LA-9086-PR
Progress Report

c. 3

Los Alamos National Laboratory is operated by the University of California for the United States Department of Energy under contract W-7405-ENG-36.

Inertial Fusion Program

January—December 1980

Los Alamos
Los Alamos National Laboratory
Los Alamos, New Mexico 87545

The four most recent reports in this series, unclassified, are LA-7587-PR, LA-7755-PR, LA-8114-PR, and LA-8511-PR.

This work was supported by the US Department of Energy, Office of Inertial Fusion.

Compiled by Frederick Skoberne

Edited by Helen M. Sinoradzki and Jody Heiken
Photocomposition by the Group IS-6 Composing Section

LA-9086-PR
Progress Report

UC-21
Issued: May 1982

Inertial Fusion Program

January—December 1980

The Inertial Fusion Program Staff

Los Alamos National Laboratory
Los Alamos, New Mexico 87545

CONTENTS

ACRONYMS

ASE	amplified spontaneous emission
BSS	Beam Simultaneity System
CCD	charge-coupled diode
CTSS	Cray Time Sharing System
CVD	chemical vapor deposition
DFP	drill, fill, and plug
DFWM	degenerate four-wave mixing
DPH	diamond pyramid hardness
EGTF	Electron-Gun Test Facility
EMI	electromagnetic interference
FCT	flux-corrected transport
FFT	fast Fourier transform
FIF	fast isothermal freezing
FOM	figure of merit
GMB	glass microballoon
g_0L	gain-length product
GWTF	Gigawatt Test Facility
HCC	Harshaw Chemical Co.
HEGLF	High Energy Gas Laser Facility
HIF	heavy-ion fusion
ICCG	Incomplete Cholesky Conjugate Gradient
ICF	Inertial Confinement Fusion
LLNL	Lawrence Livermore National Laboratory
LOM	lowest order mode
LPP	low-pressure plasma
LTSG	laser-triggered spark gap
MCNP	Monte Carlo code for neutron and photon transport
MCP	microchannel plate
MHD	magnetohydrodynamic
MI	machine interface
NBS	National Bureau of Standards
NRC	National Research Council
OAS	Optical Assembly Shop
OEL	Optical Evaluation Laboratory
OTB	optical test bed
PAM	power amplifier module
PDM	Pittsburgh-Des Moines Steel Co.
PIC	particle-in-cell
PVD	physical vapor deposition

RFQ	radio-frequency quadrupole
RIO	reinjection oscillator
SCC	subsystem-control computers
S/D	sorption/diffusion
SEM	scanning electron micrograph
SNL	Sandia National Laboratories
SPDT	single-point diamond-turning (ed)
TDR	time-domain reflectometry
TEA	transversely excited atmospheric pressure
TPA	triple-pass amplifier
TVS	target vacuum system
VPP	vapor phase pyrolysis
XRD	x-ray diode
YIG	yttrium-ion-garnet

INERTIAL FUSION PROGRAM
January—December 1980

by

The Inertial Fusion Program Staff

ABSTRACT

Our progress in developing high-energy short-pulse carbon-dioxide laser systems for fusion research is described. Because of increased efficiency and reliability, Helios, our eight-beam system, was fired 986 times, achieving on-target energies exceeding 9 kJ and pulse lengths as short as 600 ps. The Laboratory's two-beam Gemini system was fired 511 times; 479 of these shots produced the desired energy on target without measurable prepulse or prelaser energy. The Antares effort, which was redirected from a 100-kJ, six-beam system to a 40-kJ, two-beam design to have an experimental facility available 2 years earlier than originally planned, made significant progress.

This report summarizes our research and development effort in support of the Inertial Confinement Fusion program, including absorption measurements with an integrating sphere, generation of high CO_2-laser harmonics in the backscattered light from laser plasmas, and the effects of hydrogen target contamination on the hot-electron temperature and transport. The development of new diagnostics is outlined and measurements taken with a proximity-focused x-ray streak camera are presented. High gain in phase conjugation using germanium was demonstrated, data were obtained on retropulse isolation by plasmas generated from metal shutters, damage thresholds for copper mirrors at high fluences were characterized, and phase conjugation in the ultraviolet was demonstrated. Significant progress in the characterization of targets, new techniques in target coating, and important advances in the development of low-density, small-cell-size plastic foams that permit highly accurate machining to any desired shape are presented. The results of various fusion reactor system studies are summarized.

SUMMARY

(Inertial Fusion Staff)

INTRODUCTION

The goal of the Inertial Fusion Program at the Los Alamos National Laboratory is to determine the requirements for scientific breakeven in targets driven by laser fusion. Achieving this goal will allow us to appraise the feasibility of this technique for commercial power generation. This challenging scientific goal requires a broadly based program that includes the development of high-power lasers, the design and analysis of suitable targets, experiments to provide input for theoretical modeling, the development of appropriate diagnostics, and conceptual studies for the eventual commercial use of inertial fusion.

During this reporting period, the main-sequence experiments were carried out by two high-energy short-pulse CO_2 lasers, Helios and Gemini. Antares, which will come on-line in FY 1983, will provide higher energies.

OPERATING CO_2 LASER SYSTEMS

Helios

Helios, our eight-beam CO_2 laser, was operated with ever-increasing efficiency and reliability in support of our Inertial Confinement Fusion (ICF) Program. The system was fired 986 times: 468 times in support of target experiments and 518 times for system development. We achieved on-target energies greater than 9 kJ with pulse lengths as short as 600 ps. Other accomplishments include

- completion of a power amplifier modification that increased energy output, offered greater protection from retropulse damage, decreased pulse width, simplified maintenance, and improved beam quality;
- redesign of the forward beam-diagnostics area;
- design and implementation of a system to provide multiple 4-GHz data-channel recording and reduction capability;
- installation and use of the movable Hartmann target-alignment sphere;
- successful demonstration of 4-GHz data-channel recording in the control-room area; and
- continued development of a distributed computer-based control and data-processing system.

Gemini

Gemini was used mainly in support of target experiments. These experiments required 511 shots, 479 of which produced the desired energy on target without measurable prepulse or prelase energy. Noteworthy accomplishments include

- completion of 13 different target experiments.
- assembly of the new front-end screen room.
- assembly of a single-target insertion mechanism and verification of its target-alignment capability.
- testing of a triple-switchout system for the new front end. (The system produces 500 J per beam with a pulse width of 800 ps.)
- continued upgrading of the control system.
- initiation of machine modification to increase energy on target.
- installation of more reliable gridded polyimide windows on the electron gun.
- completion of new pulse-cutting front end.

ANTARES—HIGH ENERGY GAS LASER FACILITY

Redirection of Program and General Progress

The Antares program was redirected in 1979 from building a 100-kJ, six-beam machine to building a 40-kJ, two-beam machine. All design changes resulting from this redirection have been implemented. The major changes were in the target vacuum system (TVS), space frame, and beam-tube configuration.

Construction of the facility was completed, and the front end and power amplifiers were moved in and assembled. Investigations of electron-gun breakdown are continuing. The gas and electron-beam pulsers for beamline 2 have been tested and accepted.

Integrated Optics

We selected the see-through beam-alignment system, instead of the costlier flip-in detector system. The evaluation and characterization of the see-through system continued successfully. We have developed a calorimeter calibration facility for the beam-diagnostics effort that is under computer control and has standards that are referenced to the standards of the National Bureau of Standards (NBS) in Boulder, Colorado. All automatic alignment concepts, except target alignment, have been verified successfully on a mock-up beamline, and one sector in power amplifier 5 has been manually aligned. Also, lithium fluoride, which absorbs stray radiation, has been applied to critical surfaces inside the power amplifier to suppress parasitic oscillation.

Large Optical Components

The large copper mirrors and salt windows are being fabricated; the windows are 60% complete. They can now be antireflection-coated by a second source, Design Optics. Prototype mirror mounts for the large focusing mirrors have been designed and production will begin soon.

Front-End System

The Antares front end has been moved to its permanent position in the basement of the new Antares building. All the pre-amplifier stages are operational. The remaining work, which consists of setting up the beamline and hooking up the computer controls, is well under way. The Antares oscillator has reached a point in construction where it can be evaluated; first results are presented in this report.

Two experiments were performed before the move. The first measured the gain recovery of a CO_2-laser medium after saturated-energy extraction; the second determined the output of the driver amplifier during mutiplexed energy extraction. More specifically, the second experiment used two pulses separated by various times to do the extracting. The main conclusion of these two experiments is that significant gain recovery is observed within a nanosecond after extraction; therefore, the time between pulses for a multiplexed system may need to be only a few nanoseconds.

Energy Storage System

Both the gas pulsers and the electron gun Marx for beamline 2 have passed their acceptance tests. In addition, both have been operated under full computer control. However, checkout of the electron gun has been delayed because of arcing late in the discharge pulse. Overvoltage gaps for the power amplifier, which are fault-protection devices, have been assembled and installed.

Target System

Construction and testing of the TVS have been completed successfully. Work on the interior structures is proceeding well: the target-insertion cart has been equipped with an improved drive system that has been tested successfully. Also, most mirror support structures have been designed and the drawings let out for bid. A detailed study of prompt and delayed effects from target fusion neutrons was carried out with the Monte Carlo code for neutron and photon transport (MCNP).

ADVANCED LASER TECHNOLOGY

Research and development in support of the ICF program at Los Alamos included the following:

- upgrading of ICF laser systems;
- pulse propagation and gain-loss mechanisms in nonlinear media used in CO_2 laser systems;
- advanced technology for CO_2 laser systems;
- advanced concepts for other ICF systems, including short-wavelength lasers; and
- optical diagnostics for short-pulse CO_2 lasers and for laser-plasma interaction studies.

Experimental work in these areas is performed primarily on Helios and on smaller lasers in the Gigawatt Test Facility (GWTF) and the Optical Evaluation Laboratory (OEL).

The following developments are especially noteworthy:

- increased maximum energy routinely available for target experiments from 5 to over 9 kJ and improved temporal characteristics of the laser pulse through a series of experiments and design changes on Helios.

- successful modeling and experimental control of gain uniformity in the 40-cm-diam Helios power amplifiers.
- discovery and characterization of significant spatial pulse shaping for nanosecond CO_2 laser pulses through SF_6 (the essential ingredient in the gaseous saturable absorbers widely used in CO_2 laser systems).
- demonstration of high gains in phase-conjugation experiments using germanium.
- completion of the first systematic investigation of retropulse isolation by plasmas generated from metal shutters in gas and vacuum.
- characterization of single-shot and multishot damage thresholds for copper-mirror surfaces at high fluences of short-pulse 10-μm radiation.
- application of the JASON code to the Antares power amplifier configuration to calculate gain uniformity with and without dielectric shields.
- measurements of gain recovery following energy extraction by a saturating pulse in an electron-beam-controlled amplifier.
- demonstration of phase conjugation in the ultraviolet by using degenerate four-wave mixing (DFWM).
- measurement of the frequency spectrum of backscattered light from laser-driven targets at Helios.

TARGET EXPERIMENTS

Absorption measurements with an integrating sphere on microballoon targets indicate an absorption of 25% for irradiances of 0.6 to 3.5×10^{15} W/cm^2. The measured absorption was the same for polyethylene, glass, and gold microballoons. Both time-resolved and integrated data indicate that the integrating sphere is behaving as designed and that it is scalable to higher laser energies. The experimental results agree with measurements made with an ellipsoidal reflector at lower irradiance.

We measured the emission of high CO_2 laser harmonics backscattered from laser plasmas. The harmonic spectrum is constant up to a cutoff frequency that depends on laser irradiance. Theoretical analysis suggests that this spectrum provides information on the plasma's density profile near the critical surface.

We studied lateral transport by comparing the ion emission from cold and incandescent targets. From these studies we inferred a velocity of transport, 2×10^8 cm/s, and a gradient of hot-electron temperature along the target surface. Differences in ion emission demonstrate that surface contamination of targets influences the plasma expansion.

We continued investigating the plasma effects of hydrogen contamination by comparing the spectra of ion emission for carbon and CH_2 targets. The presence of hydrogen reduces the hot-electron temperature and the energy of emitted carbon ions. Theoretical modeling relates these spectra to transport and absorption processes.

DIAGNOSTICS DEVELOPMENT

We developed an integrating sphere to measure the total reflected 10.6-μm light at a high intensity (10^{15} W/cm^2). We used the sphere successfully to measure the total diffuse reflection from a variety of targets.

Two different broadband x-ray spectrometers, the APACHE and the MULTIFLEX, were installed on Helios. The APACHE system, installed to measure high-energy x rays, has 10 channels, each with a collimator, K-edge filter, and CsF scintillator optically coupled to an ITT-4014 photodiode. The scintillator-photodiode assemblies were calibrated for photon energies between 10 and 240 keV. This system was used to measure the hard-radiation environment in the chamber from both the e-beam discharge and the laser-target interaction.

The seven-channel MULTIFLEX system is designed to give both time-resolved and quick time-integrated low-energy x-ray spectra. The diodes are run at a potential of 2 to 3 keV and give a time response of <100 ps.

We are developing an electron monochrometer with a thin magnetic lens. A code written to determine trajectories of meridional electrons through the system indicates that the resolution will be good enough to image the targets with the hot electrons that are emitted during the irradiation.

Using the proximity-focused x-ray streak camera, we tried to obtain an absolute spectral calibration. We used both a 300-ps pulsed laser-plasma source calibrated with standard x-ray diodes (XRDs) and a variety of continuous x-ray sources, because some components of the system are sensitive to rate of flux as well as to total dose. The sensitivity measured with the continuous sources was 6.5 times lower than that measured with a pulsed source. The streak-tube output was very nonlinear between 2×10^8 and 1×10^{10} photons/cm^2·s.

We developed several new methods for analyzing data, including an iterative integral code for reconstructing spherically symmetric source shapes from slit x-ray photographic data, a new refraction code that numerically integrates analytical functions for unfolding the angle of emerging rays, and a least squares fitting routine to fit analytic routines to spatial-profile x-ray data.

Provisions are being made to incorporate the following six target diagnostics into the Antares TVS so that they will be ready for the first target shots: neutron counting and spectroscopy, visible and x-ray spectroscopy and photography, radiochemistry, inteferometry, charged-particle measurements, and laser energy absorption.

LASER FUSION THEORY AND TARGET DESIGN

An understanding of basic plasma physics and hydrodynamics is crucial to the extension of target concepts from experiments at Helios (8 kJ), to Antares (40 kJ), to scientific breakeven (near 1 MJ), and finally to high-gain systems (several MJ). In 1980 our emphasis has been on understanding current experiments and improving our calculational techniques.

Our modeling of current experiments includes both the design of integrated experiments and the interpretation of new diagnostics. We completed the design of a double-shell target (Polaris) for Helios, which we will use in testing how efficiently an outer pusher can transfer its kinetic energy to an inner shell surrounding the DT fuel. (An efficient transfer is essential for high-gain targets.) As one step toward a better understanding of neutron yield, we developed an analytic model relating the neutron yield of an ICF capsule to the DT fuel temperature. One new laser-plasma diagnostic is the recently observed harmonic emission in the visible range of the spectrum. The short-wavelength cutoff in this emission can be used to diagnose the plasma temperature at the critical surface.

Our major accomplishment this year was the conversion of our main design code, LASNEX, for use on the CRAY computers under the Cray Time Sharing System (CTSS). LASNEX has been completely rewritten and restructured to produce a modular and extensively annotated code. By applying structured programming, we made code maintenance and improvements easier. On-line graphics have been added to aide our designers. The Incomplete Cholesky Conjugate Gradient (ICCG) algorithm, which is used in thermal electron, ion, and radiation transport calculations, was vectorized to run 15 times faster. As a result of these and other changes, one-dimensional LASNEX calculations are three times faster on the CRAY than on the CDC-7600 computer, and two-dimensional calculations are four times faster.

We are developing a hybrid hot-electron transport scheme, which allows us to calculate self-consistent electric fields over many plasma periods. This approach is several orders of magnitude faster than the traditional particle-in-cell (PIC) calculations and should allow us to calculate transport on time scales of hydrodynamic interest.

Finally, we have developed an adaptive zoning method for our computer calculations. This technique will save user time by reducing manual rezoning of two-dimensional calculations; in addition, it will allow us to calculate two-dimensional problems containing large shear stresses and complex deformations.

LASER FUSION TARGET FABRICATION

We are developing techniques for fabricating and assembling multishell targets. We have developed a confocal alignment scheme that aligns the centers of spherical surfaces to within 1.0 μm.

Target Characterization

We have developed a new technique for determining the DT content of plastic- and metal-coated glass microballoons (GMBs). This new technique is based on counting the soft x rays resulting from tritium decay.

A proof-of-principle acoustic microscope, which has been built and successfully operated, shows promise as a characterization tool for applications requiring uniformity better than ±100 Å over an area less than 100 μm.

Our radiographic and image-analysis techniques for target characterization have progressed to the point where we are able to detect defects in opaque target coatings with sensitivities of ±0.5% to nonconcentricity, of ±2.5% to nonsphericity, and of ±6% to bump and dimple defects.

Significant progress has been made in optical characterization of targets. We have almost completed an automated sphere-mapping system, capable of measuring all types of defects in transparent shells and surface defects in metal-coated shells.

Inorganic Coatings Development

We have continued the development of high-quality metal coatings on GMBs. The deposition methods being studied are electroplating, electroless plating, physical vapor deposition (PVD), and chemical vapor deposition (CVD). In addition, we have recently concentrated on forming "gold-black" at a density no greater than 1% that of bulk gold in thicknesses up to 300 µm. We have collected material with a density as low as 0.6% that of bulk gold and have fabricated targets with 150-µm-thick coatings of 1% density. A procedure to deposit thick chromium coatings on Solacels by CVD was also developed.

Organic Coatings Development

We have developed the capability of simultaneously coating hundreds of bouncing GMBs in the vapor phase pyrolysis (VPP) process to a thickness of 5 µm. Cooling the apparatus to 153 K completely prevents agglomeration of the coated GMBs.

Among several methods to coat planar and spherical substrates with various organic coatings, we have developed a low-pressure plasma (LPP) technique that allows the deposition of smooth, ~26-µm-thick hydrocarbon coatings on rough molybdenum and tungsten substrates. A sublimation process that allows GMBs to be coated with a uniformly thick coating of NH_3BH_3 was also developed.

Organometallic Coatings Development

We have shown that metal-containing plastic coatings of graded density can be produced in the LPP process. Lead is the metal used in such coatings with a content as high as 78 wt%. We have also incorporated bismuth to 16 wt% and thallium to 1 wt% in VPP-produced coatings, and we expect to be able to control these coatings to produce graded densities.

We have invented a new technology for incorporating any metal into plastic films. This process, called the sorption/diffusion (S/D) process, can also be used for coatings of graded density and of graded or mixed atomic number. It also has a powerful surface-smoothing effect.

Low-Density Foam Development

We have improved our low-density, small-cell-size plastic foams. Molded foam hemishells have been produced at a density of 0.05 g/cm^3 and an average cell size of 2 µm. The process uses a polymer of high molecular weight, but low bulk density, and a solvent that is solid at room temperature. This solid solvent allows highly accurate machining to any desired shape before solvent extraction.

Cryogenic Target Development

We successfully tested our cryogenic laser-target processing shroud in the Helios target chamber, primarily to determine whether our hardware produced parasitic oscillations in Helios. There were none, but significant laser-induced damage occurred on the copper face of the shroud. We found a simple solution to this problem. We also simplified target processing significantly by replacing a cw laser with a small laser diode.

Target Production

During the last three months of 1980, all available manpower was devoted to the fabrication of targets in response to the accelerated experimental program. About two-thirds of our personnel were working on this effort. As a result, many efforts to develop advanced materials and technologies directed toward fabrication of high-performance hydrodynamic targets were either significantly reduced or postponed. These included precision assembly techniques for multishell targets, precision micromachining of hemispheres and other shapes, metal microballoon production, cryogenic fuel development, and high-quality metal pusher-shell coating development.

HEAVY-ION DRIVER DEVELOPMENT

One of the major issues in the Heavy-Ion Inertial Fusion program is the development of the high-current, high-energy accelerators needed as drivers. We designed and analyzed the radio-frequency quadrupole (RFQ) linear accelerator, which shows promise in meeting the requirements. Beam-transport mechanisms were studied to determine the acceptable parameters. We also reviewed the physics of the ion/target interaction and developed an energy deposition model. Based upon these studies, we are optimistic about the potential of heavy ions as a viable driver.

SYSTEMS AND APPLICATIONS STUDIES OF INERTIAL FUSION

We directed our efforts primarily toward the consolidation of previously obtained technical results and toward their incorporation into systems modeling and integration studies.

Specific activities and accomplishments included

- development and illustration of a simple approach to ICF systems integration in which approximate analytic expressions are used to model different subsystems. This approach, when used judiciously, provides insights into parametric interdependencies by revealing trends and may save significant amounts of time and effort for detailed studies and for optimizations with computer modelings.
- initiation of a revision of the ICF commercial applications system code TROFAN. Objectives of this revision are (1) to update and upgrade physical and cost models, (2) to provide access to recently accumulated data bases, (3) to increase the selection of options in subsystems and output, (4) to facilitate future modifications, and (5) to provide adequate documentation. Substantial progress has been made in achieving these objectives; the two most significant accomplishments are summarized below.
- development of a subroutine for the TROFAN Code that models and analyzes the tradeoff between reactor vessel size and its service life for four first-wall protection schemes: (1) liquid lithium film, (2) magnetic field, (3) sacrificial carbon liner, and (4) thin layer of metallic material composed of the deposited fuel pellet debris. The analysis includes neutron damage criteria, first-wall temperature rise, heat transfer, and material loss by evaporation and by sputtering.
- development of a capital cost model of a CO_2 laser driver to be used with the TROFAN Code, based on the results of a design study carried out by the AVCO-Everett Research Laboratory. Their results have been generalized and extended to configurations that appear to promise cost reductions for specified performance requirements.

I. OPERATING CO_2 LASER SYSTEMS

(J. P. Carpenter, J. F. Figueira)

Three high-energy, short-pulse CO_2 laser systems are operating routinely at Los Alamos in support of the target experimental program. Helios, which first demonstrated a 10-kJ, 1-ns output in June 1978, is operating at 10 TW on target in subnanosecond pulses. Gemini, a two-beam system that served as a prototype for Helios, operates at 600 J on target in a nanosecond pulse. A smaller system, the GWTF, comprising two lasers, operates at outputs on target in the 1- to 2-GW range with nanosecond pulses.

HELIOS LASER SYSTEM

Introduction (E. L. Jolly)

Helios continued to be our most important facility to assess the viability of CO_2 lasers for ICF. The installation of the movable Hartmann target alignment sphere caused higher shot rates, higher output energies, and greater reliability.

Operations (E. L. Jolly)

Helios continued to operate more efficiently in 1980. We fired a record 209 shots (a 6% increase over the last half of 1979) during the first 6 months of 1980 in support of the target experimental program despite a 1-month downtime for a major modification to the optical path of the power amplifier. We also fired 429 shots in support of system development and maintenance, mainly to test the amplifier modification. During the second half of 1980, we fired 259 shots (a 24% increase over the first half of 1980) despite a 1-month suspension of target shots for installation of the movable Hartmann target-alignment system. During the second half, we fired an additional 89 shots for system development and maintenance.

The system routinely delivers an output energy of 7 kJ in 0.75-ns pulses (FWHM) at a system shot rate of two per hour. As shown in Fig. I-1, the maximum energy on target continued to increase, reaching 9.4 kJ in December. We are now able to change beam alignment from a system in which all eight beams are aligned and focused at a single point to one in which the beams are split into two groups of four. We can change routinely from one configuration to the other during a shooting day. In general, 2 of every 5 workdays are shooting days; the other 3 days are used for installation of target diagnostics, modification of system hardware and software, and maintenance. However, during December, all workdays were scheduled for shooting because we wished to accelerate the main-sequence experiment. Target diagnostics were installed on a second shift, and only critical modifications and maintenance were performed.

Power Amplifier Modification (E. L. Jolly)

We modified the beam path of all the power amplifiers by replacing two 10-cm-diam salt windows, a pinhole, a concave copper mirror, and two Mylar pellicles located between the first and second passes of each triple-pass amplifier (TPA) with a single convex copper mirror. This modification produced several benefits, including increased output energy, protection from retropulse damage, decreased output pulse width, simplified alignment and maintenance, and improved beam quality. Output

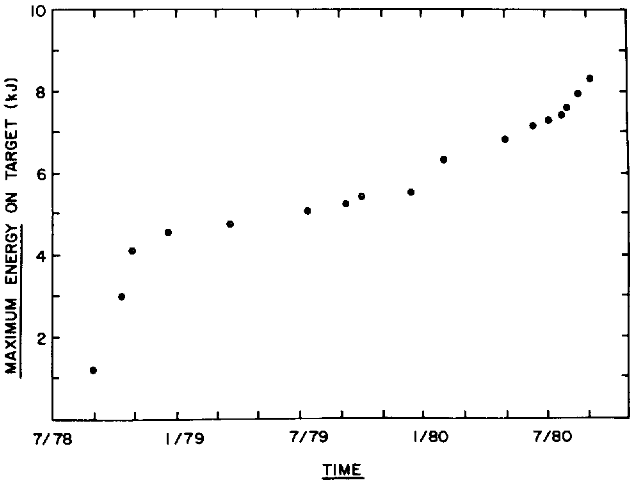

Fig. I-1. Historical record of Helios improvement.

energy was increased and pulse width decreased because the modification eliminated vignetting of the beam between the first and the second pass, thus saturating the third and final pass more completely.

Retropulse protection is now provided by gas breakdown in a beam overlap region at the convex mirror rather than by the destruction of Mylar pellicles. The modification also eliminated eight optical surfaces (4 salt, 4 Mylar).

Front End (R. Carlson, M. Weber, R. Pretzel)

Eliminating eight optical surfaces in each of the main amplifiers increased the signal-to-noise ratio of the Beam Simultaneity System (BSS) five- to tenfold. We can now easily adjust the path length of an optical beam to within 0.5 cm (15 ps) of a reference length; repeated measurements indicate that path lengths remain within 1 cm (30 ps) of the reference length over several weeks of operation. The signal-to-noise ratio will be further improved by a factor of 5 after installation of a new low-noise solid-state preamplifier. The impedance of this preamplifier matches that of the mercury-cadmium-tellurium detector at the 41.67-MHz operating frequency.

As part of the continuing effort to improve the front-end system, the following tasks were completed.

- We installed a Nova 4/S computer system to provide stand-alone capability. This system monitors the status of interlock and analog signals and provides a ready/not-ready indication to the control room computer.
- We tested a wave-guide laser for the new multiband front end for stability in power, pointing accuracy, and line selectability. We will progress more quickly on the multiband front end when the Helios building addition is completed, because it will provide space for installation of the system at Helios.
- We installed a modular triple switchout and mode-matching telescope assembly to provide improved mechanical and optical rigidity and facilitate oscillator system alignment.
- We put optical tables for the multiband front end in a room adjoining the front-end room. The preamplifiers, wave-guide oscillator, switchout, and transport optics to assemble a one-line system are available.

Beam Diagnostics (R. Carlson, J. Reay)

After reviewing the mechanical and optical integrity of the forward beam-diagnostics area, we decided to eliminate three mirrors in each diagnostic beam path; provide for simultaneous alignment of the diagnostic and amplifier beam paths; improve the mechanical stability of the system by eliminating off-axis and cantilevered optical supports; incorporate four modular prealigned and calibrated diagnostic systems, each capable of detecting postpulses and of recording the shape of the main pulse; use 5- by 5-cm Gen-Tec, Inc. detectors to measure energy content of the main pulse; provide eight 4-GHz data-recording channels to record eight pulse widths simultaneously; and incorporate a dry-run system to ensure repeatable and reliable data.

We have already installed two of the eight 4-GHz data-recording channels as a demonstration project. This system, located in an area adjacent to the Helios control room, will gather all relevant forward-beam-diagnostic, retropulse-diagnostic, and target data effectively and efficiently. The system will demonstrate that a 4-GHz bandwidth can be maintained over 38 m of equalized Heliax cable with an amplifier and displayed on a Model 1776 oscilloscope. The two channels will be fed by a fast pyroelectric detector (beam pulse-shape data) and by an XRD detector. If we are successful, we will build a system capable of recording eight pulse shapes and two retropulse shapes.

We modified two Model 1776 oscilloscopes, designed equalizers, and tested a 20-dB-gain B&H 5-GHz amplifier. The dry-run system that displays a base line, a sine wave, and a synthesized pulse on the oscilloscopes is 90% complete. When the system is complete, oscilloscope trace data will be digitized and sent to the Data General 230 central computer system for final processing and display. A laboratory prototype of the digitizing camera and software has been tested successfully.

The following tasks have been performed to improve the efficiency and reliability of the Helios beam-diagnostic system.

- We have almost completed a beam-diagnostic calibration system capable of delivering 1 J in a 1- or 100-ns pulse at 10.6 μm. We will use this system to evaluate and calibrate detectors for the beam-diagnostic system.

- We have designed and tested an amplifier/line-driver circuit for use with the Gen-Tec, Inc. ED-500 (5- by 5-cm) pyroelectric joulemeter. A joulemeter can now be calibrated to 15 V/J ±5% against a tertiary standard traceable to NBS. All beam-diagnostic energy monitors can be made directly interchangeable.
- We have built a two-segment pyroelectric detector (3 by 3 mm), which provides a linear pulse output of 6 V into 50 Ω, a sensitivity of 4 V/MW, and a time-domain reflectometry (TDR) falltime of <80 ps. We will install this detector in the beam-diagnostic system to provide pulse-shape data and to eliminate alignment problems associated with the 1- by 1-mm detector. Its higher output will also improve the signal-to-noise ratio of the recording system.

Optical Alignment (E. Jolly, R. Carlson, D. Stahl, S. Harper)

The following tasks have been performed to improve the efficiency, reliability, and versatility of the Helios beam-alignment system.

- We began construction of an electromechanical system that will allow us to position a Hartmann alignment sphere accurately within a 0.6-cm cube of space at the center of the target chamber. Because our alignment technique results in a beam being pointed and focused at the center of a Hartmann sphere, the capability to move and accurately position a sphere gives us the capability to align and focus the eight beams independently. Figure I-2 shows the movable Hartmann sphere, its translation stages, and stepping motors. The same mechanism that transports and positions the target also transports and kinematically positions the movable Hartmann target-alignment system in the target chamber.

  The microprocessor-based control system accepts and stores position coordinates from a user's terminal. These positions can be recalled and the sphere transported to the desired position by simple commands from the user. We used this new system extensively for the Chamisa target experiments in December. The system was installed at Helios near the end of 1980.
- We also constructed a Hartmann sphere mechanism. This device will be attached to the target-insertion mechanism near the center of the target chamber. The sphere can either be lowered into position at the center of the chamber or retracted upwards so that the cart carrying a target can be used. This device will decrease alignment time because we will no longer have to insert the Hartmann sphere into the target chamber through the airlock on a target cart. This system was also installed near the end of 1980.
- We have designed a new pinhole and alignment detector for the spatial filter located before the input to each power amplifier. The old detector sometimes gave ambiguous alignment signals, and the pinhole was a source of parasitics for the main amplifier. A new pinhole structure was flame sprayed with lithium fluoride to suppress reflections. We are designing a thermal quadrant detector similar to that used in the front end to swing in and out of the beam-sensing area.
- We installed silver-coated ceramic mirrors in place of solid copper mirrors in all beamlines up to the input to the main amplifiers. The increased reflectivity at visible wavelengths made it easier to align

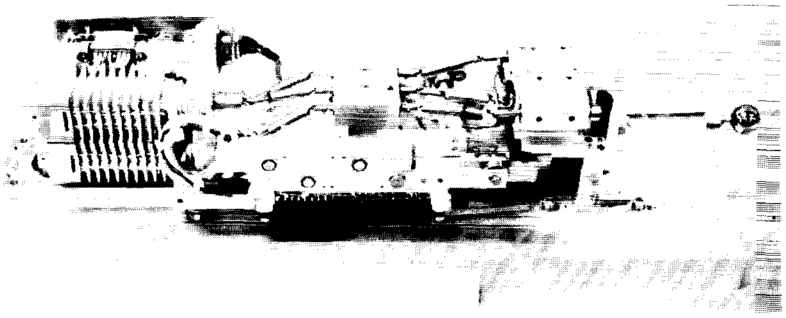

Fig. I-2. Movable Hartmann sphere.

the beam-diagnostic paths. These mirrors do not degrade the 10.6-μm beam.

Controls (E. Jolly, R. Johnson, G. Karpen, S. Garcia)

We developed a basic operating system to provide communication between the main computer (Data General Eclipse S200) and the microcomputers (Data General Micronova) located in both the beam-diagnostic and return-channel data areas. We also developed an operating system for the front-end computer (Data General Nova-4S), which allows five-level multitasking.

Programming. We wrote and debugged a program for a downline loader for our new Nova. This effort allows programs to be written and debugged with Eclipse systems, stored on disks, and later loaded onto the remotely located Nova to monitor the front-end system.

Control Hardware.

- We modified the saturable-absorber controls to permit continuous monitoring of saturable-absorber gas pressures.
- We installed a closed-circuit television system that allows us to make video recordings at shot time with either a disk or a tape recorder. It also permits disk-to-tape and tape-to-disk transfers.
- We fabricated the control chassis for the cryogenic target system, based on the Motorola MC14500B industrial control unit. The chassis is in the check-out stage.
- We installed a shutter control system to open all camera shutters in both the target and beam-diagnostics areas.
- We designed and fabricated a tester to troubleshoot the electron-beam, high-voltage trigger generators.
- We modified a CO_2 probe-laser control system by incorporating a spectrometer that provides feedback control to measure the peak of the laser output automatically.
- We installed an over-temperature alarm and automatic power shutoff in the computer room.
- We installed a movable Hartmann control system.
- We designed, fabricated, and installed controls for the Hartmann system.
- We designed and tested a new input trigger board for electron-beam trigger generators.
- We installed new cable trays and control wiring on power amplifier modules (PAMs) 2 and 4.
- We designed a system to monitor oil-tank temperatures and oil levels for the pulse-forming network remotely.

Mechanical (E. Jolly, D. Martinez)

Major mechanical accomplishments are summarized below.

- We designed and began building a new power amplifier anode. The natural vibrational frequencies of this anode will avoid those of the pumping chamber; therefore, we will prevent the failures we now have.
- We designed an improved fiber glass pumping chamber for the power amplifiers. The material and manufacturing techniques should provide a void-free structure and eliminate some problems we have encountered.
- We fabricated and began installation of a working platform on top of the target chamber.

GEMINI LASER SYSTEM

Introduction (J. Hayden)

The following experiments were performed on Gemini:

- integrating-sphere base-line tests,
- free-surface velocity measurements from laser-produced shocks,
- hot-electron measurements in laser-produced plasmas,
- microchannel-plate (MCP) intensifier evaluations,
- fiber-optic diagnostics development tests for hot-electron measurements,
- alignment stability tests on the energy absorption apparatus,
- target energy absorption measurements with the egg-shaped calorimeter,
- verification of calorimeter precision by using the digital pen recorder,
- analysis of postpulse energy generated by target-plasma reflections,
- hot-electron measurements using a fiber-optic-coupled spectrograph,
- target absorption measurements using a sphere absorption measurement technique,

- target dynamics experiments using a fast streak-camera shadowgraph technique, and
- measurements of time-resolved x-ray production.

Of the 840 shots fired in support of these experiments, 92% produced the desired energy without measurable prepulse energy.

Laser Performance and Diagnostics (S. Hackenberry, J. McLeod)

The Gemini laser was fired at energies ranging from 3.5 to 393 J per beam. Nearly one-third of the shots were low-energy shots (between 3 and 100 J) to avoid damage to the absorption-measuring apparatus.

The optical system for aligning single targets in the single-target insertion mechanism was installed in the optical diagnostics area. Misalignment caused during transport of targets aligned in the target fabrication facility is thus avoided.

A new tube with a larger bore was installed on the cw laser that powers the gain probe channel. The cavity is now more stable and produces only the line desired for probe measurements.

Delivery of the deformable recollimating mirror was delayed until October 1980 because of manufacturing difficulties encountered by the vendor.

We started upgrading the laser system by modifying the south beam to install a new saturable-absorber gas cell between passes 2 and 3 inside the dual-beam module. This change required a totally new optical design at the input to the machine. This design will properly inject the several required laser beams through the machine. When this modification is completed, the energy on target will be increased more than twice. Also, this improvement will allow the use of either the old mode-locked front end or the new pulse-cutting front end as a driver for the dual-beam module.

The poor quality of the diagnostic beam used to determine pulse shape and risetime has caused damage to optical components. The diagnostic beam pickoff device is a large 40-cm (16-in.) -diam salt window on the target chamber. By experiment, we determined that the problem was caused by an 80-μm surface distortion of the salt window.

We also improved the electron-gun portion of the machine by installing a newly designed window that incorporates a tough polyimide-aluminum sandwich material glued to a support grid. Should an arc occur and rupture the window, this grid acts as a rip stop to prevent further propagation of the rupture. The polyimide material is tougher and less brittle than the previously used titanium, and it retains the same strength.

Oscillator-Preamplifier System (V. Romero, E. Coffelt)

We are ready to install the new front end. Utility lines for the new screen room have been routed as needed. The triple Pockels cell has been assembled and tested. The oscillator produces 500 mJ with a pulse width of 800 ps (FWHM).

The old front end was fired 8951 times during the last 6 months for setup of instrumentation in the target chamber, for beam alignment, and for actual target experiments. We devised a low-jitter (<1 ns) high-voltage pulse-generation technique to obtain an early trigger for a high-speed visible-light streak camera. This technique uses a detector developed specifically for this purpose.

The new pulse-cutting front end was essentially completed. It has been operated in conjunction with the entire system and has exhibited no jitter or pretriggering problems.

Computer and Control Systems (S. Hackenberry, P. Castine, V. Romero, J. Taylor)

Work is progressing on the control system upgrade to monitor the relative timing of all triggers in the Gemini firing sequence. We have decided to use fast fiber-optic links instead of hard wires.

The data-acquisition channels were added to the computer data-monitoring system, which will be used to detect early and late arcing in the electron-beam gun.

A Nova-IV computer was ordered for the data-monitoring system because replacing parts and maintaining the old computer had become too difficult.

A major improvement was made to the control system of Gemini. A sophisticated, fail-safe interlock was designed and installed to preclude a catastrophic failure of electron-gun windows if pumping voltage were applied to the machine without proper electron-gun performance.

The data-logging software program has been improved to notify the operator if certain diagnostic power supplies are not turned on.

II. ANTARES—HIGH ENERGY GAS LASER FACILITY

(H. Jansen)

The High Energy Gas Laser Facility (HEGLF) was built to house a high-power (100- to 200-TW), six-beam, short-pulse, CO_2 laser, Antares, which will be used to investigate laser fusion phenomena. The effort, as originally conceived, has been redirected to provide two beams with 20 kJ each in 1983.

INTRODUCTION

In January 1980, the scope, schedule, and cost of the Antares project were redefined. To achieve significant results from the target experimental program at the earliest possible date, we decided to reduce the scope of the Antares program and to build the first two Antares modules with an energy of 35-40 kJ on target. Based on the presently projected funding schedule, this goal can be completed at the end of FY 1983. However, if funding could be accelerated, the completion date could be advanced accordingly.

All design changes and procurements resulting from the redirection have been implemented. The major changes made were in the TVS and space-frame configuration and beam-tube configuration. We have maintained 6-sided symmetrical target illumination for the 2-power amplifier, 24-beam system. Through a joint-occupancy arrangment with the building contractor, we have begun system installation. Thus, slippage in the building schedule has had only a limited impact on the overall Antares schedule.

A study was initiated to determine the amount of energy that an upgraded Antares could focus onto a target following a successful program at 40 kJ. The major constraint for the study was the stipulation that the upgraded Antares machine fit the facilities. A design was developed that would provide on-target energies of 300-400 kJ with acceptable costs.

OPTICAL SYSTEM (A. Saxman, W. Reichelt, Q. Appert, W. Bauke, S. Bender, C. Bjork, R. Day, J. Munroe, E. Sklar, T. Sheheen, C. Silvernail, J. Sollid, T. Swann, W. Sweatt, P. Wolfe)

Highlights

Our main tasks in the development and fabrication of the integrated optical system focus on

- evaluation of the see-through beam-alignment television-tracker system and its integration with the computer control system,
- fabrication and testing of the Antares prototype calorimeters and their data-reduction software,
- initial positioning of the power amplifier shells and final placement of the target chamber and turning chambers, and
- completion of the power amplifier assembly tolerance analysis and its antiparasitic baffle design.

These major efforts are being successfully completed on schedule.

- The Los Alamos calorimeter calibration facility is being automated and has standards that are referenced to NBS, Laser Measurements, in Boulder, Colorado.
- Large calorimeters based on the Antares design were tested successfully at Helios.
- Verification tests of all automatic alignment concepts, except target alignment, were completed successfully on a mockup beamline.
- One sector of optics and automatic alignment hardware has been installed and manually aligned for the optical test bed (OTB) in power amplifier 5.
- Lithium fluoride (LiF) low-reflectance coatings have been applied to critical elements throughout power amplifier 2, making use of both the flame-sprayed LiF and a newly developed LiF-loaded paint.

Optical System Analysis

Optical Tolerance Analysis. We completed two tolerance analyses of the Antares optical network and concluded that

- the total optical network is insensitive to both axial and radial component-centering errors (±0.050-in. errors generate less than $\lambda/100$ rms wave front error). It is also insensitive to component tilt errors (±2 mrad tilt errors generate less than $\lambda/50$ rms wave front errors).

- the radius of curvature of the powered mirrors must be held to within ±0.5% (easily achieved with the use of test plates).
- the main requirement for controlling centering and tilt errors is to avoid vignetting.

The final specifications for optical component placement have been relaxed in many areas as a result of this analysis and because the mechanical specifications are being met by the hardware vendors.

Beam-Alignment Sensitivity. The optical ray trace program developed by Optical Research Associates* is being modified for beam-alignment sensitivity calculations. The present program can only handle 150 surfaces in an analysis but will be extended to 250 surfaces so that the entire Antares beamline can be modeled from the front-end system to the target.

Beam Diagnostics

Calibration Facility. A facility to test and calibrate all the calorimeters for use in Antares is operating. The measurements are referenced to the laser measurements standards at NBS. The facility is based on a specially modified Lumonics-103, transversely excited atmospheric (TEA) oscillator fitted with a smoothing tube of Los Alamos design. The design included a gain-switched 2.0-J, 100-ns pulse, on the 10.6-µm band [P(20) line]. The calibrating pulse is monitored in a beam-splitter arrangement, whereas the calorimeter response is monitored with CAMAC analog-to-digital equipment. The entire data-acquisition and reduction process is under computer control. The control and acquisition system is identical to the one that will be used during Antares operation. Provision is made for both electrical and laser calibration. The standards that we maintain are of Los Alamos design. The total error for Antares calorimetry should be ±5%.

High-Energy Calorimeters. Several square calorimeters, 55 cm on a side, were fabricated and tested on Helios. They are based on volume absorption in type-V Kapton, a polyimide film with near-optimal absorption, damage, thermal, and electrical characteristics. Kapton-copper laminated sheet is readily available commercially. The dielectric strength is excellent and the material will not melt. Consequently, it has a very high damage threshold, ~2.8 J/cm^2 in a 10.6-µm, 1-ns pulse. The design goal was 2.0 J/cm^2. The absorption length is 330 cm^{-1} and the index of refraction is 1.33.

We demonstrated that the material (1) could stand the flux, (2) did not damage or flash, (3) did not cause parasitic oscillations in the system, and (4) had a sensitivity about as high as expected from the sum of the heat capacities. Therefore, the prototypes performed nearly as ideal isoperibol calorimeters. The prototypes did cause some air breakdown sparks from the ~2% Fresnel reflection from the front surface of the Kapton. Breakdown occurred because the separate elements in the 9 by 9 array were slightly concave, forming small mirrors that focused the 2% reflected light sufficiently well to produce air breakdown. This phenomenon is not a problem in Antares because most of the calorimeters are operated in vacuum. In future calorimeters this problem can be prevented by burnishing each element into a slightly convex shape.

Diagnostic Techniques. We have designed a wide-bandwidth measurement system for the temporal energy-distribution measurements of the Antares full power beams. The system incorporates the wide-bandwidth, 4-GHz Model 1776 MCP oscilloscopes and video digitizing scope cameras for the temporal profile of the main pulse; it also uses smaller bandwidth scopes for the postlase temporal distribution measurements. This system will soon be tested on a single beamline in Helios.

Using a perforated plate attenuator (holey plate) and a two-dimensional pyroelectric charge-coupled diode (CCD) array is being considered for the point-spread-function beam-quality measurements. Pyroelectric array detectors have been successfully tested recently. The elements in the 32- and 128-element linear arrays are separated by 0.1 mm; attempts are being made to reduce this spacing and to produce two-dimensional arrays. We will continue our search for promising arrays for beam-quality measurements at the target focal plane.

Optical Systems Engineering

Power Amplifier. The specifications for the optical design of the power amplifier have been evaluated and approved. We have successfully traced the Antares

---

*Pasadena, CA 91107.

optical system in a computer simulation from the front end to the target. Statistical information can be extracted showing the condition of the beam at selected stations. These data are useful for sensitivity studies, alignment studies, analyses of aberrations, and for determination of real or virtual image positions. Several such studies have been performed and produced useful beam-profile information. Analyses have shown that the allowed tolerances for mechanical fabrication of the large pressure- and vacuum-shell optical support structures could be doubled in some areas of the power amplifier such as the relay-optics section. This relaxation is possible because the large shells are delivered well within their specified tolerances. Also, the shells can be aligned on the stands about three times more accurately than we first estimated.

Target System. System sensitivity analyses have shown that the mechanical constraints on optical component placement can be eased. Mirror positioners can now be placed to within ±1 mm of true position. The tolerances are reduced because of the technique of nulling out alignment-induced aberrations in the target-system beamlines with the new Smartt interferometer system.

Parasitics and Retropulse Protection. Work continued on parasitics control for Antares, mainly in baffle, diaphragm, and aperture stop design, including specifications for LiF and Fe_3O_4 coatings. Specifications for the absorber and output salt windows and their mounts are being prepared.

We completed secondary-retropulse calculations and analyzed the results. Briefly, the secondary retropulse is the part of the main beam that is deflected by the last relay mirror and returned to the vicinity of the spatial filter. This returning radiation will be used to create a plasma isolation shutter in the spatial filter plane. This technique will be further refined in the GWTF.

Contamination control, especially in the Optical Assembly Shop (OAS), was a topic of considerable concern. We prepared a Contamination Control Handbook and will distribute it to installation personnel. Particular attention is given to maintaining a clean environment around the large salt windows and mirrors in the beam-overlap retropulse-protection area at the last relay mirror.

LiF-loaded paints have been developed and tested for use in Antares. These low-reflectivity (at 10.6 µm) paints will be used in place of the LiF flame- and plasma-sprayed materials for many components. The paint samples have been tested for cleanability, reflectivity at 10.6 µm, uv damage susceptibility, 10.6-µm damage thresholds, and outgassing rates. Typical specular reflectivities at 10 µm are $<2.0\%/\mathrm{sr}$ and the diffuse scatter is $<0.1\%/\mathrm{sr}$. The use of paints is very cost effective and flexible in application. These paints constitute a breakthrough in controlling parasitic oscillations. The medium is easy to apply on varied geometrical shapes compatible with high-vacuum environments and highly durable in the laser beam and uv environments of laser cavities. The LiF flame-sprayed materials will only be used where the intense primary 10.6-µm beam may exceed 2.0 J/cm^2, as is possible on the salt window apertures of the output beam train.

Beam Alignment

Automatic Alignment System. Tests of the automatic alignment system on a mockup beamline have been completed successfully with an LSI-11 microprocessor. These tests verified all alignment concepts except final target alignment, which will be addressed in the second half of 1981.

One sector of optics and alignment hardware has been installed in power amplifier 5 for the OTB. The alignment station for this beamline was nearing completion; testing is scheduled to begin in January 1981.

We have completed detailed calibration and automatic alignment procedures and are using them to generate software for the Antares control system. We will check out the software as part of the OTB tests.

In support of the OTB tests, all optical parameters from the front end through to the target were set up on the optical design program, Code V. These data will also be useful for optical adjustments during Antares installation and operation.

Design of an alignment gimbal positioner for the target chamber was essentially completed. This device is used for initial optical alignment in the target chamber and will also be an integral part of the automatic alignment system for final alignment of the beams to the target position.

The automatic alignment telescope will be delivered in August 1981. We designed a telescope, now in operation but lacking some required capabilities, to be used in the interim.

Hardware development efforts centered around the installation of optical components for the OTB. Alignment hardware installations continued in the front-end room and were completed for the input/output optics structure in the OAS. Installation of the polyhedron alignment device, the fiber optics and their light-source boxes, and the rotary wedge alignment device has been completed in the OAS. The pit mirror has been assembled and aligned to power amplifier 5. The various mirrors of the beamline 5 alignment station have been installed and are being aligned. The optical table for the beamline 2 alignment station has been moved into position in the front-end room, and equipment is being prepared for it. Other hardware for beamline 2 is partially completed. The polyhedron alignment device, the pit mirror assembly, and the periscope/carousel are all complete; the rotary wedge assembly is being built. We are making final drawing changes before buying the back-reflector flip-in light sources. Contracts for safety devices, the pit cover, and shroud design and fabrication have been awarded to EG&G, Inc., and the first units are being installed on beamline 5.

Manual Alignment. Placement measurements were made to install optical components in the OTB shells and to align the shells to beamline 5 (Figs. II-1 and II-2). Bench marks and grid references in the Laser Hall were transcribed from the floor to permanent brass markers, which are grouted into the floor and protected from abrasion and wear. The pit mirror in pit 5 has been located and installed. Permanent reference marks for beamlines 2 and 5 were extended through the pits into the front-end room, and station-line references have been determined. These references were then used to locate alignment tables in relation to beamlines.

In power amplifier 2, we determined the position of the anodes and the degree of their movement during removal of the anode bushings. The anodes remained well within tolerance. In the target chamber, we measured the final level of space-frame support and rollout surfaces.

During the power amplifier pressure tests, we measured deflection at various points outside and inside power amplifiers 2 and 5. We recorded movements that had both positive and negative hysteresis characteristics, as well as the expected deformations, which caused a slight permanent change of shape in power amplifier 2. However, all recorded movements were less than previously calculated and all resultant configurational changes were well within allowed error.

Pumping-chamber sections 1 and 2 for power amplifier 2 were lined up in the global X-, Y-, and Z-directions before they were welded, and their movement during and after welding of the base plates was measured. After initial tack-welding, the centering targets on the shells were well within the tolerance limit of 0.020 in. The shells can typically be placed back into position to within 0.030 in. This possibility was demonstrated recently on the OTB with all the optics for one sector prealigned inside the power amplifier shells. We demonstrated that the optical train was aligned sufficiently after the installation of the shells so that initial beam acquisition with the automatic alignment system would be possible.

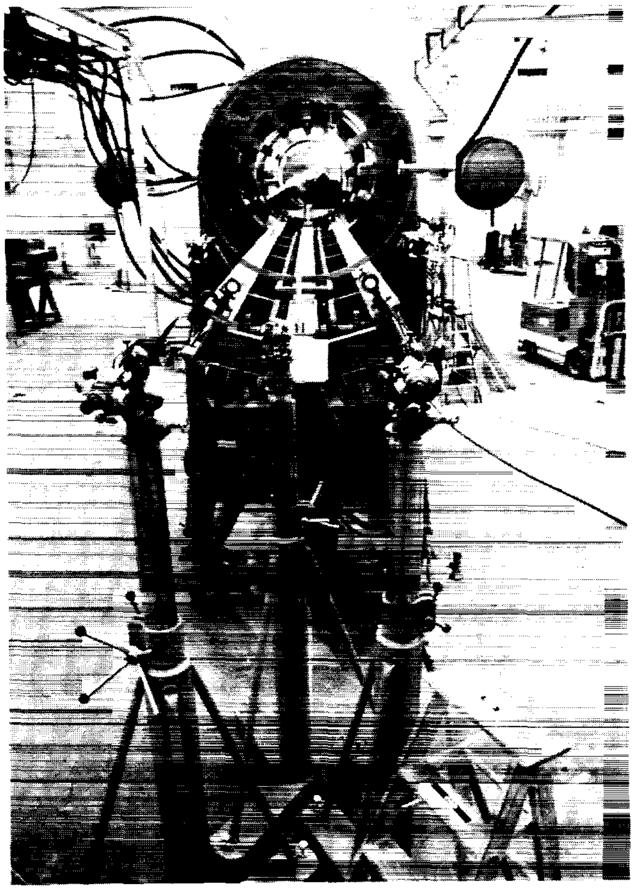

Fig. II-1. Alignment of power amplifier 5.

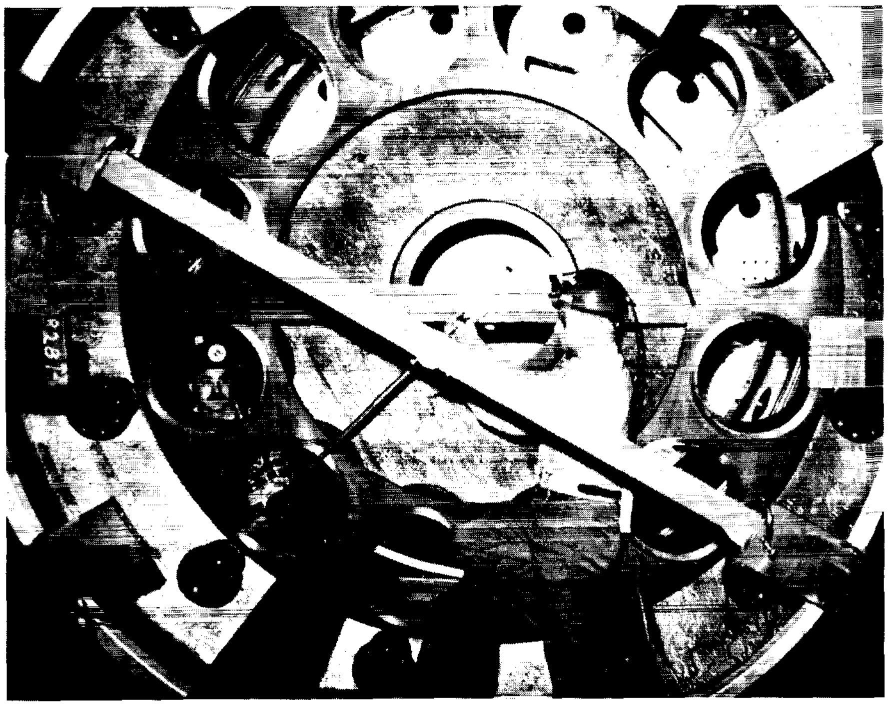

Fig. II-2. Alignment activities inside of power amplifier 5.

LARGE OPTICAL COMPONENTS (W. Reichelt, D. Blevins, R. Cutler, J. Munroe)

Highlights

The following items are particularly important.

- The 45-cm (18-in.) -diam salt windows are on schedule. Four have been delivered to Los Alamos.
- The manufacturing schedule for mirror positioners has been established.
- Incorporation of optical components into Antares is on schedule.
- An additional source for antireflection coating the salt windows has been established.
- The Z-axis drive for the target-system focusing mirrors has been prototyped and will be in production shortly.

Salt Windows

Delivery of the salt windows awaits the manufacture of frames to protect the windows during shipment. The machined forgings should be ready and the frames complete early in 1981. Partial shipments of the finished frames may somewhat expedite this schedule. Harshaw Chemical Company (HCC) is well along on their production schedule for the salt windows and can begin deliveries as soon as frames are available.

Four wedged output windows were assembled into preliminary frames by HCC and were received at Los Alamos. Two parallel saturable-absorber windows have been received from HCC and are being assembled into the two remaining preliminary frames. These shipments should keep Antares on schedule despite the delay in frame acquisition. The HCC specifications are being rewritten because the redirection of the Antares program will require fewer windows.

A second source, in addition to Optical Coatings Laboratory, Inc., has been developed for antireflection coating of the large salt windows. Recently Design Optics has also demonstrated this capability. Coatings from both sources are of equal quality and meet the damage threshold requirements.

Mirrors

All large mirrors for the power amplifier and target systems are being procured. Electroplating of copper onto the substrate has been a constant problem. Generally, the main problem has been in coating the aluminum substrate with zinc before copper plating. This problem has been resolved through proper process control. Another problem, delamination in the copper plating itself, became evident recently while we were machining the copper after plating. A thorough review indicated the high probability that insufficient process control was again the culprit. This situation too has been corrected. No effect on the overall schedule caused by these problems is expected.

Large Mirror Positioners

Seventeen production-type mirror positioners have been completely assembled and checked out. Twelve more are being assembled. No major problems were encountered. Orders for 100 more positioners have been placed and units are in fabrication.

A prototype Z-axis drive unit for the focusing parabolas has been assembled and tested. It operated satisfactorily. Components for three preproduction units have been procured. One has been assembled for more testing before we order components for production.

FRONT-END SYSTEM (G. York, D. Brown, E. Foley, R. Gibson, D. Gutscher, M. Kircher, C. Knapp, W. Leland, R. Sierra, E. Yavornik)

Highlights

The following achievements are noteworthy. We have

- completed the prototype front end.
- made a prototype for the fiber-optic controls.
- performed gain recovery experiments.
- performed multiplexing experiments on the driver.
- installed the front end in Antares.
- demonstrated multiline oscillation.
- evaluated the multiline oscillator spark gaps.

Prototype Front End

The prototype front end has been assembled completely and tested. The interim oscillator, which is similar to that in Helios, generates ~500 mJ in a 70-ns (FWHM) gain-switched pulse of variable line content. Energy, pulse width, and line content are being determined on each shot. Shot-to-shot amplitude variation is ±25%.

A 1-ns (FWHM) pulse is chopped out of the 70-ns pulse by means of a laser-triggered spark gap (LTSG) and a conventional three-stage Pockels cell arrangement. We use large germanium crystals (15 by 15 by 70 mm) to minimize beam-edge interactions and to produce a contrast ratio of $>5 \times 10^6$. The energy after switchout ranges from 0.3 to 0.5 mJ.

The short pulse is routed to the preamplifiers through a spatial filter and an alignment beam injection station. Two preamplifiers are available in the chain. The first is a Lumonics, Inc. 922 double-discharge laser in which the energy is amplified to ~25 mJ in a single-pass energy extraction. The second is a Lumonics 602 laser that has a peak gain-length product (g_0L) of ~4 and is equipped with on-axis, triple-pass Cassegrainian optics. The optical quality and configuration of the system resulted in the generation of a single undesirable parasitic pulse. We have redesigned the system to overcome this problem and have ordered new components.

To evaluate the driver optics, we removed the preamplifier Cassegrainian optics and used the preamplifier in single-pass operation to produce ~200 mJ in a 2.5-cm-diam beam. This beam was routed through another spatial filter and beam injection station to the TPA. The threshold for parasitic oscillation was determined to be at a g_0L of ~3.6, in good agreement with theoretical calculations. We were able to suppress these oscillations at the design g_0L of 7.5 by using ~150 torr•cm of saturable absorber (Mix 804 with 1.5% SF_6).

With this saturable absorber and an input of ~200 mJ, we were able to extract ~70 J in a 15-cm-o.d. by 9-cm-i.d. annular beam at a g_0L of ~3 at 1500 torr. The timing was well established and all units of the front end were triggered at the appropriate time without crosstalk. We did not observe any prelasing or retropulse damage, and a burn pattern of the output beam indicated fair to good uniformity.

Antares Front End

After the physics experiments, we disassembled the prototype front end and moved it to the basement of the Antares building. We discovered a number of problems in the building, including failures of the oil and chilled water systems; however, conditions are now satisfactory for operation. We have written a Standard Operating Procedure to permit operation of the system with a temporary safety system that has been constructed and installed. This safety system monitors door positions. To activate a Class-IIIb or Class-IV laser, the yellow warning light must be activated at the entrances to the room. If a door is opened while one of these lasers is energized, a buzzer sounds to alert the operator, who must take appropriate action. To activate the driver amplifier, the red light must be energized. If any door into the driver room is opened while the driver is charged or being charged, the safety system will dump the energy supplies to a safe state.

We have installed and checked out all preamplifiers and the driver. The beamline is being installed with the following additions. A calorimeter/beam stop at the output of the driver has been constructed. The secondary Cassegrainian mirror for the driver has been moved to a position inside the output salt window to aid in retropulse damage protection. A vacuum chamber has been built for spatial filter 3 to provide better control of the breakdown threshold.

All manual controls have been installed and can be operated through the fiber-optic interface boxes. We anticipate that the front end will be operated for some time with these controls, whereas timing and fast-pulse data-acquisition capabilities will be provided by the computer system.

A contractor is working on a second driver and delivery is expected on schedule in April 1981.

Controls

Prototype fiber-optic controls were constructed for both the Lumonics 602 preamplifier and the driver amplifier. The two controls are of slightly different design: the receivers and transmitters for the preamplifier are located at the laser, whereas, for the driver, they are located at the outside screen room wall. The latter installation obviously requires a long cable (20 m) to transmit electrical signals to the shielded box but permits short runs of fiber-optic cable. Because many signal runs in the Laser Hall are longer than the maximum permissible fiber-optic cable run (because of signal attenuation in long light pipes), we must be able to operate with long cables attached to the fiber-optic electronics. Both schemes are essentially immune to noise, and neither suffered any transmission loss in the fiber-optic circuitry, even in the most severe case of an arc in the driver amplifier discharge.

The driver amplifier is operated routinely from inside the screen room through the fiber-optics system with manual controls, whereas the preamplifier has been operated on a device-control basis by a PDP-11/03 microprocessor through a fiber-optic system.

Multiline Oscillator

The P(14), P(16), and P(18) lines have been switched, combined both temporally and spatially, and amplified through the four-pass amplifier. The typical output is ~150 μJ in a 1-ns pulse. The cw beams were not sufficiently stable, however, and we are trying to remedy this situation.

The multioutput spark gap was constructed and tested by Maxwell Laboratories, Inc. The 10-output gap produces a subnanosecond risetime pulse of ~12 kV. All gaps appear to be firing, although simultaneity has not been measured and the voltage is somewhat lower than anticipated. We have given Maxwell an additional contract to further characterize this gap.

The prototype rail gap was finished and tested. Unfortunately, it was not satisfactory so a new type of gap has been designed and is being fabricated and tested.

We have completed the controls for attenuators, wave plates, and diagnostic mirrors. Prototype temperature and pressure transducers have been assembled and tested.

POWER AMPLIFIER SYSTEM (R. Stine, G. Allen, W. Bartlett, J. Brucker, W. Gaskill, R. Kennedy, W. Miller, J. Ratliff, G. Ross, R. Scarlett, W. Turner, B. Weinstein, M. Wheeler, N. Wilson)

Highlights

Major achievements are summarized as follows.

- Power amplifiers 2 and 5 were disassembled, cleaned, painted, reassembled, and pressure tested.
- The high-voltage cables for power amplifier 2 were terminated, tested, and installed in the Laser Hall.
- The gas and vacuum system for power amplifier 2 was installed and checked out.
- The electron gun was checked in power amplifier 2 in the Laser Hall.
- The electron gun exhibited internal breakdown and is being fitted with a new grid.

Pumping Chamber

Electrical and Optical Design Testing. We have selected a polyurethane paint for coating the inside of the pressure vessel to prevent oxidation of the carbon steel and to absorb the 10.6-μm light.

The first two prototype double-tapered anode bushings were received, assembled onto the high-voltage cable, and tested at 900 kV (Fig. II-3). The production tooling was acceptable; therefore, delivery of production units can begin.

We developed an antireflection coating (Fe_3O_4) for the anode and selected a vendor to coat the anodes by flame-spraying.

Mechanical. Molds were designed for dielectric dividers; however, the first eight units were machined from solid, cast polyurethane blocks because of the long lead time for mold tooling. They have been installed in section 9 of power amplifier 2. We have received the first mold for casting the remaining divider.

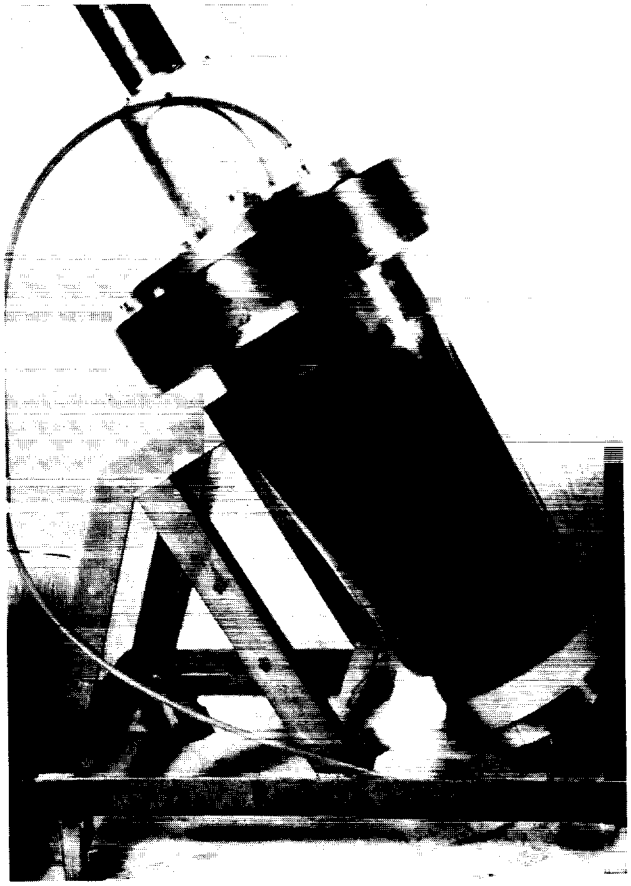

Fig. II-3. Double-tapered anode bushing.

Both amplifers (Fig. II-4) have been cleaned, painted with the polyurethane paint, and reassembled and pressure tested to 1.25 times the maximum operating pressure. The input/output optics shells for power amplifier 5 were assembled (Fig. II-5) on the stand and bolted to the bellows on the beam tube as a fit check. We measured the alignment optically to demonstrate that all the assembly tolerances had been met.

The anodes for power amplifier 2 have been fabricated, coated with the Fe_3O_4 antireflective coating, and assembled into the amplifier. Measurements showed they were within 0.25 in. of the true position, which is within assembly tolerances.

The other internal hardware, that is, secondary rails, nonsupport rails, and foil protection grills, has been installed in power amplifier 2 in preparation for inserting the electron gun for the small-signal gain test.

We assembled power amplifier 5 and have begun installing one sector of optics for the alignment test.

Electron Gun

Electrical Design and Testing. We assembled the electron gun and began testing it in the Electron-Gun Test Facility (EGTF). Over 1000 shots have been fired. The maximum operating voltage is ~480 kV, although the unit was conditioned to 600 kV without the grid. Most of the shots have been fired at 450 kV to map the current-density distribution. However, the electron gun (Fig. II-6) would not recondition after a breakdown so a new grid is being installed.

Mechanical Components. The first grid (Fig. II-7) was fabricated from stainless steel panels that had been perforated by the single-punch method. However, punching caused the material to roll, warping panels. We have fabricated an alternative grid that has a much better finish and uses a gang-punched metal grid. In addition, a design has been completed that uses small-diameter stainless steel tubes for the skin instead of the punched metal. This grid will provide a much smoother profile and will be fabricated if the punched metal is the cause of the grid emission.

The initial set of prototype electron-gun windows, made from titanium foil bonded to a stainless steel rip-stop grid, leaked in vacuum. Therefore, we changed to Kapton-aluminum laminate film, which has been used

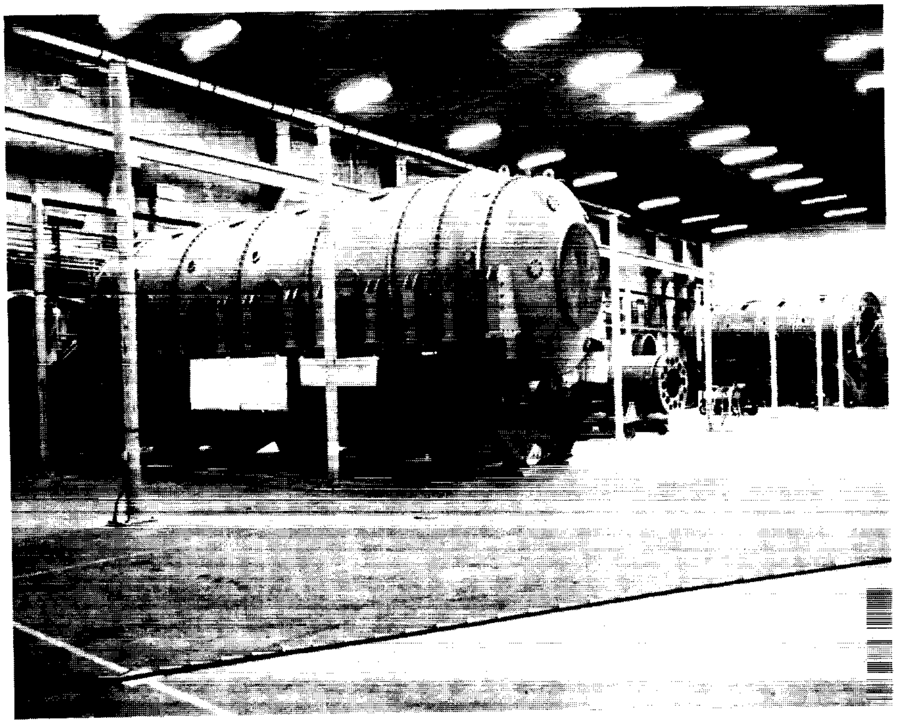

Fig. II-4. Power amplifiers 2 and 5 being assembled.

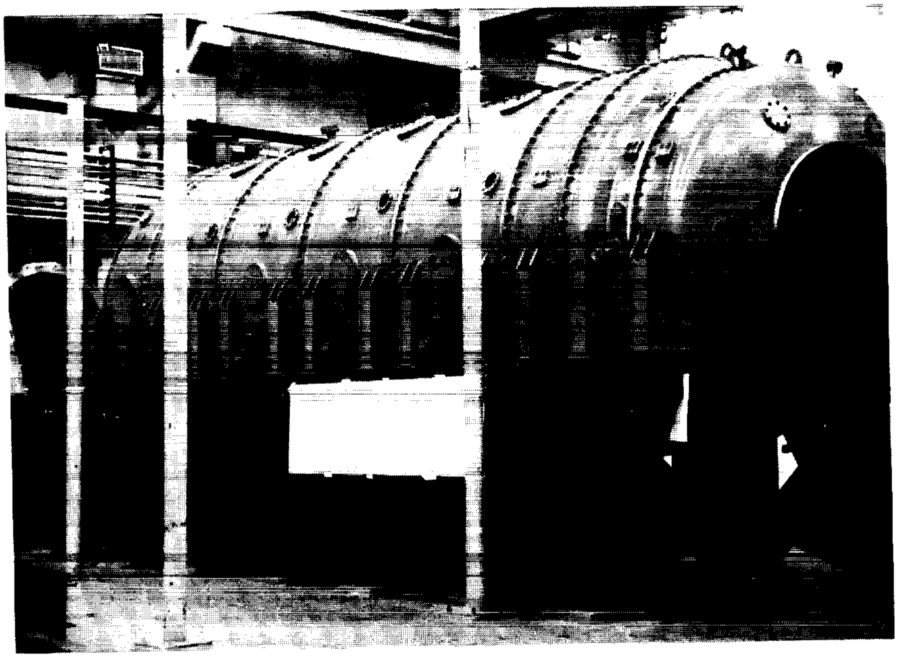

Fig. II-5. Power amplifier pressure test configuration.

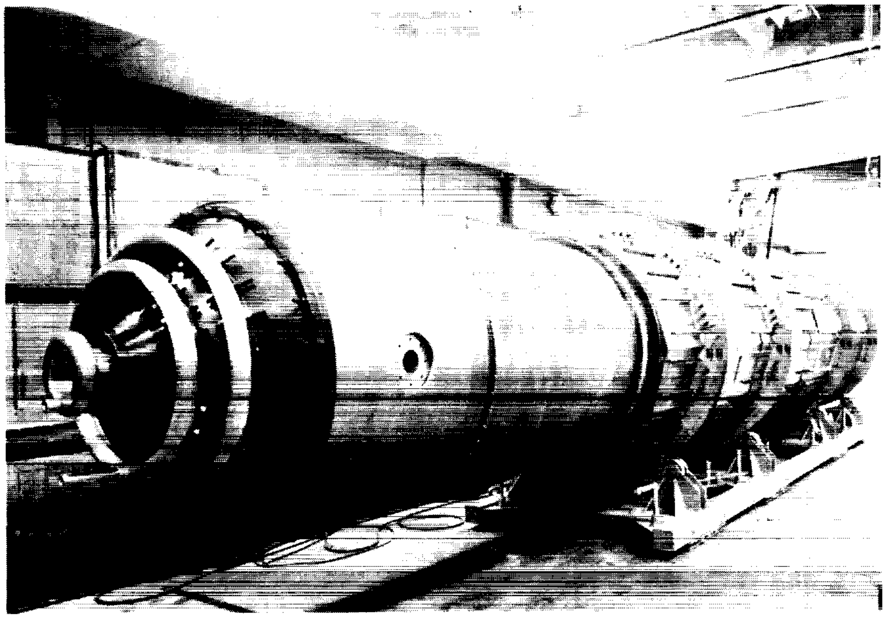

Fig. II-6. Electron-gun assembly.

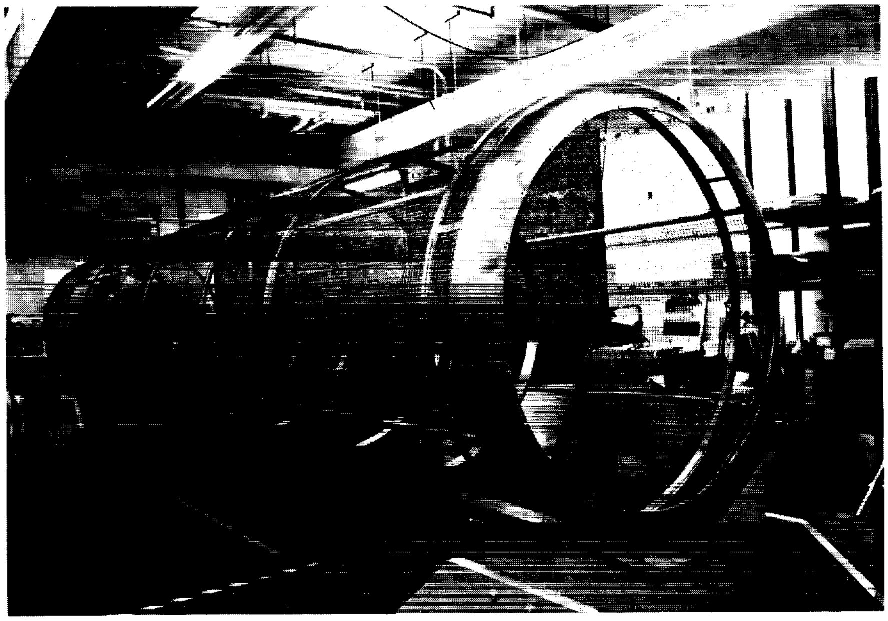

Fig. II-7. Initial electron-gun grid.

successfully on Helios. A complete set of Kapton-aluminum foil windows has been fabricated and installed on the electron gun.

The second electron gun is being procured. The vacuum shell has been machined and is being welded.

Gas and Vacuum Subsystem

All the vacuum pumps and gas-mixing hardware have been assembled and installed in the Laser Hall. The Laser Hall vacuum system, which is used as a roughing pump to evacuate the electron gun and to pump out the pressure vessel, was tested and accepted. The electron gun vacuum system for power amplifier 2 was also tested and accepted.

Handling Equipment

We have received and checked out all the large handling equipment. We used the optics shell transporter to move the shells between the Laser Hall and the OAS. The electron-gun shell was moved successfully to the Laser Hall on an air spring saddle and has been inserted into the power amplifier using the high-boy insertion fixture (Fig. II-8).

The anode-bushing loader was used to install all the bushings in the first power amplifier.

Optical Support Structures

All these units have been received and installed in the power amplifier. They have been measured optically to confirm that all the dimensions are within tolerance as assembled. The units are now in the OAS, where optical mounts are being installed for the one-sector alignment test in power amplifier 5.

Support Stands

The support stands for the first two power amplifiers were installed in the Laser Hall. The units were aligned with optical tooling and grouted into place. A vibration test on the installed units confirmed the initial resonant-frequency calculations. These units are complete except for painting after all piping has been installed.

High-Voltage Cables

The first set of 24 high-voltage cables has been terminated, tested in the cable assembly and test facility, and installed on the cable support structure in the Laser Hall (Figs. II-9 and II-10). These cables have been inserted into the power amplifier 2 anodes and are ready to be used.

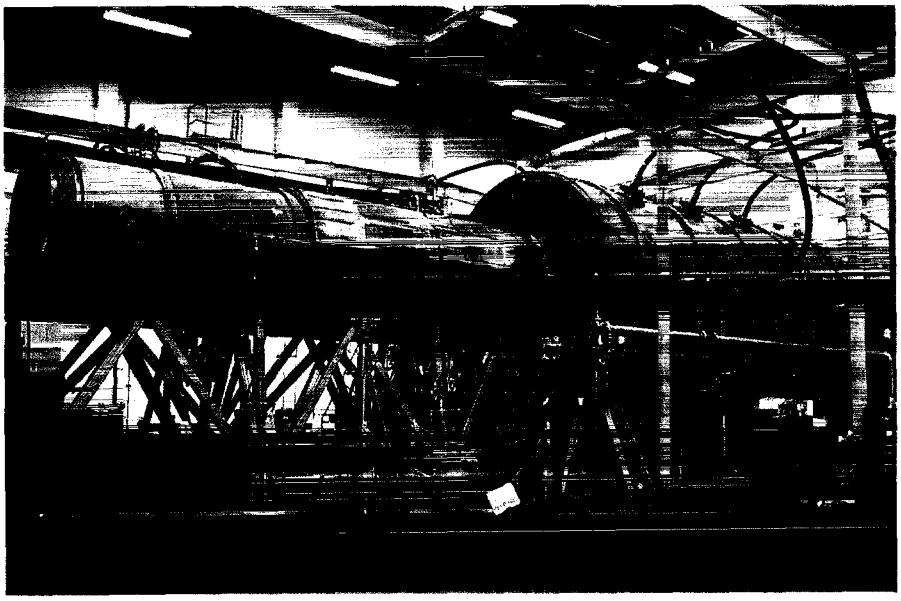

Fig. II-8. Electron gun being inserted into power amplifier 2.

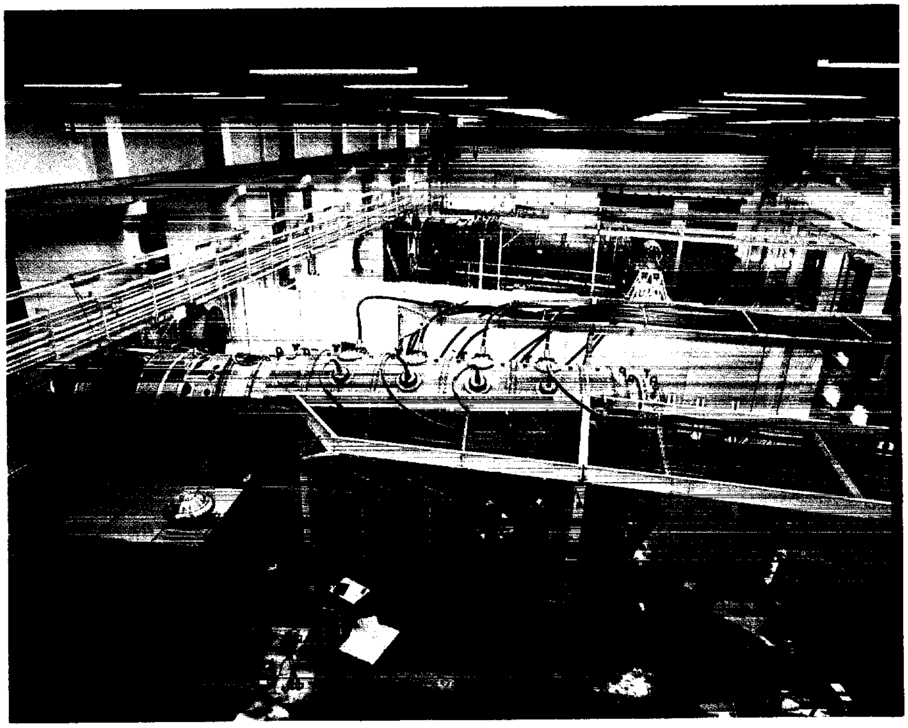

Fig. II-9. Laser Hall showing power amplifiers 2 and 5.

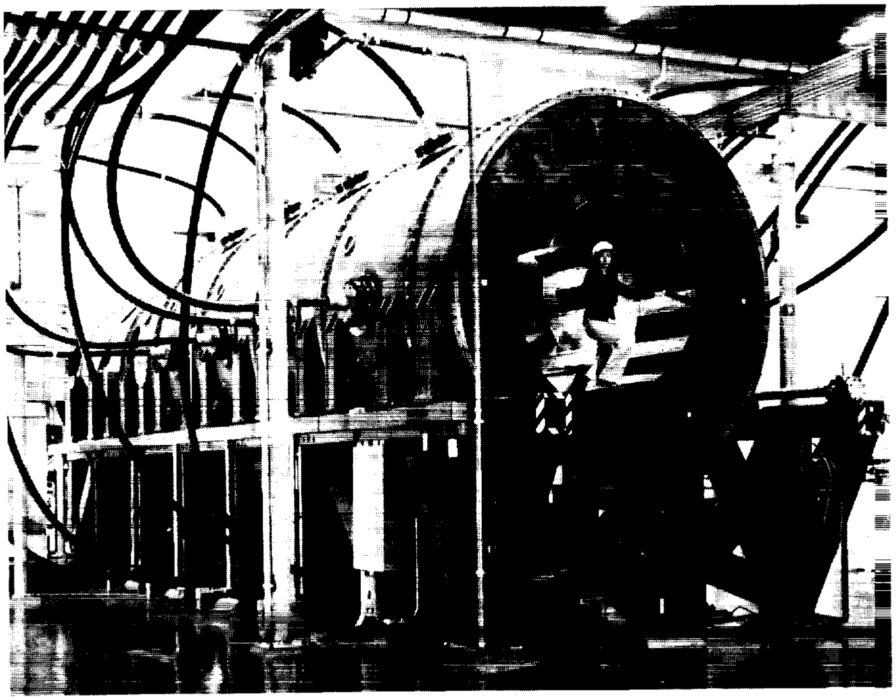

Fig. II-10. Power amplifier 2.

ENERGY STORAGE SYSTEM (G. Allen, W. Scarlett)

Highlights

- Development of the overvoltage gap was completed.
- The gas pulsers for beamline 2 have been tested successfully.
- The gun Marx has also been tested successfully.
- Both the gas pulsers and the gun Marx have been operated successfully under full computer control.

Gas Pulsers

The four gas pulsers for beamline 2 have been tested successfully. We fired 100 consecutive full-energy discharges into an internal dummy load with no prefires and with a delay jitter of <10 ns (1 σ).

Computer control integration of the four production pulsers is 90% complete. Using version-I software, we have fired all four pulsers simultaneously, at full energy, into a common external dummy load under complete computer control. All controls, diagnostics, and displays function properly with no indication of electromagnetic interference (EMI) problems. Final calibration of the fiber-optic links measuring output current and checkout of the timing delay system remain to be completed.

We have contracted for the construction of the next four pulsers required for beamline 5. Delivery of subassembled units is to begin in mid-May 1981.

We are constructing a new control system for the gas-pulser test and repair facility that will allow either manual or computer control of pulsers undergoing tests. We plan to complete the system in May 1981.

Gun Marx—Antares

We have tested the first gun Marx (Fig. II-11). The final test sequence of 200 full-energy discharges resulted in a delay jitter of 10 ns (1 σ) with only one prefire.

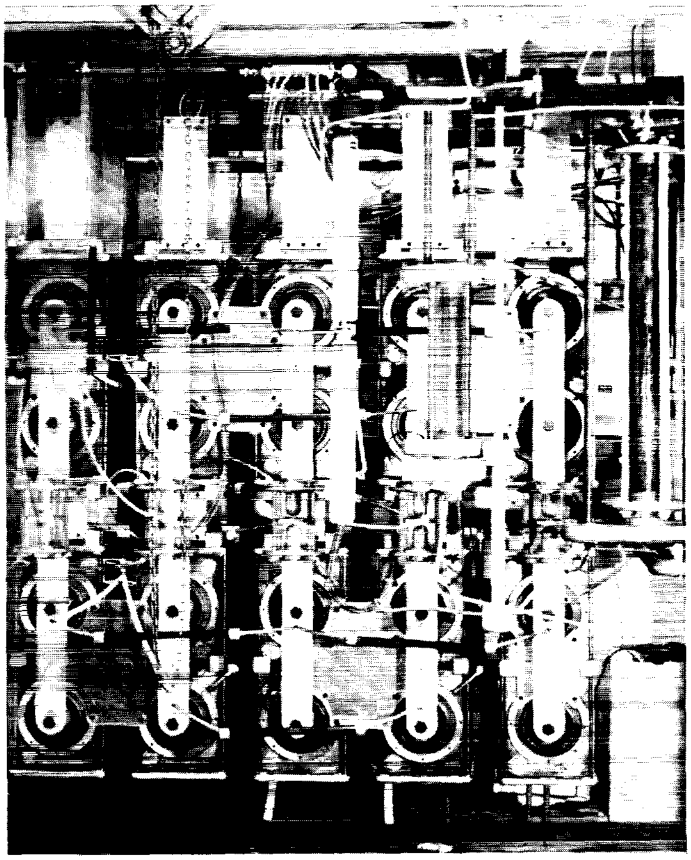

Fig. II-11. Gun-Marx generator.

We have moved the gun Marx to the Laser Hall, installed all computer control hardware, and connected the system to facility lines. The Marx has been operated successfully under complete computer control. To complete the control integration, we must perform a final calibration of the high-speed analog fiber-optic links.

Arcs occurring late in the discharge pulse have slowed down the checkout of the electron gun. To alleviate this problem, we are developing a water spark gap, which will be installed in the gun Marx to divert the remaining Marx energy after 4 μs. Initial low-energy tests indicate that the diverter timing jitter is sufficiently low to be operationally effective. We are conducting high-energy tests under operating conditions.

Fabrication of the second gun Marx has begun and will be completed in July 1981.

Power Suppliers

The energy storage units for the electron gun and the gas pulser have been received and tested into dummy loads. The first gun-Marx supply and gas-pulser supply have been operated successfully under full computer control in conjuction with the gun Marx and gas-pulser control integration tests.

Gap Gas System

We have installed the spark-gap gas-distribution system for beamline 2. Computer control of the gap pressure and venting systems has been operationally checked out in conjuction with the gun Marx and gas-pulser control integration tests.

We have ordered hardware for the beamline 5 gap gas system and will begin assembly in July 1981.

Fault Protection

The design, fabrication, assembly, and installation of the power amplifier overvoltage gaps have been completed. Delivery of gap housings for the gas-pulser overvoltage gaps has been delayed. One gas-pulser gap has been installed. Final testing will begin in March 1981. Installation of the remaining gas-pulser gaps will occur when there is a break in operations.

The design, fabrication, and installation of all cable fault sensors for beamline 2 have been completed. The design consists of a six-turn 1.27-cm-diam current loop to be placed at the ground end of the power amplifier anode bushing. This arrangement provides a signal that is adequate to drive an inexpensive laser diode transmitter. We are simulating cable faults to provide information for scaling from test conditions to actual fault conditions.

ANTARES TARGET SYSTEM (P. Wolfe, J. Allen, D. Bannerman, D. Blevins, C. Cummings, R. Day, L. Dodd, W. Dorris, A. Englehardt, M. Gardner, R. Juzaitis, J. Miller, J. Murphy, P. Soran, V. Viśwanathan, C. Winkelman, V. Zeigner)

Highlights

The decision to reduce the scope of the Antares program necessitated redesigning much of the target system rapidly. The following achievements are particularly noteworthy.

- We completed a detailed study of prompt and delayed effects from target fusion neutrons.
- We completed construction of the TVS and carried out initial vacuum tests with good results.
- We completed most of the design for the massive mirror support structures and sent several out for bid.
- We developed and tested an improved drive system for the target-insertion cart.

Target Neutron Effects

Three distinct but related studies are being conducted.

- To facilitate estimates of permanent displacement damage, we are calculating neutron fluences seen by critical semiconductor components in the motor cans of the folding-mirror positioner.
- To ascertain transient effects on electronics, we are characterizing the time-behavior of prompt-gamma-ray and neutron fluxes in a representative electronic test cell at various locations in the target building.
- We are analyzing long-term activation for critical components of the system, such as the cryogenic shroud and the folding-mirror positioner motors.

Early in 1980 we completed a computer model incorporating the target-insertion mechanism, all mirrors, the space frame, and the target chamber, with as much detail as permitted by the MCNP code. Because the two-beam configuration of Antares places folding mirrors, positioners, and mounting structures about four times closer to the target than the previous six-beam design, we modified the model to account for these and other changes, such as the relocation of the target-insertion mechanism and the decreased number of focus mirrors. Reaction rates, optical thickness, and other information from the detailed model remained unchanged.

We used MCNP in an extensive series of calculations designed to assess the effects of neutron and induced gamma radiation on the Antares target system. We conducted two general types of calculations, each relating to a particular area of concern from a broad class of radiation effects, namely, permanent damage effects and transient (prompt) effects on electronics.

Calculations were performed to quantify the high-energy (<10 keV) neutron fluences seen by critical semiconductor components in the radiation source within the target chamber. Results indicate that critical motor control diodes in the Antares target system (for example, in the folding-mirror positioners or the target-insertion mechanism) will tolerate approximately one thousand 15-kJ shots before displacement damage from neutron fluence becomes important.

The second and major part of this radiation effects study involved a series of calculations for the prompt, time-dependent neutron and for induced gamma-ray fluxes inside a representative electronic test cell at the time of the fusion shot. The test cell could be located in various places in the Target Building; in essence, then, this series of calculations could be characterized as a (restricted) time-dependent flux-mapping in the Target Building. The results of these calculations would help other experimenters in ascertaining the short-term, temporary disruptions in electronic component operation brought about by radiation-generated disturbances in the charge-carrier concentration equilibrium.

An overall geometry model was employed for these calculations (Fig. II-12). Note the location of the test cell inside the Target Building screen room.

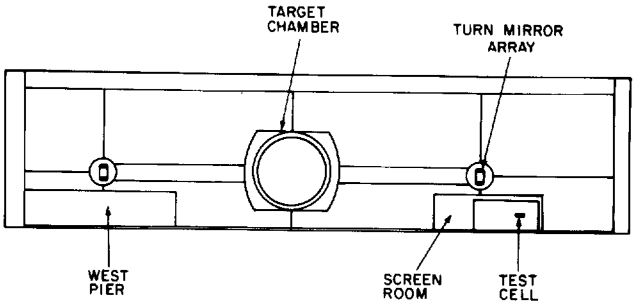

Fig. II-12. Geometry model employed in prompt flux calculations for the Antares two-beam configuration.

The time-dependent studies of the prompt neutron and induced gamma-ray fluxes (and heating) at four representative locations inside the Antares Target Building indicate some general trends. First, despite consistently higher neutron flux levels at all sites, the cumulative heating of the material inside an electronic test cell (calculated in MeV/cm^3·J of neutron fusion output) was dominated by the gamma rays generated in local structures, for example, reinforcing steel, target chamber, and turn mirrors (depending on the location of the test cell). Heating rates were highest during the first 500 ns after the fusion shot and quickly dropped by many orders of magnitude to insignificant levels by 100 s after shot. In all cases (excluding the screen room interior), heating from neutrons was attributable, for the most part, to the particles of highest energy (12-14.1 MeV). On the other hand, gamma-ray heating was more fairly distributed as a function of gamma energy above 1 MeV; heating by gamma rays with energy less than 0.10 MeV was relatively insignificant.

The lowest flux and heating levels were computed inside the Target Building screen room. Total heating to 100 s after the fusion shot was calculated as 1.225 MeV/cm^3·J caused by gamma rays and a relatively unimportant 0.066 MeV/cm^3·J attributed to neutrons. Peak gamma heating occurred in the time interval 500-1000 ns at a rate of 2.736×10^5 MeV/cm^3·s per joule of (neutron) fusion output. At 100 s, the rate was only 9.246×10^{-3} MeV/cm^3·s per joule.

The highest neutron and gamma fluxes were calculated for the test cell located outside and adjacent to the target-chamber wall. Peak gamma heating of 71.91×10^8 MeV/cm^3·s per joule of (neutron) fusion output occurred in the time interval of 50-100 ns after shot. Total heating accumulated over the first 100 s was computed as 464.2 MeV/cm^3·J caused by induced gamma rays and 356.7 MeV/cm^3·J caused by neutrons.

A representative curve showing the induced gamma-ray flux as a function of time (in this case for the test cell located adjacent to, but outside, the target chamber) has been generated (Fig. II-13).

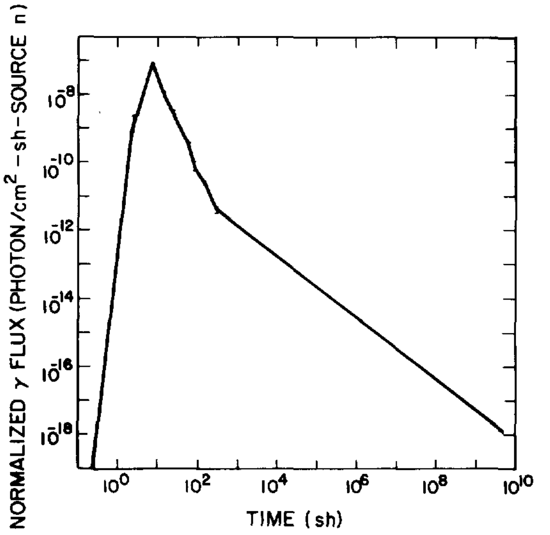

Fig. II-13. Time-dependent gamma-ray flux (test cell located adjacent to target chamber).

Operations

To take advantage of the hands-on experience available as the contractor completed the TVS and carried out debugging activities, a staff member and a senior technician were assigned full time to the Target Building. A set of color slides showing the TVS in various stages of assembly has been prepared to aid in training future personnel and to document the system. Additional training by the contractor will be provided during and after the formal acceptance-test program.

Two major items of special equipment have been purchased for the facility. Because we will install a wide variety of materials in the TVS during fusion experiments (some of which may contribute unduly to the gas load of the system), we are installing a residual gas analysis system. The second item we obtained is a heavy-duty mobile lift platform needed for working on those upper portions of the TVS not served by the permanent work platforms.

The TVS, as well as the rest of Antares, contains many vacuum components (and much other equipment) that require periodic preventive maintenance if system reliability is to be maintained and operating costs are to be minimized. We are setting up a computer data base with maintenance and parts information and a program to use this data base for scheduling and tracking actual maintenance. As part of this activity, an optical spare parts inventory for the TVS has been established.

Target Vacuum System (TVS)

PDM Fabrication Project. Pittsburgh-Des Moines Steel Co. (PDM) has completed almost all TVS fabrication, on-site erection, and installation. An order for changes required for early two-beam Antares operation was incorporated in the PDM contract.

This $4.5 million contract, covering the stainless steel vacuum envelope (Fig. II-14) with its pumps and controls, is the major item of the Antares target system. In the two-beam configuration, there are two 2-m-diam beam tubes extending over 30 m underground from the Laser Hall to the Target Building. These tubes terminate in 3-m-diam turning chambers to redirect each beam toward the 7-m-diam target chamber in the center of the hall. Two more beam tubes, each about 14 m long, connect the turning-mirror chambers to the target chamber.

PDM had almost completed construction on December 7, 1980, when the boiler makers went on strike for 6 weeks. PDM engineers carried out some functional testing and some debugging of electrical parts and pumps during the shutdown, but overall progress was limited by their inability to repair structural leaks. Fortunately, the schedule will not be affected by this delay.

At the end of 1980, functional testing and leak-checking of the envelope and its ancillary components was progressing well. Roughing-down times were well within the 4-h specification. The cryogenic pumps achieved cold-surface temperatures of 10 to 14 K and blanked-off pressures in the 10^{-7}-torr range. The beam tubes, without the target chamber, were reaching $\sim 10^{-5}$ torr with their cryogenic pumps. Because thorough leak checking is yet to be done, there is every reason to expect that the system will surpass its operating specification of 2×10^{-6} torr.

The acceptance-test program submitted by PDM has been reviewed, revised several times, and approved. Vacuum gauge tubes to be used as references for the tests have been calibrated by Sandia National Laboratories (SNL).

PDM will paint the exterior of the TVS and the interior of the Target Building as part of its contract to minimize damage risk from the operation. A contract change for this work was negotiated.

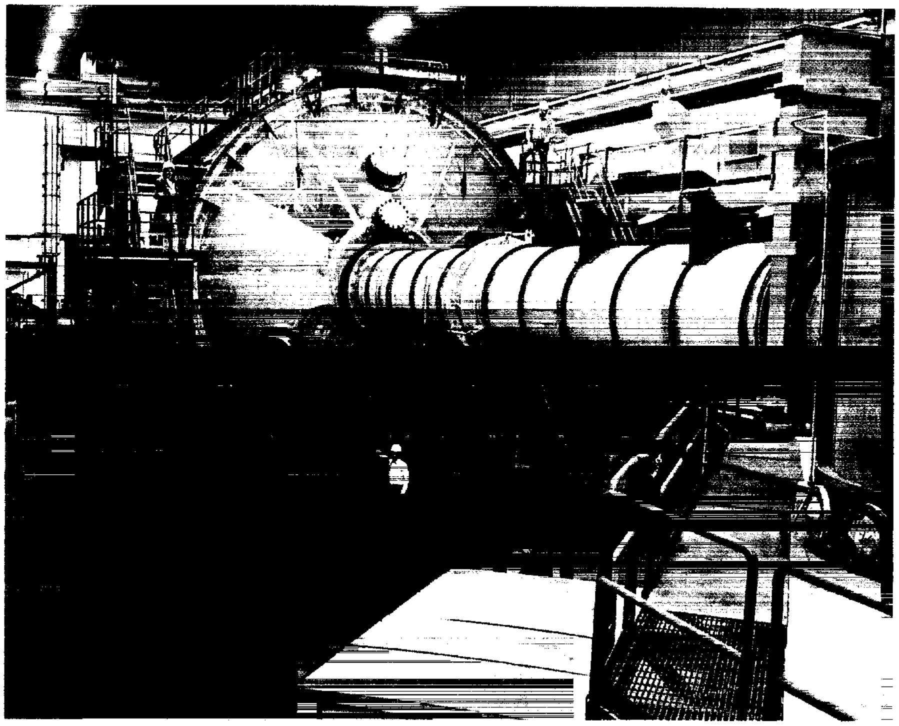

Fig. II-14. Target chamber.

Component Qualification Program.

Characterization of Cryogenic Pumps. The spare cryogenic pump from Helios, which is typical of those to be installed in the TVS, was tested for pumping speed, ultimate pressure, and total amount of gas pumped as a function of gas loading rate. This information is of considerable value for defining an optimum operational sequence for the cryogenic pumps of the TVS.

One of the Antares cryogenic 50-cm (20-in.) -diam pumps was performance tested at the vendor's plant. The tests included were (1) ultimate pressure, (2) cooldown to 20 K from room temperature, (3) hydrogen gas burst, and (4) nitrogen gas burst/crossover pressure simulation. Base pressure for the pump was 1.1×10^{-7} torr. Cooldown time for the pump was ~150 min. No significant second-stage warmup was observed with 10 atm/cm^3 hydrogen gas injection. Seven hundred torr/L of N_2 gas were accommodated without warming the condensing array unacceptably. All characteristics are within the specification quoted by the vendor to PDM. The pump tested is the last of six to be supplied to PDM for the TVS; the other five pumps have been received by PDM at Los Alamos.

Outgassing Rate Measurements. Many components and materials for use in the TVS and in the in/out optics portion of the Antares power amplifiers have been evaluated, and acceptable items have been identified, such as electrical connectors and feedthroughs, stepper motors, surface preparations and finishes, and wire for in-vacuum cables.

Outgassing measurements have been made on several wires considered for cable use in the TVS and in the vacuum portion of the power amplifiers. Only Durad wire, manufactured by Haveg Industries, had a low enough outgassing rate to satisfy our needs. This material has been ordered and will arrive early in 1981. Other materials evaluated include electrical feedthroughs, components for the target-chamber full-power calorimeter, and an epoxy for possible use in shimming the space-frame runout rails in the target chamber.

Vacuum Measurements. Six ionization gauge tubes to be used in the TVS acceptance tests were submitted to SNL for calibration. By agreement with PDM, these tubes will be the principal performance evaluation sensors for the tests.

Vacuum Locks. A standard generic design covering pumps, gates, valves, and controls has been defined for use wherever needed on the Antares TVS. The first implementation of this standard will be the lock for the cart of the target-insertion mechanism. A review of the special mechanical and contamination control requirements of the lock has led us to include a laminar flow hood at the lock access. The design of the pump station for this lock is almost finished.

Time-of-Flight System. The TOF pipe installation was leak tested. No leaks were detected in the pipe installation with a leak detection setup adequate to resolve a leak of $\sim 1 \times 10^{-7}$ atm•cm/s; maximum acceptable leakage is 5×10^{-7} atm•cm/s.

A pumping station was required to evacuate the TOF system. The station makes use of a 360-L/s turbomolecular pump to produce a pressure of less than 2×10^{-6} torr after pumping for 24 h. The addition of diagnostic devices with outgassing rates higher than the rate expected from clean, dry TOF walls will increase this operating pressure accordingly. The configuration provides for substitution of a 1500-L/s speed turbomolecular pump, if diagnostic devices indicate it is needed.

Target Mechanical System

Space Frame. The focus geometry selected for the two-beam (24-sector) system allows us to retain about the same locations for focusing-mirror arrays as in the six-beam system (each having only 4 instead of 12 sectors), but requires entirely new locations for the folding-mirror arrays. Therefore, we had to design a supplementary support stand for the folding-mirror arrays to fit into the space frame. Two alternative designs for this stand are being analyzed for rigidity as a mechanical extension of the space-frame structure.

To aid in the layout of mirrors and diagnostics equipment in the target chamber, a one-fifth scale model of the space frame has been built and fitted with mockup optics (Fig. II-15). A transparent target-chamber model that encloses the space frame was also built; the combination is very valuable in preventing errors in locating various components in this rather complex configuration.

Mirror Support Structures. Each of the two beams originating in the Laser Hall is an annular array of 12 beamlets (sectors), each ~ 100 cm^2 in cross section. The two beams, which are separated by ~ 38 m, travel

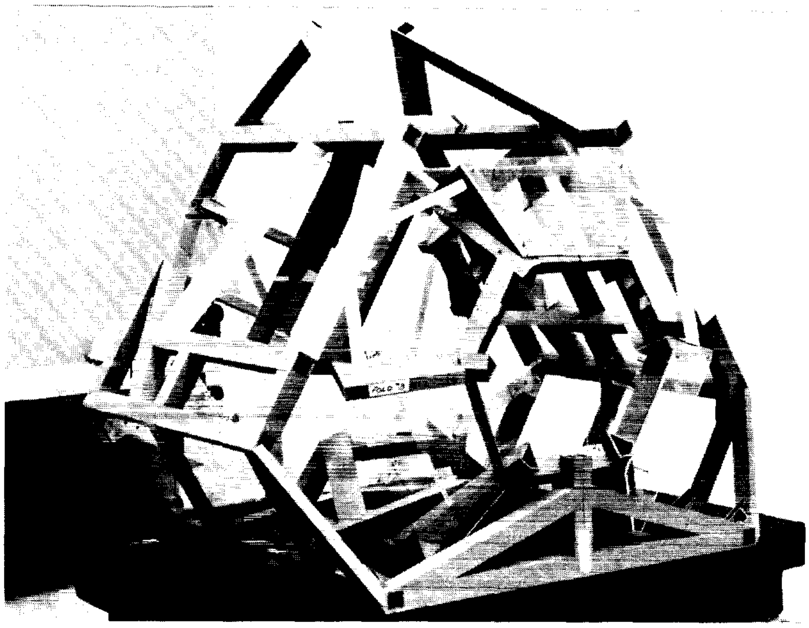

Fig. II-15. Scale model of Antares target-chamber space frame.

roughly northward from the Laser Hall into the Target Building, where they are turned ~90°, one eastward and one westward, toward the target chamber. The turning-mirror structures are essentially large plates, about 2 m high and 3 m wide. Twelve individual mirror positioners and mirrors are mounted on each of the structures in an ellipitical pattern. Completing the massive structure are two post-like stands that support each end of the plate from the floor of the turning-mirror chamber. Design objectives for these structures included optical stability, ease of precisely locating the individual mirrors, clearance for mirror positioner motors, and access for mirror installation. A reshuffling of the beamlet pattern occurs between the turning chamber and the target chamber, implemented by adjustable wedge adapters under each mirror positioner. Similar wedges are used under the folding mirrors in the target chamber. Design, analysis, drafting, and checking for the turning-mirror structures and the turn and fold wedges have been completed. These items are out for bid.

In the target chamber, the 12 beamlets entering from the west are reflected by 12 folding mirrors into 3 groups of 4 beamlets each. The 12 folding mirrors are located just west of the target position and close to the east-west axis of the chamber. The beamlets then illuminate the three sets of focusing mirrors, which are located at the 2-, 6-, and 10-o'clock positions, away from the east-west axis and somewhat west of the folding mirrors. From the focusing mirrors, the beamlets converge to the target. The configuration for the beam entering the target chamber from the east is the mirror image of that just described. A large stainless steel space frame, originally designed for the 6-beam Antares optics, holds 6 support plates for the 24 focusing mirrors. An adapter stand for the folding-mirror support plates is mounted on the space frame. This stand is needed because the original six-beam locations for the folding-mirror arrays were not suitable for the two-beam configuration. At the end of 1980, the folding-mirror support stand drawings were completed and checked. The focusing-mirror support plates went out for bid. The folding-mirror support plates had been drawn and checked. They are being modified before going out for bid.

The target-chamber space frame has been contracted to PDM for detailed design, factory fabrication, and on-site erection. At mid-year, design had been completed and PDM began fabrication of structural members at its plant in Provo, Utah. The structure is rather complicated geometrically, and a number of discussions were held with PDM to work out plans for cooperatively verifying the correct placement and orientation of various parts, in plant and on site. Our optical tooling team visited Provo in December and found that the work to date was satisfactory.

Handling Equipment. A variety of special fixtures is needed for moving and installing the space frame and the various mirror support plates and stands. Design of these components is complicated by considerations such as safety analyses and the center-of-gravity requirements of both the fixture and the item to be handled. At the end of 1980, two fixtures were out for bid: the air bearing dolly for supporting the space frame and the drive mechanism for moving it. The handling system for the focusing-mirror support plate has been designed, drafted, and is ready for checking. Drafting has started on handling systems for the turning-mirror support structure and the folding-mirror support plates.

Target Optical System

Mirror Arrays. The focal length, shape, and distance off-axis of the parabolic focusing mirrors for the two-beam system have been defined. All 24 mirrors are identical. Substrate drawings for the new turning, folding, and focusing mirrors have been completed and approved. The concept of a beam-pointing/target-insertion sequence has been developed, which includes rough target-chamber mirror alignment, calibration of all motions, and the normal alignment sequence.

Because the major design effort is behind us and the actual installation of large mirrors is not scheduled until late 1981, this activity consists only of miscellaneous tasks. Procedures were completed for prealigning the large mirrors during installation in their support plates in the OAS. A fixture was designed for properly centering and orienting the off-axis parabolic focusing mirrors used in the target chamber. Ray-tracing calculations in the vicinity of the target were carried out to aid in the design of the target-insertion mechanism.

Alignment Devices. The reference telescope system is a pair of orthogonal telescopes with associated illuminators and video equipment used in precisely positioning targets and beam-alignment devices at the target location. The design allows the vidicons and the cryogenic target heater to be located outside the vacuum shell. The only movable parts inside the shell are (1) an XYZ stage holding the reticle, (2) a barn-door shutter that protects the objective from flying debris, and (3) a tip-tilt mirror to facilitate initial alignment. Light sources and target fiducials for use with this system have also been worked out, with fiber optics carrying light to the fiducials at the target location from outside the vacuum shell.

We constructed and evaluated the optical breadboard for a previous concept and found it lacking. In particular, it does not seem practical to relay the telescope image over a 3-m-long path to the outside of the target chamber without unacceptable loss of resolution. In addition, the proper matching of available optical components turns out to be cumbersome in this design. Accordingly, we are planning to subcontract the design and fabrication of the telescope optical package. The configuration has been modified to place the vidicon close to the telescope within a reentrant enclosure extending into the target chamber so that the video components can be in an atmospheric environment and yet be located optimally for optical performance.

The size of the reentrant enclosures and the limited space in the space frame in the vicinity of the folding-mirror support structure made it necessary to relocate the telescopes. The new locations, one slightly below the target-insertion mechanism and the other almost directly overhead, provide convenient access to the telescope enclosures and no longer obscure prime space for target fusion experiments. The overhead location, just south of the 1-m^2 access port on top of the target chamber, requires an additional penetration in the chamber. Arrangements have been made with PDM for us to install it before they complete their work.

Target-Insertion System

This system provides for loading targets onto a cart outside the target chamber in a clean environment, transporting the loaded cart through a vacuum lock into the chamber, and then precisely seating the target holder onto a kinematic mount, which is rigidly located in the optical space frame. We have designed the vacuum lock and prototype doors are being fabricated. A design for the cart drive mechanism was carried to the point where a model could be built and evaluated, with some improvement over the systems used in Gemini and Helios. To carry the cart along the rail, a self-storing metal tape is driven by pinch rollers into a T-shaped slot in the cart rail (Fig. II-16). The design of the mechanism for seating the target holder on the kinematic mount has also been completed.

The target-insertion design has two new features. A manually settable 8-bit encoder has been provided so that target information can be set when the target is loaded in the laboratory and then read out automatically into the computer data base when the target has been installed in the chamber. To aid in keeping particulate contaminants off the target, we will install a protective cap when the target is mounted. This cap will be removed only when the target is within the vacuum lock and after evacuation.

The location of the target-insertion mechanism for the Antares two-beam design has been changed. Because the former location, on the west end of the target chamber, is now occupied by the relocated beam tube 2, we have moved the target loading station to the access plate on the south side of the chamber, 15° above horizontal. We have also decided to orient the kinematic mount at 15° to the horizontal because only certain locations are workable for the auxiliary equipment needed to handle cryogenic targets. We completed the design for the mechanism to seat the target holder on the kinematic mount. It is similar to the one used in Helios and Gemini but accommodates the more complex geometry and greater weight of the Antares auxiliary optical alignment devices.

Components such as bearings, motors, encoders, and remote-mating connectors are being evaluated. Completion of these numerous essential tests will permit the final design work to proceed without delay. For example, the tests of two motors considered for powering the target-cart drive show an average outgassing rate after 24 h of 4.1×10^{-5} torr·L/s. This rate should be acceptable in view of the total outgassing budget for the target-insertion mechanism of 3.0×10^{-3} torr·L/s.

Diagnostic Development—Antares Target Chamber (A. G. Engelhardt)

Beginning in April 1980, we allocated more effort for creating an effective interface between target diagnostics and the Antares target chamber during its construction to ensure maximum accessibility of the chamber for current or future diagnostic techniques. Apart from the rather obvious need for plasma measurements, there is a separate and distinct need for beam diagnostics for determining parameters like beam energy, pulse shape, and

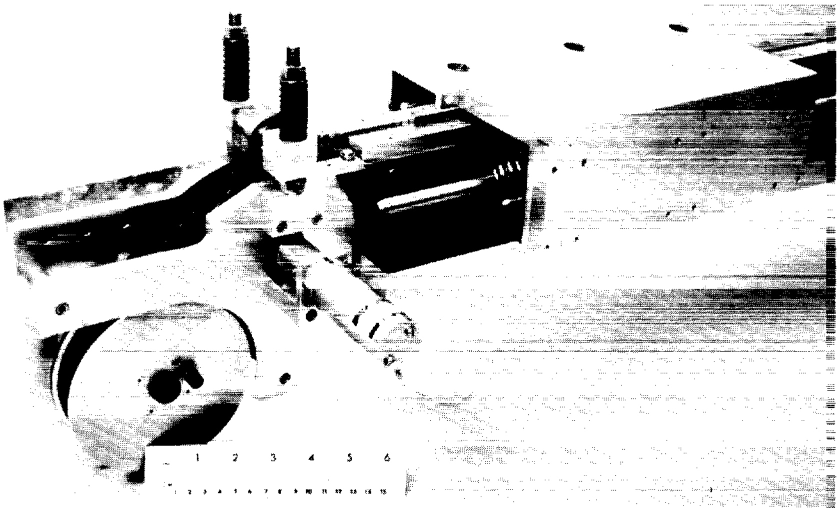

Fig. II-16. Prototype model of metal tape drive mechanism for target-insertion system.

prepulse levels. Before any of these quantities can be measured in the course of a shot, the target must be located at the focal spot and the system suitably aligned. It is the mission of the coordination effort to integrate these three tasks spatially and temporally.

We have identified these types of diagnostics for the Antares target-chamber operations:

(1) neutron counting and spectroscopy,
(2) visible and x-ray spectroscopy and photography,
(3) radiation chemistry,
(4) interferometry,
(5) charged-particle measurements, and
(6) laser energy absorption.

At present, items (1), (2), (5), and (6) have priority as primary diagnostics, but we have ascertained that the target chamber should be able to accommodate all six types of diagnostics. As the various instruments are developed and built, they will be scaled into the target chamber. A one-fifth scale model of the target chamber was delivered in late May.

With regard to target-chamber construction, beam diagnostics, and target insertion, we have determined the preliminary design of the following systems so that they will not interfere with the proposed six diagnostic techniques:

(1) cryogenic and noncryogenic target-insertion mechanisms,
(2) target-alignment telescope and Smartt interferometer,
(3) turning and focusing mirrors, and
(4) beam calorimeters.

These coordination activities also contributed to the specification of the following auxiliary systems and studies:

(1) Antares control system,
(2) television-monitoring network,
(3) telephone and intercom network,
(4) target-chamber neutron activation studies, and
(5) TVS and controls.

CONTROL SYSTEM (M. Thuot, D. Call, L. Burczyk, D. Carstensen, R. Dingler, H. Egdorf, B. Felkner, R. Jones, A. Kozubal, C. Odom, J. Parker, K. Spencer, J. Sutton, S. White, R. Wright)

Highlights

Noteworthy achievements included the following items:

- the control system architecture was modified to accommodate a two-beam Antares system.
- the central control and front-end control shielded rooms were installed and EMI tested.
- a fully implemented computer-control and data-acquisition system has been installed in the energy storage system.

Control System Architecture

The change in scope of Antares led to a modification of the control system architecture. The modified system shows some reduction in complexity and cost. The lowest level of control, the machine interface (MI) (Fig. II-17), remains unchanged: ~42 LSI-11 microprocessors serve as data multiplexers and have direct control of valves, relays, and data-collection devices. Four subsystem-control computers (SCCs), PDP 11/60s, control the major subsystems: optics and target, front end, beamline 2, and beamline 5. Most of the closed-loop control resides at this level. These computers also support a man-machine interface so that each subsystem can be operated separately and concurrently. A PDP 11/70 computer provides the overall system control by coordinating the operation of the four subsystem computers and providing the operator-machine interface for the entire system. The system design accommodates 4000 control and data channels while providing control of nearly 150 interacting processes. The control system has been designed and tested to operate without errors in the severe EMI environment generated by the laser.

Project Engineering

We have established a standard format for subsystem documentation. The format lists all functional inputs and outputs of each subsystem, defines procedures for normal and faulty operation, and defines every physical control or data channel. The computer now provides an updated list of all the data and control channels for the Antares front end, for power amplifier optical alignment, and for the energy system. This information is the basis for our wire-run data base and data dictionary.

We have completed the interface-data documents for the laser diagnostics, the energy system, and the power amplifier electrical diagnostics and have almost finished the vacuum/gas, front-end, and optics alignment documents.

Energy System Project

Hardware implementation of the energy storage system controls includes 10 computers operating in a hierarchical network. A Digital Equipment 11/60 minicomputer functions as the beamline controller, actively

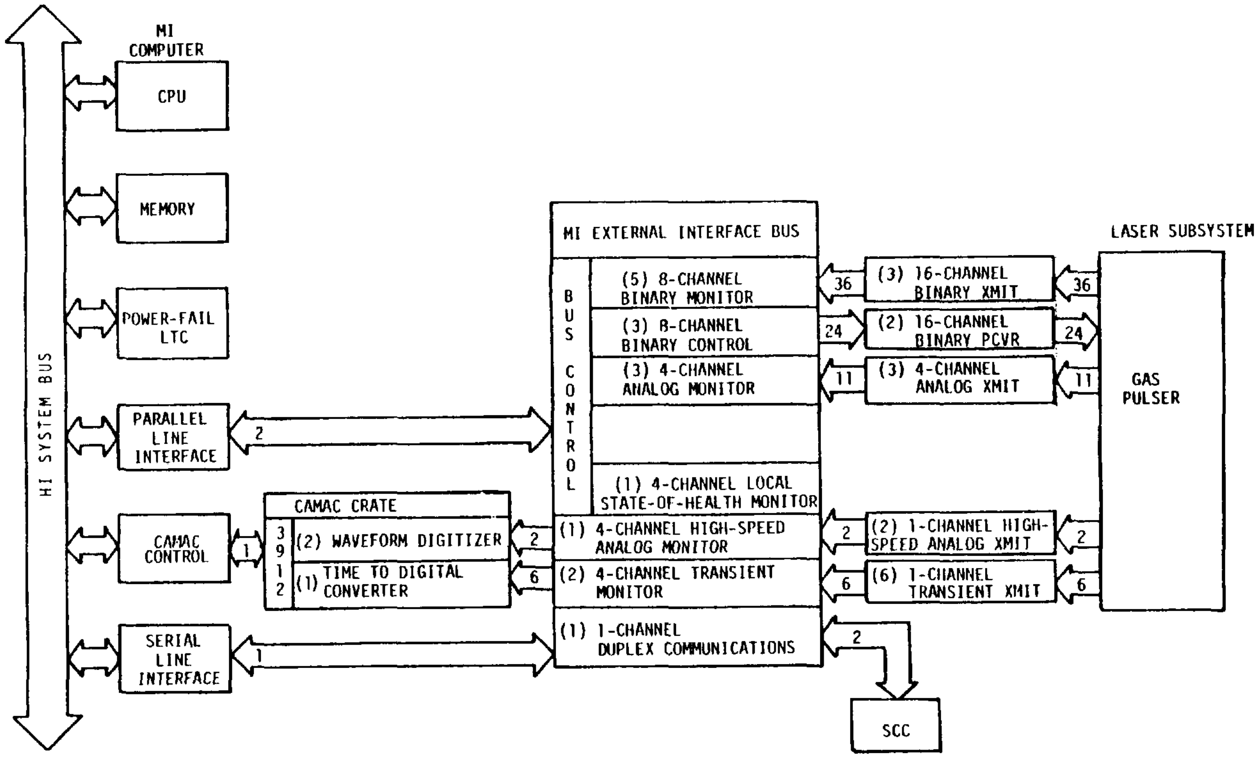

Fig. II-17. Typical Antares MI processor.

supervising nine MI computers. The nine LSI-11 MI microcomputers are assigned to functionally and physically independent devices in the energy storage system. Two MIs are assigned to each of two high-voltage power supplies (Fig. II-17). One is used to control the charging of the four gas pulsers, and the other controls the charging of the electron-gun pulser. One MI computer-control and data-acquisition package is attached to each of the five pulsers (Fig. II-18). Each has high-quality EMI-shielded enclosures that allow error-free operation in the high electromagnetic fields that surround the pulsers (Fig. II-19). In addition, all data and control connections to these MIs are made with fiber-optic cables to eliminate electrical noise. Another MI-controlled data-acquisition subsystem is located in the shielded room adjacent to the laser power amplifier. This subsystem has >100 fiber-optic data channels that record voltage and current waveforms as well as timing information from the power amplifier during operation. The ninth MI is the central timing controller that provides triggers transmitted by fiber-optic cables to the pulsers and data-acquisition systems. This timing controller coordinates system operation to within 10 ns. This computer hardware has been tested in hundreds of pulser operations, some up to full pulser charge voltage. No data or control errors caused by EMI occurred during these tests.

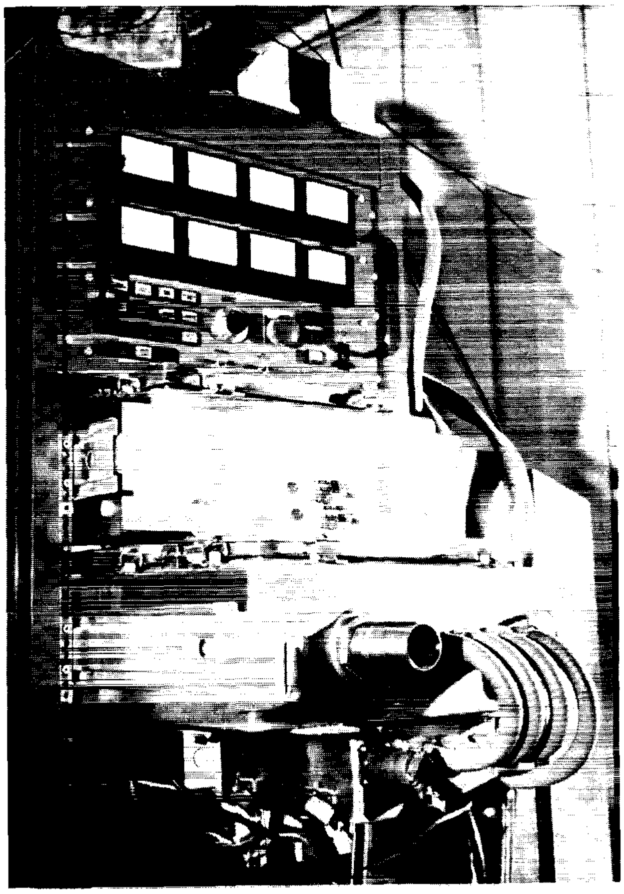

Fig. II-18. Computer controller for high-voltage power supply.

The pulser control system also incorporates a unique fiber-optic prefire diagnostic system (Fig. II-20). This system detects prefires in each stage of trigger amplification and sends the information through the computers to the energy system operator. The operator can observe prefires with a 2-ns resolution in any of five trigger amplifier stages in each pulser. The system operator identifies the stage that prefired for maintenance.

The installation of one beamline energy storage system required the construction and installation of >700 fiber-optic data, control, and communication links. These links had computer interfaces on one end, and most had laser pulse-power interfaces on the other end. To provide the manpower for this effort, an electronic fabrication facility, with as many as 11 electronic technicians, was established. Almost all EMI enclosures, chassis, fiber-optic cables, backplanes, printed wiring boards, and data-acquisition subsystems were assembled here.

Integrated Control Project

The central control and the front-end control shielded rooms have been installed and tested for EMI. Both rooms passed the tests.

The Antares control-system minicomputers have been moved into the central control room. All machines are operational under the UNIX/TENnet system. Subsequent tests demonstrated full computer control of the energy system including recording and plotting output waveforms from the central control console.

Antares Software

General. The software team has produced several versions of control software for Antares. Each successive version provided increased capabilities over previous versions. We can thus add capability and performance as required to support increasingly complex system operations. Also, we are thus able to evaluate new requirements so that changes can be made to the subsequent versions without disrupting the operating version.

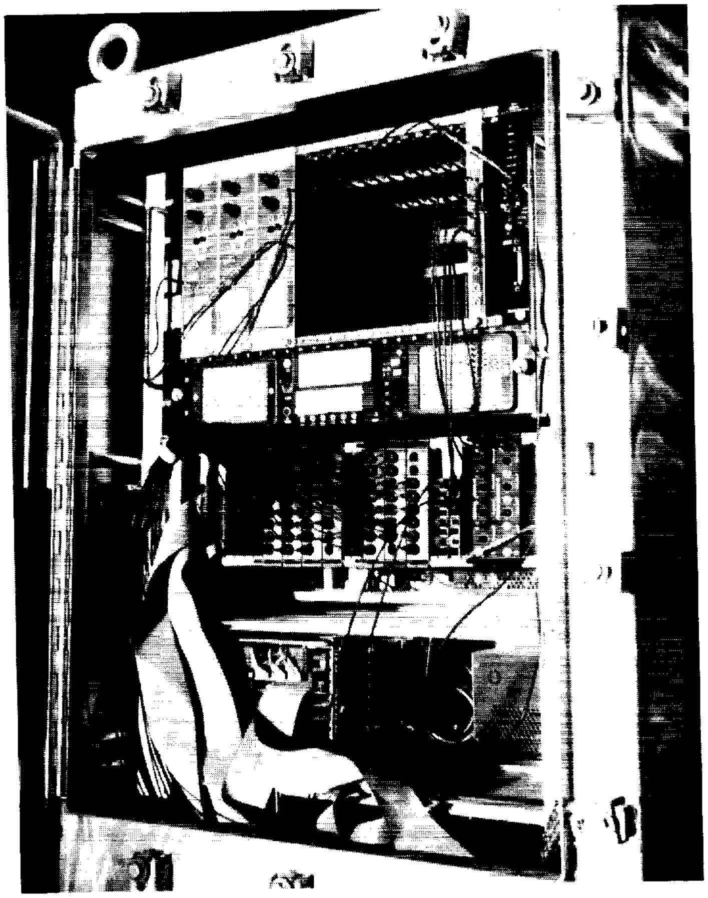

Fig. II-19. Shielded enclosure for Marx controller and data system.

Fig. II-20. Prefire diagnostic transmitter in Marx trigger system.

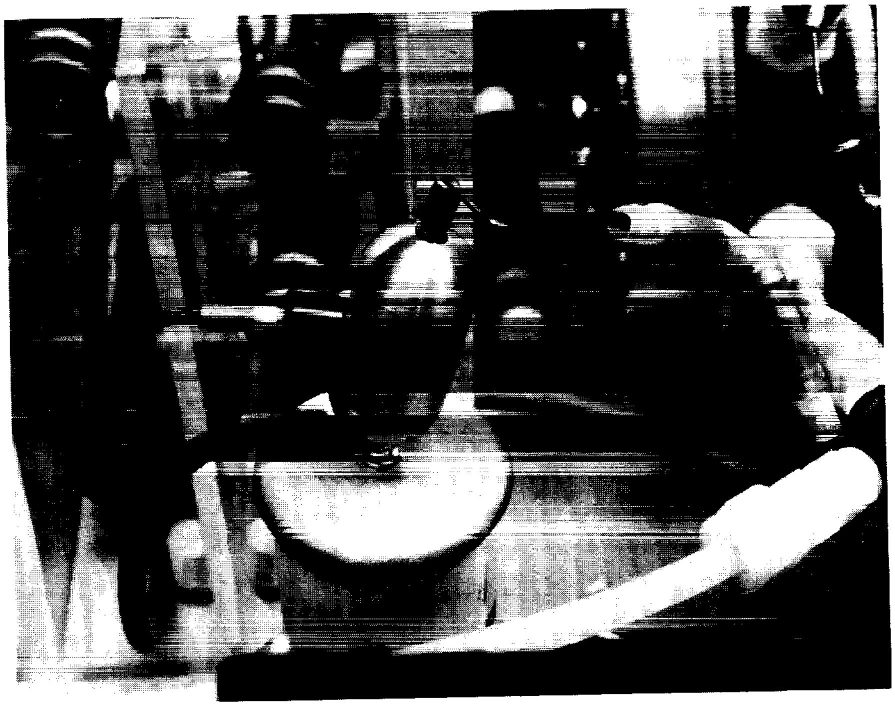

We have defined four categories of software modules: applications, operator interface, laser interface, and data base interface. Applications processes perform control, monitor, or data-acquisition functions for specific Antares hardware, whereas the other three categories are common to all subsystems and are called kernel modules.

The locally developed communications software TENnet was tested and found adequate to support the communication between all the computers in the energy system network. This software also provides the required error-detection and recovery functions for link errors, loss of link, loss of a network processor, and loss of power.

Energy System Software. The software design now supporting the energy operation is the first version. It is based on several general kernel software modules used by all the application processes to provide the required control functions. These kernel modules provide plug-in functions that are customized to the specific application by adding data about the application. The kernel modules are device independent interfaces among the application processes, the operator consoles, and Antares hardware.

There are three kernel modules: the MI handler, the resource manager, and the console manager. The MI handler connects the laser data and control channels to the supervisory computer. This module resides in the MI computer and controls all the laser interfaces and CAMAC data-acquisition equipment. The resource manager kernel resides in the beamline controller. Its function is to allocate access for laser resources to the various application programs. It provides some interlock functions and fault protection. The third kernel module, the console manager, provides access to the console terminal from the application program. This module provides keyboard control of the laser devices and graphic representation of the control process.

The application programs are written to use the modular interfaces defined above. This simplifies the application program so that it is easier to check for proper control operation. Two levels of applications programs have been written for energy system control. The first, component control, allows a low-level interface to each component (for example, a relay, valve, or switch) in any controlled device. The use of the predefined kernel software modules now allows this application software to be generated almost entirely by the computer from the signal name list prepared by the project engineer. The low-level control access is used extensively in installation, checkout, and maintenance of the hardware.

The second-level control for the energy storage system is provided by an application program called charge and fire. This program provides integrated operation of a beamline energy system. The operator selects which of the five pulsers he wants to operate and the level of charge voltage for each pulser. The computer then runs a test on the laser interfaces and control equipment and begins charging the pulsers. The charge process is represented graphically on the operator's console. The operator is notified when the charge is complete and the energy system is fired. After the shot the voltage and current waveforms and the timing data are displayed to the operator and recorded for future access. If prefires occur, data are saved that identify the problem and the operator can recharge the prefired device on command.

III. ADVANCED LASER TECHNOLOGY

(J. F. Figueira)

Each of the CO_2 lasers used in fusion experiments at Los Alamos represents a significant advance in the state of the art for reliable CO_2 laser subsystems, components, and diagnostics. Thus the design, construction, and improvement of these systems rely heavily on our basic supporting research and development in various areas of CO_2 laser pulse amplification and propagation, suppression of parasitic oscillations, measurements of optical damage thresholds for optical components, and basic physics studies that improve the performance of fusion lasers. In addition, we conduct research in advanced laser concepts, such as multiplexing and phase conjugation, and in optical plasma diagnostics for target experiments.

STUDIES OF ANTARES AND HELIOS LASER SYSTEMS

Introduction

Considerable effort was devoted to improving the routine performance of Helios. We redesigned the optical configuration of the TPAs, substantially increasing the energy available for target experiments. Then we tested the optical quality of this new configuration and measured both the spatial gain profile and the gain-vs-frequency spectrum. The goal of these modifications was not only to increase the laser system output, but also to measure quantities needed as benchmarks for design codes and to point the way for engineering improvements in other CO_2 laser systems. We studied the gain-vs-frequency data obtained at Helios to determine how the Helios saturable-absorber performance could be improved.

To characterize the Antares power amplifiers, we began computer calculations on their spatial gain profile. In addition, we assembled and tested components and subsystems for a multichannel small-signal-gain measurement.

Helios Modifications (R. B. Gibson)

Under the extreme pumping conditions of the FIST-II tests in June 1978, Helios delivered a 0.7-ns, 11-kJ pulse into calorimeters. However, the maximum energy routinely delivered onto fusion targets was limited to ~5.5 kJ. A series of experiments and subsequent optical and mechanical modifications to the Helios power amplifiers increased the available energy for target illumination to the 7- to 8-kJ range with no change in discharge pumping levels. Illumination symmetry, beam-to-beam energy uniformity, and shot-to-shot reproducibility were improved; routine maintenance requirements were reduced; and our understanding of large-aperture laser amplifiers was considerably enhanced.

The increased energy and other operational improvements cited above were the results of extensive measurements on, and modifications to, the optical path through the Helios power amplifiers. In the original configuration (Fig. III-1), the beam was deflected into a sidearm after one pass through the amplifier. This sidearm contained a spatial filter and concave mirror, which produced the expanding beam required for the second amplifying pass. The sidearm was maintained at a pressure just sufficient to allow plasma breakdown for target-produced retropulses (about 2 torr) using a vacuum pump controlled by a feedback loop.

Operational experience in Helios during the past 2 years shows that the spatial filter did not appreciably improve beam quality. Moreover, the current series of experiments demonstrates that accurate, reproducible alignment through the sidearm is virtually impossible because of the restrictive apertures. In addition, the sidearm salt windows and the Mylar sheets used to protect the windows from retropulses introduced energy losses and wave front aberrations in the beam.

In the new amplifier configuration (Fig. III-2), the sidearm is no longer isolated from the amplifier chamber. Therefore, the two salt windows, the Mylar retropulse isolator, the pinhole spatial filter, and the sidearm vacuum pump and pressure controller are eliminated.

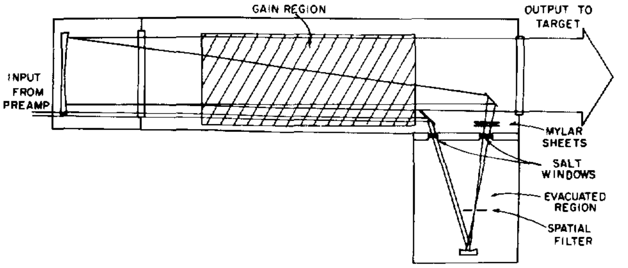

Fig. III-1. Old optical layout of Helios power amplifier.

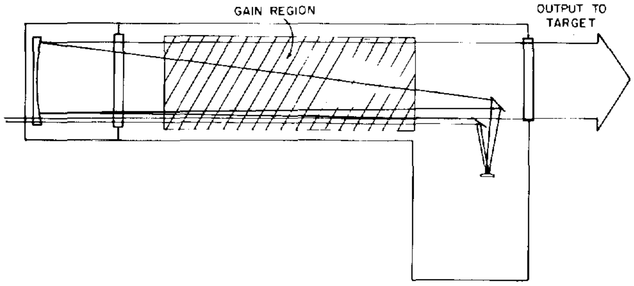

Fig. III-2. Modified optical layout of Helios power amplifier.

The virtual focus of the new mirror is where the old spatial filter was. Retropulse protection is provided by plasma breakdown in the laser gas where the beam overlaps itself above the sidearm mirror. This method of retropulse protection (also used in Gemini) has proven completely satisfactory in the several months since its installation.

Although this modification improved the performance of Helios substantially, there are many areas where our understanding is still incomplete and performance is less than optimum. For instance, variations in gain and energy output across the aperture are more complex than previously realized. This complexity has a major impact on pulse shaping, parasitics suppression, and optical damage problems. Discharge timing is more critical than we believed previously, and both laser and saturable-absorber gas mixes still need to be improved for present and projected discharge pumping levels. We are investigating all these areas.

Optical Analysis of Upgraded Helios Facility and GWTF (V. K. Viswanathan)

Our optical analysis techniques and experimental methods have been discussed in detail earlier.[1,2] Briefly, the techniques involve (1) experimentally obtaining Twyman-Green or Smartt interferograms of the various components, subsystems, or systems at 0.633 or 10.6 µm, (2) digitizing the interference patterns to obtain a Zernike polynomial representation, and (3) using propagation codes and fast Fourier transform (FFT) techniques to obtain the optical parameters of interest.

We modified the sidearm of the Helios TPA extensively. Specifically, we replaced the concave-mirror/spatial-filter/Mylar beam-transport system with an equivalent convex mirror system. This change produced more reliable machine operation with fewer optical components (Fig. III-2). We also replaced many older optical components with better ones. Then we analyzed the eight beams in this new configuration.

Although the interferograms for all eight Helios beams were digitized, only beamline 3B was analyzed in detail. For this beamline, the Strehl ratio increased from 0.2 to 0.5, indicating a substantial improvement in wave front quality. We are still analyzing the other seven beams.

As part of a similar analysis, we measured the optical quality and stability of the reinjection oscillator (RIO) and Lumonics-600 amplifier in the GWTF. This facility supports both laser physics studies and target interaction experiments.

A surrogate laser (cw CO_2) and a focusing lens produced Smartt interferograms of the various subsystems in the RIO/Lumonics system. We eliminated the effects of the laser and focusing lens on overall focal-spot quality in the computer analysis so we could define the contributions of each subsegment. The results are summarized in Tables III-I and III-II.

We concluded that (1) the various parts of the RIO/Lumonics system have reasonable optical stability, (2) the Lumonics amplifier has the best and the RIO the worst optical quality, and (3) defects in the optical quality of individual components are canceled out as the beam traverses the RIO/Lumonics system.

As a result of this study, we intend to look at the optical design and engineering details of the RIO next,

TABLE III-I. Typical Results of Analysis of Smartt Interferograms[a]

	Wave Front Errors[b]		Encircled Energy		
System Tested	RMS	PV	Strehl Ratio	70-80% Diam (μm)	3rd-Order Aberrations[b]
RIO (without four-pass amplifier)	0.32	1.4	0.01	240 308	SPH→– 4.3 COMA→+0.2 AST→+0.2
Lumonics amplifier	0.14	0.7	0.5	46 88	SPH→+1.6 COMA→+0.4 AST→+0.2
Test lens	0.13	0.6	0.5	51 82	SPH→+1.5 COMA→+0.1 AST→0.0
Whole system including test lens	0.13	0.8	0.6	34 67	SPH→ – 1.0 COMA→+ 0.7 AST→+0.2[c]

[a]Key to Abbreviations
AST = astigmatism
PV = maximum peak-to-valley wave front error
RMS = root-mean-square average of peak-to-valley errors (should be about 0.2 × PV)
SPH = spherical aberration

[b]All quantities, as well as the COMA, are given in units of λ (10.6 μm).

[c]COMA and AST cannot be added properly.

with special emphasis on the effects of its four-pass amplifier geometry on optical quality. We also hope to study the optical parameters at the focal plane and to use the pulse itself to produce the interferograms, if possible.

Optimization of Helios Saturable-Absorber Mixture (R. F. Haglund)

The current gas mixture used for stabilizing the Helios power amplifiers, Mix 907, contains SF_6 and six other fluorocarbon gases (Table III-III). We derived this mix by improving[3] another gas isolator, Mix 804, which was developed in experiments described elsewhere[4] to stabilize the Helios amplifiers without a target. In Helios, the absorber cell is 77.5 cm long, and typical operating pressures are ~18 torr. The fluence of pulses entering the cell ranges from 20 to 200 mJ/cm^2. The length of the active laser medium is 200 cm.

To achieve adequate isolation, a gaseous absorber must reduce the net small-signal gain on each laser line to a value below the parasitics threshold. It is instructive to compare the performance of Mixes 804 and 907 in this regard. In Fig. III-3 we have displayed the net small-signal gain experienced by each of the 9- and 10-μm lines for a single pass through the Helios amplifier and saturable-absorber cell. This net gain G(λ) is given by

$$G(\lambda) = g_0(\lambda)\,L - P\ell \sum_i \alpha_i(\lambda)\omega_i \ , \qquad \text{(III-1)}$$

where $g_0(\lambda)$ is the small-signal amplifier gain at wavelength λ, L is the length of the amplifier medium, P is the pressure of the absorber gas in a cell of length ℓ, α_i is the small-signal loss, and ω_i the mole fraction of gas i in the mixture. The amplifier gains $g_0(\lambda)$ in this computation are measured values taken under current Helios operating conditions. The losses $\alpha_i(\lambda)$ in the absorber for both Mix 804 and Mix 907 are calculated from the

TABLE III-II. Typical Results From Studying Stability of GWTF System

System Tested	Wave Front Error[a]		Encircled Energy		3rd-Order Aberrations[a]
	RMS	PV	Strehl Ratio	70-80% Diam (μm)	
RIO (without four-pass amplifier)					
9:30 a.m.	0.32	1.4	0.01	240 308	SPH→+ 4.3 COMA→+0.3 AST→+0.3
11:30 a.m.	0.37	1.5	0.02	240 295	SPH→–5.2 COMA→+0.9 AST→+0.7
Lumonics amplifier					
3 p.m.	0.14	0.7	0.45	42	SPH→+ 1.1 COMA→+0.8 AST→+0.2
3:30 p.m.	0.14	0.7	0.52	46 88	SPH→+ 1.6 COMA→+0.4 AST→+0.2
Whole system including test lens					
3 p.m.	0.13	0.8	0.62	34 67	SPH→–1.0 COMA→+0.7 AST→+0.2
3:30 p.m.	0.12	0.8	0.63	34 67	SPH→–0.7 COMA→+0.2 AST→+0.5
4 p.m.	0.10	0.6	0.75	37	SPH→–0.6 COMA→+0.5 AST→+0.2

[a] All quantities, as well as the COMA, are given in units of λ (10.6 μm).

measured transmission spectra of their component gases (Fig. III-4). The highest net small-signal gain for a gas mix and pressure that just stabilizes the laser should be equal to the threshold gain for parasitic oscillations, that is, the gain at which the amplifier is stable in the presence of a target but without any saturable absorber in place. (This is true if one assumes that the threshold gain is independent of wavelength.) The value of g_{th} found in this way (~1.5%/cm) is in reasonable agreement with the value g_{th} = 1.75%/cm estimated by Montgomery et al.[4] The prediction that the lines with the highest net gains are the 10-μm P(10) line for Mix 907 and the 9-μm P(26) line for Mix 804 is also in agreement with experimental observations.

The salient differences between the two gas mixtures are the higher transmission of Mix 907 at the operating wavelengths and the greater absorption of Mix 907 in the 9-μm P-branch. Fig. III-4 shows that the higher transmission of Mix 907 is due to a smaller nonsaturable loss (that is, higher net small-signal gain) near the 10.6-μm P(20) lines where the laser is designed to operate. Moreover, the absorption of Mix 907 in the 9-μm band is

TABLE III-III. Composition of Mix 804 and Mix 907

	Gas Content (%)	
Gas	Mix 804	Mix 907
SF_6	1.51	0.82
C_4F_8	4.04	2.27
FC-115	12.20	6.64
FC-152a	0	9.09
FC-1112a	0	13.63
FC-12	62.40	25.00
FC-1113	19.85	42.55

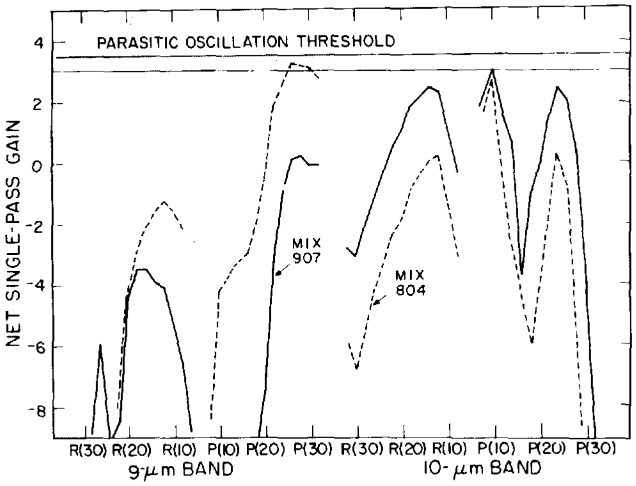

Fig. III-3. Net single-pass small-signal gain G(λ) for all the 9- and 10-µm CO_2 laser lines having significant gain in the Helios power amplifiers for Mix 804 and Mix 907. The parasitics threshold region for these amplifiers with a target in place lies between a net gain of 3 to 3.5. The pressures of the gas mixes used for this calculation were 18 torr of Mix 907 (a pressure that just stabilizes the Helios amplifiers) and 20 torr of Mix 804. Both had an absorber-cell path length of 77.5 cm.

higher than it needs to be for effective parasitics suppression.

Therefore, it should be possible, using the measured gains for the Helios PAMs and Eq. (III-1) to predict an optimum gas mix with some confidence. In fact, calculations indicate that it is possible, by eliminating FC-1112a and either C_4F_8 or FC-152a, to design a five-component gas mixture that will have a smaller nonsaturable loss near 10-µm P(20) and a net single-pass gain adequate to suppress self-lasing throughout the 9-µm and 10-µm bands. The current expenditures for FC-1112a in Helios are approximately $15 to 20 thousand per year, and the gas is difficult to handle (its boiling point is 292 K). Therefore, it seems prudent to consider a test of a different gas mixture at the earliest practical date.

Another feature of this study should also be emphasized. Because of the properties of the absorber gases that are suitable for parasitics suppression (Fig. III-4), the lines hardest to suppress are the *low-gain* lines [for example, 10-µm R(12) and P(10)]. Given the uncertainties in available gain calculations at these lines, it would be wise to measure complete gain spectra for each amplifier requiring saturable absorbers for parasitics suppression. Helios experience shows this is not particularly time consuming, and the task of improving a saturable absorber is thus made much easier. Hence, the acquisition of detailed gain-vs-frequency data should have high priority in the Antares small-signal gain tests.

Small-Signal Gain Spectrum in an 1800-Torr CO_2 Amplifier (R. F. Haglund, J. C. Goldstein, J. Comly)

Suppression of parasitic oscillations is essential for the operation of high-energy, high-gain, short-pulse amplifiers in ICF laser systems. In our CO_2 laser systems, parasitics are suppressed by multicomponent gas mixtures that reduce the net small-signal gain at all frequencies below parasitics threshold but simultaneously allow maximum transmission of the amplified short pulse.[3] Definition of these mixtures, in

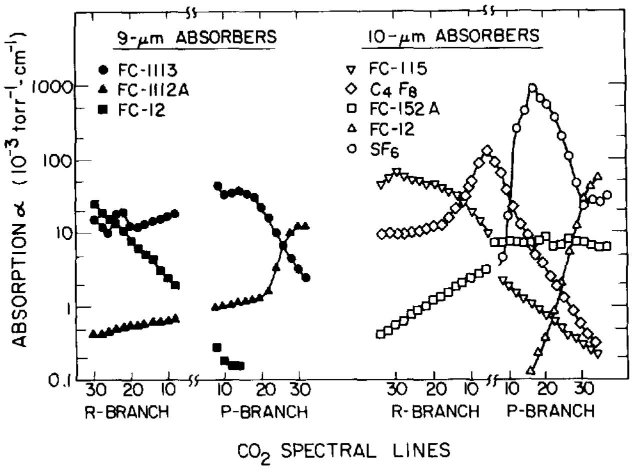

Fig. III-4. Small-signal absorption coefficients for various gases as a function of CO_2 laser line. SF_6 and FC-152a saturate in the 10-µm P-branch.

turn, requires an accurate gain-vs-frequency profile of the amplifier.

The measurements we have made of the small-signal gain coefficients for 53 different lines in the P- and R-branches of the 9.4- and 10.6-µm bands of an 1800-torr electron-beam-controlled CO_2 amplifier in Helios are the most complete gain-vs-frequency measurements for this type of CO_2 laser. They are also in good agreement with a theoretical calculation that uses as input only the measured electrical characteristics and that has no variable parameters. An important feature of this calculation is the inclusion of hot-band and line-overlap effects,[5] which can change the basic two-level gain coefficients of many lines by 10 to 20%. Agreement between theory and our measurements confirms the usefulness of the model for application to other pumping conditions.

The gain was measured by using a mechanically chopped probe-laser beam with an incident waveform [Fig. III-5(a)]. The amplifier was pumped so that peak gain occurred simultaneously with the attenuated part of the chopped probe signal [Fig. III-5(b)]. The attenuation factor was chosen so that both the attenuated and unattenuated probe pulses produced detector output signals ranging from 0.5 to 3.0 V. Comparing signals of similar amplitude avoids errors in the gain from nonlinear detector response.

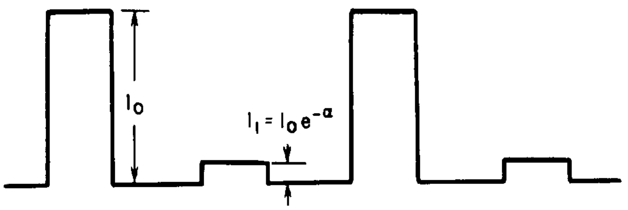

Fig. III-5(a). Chopped pulse train from cw probe laser before the power amplifier is pumped. The chopper wheel has four holes, two of which are open and two of which are covered by CaF_2 or Mylar attenuators. The attenuation α ranges from about 3 to 6.5.

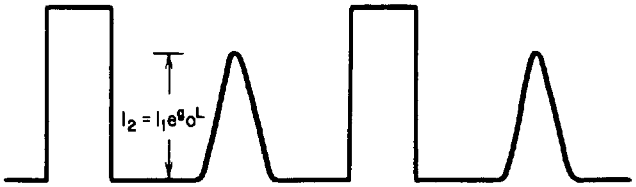

Fig. III-5(b). Timing of pump pulse for the amplifier is arranged so that the attenuated pulse of intensity I_1 is amplified by $\exp(g_0L)$. L is the length of the active region and g_0 is the small-signal gain coefficient in cm^{-1}.

In these measurements, two chopped probe beams from Sylvania-950 CO_2 lasers were routed down the center of Helios amplifier 4B[6] (Fig. III-6). The frequency of one probe was held constant on either the 10-µm P(22) or the 10-µm P(20) line; thus, it monitored shot-to-shot variations in the amplifier gain. The frequency of the second probe was verified throughout the 9- and 10-µm bands. For a given frequency ν, the measured gain g_0 was then normalized by the factor $<\gamma_0>\gamma_0$, where γ_0 is the monitor gain measured on a given shot and $<\gamma_0>$ is the average value for a sequence of shots in a given branch. Both probe beams were injected into the amplifier through 2-cm holes in Plexiglas disks mounted at either end of the amplifier. This arrangement helped prevent contamination of the measurements by stray light.

The probe signals were monitored with two mercury-cadmium-tellurium detectors at 77 K. Calcium fluoride attenuators reduced the signal at the detector surface to a level well within the linear response range of the detectors. With this measurement technique, the relative error in the gain-profile measurements is independent of detector response, provided one remains in the region of linearity.

The formula for calculating the g_0L from the measured voltages [Fig. III-5(b)] is

$$g_0L = \alpha + \ln\left(\frac{I_2}{I_0}\right) ,$$

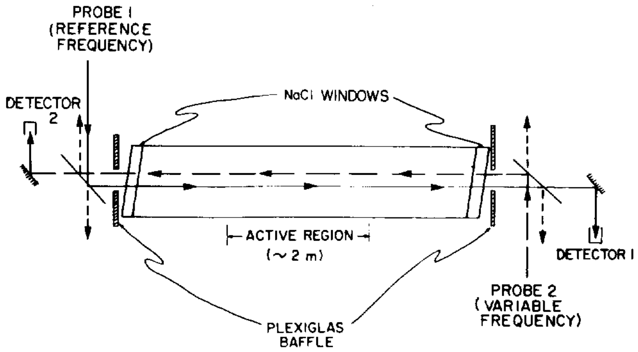

Fig. III-6. Experimental layout for gain-vs-frequency measurements in Helios.

where I_2 and I_0 are, respectively, the peak detector voltages induced by the *attenuated/amplified* beam from the probe and by the *unattenuated/unamplified* beam and α is the small-signal loss of the CaF_2 or Mylar chopper-wheel attenuator. The voltages (including any dc offsets in the detector) are known to within ±0.05 V. The values of α used are believed accurate to within ±2% of α. We ignored the change in attenuation from temperature variations, which we did not measure and which are believed to be insignificant. The nominal attentation values were corrected for the surface reflection losses.

The errors in the gain calculation can be assessed by observing that

$$\frac{\Delta g_0 L}{g_0 L} = \frac{1}{g_0 L}\left[(\Delta\alpha)^2 + \left(\frac{\Delta I_2}{I_2}\right)^2 + \left(\frac{\Delta I_0}{I_0}\right)^2\right]^{1/2} . \qquad \text{(III-2)}$$

For lines in the wings of the R- and P-branches, the gains are low, and uncertainties in I_2 (of ~10%) predominantly contribute to the errors in g_0L, which are around 3%. For lines near the branch centers, the errors in I_2 and α are small compared to the errors in I_0; the errors in g_0L are around 2%. For most points, we assigned a relative error of 3% of g_0L, which we believe is the minimum reasonable value. A few points have relative errors ranging up to ~7%. The scale (or overall normalization) errors in g_0L are believed to be ~5%, based on variations in gain in different Helios modules under nominally equal operating conditions.

Figure III-7 shows the measurements of peak gain coefficients and the corresponding theoretical results. The solid lines represent theoretical values that ignore all hot- and sequence-band contributions, as well as line-overlap contributions caused by the finite line width of each transition. The theoretical points were obtained from a spectrum synthesis program[7] that used as input CO_2 vibrational temperatures calculated from a discharge kinetics code.[8] The kinetics code, using only currents and voltages derived from measurements and no other fitting parameters, computed the excitation temperatures. In this computation, we assumed a spatially homogeneous discharge to obtain approximate pumping conditions at the center of the laser amplifier.

The rotational temperature for the solid curve is ~360 K, which is in good agreement with other information about the gas temperature during the laser pump pulse. However, as Fig. III-7 clearly shows, the simple two-level model from which this curve is calculated is wholly inadequate to describe the data. Instead, one is forced to take into account the many overlapping hot-band and sequence-band contributions to the gain. This is true not only for the lines in the center of the 10-μm P-branch, which have long been known to have anomalously high gain, but also for the entire 9-μm spectrum.

Modeling and Control of Spatial Gain Distribution in Helios (E. T. Salesky, D. E. Casperson)

The model for analyzing the performance of the Helios PAMs in detail was generated by the need to

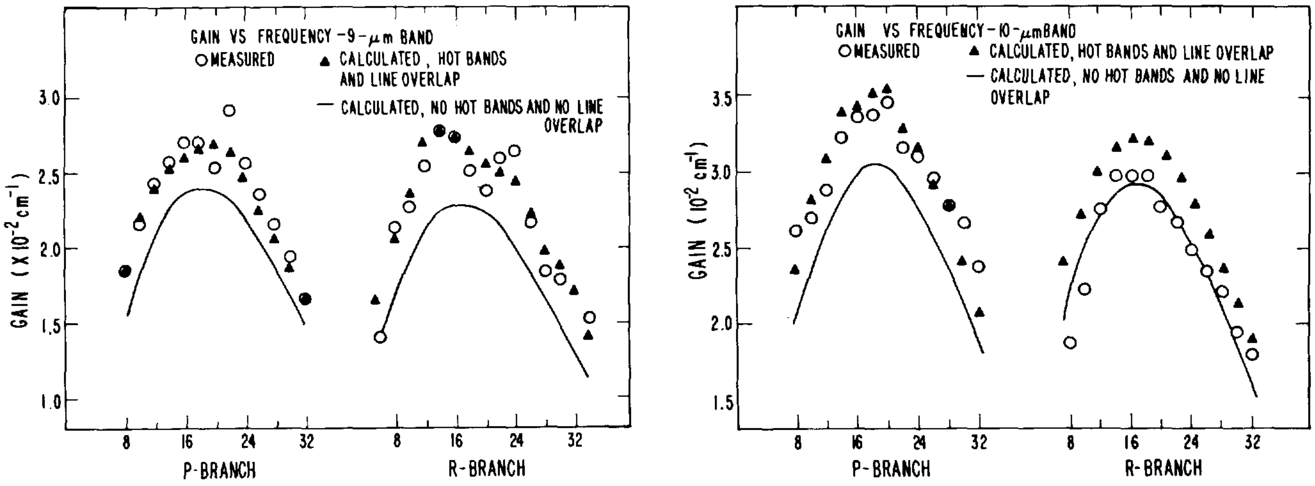

(a) (b)

Fig. III-7. Calculated and measured gains in the (a) 9-μm and (b) 10-μm bands of an 1800-torr CO_2 amplifier.

predict the discharge scaling laws for future large CO_2 laser fusion systems. We developed an improved computer model of the electron-beam-controlled discharge used to pump CO_2 fusion lasers. This model allows for arbitrary discharge geometries, so that exact electrode shapes, discharge shields, the influence of magnetic fields, and electron-beam parameters can all be studied. The code generates two-dimensional maps of gain, electron temperature, electric field, energy deposition, and electron density. These maps help assess engineering tradeoffs.

We used the improved model to analyze the data from an experiment in which the spatial distribution of small-signal gain in a Helios PAM was measured and found to be highly nonuniform. Our model verified that the principal causes of this nonuniformity in the gain distribution are (1) anisotropic magnetic fields resulting from the discharge return currents, and (2) lower than optimum electron temperature in the laser discharge. Both results have been verified experimentally on the Helios PAM. However, these experiments were intended to yield only qualitative results, that is, to determine if the gross effects could be controlled. Because both experiments were successful, we are planning an experiment to provide accurate data on the improved gain profile in Helios.

The core of our model is the two-dimensional electrostatics JASON code developed by S. Sackett of Lawrence Livermore National Laboratory (LLNL).[9] This code solves the Poisson equation for arbitrary boundary conditions, so that exact geometries (for example, electrode shapes of the Helios PAM) can be specified. In previous treatments at Los Alamos, this was not the case. As a result, we could not consider many interesting features, such as electrode designs that would maximize electrical efficiency in the optical extraction region and minimize streamer formation[10] caused by high electrical stress at critical regions.

In our work, JASON is used to solve the nonlinear two-dimensional electrostatic problem specified by

$$\vec{\nabla} \cdot (\sigma \vec{\nabla} \phi) = 0 \ , \qquad \text{(III-3)}$$

where ϕ is the two-dimensional electrostatic potential and σ is a two-dimensional conductivity. This conductivity is given by Ohm's Law,

$$\vec{J}_s = \sigma \vec{E}_s \qquad \text{(III-4)}$$

with $\vec{J}_s$ the discharge current density and $\vec{E}_s$ the electric field $\vec{\nabla}\phi$. In terms of plasma parameters, $\vec{J}_s$ is given by

$$\vec{J}_s = e n_e \vec{V}_d , \qquad \text{(III-5)}$$

where e is the electronic charge, n_e is the electron number density (ion transport is negligible), and $\vec{V}_d$ is the electron drift velocity against the sustainer electric field $\vec{E}_s$ in the presence of elastic and inelastic collisions with the neutral gas species. (Electron-electron and electron-ion effects are negligible.) The functional form of $\vec{V}_d$ was taken to be

$$\vec{F}_d = \vec{F}_0 \left(\frac{E}{N} \right)^{1/2} , \qquad \text{(III-6)}$$

where E/N is the electric field $\vec{E}_s$ normalized to the neutral gas number density.

The electron number density n_e is determined by the differential equation

$$\frac{dn_e}{dt} = S - \alpha n_e n_+ - \beta n_e \ , \qquad \text{(III-7)}$$

where S is the electron-ion production rate given by the Monte Carlo calculation, α is the recombination rate, and β the attachment rate. We assumed the discharge to be recombination dominated, so that $n_+ = n_e$ and $\alpha n_e \gg \beta$. If we ignore the initial build-up of the plasma and the afterglow following the discharge, most of the discharge is in equilibrium and the electron-beam ionization rate is balanced by electron-ion recombination. Therefore,

$$\frac{dn_e}{dt} = 0 = S - \alpha n_e^2 \qquad \text{(III-8)}$$

and

$$n_e^2 = \frac{S}{\alpha} \ . \qquad \text{(III-9)}$$

Generally speaking, α is a function of the electron energy (or temperature, in the loose sense of the word). Only a few measurements of α have been made,[11] so that, in practice, the functional form must be estimated. We assume that

$$\alpha = \alpha_0 \left(\frac{E}{N} \right)^{-2} \qquad \text{(III-10)}$$

is a reasonable approximation in the present case.

With these inputs we use the JASON solution to give a two-dimensional map of E_s and J_s, which in turn determine the two-dimensional small-signal gain distribution for a specified integration time.

Fig. III-8 shows the experimental gain measurements and our model predictions. Agreement is good and indicates that we have accounted for the major gain-profile-shaping effects caused by the nonuniform discharge conditions. The cathode-to-anode asymmetry is caused mainly by the low electric field (electron temperature) in the discharge, and the top-to-bottom asymmetry is caused mainly by the nonuniform magnetic fields produced by the return currents. We have verified these conclusions experimentally on a Helios PAM in a series of qualitative experiments.

The code development program is a valuable tool for the analysis of Helios performance and will improve the output of the device. The experiments verified the predicted magnetic-field effects and yielded a 15% increase in laser output energy, with a corresponding improvement in the spatial uniformity of the energy output. More detailed experiments are planned for Helios to further test the code.

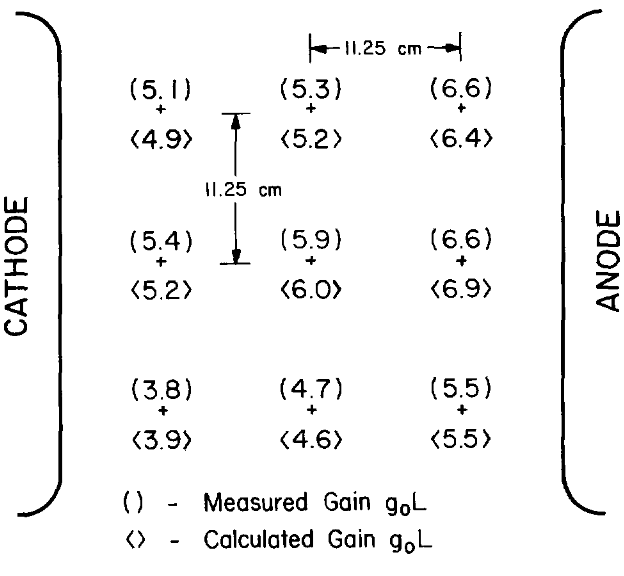

Fig. III-8. Measured and calculated spatial profile of gain in Helios PAM 4B. The gain was measured in a grid pattern centered on the optical axis of the PAM, with a spacing of 11.25 cm point-to-point. The diameter of the extracted optical beam is 34 cm. The amplifier parameters were gas mix, 3:1/4:1::He:N_2:CO_2; pressure, 1800 torr; electron-beam voltage, 230 kV; sustainer voltage, 210 kV; and discharge time, 30 μm.

CO_2 Laser Discharge Physics: Antares (E. T. Salesky)

We have begun to study the electrical discharge of the annular Antares geometry using the JASON model. In addition to a new geometry, we are also considering different laser-gas mixtures and the effect of using dielectric shields to confine the discharge plasma.

Figures III-9 and III-10 show some results of our work on the Antares discharge. They present models of the gain profile across the discharge from cathode to anode for the Antares design both with and without dielectric shields. The discharge parameters considered are the design specifications of 500 keV for the electron-beam electrons and 556 kV for the sustainer voltage for the laser mixture (0.25:1::N_2:CO_2) at 1800 torr. The predicted uniformity is good in the optical extraction region in both cases and does not seem to indicate that dielectric shields are necessary. However, these results are deceptive because they show the gain profile under optimum conditions. No magnetic pinching has been included, the longitudinal discharge profile is assumed uniform, and square electrical input pulses are assumed.

Furthermore, in other calculations (not shown), the shields appear, at least under these conditions, to have an important effect on the electrical stresses at the edges of the discharge. We are studying the sensitivity of these effects. At present, because of a lack of experimental data on the gain profile and current-density profile on the Antares PAMs, we are studying the data obtained on the prototype module.

In addition to this technical effort, we have improved the code so that it can be used by those who are not familiar with the details of the JASON calculation or with the auxiliary codes that generate input files. We have reduced the number of input parameters and auxiliary codes necessary to run a complete calculation.

- We have implemented a number of option switches so that unnecessary calculations are not performed during the input testing stage, the major solution stage, and the output postprocessing stage.
- We are converting the code from LTSS (for the CDC 7600 machines) to the CTSS operating system for the CRAY-1 computer. We are preparing a detailed user's guide to the code.

At the request of the Air Force Weapons Laboratory (Kirtland AFB, New Mexico), we provided technical assistance in the evaluation of their proposed CO_2 laser program. We offered technical expertise while paving the way for a mutually beneficial discharge scaling program, both experimental and theoretical.

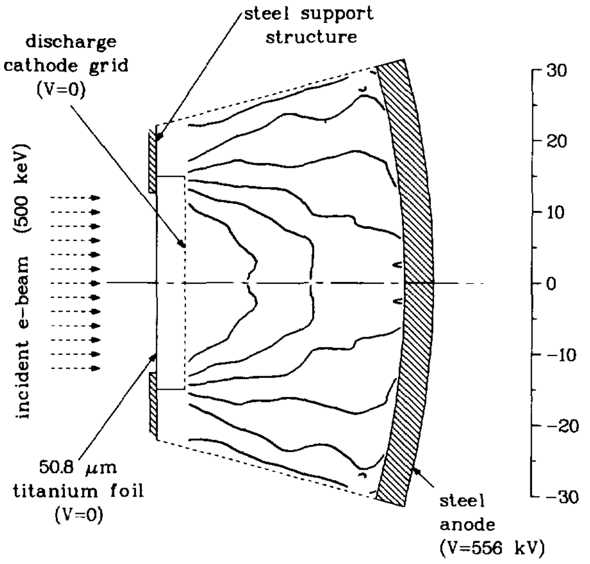

Fig. III-9. Transverse view of a single section of an Antares PAM showing the gain profile at 2 μs without a dielectric shield.

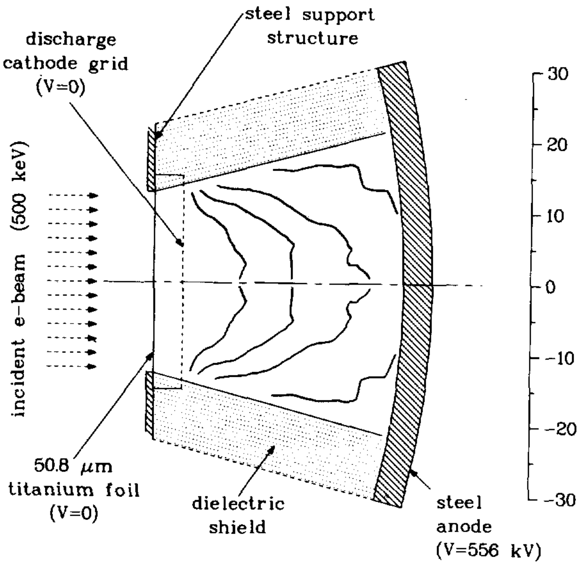

Fig. III-10. Transverse view of a single section of an Antares PAM showing the gain profile at 2 μs with a dielectric shield to confine the discharge.

STUDIES IN NONLINEAR MEDIA

Introduction

For CO_2 fusion lasers, the physics questions of current interest center on the propagation of high-power, subnanosecond pulses in CO_2 laser gain media and in saturable-absorber media.

Strong spatial-profile modification was observed for nanosecond pulses passing through SF_6 (SF_6 is the basic component of saturable-absorber mixes now used in our fusion lasers.) In SF_6 and Mix 907, we demonstrated substantial risetime degradation as well as frequency- and fluence-dependent pulse dispersion. Both effects are potentially damaging to the production of terawatt-level multifrequency pulses. Also, we made the first measurements of gain recovery in an electron-beam-controlled amplifier. The data confirm that significant repumping occurs on time scales shorter than 25 ns, which has favorable consequences for amplifier multiplexing. We also investigated subnanosecond pulse propagation in a CO_2 TEA amplifier, nanosecond pulse behavior in hot CO_2, and line-broadening effects on gain coefficients.

Temporal Pulse-Shape Distortion in Saturable Absorbers (R. F. Haglund)

The power amplifiers used in the Helios CO_2 fusion laser are stabilized against parasitic oscillations by the use of SF_6-based gaseous saturable absorbers. The single absorber cell in the Helios power amplifier chain must not only provide gain isolation between the preamplifiers and the first pass through the power amplifier, but also between the second and third passes through the power amplifier. Therefore, the absorber loss characteristics cannot easily be optimized to match the varying fluence and intensity at each stage of amplification. This variation also introduces the possibility of nonlinear pulse-shaping effects in the absorbing medium.

In a recent paper,[12] Nowak and Ham have reported severe spatial pulse distortion for nanosecond CO_2 laser pulses traversing SF_6 gas samples at modest pressure-length products. Preliminary experiments showed no spatial effects in the Helios saturable-absorber mixtures. However, we have looked for and found substantial temporal pulse distortion both in SF_6 and in Mix 907, which is used for parasitics suppression in the Helios laser. The observed effects of most concern in an operating fusion laser system are a wavelength- and fluence-dependent increase in pulse risetime and a wavelength-dependent dispersion in the transit time of a nanosecond laser pulse through the absorbing medium. Both effects are undesirable in current CO_2 fusion laser systems, which use multiwavelength pulses to maximize energy extraction and which must have the fastest possible risetimes.

The laser used for the experiment[13] produces an approximately triangular pulse shape with a 10-90% risetime of 450 ps, a fall time of 1750 ps, and a width (FWHM) of 1700 ps. The experimental arrangement is shown in Fig. III-11. The gas cell used for the pulse-shape measurements is 19.8 cm long and is sealed by salt windows mounted at Brewster's angle. The incident fluence on the cell is controlled by putting calibrated CaF_2 attenuators in front of the entrance window of the gas cell. The signal incident on the pyroelectric detector at the cell exit is kept to reasonable limits by keeping the *total* attenuation before and after the cell constant. The values of the attenuators in the stack are chosen to give appropriate fluence increments between 0.01 and 1000 mJ/cm^2. We use a pair of matched salt wedges to split off a portion of the incident beam for diagnostic purposes. This diagnostic beam is further split with a single salt wedge; the two beams are then directed into fast and slow pyroelectric detectors to measure pulse shape and incident energy, respectively. A second fast pyroelectric detector is used to measure the pulse shape at the end of the gas cell. The output signals from the fast pyroelectric detectors are delayed with respect to one another so that the signals can be added to the input of a 5-GHz oscilloscope and appear on the same trace.

Figure III-12 shows pulse traces for a 1.7-ns laser pulse on the 10-μm P(16) line, incident on 60 torr•cm of SF_6, at a peak fluence of ~600 mJ/cm^2. If one corrects for sweep nonlinearity in the 5-GHz oscilloscope, one finds that the pulse risetime in SF_6 is lengthened from ~450 to ~600 ps. Similar results are obtained at other frequencies (Table III-IV).

The data in Table III-IV were all taken with 60 torr•cm SF_6 in the gas cell. Risetime ratios are normalized to the average vacuum risetime. Peak incident fluence in each case is ~600 mJ/cm^2. At low fluences (~60 mJ/cm^2), the risetime ratios remained constant,

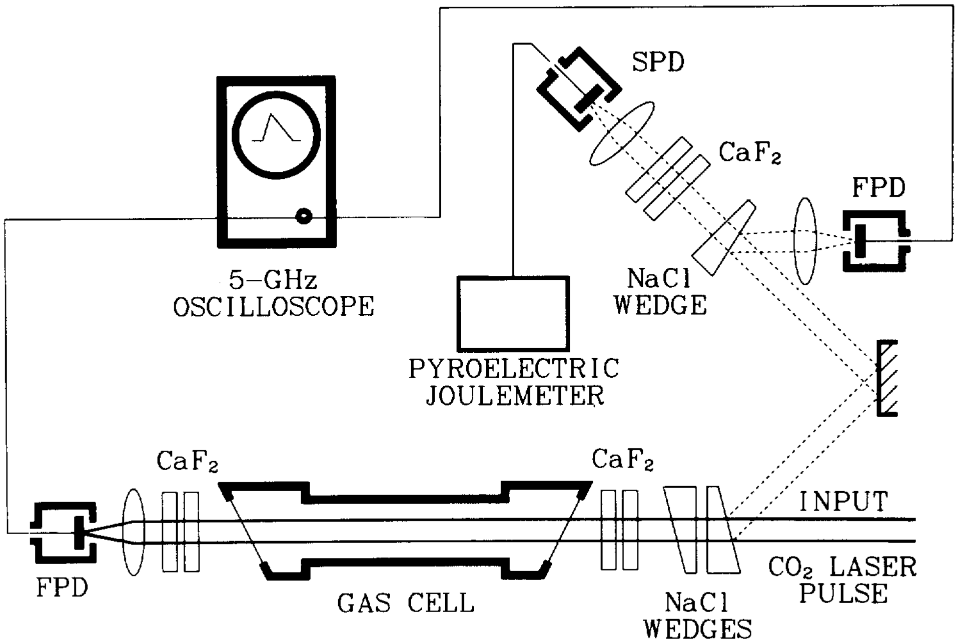

Fig. III-11. Experimental layout for pulse-shape measurements. The laser pulse is incident from the lower right. Wedges of NaCl are used to provide diagnostic pick-offs. The labels "SPD" and "FPD" refer to slow and fast pyroelectric detectors, respectively.

TABLE III-IV. Wavelength Dependence of Pulse Shape

Wavelength	Risetime Ratio	Peak Delay (ps)	Gas
10.6-μm P(20)	1.0	580	Vacuum
10.6-μm P(14)	1.0	610	60 torr•cm SF_6
10.6-μm P(20)	1.3	640	60 torr•cm SF_6
10.6-μm P(24)	1.3	630	60 torr•cm SF_6

whereas the peak delay time increased by 5-8%. The pulse delays indicated in Table III-IV are simply those between incident and exit pulse peaks. Because a greater fraction of the leading edge of the pulse is absorbed as the gas saturates in the low-fluence case, there is a change in delay between high-fluence and low-fluence exit pulses.

Figure III-13 shows the fluence dependence of the risetime ratio for 10 torr•cm of pure SF_6 and for 800 torr•cm of Mix 907. The data fall reasonably well on the best fit straight line. The experimental errors (approximately ±0.10% in the risetime ratio) do not justify a more sophisticated fitting procedure. Because the mole fraction of SF_6 is nearly identical in the two cases, we conclude that the risetime degradation is determined primarily by the pressure-length product of the SF_6. It should be noted that the pulse shaping is not negligible even at moderately high fluences. In particular, because absorber pressure-length products in Helios are approximately 2500 torr•cm, the effects are likely to be observable even above 50 mJ/cm^2.

Because the risetime degradation of nanosecond pulses at high fluences is not what one normally expects of a saturable absorber, we calculated some parameter-space scans with a simple model to see if a simple theory would predict such behavior. We used the Frantz-Nodvik[14] model because it can be expressed analytically in terms of parameters that have a readily apparent physical significance. In this model, the pulse intensity after passing through a saturable absorber with total small-signal loss αL and saturation energy E_{sat} is given by

$$I(t) = \frac{I_0(t)}{1 - [1 - \exp(\alpha L)] \exp[-E_0(t)/E_{sat}]} , \quad \text{(III-11)}$$

where I_0 (t) is the input pulse intensity and the integrated energy E_0 (t) is

$$E_0(t) = \int_0^t I_0(\tau) d\tau . \quad \text{(III-12)}$$

Figure III-14 shows how a Frantz-Nodvik absorber compares to an ideal saturable absorber and to a multiphoton absorber (Mix 907). Mix 907 goes into

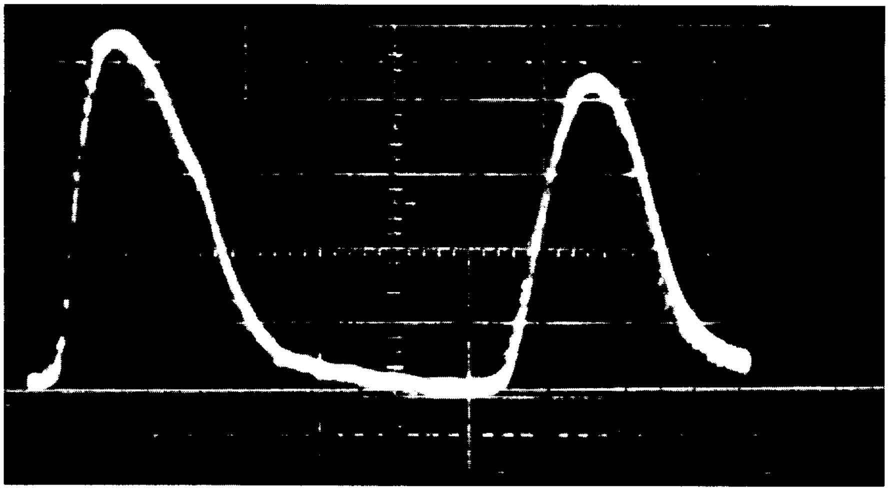

Fig. III-12. Oscilloscope trace showing input (left) and exit (right) pulse shapes for a 10.6-μm P(16) pulse traversing the gas cell when it contains 3.0 torr of SF_6. The horizontal scale is 1 ns per division.

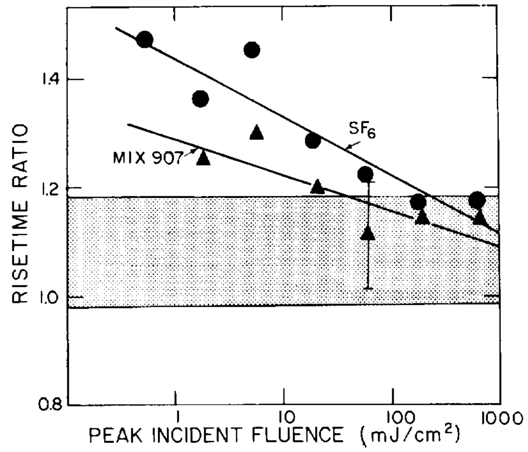

Fig. III-13. Risetime ratio of pulses traversing a gas cell. The pulse wavelength is 10.6-μm P(20).

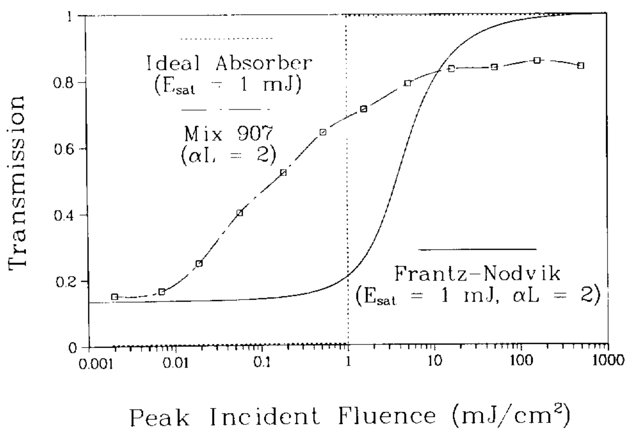

Fig. III-14. Comparison of the transmission behavior of an ideal saturable absorber with a saturation energy of 1 mJ, a Frantz-Nodvik absorber with a small-signal loss of 2 and saturation energy 1 mJ, and a multiphoton saturable absorber (Mix 907) with a small-signal loss of 2.

saturation sooner but takes three decades in fluence to saturate; even then it fails to saturate completely. Therefore, we should not expect to see detailed quantitative agreement between the simple model and the behavior of pulses passing through a multiphoton absorber.

Figure III-15 shows the triangular pulse used as input in all the calculations, whereas Figs. III-16 and III-17 show the output pulse shapes computed from Eq. (III-11). Figure III-16 indicates that the loss αL has little effect on the pulse shape by itself, because tripling αL only results in a loss of slightly more of the leading edge of the pulse. On the other hand, Fig. III-17 shows that the ratio of the incident pulse energy to the saturation

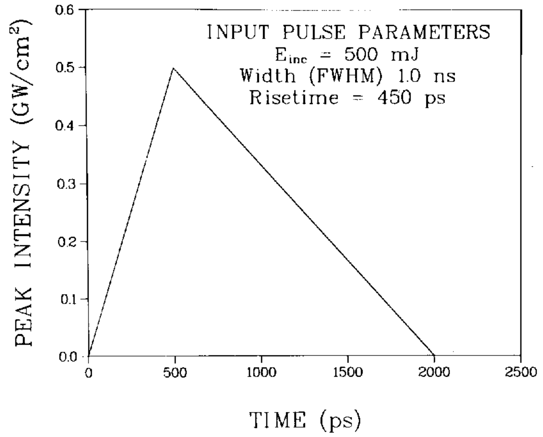

Fig. III-15. Input pulse used for Frantz-Nodvik calculations.

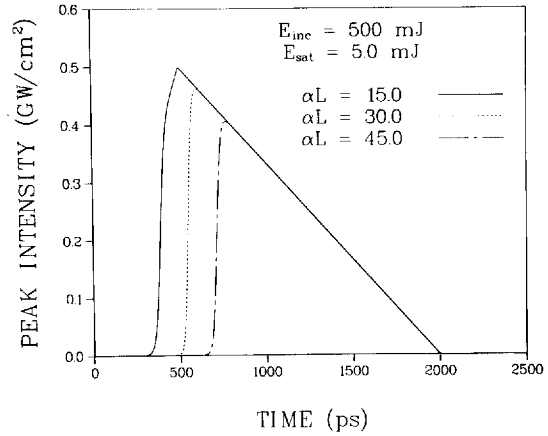

Fig. III-16. Frantz-Nodvik calculation of pulse shapes (intensity vs time) following transmission through an absorber of varying losses αL.

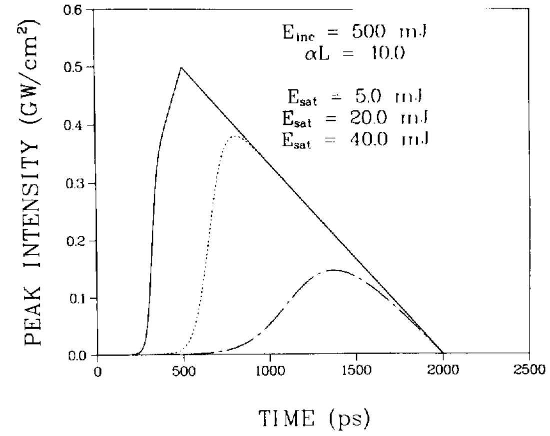

Fig. III-17. Frantz-Nodvik calculation of pulse shapes for transmission through an absorber with varying saturation energy E_{sat} for a fixed incident energy E_{inc} and loss αL.

energy is crucial to the temporal behavior of the pulse. It would appear that for $E_{sat} > 0.05\ E_{inc}$, one can expect significant risetime effects.

The situation depicted in Fig. III-17 is in the range of physical parameters encountered in operating high-gain CO_2 laser systems. Small-signal losses are high, typically about $15 \leq \alpha L \leq 30$. Using the Frantz-Nodvik model, one cannot easily say what E_{sat} is for a multiphoton absorber, but it is clearly much higher than the energy at which the absorber first begins to bleach.

An effective saturation energy of several millijoules seems a reasonable number to assign, especially in view of the nonsaturable loss that the multiphoton absorber experiences. In this regime of high small-signal loss and low saturation energy, it is evident that even a simple two-level absorption model predicts pulse-shaping effects that are qualitatively similar to experimental observations.

Figure III-18 shows one difficulty that arises when a multiwavelength pulse is propagated through a Frantz-Nodvik absorber. Here we have used a saturation energy of 5 mJ, and the input pulse is the same as that in Fig. III-15. The loss α is varied to correspond to the values of α experienced by 10.6-μm P(16), P(18), and P(20) pulses passing through 60-torr•cm SF_6. It is evident that the peak of the P(16) pulse is delayed almost 300 ps with respect to the P(20) pulse. This implies that multiwavelength pulses passing through a saturable absorber will be "stretched" by a delay time related to the attenuation. Qualitatively similar results appear in Table III-IV, where the pulse delays for P(14) and P(24) are less than those for P(20), which experiences a greater attenuation than either of the other two lines. Moreover, the stretching effect will be aggravated in any amplification process occurring after the saturable absorber. Therefore, for a given pulse energy, a multiwavelength pulse will have reduced peak power after traversing a saturable absorber when it is compared with a monochromatic pulse of the same initial energy and time history.

Self-Focusing and Defocusing in SF_2 at 10 μm

(A. V. Nowak, D. Ham)

The saturable-absorber characteristics of SF_6 have been of immense practical value in the operation of high-gain CO_2 laser amplifiers. Saturable-absorber mixes containing SF_6, for example, made it possible to operate the Helios PAMs at high gain without the danger of parasitic oscillations.

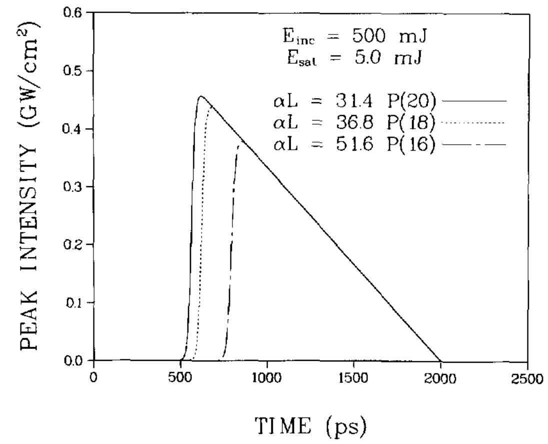

Fig. III-18. Pulse shapes for 10.6-μm laser lines of different wavelengths in the vicinity of the absorption peak in SF_6. Loss coefficients αL are shown corresponding to the actual loss in 60 torr•cm of SF_6.

The saturation behavior of Mixes 804 and 907^3 was determined in small-scale experiments with a 0.5- to 1.0-cm-diam GWTF beam of Gaussian profile. We assumed that these small-scale single-line measurements could be extrapolated directly, without modification, to the multiline, large-diameter Helios beam—an assumption that has never been properly justified. With the discovery of severe self-focusing/defocusing in pure SF_6 and SF_6-helium mixes in small-scale experiments, we cannot justify direct extrapolation to Helios conditions without addressing two questions of particular concern. Does self-focusing/defocusing in Helios degrade its performance? Does self-focusing/defocusing in the small-scale experiments yield saturation data that cannot be extrapolated to large-scale (Helios) conditions? The experiments on pure SF_6 and SF_6-helium mixes described below go to the heart of these questions. We introduce the results of self-focusing in SF_6 with the following two observations.

First, in an experimental run with an evacuated 108-cm-long gas cell, a 300-mJ/cm² pulse at 10-μm P(10) passed through the cell without incident, but after we added 1.03 torr of SF_6, the pulse was so strongly self-focused that the salt exit window was severely pitted after four or five shots and had to be replaced.

Second, in another experiment at 10-μm P(14) with an evacuated 19-cm-long gas cell, the transmitted pulse produced a smooth burn on black photographic film, but when the cell contained 9.2 torr of SF_6, the burn consisted of many dozen pinpoints and speckles that indicate beam filamentation. This is the first known observation of such an effect in a gas at 10 μm.

A collimated 1.5- to 1.7-ns pulse from a CO_2 oscillator-amplifier combination was passed through a gas cell containing SF_6 at pressures between 0.1 and 10.0 torr. The vertical spatial profile of the transmitted beam was recorded on a Molectron Corp. PLS-128 pyroelectric array of 1.0-mm interelement spacing, placed at distances from 5 to 100 cm beyond the cell's exit window. The incident beam profile was Gaussian with a nominal radius of 4 mm at e^{-1} of peak energy. Single-line output was used at 10-μm P(8), P(10), P(14), P(16), P(20), and P(28). Maximum pulse energy was 300 mJ.

Figure III-19 shows the dependence of self-focusing/defocusing upon wavelength for P(10), P(20), and P(28) lines at several SF_6 pressures in a gas cell 107.7 cm long. We measured the beam radius by locating the pyroelectric array 15 cm beyond the exit window of the gas cell. A true measure of beam-radius variation is obtained by plotting the ratio of the 1/e radii of the beam in vacuum and in SF_6.

The results shown in Fig. III-19 may be summarized as follows.

- At P(28), where the SF_6 spectrum arises exclusively from hot-band absorption caused by vibrational levels near 1000 cm^{-1}, self-defocusing occurs over the entire fluence range of the laser.
- At P(20), where the SF_6 spectrum consists of both ground-state and hot-band absorption, self-focusing occurs, followed by defocusing and self-focusing as the laser input fluence is increased.
- At P(10), where the pulse is absorbed by ground-state SF_6 molecules, only self-focusing is observed over the range of fluences produced by the laser.

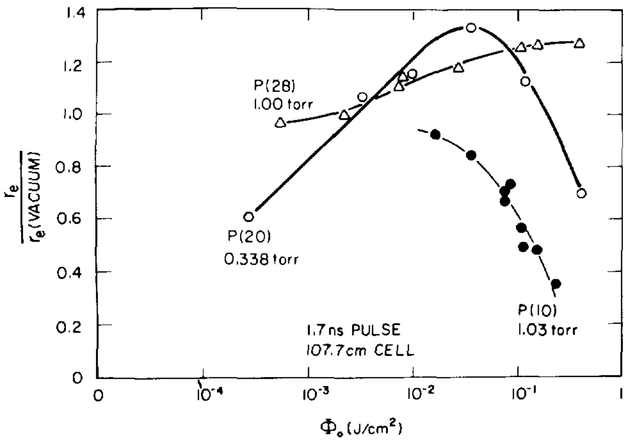

Fig. III-19. Wavelength dependence of self-focusing and defocusing in SF_6 near 10 μm for a range of input laser fluences.

In addition, self-focusing was observed only for incident pulses at the P(8), P(14), and P(16) frequencies. Thus, the modification of beam radius for a given frequency depends to some extent on the dominant absorption mechanism in SF_6 at that frequency.

Figure III-20 shows how self-focusing causes the beam at 10-μm P(10) to converge after passing through a gas cell 19 cm long, filled with 6.1 torr of SF_6. In one case the beam collapses to 40% of its original size.

Adding helium buffer gas did not destroy the self-focusing. Figure III-21 shows that the effect occurred even at a helium pressure of 1030 torr. The results with helium indicate that coherent processes do not play an important role in the self-focusing caused by SF_6.

We offer no explanation yet for the observation of self-focusing/defocusing in SF_6. We plan more comprehensive studies of beam filamentation and further experiments with the 10-μm CO_2 R-branch lines to determine how far away from resonance self-focusing persists. We will also study the dependence of self-focusing/defocusing on beam diameter, on gas cooling to depopulate the hot bands, on pulse duration, and on multiline excitation. We will study other gases, including hot CO_2 and the halocarbons in Mixes 804 and 907.

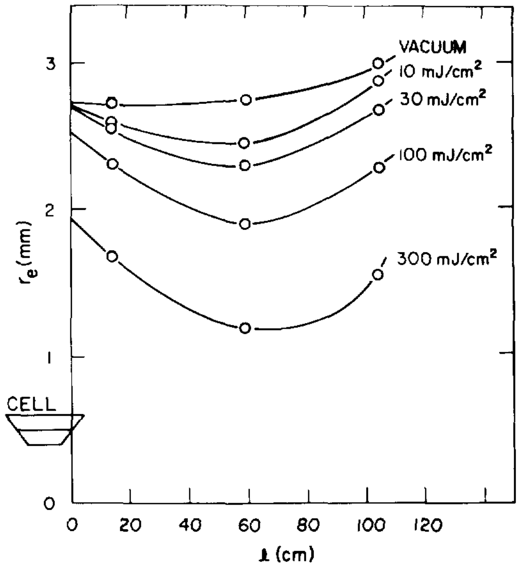

Fig. III-20. Effect of self-focusing on the transmission of a 1.5-ns, 10-μm P(10) pulse through SF_6. The pyroelectric array was located at distances of 14, 59, and 104 cm beyond the exit window of the gas cell.

Pulse Propagation in Helios Amplifiers (I. Bigio)

Rate-equation models for large CO_2 laser amplifiers predict increased energy output for multiline operation. However, because of extreme sensitivity to the very early (and at present unmeasurable) details of the input-pulse leading edge, no calculation is able to predict the effects of multiline energy extraction on output pulse shape with any accuracy.

To identify dispersion effects on multiline pulse propagation, we are sampling the Helios output with a spectrometer that uses a detector array to determine the individual rotational transitions, ranging from P(14) to P(24). The detectors may be either the integrating energy-measuring type or ultrafast pyroelectric units designed by Los Alamos. Figure III-22 shows the apparatus.

Using the krypton-ion laser, we can align the spectrometer in the Helios diagnostic gallery (Gallery West) in about 5 min. We can align the spectrometer internally by using test pulses in the Helios master-oscillator room; however, this step is required only if alignment has been disturbed.

In Helios, the oscillator is adjusted to extract energy simultaneously on several different rotational transitions. In principle, multiline short-pulse energy extraction is more efficient than single-line extraction. However, the distribution of energy among different laser frequencies also affects the temporal shape of the pulse. Temporal pulse shaping arises not only because of the frequency-dependent gain saturation characteristics of a laser amplifier, but also because of the dispersion in propagation velocities caused by the linear and nonlinear refractive indexes. Therefore, both the risetime and pulse width for a given total energy output are functions of the distribution of that energy among the various rotational lines. It is desirable to quantify this effect so that future designs, including Antares, can account for and take advantage of these effects by controlling the timing of individual lines from the oscillator.

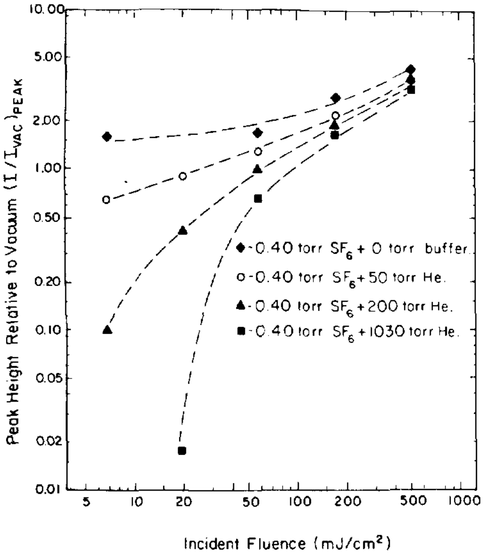

Fig. III-21. Dependence of self-focusing in SF_6 on helium buffer pressure. The laser was tuned to the 10-μm P(14) line. The array was located 75 cm beyond the exit window of the 108-cm-long gas cell, where the incident beam had a diameter of 7.3 mm at e^{-1} of its peak intensity.

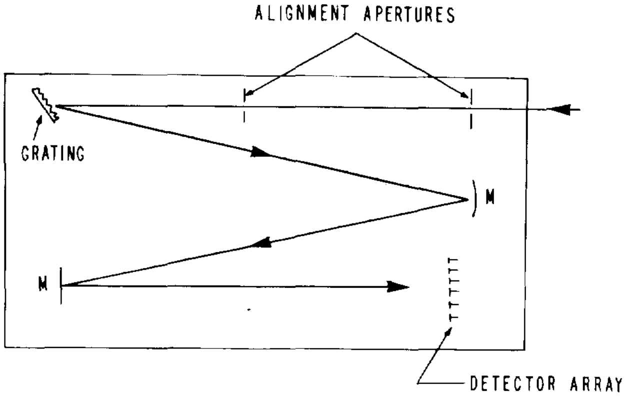

Fig. III-22. Multiline spectrometer for pulse-shape and line-content measurements in Helios.

Initial measurements of the energy-frequency distribution changes in the input and output of Helios PAMs have shown a predictable and interesting relationship. As a result of gain saturation, energy ratios between pairs of lines tend to diminish after propagation through the amplifier except when those ratios are greater than ~5:1. Then, the frequency carrying the lesser energy is diminished relative to the other after propagation through the amplifier. This latter effect may be caused by the saturable-absorber cells in the amplifier. Also, while energy-extraction efficiency from the amplifier appears to be definitely improved by two-line operation, the further improvement achieved in going from two lines to three is small, and for four, unmeasurable.

Temporal pulse-shape variations caused by propagation effects have been more difficult to measure. Figure III-23 shows two temporal pulse-shape traces made on the P(20) line with a fast pyroelectric detector and 5-GHz oscilloscope. The traces in Fig. III-23 represent two shots. In Fig. III-23(a), >80% of the total energy was in

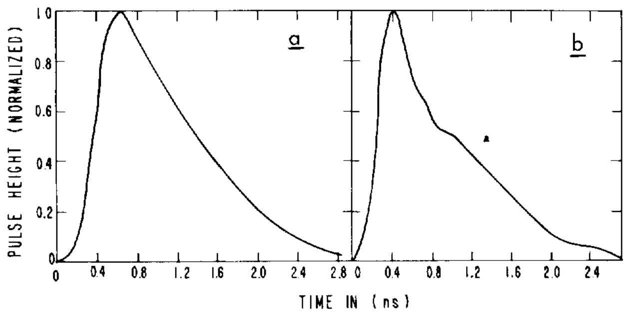

Fig. III-23. Comparison of measured Helios pulse shapes with differing line content.

the P(20) line, with only small amounts of energy in several other lines. In Fig. III-23(b), the energy was more equally distributed among the P(16), P(18), and P(20) lines. Our tentative explanation for the more sudden drop after the peak in trace [Fig. III-23(b)] is that the P(18) and P(16) components, delayed by propagation effects while the beam travels through the amplifier, make the final saturating pass about 100 to 200 ps after P(20) and rob gain from the P(20) line through Fermi resonance and rotational relaxation effects. A more complete study should allow us to quantify the phenomena with better accuracy.

Recovery Following Saturated Extraction in Electron-Beam-Controlled CO_2 Laser Amplifiers

(R. B. Gibson, G. W. York, R. Sierra)

Vibrational relaxation and repumping in a CO_2 laser amplifier can be studied by measuring gain recovery after saturated extraction with a short (~1 ns) pulse. Two experiments were done to measure recovery in a representative large-aperture electron-beam-controlled CO_2 laser amplifier. In the first experiment, we measured small-signal gain as a function of time before and up to 1000 ns after extraction. In the second experiment, we sent two saturating pulses through the amplifier 3 to 25 ns apart. Energy extracted in the second pulse indicated the amount of repumping in the time interval after initial extraction.

The prototype Antares driver amplifier, which has a 17- by 17- by 200-cm active volume, was used for both experiments. It was operated at 600 and 1200 torr with an E/N range of 1.2 to 3.8 × 10^{-16} V•cm^2. Under these conditions, the amplifier gain length ranged from 1.0 to 9.2 on the 10-μm P(20) line. Helium-free 1:4 and 1:1 N_2:CO_2 gas mixes were used.

In the first experiment, we measured gain along the axis of the amplifier. A spatially uniform 1-ns (FWHM) input pulse of 100 to 300 mJ/cm^2 was sent through the amplifier. We varied the timing of this pulse up to ±800 ns from gain peak. We used both single- and multiline pulses consisting of high-gain 10-μm P-branch lines. Pyroelectric joulemeters measured amplifier input and output energies. The gain probe was a 1-W chopped cw beam on the 10-μm R(16) line propagating on the same axis but in the opposite direction to the extracting pulse. This probe beam was detected by a spectrum analyzer and helium-cooled mercury-germanium crystal.

Maximum recovery and the time required to reach it depended more on time of extraction relative to peak gain than on any other parameter scanned. For gain (g_e) at extraction, gain recovered to ~0.75 g_e for extraction near the gain peak; to ~0.65 g_e for extraction >500 ns after peak gain; and to ~0.9 g_e for extraction >500 ns before peak gain. Maximum gain recovery occurred 350 to 550 ns after extraction for the 1:4 mix and ~25% faster for the 1:1 mix. Earliest extraction caused longest recovery times for both mixes; latest extraction produced shortest times. In all cases, most of the gain recovery took place in <20 ns, which is the temporal resolution of the detection system. Figure III-24 shows a typical case.

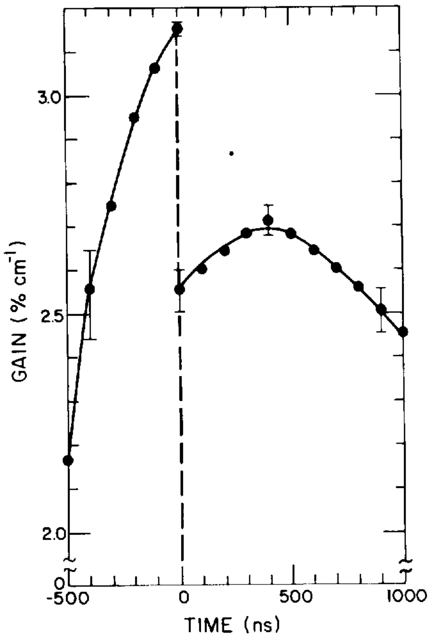

Fig. III-24. Gain vs time data for 1:4::N_2:CO_2 laser mix at 1200 torr. E/N = 2.5 × 10^{-16} v•cm^2. Saturated extraction occurs at t = 0. Note the nearly instantaneous recovery to 80% of preextraction gain.

Because practical difficulties preclude improving the temporal resolution of this technique, we used another approach to look at recovery in the first few nanoseconds after extraction. For this experiment, two spatially uniform, collinear, 1-ns pulses, separated in time by 3, 6, 10, or 25 ns, were directed along the axis of the discharge region. Line content varied from shot to shot; it was measured with a spectrum analyzer and scanning pyroelectric array at the amplifier input. Energy in each pulse was 100-200 mJ/cm^2, enough to saturate the amplifying medium throughout its length. Pyroelectric joulemeters measured total input and output energies, whereas photon drag detectors measured pulse-height ratios between the two pulses, allowing deduction of the energy in each pulse. Small-signal gain in the medium was measured as a function of time to confirm pumping conditions and timing.

At low E/N, we could extract nearly as much energy in the second pulse as in the first, even for pulse separations of 3 ns at 600 torr. Gain recovery was less complete and slower as E/N increased but was no less than 50% at $\Delta t = 10$ ns for any pumping condition. Characteristic recovery times were <5 ns for all discharge conditions studied. Energy extracted and subsequent recovery for both short and long time scales seemed independent of the number of lines in the input laser pulse. This unexpected result will be the subject of further investigation.

We conclude that most gain recovery in CO_2 is a result of fast vibrational processes, principally the rapid equilibration of the Fermi-resonant 10°0 and 02°0 levels and intramode vibrational relaxation. These processes occur in a few nanoseconds, whereas repumping the inversion by electronic collision and intermode energy transfer requires several hundred nanoseconds. These slower processes can be described quantitatively by conventional four-temperature kinetic models, but the fast processes that are clearly very important are not yet well characterized in the theory.

These observations indicate that studies of pulse propagation in high-pressure CO_2 amplifiers must take fast vibrational processes into account. Furthermore, long interpulse delays may not be necessary for practical, multiplexed CO_2 fusion driver systems. Efficiency increases of at least 50% over conventional single-pulse operation are possible using only two pulses separated by a few nanoseconds. The use of additional pulses should result in further, though diminishing, improvement in efficiency.

Line Broadening in CO_2 (E. T. Salesky)

The small-signal gain of a laser is

$$G_0 = \text{const}\ \frac{\Delta N}{\Delta \nu}$$

where ΔN is the population difference between the upper and lower laser levels and $\Delta \nu$ is the half-width of the transition. Thus the theory of spectral line shapes can be useful in understanding how energy is stored and extracted in high-power laser systems.

In the case of the CO_2 laser, energy is stored in a population inversion of vibrational states that are rotationally degenerate, with rotational substates labeled by the angular momentum quantum number J and spaced about 1.2 cm^{-1} apart. The population inversion ΔN has a J-dependence given by

$$\Delta N = N_{001}\, P(J) - \frac{\theta_J}{(\theta_J + 1)} N_{100}\, P(J + 1) ,$$

where P(J) is the occupation probability of the state with rotational quantum number J, N_ν is the population density in the vibrational state ν, and θ_J is the rotational degeneracy factor (2J + 1). The inversion ΔN can usually be determined by using our CO_2 kinetics code because the transition rates for various vibrational energy channels are reasonably well known and because the J-dependence of the occupation probabilities can be modeled adequately.

Therefore, the uncertainties in calculating the variation in gain from one rotational line to another arise primarily because of uncertainties in our knowledge of the line width. These uncertainties appear to be of two main types:

(1) the probable J-dependence of $\Delta \nu$, and

(2) higher level transitions within $\Delta \nu$ of lower laser transition frequencies that increase the effective gain.

The best known example of item (2) is the hot-band contribution to the P(20) 001-100 transition caused by the R(23) 011-110 transition for which the lines overlap almost exactly.

We know that the energy broadening of rotational lines caused by molecular collisions is approximately 0.1 cm^{-1}/atm for CO_2 lasers. However, precise specification of the line width depends not only on the pressure, but also on the character of the collision partners in the laser gas. For most CO_2 lasers, the collision partners include the triatomic CO_2 molecule itself, the diatomic molecule N_2, and the noble gas helium. Unraveling the J-dependence of the collisional perturbations in such a complicated mix is difficult. In the past, the 10-μm P(20) transition has been modeled successfully; however, this success indicates only that ΔN is calculated well, because $\Delta \nu$ is known for this particular transition for the various perturbing molecular species.

In general, past treatments of CO_2 broadening showed neither the consistency nor the detail we require. The "full" quantum mechanical treatments have been limited to diatom-atom systems because of computational expense; even then too many parameters were varied to allow a consistent treatment for different conditions. The treatment of CO_2-N_2 and CO_2-CO_2 collisions is not now considered feasible with these methods, and the quantum mechanical calculation of even the CO_2-He collisional effects on line width would be extremely difficult and time consuming. Furthermore, the temperature dependence of the line shape is usually neglected, again because of computational expense.

We have developed a semiclassical theory of line broadening[15] that is computationally simple enough to include collisional perturbations by diatomic and symmetric-top molecules and temperature effects. Before testing the code, a lengthy literature search was required, because data on broadening of CO_2 by helium and N_2 are scarce. Thus, other systems involving these molecules had to be modeled to establish a consistent set of parameters.

As a first check on the semiclassical theory of line broadening for short-range interacting systems, we considered the broadening of lines in HCl perturbed by argon. This system was well chosen for study because of the substantial body of available data and because it has frequently been the subject of full quantum mechanical calculations. In all cases good agreement with experimental data was obtained.

CO_2 self-broadening has also been calculated by using our model. The results are presented in Table III-V along with some experimental data.[16] Agreement is good and indicates that the semiclassical theory is still valid even for the short-range forces that dominate CO_2-CO_2 collisions. However, the problem of temperature dependence has not yet been addressed.

CO_2 broadening by noble gases cannot be calculated accurately without including higher order contributions to the interaction arising from the weak intermolecular potential.

TABLE III-V. Half-Widths for CO_2 Self-Broadening

Initial State (J)	Line Width $\Delta \nu$ (cm^{-1})	
	Experiment[a]	Calculation
8	0.125 ± 0.006	0.109
10	0.121 ± 0.007	0.109
12	0.113 ± 0.007	0.110
14	0.119 ± 0.007	0.111
16	0.113 ± 0.005	0.112
18	0.109 ± 0.004	0.112
20	0.108 ± 0.006	0.112
22	0.109 ± 0.004	0.112
24	0.105 ± 0.004	0.111
26	0.105 ± 0.005	0.109
28	0.101 ± 0.003	0.107
30	0.101 ± 0.003	0.104
32	0.098 ± 0.006	0.101
34	0.097 ± 0.004	0.097
36	0.093 ± 0.006	0.093
38	0.084 ± 0.004	0.088
40	0.085 ± 0.003	0.084

[a] Data are from Ref. 16.

In applying our semiclassical treatment to the problem, we have concentrated on the CO_2-argon system because good experimental data[17] exist for comparison and because we expect the semiclassical scattering approach to be valid for this system. The main problem is determining the correct interaction potential.

Leavitt[18] indicates that the most important contributions to the interaction are due to the long-range dispersion interactions that behave as R^{-6}, where R is the radial separation between molecules. This interaction yields a b^{-10} dependence (b is the impact parameter) for the second-order matrix element in the line-width calculation (see Ref. 19). Furthermore, the induction interaction caused by the permanent quadrupole moment of CO_2 behaves as R^{-7} producing a b^{-12} in the matrix elements, because the cross terms vanish as a result of symmetries of spherical tensors.

Calculations with these terms are presented in Table III-VI, column A. The R^{-7} term improves the agreement with the data, but the agreement is still poor. A

TABLE III-VI. Raman Line Widths: CO_2 Broadened by Argon[a]

(J)	Data (Ref. 15)	Col. A	Col. B
4	0.075	0.054	0.071
6	0.078	0.053	0.069
8	0.076	0.051	0.066
10	0.074	0.049	0.064
12	0.073	0.047	0.061
14	0.069	0.045	0.058
16	0.069	0.043	0.055
18	0.069	0.041	0.053
20	0.065	0.039	0.050
22	0.064	0.038	0.048
24	0.063	0.036	0.046
26	0.062	0.035	0.044
28	0.059	0.033	0.043
30	0.060	0.032	0.041
32	0.059	0.031	0.039
34	0.059	0.030	0.038
36	0.058	0.029	0.037
38	0.058	0.028	0.035
40	0.056	0.027	0.034

[a]Values are in cm^{-1}/atm.

substantial improvement can be obtained by employing Leavitt's formalism[18] to calculate the next higher interaction, the "quadrupole-induced-quadrupole" moment, which behaves as R^{-8}. This is not normally considered in the literature because its second-order matrix element behaves as b^{-14} and is thus quite insignificant. However, because of its spherical tensor characteristics, there is a cross product between this term and the induction term resulting in a matrix element dependence of b^{-12} that is of the same order as the second-order matrix contribution of the R^{-7} interaction. Using this new term, we obtained the results in column B. Clearly, a 20 to 30% improvement has been realized; more importantly, agreement at low J is good when the new interaction term is added. However, there remain significant discrepancies between theory and experiment at high J. Similar results were obtained by Smith et al.,[19] who used a different long-range interaction model. They decided to incorporate short-range contributions to the potential, and we are now examining this possibility.

The new quadrupole-induced-quadrupole interaction term included in our calculations is given below. Reference 18 provides an explanation of the notation. Once a consistent model is obtained, the temperature dependence of the line widths can be studied.

$$V\theta_1\alpha_2\theta_1 = -\frac{21}{2}\frac{\theta_1^2\alpha_2}{R^8}\left[7\{00|0\} + 8\{20|2\} + 6\{40|4\}\right] \cdot$$

Second-order matrix element (cross-term with R-6 term)

$$S_i^{2\ \text{outer}} = \frac{315\ \pi^2}{512}\ (\mu_1^2\alpha_2)\left[\mu_1^2\alpha_2 + \alpha_1\gamma_1\mu_2^2 + \frac{3}{2}\bar{U}\ \alpha_2\gamma_2\alpha_1\right]$$

$$\sum_i\ <J_i(0)2(0)|J_i^1(0)>^2\ \{\ g(k_8) + i\ Ig_8(k)\} \quad ,$$

where

$$g_8(k) = \frac{1}{450}\, e^{-2k}\left[2k^7 + 18k^6 + 85k^5 + 264k^4 + 576k^3 + 888k^2 + 900k + 450\right] .$$

$Ig_8(k)$ is the Hilbert transform of $g_8(k)$.

Pulse Propagation in Hot CO_2 Absorber (J. Goldstein, S. Czuchlewski, A. Nowak)

We have discussed the absorption of 1.6-ns laser pulses by hot (673 K) CO_2 gas previously.[20] The absorption saturated when the fluence of the incident laser pulses exceeded ~20 mJ/cm^2 (Figs. III-25 and III-26). We demonstrated that the triatomic hot CO_2 molecule saturates almost like a two-level system, in marked contrast to the observed behavior of heavier polyatomic molecules, such as SF_6. By using a fully coherent computer model,[21-23] we have completed a detailed analysis of laser pulse propagation through the hot CO_2 *absorbing* medium. This analysis complements and extends related studies[23,24] on pulse propagation in CO_2 *amplifying* media.

In the past, direct comparisons of experiments with theory were difficult because the characteristics of the amplifying or absorbing medium and the temporal and spatial profiles of the laser pulses were not well defined. In contrast, our latest experiments were performed under *carefully controlled* thermal and optical conditions that permit direct comparison. The calculations reveal the importance of hot-band[7] effects on the P(20) saturation curve.

Figure III-25 shows the measured transmission of hot CO_2 for short 10-μm P(20) laser pulses as a function of

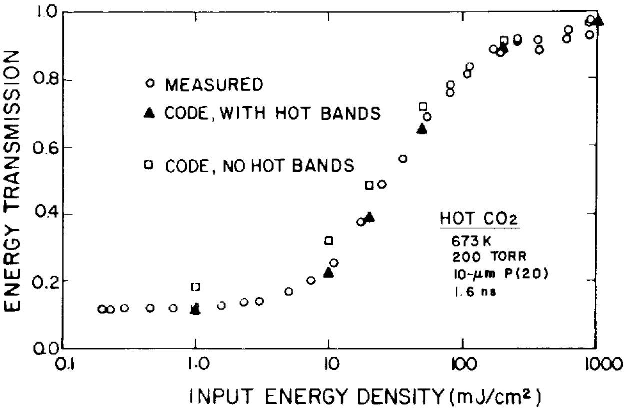

Fig. III-25. Transmission of 1.6-ns, 10-μm P(20) laser pulses through 118 cm of hot CO_2 at 200 torr; the spatial profile of the input pulse is flat.[20] Circles, measured data; squares, theory without hot-band contribution; and triangles, theory with hot-band effects.

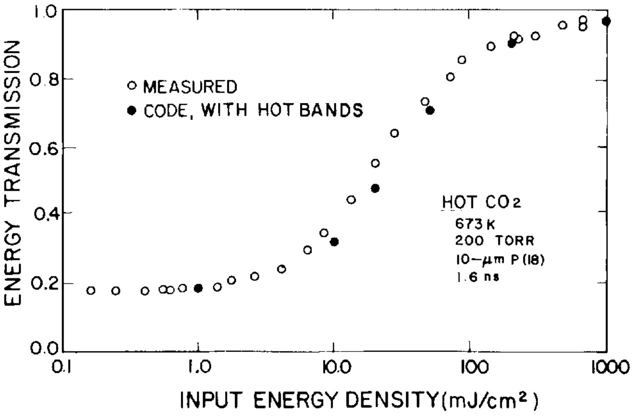

Fig. III-26. Transmission for 10-μm P(18) laser pulses. Other parameters are the same as in Fig. III-25.

input fluence; it also shows two sets of theoretical predictions. The squares indicate the calculated transmission when hot-band contributions are ignored; the triangles represent the theoretical values when hot bands are included. We did not use adjustable parameters in the coherent-propagation density-matrix calculations.[21] Spectroscopic data provided the small-signal absorption coefficient, including hot-band effects.[7] We used the measured temporal shape of an input pulse with nearly constant transverse spatial intensity in the calculations. The results (Fig. III-25) clearly indicate the importance of hot bands, which contribute ~21.5% of the P(20) absorption coefficient under these conditions. Without the hot-band contribution, no agreement between theory and experiment is possible.

Figure III-26 shows similar experimental and theoretical saturation data for P(18) laser pulses. Hot-band contributions at this wavelength are almost negligible (~1%).

Figure III-27 shows that measured small-signal transmissions of the very weak P(18) 1.6-ns pulses through the cell at various pressures are in good agreement with theoretical results. For cw or long pulses, the theoretical small-signal transmissions of the medium vary only slightly with pressure. At 50 torr the measured short-pulse transmission is almost 2.5 times that of the cw small-signal loss. These results demonstrate the effects of varying the ratio of the pulse bandwidth to that of the resonant medium.

Coherent theory also predicts a dramatic nonmonotonic variation in the temporal width of the output pulse with increasing input pulse fluence. These predictions, which depend sensitively on the exact input pulse shape, will be tested in a future experiment.

Pulse Propagation in CO_2 Laser Amplifiers

(S. J. Czuchlewski)

The general coherent density-matrix theory for pulse propagation in a laser gain medium has been well developed for several years.[22,23,25-28] However, few calculations have dealt with short-pulse (≤1 ns) propagation in real CO_2 laser systems. It is well known that the

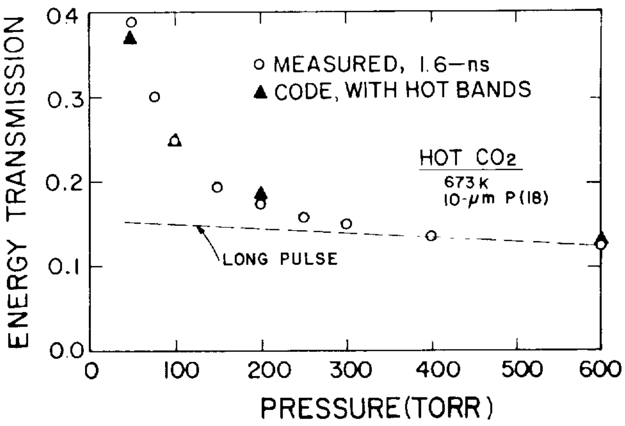

Fig. III-27. Small-signal transmission of weak 1.6-ns, P(18) laser pulses through 118 cm of hot (673 K) CO_2 at various pressures. The dashed line is the theoretical transmission for long (or cw) pulses.

total output energy of an amplifier is relatively insensitive to details of the coherent theory. However, pulse shape and peak power depend on both gross and subtle coherent effects, particularly if risetime and total pulse width are on the order of the dipole dephasing time T_2 or of the rotational relaxation time T_1. The dipole dephasing time T_2 is also a measure of the pressure broadening in the laser gas.

Detailed experimental results have been compared with theoretical predictions in only two studies. Volkin found good agreement with theory for propagation of 1.8-ns pulses in the Los Alamos 1800-torr, 0.5-TW Gemini laser system.[23] However, because the pulse length was much greater than the T_2 and T_1 times (23 and 46 ps, respectively), this investigation did not provide a critical test of coherent aspects of the theory. In another experiment,[24] we found an apparent discrepancy between the propagation of 600-ps pulses observed in a 600-torr amplifier and that predicted by theory. Because the T_2 and T_1 times (83 and 171 ps, respectively) are longer for a lower pressure amplifier and because shorter pulses with faster risetimes (200 ps) were used, this experiment was expected to be more sensitive to coherent effects than that reported by Volkin.[23] However, modeling of the experiment was complicated because the pulse traverses the gain medium three times. We plan to continue these experiments under more carefully controlled conditions that will allow unambiguous comparisons between theory and experiment.

As a prelude to these experiments, we are using the computer code developed by Feldman[22,26] to investigate the predictions of a coherent theory under a variety of conditions that will elucidate the effects of various properties of the medium on pulse propagation, with emphasis on those conditions that can be readily tested in the laboratory. For example, in the small-signal regime, this code indicates that the response time of the medium limits the risetime of an output pulse to $\sim g_0LT_2$, where g_0L is the gain-length product of the amplifier. This agrees with an earlier analytical calculation (Ref. 29); however, even this very fundamental phenomenon has not been confirmed experimentally. Verification should be straightforward with the laser system described in Ref. 24.

For high-intensity input pulses, the coherent model predicts output pulses with the general shape shown in Fig. III-28. The width of the sharp spike is $\sim T_2$, and the peak intensity is $\sim g_0LE_sT_2$, where E_s is $\hbar\omega/2\sigma$, the saturation energy for a pair of rotational sublevels. The long decay time of the output pulse depends on T_1, which determines the rotational repumping time. According to the coherent model, the situation shown in Fig. III-28 represents the maximum peak power that can be extracted from an amplifier under single-pulse conditions.

If the amplifier is driven more heavily into saturation, self-induced transparency (or optical nutation) develops, leading to outputs of the type shown in Fig. III-29. This figure has several notable features. The risetime is considerably shorter than T_2, the first minimum is significantly below the intensity of the input pulse, and the period of the oscillations is constant.

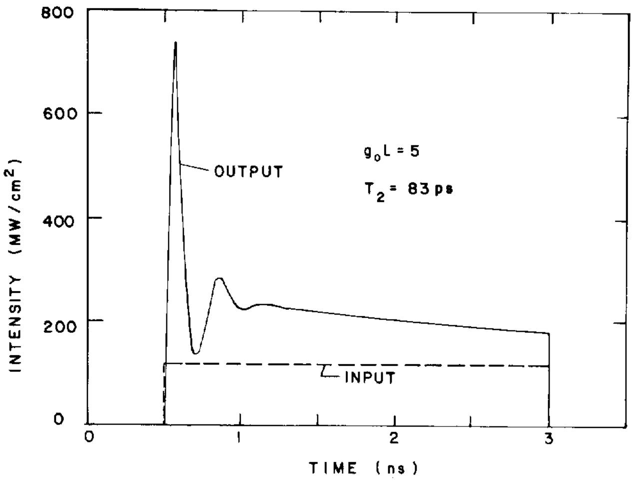

Fig. III-28. Coherent calculation of maximum peak power extractable in a single pulse.

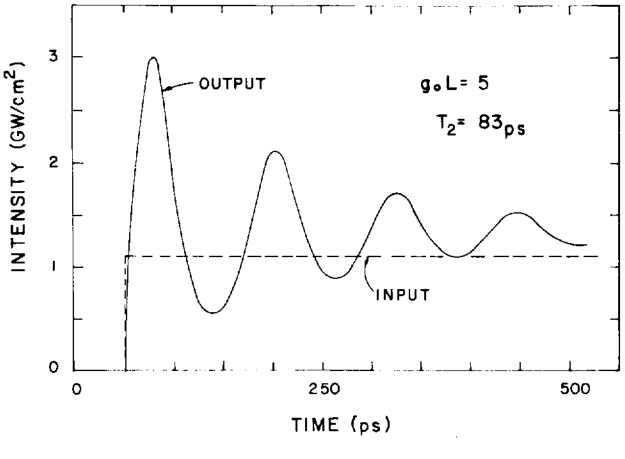

Fig. III-29. Output intensity vs time for a step-function saturating input pulse.

The present theoretical model ignores magnetic sublevels in the rotational states of the CO_2 molecules.[27] We do not know whether these states will diminish the coherent ringing that appears in Fig. III-29 or what the resulting shape of the amplified pulse would be. We plan to look for these effects experimentally in a low-pressure CO_2 gain medium in which T_2 and the period of the oscillations in Fig. III-29 are long enough to be measured conveniently. We will also investigate effects of T_2, T_1, and multiline operation on amplified pulse shapes.

ADVANCED CO_2 LASER DEVELOPMENT

Introduction

We are continuing a variety of studies to develop technology for upgrading Gemini and Helios and for possible application to Antares, including CO_2 laser kinetics, deformable optics, saturable absorbers, plasma shutters, phase conjugation, and damage to optical components induced by a laser pulse. In each of these areas, basic physics studies and parameter-space mapping can contribute both to fundamental understanding of the phenomena and to engineering design concepts. During 1980, work on gas and solid-state isolators and plasma shutters, multishot laser damage studies on copper mirrors, and the demonstration of high gains in a germanium phase conjugator were especially significant.

Optimization of Parasitic Isolators in Laser Fusion Systems (J. F. Figueira, C. R. Phipps, R. F. Haglund)

The selective use of nonlinear saturable absorbers distributed throughout a high-gain amplifier chain is an effective means of controlling unwanted parasitic oscillations in CO_2 fusion lasers. Much work has been done to characterize these absorbers. Below, we discuss the extension of these specific techniques and develop a useful figure of merit (FOM) to describe the performance of this class of parasitics isolators in specific laser geometries.

The transmission T(I) of a nonlinear saturable absorber is a function of the incident laser power (energy). At a given intensity (fluence) level, an effective absorption coefficient can be defined by

$$\alpha(I) = \frac{\ell n\, T(I)}{\ell} \qquad \text{(III-13)}$$

for a material of length ℓ irradiated at a laser intensity I. If the small-signal loss coefficient is denoted by α_0, then a FOM for the saturable absorber can be defined by

$$\mathrm{FOM} = \frac{\alpha_0}{\alpha} > 1 \ . \qquad \text{(III-14)}$$

With these definitions we can express energy absorbed by a given material as

$$I_{abs} = I_0 - I_t = I_0(1 - e^{-a\ell}) \ .$$

Then, in the high-field limit using Eq. (III-14), we find

$$I_{abs} = \frac{\alpha_0 \ell}{\mathrm{FOM}} I_0 \ . \qquad \text{(III-15)}$$

In all applications of saturable absorbers to the stabilization of high-gain laser fusion systems, one attempts to optimize the overall performance of the laser-isolator system by minimizing the laser energy absorbed by the isolator. As can be seen above, minimization of I_{abs} implies the maximization of the FOM of the saturable absorber.

The functional dependence of the FOM on input intensity is related to the physical parameters of the saturable absorber. To illustrate the usefulness of this FOM definition, we consider the case of an intense beam of light propagating through a homogeneously broadened saturable absorber whose characteristic recovery time is short compared to the length of the interacting laser pulse (a Rigrod-type absorber). Under these conditions the incremental change in intensity of the incident pulse in a distance dz in the absorber can be written as

$$\frac{dI}{dz} = -\frac{\alpha_0}{1 + I/I_s} - \alpha_{NS} I \ . \qquad \text{(III-16)}$$

In this expression, α_0 is the small-signal loss coefficient, I_s is the saturation intensity for the absorber, α_{NS} is the nonsaturable loss coefficient for the absorber, and I is the local laser intensity. In the limit of high intensities, $I \gg I_s$, this expression can be solved for an input fluence I_0 to give

$$\mathrm{FOM} = \frac{\alpha_0 \ell}{\ell n(I/I_0)}$$

$$= \frac{\alpha_0 \ell}{\ell n[\alpha_0/\alpha_{NS}\,(I_s/I_0)\ (e^{-aNS\ell} - 1) + e^{-aNS\ell})} \cdot \qquad \text{(III-17)}$$

In the high-field limit, we find several special cases. For $\alpha_{NS} = 0$, the FOM $= I_0/I_s$ and the energy absorbed by the isolator is given by

$$I_{abs}(\alpha_{NS} \neq 0)\, d = \alpha_0 \ell I_s \qquad \text{(III-18)}$$

and is a constant, independent of input intensity. For $\alpha_{NS} \neq 0$, we find FOM $= \alpha_0/\alpha_{NS}$, limited to a maximum value that depends on the parameters of the material. In this limit the energy absorbed by the isolator is given by

$$I_{abs}(\alpha_{NS} \neq 0) = \alpha_{NS} \ell I_0 \qquad \text{(III-19)}$$

and increases in direct proportion to the input intensity.

For the general case of intermediate values of I_0, Eq. (III-16) must be numerically integrated in space and time to obtain the FOM. Figure III-30 shows a typical calculation for a Rigrod absorber with homogeneously broadened absorption and no nonsaturable loss ($\alpha_{NS} = 0$). As can be seen, the nonsaturable loss has a profound effect on the efficiency of the saturable-absorber performance.

For homogeneously broadened absorbers, FOMs in excess of 50 are easily obtained for input fluences of $10^2 \times I_s$.

Figure III-30 also shows that variation of the value of $\alpha_0 \ell$ from 3 to 9 has only a minor effect on the dependence of the FOM on input intensity. This independence of the FOM from the small-signal loss is only true for the case for which $\alpha_{NS} = 0$.

In Fig. III-31 we calculate the FOM for a Frantz-Nodvik absorber that has recovery times that are long compared with the laser pulse duration. Here, for high fluences we see the limiting behavior described previously by Eq. (III-19).

For use in a broadened CO_2 laser fusion system, a parasitic isolator must have the proper spectral absorption characteristics to provide loss for all laser wavelengths having excess gain. In addition, the isolator must saturate efficiently, as described above, so that its use does not represent an unacceptable energy loss to the output laser beam. Many materials possess saturable absorptions in the infrared. Table III-VII lists several characteristic materials.

The FOMs range from 5 for inhomogeneously broadened germanium, through 10-20 for multiphoton absorbers (SF_6 and Mix 907), to 30-40 for two-level homogeneously broadened CO_2 and KCl doped with ReO_4^-. Practical considerations against heating CO_2 to 723 K (450°C) in large cells and poor spectral match of

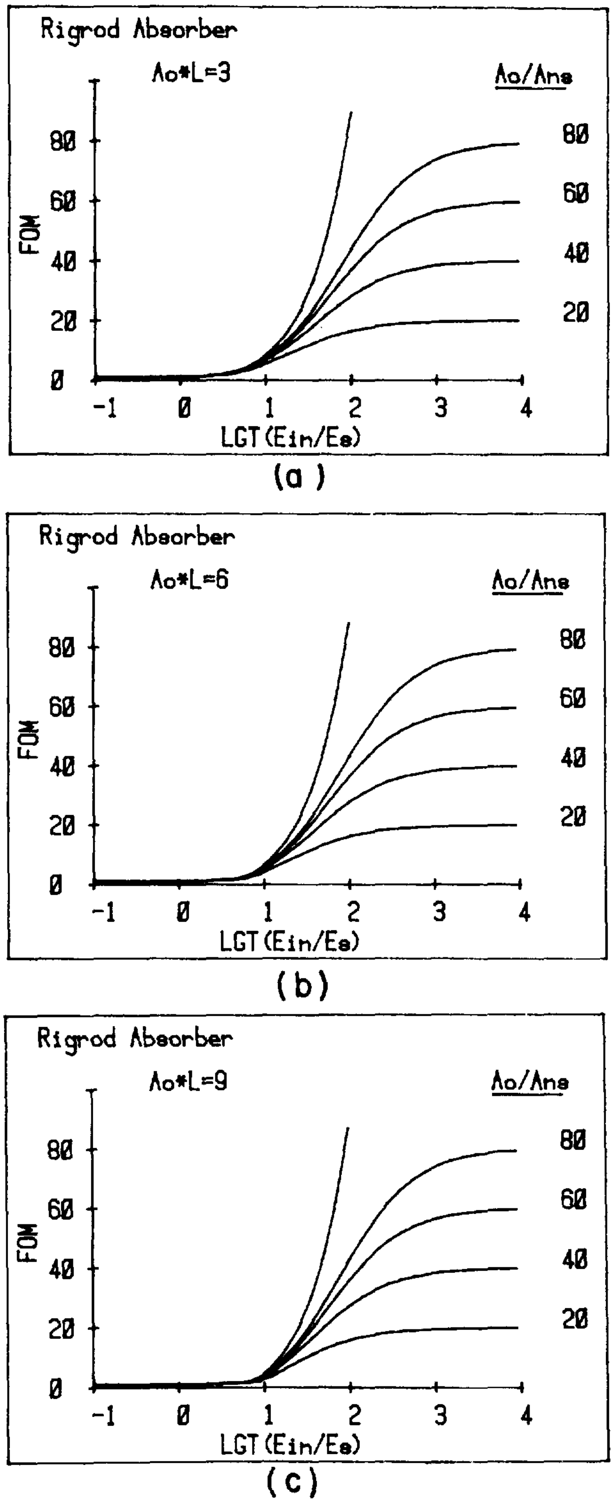

(a)

(b)

(c)

Fig. III-30. Model calculations of the FOM of a Rigrod absorber for a homogeneously broadened absorber. Calculations for $\alpha_0 L$ of 3, 6, and 9 are shown.

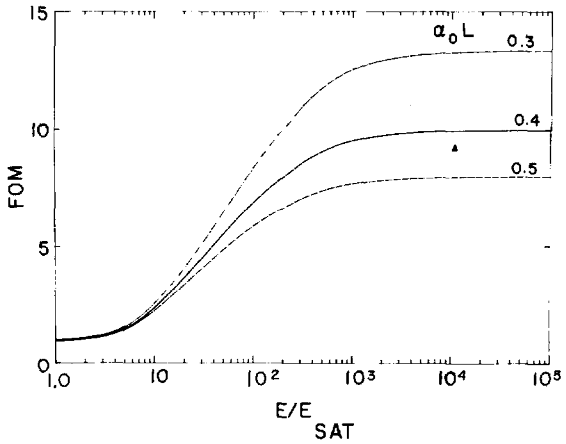

Fig. III-31. Model calculations for a Frantz-Nodvik absorber with a nonsaturable loss and α_0L of 4. A nonsaturable loss of 0.35 represents the practical case of Mix 907.

TABLE III-VII. Saturable-Absorber FOMs

Material	Bandwidth	I_0 (1 ns)	FOM
SF_6	20 cm^{-1}	200 mJ/cm^2	23
Mix 907	9 μm + 10 μm	200 mJ/cm^2	12
Ge	9-11 μm	200 MW/cm^2	5
CO_2 (Hot)	9-11 μm	500 MW/cm^2	40
$KCl:ReO_4^-$	1 cm^{-1}	500 MW/cm^2	30

the currently available doped alkali halides dictate the use of polyatomic gas mixtures. These mixtures are typified by Mix 907, which contains SF_6 plus a variety of other fluorinated hydrocarbons.* Figure III-32 shows a typical measured FOM curve for Mix 907 for a variety of small-signal loss lengths ranging from 2 to 6. The FOM tends to a limiting value of 12, implying that $\alpha_{NS} = 0.08\ \alpha_0$. This value is consistent with the known nonsaturable losses due to the other components in the mixture, including the multiphoton absorption of the SF_6 itself, which accounts for about one-third of the nonsaturable loss. Thus, for practical isolators currently available, FOMs of 12 can be expected.

The optimization of an isolated laser fusion system requires consideration of its detailed architecture to determine the proper staging of the isolator. The system shown in the insert of Fig. III-33 illustrates this behavior.

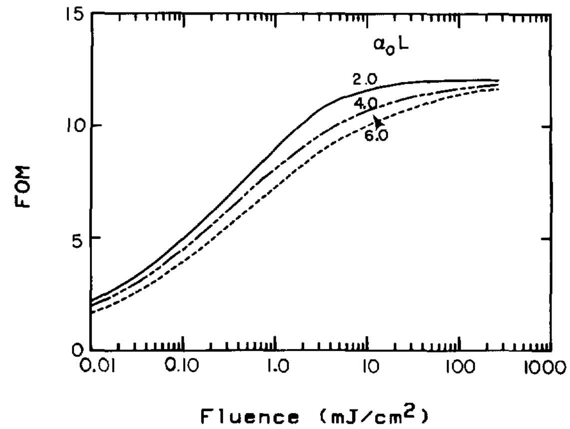

Fig. III-32. Measured FOM of Mix 907 for small-signal loss lengths of 2, 4, and 6 at P(20)-10 μm with 1.7-ns pulses of Gaussian space-time radiation. Cell length is 119 cm; gas pressures are 3, 6, and 9 torr, respectively.

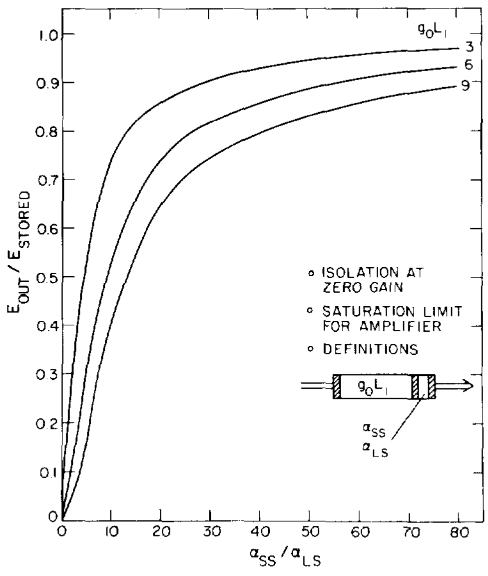

Fig. III-33. Single-pass amplifier efficiency for isolation of zero gain for various amplifier gain lengths. Isolator is located at output of amplifier.

A laser amplifier is operated in single pass at the saturation limit. To stabilize the system against unwanted parasitic oscillations, we place a saturable absorber at the output of the amplifier and adjust the loss in the absorber so that the amplifier small-signal gain is numerically equal to the absorber loss. This is isolation at zero gain. Under these conditions we have

$$g_0L_1 - \alpha_{ss}L_2 = 0 \ , \qquad \text{(III-20)}$$

---

*Mix 907 is a mixture of SF_6, C_4F_8, FC-115, FC-152A, FC-12, and FC-1113 in volume proportions of 0.82%, 2.27%, 6.64%, 9.09%, 13.63%, 25.0%, and 42.6%, respectively.

where g_0L_1 is the amplifier gain length ($G = e^{g_0L_1}$) and $\alpha_{SS}L_2$ is the isolator loss length. If E_s is saturation fluence for the amplifier, then the output of the amplifier in the absence of any isolator is

$$E_{stored} = E_s\, g_0L_1 + E_{in} .$$

With an isolator, it is

$$E_{out} = (E_s g_0 L_1 + E_{in})\, e^{-\alpha_{LS}L_2} .$$

By using Eq. (III-14), we can calculate an effective amplifier efficiency

$$\frac{E_{out}}{E_{stored}} = e^{-\alpha_0 L_2/FOM} . \tag{III-21}$$

For constant efficiency α_0L_2/FOM is constant; higher gain amplifiers required increasingly more efficient isolators. Figure III-33 graphs Eq. (III-21): the laser efficiency (E_{out}/E_{stored}) is plotted for various values of the FOM (α_{SS}/α_{LS}) for different values of the g_0L, ranging from 3 to 9. For efficiencies of 90% or higher, FOMs between 25 and 100 are required. For more optimal staging with multipass lasers, proper design can reduce the number of required FOMs to 10-20.

Pressure, Pulse Length, and Frequency Dependence of Mix 907 Transmission (R. F. Haglund, A. V. Nowak)

Extrapolation of saturable-absorber technology to new situations (for example, Antares) requires a fundamental understanding of the optical properties of the mixes as functions of pressure, pulse length, and incident pulse frequency. It is particularly important to know how the nonsaturating components of the gas mix affect the behavior of SF_6, the vital ingredient in all the saturable absorbers used in CO_2 lasers.

As a reference point for our investigations, we used the transmission curves shown in Fig. III-34. These data, and the data on Mix 907, were obtained on the GWTF System 1 laser, which delivers a 1.6-ns FWHM pulse with a 400-ps risetime at a peak incident fluence of ~750 mJ/cm^2, or an 80-ns pulse of several joules. The spatial profile of the pulse is Gaussian, with a diameter of ~0.65 cm at 1/e of peak intensity.

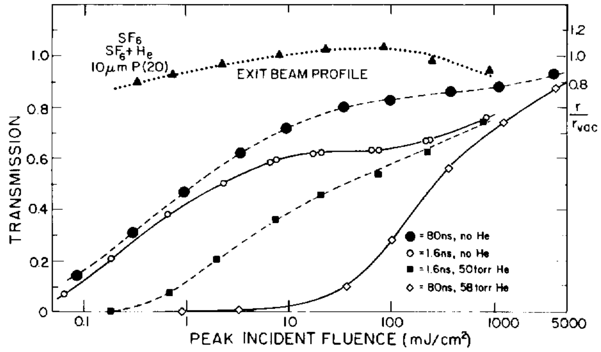

Fig. III-34. Transmission of 10-μm P(20) pulses through SF_6 and SF_6 buffered by He. Cell length was 19 cm and SF_6 pressure was 1.02 torr for all four transmission curves. The dotted curve shows the profile (referred to the right-hand axis) of the transmitted 1.6-ns pulse through the unbuffered SF_6 at a point 18 cm beyond the cell, where r_{vac} is the radius with the cell evacuated.

Figure III-35 shows a large-signal transmission curve for Mix 907. The small-signal transmission measured with the pulsed laser is in good agreement with the sum of the small-signal absorptions of the mix components and with values measured on an ir grating spectrophotometer. When we take into account the unsaturated small-signal losses of the other components at this wavelength, the large-signal transmission agrees well with the value calculated from the saturated losses of SF_6 and FC-152a, the two saturable components of the mixture.

In Fig. III-36, we show the measured transmission curves for short- and long-pulse transmission in 6 torr of Mix 907. A comparison with Fig. III-34 immediately shows that the transmission curves do not behave like those of low-pressure SF_6, which the long pulse saturates more readily than the short pulse. Instead, we find a behavior more like that of buffered SF_6, which saturates more slowly for the longer pulse than for the shorter one.

This behavior may be understood from a check of the collision times for these gases. At a temperature of 300 K, the collision frequency of SF_6 and FC-152a with the other constituents of Mix 907 is[30]

$$\nu = \frac{3.6\sigma^2}{\sqrt{M}}\ \text{MHz} \cdot \text{torr}^{-1} ,$$

where M is the atomic mass number and σ is the Lennard-Jones diameter. At 6 torr, there is a collision approximately every 17 ns for SF_6 and FC-152a. Alternatively, using the fast SF_6-SF_6 relaxation rate of ~35 ns torr (possibly rotational) observed by Fuss and Hartman[31] and Moulton et al.,[32] we calculated a relaxation time of ~6 ns assuming the gas was entirely SF_6 at 6 torr. This value is most likely an upper boundary to the relaxation time because the majority of gases in Mix 907 are lighter than SF_6 and also polar. This means that

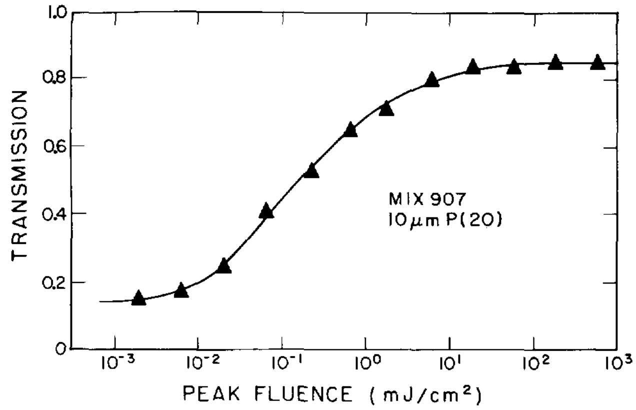

Fig. III-35. Saturation curve for Mix 907 measured with a 1.6-ns, 10.6-μm P(20) pulse having a 1/e diameter of 6.8 mm. The pressure of Mix 907 in the gas cell was 6 torr; cell length was 108 cm.

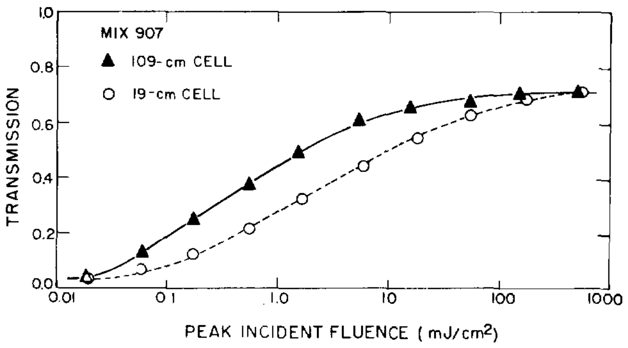

Fig. III-37. Saturation curves for Mix 907 in two different gas cells with different pressures but nearly equal pressure-length products. The pressure of Mix 907 in the long cell was 6 torr; in the short cell it was 31.5 torr. The laser pulse in both cases was 1.6 ns FWHM at the 10.6-μm P(20) wavelength.

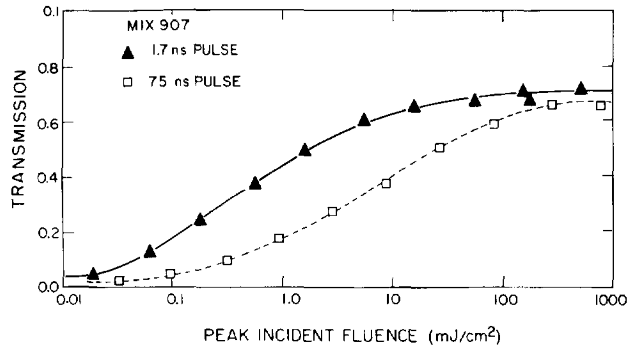

Fig. III-36. Transmission curves for short (1.7-ns) and long (75-ns) pulses at 10-μm P(20).

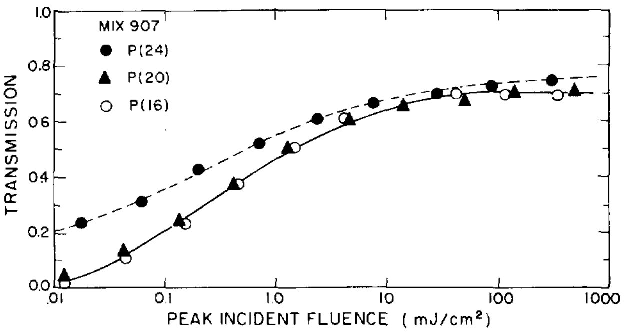

Fig. III-38. Saturation curves for Mix 907 for three different wavelengths in the 10.6-μm P-branch. The gas sample was contained in a 109-cm-long cell at a pressure of 6 torr. The laser pulse length in each case was 1.6 ns FWHM, and the beam spatial profile was the same for all wavelengths.

many relaxing collisions occur during the passage of the long pulse, whereas the short pulse is transmitted with few collisions. Thus the gas is more difficult to saturate with the long pulse than the short.

A similar explanation may be involved for the curves shown in Fig. III-37, where the short-pulse transmission for two cell lengths with nearly the same pressure-length product differs significantly. At 6 torr, the mean time between collisions is ~17 ns, whereas at 31.5 torr, it is 3.2 ns. Again, using the fast SF_6-SF_6 relaxation rate, the relaxation time has an upper limit of 1.1 ns at 31.5 torr. Thus, the transmission at 31.5 torr is collision influenced and the gas requires more energy to saturate.

Figure III-38 compares the saturation properties of Mix 907 for three different lines in the 10.6-μm P-branch of the CO_2 spectrum. The P(16) line coincides with the Q-branch of SF_6 and has the greatest small-signal loss of all the CO_2 laser lines in the 10.6-μm P-branch. The P(20) line is in the P-branch of SF_6 and has almost half the small-signal loss of P(16), although its large-signal transmission level is nearly identical to that of P(16). The P(24) line, on the other hand, is well over into the P-branch of both SF_6 and FC-152a. Moreover, it lies near the center of the multiphoton absorption pathway in SF_6. Therefore, the P(24) line should be more difficult to saturate than either P(16) or P(20), as is in fact the case.

These experiments suggest that the behavior of the mixes is, in general, similar to that of helium-buffered SF_6 at much higher pressures. The rotational relaxation effects in the large fluorocarbon molecules, which in effect couple a sizable reservoir of collisional states to the SF_6, are significant even at relatively low pressures. Moreover, the use of short absorber cells at higher gas pressures requires a penalty, that is, reduced transmission performance.

Although our data seem to bear out the premise of "linearity"—that an absorbing gas mixture behaves as the sum total of its components—there are some inconsistencies. In particular, some data show that SF_6 + FC-1113 has a lower large-signal transmission for 10-μm P(20) than pure SF_6, even though FC-1113 is transparent at this wavelength. These and related problems will be the subjects of further investigation.

Energy Transfer Kinetics in CO_2 (M. D. Thomason, B. J. Feldman)

The development of Gemini, Helios, and Antares has significantly advanced the technology of high-energy, short-pulse, CO_2 amplifiers. However, multiline energy extraction and advanced schemes such as multiplexing require more detailed knowledge of the physical processes involved in these devices. For example, optimization of short-pulse amplifiers demands a thorough understanding of energy transfer pathways in excited CO_2. To explore this phenomenon, we have begun experiments designed to determine the various vibrational and rotational relaxation rates in CO_2.

In these studies we used saturation double-resonance spectroscopy, which is a proven, valuable tool in the study of CO_2 laser kinetics.[33] This method studies individual laser transitions by using separate pump and probe lasers, so that one can, in principle, study vibrational and rotational energy exchanges on a line-by-line basis. Unique to our experiment is the use of probe lasers that can be operated at hot-band and sequence-band frequencies. These frequencies allow us to observe population transfers to higher energy levels than those excited in normal laser transitions. The combination of these data with fluorescence results obtained by others[34,35] should yield key information in the CO_2 energy-migration puzzle. In addition, we used a 2.5-m-long hot cell to contain the absorbing medium, so that we could control the temperature, pressure, and composition of the gas mixtures accurately.

Despite the paucity of experimental data, we have made significant advances in our theoretical efforts to describe CO_2 collisions in recent years.[36,37,*] Further refinement of the models requires more carefully controlled exploration of the experimental parameter space.

The detailed experimental design has evolved over several years. The apparatus consists of a TEA laser, designed and built by Los Alamos, which produces a smoothed, saturating pump pulse, a low-power cw-probe laser, and a hot cell containing the gas sample. The cross-polarized outputs of the lasers are joined to produce a unidirectional, collinear beam path. The combined beams traverse the hot cell and pass to a screen room where the low-power probe signal is discriminated from the megawatt pump pulse by polarizers and grating filters. Each laser is grating tuned so that a wide variety of pump- and probe-frequency combinations is available.

One key to the success of this experiment is the operation of the probe laser. Rotational relaxation studies can be performed at the normal CO_2 frequencies. However, studies of vibrational relaxation require lasing operation on sequence-band and hot-band lines, a difficult task because the sequence-band transitions are interspersed among the normal higher gain transitions. Placing a short intracavity hot cell, containing 40 torr of CO_2 at 683 K, in the cavity absorbs the normal frequencies without affecting the sequence band. By using this technique,[38] we have been able to obtain sequence-band lasing on several lines. Hot-band gain is lower yet and several trial arrangements have yielded only marginal lasing. We decided, therefore, to operate the probe laser in a pulsed mode because such operation increases the gain on all lines substantially. We have obtained 3-ns pulses (essentially cw for our experiments) on hot-band lines in the P(20) to P(33) region.

We have obtained some data on sequence-band, hot-band, and normal-band transitions, but these results require a careful, multilevel rate-equation analysis to extract the model parameters of interest. Our preliminary computer analyses have indicated a need for faster risetime pump pulses. To this end, a Pockels-cell optical gate will be assembled for the output of the TEA laser. When this improvement to the laser is complete, we expect to begin an extended period of data collection.

Deformable Mirrors (V. K. Viswanathan)

The use of a deformable mirror in our CO_2 laser fusion system to improve the system performance has been discussed previously.[39] Hughes[39] and Rocketdyne[40]

---

[*] E. T. Salesky, Los Alamos Group P-1, is currently applying the method of Salesky and Korff, Phys. Lett. 72A, 431 (1979) to CO_2.

have designed and manufactured such mirrors as replacements for the collimating mirrors in the Gemini power amplifiers. The Rocketdyne mirror, in tests at Los Alamos, was easy to use, stable, and capable of producing the proper conjugate wave front for the kinds of aberrated wave fronts typically encountered in CO_2 laser fusion systems. The experimental setup duplicated the target-chamber area of Helios and used typical Helios components. We obtained Smartt interferograms[2] at the focal plane and performed an optical analysis with the code FRINGE.* The results are shown in Tables III-VIII and III-IX.

Discharge and Kinetics Modeling in Electron-Beam-Controlled CO_2 Laser Amplifiers (J. C. Comly, Jr., W. T. Leland, C. J. Elliott, A. M. Hunter II, and M. J. Kircher)

For the study of laser fusion, CO_2 laser systems[41,42] have been designed that use electron-beam-controlled discharges in the main amplifiers.[43-45] When used to pump laser media, such discharges are efficient, stable, and scalable to large sizes and pressures; consequently, they have been applied to a wide variety of laser devices. In this section, we will discuss high-power, short-pulse CO_2 amplifiers. First, we will briefly present the operation of these devices and the logical structure of the model. Then, we will describe two representative calculations: one allowing direct comparison with experiment

TABLE III-VIII. Stability of Rocketdyne Mirror

Time of Test	Strehl Ratio	Diam 80% Encircled Energy Spot (μm)	Diam 84% Encircled Energy Spot (μm)
9:00 a.m.	0.54	58	80
12:00 p.m.	0.52	59	81

TABLE III-IX. Ability to Correct Aberrations

Energy Description	Strehl Ratio	Diam 80% Encircled Energy Spot (μm)	Diam 84% Encircled Energy Spot (μm)
Initial state	0.63	59	79
Aberrated wave front introduced	0.09	141	164
Corrected state using deformable mirror	0.63	59	88

---

*FRINGE is the generic name for an interferometer analysis code developed by the Optical Sciences Center, University of Arizona, Tucson, AZ 85721 and the other illustrating the use of the model as a design tool for future systems.

The model can be applied to amplifier systems having a wide variety of geometries, components, and extraction schemes; however, for illustrative purposes, we will consider amplifiers similar to those in Helios.[46] A schematic of such a device is shown in Fig. III-39, which indicates that there are two distinct electron currents of interest. The first is a beam of high-energy electrons $\vec{j}_b$ that is generated in an electron-beam gun and injected (through a foil) into the laser-gas region. Collisions of these beam electrons with the gas produce ion-electron pairs; this allows a second power supply to draw a discharge current $\vec{j}$ through the conducting medium. In this discharge, collisions of the (low-energy) "discharge" electrons excite the CO_2 and N_2 molecules, producing population inversions.[47] In the application considered here, this pumping continues until a short, intense (saturating) optical pulse propagates through the amplifier, extracting energy from the inversion.

The modeling approach is based on Fig. III-40, which shows the dominant processes (and interrelations) occurring in this type of amplifier.[48] We analyze each process separately, while limiting the couplings between them to those shown in the figure. This approach will be justified in terms of the operating parameters of the device, examples of which are given in Table III-X. The modeling must incorporate a wide range of processes: microscopic collision cross sections, macroscopic transport coefficients, and phenomenological circuit descriptions. One major advantage of the logic structure shown in Fig. III-40 is that each calculation deals with effects on only one "scale."

Actual systems can vary widely from the nominal conditions shown in the table. We will not discuss the many constraints placed on the design of an amplifier by fundamental physics, engineering, and cost considerations. However, we will assume that the designs being modeled share certain desirable qualities; for example, the pumping time τ_{pump} will be consistent with the kinetics time scales, and the electric field $\vec{E}(\vec{r},t)$ will be well below the breakdown threshold. In this case, we can neglect ionization produced by the discharge electrons,[49] so that only "beam" electrons generate the ion-electron source $S(\vec{r},t)$. Furthermore, as shown later, the remaining feedback couplings (indicated by dotted lines in Fig. III-40) are weak effects, largely constrained by integral properties. Physically, this leads to electron-beam-controlled discharges that are stable, relative to self-sustained discharges;[50] it also vastly simplifies the model conceptually and computationally. The state of the system is modeled by separately calculating each process in turn, following the solid arrows in Fig. III-40; then, self-consistency is achieved by modifying the quantities in the feedback couplings and iterating the procedure. In practice, these iterations converge rapidly;

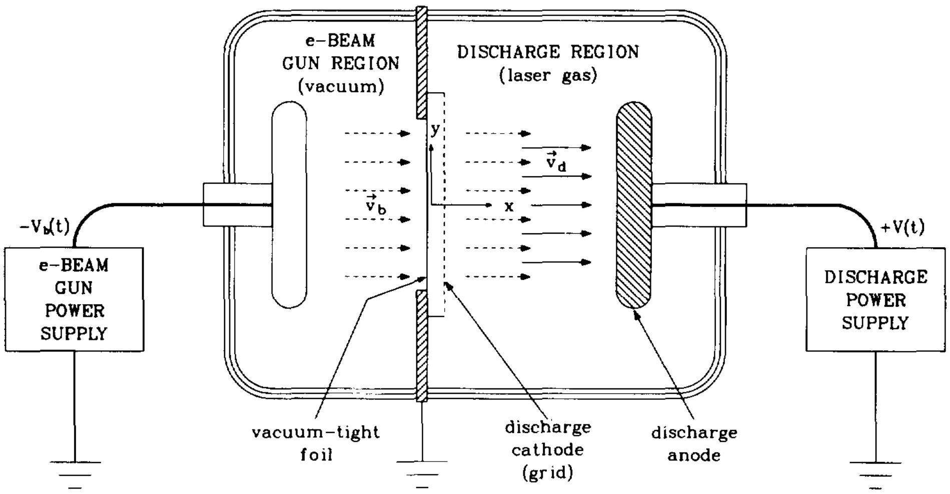

Fig. III-39. Schematic of electron-beam-controlled amplifier showing coordinate system used. The high-energy-beam electron current is shown as dotted arrows, whereas the discharge current is shown with solid arrows. Electrodes and chamber walls are schematic only. The z-axis, along which the optical pulse propagates, is out of the plane of the figure.

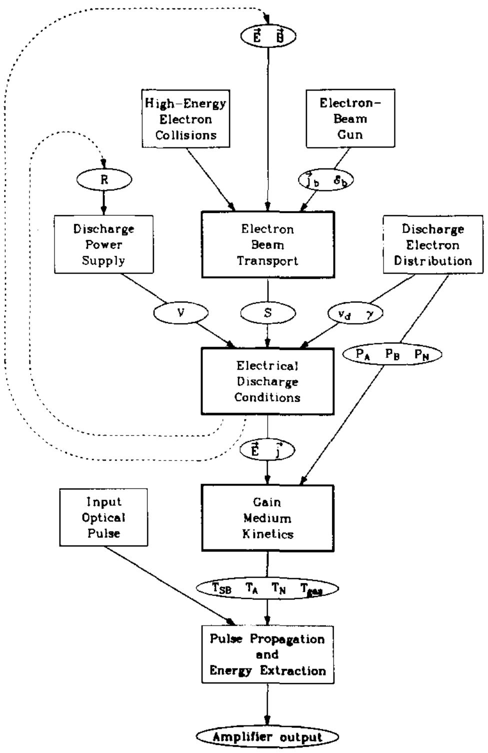

Fig. III-40. Logic structure of model. The boxes indicate the processes included in the model, and the arrows show how they relate to each other. (The ellipses contain the variables producing the interdependencies.) The solid arrows indicate computational flow, whereas the dotted arrows indicate feedback loops producing self-consistency. Several approximations discussed in the text have been used to simplify the interconnections as much as possible.

usually, a single pass is adequate, with the proper first guess.

Because distinct calculations are used to model each process, we have been able to incorporate new or improved capabilities easily. An effort has been made to model correctly the processes that are most important, for example, to match the observed gain build-up and peaking when a discharge pulse is applied. Although details of the calculations may be open to criticism, the complete modeling procedure has proved successful, both in describing several operating Los Alamos systems and as a design tool.

We have used our modeling approach to simulate an experiment that measured the peak gains achieved on a large number of laser lines in one of the Helios amplifiers. The purpose of the experiment was to obtain data needed in the design of an efficient saturable absorber for the amplifier.[3] Table III-X and Fig. III-41 show the Helios operating parameters during the experiments. Figures III-42 and III-43 show the computed electron-beam deposition and discharge power uniformities, respectively. The gain measurements were made over a path along the geometric center of the amplifier, at the point indicated in Fig. III-43; however, we observed[47] that the discharge was displaced from the amplifier midplane, as is also shown in the figure. We used the offset in the calculations for Figs. III-42 and III-43 to match the experimental uniformity data approximately. (This asymmetry in the discharge was probably caused by an asymmetry in the return-current paths around the discharge chamber.)

TABLE III-X. Parameters of Electron-Beam-Controlled Amplifiers

		Helios	Nominal
Discharge dimensions	discharge gap, D (cm)	35	10
	discharge width, W (cm)	35	10
	discharge length, L (cm)	200	100
Gas mixture	pressure (torr)	1800	760
	$He/N_2/CO_2$	3/0.25/1	(variable)
Electron beam	energy, ξ_b (keV)	230	100-300
	beam current, j_b (A/cm^2)	~0.8	0.1-1
Discharge	average field, E (kV/cm)	6	5-8
	average current, j (A/cm^2)	11	3-10
	pump time τ_{pump} (10^{-6} s)	~3	2-10
Optical pulse length	τ_{pulse} (10^{-9} s)	1.6	3-10

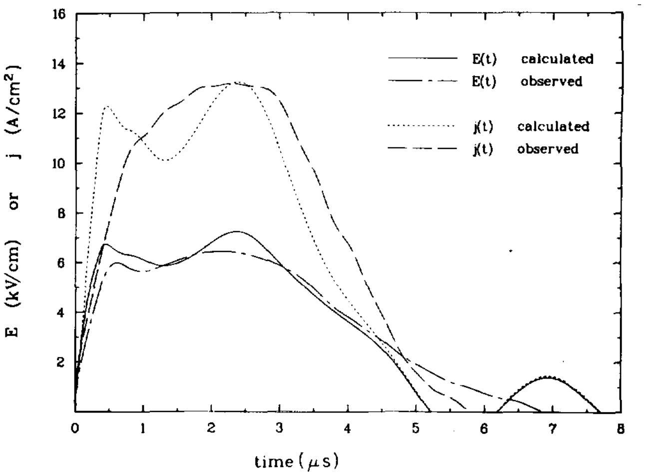

Fig. III-41. Comparison of calculated and observed Helios electrical pumping characteristics. The discharge in this case is assumed to be uniform, to have the spatial dimensions shown in Table III-X, and to be driven with the circuit described by Riepe.[51]

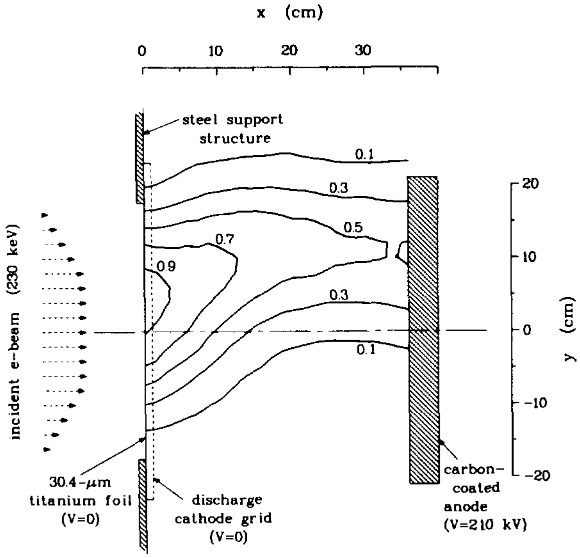

Fig. III-42. Calculated distribution of the energy deposited by the beam electrons in a geometry representing the Helios laser amplifier, under the conditions shown in Table III-X. The contours show the distribution values normalized to the maximum. The discharge magnetic field has been displaced toward positive y relative to the electron-beam entrance and the electron trajectories show a strong tendency to follow the displacement.

The discharge calculation (Fig. III-43) indicates that the ratio of the local electric field (at the gain measurement point) to the average field was $F_E = 1.08$, whereas the corresponding ratio for the current density was $F_j = 0.81$. These ratios were used to scale the electrical histories shown in Fig. III-41, giving values for E(t) and j(t) at the measurement location. A kinetics calculation then predicted the following mode temperatures at the time of peak gain:

386 K (CO_2 symmetric stretch and bending),
1381 K (CO_2 asymmetric stretching),
1448 K (N_2 vibrational), and
361.5 K (bulk gas and rotational equilibrium).

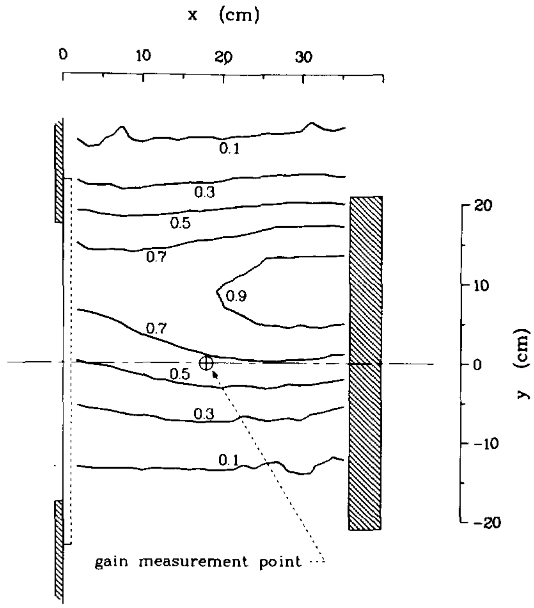

Fig. III-43. Distribution of discharge power $P = \vec{E} \cdot \vec{j}$, in Helios amplifier, under the conditions shown in Fig. III-42. Contours are normalized to peak pumping = 1.05×10^5 W/cm^3.

To calculate the gains on the lines as accurately as possible, we used the improved gain program of Goldstein.[7] This program accounts for contributions to the gains from lines outside the fundamental transitions: lines from eight hot and sequence bands[5] have been included, as well as line overlaps caused by the Lorentzian line width of each transition. The predicted gains, using the mode temperatures listed above, are shown in Fig. III-44, along with the experimental points. Because there is no arbitrary normalization involved with the theoretical points, agreement seems good; however, this may be partly fortuitous, because of the uncertainty of the discharge displacement.

As a second example of using the modeling capabilities, we will consider the design of an amplifier whose aperture dimensions have been scaled up from present devices. The operating parameters of such a

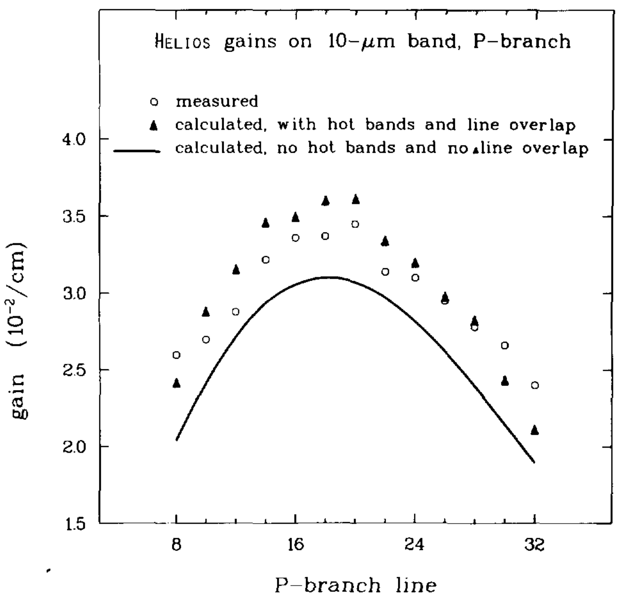

Fig. III-44. Comparison of calculated and observed gain vs line on the 10-μm P-branch transitions.

device can be chosen only after considering many constraints and tradeoffs[48] that we will not discuss here. However, before any system design could be completed, it would be necessary to model the amplifier in sufficient detail to quantify (and, we hope, optimize) its performance.

Figures III-45 and III-46 show the computed electron-beam energy deposition and discharge power (P($\vec{r}$)), respectively, for a discharge with the following characteristics:

geometry D,H,L : 46, 46, 300 cm
gas : 0.25:1::N_2:CO_2 (1800 torr)
electron-beam voltage : 500 keV
power-supply voltage : 1188 kV (18 kV/cm or 7.6 kV/cm•atm)
power-supply current : 132 kA (6 A/cm^2 average).

The system is symmetrical about the midplane in y. A measure of the uniformity can be found by considering the discharge power density inside the optical beam extraction region (the dotted circle in Fig. III-46). The average-to-peak value is 0.86, which indicates good uniformity for many applications. Several techniques have been employed to improve the uniformity of the discharge.

- The anode is curved, leading to a higher field and higher discharge power near the edge of the discharge. This counteracts the pinching of the electron beam toward y = 0.

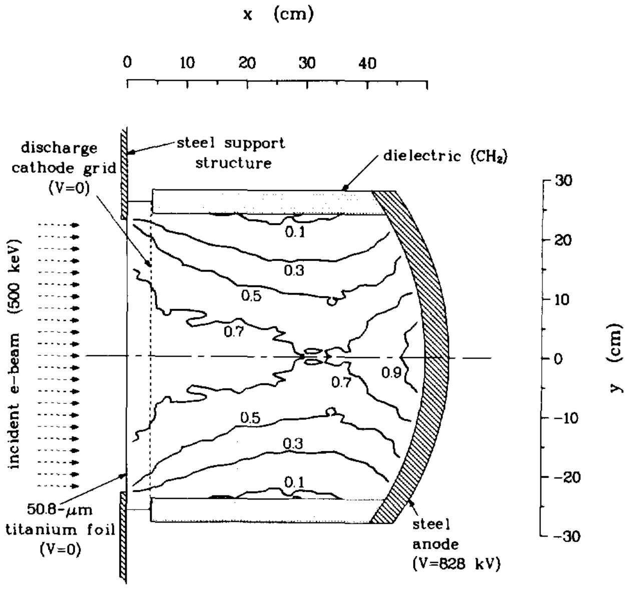

Fig. III-45. Energy deposition by an electron beam in a large-aperture amplifier. Contour values are normalized to peak deposition. Uniformity is improved by backscattering from the steel anode and by assuming a low discharge current (6 A/cm^2). The gas (0.25:1::N_2:CO_2) is at 1800 torr; the cathode grid is 4 cm from the foil and 46 cm from the anode.

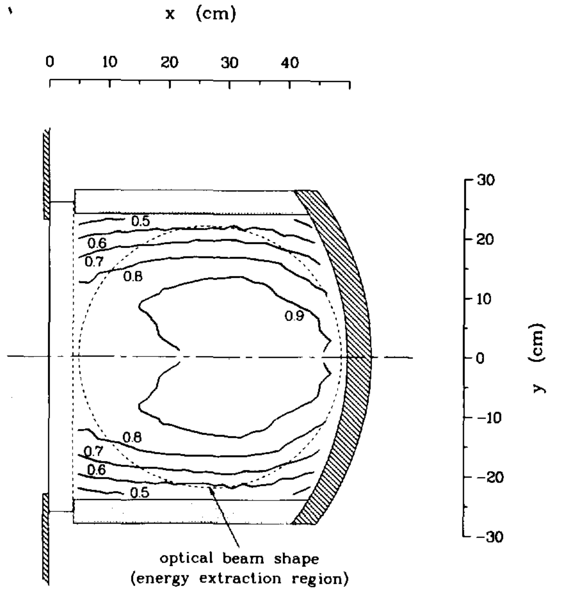

Fig. III-46. Discharge power uniformity corresponding to conditions shown in Fig. III-45. The curved anode and dielectric shields increase the power-loading at the edges of the discharge. (Structures shown are theoretical only, because any real dielectric and anode would have to be shaped to avoid excessive electrical stresses.) The figure shows a 44-cm-diam optical beam extraction region.

- Dielectric shields near the edge of the discharge constrain the current and prevent power from being wasted in fringe regions.
- A steel anode backscatters beam electrons into the gas; this is particularly beneficial in smaller devices but also has a useful effect here.
- The current density is low, but the amplifier length can be extended to achieve the desired output fluence.

Figures III-47 and III-48 show the results of using another technique[52] to improve the transverse discharge uniformity. These examples suggest that no scalability limit has been reached for electron-beam-controlled CO_2 discharge amplifiers, up to the sizes considered here.

Our modeling approach contains a logic structure and computational elements that would allow a three-dimensional, time-dependent discharge and kinetics description. Acceptable accuracy is retained in a much simpler set of calculations. Modeling with this method is both accurate in describing details and versatile in application to conceptual device designs.

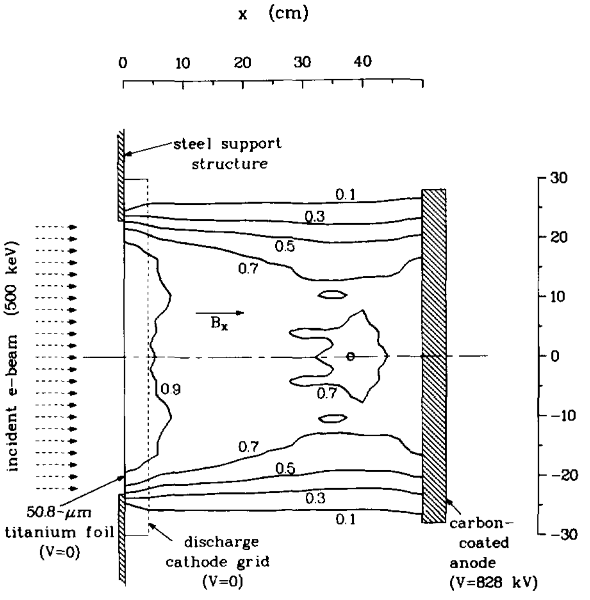

Fig. III-47. Energy deposition by an electron beam in a large-aperture amplifier containing a uniform 750-G guide magnetic field. This device is similar to that shown in Fig. III-45 except that a different method is used to improve the transverse uniformity.

Influence of Amplified Spontaneous Emission (ASE) on Angularly Multiplexed KrF Laser Systems (A. M. Hunter II)

Introduction. Questions have been raised regarding the suitability of KrF as an amplifying medium to be used in conjunction with angular multiplexing schemes. The criticisms are twofold: (1) ASE reduces the extraction efficiency considerably below the levels predicted in the absence of ASE or parasitic oscillations, and (2) ASE damages the ICF target before the main pulse arrives. We address both criticisms below, concentrating on the ASE output from a 50-kJ, double-pass final PAM and its subsequent influence on a target.

- We included nonsaturable absorption loss in the gain calculation.
- We solved the steady-state optical propagation through a saturating medium analytically for combinations of counterstreaming coherent and incoherent beams.
- We estimated the ASE fluence intercepting an ICF target for a 50-kJ angularly multiplexed KrF power amplifier.

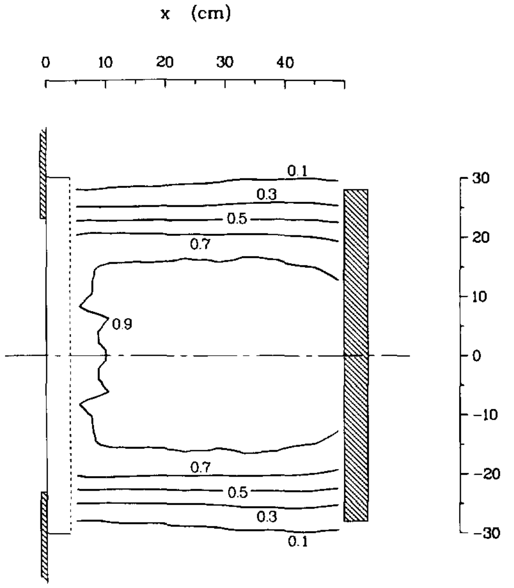

Fig. III-48. Discharge power uniformity for the conditions shown in Fig. III-47. By combining the techniques shown in Figs. III-44 and III-47, larger amplifiers than those shown here could be designed with high uniformity.

We conclude that the extraction efficiency is not seriously reduced; prepulse on target should not be a problem.

Amplifier Results and Conclusions. The equations for a double-pass amplifier have been solved, and the results are displayed in Figures III-49 through III-55. The integrated single-pass gain-length product g_LL is shown in Fig. III-49 as a function of g_0L and g_0/α where g_0 is the small-signal gain, α is a nonsaturable absorption loss coefficient, and L the amplifier length. Figure III-49 does not include ASE effects: the graph would be virtually identical. Increasing absorption at fixed g_0 decreases g_LL, but the three curves do not differ substantially as long as the medium is saturated.

The stage gain G (Fig. III-50) exhibits a stronger dependence on g_0/α than does g_LL because $G = \exp(2g_LL)$. ASE reduces the stage gain (Fig. III-51), but G is more sensitive to g_0/α than to ASE for a saturated amplifier.

Figure III-52 shows that the average extraction efficiency π is very sensitive to g_0/α. Extraction efficiency initially increases with increasing g_0L at fixed g_0/α indicating that the medium is beginning to saturate. The unbleachable absorber imposes a lower limit to which the gain can be reduced by stimulated emission. For that reason, π begins to decrease as g_0L (which is a measure of energy addition to the medium) increases beyond an optimum value. Figure III-53 shows the sensitivity of π to ASE. Extraction efficiency is not seriously reduced by ASE for reasonable amplifier aspect ratios ($\sim$2) and saturated operation.

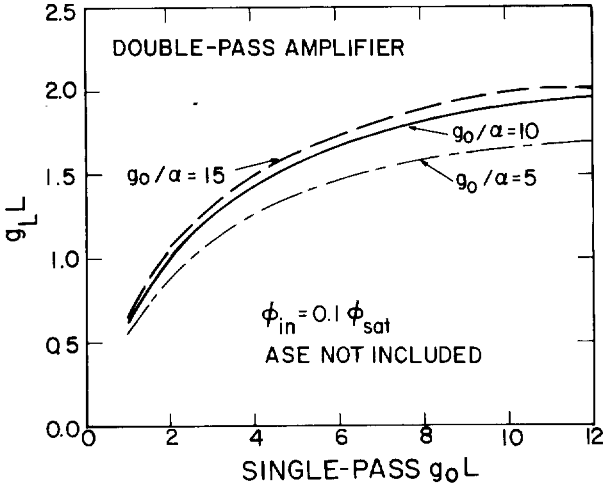

Fig. III-49. Integrated single-pass gain minus absorption for a double-pass amplifier.

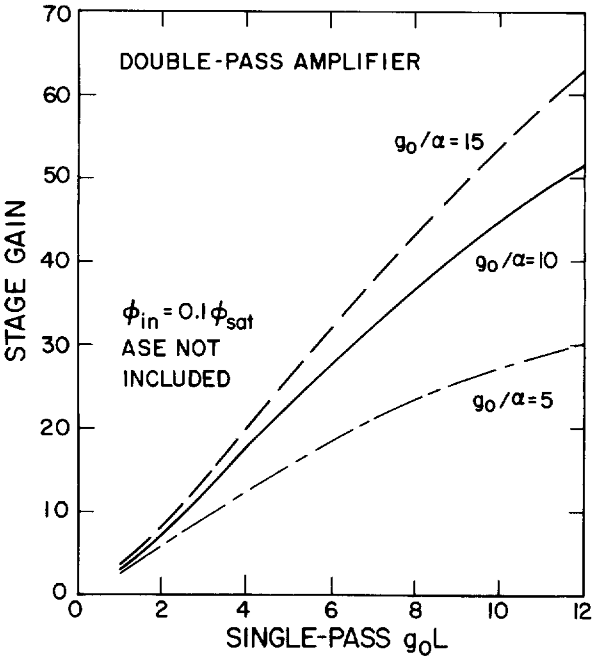

Fig. III-50. Stage gain for a double-pass amplifier without ASE.

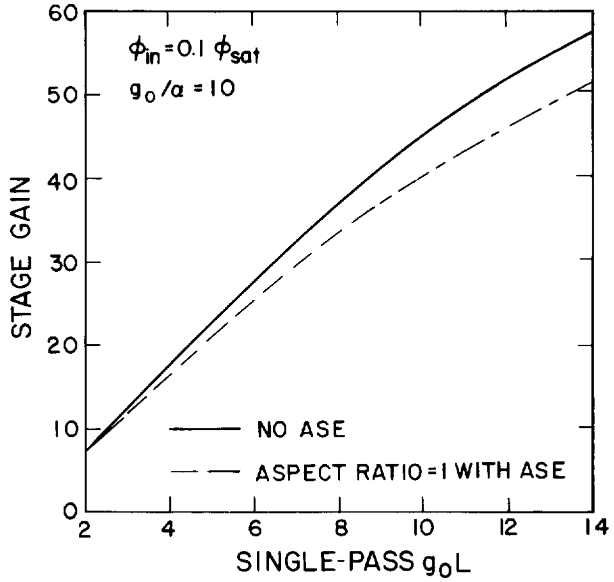

Fig. III-51. Stage gain for a double-pass amplifier subject to ASE.

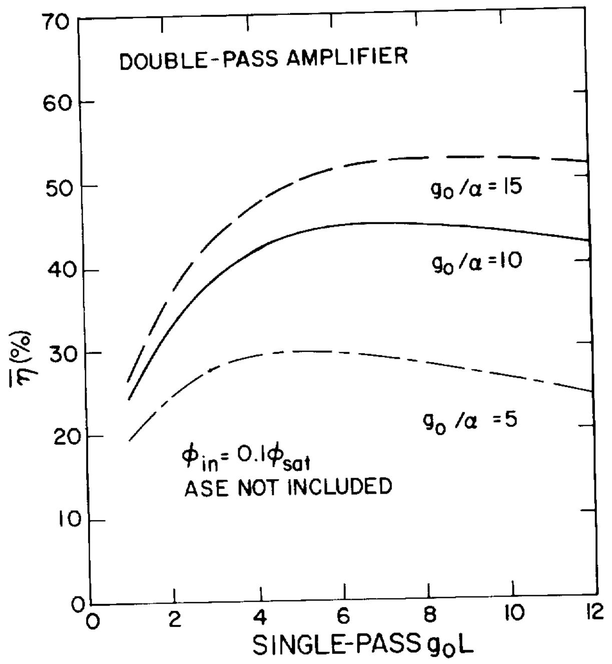

Fig. III-52. Average extraction efficiency for a double-pass amplifier with different gains g_0.

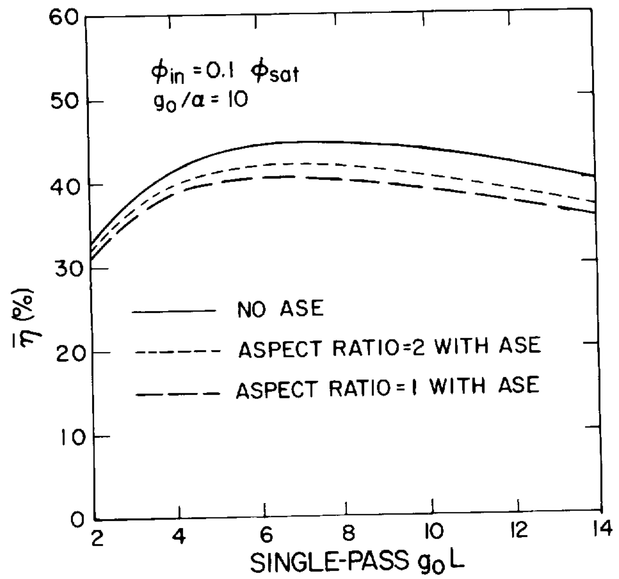

Fig. III-53. Average extraction efficiency for a double-pass amplifier with different aspect ratios.

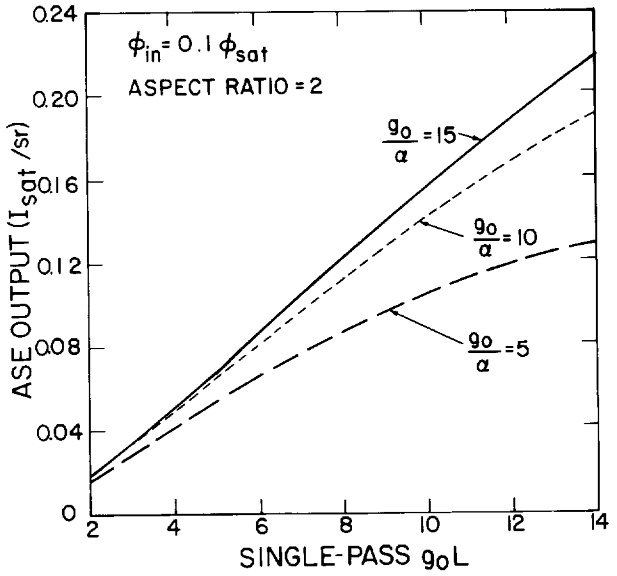

Fig. III-54. ASE output from a double-pass amplifier driven at 10% of saturation intensity.

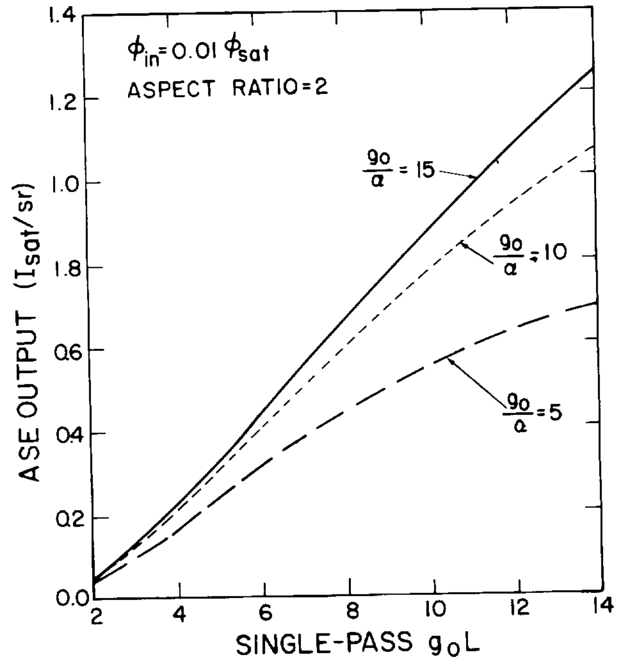

Fig. III-55. ASE output from a double-pass amplifier driven at 1% of saturation intensity.

Finally, the ASE output from a double-pass amplifier is shown in Figs. III-54 and III-55. ASE increases with decreasing α because the spontaneously emitted photons are much more likely to be amplified than absorbed. ASE increases as the input flux is reduced because the gain is not saturated by the coherent signal. Therefore, the ASE source, proportional to g, and the ASE stage gain increase with decreasing coherent input.

ASE Prepulse Results and Conclusions. Suppose that we want to estimate the ASE prepulse on target from a 50-kJ power amplifier. If we assume that the optical damage limits are 5 J/cm^2 for the slow (500-ns) optics and 1 J/cm^2 for the fast (10-ns) optics, the relay, compression, and focusing system requires 10^4 cm^2 per operation of slow optics and 5×10^4 cm^2 per operation of fast optics. One version of an angular multiplexing system is shown in Fig. III-56. The PAM aperture and relay array are slow optics with area A_s, and the compression and focusing optics are fast, with areas A_f. It is necessary to determine the solid angle into which radiation can be transmitted by the power amplifier and subsequently intercepted by the target.

Because the distances ℓ_1, ℓ_2, and ℓ_3 are each several tens of meters and $A_s = 10^4$ cm^2 and $A_f = 5 \times 10^4$ cm^2, the solid angles subtended by the optical arrays are on the order of 10^{-4} sr. As shown below, a reasonably designed power amplifier will transmit a fairly large fluence of ASE into that solid angle; however, this is not a problem because very little of that ASE hits the target.

A geometrical optics calculation shows that the maximum angle at which a ray may deviate from the optical axis at the power amplifier and intercept the target is

$$\alpha_{max} = \frac{\text{target radius}}{\text{focal length}} \ .$$

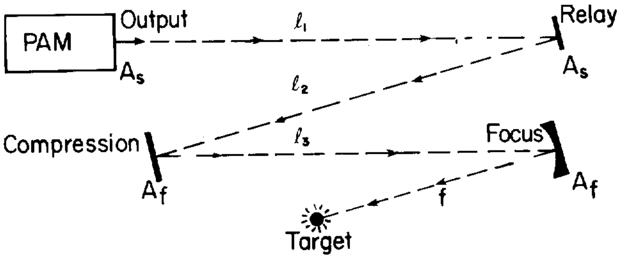

Fig. III-56. Schematic of angular multiplexing output optics.

Using 150 μm as the target radius and 30 m as the focal length,

$$\alpha_{max} = 5 \times 10^{-6} \text{ rad} \ .$$

The corresponding solid angle viewed from the amplifier aperture is

$$d\Omega = 4\alpha_{max}^2 = 10^{-10} \text{ sr} \ .$$

A power amplifier that transmits 50 kJ through a 1-m^2 aperture in 500 ns operates at an average intensity of 10 MW/cm^2. At P = 2 atm, that intensity is equivalent to 5 I_{sat}. The amplifier could operate with a stage gain of 50, $g_0L = 12$, extraction efficiency of 38.5%, aspect ratio of 2, and an ASE output of 0.17 I_{sat}/sr. The fluence at the target is

$$\text{Total Fluence} = \frac{(\text{ASE output})\,(I_{sat})\,(d\Omega)\,(A_s)\,(\tau p)}{(\pi/4)\,d_{target}^2)}$$
$$= 2.4 \times 10^{-4} \frac{\text{J}}{\text{cm}^2} \ .$$

Only half of the total fluence will arrive before the main pulse.

The ASE fluence on a 300-μm target for a 50-kJ module is about 10^{-4} J/cm^2 for reasonable focal lengths. This fluence is three orders of magnitude smaller than the fluence required to damage a GMB with CO_2 light.[53] The contrast ratio between the main pulse and the ASE is 5×10^{11}.

The total ASE fluence transmitted by the optical system is formidable—roughly 200 J/cm^2. However, because only one millionth of the total ASE hits the target when it enters the target chamber, the ASE prepulse should not pose a serious threat to the target.

Solid-State Saturable Absorbers (J. F. Figueira)

The development of solid-state saturable absorbers for use with CO_2 lasers continued at Los Alamos, at Cornell University, and at HCC. These materials are being developed as potential replacements for the conventional gas mixtures used as parasitics suppressors and prepulse attenuators in large-aperture CO_2 laser fusion systems. For the first time, HCC has successfully produced $NaReO_4$-doped NaCl isolators with an absorption spectrum appropriate for use with CO_2 lasers. In addition, work at Los Alamos and Cornell has demonstrated that entrainment of SF_6 molecules in alkali-halide host material yields nonlinear optical properties that are particularly well matched to the CO_2 laser.

Doped Alkali-Halide Crystals. Single crystals of KCl doped with ReO_4^- have been successfully grown previously; however, attempts to extend the technique to NaCl have met with repeated failures. Recently, HCC prepared samples of NaCl single crystals *double-doped* with $NaReO_4$ and $CaCl_2$. The long-sought V_3 resonance of the ReO_4^- ion has been seen for the first time in these crystals. Figure III-57 shows a spectrophotometer scan of the material. The center of the V_3 resonance is at 946 cm^{-1} with a bandwidth of ~ 6 cm^{-1}, providing an excellent match to the P(20)-P(14) lines in the 10-μm band of the CO_2 laser. The position of the V_3 mode agrees with earlier estimates based on the known variations of the V_3 resonance with lattice spacing.

Figure III-58 shows the measured dependence of the V_3 resonance energy on crystal lattice spacing for six different alkali halides.

HCC is continuing to refine growth techniques for samples of NaCl with larger ReO_4^- concentrations. (Current samples contain $\sim 10^{14}$ $ions/cm^3$.) As denser samples become available, we will make a more complete spectroscopic examination (both at high and low power) of the optical properties of this material.

Entrained Impurities. Cornell has developed a new method of altering the optical properties of normally transparent alkali-halide host materials. Using hot-forging techniques, SF_6 molecules have been entrained successfully in KCl and NaCl. Figure III-59 shows typical absorption spectra for $KCl:SF_6$ and for normal gas-phase SF_6. A comparison reveals that entrainment dramatically alters the optical properties of the SF_6 impurity, broadening the resonance and shifting it to lower energies.

Table III-XI summarizes the measured optical properties of both $KCl:SF_6$ and $NaCl:SF_6$. Although their optical behavior depends to some extent on fabrication techniques, the characteristics quoted in Table III-XI are fairly representative. Because of the broadband nature of absorption resonance and the moderate value of the saturation parameter (~ 10 MW/cm^2), these materials show great promise for use with CO_2 lasers. Fabrication technology issues, residual scattering losses, and damage levels remain to be investigated.

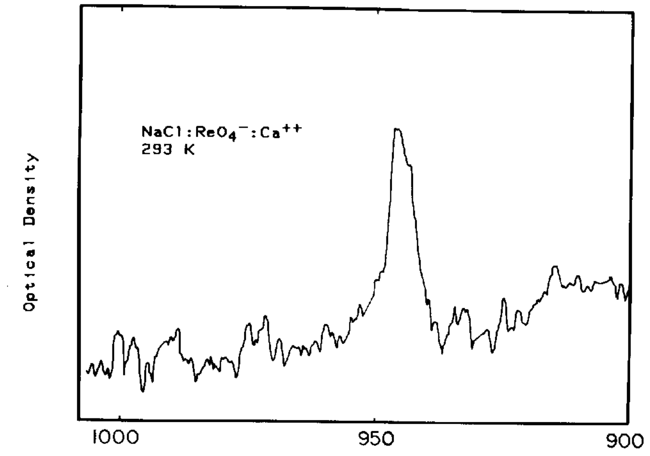

Fig. III-57. Optical density as a function of wavelength for an NaCl crystal double-doped with $NaReO_4$ and $CaCl_2$.

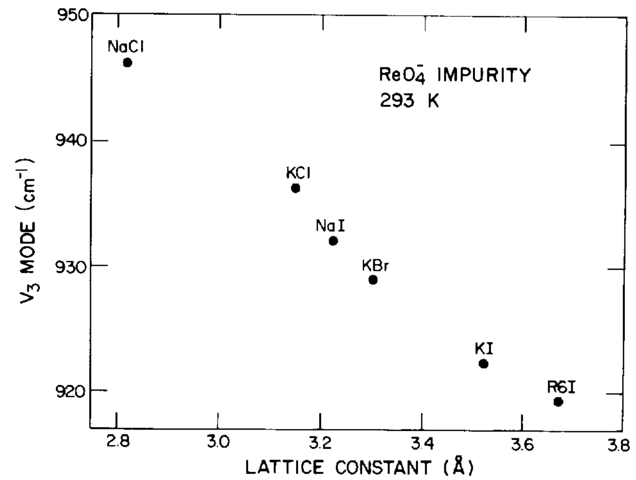

Fig. III-58. V_3 resonance for the ReO_4 impurity for six crystals with different lattice constants.

Plasma Shutters (S. J. Czuchlewski, J. F. Figueira)

Retropulse isolation is an important design consideration in high-power laser fusion systems. Gemini, Helios, and Antares depend on laser-initiated plasma-breakdown shutters (usually an iris located in the focal plane of a spatial filter) to limit the return flux incident on critical front-end optical components. In an extensive, systematic study, we are trying to characterize the performance of these devices and to clarify the physics of the plasma-breakdown phenomenon. In general, the desirable

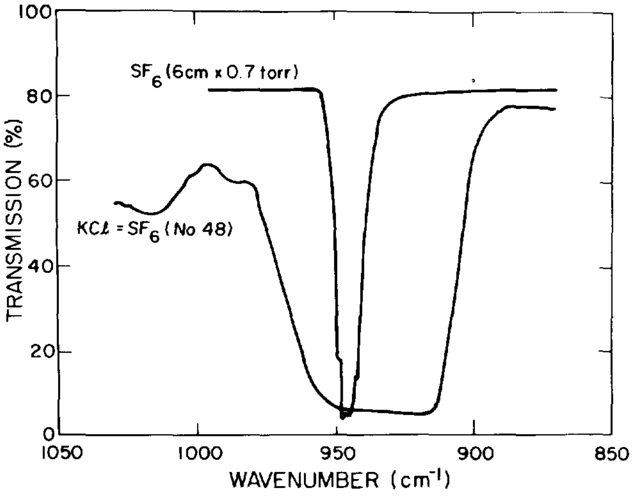

Fig. III-59. Comparison of absorption spectra for gaseous SF_6 and for SF_6 entrained in KCl.

TABLE III-XI. Parameters of Alkali Halides with Entrained Impurities

Host	Impurity	λ_0 (cm^{-1})	$\Delta\lambda$ (cm^{-1})	I_s (MW/cm^2)
NaCl	SF_6	~955	~20	~8
KCl	SF_6	~940	~50	~10

properties of such an isolator are (1) high forward transmission, (2) low reverse transmission, and (3) passive initiation of breakdown to ensure simple and reliable operation. We have demonstrated that these criteria could be met with a plasma shutter in which a small fraction of the forward-going laser pulse is used to initiate a plasma at the edge of a metal iris, located in the focal plane of a spatial filter.[54,55]

We have investigated the plasma initiation process and forward-transmission characteristics of these shutters for irises of different diameters, using subnanosecond CO_2 laser pulses. The experiment consisted of measuring the energy transmitted through an aperture as a function of the laser pulse fluence incident on the edge of the iris (in a 600-torr ambient N_2 atmosphere). Figure III-60 shows typical data. At low fluences, ~23% of the beam is transmitted, a fraction that is determined by the relative diameters of the beam and the aperture. At an input fluence of ~2.1 J/cm^2, plasma formation is initiated and the transmission decreases. The dashed curve shows the total energy transmitted through the iris. For large inputs the transmitted energy clamps to a constant value (in this case ~6 mJ). This clamping phenomenon makes these shutters useful as retropulse isolators.

Figure III-61 plots transmission (normalized to unity for low-intensity inputs) as a function of iris-edge fluence for both long (60 ns) and short (0.7 ns) pulses.[54,55] The curves are nearly coincident, which demonstrates that the breakdown process is essentially fluence dependent rather than intensity dependent. (Intensities differ by a factor of 85 between the two cases.)

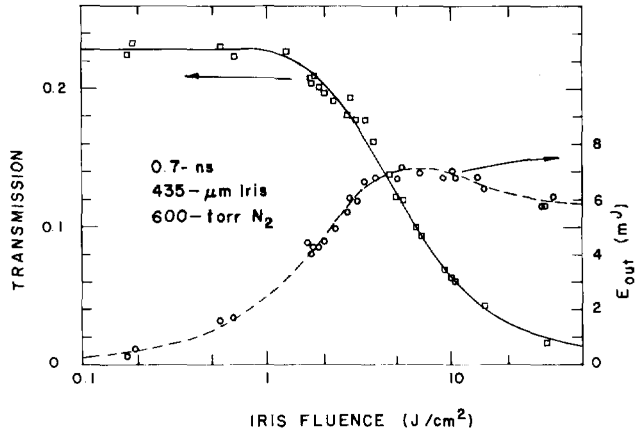

Fig. III-60. Transmission vs input fluence at the iris edge for 0.7-ns pulses. Beam radius a_0 was 445 μm. Transmitted energy was collected with an f/2 optical system.

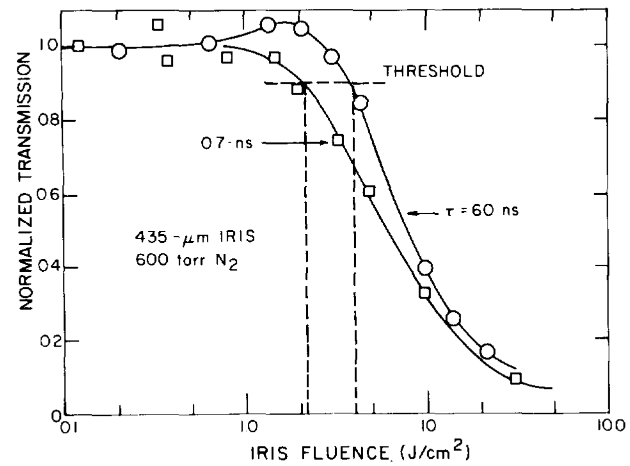

Fig. III-61. Normalized transmission vs input fluence at the iris edge. Transmissions are normalized to the small-signal values. The breakdown threshold fluence is a weak function of pulse length.

Observed breakdown thresholds are plotted in Fig. III-62 for both the long- and short-pulse cases.* Breakdown threshold is defined as the fluence for which the transmission has decreased to 90% of its small-signal gain. The measured spatial profile of the beam was approximately Gaussian in both experiments at a radius a_0 of 230 ± 30 and 445 ± 60 μm for the long- and short-pulse cases, respectively. The Gaussian intensity profile is defined by

$$I(r) = \exp\left(\frac{-r^2}{a_0^2}\right) \quad . \tag{III-22}$$

Within the uncertainty of the data, the breakdown threshold exhibits no dependence on iris diameter, but there is a slight dependence on pulse length. The measured breakdown thresholds on stainless steel irises in 600-torr N_2 are 1.4 ± 0.6 and 4.0 ± 1.0 J/cm^2 for 0.7- and 60-ns laser pulses, respectively. When we removed the irises, breakdown occurred in the nitrogen gas only at substantially higher input fluences.

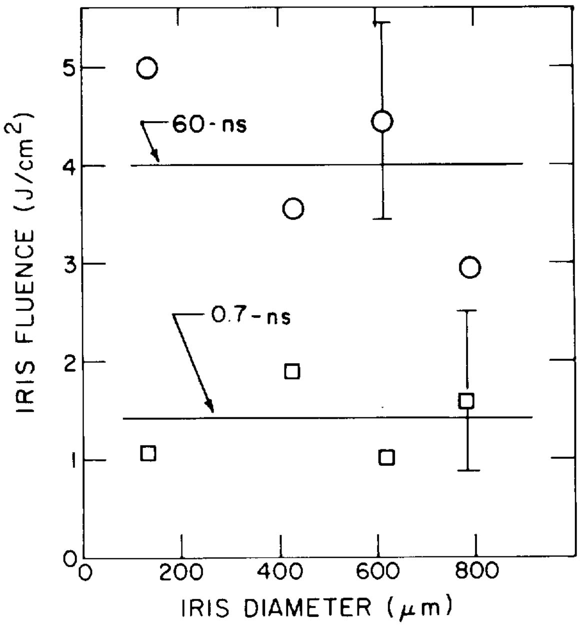

Fig. III-62. Fluence at iris edge at breakdown threshold for 60- and 0.7-ns pulses as a function of iris diameter. Beam radius a_0 was 230 and 445 μm for the long- and short-pulse cases, respectively. An f/2 collecting system was used in both cases.

For a Gaussian beam [Eq. (III-22)], when the iris threshold fluence F_t and beam radius a_0 are known, we predict that the clamping fluence E_C is

$$E_C = \pi a_0^2 F_t \left[\exp\left(\frac{R^2}{a_0^2}\right) - 1\right] \tag{III-23}$$

for an iris of radius R. For both long and short pulses, this equation produces results that generally agree with the measured clamping energies to within a factor of 2.

This research is continuing to investigate plasma-shutter designs for Antares. We will study the decay of laser-initiated plasmas at long times (~0.5 μm) after formation. The effects of large f-number, different iris material, and vacuum environment on the efficiency of these plasma shutters is also being investigated.

Phase-Conjugation Studies (C. R. Phipps, Jr., D. E. Watkins, S. J. Thomas, W. W. Rigrod)

Our interest in phase conjugation using DFWM stems from its unique ability to reverse both the propagation vector and the phase distortion of an aberrated wave. For example, in a double-pass, static optical configuration such as that of our ICF power amplifiers, the optical wave arising from a point source will return to that point with fixed wave front distortions removed. Thus both automatic target alignment and improved beam quality are possible by means of phase conjugation.

In a previous report,[54] we discussed studies designed to identify the best materials for phase conjugation at CO_2 wavelengths and to characterize their performance accurately. Desirable characteristics include moderate reflectivity (≥10%), an operating bandwidth consistent with the Antares power spectrum, adequate optical damage threshold, freedom from undesirable side effects such as self-focusing, acceptable material availability, and low installation cost. Germanium emerged as the best choice, a decision corroborated by extensive theoretical and experimental investigations.[54]

Although differing only in the type and density of doped impurities, intrinsic (pure) and p-type (gallium-doped) germanium produce phase-conjugate reflections by quite different means in the infrared. At CO_2 wavelengths, intrinsic germanium is a Kerr-type DFWM material in which refractive index gratings are built up by the interference of pump and probe beams acting on the

---

*A slightly different definition of breakdown threshold was used in Refs. 54 and 55, so that there is a small discrepancy between the values that appear in Fig. III-62 for the long-pulse data and the values that appear in these references.

very large nonlinear index of the material. On the other hand, P-type germanium is a resonant, inhomogenously broadened absorber normally used for laser isolation and modelocking. Its DFWM response is primarily caused by gratings formed by spatially modulated absorption rather than caused by the refractive index.[56,57] P-type germanium is an example of a class of DFWM materials that also includes homogeneously broadened absorbers such as KCl:KReO$_4$.

Both materials share a third type of behavior at high intensities in which nondestructive internal free-carrier plasma formation[58,59] dramatically enhances DFWM response and completely dominates both mechanisms discussed above. Although this regime is characterized by a highly nonlinear reflectivity, limiting immediate ICF system applications, it offers the first instance of *amplified* phase-conjugate reflections by unassisted DFWM.

In addition to reporting our experimental results in these three areas, we will discuss substantial improvements in our ability to model the observed response, including most notably the effects of pump attenuations and of pump depletion on the predicted reflectivity. These results are not restricted to CO$_2$ wavelengths.

Effects of Pump Attenuation. Pump attenuation, as distinguished from pump *depletion* refers to loss of pump-beam intensity caused by ordinary absorption processes in a DFWM material. This effect is particularly important in choosing a design for a phase conjugator based on saturable absorption. Before our work, the best available theory[60] (which ignored pump attenuation) predicted the highest reflectivity from samples with the smallest transmission, used with partially saturating pump intensities. However, extinction of the pumps obviously leads to zero DFWM response, and no method existed for assessing the implied tradeoffs between these contradictory features in a practical phase-conjugator design. We have developed a new model that includes these effects and substantially improves our ability to predict the DFWM reflectivity of both inhomogeneously and homogeneously broadened absorbers, typified by p-type germanium and KCl:KReO$_4$.

A KCl:KReO$_4$ absorber with 5% small-signal transmission exhibits a reflectivity nearly an order of magnitude lower than predicted by Ref. 60 at low to moderate intensities. In contrast, our improved model[61] accurately predicts reflectivities in this range. At higher intensities (Fig. III-63), both models are inaccurate in this material as a result of two-photon effects that will be described in a future report. Figure III-64 shows the excellent agreement between our theory and results from p-type germanium for intensities below the threshold of internal plasma formation.

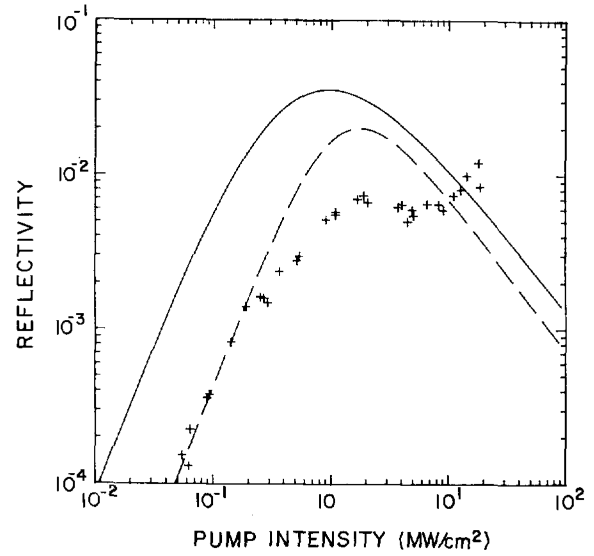

Fig. III-63. Phase-conjugate reflectivity in a 2-cm-long sample of KCl:KReO$_4$ with small-signal absorption coefficient of 3. The solid line is the Abrams-Lind model. The dashed line is the revised model.

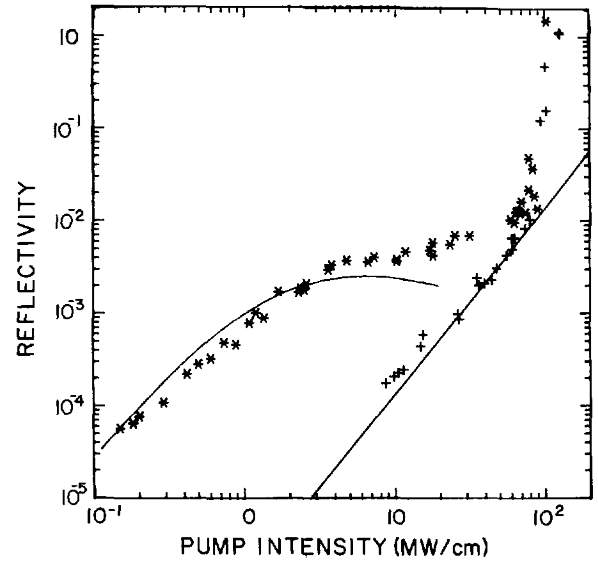

Fig. III-64. Phase-conjugate reflectivity in 3-mm-long sample of n-type (+) and p-type (*) germanium. The plasma threshold is 80 MW/cm^2; above this value, a dramatic increase in reflectivity is observed.

DFWM from Free-Carrier Plasma Gratings. Free-carrier plasma with densities up to 2.5 x 10^{15} cm^{-3} can be formed in lightly doped or intrinsic germanium with CO_2 laser intensities of 100-200 MW/cm^2. This process has been studied intensively at Los Alamos[58,59] and elsewhere.[62,63] We have been able to induce plasma gratings capable of amplified reflections in the DFWM configuration in optical grade (slightly n-type) and in slightly p-type germanium. Above the threshold for this process, the plasma contribution totally dominates the contribution of the standard mechanisms for DFWM, giving measured reflectivities as high as 800%. Because the intensity-dependence of plasma density is well known from previous work,[59] it is a simple matter to compute the refractive index modulation created by the plasma,[56] and, from this, the expected reflectivity. We have obtained a factor-of-2 agreement between experiment and theory in this regime, despite the eleventh-power intensity dependence of the plasma reflection coefficient. Possible applications of this work include phase-conjugate oscillators with nearly perfect phase and intensity profiles, as well as efficient point-illumination geometries analogous to highly aspheric optics. Figure III-64 illustrates typical results we obtained in optical-grade germanium.

Theoretical Treatment of Pump Depletion. Because theories of phase conjugation are essentially small-signal theories in which the pumps are always assumed much more intense than either the probe or the signal, it is natural to inquire how small the pump may be to give the expected reflection. This consideration is important in system designs, where pump beams of energy ≥100 J might be required to satisfy the assumption of the small-signal theory. Figure III-65 shows the results of a computer simulation designed to provide answers for these questions. Clearly, the correction to the small-signal theory is small when the reflectivity is small but becomes much more dramatic as the reflectivity approaches 100%. For the base-line case identified as being relevant to ICF systems applications, we can achieve the desired reflectivity of 10% when the pump intensity is as low as five times that of the signal to be conjugated.

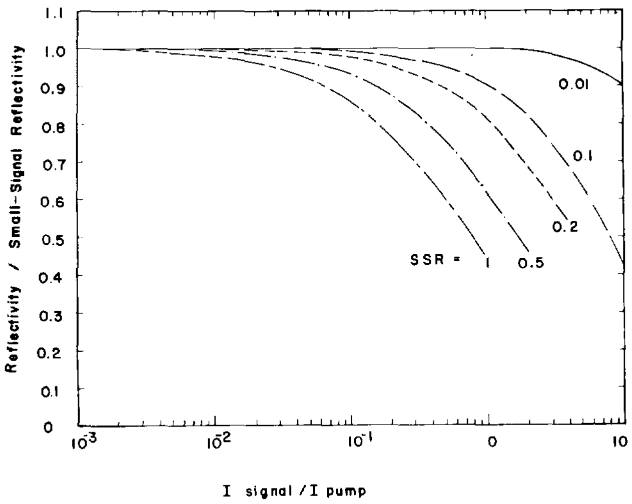

Fig. III-65. Calculations of pump depletion and its effects on phase-conjugate reflectivity. The ratio of actual reflectivity to that predicted by small-signal theory is plotted as a function of the ratio of probe-to-pump signal intensities for several values of small-signal reflectivity (SSR).

Optical Damage Limitations for Copper Mirrors Used in CO_2 Laser Systems (S. J. Thomas)

CO_2 laser systems use copper mirrors extensively. Such mirrors must be used at high fluence levels and for repeated short pulses in air and vacuum environments. However, the single-shot damage thresholds that have been reported[64,65] give no hint of the fluence levels a mirror can survive in a multishot system. In this section, we compare the performance of copper mirrors finished by different techniques, including single-point diamond turning (SPDT). We present for the first time the relative decrease in 10-μm damage thresholds for multiple shots and the loss of brightness of a reflected beam at high fluence levels. In our experiments, we measured mirror lifetime by comparing the focusability of the reflected beam in vacuum at various energy levels near threshold. We fired up to 100 shots per site.

Plasma formation causes a loss in intensity and energy when copper mirrors are used in air. Damage thresholds in air are difficult to measure because of the formation of a plasma at the mirror surface; indeed, some mirror surfaces cannot be damaged at all in air.[66] We have measured the loss of energy and intensity caused by the air-breakdown plasma absorbing the tail of the pulse. Mirrors with many polishing scratches or machining marks could not be damaged because these surface irregularities caused the early formation of a plasma that protected the mirror surface. Such mirrors, however, did not perform well in multishot lifetime tests in vacuum because no protective plasma could form.

Description of Test Mirror. Mirrors used for these measurements were fabricated from 10-cm (4-in.) copper-plated aluminum bronze substrates of the type used in Antares. We supplied the substrates. The copper plating was 0.040 in. thick. Several vendors used standard optical fabrication techniques for the test mirrors, whereas some mirrors were finished by SPDT at the DOE Y-12 facility.

Experimental Setup and Procedure. We conducted laser damage studies at the GWTF, which produces a Gaussian 1.7-ns pulse tuned to 10.59 µm [P(20)]. Figure III-66 shows the test setup. We placed the samples 10 cm inside the focal point of a 1-m (focal length) lens whose $1/e^2$ spot radius was 1 mm and measured the peak fluence (J/cm^2) at the sample plane on each shot using a 200-µm pinhole. The pinhole was located in the split-off reference beam, at the same distance from a 1-m (focal length) lens as was the sample. To record the incident and reflected energies of each laser shot, we used a Laser Precision Corp. ratiometer that was regulated with calibrated CaF_2 attenuators. Before each test series, a calibration was performed with an identical pinhole centered at the sample plane. Using this technique, we determined damage-plane fluence to within ±2%.

We determined absolute fluences by comparing the Laser Precision Corp. calorimeters to Scientech Inc. disk calorimeters, which are widely used at Los Alamos as measurement standards. This cross calibration shows that the Laser Precision meter reads 25% low. Because Scientech disk calorimeters are used as standards throughout the inertial fusion program, we have corrected our data to show Scientech joules.

For vacuum studies, samples were placed in a vacuum chamber with NaCl windows (Fig. III-67). Pressure was less than 100 mtorr for all tests. We used a liquid nitrogen cold trap to prevent oil vapors from reaching the test mirrors. Damage, defined as any change in the mirror surface, was observed visually with the aid of a 60X microscope and a bright-light source. Damage spots in air were characterized by a diffraction pattern, whereas the damage created in a vacuum was always a smooth crater that grew from a single point. We believe that the diffraction in the former case is caused by plasma formation.

Single-Shot Damage Thresholds. We measured single-shot damage thresholds by irradiating the sample at 25 different sites one-on-one at or near threshold and taking the average of the measured threshold fluences. Table III-XII tabulates the thresholds for air and vacuum.

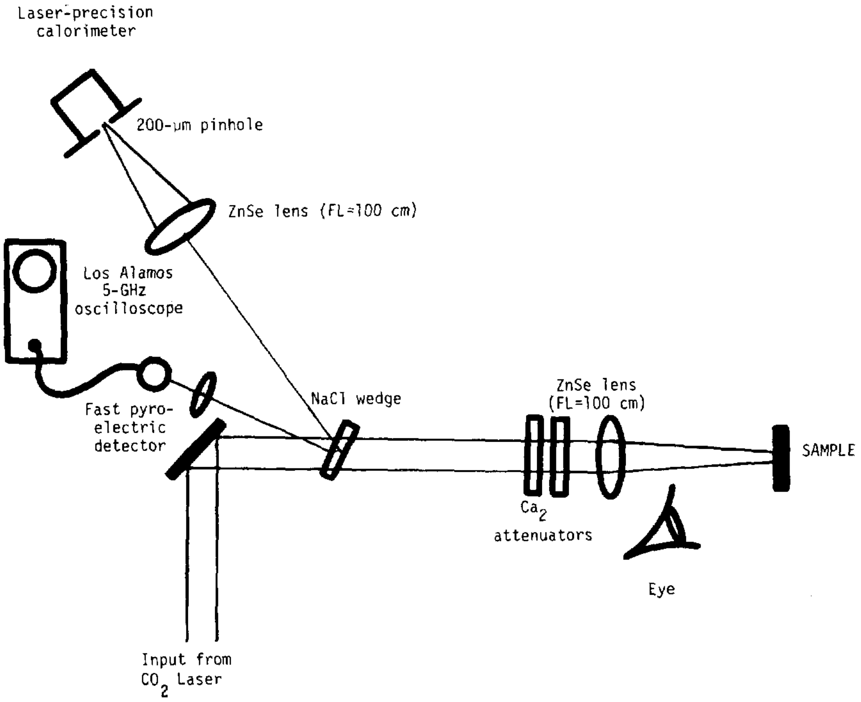

Fig. III-66. CO_2 laser-damage test setup. The ZnSe lenses are located at a distance of 90 cm from the sample and from the Laser Precision Corp. ratiometer—that is, just slightly forward of the focal plane of the lens.

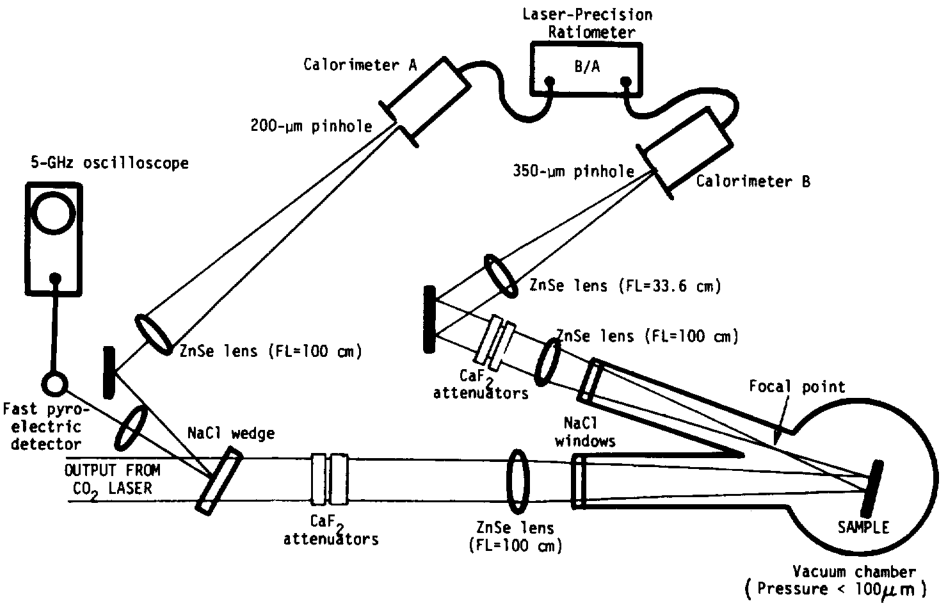

Fig. III-67. Experimental setup for measuring degradation of beam brightness for samples irradiated in vacuum.

Vacuum thresholds were nearly the same, indicating that we may have reached the melting point of copper.

Multishot Studies. The focusability of the reflected pulse for multiple shots on the same site was measured as shown in Fig. III-67. We placed the B-calorimeter of the Laser Precision ratiometer behind a 350-μm-diam pinhole. Any change in transmission or focusability was indicated by the energy ratio of the B and A calorimeters of the ratiometer. We normalized the B/A reading to unity for each energy level and plotted it as a function of shot number. Our goal was to find the highest fluence level that would allow us to obtain 100 shots without a loss in brightness greater than 10%.

Typical multishot data are shown in Fig. III-68, and summarized in Table III-XIII where we have listed the maximum fluence (in J/cm^2) that would allow 100 shots before losing 10% brightness and the percentage of the single-shot threshold for each mirror. On an average mirror, 8.49 ± 1.09 J/cm^2 is a safe fluence level. This corresponds to ~71 ± 12% of the single-shot threshold.

Pulse Transmission in Air and Vacuum. When a mirror is used in air, a plasma forms at the mirror surface at ~5 J/cm^2 with a 1.7-ns pulse. To measure the effect of this plasma on the reflected pulse, we used two fast pyroelectric detectors and a 5-GHz oscilloscope to compare the input pulse to the reflected pulse. The mirror was placed at the focal point of the 1-m (focal length) lens, and the reflected beam was focused into the second detector with a 33-cm (focal length) lens. Both pulses were displayed on the same sweep with the reference input pulse first. Figure III-69 shows a sample set of photographs. As the energy is increased, the plasma forms and absorbs the tail of the pulse.

We performed a computer analysis to compare the output pulse with the input pulse. Results for two mirrors in air and vacuum are plotted in Fig. III-70 showing transmission of energy and intensity as a function of fluence. There is a spark on the mirror surface in vacuum caused by spallation of material from the surface. However, we observed no transmission loss until the mirror was damaged. The effect of the plasma formation in air was not as severe for the SPDT mirror.

Conclusions.

- Single-shot damage thresholds in air do not show the true limitations of a mirror.
- Single-shot thresholds for 23 mirrors in vacuum averaged 11.73 ± 1.64 J/cm^2, indicating an upper limit had been reached.
- The SPDT mirrors could be used at their vacuum 100-shot damage level (8.3 J/cm^2) without noticeable pulse distortions. However, the polished mirrors (for example, Spawr No. 12-19-78-23) generated noticeable pulse distortions at fluences of 4 J/cm^2 or ~53% of their vacuum 100-shot level.

TABLE III-XII. Damage Thresholds in Air and Vacuum[a]

		Damage Threshold (J/cm^2)	
Mirror No.	Manufacturer	Air	Vacuum
56SN056	Kodak	>25	13.05 ± 1.2
39SN039	Kodak	>25	9.65 ± 1.15
7-9-79-1	Zygo	>25	13.85 ± 0.44
7-9-79-3	Zygo	19.11 ± 1.7	13.13 ± 0.54
3-7-79-53	Kodak	16.39 ± 1.4	9.93 ± 1.2
12-11-78-26	Applied	15.68 ± 1.3	13.05 ± 0.85
12-11-78-24	Applied	15.01 ± 0.67	13.77 ± 0.21
3-27-79-45	Zygo	16.16 ± 1.47	14.57 ± 0.57
4-23-79-01	Alpha	13.91 ± 0.78	9.64 ± 0.21
12-11-78-22	Applied	13.51 ± 0.61	12.07 ± 0.23
4-23-79-2	Alpha	12.12 ± 0.54	9.67 ± 0.79
4-17-79-04	OSTI	12.24 ± 0.43	12.01 ± 0.43
1-18-79-43	Design Optics	12.18 ± 0.63	11.48 ± 0.45
1-18-79-42	Design Optics	11.02 ± 0.46	10.43 ± 0.68
4-17-79-01	OSTI	12.56 ± 1.25	11.72 ± 0.45
12-19-78-22	Spawr	8.51 ± 0.73	7.96 ± 0.15
12-19-78-23	Spawr	11.75 ± 0.63	11.17 ± 0.35
3-23-79-23	Y-12 SPDT	12.90 ± 0.31	12.62 ± 0.33
3-23-79-26	Y-12 SPDT	13.31 ± 0.51	12.35 ± 0.1
3-23-79-25	Y-12 SPDT	21.63 ± 4.6	12.26 ± 0.352
3-23-79-22	Y-12 SPDT	12.39 ± 0.95	12.85 ± 0.20
3-23-79-24	Y-12 SPDT	23.82 ± 1.0	12.19 ± 0.15
Stock Copper	Los Alamos SPDT	>25	10.47 ± 1.25
Stock Aluminum	Los Alamos SPDT	0.413 ± 0.27	---

[a] To convert J/cm^2 to GW/cm^2, multiply by 0.602.

- For multishot use, a high-quality mirror can be employed at ~71 ± 12% of its single-shot threshold in vacuum.
- Care must be taken when mirrors are used in air to avoid energy loss and pulse distortion caused by the air spark. In large-diameter beams, the center of the beam could be absorbed, leading to undesirable diffraction effects.

Multiple Pulse Damage to Copper Mirrors
(J. F. Figueira, S. J. Thomas)

The maximum performance that can be obtained reliably from a high-power laser such as Helios is determined to a large extent by the ability of the optical components to survive the high laser fluences present during an extended period of operation. To determine the practical limitations to laser system performance, we have maintained a continuing program of material evaluation. Both single-point damage thresholds and multishot damage thresholds have been determined for many optical materials and components most frequently used in Helios.

To fully characterize the long-term behavior of optical components, we are conducting lifetime tests to determine how well a given material withstands repeated exposure to high-power laser radiation. As an example, let us consider the results for copper mirrors in vacuum.[67] A sample is positioned so that a series of laser pulses at a fixed fluence can be directed to a single fixed point on the mirror surface. The peak brightness of the reflected beam is then measured as a function of the number of laser shots. Figure III-71 shows the result of such a test for several different fluence levels. At one-half the single-shot damage level, the mirror lifetime is essentially unlimited. If the irradiating fluence is increased, the brightness of the reflected beam degrades, indicating a tradeoff between operating fluence and mirror lifetime.

In these tests we determined mirror lifetime, that is, the number of laser shots required at a fixed fluence level to reduce the brightness of the beam reflected from the mirror to 90% of its original value. These tests included mirrors from several vendors: Union Carbide Corporation's Y-12 (micromachined mirrors), Spawr Optical Research, Inc., Applied Optics Corp., Design Optics Inc., and Eastman Kodak Co. (conventionally polished mirrors). From data obtained, we constructed lifetime curves for a given optical component. Figure III-72 shows such a lifetime curve for copper mirrors in vacuum, where the number of shots required to produce a 10% reduction in beam brightness is plotted as a function of beam fluence. Data for mirrors from all five vendors are used. Input fluences have been normalized to the measured single-shot damage fluence F_0. The data for all mirrors scatter about an exponential trend line and can be fit by the function

$$N = 10^{7(1 - F/F_0)} \quad , \qquad \text{(III-24)}$$

where N is the number of shots at fluence F required to reduce the beam brightness to 0.9 of its starting value and F_0 is the single-shot damage threshold. The prefactor 7 is determined by a least squares fit to the data. The universality of the trends among polishers suggests that the failure mode is dominated by intrinsic properties of the copper (such as melt levels) rather than by details of the mirror preparation technique. In general, for extended lifetimes ($N > 100$), operation at half the single-shot damage threshold is required for copper mirrors in vacuum.

Of course, different damage criteria will lead to different conclusions. In particular, if higher beam brightness degradations are allowed, much more detail appears in the lifetime data, and the conventionally polished mirrors show a lifetime advantage over the SPDT mirrors.

Laboratory tests as described above and the continuing practical experience gained on Helios are generating a data base on component survivability for high-power ir lasers. In addition, we are developing a general methodology for the characterization of material interactions with high-power laser beams that will be applicable to a wide variety of laser wavelengths and operating conditions.

ADVANCED CONCEPTS

Introduction

Although the bulk of our research is directly related to current and planned short-pulse CO_2 lasers for ICF applications, a limited effort in advanced laser fusion concepts is also in progress. Though small in terms of time and level of effort, these activities help to maintain a state-of-the-art posture in the laser technology field. Moreover, our direct involvement in current ICF programs helps to point these advanced projects in directions that have a high probability of contributing to ICF laser development. At present, advanced concepts work is focused on phase conjugation and on the development of high-brightness pulsed uv lasers.

Transient Analysis of Kerr-Like Phase Conjugators Using Frequency-Domain Techniques (B. R. Suydam, R. A. Fisher, B. J. Feldman)

The subject of optical phase conjugation (or "wave front reversal") using DFWM in Kerr-like media has recently become extremely popular.[68] The unusual aberration-free image-transformation properties of phase conjugators suggest many practical applications in fields as diverse as adaptive optics, laser fusion, image restoration, real-time holography, high-resolution microscopy, and optical computing.

The steady-state on-resonant theory gives the now familiar expression for the conjugate wave strength as $\tan(\kappa\ell)$ times the input wave strength. In this expression, $\kappa = \kappa_0 \Delta n$ is the coupling constant (the product of the free-space wave number and the changes in refractive index) and ℓ is the length of the conjugator. But for cases of interest to the laser fusion program, one cannot rely on predictions for this steady-state theory. We have, therefore, developed a transient theory, which permits us to calculate the conjugate waveform for any arbitrary input pulse. We assume that the pump waves are cw.

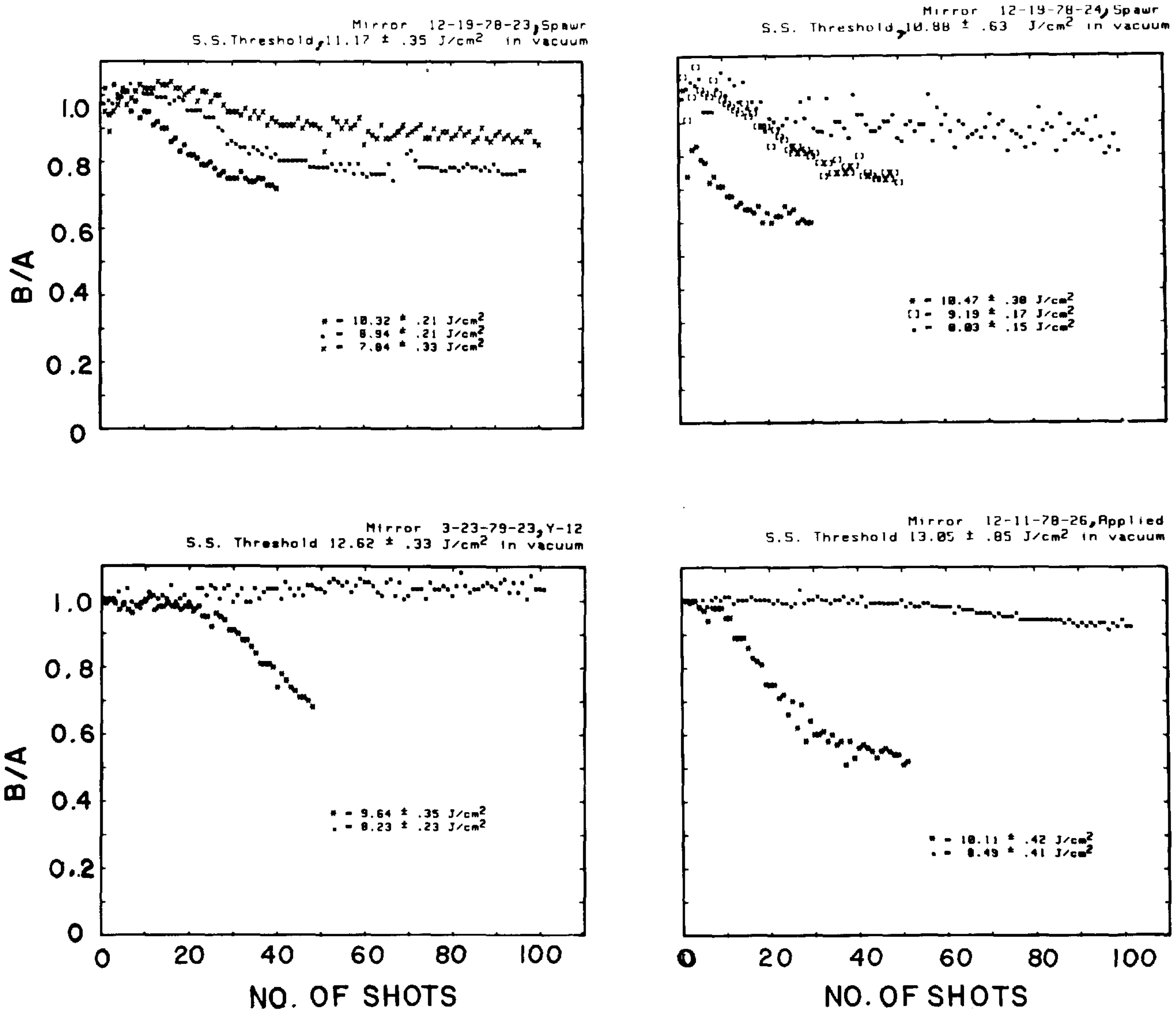

Fig. III-68. Comparison of multishot damage on mirrors from different vendors. The ratio B/A is a measure of the focal-spot quality produced by the mirror.

The theoretical expressions for the conjugate waveform are expressed as an antilinear double Fourier-transform relationship. With the use of FFT techniques, these expressions can be evaluated readily with a computer. We have demonstrated both analytically and numerically that the response to a temporal delta function input agrees with that in the literature.[69]

Figure III-73 shows a representative set of calculations. We conjugate a 0.5-ns pulse in a germanium conjugator set for unit conjugate reflectivity on-resonance, but with ℓ and κ varied to show the deleterious effects of temporal spreading and of pulse reduction. These results are recast in Fig. III-74 and show that to avoid serious efficiency degradation, the round-trip transit time of the conjugator must be less than the duration of the input pulse. Pulse spreading is the reason that the peak intensity falls off faster than the energy. Figure III-75 shows a calculation of the degradation in chirp reversal when the conjugator becomes too long. The same input pulse as that in Figs. III-73 and III-74 has impressed upon it a positive linear chirp just sufficient to double the spectral width. Only the thinnest conjugator (0.1 cm) truly reversed the chirp.

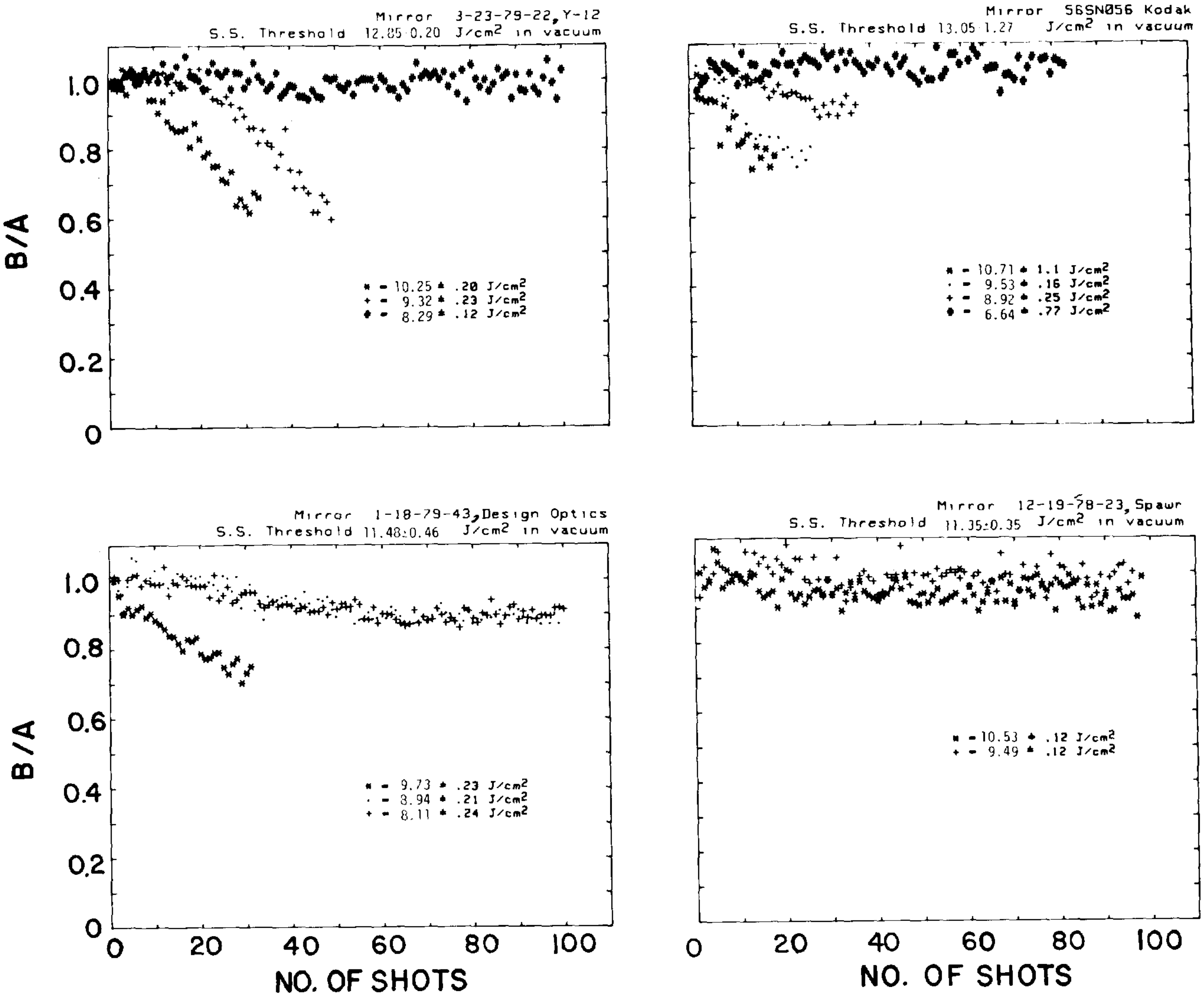

Fig. III-68. (cont)

These are only a few examples of the many calculations that can now be performed with this newly developed computer technique. Our predictive capability for anticipating the waveform modification during the conjugation of arbitrarily shaped pulses will thus be greatly enhanced. A more complete description of these calculations can be found in Ref. 70.

Practical Applications of Ultraviolet Phase Conjugation (B. J. Feldman, R. A. Fisher, S. L. Shapiro)

Introduction. The desirability of phase conjugation in the uv is widely acknowledged. The highly nonlinear liquid CS_2 is a natural choice for an efficient conjugator. Unfortunately, pure CS_2 is opaque over most of the uv spectrum. However, we have found that by diluting CS_2 in uv-transmitting solvents, the absorption bands are significantly shifted, opening up a concentration-tunable transmission window in the important 2450- to 2850-Å range. Establishing this transmission window in CS_2 allows one to take advantage of its large Kerr effect, which, in the uv, is enhanced over its visible value.[71] Within this concentration-tunable window, we have obtained a phase-conjugate 2660-Å, 0.1% reflection in a 1-mm-thick sample consisting of a mixture made up by volume of 60% CS_2 and 40% hexane. This reflection is consistent with the large nonlinearity of CS_2.

In DFWM,[72] a probe wave impinges upon a nonlinear material that is illuminated by a pair of counterpropagating pump waves. Even though an aberrator may be in the

TABLE III-XIII. Allowable Pulse Energy for One Hundred Shots Before Loss of 10% Brightness

Mirror No.	Manufacturer	Max Fluence in Vacuum Permitting 100 Shots Without 10% Loss of Brightness (J/cm^2)[a]	Percentage of a Single-Shot Threshold (%)[b]
3-23-79-26	Y-12	9.46 ± 1.0	77
3-23-79-23	Y-12	8.23 ± 0.23	65
3-23-79-22	Y-12	8.29 ± 0.12	65
12-19-78-23	Spawr	7.48 ± 0.33	70
12-19-78-24	Spawr	8.03 ± 0.15	74
12-19-78-23	Spawr	10.53 ± 0.12	Different Spot 94*[c]
12-11-78-26	Applied	8.49 ± 0.41	65
56-SB056	Kodak	6.64 ± 0.77	51
1-18-79-43	Design Optics	8.94 ± 0.21	78

[a] Average fluence for 100 shots = 8.49 ± 1.09 J/cm^2.
[b] Average fraction of single-shot threshold = 71 ± 12%.
[c] Did not repeat.

way, the medium reradiates a fourth phase-conjugate wave precisely retracing the k vector of the probe wave.

These distortion-correcting features of phase conjugation suggest widespread applications, in particular in the uv range. First, all high-energy uv lasers are high-gain excimer systems, characterized by severe optical inhomogeneities. These lasers are particularly promising for laser fusion, laser isotope separation, and very long distance propagation. An appropriate conjugator could minimize the effect of static aberrations both in the laser and between the laser and the target.[73] Thus, a highly aberrated excimer laser system could be converted into one providing a well-collimated, focusable beam. As a second application, uv phase conjugation could be used in conjunction with photolithography (or other laser processing techniques) to produce small integrated-circuit components. Lastly, in the uv, optical tolerances are hard to attain; phase conjugation may permit the use of inferior elements in uv optical systems.

Solvatochromism in CS_2. In choosing nonlinear uv phase-conjugation samples, we sought transparent materials with a strong optical Kerr effect and a short response time. Although liquid CS_2 is useful for visible and ir wavelengths, it is opaque below 3600 Å because of strong and broad electronic absorption bands at 3100 and 2200 Å. Nevertheless, we have observed that when CS_2 is mixed with uv-transmitting organic solvents, a window appears between the two absorption bands whose width and center frequency depend upon the specific solvent and its concentration.

Figure III-76 shows uv transmission curves for 1-mm-thick samples of various mixtures of reagent-grade CS_2 and uv-grade hexane. The region of transparency broadens and the peak transmission wavelength shifts by 3000 cm^{-1} toward the blue as the CS_2 concentration is reduced. Without solvent-solute interaction, the peak transmission wavelength would not have changed. Although solvent shifts for dilute systems are well known,[74] we are not aware of any concentration-dependent studies in CS_2-hexane. At 60% CS_2 concentration, the 2660-Å transmission is 50%, making this mix suitable for phase conjugation at this wavelength and at the 2680-Å wavelength of CH_4-Stokes-shifted KrF laser light. Further dilution of the CS_2 increases the transmission at both 2485 and 2820 Å, suggesting that longer dilute samples would be suitable phase conjugators at KrF and XeBr excimer wavelengths.

In our experiments, a single, collimated, 5-mm-diam, 400-mJ, 15-ps, 2660-Å pulse (quadrupled Nd:YAG) entered the experimental arrangement (Fig. III-77). The pulse first encountered a 90% reflecting beamsplitter,

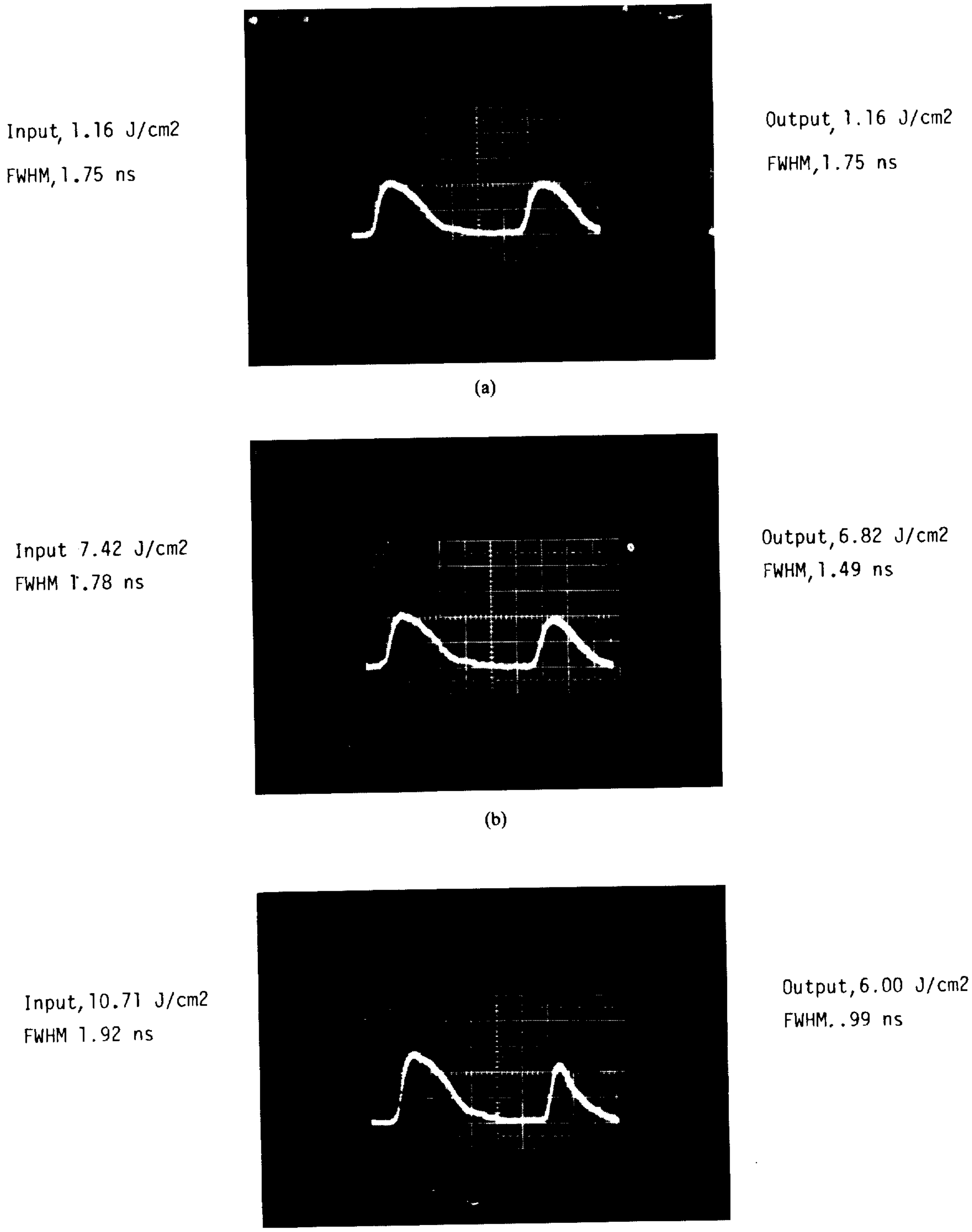

(a)

(b)

(c)

Fig. III-69. Comparison of input and output pulse shapes when an air-breakdown plasma forms at the mirror surface. As the input fluence increases from (a) to (c), the fraction of transmitted energy and the FWHM of the pulse decrease.

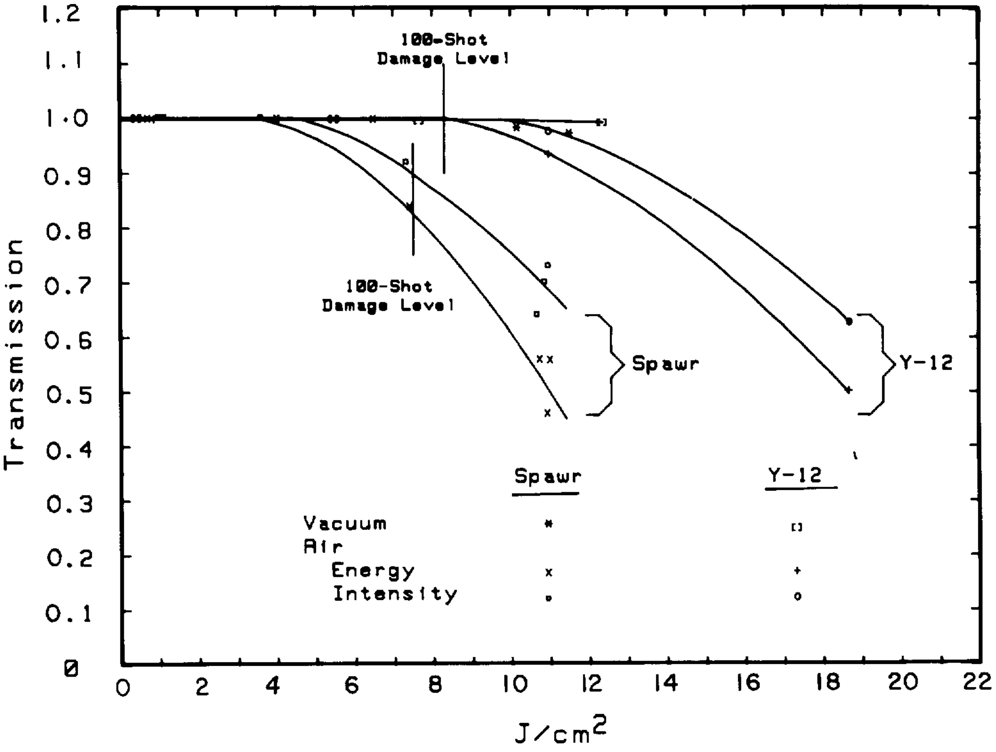

Fig. III-70. Measured transmission as a function of incident fluence in air and vacuum.

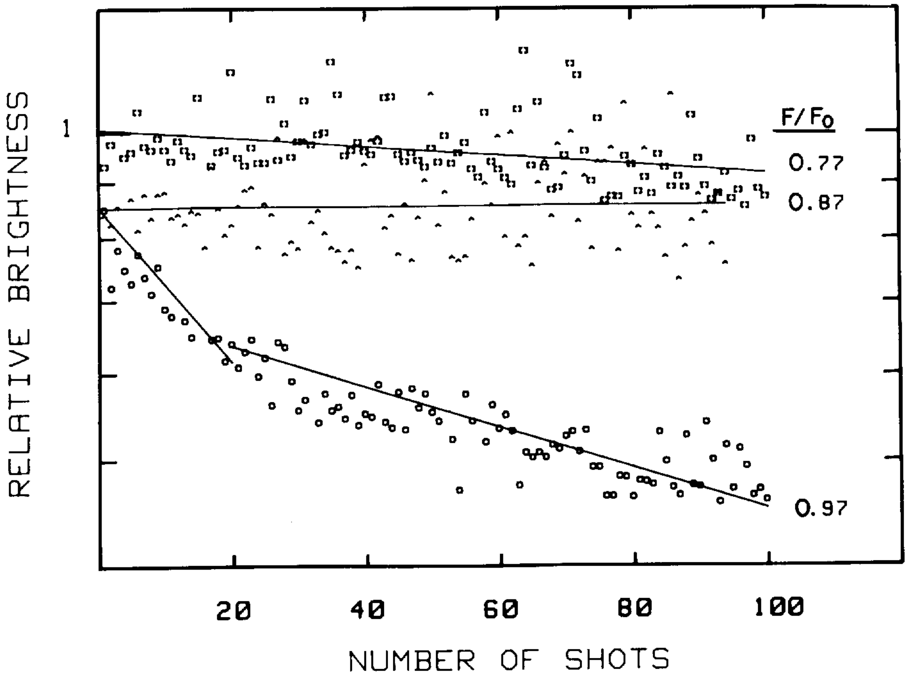

Fig. III-71. Brightness degradation of a conventionally polished copper mirror illuminated with successive laser pulses at a fixed peak fluence. Pulse duration 1.7 ns, 10-μm P(20) radiation.

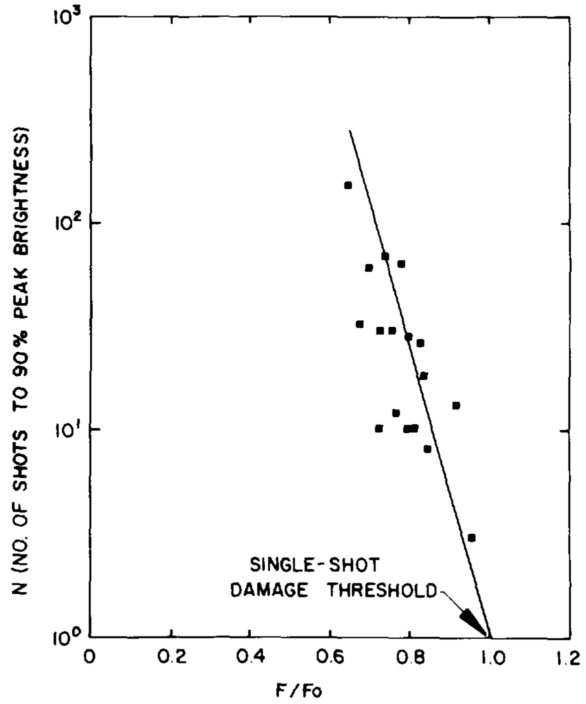

Fig. III-72. Mirror lifetime curve for conventionally polished and micromachined copper mirrors for various fixed values of the irradiating fluence.

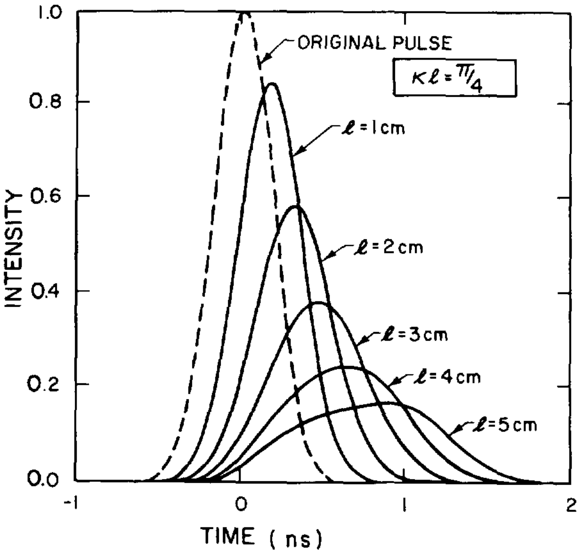

Fig. III-73. Temporal spreading of the conjugate pulse. This calculation was performed by keeping $\kappa\ell$ set to $\pi/4$ (so that the conjugate reflectivity on resonance is unity), but with ℓ and κ variable. This procedure varies the effective bandwidth of the conjugator. The original pulse (0.5 ns FWHM) is shown by the dashed line. The conjugator material is germanium with a refractive index of 4.0.

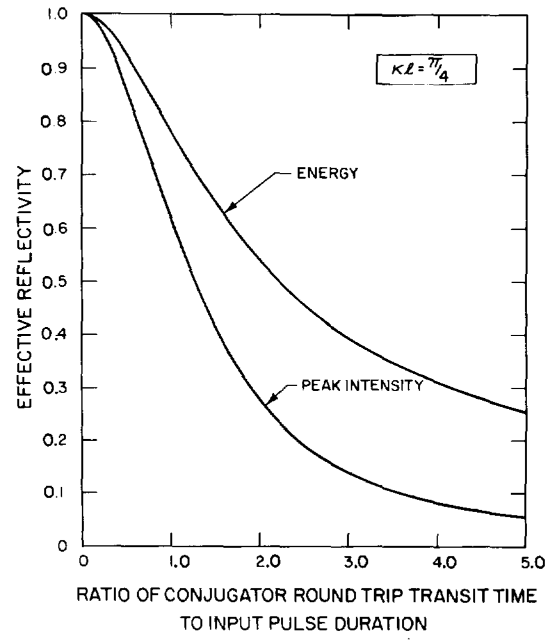

Fig. III-74. Calculated degradation in effective reflectivity when the probe pulse duration becomes shorter than the thickness of the conjugator. Both the integrated conjugate energy and the intensity at the peak of the conjugate pulse are plotted. All other conditions are like those in Fig. III-73.

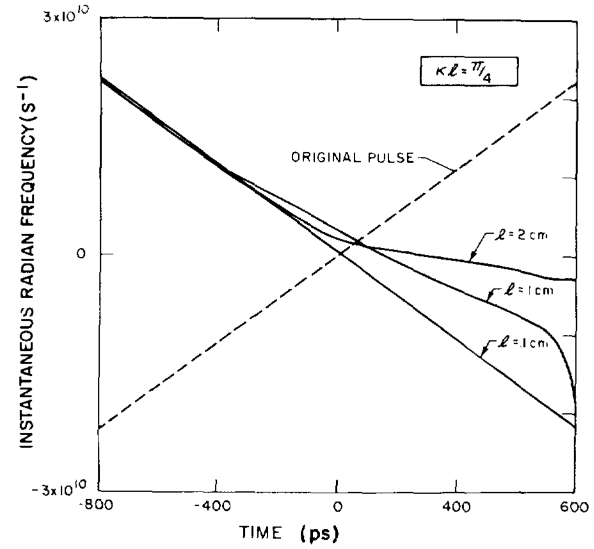

Fig. III-75. Study of the chirp-reversal process. The instantaneous frequency shift vs time curve is shown for the positively chirped input pulse. Again (as in the previous two figures) the cw on-resonance conjugate reflectivity is set to unity, but the physical thickness of the conjugator is varied. For a physically thin conjugator (one that is sufficiently broadband), the chirp reversal is nearly perfect, but for thicker conjugators, the chirp at the peak of the pulse is significantly reduced.

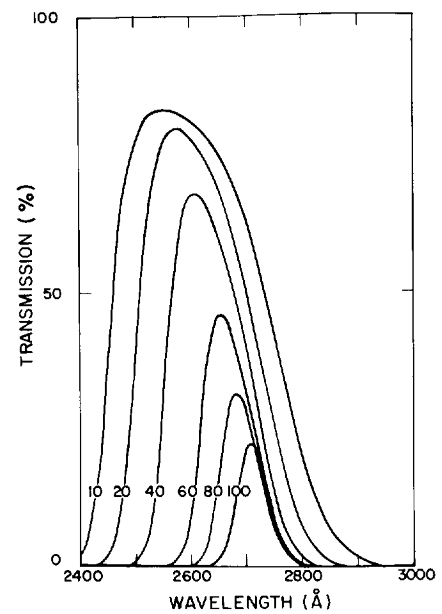

Fig. III-76. Transmission spectra of 1.0-mm-thick CS_2-hexane mixes. The number associated with each line refers to the percentage (by volume) of CS_2 in the mixture. These curves have not been corrected for the Fresnel losses of our quartz cell.

and the larger portion was directed into a ring to provide counterpropagating pump waves within the 1-mm sample. The beam that passed the 90% reflecting beamsplitter passed through a 50% reflecting beamsplitter and impinged (as a probe beam) onto the sample at a 30° angle. All beams were linearly polarized in the same direction. A curved mirror focused the probe beam to a point beyond the sample, halving the diameter at the sample to ensure complete overlap of the three beams. A 100% reflector could be placed before the curved mirror as a reference for evaluating conjugate reflectivities. Any conjugate emission retraced the path of the probe beam, and a portion was redirected by the 50% reflecting beamsplitter for detection and analysis.

With a CS_2-hexane solution (60% CS_2) in a 1-mm cell, we observed signals on a uv-sensitive video monitor. Their phase-conjugate nature was confirmed by their disappearance when we blocked either of the two pump beams or the probe beam (blocked between the 50% and 90% beamsplitters). Also, the spot on the video monitor did not move with minor angular adjustment of the curved mirror, thereby satisfying a one-dimensional aberration test.

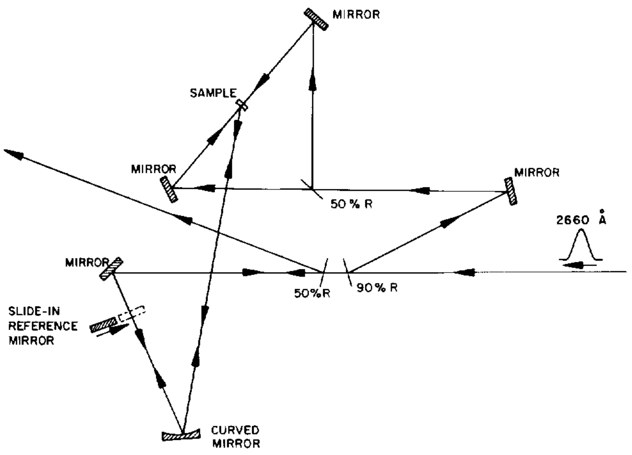

Fig. III-77. Experimental arrangement. Most of the ultrashort pulse is directed to provide the counterpropagating pump waves; the remainder is brought to the sample as a probe beam.

Separate photomultipliers monitored the conjugate and the input signals. The 1.5-ns-response photomultipliers acted as high-speed calorimeters. The conjugate channel gave two peaks; the true conjugate signal was preceded (by 3 ns) by scattering from the 50% beamsplitter. We measured the height of the second peak only. The data are shown in Fig. III-78. We made a least squares fit to the data using the equation

$$E_s = a(E_{in}) + b(E_{in})^c , \qquad \text{(III-25)}$$

where E_s is the observed signal energy and E_{in} is the input signal energy. The first term represents the residual linear scattering. We found that $a = 0.15$, $b = 0.028$, and $c = 2.96$. The value of c is in excellent agreement with the expected value of 3, indicative of the DFWM process.*

At the highest input intensities, we obtained 0.1% conjugate reflectivity. To compare these results to theory, the simple DFWM model must be modified to include nonsaturable absorption. The low-reflectivity expression becomes

$$R = [k\ell\, \delta n_0 \exp(-\alpha\ell)]^2 , \qquad \text{(III-26)}$$

where $k = \omega/c$, δn_0 is the nonlinear index change induced by one pump wave at its entry face, and α is the

---

*For a low-reflectivity conjugator, the reflectivity is proportional to the square of the pump wave intensity. The probe signal is also proportional to the pump wave intensity, giving overall cubic dependence.[75]

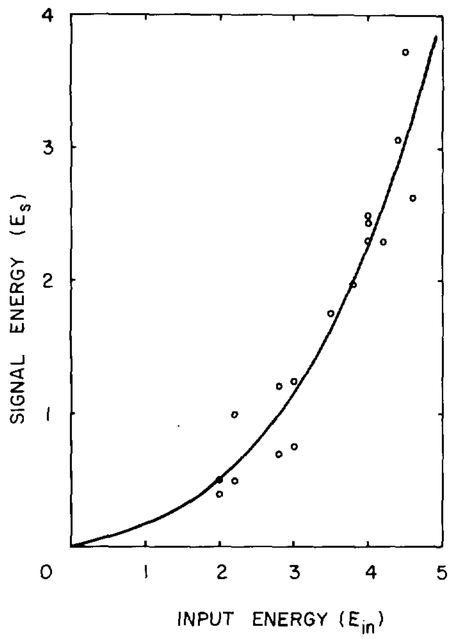

Fig. III-78. Input vs output energy (arbitrary units) for a 1-mm-thick conjugator containing (by volume) 60% CS_2 and 40% hexane. To include spurious scattering, we fit the data to the expression in Eq. (III-25), giving c = 2.96 and a nearly cubic dependence for the nonlinear term. The best fit curve is also drawn.

nonsaturable-absorption coefficient. To estimate the induced index change from the pump, we note that $\delta n = 1/2 n_2 \epsilon^2$, where ϵ is the slowly varying envelope function of one of the pumps. For CS_2, $n_2 \sim 4.34 \times 10^{-11}$ esu at 2660 Å.[71,76] We assume for a 60% CS_2 mix that n_2 is reduced by a factor of 0.6 (ignoring small local field and volumetric corrections[76]). The peak intensity of each pump was 40 MW/cm^2, corresponding to $\delta n_0 = 3.1 \times 10^{-6}$. Using Eq. (III-26), we find that R = 0.12%, which is in good agreement with the measured value.

The signal vanishes for CS_2 concentrations below 5%. Furthermore, introducing a 40-ps delay into either of the two pump paths decreased the 60% CS_2-generated conjugation signal more than tenfold. The disappearance of the signal with dilution and the reduction with delay rule out the roles of solvated electrons[77] and thermal gradients,[78] respectively, leaving only the optical Kerr effect in CS_2 as the dominant nonlinearity responsible for our conjugate signals.

We obtained phase-conjugate signals of approximately the same reflectivity for 60% CS_2 mixtures in cyclohexane, ethyl alcohol, 1-2 dichloroethane, and N-butanol. These results indicate that the n_2 of dilute CS_2 is not strongly solvent dependent. We have also seen weaker phase conjugation in pure dimethyl sulfoxide (DMSO); in 1,2-dichloroethane; and in β-carotene-hexane mixes. Because of the high absorption, we observed no signals in pure CS_2.

In addition to the above Kerr-conjugators, we have studied conjugation in various saturable absorbers. The precise mechanism for the observed effects is not clear now. Heating,[78] saturation,[60] and photochemical reactions[79] may play roles. Fluorescein in ethyl alcohol, rhodamine 6G in water or in ethyl alcohol, Kodak A9740 dye in 1,2-dichloroethane, pyrene in hexane, and 2-Napthol 6-Sulfonate in water (pH 4.5) all exhibited ~0.01% conjugate reflectivity. Neither water nor ethanol gave a signal.

Conclusion. We have obtained the first demonstration of phase conjugation in the uv. Because we used ultrashort pulses, we had to limit sample thicknesses to millimeter dimensions. For lasers with greater coherence lengths, thicker samples could be used with correspondingly higher conjugate reflectivities.

Excimer Laser Development (I. J. Bigio)

Research and development in the area of ultraviolet gas discharge lasers is done for a multiplicity of motivations. Recent interest in the development of excimer lasers as laser fusion drivers opens up many areas requiring research and development. The desire to use short-wavelength lasers as diagnostic tools in laser fusion gives impetus to the development of excimer lasers as the originating source of nonlinear processes. Yet another area of interest is nonlinear phase conjugation, particularly the uv range, which appears to have great promise in applications to various optical fields.

Our effort has been directed toward the development of an electrical discharge krypton-fluoride laser with a very narrow line width and very high brightness at the same time. Other excimer systems would also naturally benefit from these developments. We want to use a small but highly controlled krypton-fluoride laser as a master oscillator to injection-lock a much larger krypton-fluoride oscillator, which then becomes the slave oscillator. This scheme has worked successfully in other high-gain laser systems that exhibit problems similar to those of krypton-fluoride lasers.[80] Figure III-79 shows the experimental apparatus.

The master oscillator is controlled with etalons and spatial filters and has a large aspect ratio, yielding a

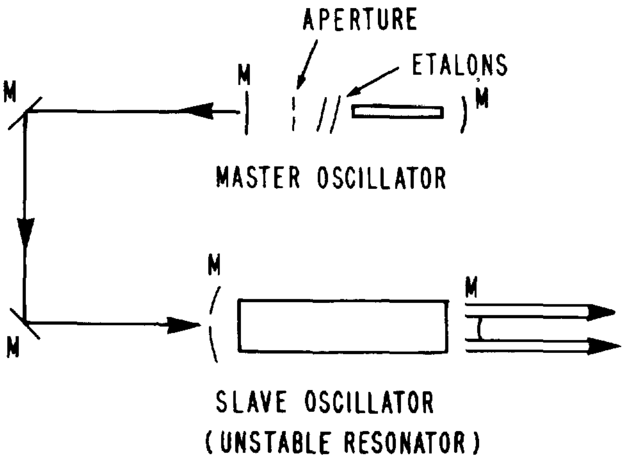

Fig. III-79. Injection-locked KrF master-slave oscillator system.

beam of high brightness and narrow line width, although one of low power. The master oscillator beam is injected through a hole in the rear mirror of an unstable resonator cavity surrounding the larger (slave) oscillator. We hope that these experiments will result in a narrow line width laser pulse with a divergence only a few times larger than the diffraction limit and an energy greater than 100 mJ. This result would represent a much simpler, more reliable, and less expensive way to achieve these results than methods currently employed.[81]

Almost all the hardware for this system has been constructed. The master oscillator, based on a Los Alamos design, is essentially a miniaturized Blumlein device with corona preionization and thyratron switching. Diffraction-limited operation has been achieved, although at reduced power, whereas ongoing studies are directed at combining the low divergence with narrow line width (≤0.1 Å) and a longer pulse duration (>20 ns).

The slave (power) oscillator is an LC-inverter discharge with a cross section of ~2 by 2 cm and a length of 60 cm. It is passively preionized by the displacement-current-induced corona discharge on the surface of dielectric boards located on either side of the discharge region. This type of preionization, which has been reported previously,[80] is remarkable because of its simplicity: it requires no separate discharge circuits or timing. In addition, pulse shape and energy are very stable from shot to shot, varying less than ±3%. Experiments to date have yielded pulse energies approaching 250 mJ, and further improvements are expected with minor modifications and optimization. With a stored energy of ~25 J, this yields an overall efficiency of ~1%. The discharge has a square cross section. We expect it to be well suited to an unstable-resonator configuration.

We have purchased and installed a commercially available gas-processing system for the slave oscillator. It will allow stable operation over a much longer time with a single gas fill. In addition, timing electronics to properly correlate the two-laser system have been assembled and are being tested.

Larger Systems. As part of a design study for larger KrF short-pulse laser systems, we redesigned a front end based on the concept of an injection-locked unstable resonator. Emphasis was placed on maximizing the use of commercially available components, on reliability, and on simplicity of operation. We expect this redesigned system to yield an output >1 J in 10 to 20 ns with a divergence of ~1.5 times the diffraction limit and with a line width of ~0.1 Å. We have ordered the components and are preparing laboratory space.

Theoretical Studies. The behavior of an unstable resonator with short-lived gain has been analyzed by several authors.[81] Their studies showed that the achievement of diffraction-limited output depends on cavity parameters such as length and magnification, as well as on the gain of the medium, the saturation parameter, and the duration of the gain. We are studying the effects of injection-locking by a small master oscillator and correlating the results of a numerical analysis with the experiments.

To the extent that the injected beam has been mapped with maximum efficiency onto the lowest order mode (LOM) (sometimes referred to as the dominant mode) of the unstable resonator, the two extremes of either ultrashort or very long gain duration are well understood. In the long-duration case, particularly with high gain and large magnification, the large loss differentiation between the LOM and all other modes allows the LOM field to dominate the cavity after several round-trip times. Then the output is nearly diffraction limited. In this case the injected master oscillator beam would somewhat accelerate the dominance of the LOM (compared with a build-up from noise) but would mainly determine the bandwidth of the output. Thus, the well-known steady-state solutions apply and the output can be described accurately.

At the other extreme, if the gain duration is shorter than the time for a single cavity pass and if the effective

g_0L is not large enough for single-pass superradiance, then the injected master oscillator beam undergoes simple amplification. In this case the energy from the slave oscillator (now just an amplifier) is not efficiently extracted unless the injected field is of saturating intensity. However, such a configuration misses the intended advantage of injection-locking, that is, that a large oscillator can be controlled by a *much* smaller oscillator.

Somewhere between these two extremes lie the parameters of discharge-pumped excimer lasers. Their gain tends to be high, with single-pass gains of e^6 to e^{15}, and the duration of the gain ranges from one to several round-trip cavity passes.

We have carried out a qualitative analysis and are planning a numerical study to identify the essential criteria for successfully locking a large (>10 MW) slave oscillator with a small (<10 W) master oscillator.

Other Systems. The argon-ion laser operating in the doubly ionized (Ar-III) chain has a lasing transition that is in good agreement with the 3511-Å line of XeF. We intend to build a pulsed Ar-III laser to investigate its usefulness as a master oscillator for injection-locking the XeF laser. Among the potential applications is the use of this system as a diagnostic tool in the inertial fusion program. We are studying other areas that could benefit the program, such as Raman scattering, Brillouin scattering, vuv generation, and phase conjugation.

GIGAWATT TEST FACILITY

The GWTF provides high-quality laser energy for a wide variety of short-pulse CO_2 laser technology experiments. The facility has two lasers, two screen rooms, five large optical tables, and state-of-the-art diagnostic equipment. Laser System 1 consists of a TEA oscillator (designed at Los Alamos) with a pulse-smoothing tube feeding a 2-m-long TEA amplifier (also designed at Los Alamos). The oscillator has a tunable grating for single-line operation. A LTSG and two Pockels cells clip the 60-ns pulse from the oscillator to 1.5 ns before the power enters the two-pass amplifier. The amplified pulse energy is 0.3 to 0.8 J. Laser System 2 consists of a 3-atm oscillator/amplifier (built at Los Alamos) with a pulse-smoothing tube and a 1-atm Lumonics 600 TEA amplifier. A system of Pockels cells clips the oscillator output pulse to 0.7 to 1.5 ns; the pulse is then reinjected into the amplifier section for four passes. The 200-mJ pulse from the amplifier makes three passes through the Lumonics amplifier, emerging with 5 J of energy. The outstanding feature of this laser is its Gaussian spatial distribution and reproducible pulse shape. Experiments performed on this system include (1) spatial and temporal pulse shaping in SF_6 and gas isolation mixes, (2) transmission measurements in hot CO_2, and (3) multishot damage studies on copper mirrors.

Our major experiment was the CO_2 phase-conjugate reflector experiment. We used the complete System 1 laser plus the Lumonics amplifier from System 2 for this purpose. We also conducted surface-damage experiments and gas-absorber performance tests on System 1. Target interaction experiments on System 2 were completed; no further target tests are planned. In the future, we will use System 2 for CO_2 laser development experiments.

Several improvements were made to the GWTF in a continuing effort to increase the facility's reliability and to extend its capabilities. We enlarged the 7- by 10-ft screen room to 10 by 10 ft and installed a new 3- by 9-ft optical table in the screen room to increase the space available for measurements in a low-noise environment. A gas-circulation system added to the System 2 oscillator/amplifier appears to have reduced its tendency to arc. We are evaluating a Tachisto, Inc. CO_2 TEA laser to determine the feasibility of using it as the oscillator in System 2. By adding the new oscillator, we can use the present oscillator/amplifier as a five-pass amplifier, and the timing between the oscillator and amplifier can be adjusted so that the laser pulse reaches the amplifier at peak gain. This modification should increase the output energy from System 2 markedly. Results indicate that the proposed modifications are feasible.

We recently acquired a precision calorimeter that is directly traceable to the NBS standard and will be used to calibrate and verify all detectors used in the GWTF. The availability of the reference calorimeter will increase the consistency and accuracy of pulse energy measurements.

REFERENCES

1. V. K. Viswanathan, "Optical Design and Analysis of Carbon Dioxide Laser Fusion Systems Using Interferometry and Fast-Fourier Transform Techniques," Proc. Los Alamos Sci. Conf. Opt. '79, D. H. Liebenberg, Ed., Los Alamos, New Mexico, May 23-25, 1979 (SPIE, 1979) Vol. 190, pp. 158-164.

2. V. K. Viswanathan, I. Liberman, G. Lawrence, and B. D. Seery, "Optical Analysis of Laser Systems Using Interferometry," Appl. Opt. **19**, 1870-1874 (1980).

3. R. F. Haglund, Jr., D. E. Casperson, S. J. Czuchlewski, C. J. Elliott, J. C. Goldstein, J. S. Ladish, and A. V. Nowak, "Optimization of a Multicomponent Gaseous Saturable Absorber for the Helios CO_2 Laser System," Proc. Los Alamos Sci. Conf. Opt. '79, D. H. Liebenberg, Ed., Los Alamos, New Mexico, May 23-25, 1979 (SPIE, 1979), Vol. 190, pp. 178-185.

4. M. D. Montgomery, R. L. Carlson, D. E. Casperson, S. J. Czuchlewski, J. F. Figueira, R. F. Haglund, Jr., J. S. Ladish, A. V. Nowak, and S. Singer, "Stabilization of High-Gain Multipass Power Amplifiers Using Saturable Absorbers," Appl. Phys. Lett. 32, 324-326 (1978).

5. J. Reid and K. J. Siemsen, "Gain of High-Pressure CO_2 Lasers," IEEE J. Quantum Electron. **14**, 217 (1977). R. S. Taylor, A. J. Alcock, W. J. Sargeant, and K. E. Leopold, "Electrical and Gain Characteristics of a Multiatmosphere uv-Preionized CO_2 Laser," IEEE J. Quantum Electron. **15**, 1131 (1979).

6. G. T. Schappert, "The LASL Gemini and Helios Laser Systems in Operation," in *Electro-Optics/Laser '79 Conference and Exposition*, Anaheim, California, October 23-25, 1979 (Industrial and Scientific Conference Management, Inc., Chicago, 1979), p. 457.

7. J. C. Goldstein, "Calculation of Small-Signal Gain Coefficients in CO_2," Proc. Los Alamos Sci. Conf. Opt. '79, D. H. Liebenberg, Ed., Los Alamos, New Mexico, May 23-25, 1979 (SPIE, 1979), Vol. 190, pp. 327-331.

8. A. M. Lockett III, "Kinetic Modeling of Electrically Excited CO_2 Lasers," Twenty-Sixth Annual Gaseous Electronics Conference, Madison, Wisconsin, October 16-19, 1973.

9. S. J. Sackett, "JASON User's Manual," Lawrence Livermore Laboratory report UCID-17814 (January 6, 1978).

10. D. H. Douglas-Hamilton, "Dissociative Recombination Rate Measurements in N_2, Co, and He," AVCO Everett Research Laboratory report RR 343 (November 1971).

11. C. Cason, A. H. Werkheiser, W. F. Otto, and R. W. Jones, "Gain Spiking and Mode-Beating Control by Signal Injection in CO_2 Lasers," J. Appl. Phys. **48**, 2531 (1977).

12. A. V. Nowak and D. O. Ham, "Self-Focusing of 10-μm Laser Pulses in SF_6," Opt. Lett. 6, 185-187 (1981).

13. J. F. Figueira and A. V. Nowak, "Carbon-Dioxide Laser System with Zero Small-Signal Gain," Appl. Opt. **19**, 420-421 (1980).

14. L. M. Frantz and J. S. Nodvik, "Theory of Pulse Propagation in a Laser Amplifier," J. Appl. Phys. **34**, 2346-2349 (1963).

15. E. T. Salesky and D. Korff, "Calculations of HCl Linewidths Using a New Impact Parameter Theory," Phys. Lett. **72A**, 431 (1979).

16. E. Arie, N. Lacome, and C. Rossetti, "Spectroscopie Par Source Laser," Can. J. Phys. **50**, 1800 (1972).

17. M. Herpin and P. Lallemand, "Study of the Broadening of the Rotational Raman Lines of CO_2 Perturbed by Rare Gases," J. Quant. Spectrosc. Radiat. Transfer **15**, 779 (1975).

18. R. P. Leavitt, "An Irreducible Tensor Method of Deriving the Long-Range Anisotropic Interactions Between Molecules of Arbitrary Symmetry," J. Chem. Phys. **72**, 3472 (1980).

19. E. W. Smith, M. Giraud, and J. Cooper, "A Semiclassical Theory for Spectral Line Broadening in Molecules," J. Chem. Phys. **65**, 1256 (1976).

20. Roger B. Perkins and the Inertial Fusion Program Staff, "Inertial Fusion Program, July 1—December 31, 1979," Los Alamos National Laboratory report LA-8511-PR (October 1981).

21. J. C. Goldstein and F. A. Hopf, "Pulse Propagation in High Pressure CO_2 Laser Amplifiers," Bull. Am. Phys. Soc. **17**, 1053 (1972). J. C. Goldstein, S. J. Czuchlewski, and A. V. Nowak, "Saturation of Hot CO_2 at 10.6 μm, Proc. of the 1980 Int. Conf. on Lasers," Carl B. Collins, Ed. (STS Press, McLean, Virginia, 1981), p. 623. John C. Goldstein, Stephen J. Czuchlewski, and Andrew V. Nowak, "Saturation of Hot CO_2 by Short 10.6 μm Laser Pulses," IEEE J. Quantum Electron. **17**, 1299 (1981).

22. B. J. Feldman, "Multiline Short Pulse Amplification and Compression in High-Gain CO_2 Laser Amplifiers," Opt. Commun. **14**, 13 (1975).

23. H. C. Volkin, "Calculation of Short-Pulse Propagation in a Large CO_2-Laser Amplifier," J. Appl. Phys. **50**, 1179 (1979).

24. S. Czuchlewski, E. McLellan, J. Figueira, E. Foley, C. Knapp, and J. Webb, "A High-Power, Short-Pulse CO_2 TEA Amplifier," Proc. of the 1978 Int. Conf. on Lasers, Orlando, Florida December 11-15, 1978, V. J. Corcoran, Ed. (STS Press, McLean, Virginia, 1979), pp. 498-505.

25. A. Icsevgi and W. E. Lamb, Jr., "Propagation of Light Pulses in a Laser Amplifier," Phys. Rev. **185**, 518 (1969).

26. B. J. Feldman, "Short-Pulse Multiline and Multiband Energy Extraction in High-Pressure CO_2 Laser Amplifiers," IEEE J. Quantum Electron. **9**, 1070-1078 (1973).

27. F. A. Hopf and C. K. Rhodes, "Influence of Vibrational, Rotational and Reorientational Relaxation on Pulse Propagation in Molecular Amplifiers," Phys. Rev. **A8**, 912 (1973).

28. F. A. Hopf, "Amplifier Theory," in *Physics of Quantum Electronics*, S. F. Jacobs, M. Sargent III, and M. O. Scully, Eds. (Addison-Wesley, Reading, Massachusetts, 1974), Vol. I, pp. 77-176.

29. G. T. Schappert, "Medium Response Limitations in Short-Pulse Amplifiers," Max-Planck Institute report IPP IV/89 (July 1976).

30. J. O. Hirschfelder, C. F. Curtiss, and R. B. Bird, *Molecular Theory of Gases and Liquids* (John Wiley & Sons, Inc., New York, 1964).

31. W. Fuss and J. Hartmann, "IR Absorption of SF_6 Excited up to the Dissociation Threshold," J. Chem. Phys. **70**, 5468-5476 (1979).

32. P. F. Moulton, D. M. Larson, J. N. Walpole, and A. Mooradian, "High Resolution Transient-Double-Resonance Spectroscopy in SF_6," Opt. Lett. 51-53 (1977).

33. R. R. Jacobs, S. J. Thomas, and K. J. Pettipiece, "J-Dependence of Rotational Relaxation in the CO_2 00^01 Vibrational Level," IEEE J. Quantum Electron. **10**, 480 (1974).

34. J. Finzi and C. B. Moore, "Relaxation of CO_2 (10^01), CO_2 (01^01) and N_2O (10^01) Vibrational Levels by Near-Resonant V → V Energy Transfer," J. Chem. Phys. **63**, 2285 (1975).

35. L. Doyennette, M. Margottin-Maclou, A. Chakroun, H. Gueguen, and L. Henry, "Vibrational Energy Transfer from the (00^01) Level of $^{14}N_2O$ and $^{12}CO_2$ to the (m, n, 1) Levels of These Molecules and of Their Isotopic Species," J. Chem. Phys. **62**, 440 (1975).

36. R. K. Preston and R. T. Pack, "Mechanism and Rates of Rotational Relaxation of $CO_2(001)$ in He and Ar," J. Chem. Phys. **69**, 2823 (1978).

37. R. T. Pack, "Analytic Estimate of Almost Resonant Molecular Energy Transfer due to Multipolar Potentials VV Processes Involving CO_2," J. Chem. Phys. 72, 6140 (1980).

38. J. Reid and K. Siemsen, "Laser Power and Gain Measurements on the Sequence Bands of CO_2," J. Appl. Phys. **48**, 2712 (1977).

39. V. K. Viswanathan, J. V. Parker, T. A. Nussmeier, C. J. Swigert, W. King, A. S. Lau, and K. Price, "Use of Adaptive Optics Elements for Wavefront Error Correction in the Gemini CO_2 Laser Fusion System," Proc. Los Alamos Sci. Conf. Opt. '79, D. H. Liebenberg, Ed., Los Alamos, New Mexico, May 23-25, 1979 (SPIE, 1979), Vol. 190, pp. 251-257.

40. S. V. Gunn, T. A. Heinz, W. D. Henderson, N. A. Massie, and V. K. Viswanathan, "Novel Deformable Mirror Design for Possible Wavefront Correction in CO_2 Laser Systems," Proc. Los Alamos Sci. Conf. Opt. '79, D. H. Liebenberg, Ed., Los Alamos, New Mexico, May 23-25, 1979 (SPIE, 1979), Vol. 190, p. 258.

41. T. F. Stratton, F. P. Durham, and C. A. Fenstermacher, "Antares and Advanced CO_2 Laser-Fusion Systems," Trans. Am. Nucl. Soc. 33, 31 (1979).

42. M. Matoba, H. Nishimura, H. Toya, H. Fujita, X. Iba, S. Nakai, and C. Yamanaka, "High-Power Electron-Beam-Controlled CO_2 Laser System for Laser Fusion Research," Sov. J. Quantum Electron. **6**, 480-485 (1976).

43. C. A. Fenstermacher, M. J. Nutter, W. T. Leland, and K. Boyer, "Electron-Beam-Controlled Electrical Discharges as a Method of Pumping Large Volumes of CO_2 Laser Media at High Pressure," Appl. Phys. Lett. 20, 56-60 (1972).

44. T. F. Stratton, "CO_2 Short-Pulse Laser Technology," in *High Power Gas Lasers 1975*, E. R. Pike, Ed. (The Institute of Physics, Bristol, 1976), pp. 284-311.

45. N. G. Basov, E. M. Belenov, V. A. Danilychev, and A. F. Suchov, "High-Pressure Carbon Dioxide Electrically Excited Preionization Lasers," Sov. Phys.-Usp. (Engl. Trans.) **17**, 705-721 (1975).

46. R. L. Carlson, J. P. Carpenter, D. E. Casperson, R. B. Gibson, R. P. Godwin, R. F. Haglund, Jr., J. A. Hanlon, E. L. Jolly, and T. F. Stratton, "Helios: A 15 TW Carbon Dioxide Laser Fusion Facility," IEEE J. Quantum Electron. **17**, 1662-1678 (1981).

47. P. K. Cheo, "CO_2 Lasers," in *Lasers*, A. K. Levine and R. J. DeMaria, Eds. (Marcel Dekker, Inc., New York, 1971), Vol. 3, Chap. 3, pp. 111-267.

48. W. T. Leland, "Design Engineering of Large High-Pressure Gas Laser Amplifiers," In *Advances in Laser Technology (Emphasizing Gaseous Lasers)*, Proc. Soc. Photo-Opt. Instrum. Eng., D. Finkleman and J. Stregack, Eds. (SPIE, 1978), Vol. 138, pp. 39-45.

49. J. J. Lowke, A. V. Phelps, and B. W. Irwin, "Predicted Electron Transport Coefficients and Operating Characteristics of CO_2-N_2-He Laser Mixtures," J. Appl. Phys. **44**, 4664-4671 (1973).

50. K. Smith and R. M. Thomson, *Computer Modeling of Gas Lasers* (Plenum Press, New York, 1978), Chap. 7.

51. K. B. Riepe, "High-Voltage Microsecond Pulse-Forming Network," Rev. Sci. Instrum. **48**, 1028 (1977).

52. K. Boyer, D. B. Henderson, and R. L. Morse, "Spatial Distribution of Ionization in Electron-Beam-Controlled Discharge Lasers," J. Appl. Phys. **44**, 5511-5512 (1973).

53. R. F. Benjamin and G. T. Schappert, "Prepulse Damage to Targets and Alignment Verification," J. Appl. Phys. **50**, 7 (1979).

54. Roger B. Perkins and the Inertial Fusion Program Staff, "Inertial Fusion Program, January 1—June 30, 1979," Los Alamos National Laboratory report LA-8114-PR (June 1981).

55. J. F. Figueira, S. J. Czuchlewski, C. R. Phipps, and S. J. Thomas, "Plasma-Breakdown Retropulse Isolators for the Infrared," Appl. Opt. **20**, 838 (1981).

56. D. E. Watkins, C. R. Phipps, Jr., and S. J. Thomas, "Determination of the Third-Order Nonlinear Optical Coefficients of Germanium through Ellipse Rotation," Opt. Lett. 5, 248-249 (1980).

57. D. E. Watkins and W. W. Rigrod, "Degenerate Four-Wave Mixing in Inhomogeneously Broadened Absorbing Media," Int. Conf. Lasers 1979, Orlando, Florida, December 17, 1979, paper S.4.

58. Roger B. Perkins and the Laser Fusion Program Staff, "Inertial Fusion Program, July 1—December 31, 1978," Los Alamos Scientific Laboratory report LA-7755-PR (November 1980).

59. C. R. Phipps, Jr., and S. J. Thomas, "Subnanosecond Extinction of CO_2 Laser Signals Via Bulk Photoionization in Ge," Topical Meeting on Inertial Confinement Fusion, San Diego, California, February 26-28, 1980, paper TuB5.

60. R. L. Abrams and R. C. Lind, "Degenerate Four-Wave Mixing in Absorbing Media," Opt. Lett. 2, 94 (1978) and Erratum, Opt. Lett. 3, 205 (1978).

61. D. E. Watkins, J. F. Figueira, and S. J. Thomas, "Observation of Resonantly Enhanced Degenerate Four-Wave Mixing in Doped Alkali Halides," Opt. Lett. 5, 169 (1980).

62. Y. Danileiko, A. Epifanov, T. Lebedeva, A. Menkov, V. Milyaev, and A. Sidovin, "Excitation of Nonequilibrium Carriers in Ge and Si by CO_2 Laser Radiation," P. N. Lebedev Physical Institute, Moscow, report No. 10 (1977).

63. S. Y. Yuen, R. L. Aggarwal, N. Lee, and B. Lax, "Nonlinear Absorption of CO_2 Laser Radiation by Nonequilibrium Carriers in Germanium," Opt. Commun. **28**, 237 (1979).

64. B. E. Newnam and D. H. Gill, "Damage Resistance of CO_2 Fusion Laser Optics," Opt. Eng. **18**, 579-585 (1979).

65. J. J. Hayden and I. Liberman, "Measurements of 10.6 μm Damage Thresholds in Ge, Cu, NaCl, and Other Optical Materials at Levels up to 10^{10} W/cm^2," in *Laser Induced Damage in Optical Materials*, A. J. Blass and H. Guenther, Eds., National Bureau of Standards Special Publication 462 (U.S. Government Printing Office, Washington, 1976), p. 173.

66. S. J. Thomas and R. F. Harrison, "Damage Test of L-10 Copper Mirrors," Los Alamos Scientific Laboratory memorandum L-9/80-116, to J. F. Figueira, April 1, 1980.

67. S. J. Thomas, C. R. Phipps, Jr., and R. F. Harrison, "Optical Damage Limitations for Cu Mirrors Used in CO_2-ICF Laser Systems," in *Laser Induced Damage in Optical Materials: 1980*, 12th Boulder Damage Symposium, Boulder, Colorado, September 30-October 1, 1980 (NBS, Boulder, Colorado, 1981).

68. See, for example, A. Yariv, "Phase Conjugate Optics and Real-Time Holography," IEEE J. Quantum Electron. **14**, 650 (1978).

69. W. W. Rigrod, R. A. Fisher, and B. J. Feldman, "Transient Analysis of Nearly Degenerate Four-Wave Mixing," Opt. Lett. 5, 105 (1980).

70. R. A. Fisher, B. R. Suydam, and B. J. Feldman, "Transient Analysis of Kerr-like Phase Conjugators using Frequency-Domain Techniques," Phys. Rev. A. 23, No. 6, 3071-3083 (1981).

71. J. W. Lewis and W. H. Orttung, "The Kerr Effect of Carbon Disulfide and Other Organic Liquids in the Ultraviolet," J. Phys. Chem. **82**, 698 (1978).

72. R. W. Hellwarth, "Generation of Time-Reversed Wavefronts by Nonlinear Refraction," J. Opt. Soc. Am. 67, 1 (1977). A. Yariv and D. M. Pepper, "Amplified Reflection, Phase Conjugation and Oscillation in Degenerate Four-Wave Mixing," Opt. Lett. 1, 16 (1977). D. Bloom and G. C. Bjorklund, "Conjugate Wave-Front Generation and Image Reconstruction by Four-Wave Mixing," Appl. Phys. Lett. 31, 592 (1977). See also Ref. 69 and its reference list.

73. N. F. Plilpetskii, V. I. Popovichev, and V. V. Ragul'skii, "Concentration of Light by Inverting its Wavefront," JETP Lett. (Engl. Trans.) **27**, 585 (1978). G. V. Peregudov, M. E. Plotkin, and E. N. Ragozin, "Use of the Wave-Front Reversal Effect to Investigate a Jet Formed by Focusing Laser Radiation on a Plane Target," Sov. J. Quantum Electron. **9**, 1413 (1979). A. A. Ilyukhin, G. V. Peregudov, M. E. Plotkin, E. N. Ragozin, and V. A. Chirkov, "Focusing of a Laser Beam on a Target Using the Effect of Wave-Front Inversion (WFI) Produced as a Result of Stimulated Mandel'shtam-Brillouin Scattering (SMBS)," JETP Lett. (Engl. Trans.) **29**, 328 (1980). D. T. Hon, "High Brightness Nd:YAG Laser Using SBS Phase Conjugation," 11th Int. Quantum Electron. Conf. Dig. and J. Opt. Soc. Am. **70**, 635 (1980).

74. W. Liptay, "Electrochromism and Solvatochromism," Angew. Chem. Internat. Edit. **8**, 177 (1969). P. Baraldi, P. Mirone, and E. S. Guidetti, "Solvent Dependence of the Intensity of the Absorption Band of Carbon Disulfide at 316 nm," Z. Naturforsch. **26a**, 1852 (1971).

75. See, for example, E. E. Bergmann, I. J. Bigio, B. J. Feldman, and R. A. Fisher, "High-Efficiency Pulsed 10.6-µm Phase Conjugate Reflection Via Degenerate Four-Wave Mixing," Opt. Lett. **3**, 82 (1978).

76. R. W. Hellwarth and N. George, "Nonlinear Refractive Indices of CS_2-CCl_4 Mixtures," Opto-electronics (London) **1**, 213 (1969).

77. G. A. Kenney-Wallace and C. D. Jonah, "Picosecond Observations of Electron Solvation in Dilute Polar Fluids," Chem. Phys. Lett. **47**, 362 (1977).

78. G. Martin and R. W. Hellwarth, "Infrared-to-Optical Image Conversion by Bragg Reflection from Thermally-Induced Index Gratings," Appl. Phys. Lett. **34**, 371 (1979).

79. J. H. Clark, S. L. Shapiro, A. J. Campillo, and K. R. Winn, "Picosecond Studies of Excited-State Protonation and Deprotonation Kinetics. The Laser pH Jump," J. Am. Chem. Soc. **101**, 747 (1979).

80. I. J. Bigio, "Injection-Locked, Unstable Resonator Dye Laser," in *High Power Lasers and Applications,* K. K. Kompa and H. Walther, Eds. (Springer-Verlag, Berlin, 1978), pp. 116-118.

81. See, for example, R. T. Hawkins, H. Egger, J. Bokor, and C. K. Rhodes, "A Tunable, Ultrahigh Spectral Brightness KrF* Excimer Laser Source," Appl. Phys. Lett. **36**, 391 (1980).

IV. TARGET EXPERIMENTS

(R. P. Godwin)

Our experimental program continued to address the fundamental issues of laser target interactions in the areas of absorption, energy transport, nonlinear optical processes, and hot-electron temperature physics; we provided input to the theory for model development.

I. INTRODUCTION

Four areas of investigation were addressed, including new techniques to measure absorption of laser light by the targets, lateral energy transport in targets, hot-electron characterization by x-ray bremsstrahlung measurements, and nonlinear processes that produce very high harmonics of 10.6-μm light.

The absorption measurements provided input to models to ensure a better understanding of the energy inventory; the integrating sphere allowed absorption measurements at full laser energy.

Using a recently developed multichannel hard-x-ray spectrometer, we began an investigation of the high-energy bremsstrahlung from targets, which is believed to be directly related to the hot-electron temperature. We investigated the effect of target cleanliness upon the fast-ion data as it relates to hot-electron temperature; studies of nonlinear processes in laser plasma interaction revealed the presence of extremely high harmonics of 10.6-μm light.

INTEGRATED ABSORPTION EXPERIMENTS ON CO_2 LASER-GENERATED PLASMAS (R. Kristal)

Absorption in laser-generated plasmas is an important factor in understanding the physics of laser energy deposition. A straightforward method for determining absorption by a plasma is to measure the reflected light fraction. We assume that what remains is absorbed, but we have no information as to the way the energy is partitioned. Because laser targets can scatter light in all directions, it is essential to include diffuse reflection as well as backscatter in the reflection measurement. In fact, for CO_2 light on microballoon targets, diffuse reflection is the dominant component.

A variety of methods exists for measuring absorption in laser-generated plasmas. One method uses a polished ellipsoidal cavity[1] where the target is at one focus and the laser light scattered from it is collected at the other focus. This technique measures the diffuse scatter over 4π sr and offers the possibility of angularly and time-resolved measurements. When the target is at the focus, however, the laser energy must be limited to prevent damage to the polished surface. Another method is the use of a box calorimeter;[2] it can accept a high-energy laser pulse but involves the complications of an absolute energy measurement. A third method, which is used in the present study, involves the integrating sphere.[3] This device can accept high laser energies and is relatively simple to calibrate. It has a lower transmittance of scattered laser light than the other methods, but when it is used with a high-energy laser source, this is not a serious limitation. The integrating sphere has been used previously at shorter wavelengths and lower energies.

A diagram of the experimental layout is shown in Fig. IV-1. The target is held in the center of a 30-cm (12-in.)-diam sphere that has a diffuse, gold-coated interior surface. The laser beam enters through a f/2.4 entrance hole slightly larger than the beam. The gold surface is highly reflective at 10 μm, and light incident on it from the target is scattered in all directions. This light continues to echo inside the sphere, except for a small amount that is lost on each reflection by absorption at the walls or leakage through the various holes that provide coupling to 10-μm optical detectors inside the sphere. Two detectors are integrating and the third is time resolved. The sphere is mounted inside the evacuated target chamber, and the optical detectors are mounted on the outside of the chamber to facilitate adjustments and reduce noise. Other holes in the sphere provide LOS access to a visible-light detector and to ion detectors mounted inside the target chamber.

The optical coupling holes are baffled to prevent measurement of direct light from the target or first-bounce light from the opposite wall. For the sphere to give a true measure of target scatter, it should be equally responsive to scattered light from all directions off the target. Baffle detail is shown in Fig. IV-2. The design was

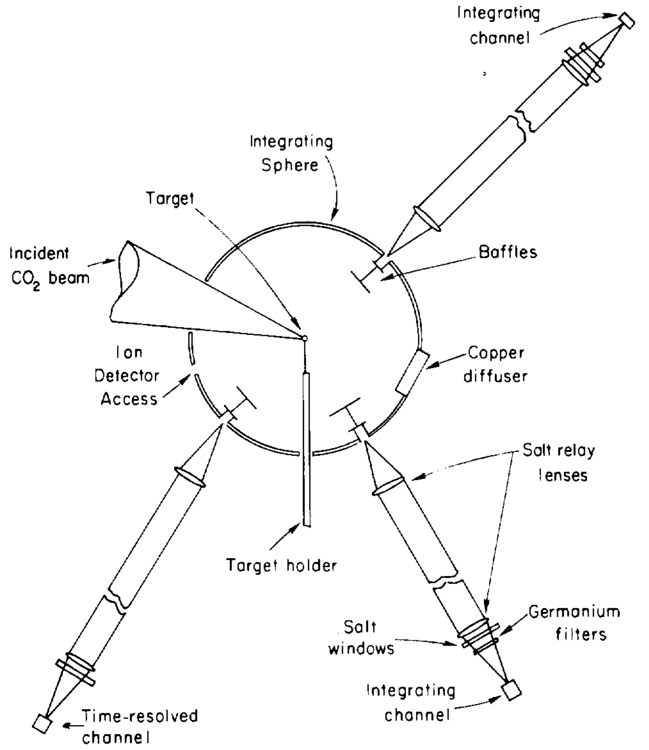

Fig. IV-1. Experimental configuration of an integrating sphere.

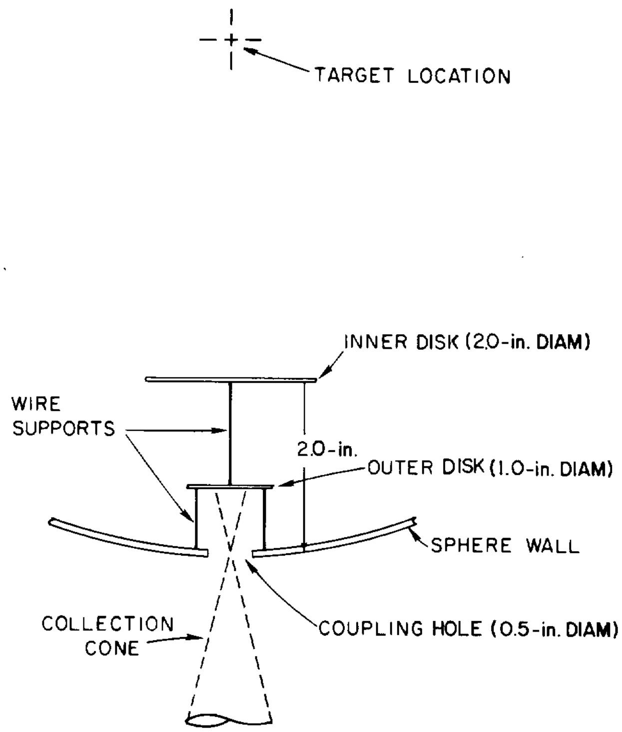

Fig. IV-2. Integrating sphere baffle detail.

achieved experimentally and provides a reasonably uniform angular response of the sphere, as determined by low-level scanning tests. These tests, at 10 μm, show a total rms variation for the sphere of <10%. This cannot be simply translated into experimental accuracy because of the angular distribution of the scattered light. The optical elements in front of the detectors are salt and germanium; at wavelengths longer than ~2 μm, they filter out all radiation except the infrared, which is composed almost entirely of scattered 10-μm light.

The system is calibrated by firing into an empty sphere and defining the result as 100% reflection. The area of the sphere on which the beam impinges should be highly reflecting, because reflectivity has an important effect on the calibration. Therefore, and because the reflectivity decreases as flux levels may approach 10^{10} to 10^{11} W/cm^2 on this surface, the section of wall directly illuminated by the laser was replaced by a cleanable solid copper diffuser plate. The sphere and associated apparatus are shown in Fig. IV-3.

The experiments were performed with one beam of the Gemini two-beam CO_2 laser. We used the sophisticated alignment aids at Gemini to correctly position the target with respect to the beam focus on each shot, with a reproducibility of ~20 μm (both in focus and transverse).

Samples of the data output are shown in Fig. IV-4. The detectors used for absorption measurements are integrating pyroelectric devices whose peak output depends on input energy. Unfortunately, these detectors are also piezoelectric, and one of the units (nearest the laser source) showed a very high acoustic noise level. Consequently, all the data used came from the other detector, which was relatively noise-free.

Target data are plotted vs intensity in Fig. IV-5 for a variety of materials ranging in atomic weight from <12 to 197. The diffuse reflectance is 72%, independent of energy and atomic number, with a rms deviation of 5% (the calibration rms deviation is 9%). If we assume small backscatter, this implies an absorption in the range of 25-28%.

Typical data from the time-resolved detector are shown in Fig. IV-6. The data show qualitatively different decay pulses for target and calibration shots. The latter show much more structure, typified by the spike at early time, whereas the target pulses show a longer risetime (by ~1 ns) and much less structure. Presumably, this

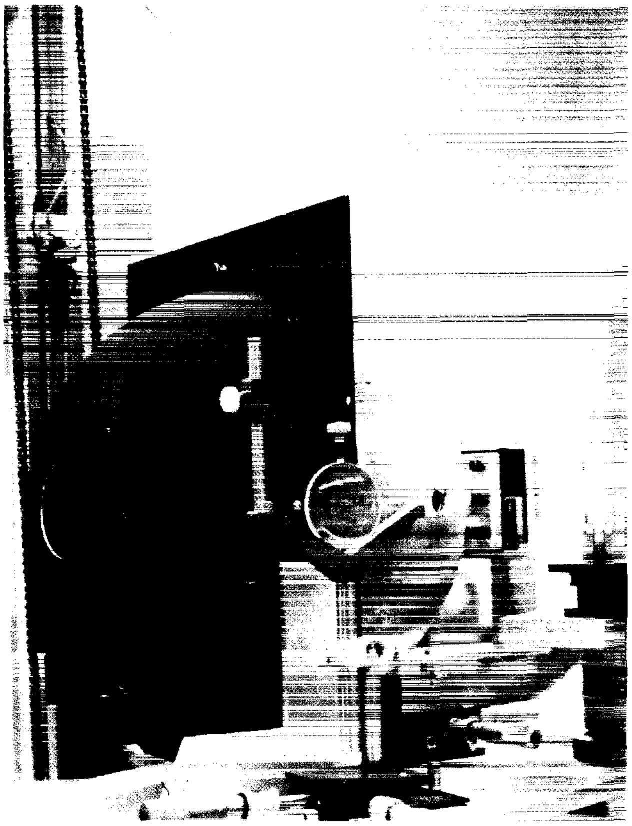

Fig. IV-3. Integrating sphere. The inner gold surface has been polished to provide very high reflectance (~98%) for 10.6-μm wavelength light. The black matte finish on the outside minimizes reflections that can produce parasitic oscillation in the laser system.

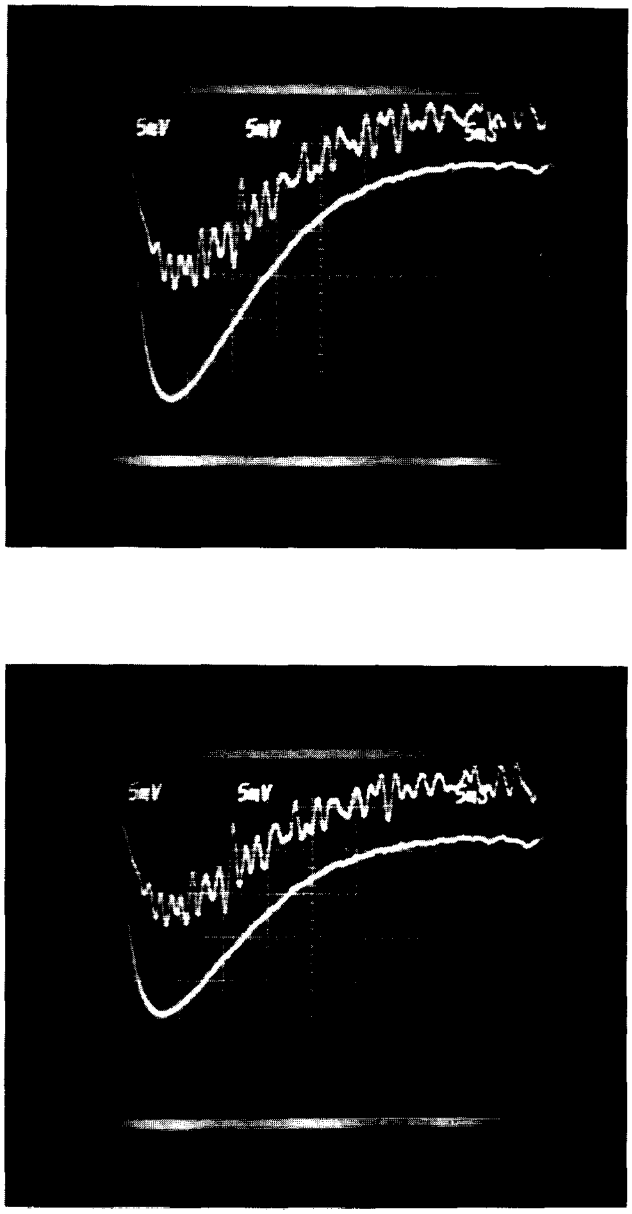

(b)

Fig. IV-4. Sample readings of energy monitors for calibration and target shots: (a) calorimeter shot, 169 J; (b) GMB, 163 J.

difference occurs because the scattered beam is more directional during calibration than during a true target shot, and because of the resulting reflections of the beam inside the sphere before homogenization occurs. The periodicity of the structure corresponds to 2-3 transits of the sphere. The longer risetime for the target pulses may result from the transit time dispersion caused by a greater portion of sphere being illuminated by scattered light than by the beam. During the decay, some target shots exhibit no structure at all, whereas others show a small amount, indicating again a difference in angular distribution of the scattered light. In spite of the different decay characteristics, the scanning results discussed earlier confirm a basically uniform angular response, which is the main requirement for the proper operation of the integrating sphere.

The decay time τ of the sphere was ~10 ns. From a simplistic model of the sphere, in which the loss per bounce is α and the time per bounce is t_B, we obtain $\tau = t_B/\alpha$. Consequently $\alpha \sim 7\%$, which is somewhat higher than expected. All the holes combined amount to a solid angle of only ~0.2 sr, implying a hole loss of 1.5%. Thus, the remaining 5.5% of loss must be caused by surface absorption, probably by contaminants on the surface. Although this loss emphasizes the need for good surface preparation, it also has implications for multiple beam studies. For the sphere to randomize target

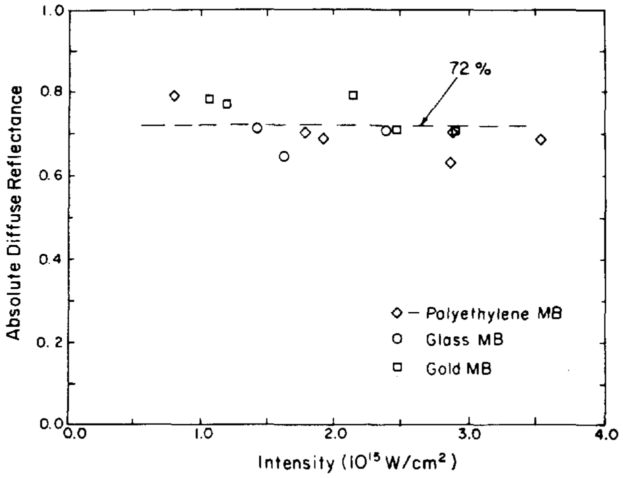

Fig. IV-5. Absolute diffuse reflectance for microballoons of various material.

reflections adequately, there must be a sufficient number of bounces. The observation that even a loss per bounce of 7% produced such a randomization indicates that more beam entrance holes can be added, provided surface losses are reduced, without degrading the angular response of the sphere. Of course, light lost directly through the holes (backscatter) would have to be independently measured.

LATERAL TRANSPORT OF ENERGY FROM A LASER-PRODUCED PLASMA (A. W. Ehler, F. Begay, T. H. Tan, P. Castine)

Experiments were conducted to measure the lateral transport of energy from a laser-produced plasma. One beam of Gemini was focused near the center of, and perpendicular to, a 1-cm-long wire target with an irradiance of 2×10^{15} W/cm^2 in a 1-ns pulse. Wires of different elements and diameters were used. Fast ions from the plasma were measured with a charge collector, a Thomson ion spectrograph,[4] and a photo-multiplier-scintillator (crab-eye) ion detector[5] located nearly perpendicular to the laser-irradiated spot (front side). Another crab-eye and a charge collector were installed 180° away to measure fast ions emitted from the back surface of the target. Three additional charge collectors were spaced at angles between the front- and back-viewing detectors.

Targets of pure carbon, titanium, or tantalum wire (250 μm in diameter) either were maintained at 1773 K (1500°C) before and during laser irradiation to boil off surface impurities or were kept at room temperature.[6] Fast protons were observed in the ion spectrograms for the cold targets, and fast ions were recorded by the backside detectors. Cold copper wire targets of various diameters were used to determine the maximum diameter for which fast ions were detected on the backside.

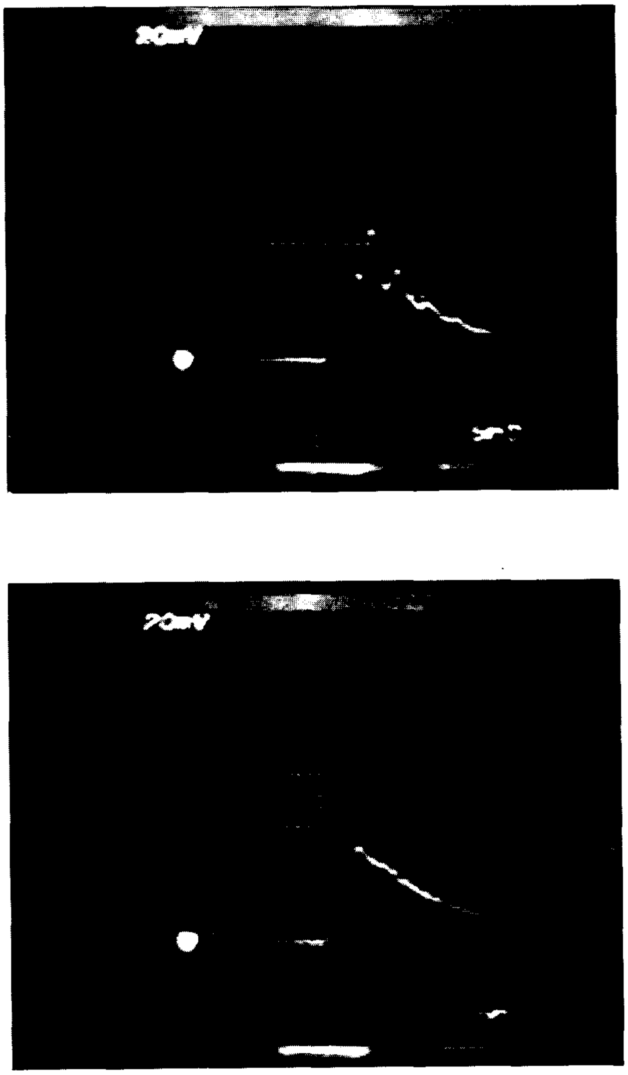

(b)

5 ns / Div.

Fig. IV-6. Sample sphere decay pulses for calibration and target shots: (a) calibration shot, 175 J; (b) GMB, 188 J.

These experiments disclosed the following information regarding lateral energy transport.

- Fast ions are highly peaked in the direction of the target normal.[7] Accordingly, the fast ions observed on the backside of a wire must have been expanded isothermally from a plasma that existed on the backside during the laser pulse.
- Hot electrons with energy less than 230, 300, and 600 keV are stopped by 250 μm of carbon, titanium, and tantalum, respectively. Consequently, energy was transported from the focal spot around the surface of the wire during the laser pulse (1 ns) to the backside of the wire.[8]
- The hot-electron temperature gradient around the wire surface was estimated from the speed of the fastest ions observed on the front and back of the 250-μm-diam target, assuming the ions were expanded isothermally. The front-side hot-electron temperature was 29 keV and the ratio of the front-to-back hot-electron temperature was 2.1. This ratio gave a value of 5×10^5 eV/cm for the gradient.
- The transport speed of energy around the surface of the wire was estimated from the distance traveled during the laser pulse (taken as 1 ns). The transport speed V was $1.5 \times 10^8 < V < 2.5 \times 10^8$ cm/s.
- If the laser plasma contained protons, the energy was transported to the backside of a wire with diameter >1000 μm [transport distance = 1/2 (π × wire diameter − laser focal diameter)]. However, for the 1773 K (1500°C) carbon target, the laser plasma was composed of only carbon ions (average ionization state of 3 to 4), and energy was not transported around a wire 250 μm in diameter. Consequently, any energy-transport mechanism considered, with a charge state and/or atomic weight dependence, must account for this ratio of 5 or more for the transport speed or distance.
- The five charge collectors, placed around the chamber perpendicular to the length of the 250-μm-diam cold wires, indicated that 7% of the total energy in fast ions is ejected from the backside. This estimate was obtained from the measured fast-ion distribution around the wire compared to that of a flat target and from the front-to-back ratio of the total fast-ion energy.

Future experiments will include visible streak photographs of the energy-transport motion for heated wires of various atomic weight materials to obtain the relationship of atomic weight and/or ionic charge of the laser plasma to the energy-transport speed.

VISIBLE HARMONIC GENERATION IN CO_2 LASER FUSION EXPERIMENTS (R. Carman, F. Wittman, N. Clabo)

A number of theoretical and experimental papers address second harmonic generation[9,10] in laser fusion experiments. Subharmonic and 3/2 harmonic generation have also been discussed.[9,10] In addition, one group reported seeing the 3rd, 4th, 5th, 6th, 10th, and 11th CO_2 harmonics in the backscattered beam direction.[9] They observed an approximately linear decrease in radiated harmonic with harmonic order, the ratio of n^{th} to (n + 1)st harmonic energies being ~6 for an incident CO_2 intensity of $>10^{14}$ W/cm^2. Similar results have been observed at 1.06 μm for intensities of $\sim 10^{16}$ W/cm^2 (impulses at both wavelengths are equal for the same $I\lambda^2$).[10]

We observe very high order CO_2 harmonics and give a theoretical explanation of our experimental results. For CC_2 incident intensities at the eight-beam Helios system of $\sim 3 \times 10^{16}$ W/cm^2, we observed harmonic light at as high as the 29th harmonic (365 nm) for GMB targets coated with plastic or metal. The effects are apparently independent of the atomic number of the coating material. In plane target experiments performed at $<8 \times 10^{14}$ W/cm^2 on Gemini, we observed up to the 20th harmonic emanating tangentially from the target, with the laser incident (in S-polarization) 15° off the target normal. In both sets of experiments, we observed a new feature, namely, that harmonic generation efficiency is nearly constant in the direction of observation from the 16th harmonic through the highest harmonic observed. Because the angular distribution of the harmonic light is not known, we are not able to quote a total efficiency with confidence, but the harmonic brightness is at least two orders of magnitude higher than plasma continuum light in the direction of observation.

The Gemini series of experiments was carried out with a single beam of 100-500 J on target in 1.0-1.2 ns (FWHM). The system operated on a single rotational line (P-20) in the 10.6-μm vibrational band. The spectra were taken by using two simple quartz relay lenses of 20-cm focal length operated at 1:1 magnification and a 1-m McPherson spectrograph (F8.7) using 2485 Kodak instrumentation film and a 300-lines/mm grating blazed for 1 μm used in second order. Several plane targets (aluminum, titanium, iron, gold, copper, CH_2, and Teflon) were used, all oriented 15° from normal incidence. A typical spectrum obtained viewing the target at grazing incidence is shown in Fig. IV-7(a). After

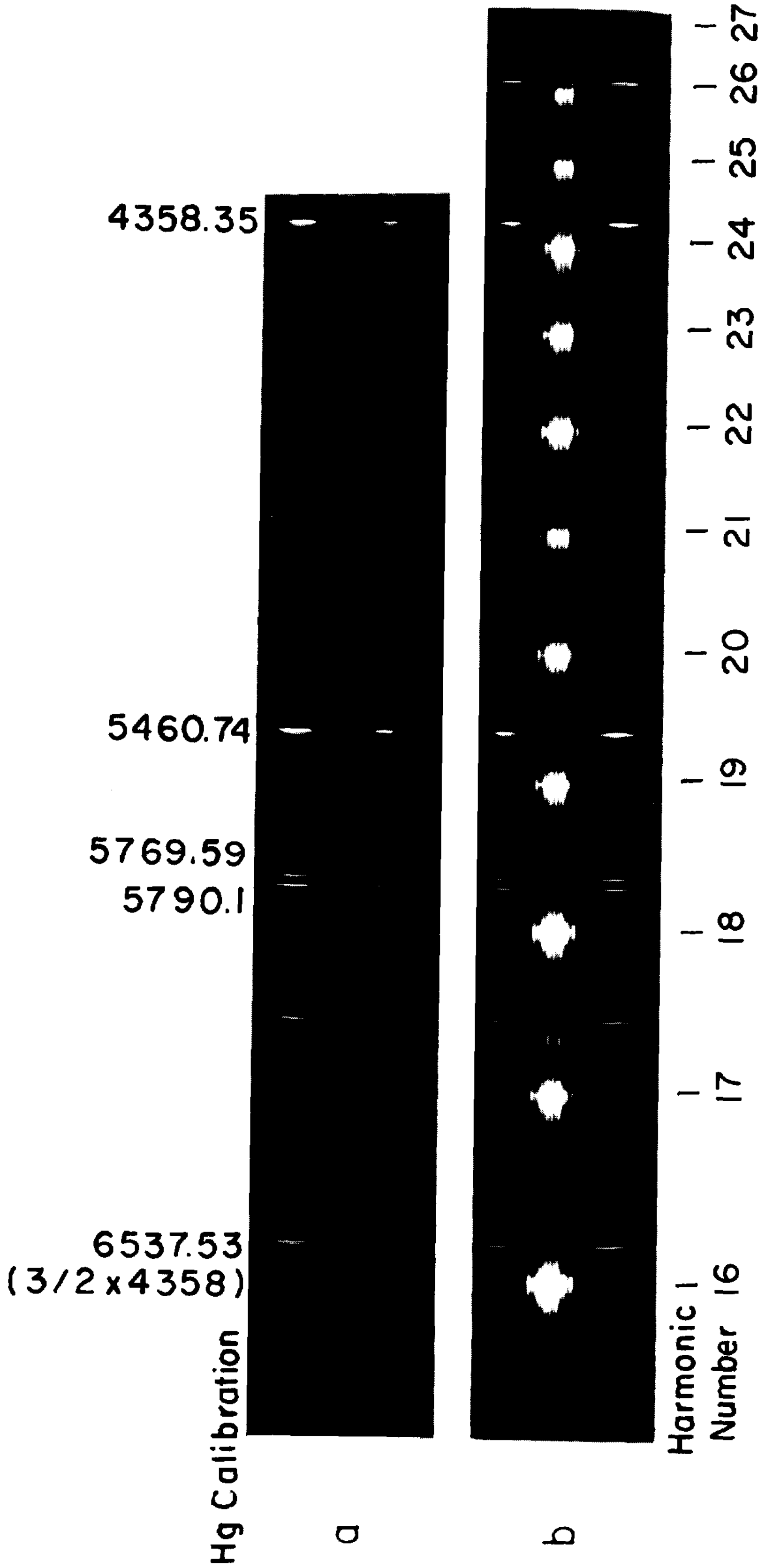

Fig. IV-7. Harmonic spectra obtained in parasitics experiments at (a) Gemini and (b) Helios.

radiometric calibration of the spectrograph and correction for transmission variations in filters and lenses, the harmonic production efficiency betweeen the 16th CO_2 harmonic and the highest harmonic observed at a fixed exposure (typically, the 18th to the 20th) was determined to be essentially constant. For higher harmonics, the production efficiency dropped rapidly. The spectral line width was observed to be $100 \pm 5\ \text{cm}^{-1}$ FWHM for all harmonics, similar to previous 1-μm laser work.[10]

The Helios series of experiments was carried out with a 750-950 J/beam in 600-750 ps (FWHM) pulses. If we defocused from the minimum spot size, the intensity in one beam could be varied from $\sim 10^{15}$ to 3×10^{16} W/cm^2. The oscillator normally operated on 3-4 rotational lines around P-20 in the 10.6-μm band. The spectra were taken by using two achromatic lenses of 25-cm focal length at 1:1 magnification and the same spectrograph and film as in the Gemini series. Spherical targets, ranging in diameter from 250 to 1000 μm and fabricated from CH_2, copper, nickel, and gold, were studied with no significant dependence noted on either target material or diameter. A typical tightly focused target spectrum in this series is shown in Fig. IV-7(b). The spectrograph direction of observation is normally 30° from the axis of one of the eight Helios beamlines. For this spectrum, we observed a constant harmonic production efficiency out to at least the 25th harmonic. This will require changing to reflective optics if we wish to eliminate the effects of chromatic dispersion. Preliminary data suggest that the harmonic efficiency is constant to the 29th harmonic and possibly beyond.

Despite the change from single-rotational-line operation at Gemini to about four-rotational-line operation at Helios (with a total spectral spread of $<5.4\ \text{cm}^{-1}$), the harmonic line widths for all Helios harmonics were still $100 \pm 5\ \text{cm}^{-1}$ FWHM. If line width were to be attributed to a Doppler shift from a moving surface, velocities up to 10^7 cm/s could be inferred, but both inward and outward velocities must occur if the shift in the center frequency from the harmonic of CO_2 P-20 (the dominant output) is to be $<10\ \text{cm}^{-1}$, as observed.

We believe that the correct interpretation of these data is intimately connected with self-consistent profile modification and the dominant energy deposition process, namely, resonant absorption. At very high laser intensities, the hydrodynamic expansion of the plasma is substantially modified by the photon momentum change that occurs near the plasma critical surface ($\omega_{Pe} = \omega_{laser}$) in connection with the reflection or turning of the incident light. This implies

$$\frac{E^2}{8\pi} = NKT_c \ , \qquad \text{(IV-1)}$$

where E is the electric field vector of the laser light, N is the plasma density, and T_c is the (cold) background plasma temperature. Actually, the plasma density required to satisfy Eq. (IV-1) can be substantially above the critical density for CO_2 light. Near the critical density where we can expect a steep jump in density, N takes on the meaning of the upper density at the jump. Rewriting Eq. (IV-1), we see that

$$N_{upper} \sim \frac{E^2}{8\pi KT_e} \sim \frac{I_L}{T_c} \ , \qquad \text{(IV-2)}$$

where I_L is the incident laser intensity ($I_L > 10^{13}$ W/cm^2 for CO_2 laser irradiation $N_{upper} > N_{critical}$), and T_c is about a few hundred eV for typical plasma.

We believe the connection between the high harmonic generation and profile modification is as follows: the profile modification process, as well as the large-amplitude Langmuir plasma oscillation, introduces a strong nonlinear response for the plasma to the CO_2 irradiation. However, we must also demand sufficient spatial overlap for the CO_2 radiation and the $(n-1)^{th}$ harmonic to produce the n^{th} order harmonic. If $N_{upper} > N_{critical}$, the turning point of the n^{th} order harmonic $n\omega_L$ will be spatially coincident with the incident laser turning point ω_L, thus providing for the necessary overlap time. From this model we infer that efficient 29^{th} harmonic generation requires

$$N_{upper} \geq N_{critical}\,(CO_2) \times (29)^2 \sim 8.4 \times 10^{21} \frac{e}{cm^3} \ . \qquad \text{(IV-3)}$$

HIGH-ENERGY X-RAY MEASUREMENTS AT HELIOS (R. H. Day)

The APACHE 10-channel x-ray spectrometer is now operational with K-edge-filtered photodiode-fluor detectors calibrated from 10 to 240 keV.

We measured the MULTIFLEX radiation environment to determine how to solve a scope-blooming problem. The radiation has two components. The first is an x-ray background that occurs at amplifier electron-beam time and consists of 80 R for 80 ns (FWHM) as viewed through 1/8 in. of lead, the amplifier chamber walls, and several meters of air. The characteristic energy of the beam is 250 keV, as determined by lead attenuation. For 90% of the shots, the signal is a single, approximately triangular pulse; the remaining 10% of the shots exhibit two or three smaller peaks separated by 70 ns. Whether this corresponds to a pathological behavior in the amplified laser beams has not been determined.

The second radiation pulse is much harder, up to several MeV, and occurs at the time of laser interaction with the target. The intensity increases with the target atomic number and has a peak of ~100 R through a 2-in.-thick lead shield. A lead attenuation measurement is consistent with a spectrum containing the most penetrating radiation of a few MeV. The time history of the pulse shows no appreciable broadening beyond the detector-scintillator response time of 5 ns.

MULTIFLEX FAST X-RAY DETECTION SYSTEM (R. H. Day)

The MULTIFLEX detection system was mated to the Helios target chamber. It is integrated with the laser controls and with a high-speed data-recording system.

MULTIFLEX consists of an array of seven XRDs designed to have <100-ps time response and to operate at a potential of 2-3 keV. The detectors are housed in a vacuum system that isolates them from the target chamber except during laser shots. This setup allows us to perform maintenance independent of the laser and to use photocathodes that would otherwise be harmed by the frequent down-to-air cycles of the main target chamber. Main gate valve operation is interlocked with the vacuum system and controlled to prevent catastrophic venting of the laser chamber.

Data are recorded in a small screen room that is configured for high-speed recording with three 1776 oscilloscopes and two 2.5-GHz-bandwidth oscilloscopes. Several 7844 oscilloscopes are available for system diagnostics and for slower recording of channels for which high-speed oscilloscopes are unavailable. Severe "blooming" of the 1776 MCP electron-beam intensifier was reduced by putting more lead shielding on the screen room door and using a slower film. After being recorded for time resolution, the signals are integrated and listed locally or with the central PDP-11/70 computer to allow us a quick look at the time-integrated spectral shape and simultaneously to provide time-resolved spectra. The relative timing of all high-speed recording traces is being determined to better than ±50 ps and provided with shot-by-shot horizontal sweep calibration.

EFFECT OF HYDROGEN IN CO_2 LASER-INDUCED PLASMAS (F. Begay, D. Forslund)

We have performed many CO_2 laser-matter interaction experiments[6] to investigate the effect of target impurities and surface contaminants on the behavior of laser-induced plasmas.

Experimentally, we observe that pure carbon plasma expands isothermally, and that C^{+6} ions acquire kinetic energies asymptotically, approaching 9 MeV. The C^{+5} and C^{+6} ions appear to attenuate self-consistently the acceleration fields for carbon ions with low ionization states. When hydrogen is present, as in the CH_2 target, carbon ion energies are greatly reduced and the hot-electron temperature is reduced by more than half.

We developed a theoretical model to treat the problem of collisionless expansion of an isothermal, electrostatic, multicold-ion, quasi-neutral plasma and will use this model to help interpret the experimental results.

Typical experimental results from a pure-carbon plasma and a polyethylene (CH_2) plasma are presented. In pure-carbon experiments, a carbon wire was irradiated with 9.6×10^{14} W/cm^2, whereas in the CH_2 experiment, a CH_2 film was irradiated with 9.9×10^{14} W/cm^2. Just before irradiation, we heated the pure-carbon wire electrically to 2273 K (2000°C) to avoid hydrogen contamination.

A Thomson parabola mass analyzer[6] and a cellulose-nitrate film particle detector were used to measure the ion velocity distribution. The entrance diameter of the aperture for the mass analyzer was 100 μm; the electric field was 750 V/cm, and the magnetic field was 385 G.

Ion velocity distributions for the pure-carbon and CH_2 plasma at various high ionization states are shown in Figs. IV-8 (a), (b), and (c). Figure IV-8 (c) shows that the presence of hydrogen induces a cutoff in the carbon velocity distribution at ~5×10^8 cm/s.

The general flattening of the dn/dv curves below 5×10^8 cm/s arises from particle track saturation of the film. The cutoff at low velocity is apparently a result of the film response. Therefore, with the cellulose-nitrate film, we can obtain good spectra for hot-electron

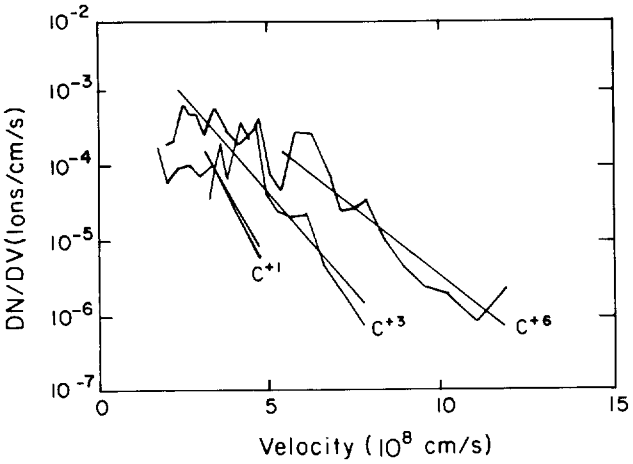

Fig. IV-8(a). Experimental ion velocity distributions for C^{+1}, C^{+3}, and C^{+6} in pure carbon plasma. Electron temperature ~31 keV. Errors for velocity <4%; for dN/dv <10%.

Fig. IV-8(b). Experimental ion velocity distribution for C^{+2}, C^{+4}, and C^{+5} in pure carbon plasma. Electron temperature ~31 keV. Errors for velocity <4%; for dN/dv ≤10%.

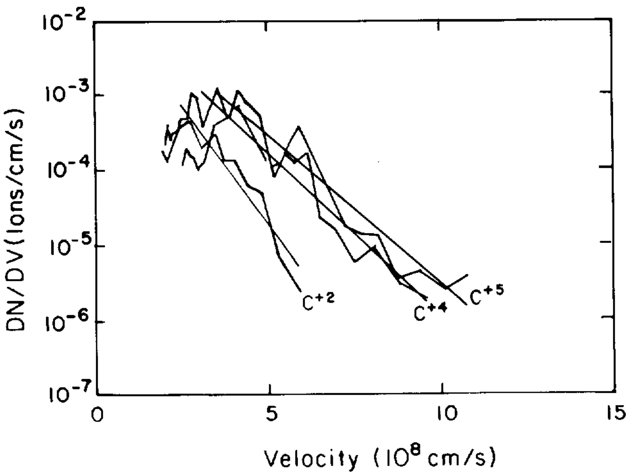

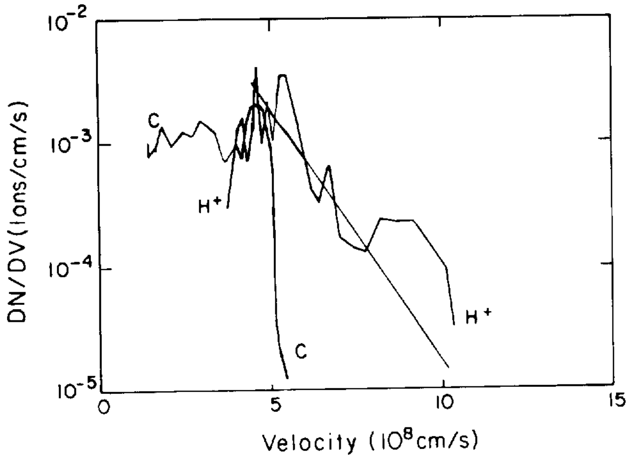

Fig. IV-8(c). Experimental ion velocity distribution for CH_2 plasma. Carbon plasma is represented as a single fluid, electron temperature ~12 keV. Errors for velocity <4%; for dN/dv <10%.

temperature determinations only from velocities $>4 \times 10^8$ cm/s.

Figure IV-8 also shows a least squares fit of the function $\exp(-v/v_0)$ to each ion species where v is the ion velocity and v_0 is the scale velocity. The scale velocities so obtained are shown in Table IV-I. If this scale velocity is interpreted as the speed of sound for the species, we can infer an electron temperature for an isothermal expansion, as shown in the table. The maximum ion energy for each species is also tabulated in Table IV-I. For the pure-carbon plasma, the inferred electron temperature is ~31 keV, and the ratio of maximum kinetic energy to ion charge is constant.

On the other hand, the CH_2 plasma is accelerated with an apparent electron temperature of only ~12 keV, and the maximum kinetic energy for the carbon ions is constant. We were unable to fit a scale velocity for the carbon flow, because most of the velocity distribution in the fast-ion region is missing.

We also attempted to determine the total energy for the fast ions with velocities $>1.5 \times 10^8$ cm/s or 11 keV/N. The ratio of total energy deposited in the carbon plasma to that deposited in the CH_2 plasma for $v > 1.5 \times 10^8$ cm/s measured at the detector was 1.6. Because observations are made at only one angle relative to the target, the angular distribution of the fast ions must be known to obtain the total energy emitted. Assuming that 35% of the incident laser energy was absorbed by the plasma,[11] we find that for the CH_2 case, 9.4% of the absorbed laser energy was expended into producing fast ions for ion velocities $>1.5 \times 10^8$ cm/s..

For pure-carbon wire, the total solid angle ω_T for the ion emission region is difficult to determine. However, if we assume $\omega_T \simeq \pi$ or 2π, we find that 24 or 97%, respectively, of the absorbed energy was expended in producing fast ions for kinetic energies greater than 11 keV/N. This underscores the necessity of more detailed angular and energy balance information.

To estimate physical conditions near the critical surface, we used experimental results from the fast-ion region and theoretical results reported by Forslund et al.[12]

Note the high densities to which the CO_2 laser apparently penetrates. These high densities can also be inferred from the extremely high harmonics of CO_2 light observed in recent experiments,[13] and they are consistent with observed profile modification[14,15] at somewhat lower intensities. The most remarkable conclusion suggests that the presence of hydrogen in the target reduces the thermal temperature near the critical surface. A reasonable explanation of this observation assumes that the absorbed laser energy does not remain in the laser spot when hydrogen is present in the target. It either goes into fast-ion blowoff or into heating material outside the laser spot. There is no evidence in our experimental data for more energy in fast-ion blowoff when hydrogen is present. However, recent experiments at the National Research Council in Canada (NRC)[15] and Los Alamos[16] indicate strong lateral heat conduction. This strong lateral conduction arises naturally from the resonance absorption itself. The hot electrons are preferentially accelerated outward toward the laser and reflect at a potential sheath to return to the high-density region. Self-generated magnetic fields may cause the electrons to

Table IV-I. Summary of Experimental Values for Scale Velocities, Electron Temperatures, and Maximum Ion Velocities

	Scale Velocities (10^7 cm/s)		Electron Temperatures (keV)		E_{max} (MeV)	
Ion Type	Carbon Plasma	CH_2 Plasma	Carbon Plasma	CH_2 Plasma	Carbon Plasma	CH_2 Plasma
H^+	---	10.6 ± 0.044	---	11.7 ± 0.02	---	0.56 ± 0.001
C^{+1}	5.45 ± 0.22	---	37.2 ± 0.05	---	0.4 ± 0.002	1.47 ± 0.002
C^{+2}	6.84 ± 0.27	---	29.3 ± 0.05	---	2.2 ± 0.004	1.47 ± 0.002
C^{+3}	8.36 ± 0.33	---	29.2 ± 0.05	---	3.8 ± 0.006	1.63 ± 0.003
C^{+4}	9.98 ± 0.4	---	31.2 ± 0.05	---	5.8 ± 0.01	1.65 ± 0.003
C^{+5}	10.9 ± 0.44	---	29.8 ± 0.05	---	7.3 ± 0.01	1.61 ± 0.003
C^{+6}	12.2 ± 0.50	---	31.0 ± 0.05	---	8.9 ± 0.01	1.87 ± 0.003

return to a region outside the original laser spot. For significant lateral energy transport, the ions must also be pulled out of the target. However, the electróns need only move a short distance from the surface to allow a strong lateral energy transport. This may contribute largely to the requirement for a flux-limiter to make simple one-dimensional models fit flat-target experiments. Note, furthermore, that the thermal pressure is the same for the carbon and CH_2 plasmas.

Table IV-II shows the results from an experiment in which a CH wire was illuminated with 18.8×10^{14} W/cm^2. Although the carbon wire was heated electrically to 2273 K (2000°C) in the CH experiment, small amounts of hydrogen remained in the target and altered the behavior of the carbon plasma. The hot-electron temperatures for the carbon wire and the CH wire experiments are approximately the same; this suggests that the hot-electron temperature depends on target geometry because a lower hot-electron temperature was determined for the CH_2 case. Furthermore, the characteristics of the carbon ion flow in CH wire are similar to the characteristics of the carbon flow in CH_2; that is, the presence of hydrogen in the CH wire does induce a cutoff in the carbon ion velocity distribution.

In future experiments we will investigate the properties of laser ablation-driven shock waves. The data will be used to calculate ablation efficiencies.

Results of numerically integrating the self-similar equations for the CH_2 case with $Z_c/M_c = 2.5/12$, $Z_H/M_H = 1.0$, $n_{co}/n_0 = 0.4$, $n_{ho}/n_0 = 0.008$, $T_e/T_0 = 1.0$ are shown in Fig. IV-9, where Z_cM_c (Z_H/M_H) is the charge-to-mass ratio for carbon (hydrogen), respectively; n_{co} (n_{ho}) is the initial ion density for the carbon (hydrogen) ions, respectively; T_e is the electron temperature normalized to an electron temperature T_0; n_{co} and n_{ho} are normalized to an ion density n_0. The choice of $Z_c = 2.5$ is based on the observation that in the CH_2 plasma the carbon ions apparently expand as a single fluid. The plots in Fig. IV-9 include results for density flow [Fig. IV-9(a)], velocity flow [Fig. IV-9(b)], the self-consistent electrostatic potentials [Fig. IV-9(c)], and the self-consistent electric fields [Fig. IV-9(d)]. Note that the potentials and the electric fields have been decomposed to show the evolution of potential and field components that depend on the relative behavior of the carbon electrons and the hydrogen electrons in the CH_2 plasma. The dotted lines in Fig. IV-9 show the calculated carbon flow, assuming it to be a single fluid without hydrogen present in the plasma.

The presence of hydrogen in the carbon plasma induces a number of modifications in its flow characteristics. The density flow characteristics show that, initially, the carbon ions expand isothermally. At a point in the expansion where the magnitudes of the

Table IV-II. Experimental Results for Carbon and CH Wire Illuminated with 18.8×10^{14} W/cm^2

Plasma	Laser Intensity I (10^{14} W/cm^2)	Hot Electron Temp T_h (keV)	Cold Electron Temp T_c (keV)	Hot Electron Density n_h (10^{19} cm^{-3})	Penetration Density n_u (10^{21} cm^{-3})
Carbon wire	9.6	31.0	1.0	2.23	0.2
CH_2 film	9.9	12.0	0.060	9.2	3.4
CH wire	18.8	28.0	0.379	5.04	1.03

Plasma	T_h/T_c	V_0/V_e	n_h/n_u	n_u/n_{crit}	Thermal Pressure P (Mbar)
Carbon wire	31.0	6.37	0.11	20.0	0.32
CH_2	211.0	26.3	0.027	340.0	0.33
CH wire	74.0	14.4	0.049	103.0	0.62

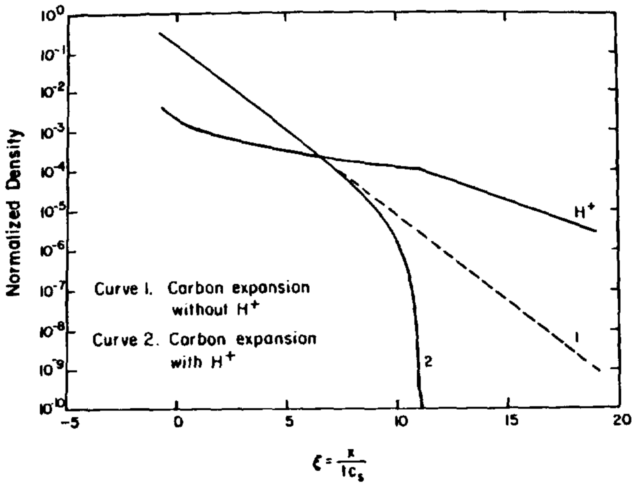

(a)

Fig. IV-9(a). Normalized carbon ion density (curve 2) and hydrogen ion density (curve H) versus self-similar parameter ξ. Dotted line is single-species (carbon) solution.

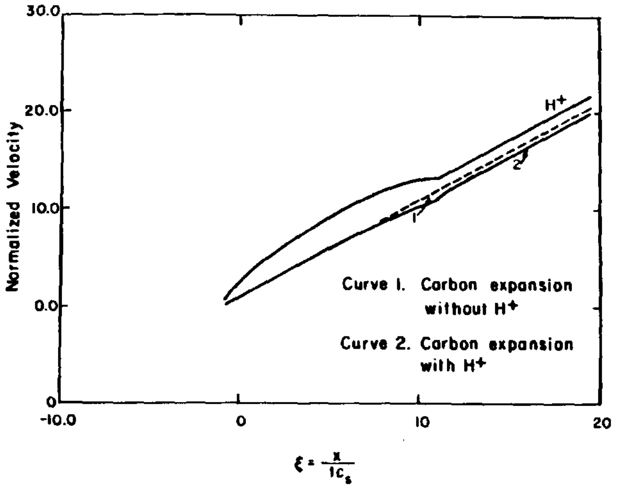

(b)

Fig. IV-9(b). Normalized carbon ion velocity (curve 2) and hydrogen ion velocity (curve H) versus self-similar parameter ξ. Dotted line is single-species (carbon) solution.

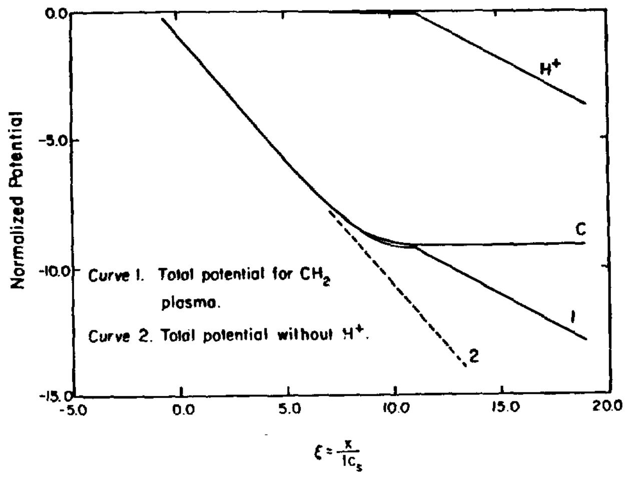

(c)

Fig. IV-9(c). Normalized total potential caused by CH_2 plasma (curve 1) and decomposed potentials caused by carbon electron flow (curve C) and hydrogen electron flow (curve H). Dotted line is single-species (carbon) solution.

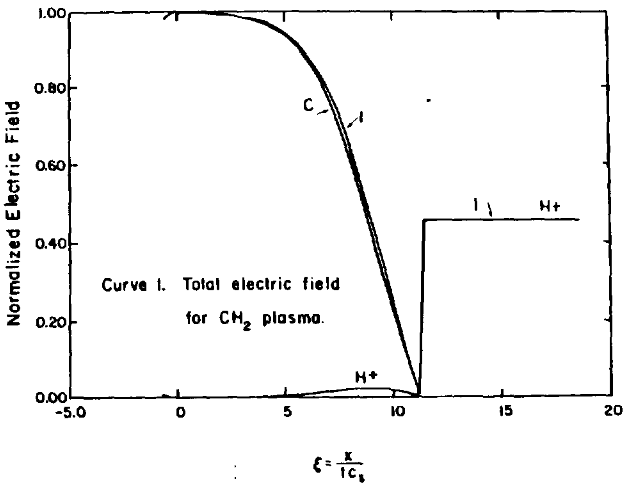

(d)

Fig. IV-9(d). Normalized total electric field caused by CH_2 plasma (curve 1) and decomposed electric fields caused by carbon electron flow (curve C) and hydrogen electron flow (curve H).

carbon and hydrogen ion densities are comparable, the carbon ion density begins to drop abruptly. The onset of this carbon density cutoff is triggered by the initial self-consistent electric field. During the early stages of the expansion, an analytic, dimensionless approximation for the electric field is

$$\frac{d\phi}{d\xi} = -1 + |\xi_o| \frac{Z_h}{Z_c} \frac{Z}{(Z - |\xi_o|)} \frac{n_{ho}}{n_c} (u_h - \xi)^{-3} \quad , \qquad \text{(IV-4)}$$

where ξ_0 is the initial value of the self-similar parameter, $Z = Z_h M_c/M_h Z_c$ is the hydrogen-to-carbon charge-to-mass ratio, n_c is the carbon ion density, and $(u_h - \xi)$ is the relative flow velocity between the hydrogen velocity flow and the uniformly moving self-similar ξ-frame. Note that if $n_{h0} = 0$ in Eq. (IV-4), $d\phi/d \simeq -1$ is the solution for the single-ion species case.

During the early stages of the expansion, where $0.185 < \xi < 5$, the carbon velocity flow can be approximated by

$$u_c - \xi \simeq \frac{Z_c}{M_c}\frac{d\phi}{d\xi} \quad , \tag{IV-5}$$

and the carbon density flow can be approximated by

$$n_c \simeq n_{c0} \exp\left[- u_c/(u_c - \xi)\right] \quad . \tag{IV-6}$$

Because Eqs. (IV-4) through (IV-6) are coupled self-consistently, the expanding plasma establishes a feedback loop between the acceleration electric field, the carbon and hydrogen velocity flow, and the carbon density flow. Note that the relative velocity $(u_c - \xi)$ is driven to zero as the acceleration electric field, caused primarily by the carbon electron density, approaches zero [Fig. IV-9(d)]; the carbon ion density n_c also approaches zero as $(u_c - \xi)$ approaches zero.

On the other hand, during the early stages of the expansion, the hydrogen flow velocity can be expressed as

$$u_h - \xi = Z - (Z - |\xi_0|)\exp(-u_h/Z) \quad . \tag{IV-7}$$

This can be approximated as

$$u_h \simeq \frac{Z}{(Z - |\xi_0|)}\{[2|\xi_0|\, Z - |\xi_0|^2 + 2(Z - |\xi_0|)]^{1/2} - |\xi_0|\} \quad , \tag{IV-8}$$

and the hydrogen density flow can be expressed as

$$n_h = \frac{|\xi_0|\, n_{h0}}{(Z - |\xi_0|)}\left(\frac{Z}{u_h - \xi} - 1\right) \quad . \tag{IV-9}$$

We see, in Fig. IV-9(a), that the hydrogen density is essentially a constant until the expansion reaches a point where the carbon density drops to zero; at this point, the hydrogen density flow expands isothermally as

$$n_h = n_{n0} \exp\left[- u_h/(u_h - \xi)\right] \quad , \tag{IV-10}$$

where $u_h - \xi$ is a constant.

The modification in the carbon velocity flow [Fig. IV-9(b)] shows some change where the carbon density approaches zero, which is where $u_c - \xi$ approaches zero. However, the hydrogen flow velocity shows high acceleration effects until the carbon density approaches zero [Fig. IV-9(b) and Eq. (IV-8)]. Near $\xi \sim 10$, the hydrogen velocity flow is constant [Fig. IV-9(b)]. This effect can be realized by considering the electrostatic potential plot in Fig. IV-9(a), where the acceleration potential is primarily caused by the carbon electron density for $\xi_0 < \xi < 10$. In the region near $\xi \sim 10$, the total electrostatic potential is a constant and the electric field is zero; therefore, the hydrogen ion velocity is a constant.

Note, furthermore, that the total electric field [Fig. IV-9(d)] is primarily caused by the carbon electrons for $\xi_0 < \xi < 11$. For $\xi > 11$, the carbon electron density drops to zero and an electric field caused by hydrogen electrons is turned on. The latter condition is required to accelerate the hydrogen ions isothermally.

Let us compare the numerical solution for carbon charge states with experimental data. Figure IV-10(a) and (b) shows the ion velocity distributions that are predicted from the model superimposed on experimentally determined ion velocity distributions. Note that in Fig. IV-10(a) the model predicts lower scale velocities than the experimental values for low charge states.

Agreement can be achieved only if we assume that the charge state in the acceleration region is different from that measured at the Thomson instrument.

We repeated the above numerical experiment with the changes indicated in Fig. IV-10(c) and (d), which summarizes the results of this run where a good fit between theory and experiment is indicated.

These changes in the degree of ionization for the different ion species suggest that the space-time evolution of the ion velocity distributions was apparently completed before the collisional-ionization and three-body recombination equilibrium was reached. In particular, the charge states $Z = 1$, 2, 3, and 4 measured on the Thomson instrument appear to have been one ionization level higher in the acceleration region. The higher charge

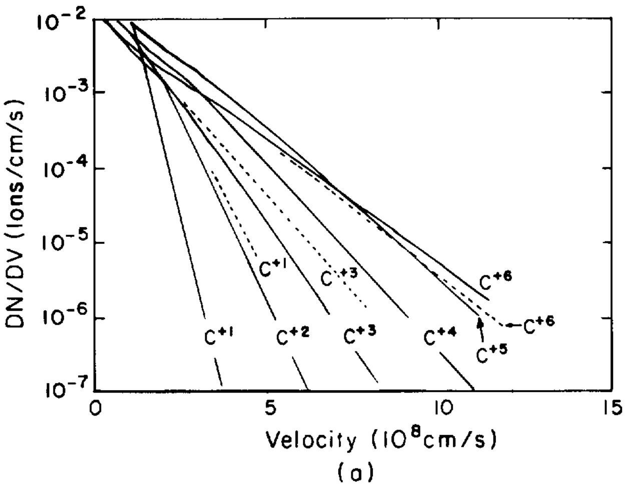

Fig. IV-10(a). Ion velocity distributions for C^{+1}, C^{+3}, and C^{+6} for theory (solid line) and experiment (dashed line) with $Z_1/M_1 = 1$, $Z_2/M_2 = 6$, $Z_3/M_3 = 5$, $Z_4/M_4 = 4$, $Z_5/M_5 = 3$, $Z_6/M_6 = 2$, $n_{10} = 0.05$, $n_{20} = 0.043$, $n_{30} = 0.08$, $n_{40} = 0.46$, $n_{50} = 0.23$, $n_{60} = 0.03$, and $T_e = 1$.

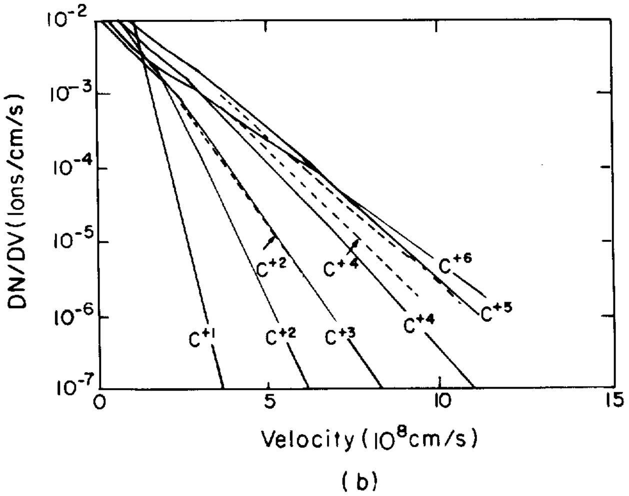

Fig. IV-10(b). Ion velocity distributions for C^{+2}, C^{+4}, and C^{+5} for theory (solid line) and experiment (dashed line). Z_j/M_j and n_{j0} are the same as used for Fig. IV-9(a).

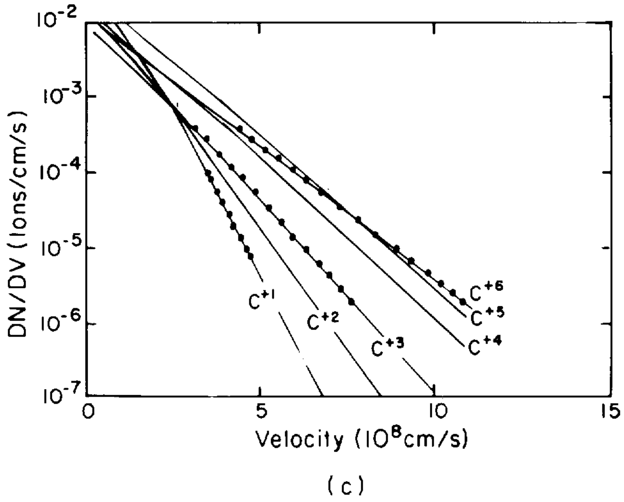

Fig. IV-10(c). Ion velocity distributions for C^{+1}, C^{+3}, and C^{+6} for theory (solid line) and experiment (dotted line) with $Z_1/M_1 = 2$, $Z_2/M_2 = 6$, $Z_3/M_3 = 5$, $Z_4/M_4 = 5$, $Z_5/M_5 = 4$, $Z_6/M_6 = 3$, $n_{10} = 0.05$, $n_{20} = 0.043$, $n_{30} = 0.08$, $n_{40} = 0.046$, $n_{50} = 0.023$, $n_{60} = 0.03$, and $T_e = 1$.

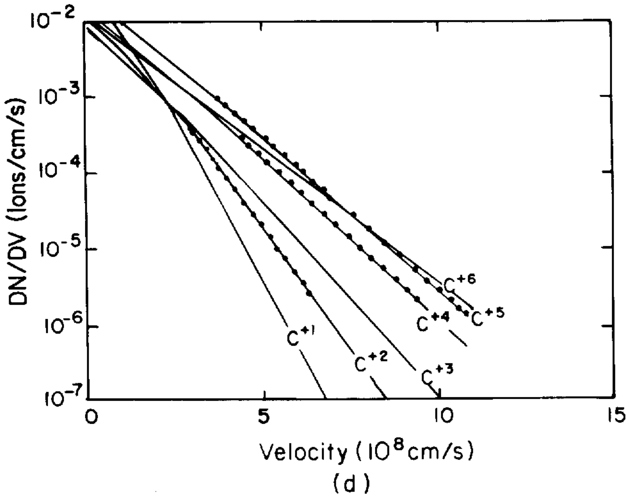

Fig. IV-10(d). Ion velocity distributions for C^{+2}, C^{+4}, and C^{+5}, for theory (solid line) and experiment (dotted line). Z_j/M_j, n_{j0} are the same as used for Fig. IV-9(c).

states appear to have been unaffected. The question of equilibrium conditions for ionization and recombination relative to evolution conditions of the ion distributions needs further investigation. This problem may also be alleviated by a lower vacuum in the target chamber.

The total electric field and the decomposed electric fields from each of the ion species are shown in Fig. IV-11. Note that for $\xi > 5$, the total electric field is primarily the result of charge densities from ions with high charge states.

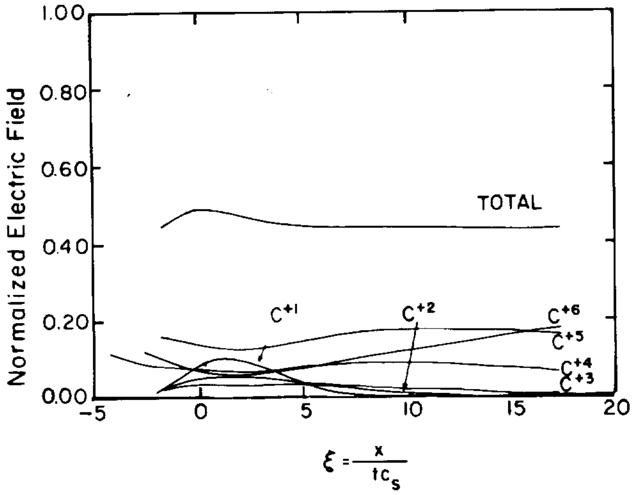

Fig. IV-11. Normalized total electric field and decomposed electric fields for each of the carbon ion species.

In conclusion, the Thomson mass analyzer has proven to be a valuable diagnostic tool for investigating quantitatively the properties of ion flows in laser-induced plasmas. It appears to be a powerful diagnostic for determining the hot-electron temperature in the low-density corona.

A carbon plasma expands isothermally with an electron temperature of ~31 keV, and the C^{+6} ions can be accelerated to maximum kinetic energies of ~9 MeV. The C^{+5} and C^{+6} ions appear to decrease the acceleration fields, which in turn decreases the expansion velocities of the ions with low ionization states. To obtain agreement between theory and experiment for the velocity distributions, the degree of ionization for ions with low ionization states had to be increased in the acceleration region. Furthermore, the presence of hydrogen in the CH_2 plasma induced an attenuation of the amplitude of the acceleration field, which self-consistently decreased the carbon velocity and density flows.

Because of the time dependence of the potential in the isothermal expanding plasma, the acceleration of ions is given by

$$\frac{dv}{dt} = \frac{Ze^2\phi}{MT_e}\frac{d\phi}{dx} \quad , \qquad \text{(IV-11)}$$

which can be integrated to give an ion kinetic energy,

$$E = Ze\phi\left(\frac{e\phi}{2T_e}\right) \quad . \qquad \text{(IV-12)}$$

Note that the ion kinetic energy varies as the square of the potential, and the ion acceleration varies as the product of the potential and the potential gradient.

The CH_2 ion flow expands both isothermally and nonisothermally as a carbon and hydrogen fluid. At ion velocities $v > 5 \times 10^8$ cm/s, the hydrogen flow induces a velocity and density cutoff in the carbon flow. In this region, changes in the hydrogen density induce a decrease in the carbon flow temperature. As the carbon gas cools, the carbon density decreases.

The ion data show that the presence of hydrogen in a plasma inhibits the transport of laser energy to the expanding plasma ions and appears to enhance the lateral transport of energy.

The cellulose-nitrate film, which was used as a particle counter in these experiments, is not useful for ion velocities $<4.0 \times 10^8$ cm/s. Improvements in detector design are being considered to conduct current measurements for ion velocities $<4.0 \times 10^8$ cm/s.

Because the cellulose-nitrate film is not useful for detecting protons with energies >0.5 MeV, a new type of plastic detector that can measure proton energies between 0.6 and 10 MeV will be used in future experiments. We also plan to modify the Thomson mass-analyzer/detector system to measure electron velocity distributions so that we can correlate these data with temperature determinations from the ion data.

We propose the following studies to increase our basic understanding of the physics of laser-induced expanding electrostatic plasmas: (1) determine the effect of the ion-ion streaming instability on the structure of the fast-ion spectra; (2) examine the initial conditions for the electrostatic potential and the electron temperature as they apply to ion flow; (3) examine ionization and recombination effects near the critical-density region with and without the presence of hydrogen; (4) conduct quantitative x-ray measurements to confirm electron temperature computation from ion data; (5) make quantitative ion measurements to determine the angular distribution of ions as a function of target geometry and charge-to-mass ratio; (6) complete quantitative measurements on the properties of the implosion process with and without hydrogen in the target material; (7) perform quantitative measurements on the laser absorption process with and without hydrogen in the target material; and (8) study anomalous transport coefficients in a turbulent collisionless plasma.

BACKSCATTER AND HARMONIC GENERATION MEASUREMENTS IN HELIOS

(D. E. Casperson)

With Helios operating reliably at 7.5 kJ on targets, we will emphasize target experiments and target diagnostics. One useful source of information in laser-plasma interactions is the backscattered radiation from the targets, that is, the laser light that interacts with the target plasma and is reflected from the critical surface in the target plasma. This light contains spectral and temporal information pertinent to the understanding of the absorption of laser light in a target.

In early experiments, one of the eight beams of Helios has provided data on direct backscatttered radiation — primarily the total time-integrated energy for a variety of targets and shooting conditions. More recently a recollimated retrobeam on Helios amplifier 2A has been routed into the Gallery West screen room where a set of detectors and interference filters has been positioned to look for the production of harmonics of the 10.6-μm laser light. Table IV-III summarizes the observed harmonic energies for three different target types.

One important result evident from the table is the reduced value of total backscattered energy from targets whose surface is not normal to the incident light (2-mm-diam gold shell with 53° angle of incidence) compared to normal incidence (plastic-coated GMB). It appears that most of the usual 6% backscatter from GMBs must be specular and that 2% is nonspecular. The 2% figure agrees with Gemini observations on slab targets.

A particularly useful diagnostic tool is the second-harmonic energy that is a substantial ~1% of the total backscattered energy (~1 J under present firing conditions). Because the second harmonic is created near the target critical surface, this harmonic could be used to investigate the evolution of the critical surface.

A double electrically isolated and x-ray-shielded screen room on the main floor of Helios was nearly completed. This screen room and its associated optical beam trains from Helios amplifiers 1A and 4A are dedicated to the study of target optical backscatter measurements. Light that is directly backscattered onto the f/2.4 focusing paraboloids inside the target chamber and is subsequently Fresnel-reflected from the NaCl windows of the amplifiers enters these two retrochannels (Fig. IV-12). The light is reflected from copper mirrors and focused through wave-guide sections into the screen room for analysis.

Spectrally resolved 10.6-μm backscatter data were obtained using a 0.75-m-long Jarrell Ash spectrometer with a high-resolution pyroelectric array detector* placed at the exit slit. This linear array has 32 elements on 100-μm center-to-center spacing that provides ~40 Å resolution at 10.6 μm. The resolution is determined primarily by the diffraction-limited spot size of the final mirror in the spectrometer and by the finite width of the entrance slit. With this resolution, the velocity of the critical surface from which the backscattered light is being reflected could theoretically be determined from Doppler shifts to an accuracy of ~1 × 10^7 cm/s. This accuracy is reduced, however, by target-plasma effects, which broaden or shift the backscattered spectrum or produce a time-dependent spectrum because the array

Table IV-III. Helios Total and Harmonic Backscattered Energies from GMB Targets and 2-mm-diam Gold Shells

Target Type	$\frac{E_{\text{Total back}}}{E_{\text{FWD}}}$	$\left(\frac{2\omega_0}{\omega_0}\right)_{\text{back}}$	$\left(\frac{3/2\omega_0}{\omega_0}\right)_{\text{back}}$	$\left(\frac{3\omega_0}{\omega_0}\right)_{\text{back}}$	$\left(\frac{4\omega_0}{\omega_0}\right)_{\text{back}}$
Plastic-coated GMB	$\frac{51\ \text{J}}{800\ \text{J}}$(6.4%)	$\frac{0.73\ \text{J}}{51\ \text{J}}$(1.4%)	-0-(1 shot)	$\frac{0.15\ \text{J}}{51\ \text{J}}$(0.3%)	---
Au shell	$\frac{14.4\ \text{J}}{928\ \text{J}}$(1.6%)	$\frac{0.14\ \text{J}}{14.4\ \text{J}}$(1.0%)	-0-(1 shot)	---	---

---

*Manufactured by Spiricon, Inc.

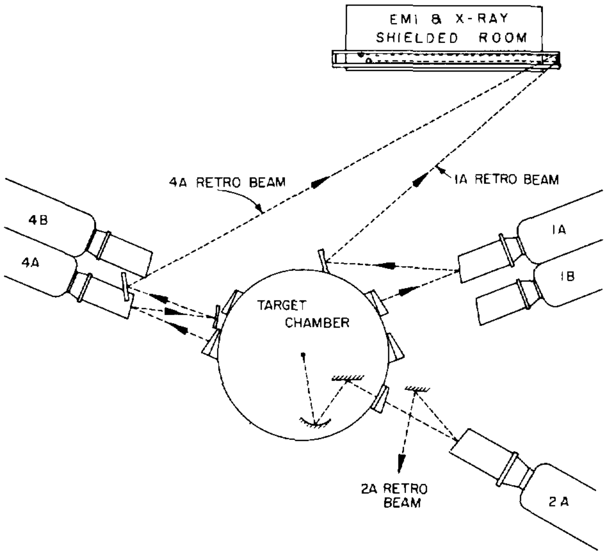

Fig. IV-12. Layout of backscatter diagnostics in Helios.

yields only a time-integrated spectrum. We are considering experiments that could yield a time-dependent spectrum by placing fast pyroelectric detectors at the exit slit of the spectrometer.

Three spectra from shots on flat and spherical copper targets are shown in Fig. IV-13. Superimposed upon each spectrum is a calibration spectrum obtained by reflecting the Helios multiline oscillator beam off the Hartmann alignment sphere in the target chamber back to the 2A retrochannel. The two calibration peaks are from the P(18) and P(20) lines of the 10.6-µm CO_2 spectrum and are separated by ~200 Å. These backscattered spectra clearly show that the individual lines are broadened to such an extent that they overlap, complicating interpretation. If the observable peaks are attributed to P(18) and P(20), then both red shifts and blue shifts are present on similar targets and under similar shooting conditions, so that systematic differences between different target types may only be inferred statistically from a large number of shots. Also, the amplitudes of the P(18) and P(20) lines are not routinely measured at the exit of the power amplifiers and are known to vary from shot to shot. Hence the Doppler shifts can be most easily interpreted if the oscillator is operated on a single rotational line.

The spectrally and temporally resolved backscattered light from the fundamental10.6-µm wavelength and from the low harmonics (for example, n = 2, 3, 4, 5) of this fundamental will also be used to help interpret target performance. Because the harmonics are generated at the critical surface in a target (that is, where the 10.6-µm incident light is absorbed, $n_{critical} = 10^{19}$ e/cm^3), the temporally resolved backscattered harmonic conveys information about time dependence of absorption in the target plasma. The dectector to be used for these measurements is a modified Santa Barbara Research Corp. Ge:Hg detector with a 100-ps risetime. The large element (5-mm diam) in this detector will facilitate total energy measurements of the weaker harmonic signals.

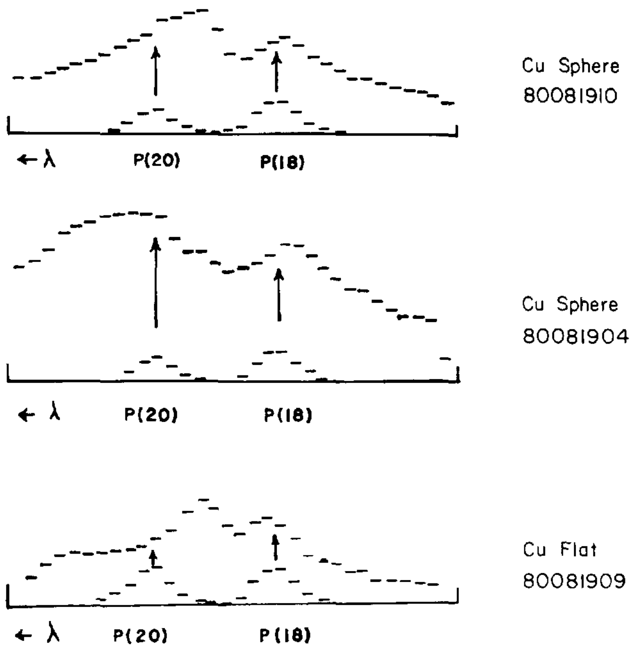

Fig. IV-13. Representative backscatter spectra from copper targets.

REFERENCES

1. V. M. Cottles, "Measurements of Absorption and Ion Production in Laser Fusion," Bull. Am. Phys. Soc. 22, 1090 (1977).

2. S. R. Gunn and V. C. Rupert, "Calorimeters for Measurement of Ions, X Rays, and Scattered Radiation in Laser Fusion Experiments," Rev. Sci. Instrum. 48, 1375 (1977).

3. R. P. Godwin, R. Sachsenmaier, and R. Sigel "Angle-Dependent Reflectance of Laser-Produced Plasmas," Phys. Rev. Lett. 39, 1198 (1977).

4. F. Young and G. H. McCall, "Measurement of Charged Particle Velocity and Population Distributions in Laser-Produced Plasma Experiments," Bull. Am. Phys. Soc. 22, 1129 (1977).

5. T. H. Tan, A. H. Williams, and G. H. McCall, "A Thin-Film Detector System for Laser Fusion Studies," Nucl. Instrum. Methods **131**, 425 (1975).

6. A. W. Ehler, F. Begay, T. H. Tan, J. Hayden, and J. McLeod, "Effect of Target Purity on Laser-Produced Plasma Expansion," J. Phys. D: Appl. Phys. **16**, L30 (1980).

7. A. W. Ehler, "High-Energy Ions from a CO_2 Laser-Produced Plasma," J. Appl. Phys. **46**, 2464 (1975).

8. R. J. Trainor, N. C. Holmes, and R. M. More, "Measurement of Electron Preheat Temperature in Laser-Irradiated Disk Targets," Bull. Am. Phys. Soc. **24**, 972 (1979).

9. N. H. Burnett, H. A. Baldes, M. C. Richardson, and G. D. Enright, "Harmonic Generation in CO_2 Laser Target Interaction," Appl. Phys. Lett. **31**, 172 (1977). The references in this article are also useful.

10. E. A. McLean, J. A. Stamper, B. H. Ripin, H. R. Griem, J. McMahon, and S. E. Bodner, "Harmonic Generation in Nd: Laser-Produced Plasmas," Appl. Phys. Lett. **31**, 825 (1977).

11. V. Cottles, A. Williams, L. White, and D. Giovanielli, "Absorption of Short Pulse 10.6 µm Laser Light by Plain and Spherical Targets," in preparation.

12. D. W. Forslund, J. M. Kindel, and K. Lee, "Theory of Hot-Electron Spectra at High Laser Intensity," Phys. Rev. Lett. **39**, No. 5, 284 (1977).

13. R. L. Carman, D. W. Forslund, and J. M. Kindel, "Visible Harmonic Emission as a Way of Measuring Profile Steepening," Phys. Rev. Lett. **46**, 29 (1981).

14. J. C. Kieffer, H. Pepin, F. Martin, P. Church, and T. W. Johnston, "Electron Energy Transport into Layered Targets Irradiated by CO_2 Laser Light," Phys. Rev. Lett. **44**, No. 17, 1128 (1980).

15. R. Fedosejevs, I. V. Tomov, N. H. Burnett, G. D. Enright, and M. C. Richardson, "Self-Steepening of the Density Profile of a CO_2 Laser Produced Plasma," Phys. Rev. Lett. **39**, No. 15, 932 (1977).

16. A. W. Ehler, F. Begay, T. H. Tan, and P. H. Castine, "Lateral Transport of Energy from a Laser-Produced Plasma," J. Phys. D: Appl. Phys. **13**, L65-66 (1980).

V. DIAGNOSTICS DEVELOPMENT

(D. Giovanielli)

The small volumes and extremely short reaction times involved in the laser fusion process create the need for new diagnostic techniques having spatial and temporal resolutions in the submicrometer and 1- to 100-ps regime, respectively. These needs are being met with a vigorous diagnostics program in such areas as laser calorimetry, charged-particle and neutron detection, x-ray spectrometry, and subnanosecond streak-camera development.

INTRODUCTION

This year the diagnostics development program addressed primarily x-ray measurements. Because the characterization of hot electrons is crucial to CO_2 target design, we developed high-energy bremsstrahlung systems that can provide information about the energy distribution of these electrons. We also emphasized time-resolved x-ray measurements using x-ray streak cameras as well as x-ray imaging systems to understand energy-transport processes. Spectrometers to directly measure energies of electrons from the target were developed to provide correlation with the x-ray data.

X-RAY DIAGNOSTICS

APACHE High-Energy X-Ray Diagnostics

(W. Priedhorsky)

We have acquired our first clean multichannel data from the APACHE high-energy spectrometer. Previous background and signal saturation problems were solved by replacing the 7764 photomultiplier detectors (photoelectron gain $\simeq 10^4$) with photodiodes (photoelectron gain = 1). These detectors provide adequate signal levels for high-Z targets. A set of typical oscilloscope traces is shown in Fig. V-1. There is no signal in the background channel with 1 in. of lead between target and detector.

The APACHE system consists of collimators, K-edge filters, and CsF scintillators optically coupled to the photodiodes. Transmission of the filters and absorption of the scintillators serve to define broad energy bands. Scintillator thickness is chosen so that it has an optical depth $\tau \sim 1$ at the filter K-edge. The scintillator response above the K-edge is thus approximately proportional to the mass absorption coefficient and falls with energy as sharply as possible. The present filter-scintillator combinations are summarized in Table V-1.

We are calibrating to determine the spectral response of the APACHE detector. However, even without calibrations, relatively high-energy x-ray signals can be compared from shot to shot. Calibration measurements of the scintillator-photodiode combinations were made on the 60-kV Picker and 300-kV Norelco x-ray systems to determine the unit photon response over the range $h\nu = 10\text{-}240$ keV. The calibration still has to be reduced to allow for signal impurity contribution, but preliminary response data indicate that the flux at $h\nu = 100$ keV is roughly equal to that predicted by our calculations.

APACHE is not now useful for low-Z shots because of the insensitivity of the photodiode detectors. The 7764 photomultipliers have too much gain and too little linear current for all but the weakest shots. Measurements were made to determine the optimum base configuration for the 7764 tubes. We find that they can be tuned to deliver 10 times more linear current at the same gain. With performance thus improved, a system based on 7764 photomultipliers would be useful for low-Z shots.

Advanced High-Energy Spectrometer

We defined the spectrometer system most likely to provide a cleaner channel response than the broad K-edge-filtered channels. We concluded that Bragg diffraction from mosaicked LiF (200) crystals would yield relatively large signals from well-defined spectral bands. Untreated crystals would yield integrated reflectivities orders of magnitude lower. A LiF system would require a modest signal amplification of $\sim 10^2$ or 10^3. We are making measurements with a lead-shielded CsF scintillator/7764 photomultiplier to determine the shielding required for such a system.

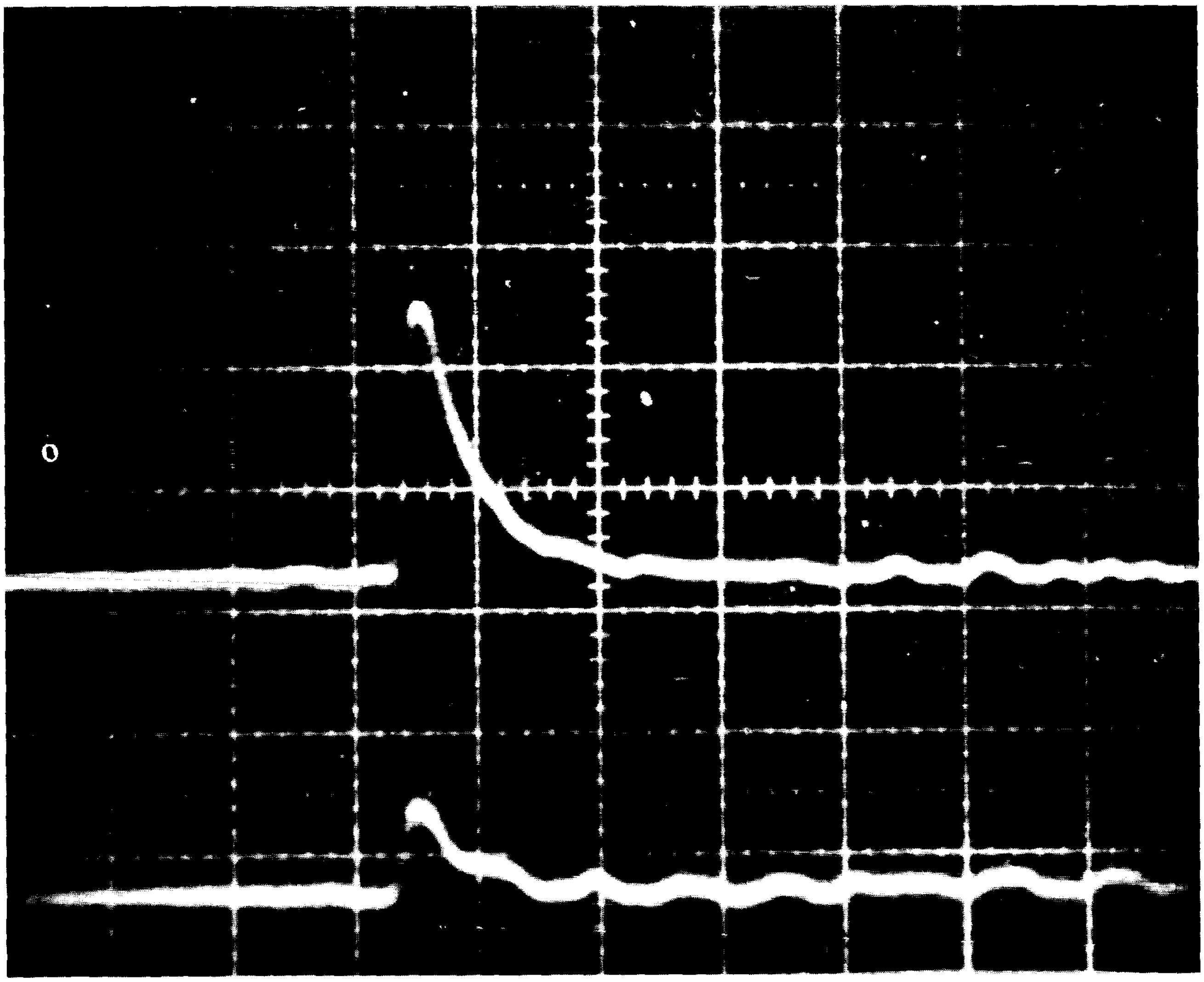

Fig. V-1. Sample oscilloscope traces for two APACHE signal channels. Target is a GMB irradiated at 8.22 kJ; input impedance 50% and scale: 10 ns/cm, 100 mV/cm.

X-Ray Diagnostic Test Source

We purchased an electron gun/lens assembly from Electron Technology, Cambridge, Massachusetts, to produce a point source of x rays for diagnostic test and calibration. The source consists of an electron beam magnetically focused on a foil target. The x rays are viewed through the target, which, for our tests, was ~6-µm-thick copper foil. The gun/lens is specified for voltages up to 25 kV. However, problems with a high-voltage junction box prevented us from making tests at >9 kV.

The electron beam is focused to the target by a current modulation scheme. A line frequency modulation is added to the focusing field by means of an auxiliary focus coil; variations in the secondary-electron yield over the foil surface produce a second-harmonic modulation in the target current, which is viewed on an oscilloscope and maximized for optimum focus. This focusing scheme seemed erratic and did not always produce a distinct focus signature. After beam operation at a given point for some length of time, the second harmonic tended to be weak, possibly because the electron beam cleaned the surface.

The electron gun/lens is specified to deliver up to a 5-µA target current into a spot size 2 µm in diameter over 15 to 25 kV. At 8.8 kV we achieved target currents up to 3.7 µA. At this voltage, the copper K-lines are not

TABLE V-I. APACHE Channel Configuration

Channel No.	K-Edge Filter (cm^2/g)	K-Edge Energy (keV)	CsF Scintillator Thickness (in.)
1	Sn 0.572	29.2	0.020
2	Er 0.206	57.5	0.020
3	W 0.285	69.5	0.050
4	Au 0.484	80.7	0.100
5	Mo 1.982	~150[a]	0.250
6	Pb 0.302	88.0	0.100
7	Mo 0.0505	20.0	0.010
8	Sm 0.138	46.8	0.010
9	U 0.549	115.6	0.250
10	Pb 28.7	Background	0.250
	or Hf 0.293	65.3	0.050

[a] Effective energy (not a K-edge filter).

excited, so the emission measured with a xenon proportional counter consisted of bremsstrahlung that fell to half peak power at 4.1 and 7.3 keV. The low-energy cutoff is set by foil absorption; the high-energy cutoff is determined by the beam voltage. The x-ray fluence was measured with a 0.75-cm^2, 12-μm-thick beryllium window proportional counter.

The beam current was reduced to 1.3 nA to obtain an acceptable counting rate. At a distance of 1.7 cm from the target, we measured 1260 counts/s in the x-ray spectra. Assuming unit window transmission and detector absorption, and x-ray yield scaling with target current, we expect 1.4×10^7 photons/sr·s from the source at 3.7 μA. Excitation of a K-line would, of course, yield a more intense and monochromatic flux.

The size of the emission region was estimated by shadowgraphing a 40-lines/mm copper mesh placed above the target. Figure V-2 shows the resultant image. The copper mesh is not completely opaque to the x-ray spectrum; this makes quantitative analysis of source size difficult. However, the resolution of the mesh clearly approaches 1 μm. Figure V-3 shows a shadowgraph of some small (~100-μm-diam) nickel Solacels placed on the same mesh. Wall defects in the Solacels are apparent.

Needle-Type Point X-Ray Source

We intend to investigate an improved version of the needle-anode point x-ray source built at LLNL by R. Price.[1] It has promise as an intense small source that can be optically aligned (the x-ray source is at the tip of a needle), but in its present version, it has a spot size of 10-15 μm. The proper use of electron optics in the source design should permit ~1-μm-diam spot sizes.

We procured the parts for an improved needle-point x-ray source that includes a focusing aperture to focus electrons electrostatically onto the needle tip. A breadboard version of this source will be constructed to test the focusing conditions required for optimum spot size.

PULSED CALIBRATION OF A PROXIMITY-FOCUSED X-RAY STREAK CAMERA (P. Rockett, J. McGurn)

Absolute spectral measurements made with XRDs have proven invaluable in diagnosing laser-target interactions. X-ray streak cameras now promise to improve the

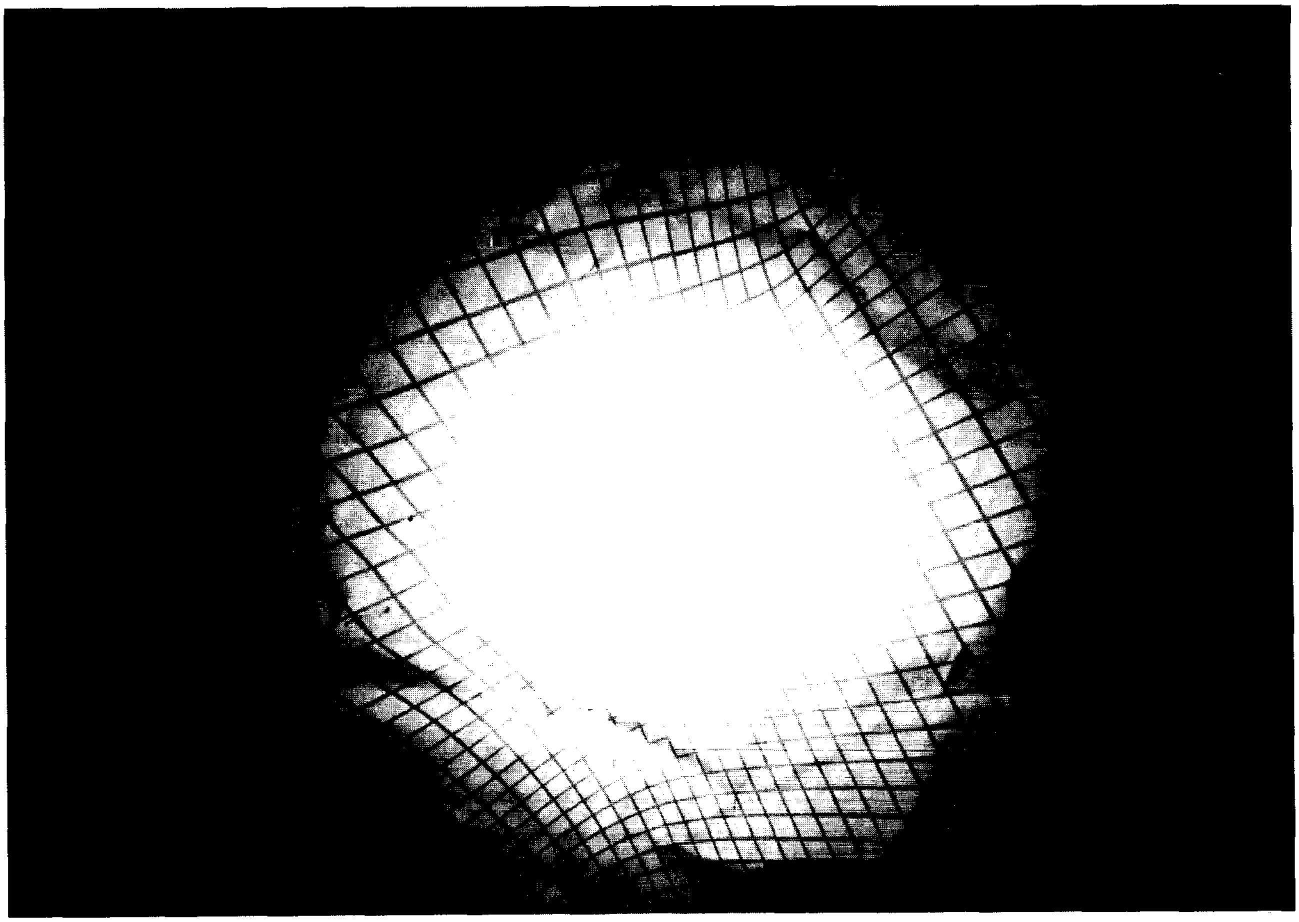

Fig. V-2. Shadowgraph of 40 lines/mm copper mesh placed above the target.

temporal resolution of the same data by a factor of 10. Absolute calibration of the streak camera, however, is not as straightforward as the calibration of XRDs, which consist simply of a filter, grid anode, and photocathode. The quantum efficiency of an XRD is the same whether measured on a dc, low-flux x-ray source or on a pulsed (10-ns) high-flux source.*[2] An x-ray streak camera is far more complicated, as shown in Fig. V-4. Several of its components may well be sensitive to both the rate of incident flux and to the total dose received. Furthermore, the camera sensitivity can only be measured by comparing the number of photons input in a given bandwidth to the resulting recording-film density.

An absolute spectral calibration was made on our GEAR, Inc.** proximity-focused x-ray streak camera. The camera photocathode is a 25-μm-thick beryllium window coated with 150 Å of gold. Initially, we made a dc calibration at x-ray energies of 0.930, 1.47, 4.5, 6.4, and 8.05 keV. We then compared these results to a pulsed calibration (300 ps) made with a laser-plasma source, whose spectrum was measured with calibrated XRDs. The results showed that measured dc sensitivities were 6.5 times lower than the pulsed sensitivity of the proximity-focused streak camera. In general, the dc calibration could not be extrapolated to a pulsed measurement.

The dc calibrations were performed by using low-energy x rays. Dosimetry measurements on each spectral line determined purity and absolute flux. The Kodak 2484 photographic film used in the streak camera was calibrated by means of a standard sensitometer and step wedge for each measurement. The camera was operated by maintaining a dc voltage on the cathode and repetitively pulsing "on" the channel-plate intensifier at 100 Hz. Results are plotted in Fig. V-5 with a model for

---

*This information was supplied by Robert H. Day, Los Alamos National Laboratory (1979).

**General Engineering and Applied Research, Inc.

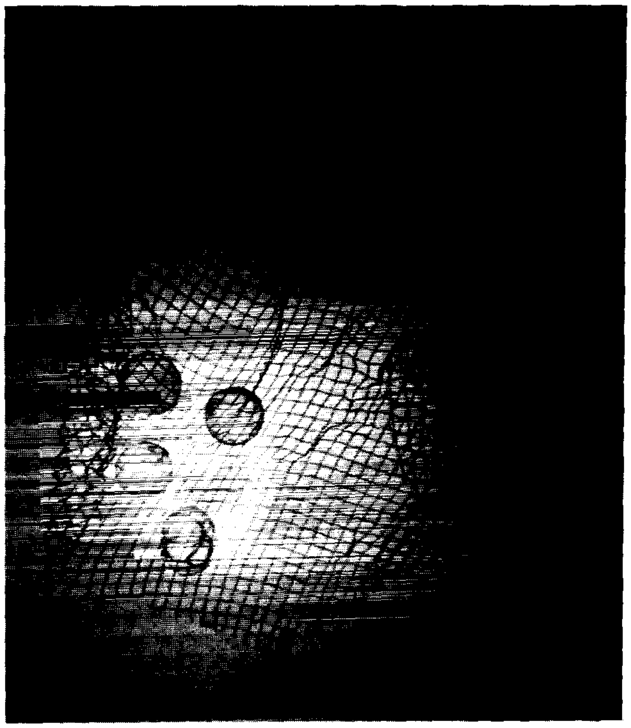

Fig. V-3. Radiograph of small (~100-μm-diam) nickel microballoons taken with the ETC point x-ray source. The scale is indicated by the 40 lines/mm mesh.

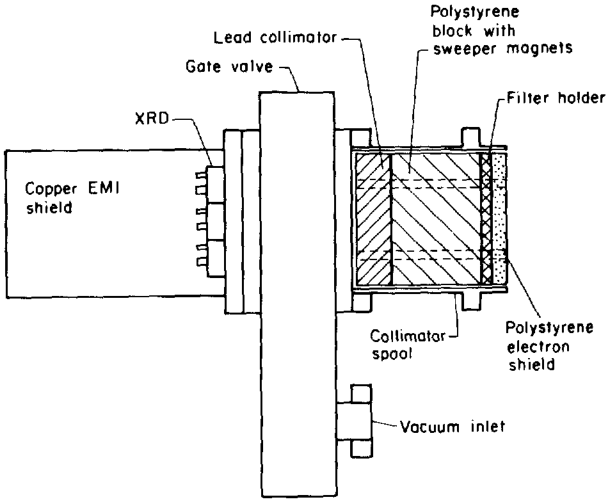

Fig. V-4. GEAR's proximity-focused streak tube, channel-plate intensifier, and fiber-optic readout.

photoelectric sensitivity proposed by Henke.[3] His well-tested model states that photoelectric yield is proportional to the product of E, the incident photon energy; μ(E), the mass absorption coefficient; and f(E), a slowly varying function describing the efficiency of converting a primary high-energy photon to secondary electrons.

The measurements fit the model well at low energies, but the model overestimates sensitivity above 6 keV. This implies that the gold photocathode is thinner than 150 Å, or that our data on f(E) are inaccurate at higher photon energies.

A pulsed comparison calibration was made by irradiating a nickel microballoon with 10 J of 1.06-μm laser light and viewing the microballoon simultaneously with the x-ray streak camera and with a five-channel array of XRDs. We used data from the XRDs to reconstruct absolutely the incident x-ray spectrum. We estimated the expected density on the streak-camera film by folding the spectrum against the data in Fig. V-5. The expected density, converted to film exposure (erg/cm^2), showed a sensitivity 6.6 times lower than that measured.

To resolve this discrepancy, we performed a dc recalibration at a variety of flux levels for each of three wavelengths, varying x-ray flux by increasing beam filtration. We then made a spectral analysis with each filter to account for the effect of changing beam purity. The results plotted in Fig. V-6 show a significant nonlinearity in the streak-tube sensitivity between 2×10^8 and 1×10^{10} photons/cm^2•s. Because the ratios between exposures at fixed flux or between fluxes at fixed

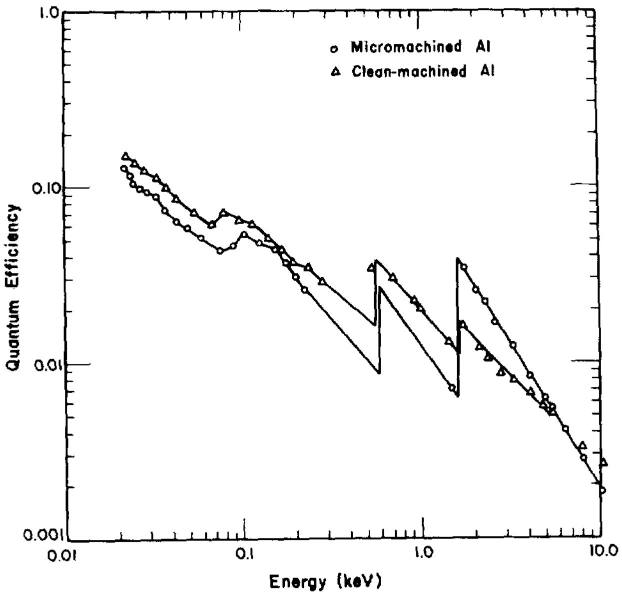

Fig. V-5. Henke's improved model shows sensitivity and experimental calibration points.

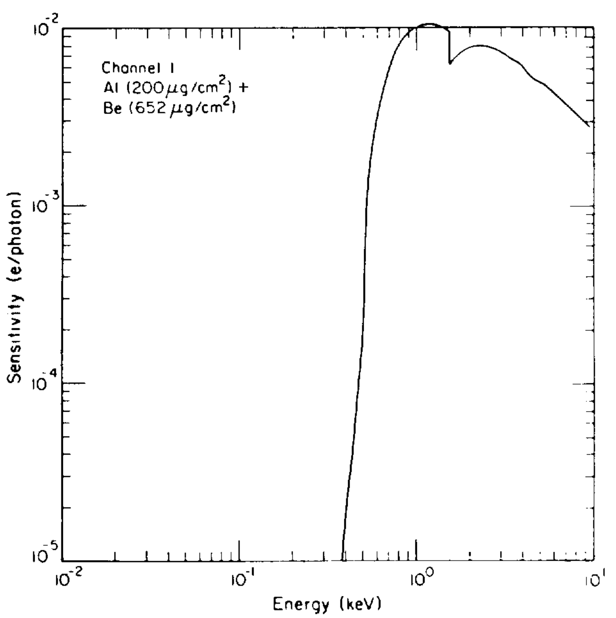

Fig. V-6. Effect of changing flux on dc calibration of a proximity-focused x-ray streak camera.

exposures remain constant over the range of fluxes and wavelengths studied, it is possible to construct a curve of relative sensitivities. Absolute calibrations clearly cannot be extrapolated to high-flux pulsed operation on the basis of low-flux dc measurements. However, the small increase in measured pulsed sensitivity over dc sensitivity indicates a saturation of the nonlinearity at high flux levels.

One might conclude that the unusual characteristics of the proximity-focused streak tube cause this nonlinear increase in sensitivity with incident flux. However, Palmer and Palmer recently reported the same observations on a conventionally designed S-1 photocathode Photocron-I streak tube.* They observed a nonlinear increase in photon gain (or sensitivity) with increasing flux from a 1.3-μm laser. The phenomenon thus appears to be related to the tubes' common features: (1) a photocathode with a high-acceleration voltage, and (2) an electron-to-photon converting phosphor. Neither has been studied independently for sensitivity.

DETECTOR RESPONSE FUNCTIONS FOR MULTIFLEX (R. H. Day)

MULTIFLEX is a seven-element XRD array arranged in a hexagonal tile geometry and mounted on a 15-cm (6-in.) Conflat* flange. A cross section of the detector system is shown in Fig. V-7. The detectors are mounted in a vacuum environment that is separated from the Helios target chamber. Maintenance operations can be performed independent of the laser system, and frequent down-to-air cycles can be avoided that would degrade the performance of high-sensitivity XRD cathodes. The collimator assembly and detector filters are housed in the Helios target chamber for easy access and frequent filter change. The detectors are well-matched 50 coaxial detectors using a Kel-F O-ring vacuum feedthrough and step-impedance matching from a General Radio connector geometry to a 0.547-in.-diam cathode. The anode-cathode voltage (2-3 kV) and separation (0.050 in.) have been chosen to yield a time response of < 100 ps.

The energy sensitivity of the detector is determined by the energy dependence of the cathode quantum efficiency multiplied by the transmissivity of the detector window. The cathode/window geometry combinations now used in MULTIFLEX are listed in Table V-II. These detectors can use clean-machined cathodes[4] or, alternatively, diamond-machined cathodes when it is desired to enhance response above the aluminum K-edge or to provide a surface less sensitive to air exposure. These two basic cathode response functions are shown in Fig. V-8.

The filter window transmissions are derived from several sources of absorption coefficients: (1) above a few hundred eV, from the Kaman Nuclear Tables,[4] and

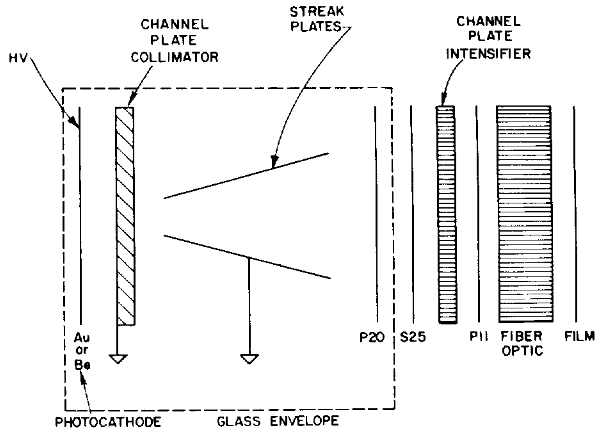

Fig. V-7. Cross section of MULTIFLEX detector system.

---

*This information was supplied by M. A. Palmer and R. E. Palmer, SNL (1980).

*Conflat is a registered trademark of Varian Associates, Palo Alto, CA 94303.

TABLE V-II. Cathode/Window Geometry Combinations Used in MULTIFLEX XRD Array

Cathode: Clean-machined aluminum
Anode: 4 lines/mm (l/mm)

Channel No.	Window	Mesh
1	200 $\mu g/cm^2$ Al 652 $\mu g/cm^2$ Be	0
2	270 $\mu g/cm^2$ Kimfoil 400 Å^+ Al	0
3	None	3 layers 4 l/mm Ni mesh
4	500 $\mu g/cm^2$ Teflon	0
5	428 $\mu g/cm^2$ Mylar	0
6	200 $\mu g/cm^2$ Al	3 layers 4 l/mm Ni mesh
7	70 $\mu g/cm^2$ Poly	3 layers 4 l/mm Ni mesh

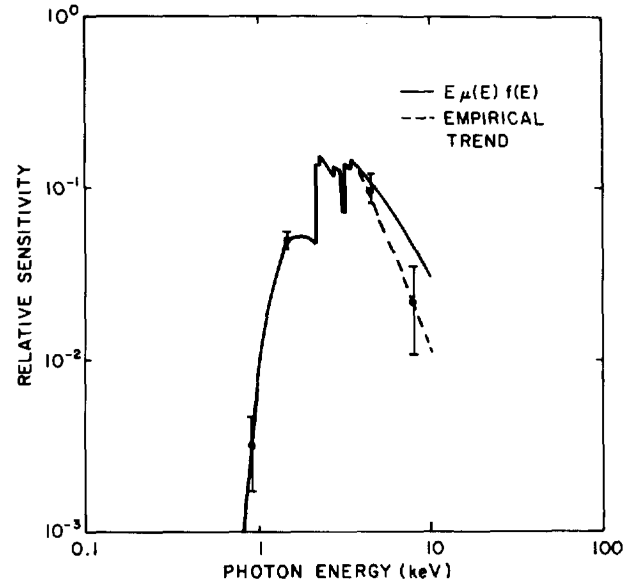

Fig. V-8. Quantum efficiencies of micromachined and clean-machined aluminum photocathodes.

(2) below that energy, from a combination of measurements made at the Deutsches Elektronen-Synchrotron[5] and some window transmissions measured at the NBS.[6] In addition, some detectors listed in Table V-II use several layers of 4 lines/mm Buckbee Meers nickel mesh as a neutral density filter for low-energy x rays. X-ray transmission studies of this material indicate that it can be represented as 84.1% open area with nickel wires of 5.1 mg/cm^2 areal density.

The measured cathode quantum efficiencies and measured or calculated window transmissions were then folded to yield a detector response. The results of these calculations for the channels listed in Table V-II are shown in Figs. V-9 to V-15.

Complete data reduction involves a spectral deconvolution using response curves to yield a best estimate of the final spectral shape. However, a simpler approach yields estimates of spectral shape and total radiated power. One method is to convolve the detector response curves against Planckian blackbody spectra at various temperatures. The results for our detector geometry and a source 200 μm in diameter folded against the various detector response curves from Table V-II are shown in Fig. V-16. Each detector yields a spectral temperature, which is a measure of the total radiated power. The channel-to-channel consistency of the temperatures reflects the conformity of the spectrum to a Planckian distribution. Both the blackbody fold code and the detector response calculator were incorporated into computer codes so that changes in the complement of MULTIFLEX detectors can be quickly calculated.

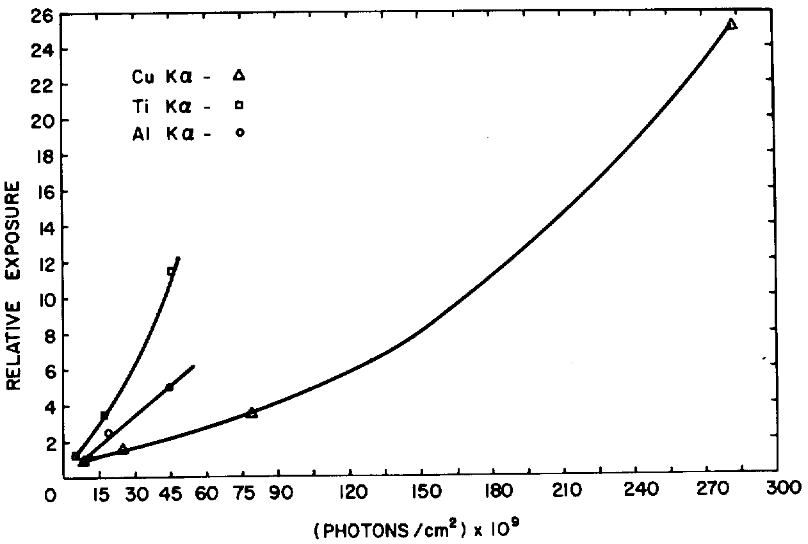

Fig. V-9. Detector response for a clean-machined aluminum cathode with a 4 lines/mm nickel mesh anode and one 200-µg/cm^2 aluminum plus 652-µg/cm^2 beryllium filter window.

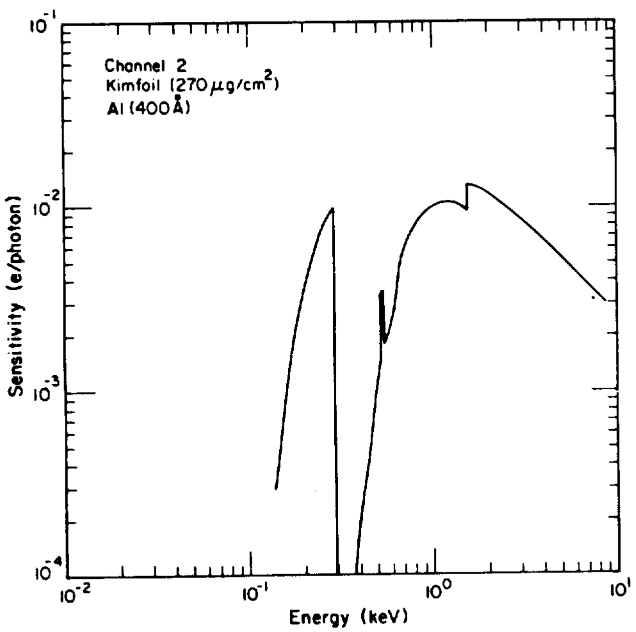

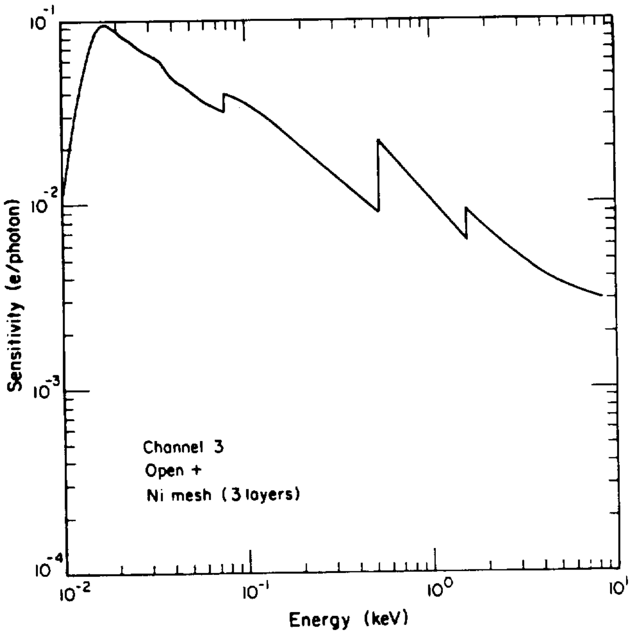

Fig. V-10. Detector response for a clean-machined aluminum cathode with a 4 lines/mm nickel mesh anode and a 270-µg/cm^2 Kimfoil plus 400 Å aluminum.

Fig. V-11. Detector response for a clean-machined aluminum cathode with a 4 lines/mm nickel mesh anode and three layers of 4 lines/1mm nickel mesh as an x-ray neutral density filter.

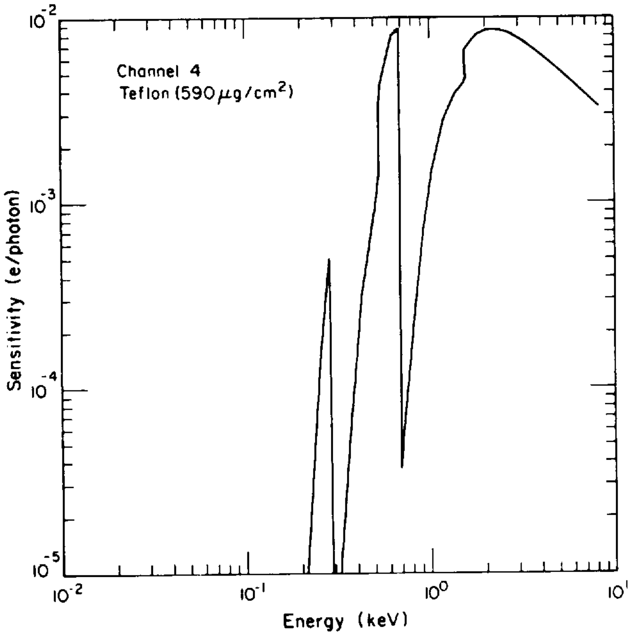

Fig. V-12. Detector response for a clean-machined aluminum cathode with a 4 lines/mm nickel mesh anode and a 590-μg/cm² Teflon filter window.

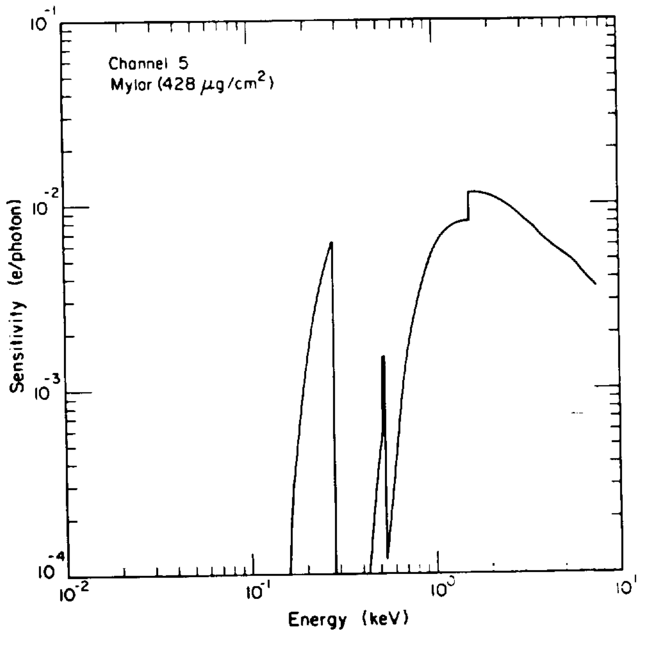

Fig. V-13. Detector response for a clean-machined aluminum cathode with a 4 lines/mm nickel mesh anode and a 428-μg/cm² Mylar filter window.

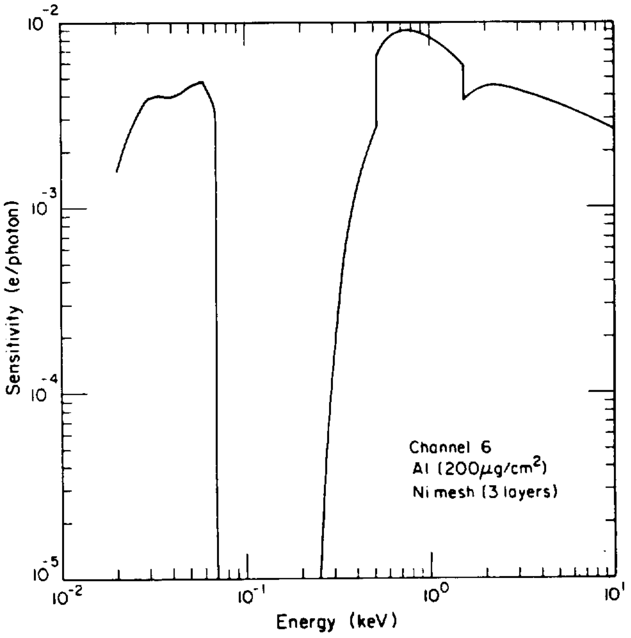

Fig. V-14. Detector response for a clean-machined aluminum cathode with a 4 lines/mm nickel mesh anode and a 200-μg/cm² aluminum filter window with three layers of 4 lines/mm nickel mesh as an x-ray neutral density filter.

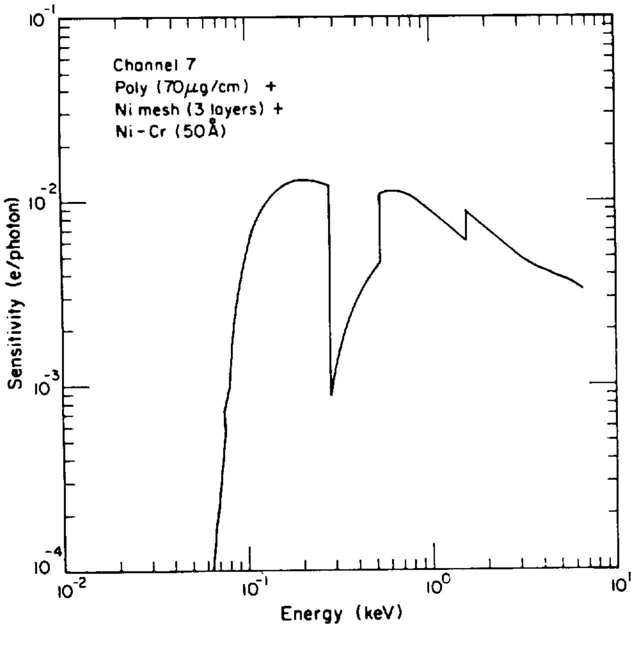

Fig. V-15. Detector response for a clean-machined aluminum cathode with a 4 lines/mm nickel mesh anode and a 70-μg/cm² polypropylene plus 50-Å, nickel-chrome filter window with three layers of 4 lines/mm nickel mesh as an x-ray neutral density filter.

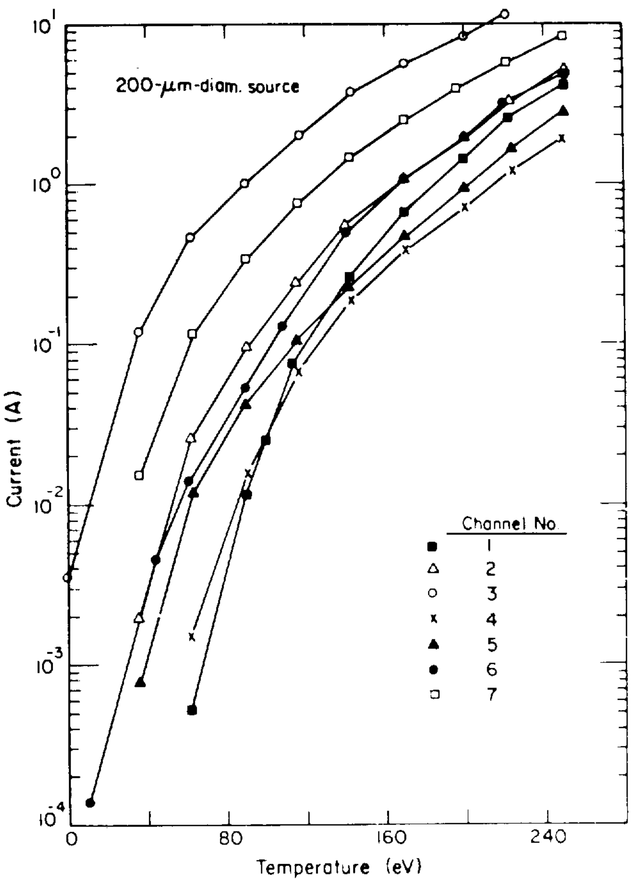

Fig. V-16. Detector current vs blackbody temperature of a 200-µm-diam source.

A "THIN LENS" ELECTRON MAGNETIC SPECTROMETER AND AN ELECTRON RAY-TRACING CODE FOR CYLINDRICALLY SYMMETRIC FIELDS (J. S. Ladish)

In 1926, H. Busch[7] demonstrated that a short, axially symmetric magnetic field could produce a focusing action on an incident electron beam. Since that time, the field of electron optics has developed to a level of sophistication rivaling that of light optics.[8-12] For many applications, especially at high electron energies (>1 MeV), magnetic lenses are preferable to their electrostatic counterpart, because the magnetic force is proportional to the electron velocity, whereas the electric force is not. This effect can be seen clearly in the data presented in Table V-III. One can show that for equal (small) transverse angular deflections in a uniform electric (E) or magnetic (B) field the following relationship holds:

$$\frac{E(\mathrm{V/cm})}{B(\mathrm{G})} \simeq 300\beta \quad , \tag{V-1}$$

where

$$\beta = \frac{v}{c} \quad .$$

Both Table V-III and the relation given in Eq. (V-1) indicate that from an experimental point of view, the requisite field values for the hot-electron energy range of interest in laser fusion plasmas (>100 keV) are more readily obtained in the magnetic case.

In the paraxial, weak, thin lens approximation, the focal length of an axially symmetric magnetic lens can be written[8]

$$f = \frac{4(p/e)^2}{\int_{-\infty}^{\infty} B_z^2 \, dz} \quad , \tag{V-2}$$

where p is the (relativistic) momentum, e is the electron charge, and B_z is the longitudinal magnetic-field component. This equation is usually referred to as the Busch equation. Because B_z is a function of radius r and axial position z, this equation demonstrates that even in this approximation, the axially symmetric magnetic lens exhibits spherical aberration [$f = f(r)$] and "chromatic" aberration ($f \sim p^2$).

A schematic depicting a typical spectrometer arrangement is shown in Fig. V-17. Analogous to the thin lens case in light optics, the object-image relation for the thin magnetic lens is given by[8]

$$\frac{1}{s} + \frac{1}{s'} = \frac{1}{f} \quad , \tag{V-3}$$

where s and s′ are the object and image distance, respectively, measured from the lens center ($z = 0$). It can be shown that this equation, together with the Busch equation [Eq. (V-2)], yields the following expression for the base-width energy transmission of an axially symmetric, thin magnetic lens spectrometer

$$\frac{\Delta E}{E} \sim 2\left[\frac{B(r_{\max}) - B(r_{\min})}{B(r_{\max}) + B(r_{\min})}\right] + 2\left[\frac{(w + mr_s)}{(m+1)\,r'}\right] \quad , \tag{V-4}$$

TABLE V-III. Calculated Uniform Electric and Magnetic Field Values Required to Transversely Deflect an Electron 1°/cm of Field Traversal

	Electron Energy (keV)				
	1	10	100	1000	10 000
Electric field (V/cm)	3.57×10	3.54×10^2	3.21×10^3	2.34×10^4	1.83×10^5
Magnetic field (G)	1.86	5.92	19.5	82.8	611.0

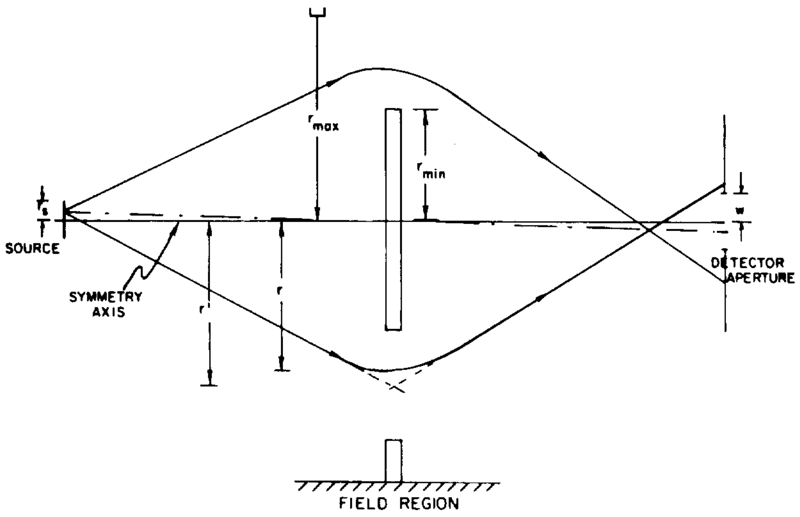

Fig. V-17. Schematic of a typical thin lens magnetic spectrometer.

where

$$B(r) = \int_{-\infty}^{\infty} B_z^2\,(r,z)\,dz,$$

$m = \frac{s'}{s}$ is the lens magnification,

$$\bar{r}' = \frac{r'_{max} + r'_{min}}{2},$$

and the remaining quantities are as defined in Fig. V-17. The first term on the right-hand side of expression (V-4) results from the spherical aberration in the lens system, whereas the second term results from the chromatic aberration in the system.

Using expression (V-4), a comparison was made with results of a spectrometer arrangement published by Deutsch et al.[13] The results of this comparison are given in Table V-IV. With the exception of case E, the agreement is within 10%; this is reasonably good in view of the approximations involved in obtaining expression (V-4), and considering the reading error ($\lesssim$10%) associated with obtaining the results from the graphical data presented.[13]

While the expressions given for the focal length and base-width energy transmission for a thin, weak, axially symmetric magnetic lens in the paraxial approximation provide a quick and valuable means of estimating spectrometer performance, they have a limited range of validity. Indeed, Goddard and Klemperer[14] have shown that serious errors can arise in applying the Busch paraxial formulation in the case of large lens apertures, even in the weak, thin lens case. The more accurate ray-tracing method proposed by Goddard and Klemperer[14] to examine axially symmetric lens behavior is discussed below.

The nonrelativistic equations of motion of an electron in an axially symmetric, static electromagnetic field are

TABLE V-IV. Comparison of Base-Width Energy Transmissions for Different Spectrometer Arrangements

	$\left(\frac{\Delta E}{E}\right)_0$		
Case[a]	1[b]	2[c]	1/2
A	0.264	0.255	1.04
B	0.153	0.143	1.07
C	0.0841	0.0820	1.03
D	0.222	0.206	1.08
E	0.0920	0.0779	1.18

[a] These cases refer to the different spectrometer arrangements given by Deutsch et al.[13]

[b] Values based upon Eq. (V-4) in the text.

[c] Values obtained from graphical data given by Deutsch et al.[13]

derived from the Lorentz force law,

$$\vec{F} = -e\,\vec{E} - \frac{e}{c}\,\vec{v} \times \vec{B} \ ; \tag{V-5}$$

the Maxwell equations,

$$\nabla \cdot \vec{B} = 0 \ , \tag{V-6a}$$

$$\nabla \times \vec{B} = 0 \ , \tag{V-6b}$$

$$\nabla \cdot \vec{E} = 0 \ , \tag{V-6c}$$

and

$$\nabla \times \vec{E} = 0 \ ; \tag{V-6d}$$

and the nonrelativistic law of dynamics,

$$\vec{F} = \frac{d}{dt}\,(m\vec{v}) \ . \tag{V-7}$$

Using cylindrical coordinates (r, θ, z) with the z-axis as the axis of symmetry and introducing the magnetic vector potential $\vec{A}$ and electric scalar potential V, where

$$\vec{B} = \nabla \times \vec{A} \tag{V-8a}$$

and

$$\vec{E} = -\nabla V \ , \tag{V-8b}$$

the equations of motion can be written (Ref. 8, p. 107)

$$\ddot{r} = \frac{\partial Q}{\partial r} \ , \tag{V-9a}$$

$$\ddot{z} = \frac{\partial Q}{\partial z} \ , \tag{V-9b}$$

and

$$\dot{\theta} = \frac{1}{r^2}\left(C + \frac{e}{mc}\,rA\right) \ , \tag{V-9c}$$

where

$$Q = \frac{e}{m}\,V - \frac{1}{2r^2}\left(C + \frac{e}{mc}\,rA\right)^2 \ , \tag{V-9d}$$

and

$$C = r_0^2\dot{\theta}_0 - \frac{e}{mc}\,r_0A_0 \ . \tag{V-9e}$$

(In these equations e is measured in esu units, namely, $e = 4.8032 \times 10^{-10}$.)

In the special case of a magnetic field only, Eqs. (V-9) can be written for skew rays (that is, $C \neq 0$),

$$\ddot{r} = \frac{1}{r^3}\left(C + \frac{e}{mc}\,rA\right)^2 - \frac{e}{mcr^2}\left(C + \frac{e}{mc}\,rA\right)\frac{\partial}{\partial r}(rA) \ , \tag{V-9a$'$}$$

$$\ddot{z} = -\frac{e}{mcr}\left(C + \frac{e}{mc} rA\right)\frac{\partial A}{\partial z} , \qquad \text{(V-9b}')$$

$$\dot{\theta} = \frac{1}{r^2}\left(C + \frac{e}{mc} rA\right) , \qquad \text{(V-9c}')$$

and

$$C = r_0^2 \dot{\theta}_0 , \qquad \text{(V-9d}')$$

and for meridional rays (that is, $C \neq O$),

$$\ddot{r} = -\left(\frac{e}{mc}\right)^2 A\frac{\partial A}{\partial r} , \qquad \text{(V-9a}'')$$

$$\ddot{z} = -\left(\frac{e}{mc}\right)^2 A\frac{\partial A}{\partial z} , \qquad \text{(V-9b}'')$$

and

$$\dot{\theta} = \frac{e}{mc}\,\frac{A}{r} . \qquad \text{(V-9c}'')$$

Although these equations appear formidable, because of the special feature that none of the right-hand sides of (V-9), (V-9′), and (V-9″) contain any velocity components, these equations can be solved numerically by applying the calculus of finite differences, in particular, by the method of ordinates.[15] This numerical method was first applied to Eqs. (V-9″) by Goddard and Klemperer.[14]

Following essentially their procedure, we have written a computer code to determine numerically the electron trajectory within a magnetic lens for a meridional electron of arbitrary energy and angle of incidence with respect to the z-axis. Note that, although Eqs. (V-9′) and (V-9″) are true only in the nonrelativistic limit (that is, $v \ll c$), these equations become rigorously correct in the relativistic case by the trivial substitution $m \longrightarrow \gamma m$, where $\gamma = 1/\sqrt{1 - v^2/c^2}$. Hence, in the case of a purely magnetic field, the numerical solution of the equations of motion in the relativistic case poses no added difficulty (because $d\gamma/dt = 0$, $\gamma =$ a constant of motion).

Table V-V compares the results obtained with this code and the results published by Goddard and Klemperer.[14] The results appear to be in good agreement.

Although our code is currently set up for meridional trajectories in a pure magnetic field, the extension to the case of skew rays is straightforward and presents no obstacles; the same may be said for the nonrelativistic case with an electric field present. In the relativistic electric field case with an electric field present, to the extent that γ may no longer be considered a constant of motion, the procedure currently used in the Los Alamos code will not work. This deficiency may be remedied at some later time.

TABLE V-V. Comparison of Electron Trajectory Calculations of Los Alamos Code with Results of Goddard and Klemperer[14]

Conditions
$E_e = 500$ eV
$B_0 = 16.5$ G
Source distance = 32 cm

Electron Trajectory Angle (deg)	Axial Focal Position (cm)		
Case	1[a]	2[b]	1/2
1.95	24.0	23.8	1.01
3.32	22.3	22.2	1.00
5.77	17.8	18.4	0.967
7.13	14.8	15.3	0.967

[a] Results obtained with Los Alamos code.
[b] Results given by Goddard and Klemperer.[14]

SLIT-VIEWING HOMOGENEOUS SPHERE: LEAST SQUARES FITTING OF ANALYTICAL EXPRESSIONS TO IMAGE DATA (M. M. Mueller)

A substantial fraction of our GMB targets are filled with DT fuel seeded with a high-Z gas such as argon. The spatial profiles of the spectroscopic x-ray lines contain much useful information concerning the degree of compression at stagnation, particularly in the case of those argon lines for which self-absorption is assumed to be negligible. For these lines, the spatial profiles are expected to be approximately what would result from the slit imaging of a homogeneous sphere of emission. Analytical expressions have been developed[16] for the image irradiance in this case. Because the spherical emission can deviate appreciably from homogeneity without causing significant departures from the analytical curves (particularly when a relatively wide slit is employed), analytical expressions for the irradiance are expected to be valid approximations for many of our shots in which self-absorption is negligible.

Hence, if such spatial profile data are used in fitting the analytical expressions by adjusting the parameters of emissivity and diameter of the argon line source, we find that the result gives a valid determination of the target compression under certain common circumstances. The fitting should be performed by a nonlinear least squares algorithm that, for speed and convenience, can be put on the local PDP-11/70 system. And, because existing nonlinear least squares codes were too large and cumbersome to be employed, we decided to develop a simple two-parameter nonlinear algorithm that can be conveniently used on the local system. The program works well even with fairly sparse, noisy data; details and results of its use are given in Ref. 17.

The algorithm described above was generalized to fit an arbitrary analytical function having no more than two parameters and possessing well-behaved first derivatives with respect to these parameters. Because only two parameters (typically one for height and one for breadth) are necessary in a large number of practical cases, this routine* should find widespread use. Statistical tests of goodness of fit are also included.

RECONSTRUCTION OF X-RAY EMISSION PROFILES OF IMPLODED TARGETS FROM SLIT PHOTOGRAPHS (M. M. Mueller)

For spherically symmetric sources, differential methods exist for performing the inversion of slit-image data to reconstruct the source emission profile.[18] These methods have the advantages of speed and uniqueness; however, in practice, data noise and aperture constraints[18] make differential methods nearly useless at present.

For circular apertures, we have developed an iterative integral technique that has worked satisfactorily[19] even with noisy data and relatively wide apertures. If we impose the additional constraint of physically reasonable reconstruction, the lack of uniqueness does not appear to be a problem in practice.

Because some of our spatial-profile data from spectroscopic argon lines are not well approximated by the assumption of a homogeneous sphere of emission, it appeared worthwhile to develop an iterative integral code for reconstructing spherically symmetric sources from slit images as well. The code has been subsequently incorporated into the local PDP-11/70 system.

However, although the code performs satisfactorily computationally, the results are far less satisfactory than for the case of pinhole apertures previously studied. There are two main problems with this method when it is applied to slit-imaging.

- The lack of uniqueness is much more serious. Additional constraints, which may not always be obvious, sometimes must be imposed to rule out solutions. For example, for much of our data taken with fairly wide slits, two classes of solution are possible: one with a hollow (low-emission) central region and one that declines monotonically from the center. Though we can usually rule out the former for argon line sources, it does impose bounds on our confidence.
- A greater problem is the lack of sensitivity to source structure—particularly evident with relatively wide slits, such as those typically employed in our diagnostics. This low sensitivity, which leads to slow (or sometimes no) convergence of the iterative model-adjusting procedure, is best discussed by numerical examples, as in Figs. V-18 through V-22.

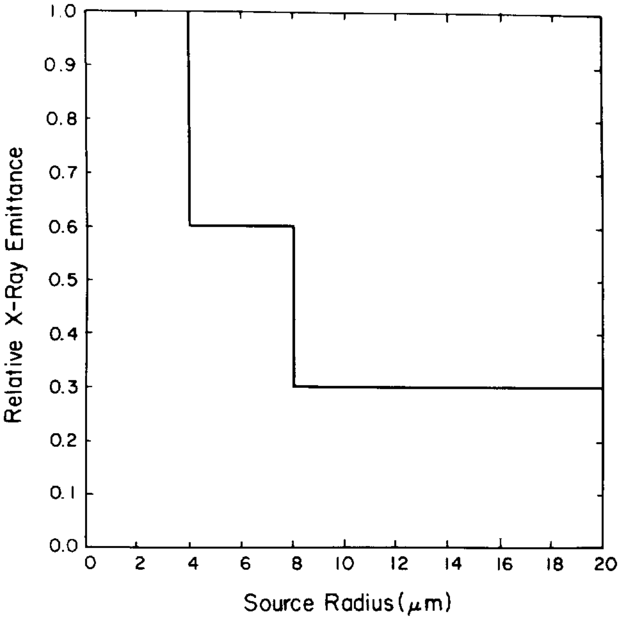

Fig. V-18. Nonhomogeneous source emission profile used for the comparisons (simulated data points) in Figs. V-19 through V-22.

---

*This code is contained in the Computer Math Library "General Math Routines" Section of the local PDP-11/70 system. A description and user's guide are given in Ref. 16.

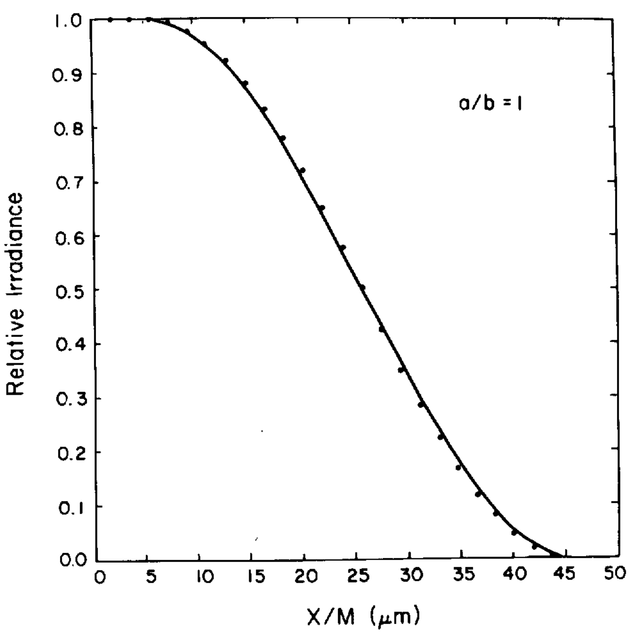

Fig. V-19. Simulated image irradiance comparison for a homogeneous sphere (curve) vs the source of Fig. V-18 (points) for a slit width equal to the source diameter (40 μm).

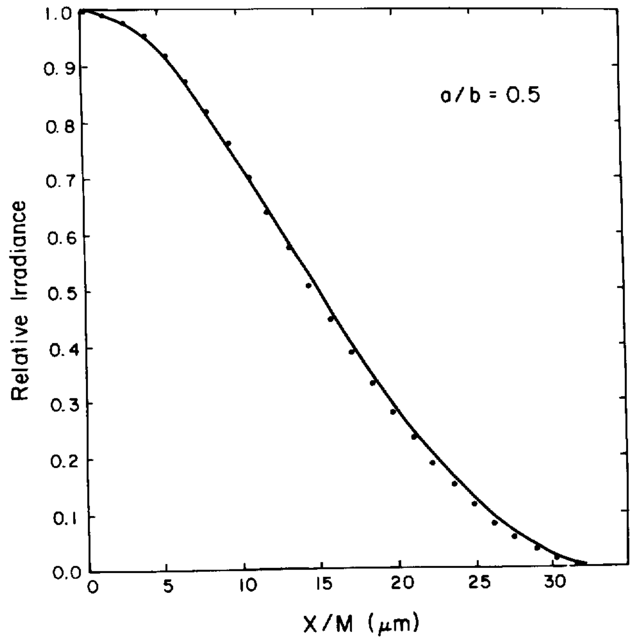

Fig. V-20. Simulated image irradiance comparison for a homogeneous sphere (curve) vs the source for Fig. V-18 (points) for a slit width equal to 0.5 of the source diameter.

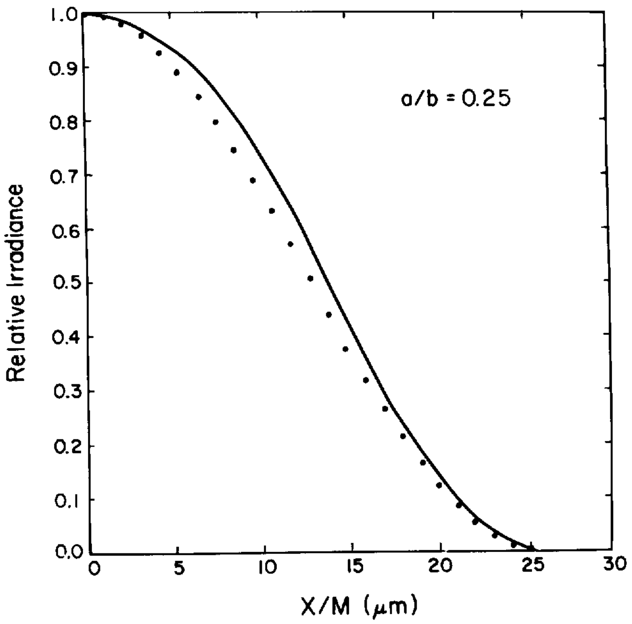

Fig. V-21. Simulated image irradiance comparison for a homogeneous sphere (curve) vs the source of Fig. V-18 (points) for a slit width equal to 0.25 of the source diameter.

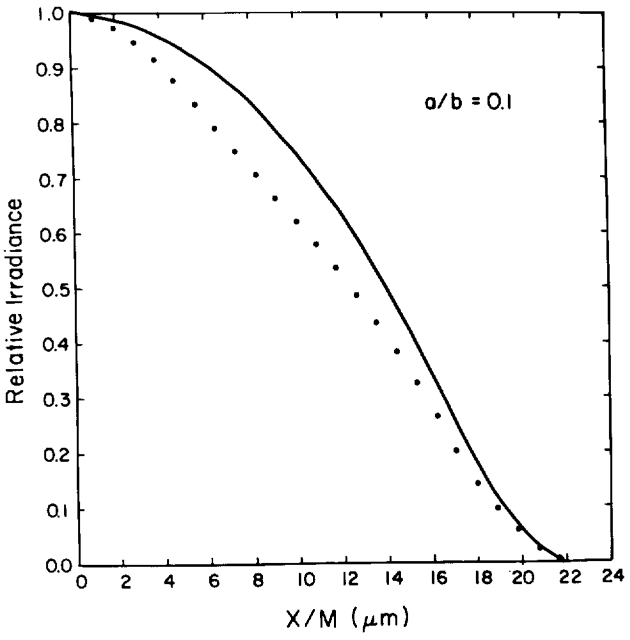

Fig. V-22. Simulated image irradiance comparison for a homogeneous sphere (curve) vs the source of Fig. V-18 (points) for a slit width equal to 0.1 of the source diameter.

Figure V-18 shows the source emission profile that will be used for comparison with the homogeneous profile (constant emittance of unity from 0- to 20-µm source radius). Such a profile could, for example, be produced if the temperature were higher in the central region of the imploded core. The abrupt histogrammic shape was chosen partly to demonstrate the astonishing degree of smoothing caused by the projection of the spherical source onto a plane combined with slit convolution. This dramatic smoothing lies at the heart of the unfolding difficulty.

In the succeeding figures, the source diameter $2b = 40\ \mu m$ and the system magnification $M = 3.5$ remain fixed although the slit width 2a is allowed to vary. The unbroken curve is the irradiance from a homogeneous sphere, whereas the dots represent a finite sampling (simulating noise-free data) of the irradiance from the emission profile of Fig. V-18. The coordinate X/M is the displacement in the image plane that is referred to the source.

Figure V-19 makes the comparison for a slit having a width equal to the source diameter, $a/b = 1$. With even a modicum of data noise, the irradiance from the source profile of Fig. V-18 would be indistinguishable from that of a homogeneous sphere of emission. As is illustrated in Fig. V-20, virtually the same result also obtains for $a/b = 0.5$. (For reasons of signal strength, this is the region of slit width employed in most of our x-ray spectroscopy.) Only for relatively narrow slits ($a/b < 0.3$, as is shown in Figs. V-21 and V-22) could the source profile of Fig. V-18 be reliably distinguished from that of a homogeneous sphere.

Note that in all cases the X-intercept is, as it must be, the same for both source models, and depends only on a, b, and M. Indeed, if determination of the source radius b is the sole goal, the use of a wide slit is indicated so that the image data can be fitted with analytical expressions for the irradiance from a homogeneous sphere, giving a unique value for b independent of the source structure. On the other hand, if source structure is desired, the smallest slit feasible should be employed to optimize unfolding by the iterative integral method.

OPTICAL PLASMA DIAGNOSTICS

Introduction

Our target-physics optical diagnostics effort comprises two major projects. One is the design of experiments and development of diagnostic instruments and techniques for probing the laser-target interaction plasma. The physical quantities to be measured are the spatial distribution of the electron density and the temporal behavior, or expansion, of the plasma. The other project deals with the design and development of a facility and the diagnostics to perform experiments on radiation backscattered from the target. The temporal history, spectrum, time-resolved spectrum, and harmonic content of the backscattered signal all give valuable information on laser-plasma interaction. Both efforts are being performed for Helios and are in their initial stages.

Interferometric Plasma Diagnostics (G. T. Schappert, J. Hanlon, K. Harrison, D. Pavlovski, V. K. Viswanathan)

We have started to develop the diagnostics and to plan an experiment for measuring the electron density and critical surface velocity of the expanding laser-target interaction plasma. This information is important because it can be used to test calculations of ablatively driven pellet compressions.

Our initial approach in these experiments is to perform interferometric measurements of the electron-density profile with a pulsed ruby laser at 0.69 µm as a probe. Double-exposure holographic interferometry or multiple, time-delayed interferograms can be analyzed to determine the electron density and motion.

The basic techniques involved are not new and have been used successfully at LLNL,[20] at Rutherford,[21] and at the NRC in Canada.[22] However, the details of the measurement are different for our CO_2 laser systems, and this fact leads to certain technical difficulties with synchronization of the laser probe. Both LLNL and Rutherford study plasmas initiated by 1.06-µm irradiation. The probe beam in this case is a portion of the 1.06-µm light that is split off the main beam, doubled or quadrupled in frequency, and delayed appropriately to arrive at the target as a perfectly synchronized optical probe. At NRC a mode-locked neodymium:glass laser is synchronized with the mode-locked CO_2 oscillator that drives the target-irradiation beam amplifiers by phase locking the two active modulators. Helios has a pulse-cutting system, where a nominal 1-ns CO_2 pulse is sliced out of the 80-ns gainswitched oscillator pulse. Therefore, we intend to synchronize a second electro-optic pulse-cutting system for the ruby laser with the CO_2 system.

We then hope to slice out a subnanosecond ruby probe pulse with subnanosecond jitter.

Most of our effort centered on trying to convert the ruby laser into a suitable short-pulse optical probe that could be synchronized with the Helios oscillator. Unfortunately, this proved to be considerably more difficult and time consuming than expected. The following section details our progress and the problems we encountered.

The Fresnel biprism interferometer described previously was assembled and set up in the laboratory. It was tested with a cw HeNe laser on a GMB and produced excellent interferograms.

Theory and code development and modification continued with the aim of generating refraction and phase-shift data from electron-density distribution models and inverting such data back to density distributions.

Because of the difficulties we encountered in synchronizing the ruby laser, we are evaluating other probe lasers and schemes for plasma-diagnostics measurement. One attractive possibility is a schlieren shadowgraph technique that would measure the location and motion of the steep electron-density gradient directly, without necessarily measuring the actual density. This scheme has the advantage of being noninterferometric; in addition, a multiple-pulse probe (several pulses separated by ~100 ps) may eliminate the restrictions of precise synchronization and temporal pulse shape that are necessary for multiple-exposure interferometry.

Theory and Modeling. In designing and analyzing the results of interferometric experiments, it is particularly important to understand the effects of a strongly refracting plasma on the ruby probe beam. We are using the codes GENRATE and REFDAT developed by A. M. Hunter[23] to generate refraction and phase-shift data from a spherically symmetric electron density. We then perform an Abel inversion on these synthetic data to reproduce the initial electron densities, thus testing the inversion technique. In another approach one starts from certain radially symmetric electron-density profiles for which the ray refraction problem (Bouger's law) can be solved analytically. With the refraction angles and phase shifts in hand, one can determine the interferogram generated by a particular interferometer. Both code calculations and analytical examples will be helpful in designing the experiment and understanding the limitations of the measurements.

We continued the theoretical modeling of the phase-shift and refraction effects for optical probe beams traversing high-density electron plasmas with steep gradients. In these studies we attempted to generate phase-shift and refraction-angle data from realistic electron-density profiles to simulate our experiments and test the procedures we need to invert such data back to a density profile.

We still intend to use a modification of the code REFDAT to invert our experimental data to electron-density profiles. The original REFDAT code was written to invert phase-shift and/or refraction-angle data from spherically or cylindrically symmetric low-electron-density profiles. Low density in this context means below the critical density of the particular probe-laser wavelength, so that all light rays propagate through the plasma. However, in our case we hope to have a spherical critical-density surface, so that only probe beam rays with impact parameters outside a certain radius propagate through the plasma and are gathered by the collection optics. The rest of the rays either deviate too strongly or are reflected.

This situation requires a modification of the original REFDAT to account for the effective truncation of impact parameters. The modified code, CEFDAT, seems to work to first order for both refraction-angle and phase-shift data inputs to within about ±20%. Higher order effects pose some problems because self-consistency iteration routines do not work yet. The code essentially inverts the original data to a density profile, then generates new data from the density profile, compares these results to the input data, and attempts to make this iteration self-consistent. The accuracy one might expect in this iteration remains to be established.

We developed two simple models to generate phase-shift and refraction-angle data for spherically symmetric electron-density distribution. One model uses a power law; the other uses a Fermi distribution.

For the power-law case, we take

$$n(r) = \left(\frac{r}{R}\right)^{\beta} = \sqrt{\frac{1 - \rho_e(r)}{\rho_{crit}}} \qquad \text{(V-10)}$$

or

$$\frac{\rho_e(r)}{\rho_{crit}} = 1 - \left(\frac{r}{R}\right)^{2\beta} \quad , \qquad \text{(V-11)}$$

where $n(r)$ is the index of refraction, $\rho_e(r)$ the electron density, ρ_{crit} the critical density, R the outer radius of the plasma, and β a parameter to adjust the steepness of the density profile. The electron density for this model is shown in Fig. V-23 for various values of the parameter β.

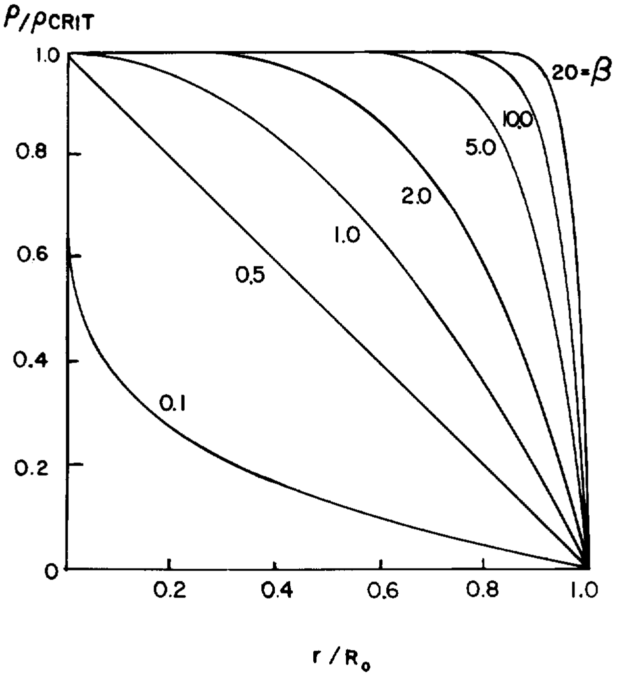

Fig. V-23. Electron density as a function of β.

Note that the $\beta \geq 1$ cases simulate a progressively steeper electron-density profile. The propagation of a collimated light beam and the accumulated phase shift for a given impact parameter (see Fig. V-24) can be calculated analytically for this model.

The result for the refraction angle α is

$$\alpha = \frac{2\beta}{1+\beta} \cos^{-1}\left(\frac{y}{R}\right) \qquad \text{(V-12)}$$

and for the phase shift ϕ_{med},

$$\phi_{\text{med}} = \frac{2}{\beta+1} \cdot \frac{1}{\lambda} \sqrt{R^2-y^2} \; , \qquad \text{(V-13)}$$

where y is the impact parameter of the probe ray as shown in Fib. V-24.

A closer look at Fig. V-24 indicates an interesting complication that arises in strongly refracting plasmas. An optical system that collects and images the strongly refracted rays extrapolates the rays back into the plasma giving an apparent impact parameter y_i in the object plane. Clearly, y_i then depends upon which plane is imaged through the target. One can show that[21]

$$y_i = y \sec\alpha + a_0 \tan\alpha \; , \qquad \text{(V-14)}$$

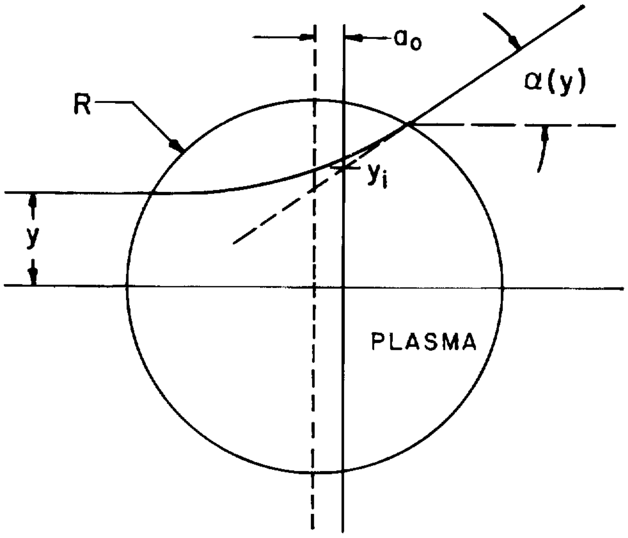

Fig. V-24. Deviation of light ray of impact parameter y by radially symmetric, strongly refracting plasma.

where a_0 is the "misfocus" distance from the central plane. Such considerations can be important in analyzing interferograms from strongly refracting plasmas.[21]

Figure V-25 shows the refraction angle α as a function of the impact parameter for various steepnesses β with this power laser-density plasma. We note that for the large-gradient cases, an f/2 collecting system, $\alpha < 0.25$, does not see far into the plasma. Rays below a certain

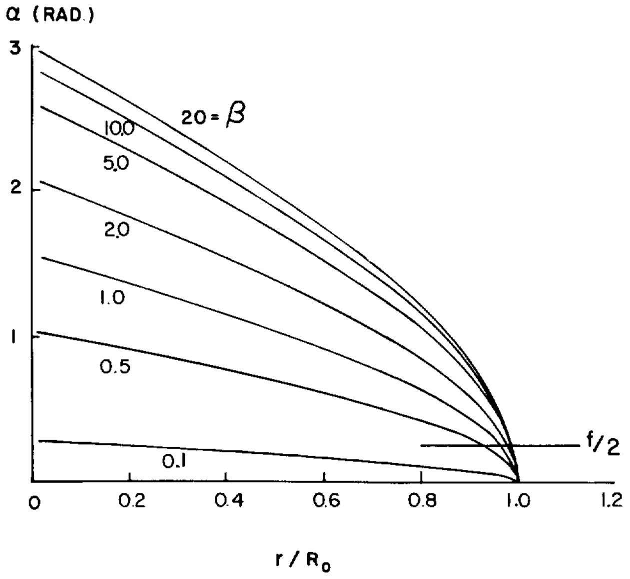

Fig. V-25. Refraction angle α as a function of impact parameter.

impact parameter are not collected, and for very small impact parameters are almost totally reflected. Similar results are obtained for a Fermi-type electron-density distribution, but the problem is no longer analytically solvable. In this case, we have more flexibility because we can simulate a lower density shelf and upper density shelf by setting the critical density for the probe somewhere on the steep portion of the curve (Fig. V-26). A code, FERMI, was developed to generate the refraction angles, phase shifts, and apparent impact parameters within the framework of this model.

Diagnostic Equipment Developments. We have begun the preliminary design and testing of a pulsed ruby laser and interferometer for use in interferometric plasma diagnostics at Helios. The layout of the ruby laser system is shown in Fig. V-27. It uses a tailored electrical pulse on the internal Pockels cell to generate a smooth 100-ns optical pulse from the ruby laser oscillator.

We intended to operate the ruby laser in a long pulse mode, then slice out a subnanosecond pulse synchronized to the CO_2 switchout.

Initially, the ruby oscillator output consisted of several interlaced trains of self-modelocked 1-ns pulses under a 100-ns envelope with 400-ns jitter relative to an internal Pockels-cell switch. Neither the smoothness nor the pulse jitter were acceptable for our synchronization scheme. Several months were spent in evaluating various schemes to obtain the desired output.

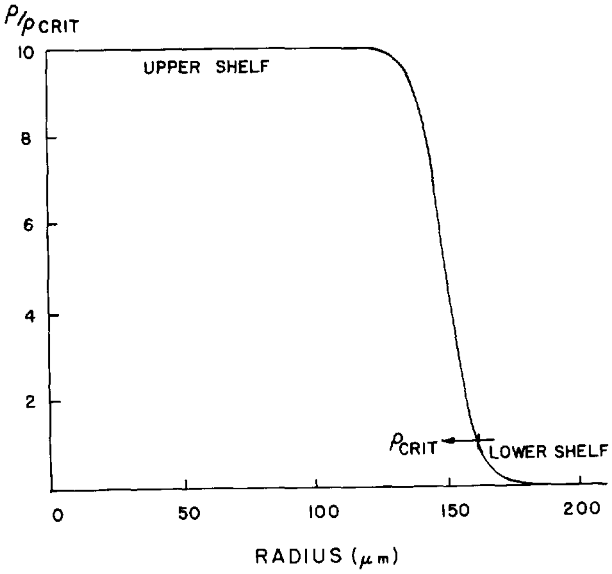

Fig. V-26. Plasma density as a function of radius for a Fermi electron-density distribution.

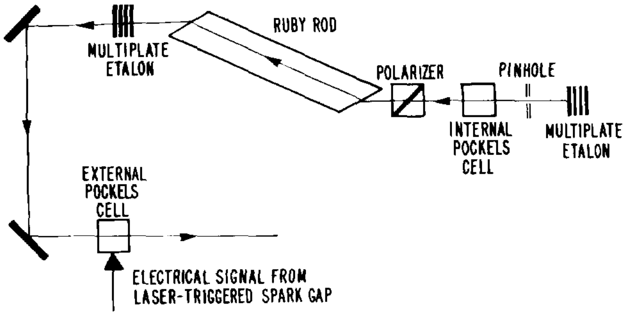

Fig. V-27. Ruby laser oscillator. The external Pockels cell is activated by a signal from the light-triggered spark gap in the Helios master oscillator.

The following changes were made.

- The cavity was shortened to spread out the longitudinal modes.
- The Pockels-cell voltage was reduced from 2000 (quarter-wave voltage) to 500 V.
- The voltage to the flashlamps, which had been set just above threshold with the Q-switch open, was raised until it was above the threshold with the Q-switch closed.

Under these conditions, the pulses were ~500 ns long, but there was still a tendency for the laser to operate in two longitudinal modes. Raising the voltage to 200 V above the threshold (with the Q-switch closed) resulted most of the time in smooth pulses, 300 to 500 ns wide. However, there were large pulse-to-pulse variations in the amplitude of the output pulse. Although the timing jitter was improved, we still expected that the system would operate satisfactorily only about half the time. More reliable operation might be possible with further modifications. However, we believe that to actively modelock either a Nd-YAG laser or the ruby laser and then use the short modelocked pulse for interferometry or shadowgraphy would be a better technique. This approach will ease the timing problems and give us a short (<30-ps) pulse without having to chop out a short pulse from a long pulse. On the other hand, it will also require some further development.

Schematics of the microinterferometer that we plan to use are shown in Figs. V-28 and V-29. This type of interferometer is built around a Fresnel biprism and recently has been used to measure electron-density profiles in the critical-density region of laser-produced plasmas in other laser fusion experiments.[21,24,25]

The layout shown in Fig. V-28 will allow operation of Helios on a noninterference basis, but the f-number of

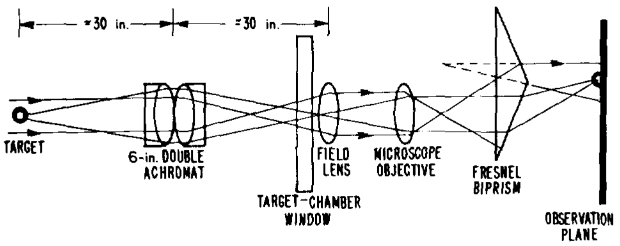

Fig. V-28. The f/5 microinterferometer scheme for Helios.

the collecting optics is only f/5 for this arrangement. An f/2 optical system that would carry the interferometer into the target chamber on a target cart is shown in Fig. V-29. However, the collecting optics for this arrangement are only ~2.5 cm from the target, so precautions must be taken to ensure that the interferometer does not cause parasitic oscillations.

We plan to test the ruby laser and the interferometer in the laboratory in both conventional and holographic modes and to prepare the system for installation at Helios.

Development of a New Refraction Code (M. M. Mueller)

The code developed previously[26] for tracing optical ray paths through spherically symmetric inhomogeneous plasmas was intended mainly for simulating interferograms. It performs well but requires considerable computation time for high accuracy in plasmas with steep gradients. For simulations of the rainbow effect, the folding operation requires information only on the angle of the emerging rays but requires these data for a large number of rays. Thus the existing, purely numerical code was too detailed and slow for applications not requiring exact ray paths, but rather requiring scattering angles for a large number of rays.

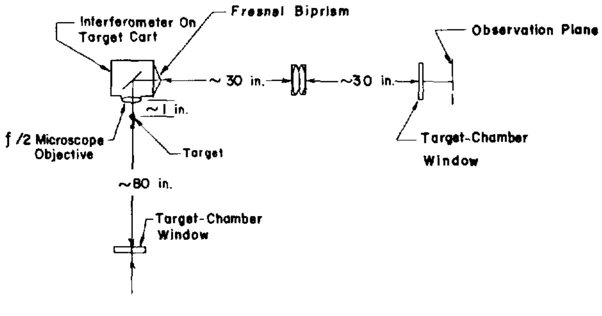

Fig. V-29. The f/2 microinterferometer arrangement for Helios.

A new code has been developed to meet this need. The basic algorithm computes the angle of emergence from the plasmas by numerical integrations of analytical integrals. It is much faster for equivalent accuracy and has been tested for plasma profiles leading to integrals that can be evaluated exactly by analytical means. A faster folding algorithm to compute scattered intensity vs angle is being developed.

Evaluation of the Rainbow Effect in Spherical Plasmas as a Possible Diagnostic of Electron-Density Profiles: Preliminary Results (M. M. Mueller)

As we have shown,[27] if white light were incident on a spherical plasma with a steepened density profile, the refracted light would be dispersed into annular bands somewhat similar to the familiar sky rainbow, but with much broader angular extent. For radiation composed of several discrete wavelengths, the dispersion into separate annular bands would be a dramatic and definitive indication of the existence of profile steepening. The rainbow effect appears to exist only if there is an abruptly steepened region of the density profile, and if the probe beam penetrates somewhat beyond the steepened region into a region of shallower gradient.

The present study begins where the earlier study stopped and explores the rainbow effect as a possible experimental diagnostic for the detailed structure of steepened density profiles. This work is by no means complete, but preliminary results are reported here. Work is under way, but not discussed in this report, to develop mathematical methods for unfolding scattered intensity to obtain the electron-density function. A unique solution may be possible for nonsteepened (smoothly declining) density profiles, but these are not the principal interest.

Figure V-30 shows the ray paths for a collimated probe beam of 0.53-μm wavelength incident on a plasma having a steep "cliff" with its top at 10^{21} cm^{-3} electron density. The bunching in angle space is evident. If the profile had declined smoothly instead, the rays would have been distributed smoothly in angle, but with a marked decline in number density as the angle increases.

Figure V-31 gives the density profile we shall employ as one of our test cases. The top of the density cliff occurs at 10^{21} cm^{-3}, and the function rises exponentially at smaller radii. The cliff itself is linear and falls to

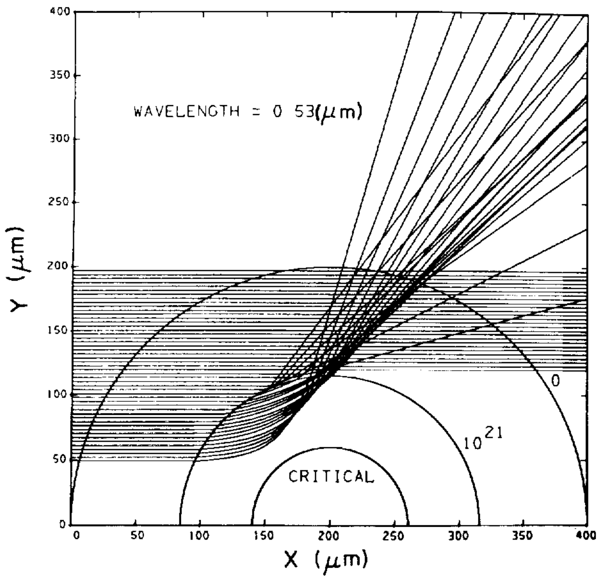

Fig. V-30. Ray paths for a collimated probe beam of 0.53-μm wavelength.

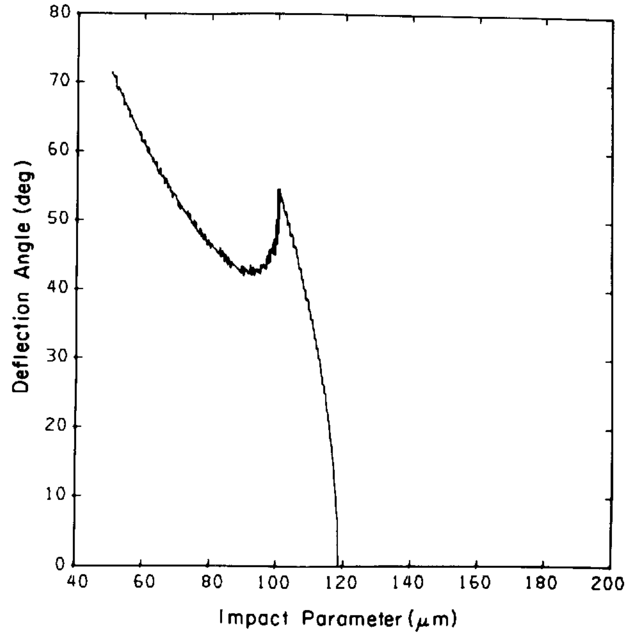

Fig. V-32. Plot of scattering angle vs impact parameter.

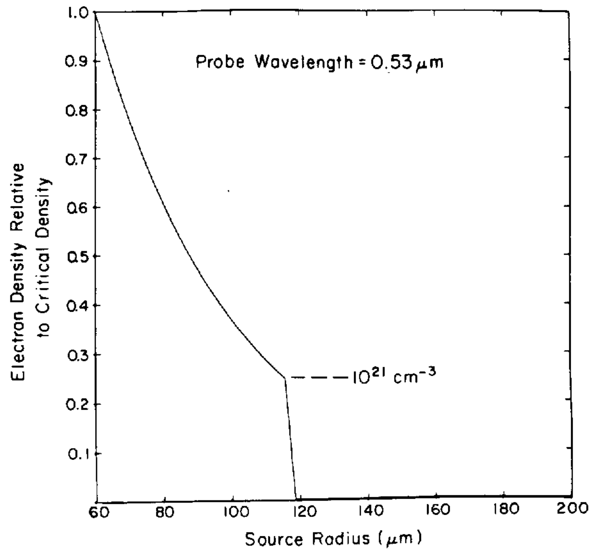

Fig. V-31. "Cliff" density profile relative to the probe critical density.

10^{19} cm^{-3} (or to zero) in a distance of 3.0 μm. (Numerical tests have shown that the presence or absence of a tail declining slowly from 10^{19} cm^{-3} makes no appreciable difference in the results unless the probe critical density is much less than 10^{21} cm^{-3}.)

A plot of scattering angle (emergent angle caused by refraction) vs impact parameter is displayed in Fig. V-32 for 0.53-μm probe light incident on the electron-density profile of Fig. V-31. The sharp cusp, which might be somewhat blunted if diffraction were taken into account, is the signature of profile steepening and is the proximate cause of the rainbow effect. However, this curve is not experimentally observable because a spot of light on the detector cannot be traced back to a particular impact parameter. The scattered light intensity can be observed as a function of the scattering angle and wavelength. (The simplest detector would be a strip of color photographic film.) Hence, the curve of Fig. V-32 must be folded with the probe beam intensity (taken to be uniform for simplicity) to produce the intensity-vs-angle plot of Fig. V-33.

This is the "rainbow effect" and should be observable. The jagged appearance of the plot is caused by folding with a finite number of rays. If a shorter wavelength probe had been used, the intensity-angle curve would have been displaced to smaller angles. Depending on the relevant parameters, the peak intensity usually occurs between ~10 and 60°.

The question of the rainbow's behavior as the plasma expands is of considerable importance and is particularly crucial if time-integrated detection is employed. For simplicity, we have used an unrealistic test case in which the density profile remains shape invariant in the steepened region as the plasma expands. As an example of the results, displacement of the steepened region from a radius of 100 μm to a radius of 200 μm shifts the intensity peak from about 41 to 49°. Thus, the effect of

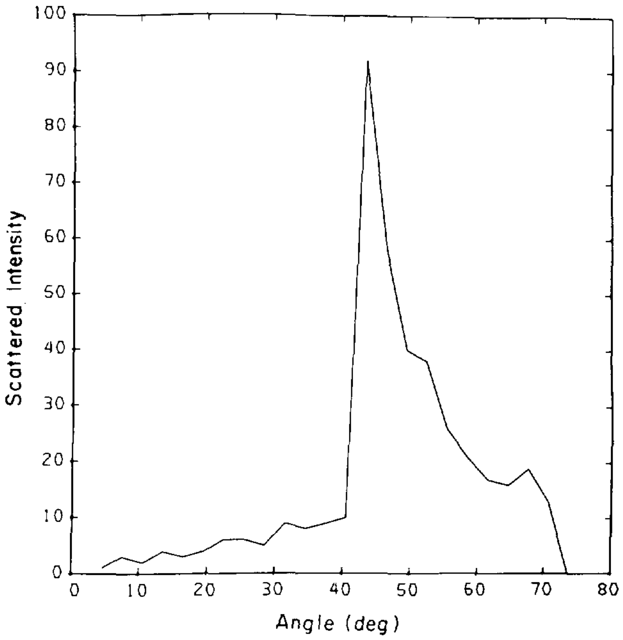

Fig. V-33. Intensity-vs-angle plot.

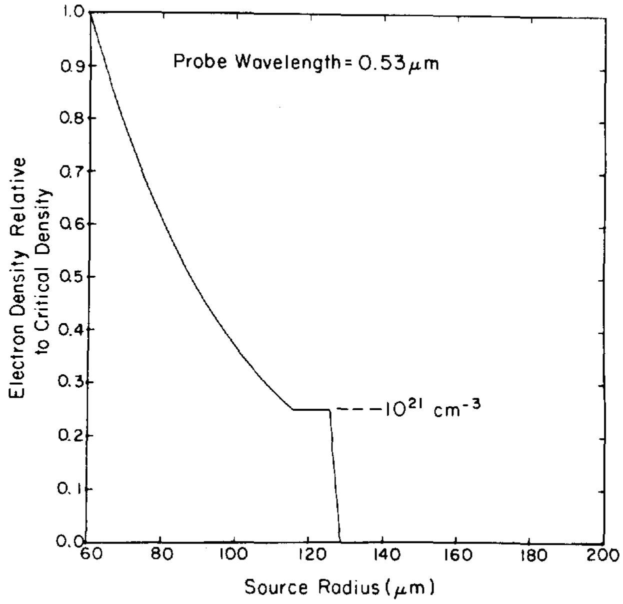

Fig. V-34. "Ledge" density profile.

expansion motion alone shifts the rainbow by an amount that, although detectable, is fairly small relative to the effects caused by shape changes in the steepened region. Hence, time-integrated blurring of the rainbow from expansion motion is minimal despite the fact that individual rays are drastically dependent on that expansion.

The question of whether the detailed structure of the steepened profile could be unfolded from rainbow effect data will not be answered at this time. We have just begun to investigate this complicated problem. However, several folding results, which have some bearing on the prospects of unfolding, will be presented here. The exponential-plus-cliff structure of Fig. V-31 is somewhat unrealistic because PIC numerical simulations studied in several laboratories have long indicated a level (or near level) shelf-like structure at the top of the density cliff during most of the laser pulse. An example is the electron-density profile shown in Fig. V-34, which we shall call the "ledge." A uniform probe beam of 0.53-μm wavelength gives the intensity-angle curve of Fig. V-35. Comparison with Fig. V-33 shows the main difference to be a much broader peak—FWHM of 30° instead of ~10°. Thus, if the sole cause of peak broadening were known to be the presence of a shelf, a broad peak would indicate a ledge instead of a cliff.

Other structures are, of course, possible. One such, which we call the mesa, is shown in Fig. V-36. A similar probe beam gives the intensity-angle curve of Fig. V-37. Somewhat surprisingly, it differs only slightly from that of the ledge and is similar to that of the cliff.

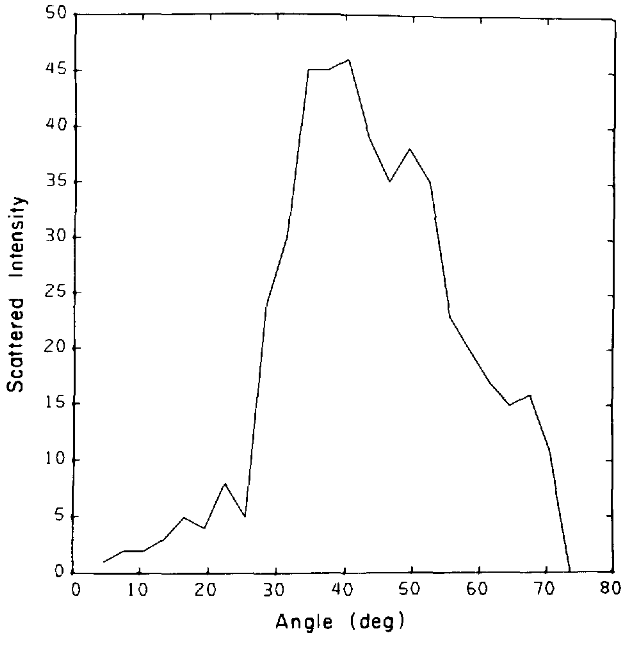

Fig. V-35. Intensity vs angle plot incident on "ledge" profile.

We conclude that the rainbow effect, being a signature of profile steepening that is little affected by expansion

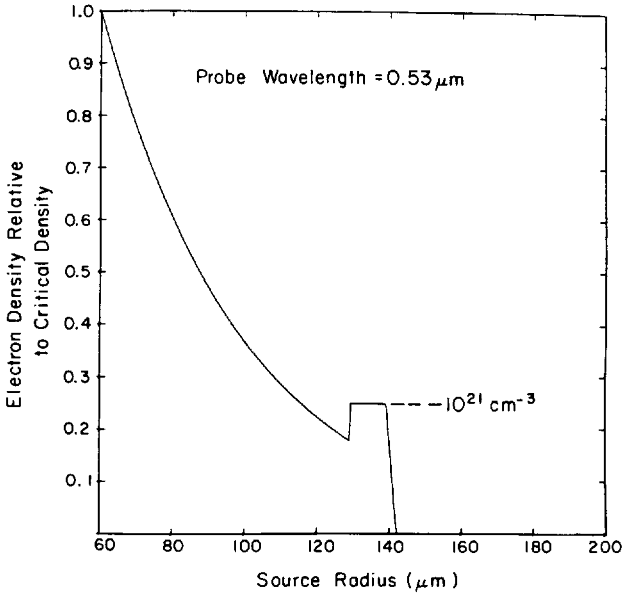

Fig. V-36. "Mesa" density profile.

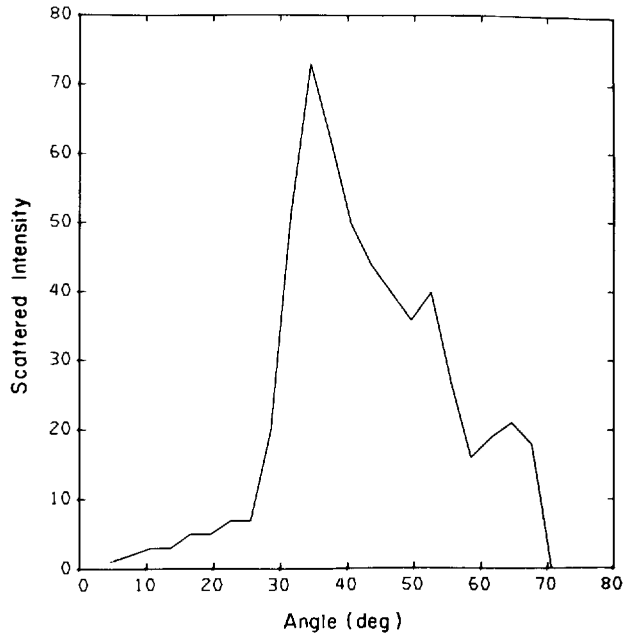

Fig. V-37. Intensity-vs-angle plot incident on the "mesa" profile.

displacement, constitutes a potentially valuable diagnostic. However, it appears from this preliminary study that its ability to discriminate among different models of steepened electron-density profiles is somewhat limited—at least if multiple wavelengths are not employed.

DATA PROCESSING (R. Peck)

Data from experiments at the Gemini and Helios lasers may be digitized immediately in Camac modules and stored in a data base of the PDP-11/70 computer. Often, however, the nature of the detector, the signal bandwidth, or the size of the data requires that the data be recorded first on film and digitized later. The trend is toward more data being recorded on film; therefore, we are expanding our capability for processing film data.

A two-dimensional scanning microdensitometer was acquired to use with film images and spectra from optical and x-ray sources. Computer programs were developed to process these data, and an operator has been trained to use the microdensitometer.

Particle tracks on the Thomson parabola films are counted by the analyzer of a locally developed microprocessor system. Other microprocessor units will be developed for fixed and portable data-acquisition needs.

Cables for the data-acquisition network were extended to the Antares location in preparation for experiments with the Antares laser.

A second, large disk unit was added to the PDP-11/70 computer. It will be used for the raw data base and will permit faster data retrieval than magnetic tape could provide.

REFERENCES

1. R. H. Price, M. J. Boyle, and S. S. Glaros, "Point X-Ray Source," (LA-UR-81-463), to be published in Rev. Sci. Instrum.

2. J. H. Sparrow and C. E. Dick, "Pulsed High Intensity Monoenergetic Low Energy X-Ray Source and Absolute X-Ray Monitor," Nucl. Instrum. Methods **141**, 283-292 (1977).

3. B. L. Henke, J. A. Smith, and D. T. Atwood, "0.1-10-keV X-Ray-Induced Electron Emission from Solids—Models and Secondary Electron Measurements," J. Appl. Phys. **48**, 1851 (1977).

4. W. J. Veigele, E. Briggs, L. Bates, E. M. Henry, and B. Braceevell, "X-Ray Cross Section Compilation from 0.1 keV to 1 MeV," Kaman Nuclear report KN-71-431 (R) (1969).

5. H. S. Hagerman, W. Gudat, and C. Kunz, "Optical Constants from the Far Infrared to the X-Ray Region: Mg, Al, Cu, Ag, AU, Bi, C, and Al_2O_3," Deutsches Elektronen-Synchrotron report DESY SR-74/7 (1974).

6. R. H. Day, P. Lee, E. B. Saloman, and D. J. Nagel, "Photoelectric Quantum Efficiencies and Filter Window Absorption Coefficients from 20 eV to 10 keV," J. Appl. Phys. 52, No. 11, 6965 (1981).

7. H. Busch, "Zur Schleiermacherschen Methode der Messung des Wärmeleitvermögens von Gasen," Ann. Phys. (Leipzig) **80**, 33-42 (1926).

8. V. E. Cosslett, *Introduction to Electron Optics* (Clarendon Press, Oxford, 1950).

9. O. Klemperer, *Electron Optics* (Cambridge University Press, Cambridge, 1971).

10. P. Grivet et al., *Electron Optics*, 2nd English Ed. (Pergamon Press, Oxford, 1972).

11. V. K. Zworykin, G. A. Morton, E. G. Ramberg et al., *Electron Optics and the Electron Microscope* (John Wiley & Sons, Inc., New York, 1945).

12. A. B. El-Kareh and J. C. J. El-Kareh, *Electron Beams, Lenses, and Optics*, Vol. I and Vol. II (Academic Press, New York, 1970).

13. M. Deutsch, L. G. Elliott, and R. D. Evans, "Theory, Design, and Applications of a Short Magnetic Lens Electron Spectrometer," Rev. Sci. Instrum. **15**, 178 (1944).

14. L. S. Goddard and O. Klemperer, "Electron Ray Tracing Through Magnetic Lenses," Proc. Phys. Soc. London **56**, 378 (1944).

15. A. A. Bennett, W. E. Milne, and H. Bateman, *Numerical Integration of Differential Equations*, (Dover Publications, New York, 1956), pp. 81-84.

16. M. M. Mueller, "Slit Viewing Homogeneous Sphere: A Simple Formulation," Los Alamos Scientific Laboratory memorandum L4 (12/79)-684, to distribution, December 19, 1979.

17. M. M. Mueller, "Two-Parameter Non-Linear Least-Squares Routine," Los Alamos Scientific Laboratory memorandum L4 (5/80)-215, to distribution, May 7, 1980.

18. M. M. Mueller, "Reconstruction of Spherically Symmetric Objects from Slit-Imaged Emission: Limitations Due to Finite Slit Width," Opt. Lett. **4**, 351-3 (1979).

19. M. M. Mueller, "Reconstruction of Spherical Source Emission Profiles from X-Ray Pinhole Photographs by Means of an Iterative Integral Technique," Bull. Am. Phys. Soc. **24**, 1053 (1979).

20. D. T. Attwood, D. W. Sweeney, J. M. Auerbach, and P. H. Y. Lee, "Interferometric Confirmation of Radiation-Pressure Effects in Laser-Plasma Interactions," Phys. Rev. Lett. **40**, 84 (1978).

21. A. Raven and O. Willi, "Electron-Density Structures in Laser-Produced Plasmas at High Irradiances," Phys. Rev. Lett. **43**, 278 (1979).

22. R. Fedosejevs, I. V. Tomov, N. H. Burnett, G. D. Enright, and M. C. Richardson, "Self-Steepening of the Density Profile of a CO_2 Laser-Produced Plasma," Phys. Rev. Lett. **39**, 932 (1977).

23. A. M. Hunter, "Refraction Diagnostics for Axisymmetric Media," Ph.D. dissertation, Ohio State University, 1975 (unpublished).

24. O. Willi and A. Raven, "Holographic Microinterferometer to Study Laser-Produced Plasmas," Appl. Opt. **19**, 192 (1980).

25. R. Tillingworth and R. K. Thareja, "An Interferometer for Use with Highly Refracting Laser-Created Plasmas," Opt. Commun. **32**, 51 (1980).

26. M. M. Mueller, "A Ray-Tracing and Simulated Interferometric Fringe-Shift Code for Gradient-Index Media with Spherical Symmetry," Los Alamos Scientific Laboratory memorandum, to distribution, May 25, 1976.

27. M. M. Mueller, "New Optical Diagnostic Methods for Determining Profiles in Spherical or Quasi-Planar Plasmas," Bull Am. Phys. Soc. **22**, 1060 (1977).

VI. LASER FUSION THEORY AND TARGET DESIGN

(D. C. Wilson)

Our theoretical support activities are closely related to our experimental efforts; we intend to gain a fundamental understanding of the relevant plasma physics and hydrodynamics. Our objective is being able to confidently predict the minimum amount of CO_2 laser energy required for scientific breakeven and high-gain target ignition. We emphasize modeling of laser experiments and computer codes directed toward this objective.

TARGET PHYSICS (D. C. Wilson)

Introduction

Theoreticians and experimenters work closely together to formulate valid models for predicting physics phenomena. Experiments either confirm or invalidate the models or lead to their modification. From this feedback, we then derive new high-yield target concepts, which again are tested in experiments to explore the crucial physics involved.

All our high-gain designs for CO_2 laser targets now use a double-shell capsule. Efficient energy transfer from an outer pusher to an inner pusher/tamper surrounding the fuel is critical. We describe below the first detailed design of Helios' double-shell target (Polaris), which attempts to satisfy this requirement.

To apply the results of experiments profitably in our design efforts, we must be able to calculate experimentally verifiable quantities. Although our computer codes can calculate the x-ray emission or neutron yield of a target, an analytic model that relates observable quantities to important physical parameters gives us much more insight than does an elaborate numerical calculation. One of these analytic models relating neutron yield of an ICF capsule to the temperature of the imploded target is described below.

Prototype Polaris Target (A. Cooper)

A double-shell, or velocity-multiplication, target drives a relatively heavy outer pusher into a lighter tamper, which in turn compresses (and ideally, ignites) a small mass of DT fuel.

The relevance of this scheme is illustrated by two colliding balls. By driving a heavy ball into an (initially stationary) lighter one, we impart to the lighter one a velocity that is higher than the initial velocity of the heavy ball, although with less energy. If in our analogy, however, both balls have equal mass, the first ball stops completely and the second rebounds with the initial velocity of the first. Here the velocity multiplication is 1 and the energy transfer is 100%. At the other extreme, a bowling ball colliding with a ping pong ball continues at almost its initial velocity, and the ping pong ball bounces off at almost twice the initial velocity of the bowling ball, but the energy transfer is almost 0.

For practical targets, the mass ratio between the colliding shells of a target is generally taken between 2 and 10. Because the shells are compressible fluids rather than rigid bodies, the actual velocity multiplication may be much less than the theoretical limit of two. On the other hand, a tamper moving at a higher velocity delivers energy to the fuel at a higher rate. Because the fuel may lose energy through thermal conduction and other mechanisms, it is very important that the tamper deliver what energy it has more quickly than the fuel can lose energy. It is in this regime, where total energy delivered to the fuel is a more sensitive function of tamper velocity than of tamper energy, that velocity multiplication is useful.

A prototype double-shell target for Helios is shown in Fig. VI-1. The outer plastic shell acts as an absorber and ablator. The pusher and tamper are typically both high-density materials; for our Polaris prototype we chose gold because of its relative ease of fabrication. The cushion is formed of a low-density, low-Z material, carbon-hydrogen foam, whose function it is to make the collision between pusher and tamper more elastic. The thin glass shell shown separating the pusher and the fuel is included for easier fabrication. (DT gas is diffused under pressure through the glass, which is then coated with the gold pusher.)

All our LASNEX calculations to model this target used a suprathermal electron temperature proportional

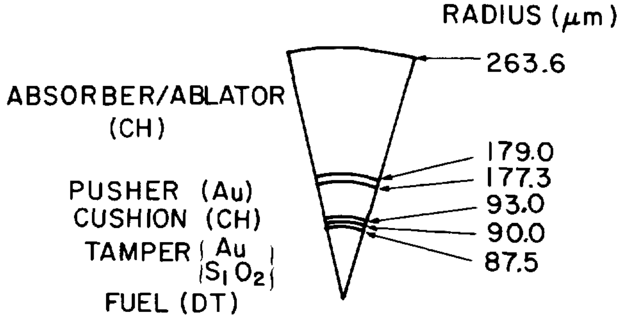

Fig. VI-1. Polaris target for Helios.

to the cube root of laser intensity. Figure VI-2 shows the laser pulse input to this target. As the laser reaches the critical-density surface, about 30% of its energy is absorbed into suprathermal electrons by means of resonance absorption. We assume that these suprathermals have a one-dimensional Maxwellian energy spectrum, with a temperature that depends on laser intensity and local background temperature in the target.

The laser-target interaction in our modeling remains an area for potential improvement. Although our modeling now reflects our theoretical understanding and agrees with the experimental data currently available, more experimental verification will be required. One deficiency may be the fact that we currently treat suprathermal energy deposition diffusively; by doing so, we find our LASNEX results are in agreement with Monte Carlo calculations for spatially isotropic distributions. This is probably a very good assumption when the absorber is a highly scattering material, such as gold. However, for plastic, the validity of the assumption depends on the initial angular distribution of the suprathermals, which in turn depends on the smoothness of the critical surface (which we have no theoretical way of determining). We hope that experiments such as those using K_α emission from layered targets will help to resolve these uncertainties in our modeling.

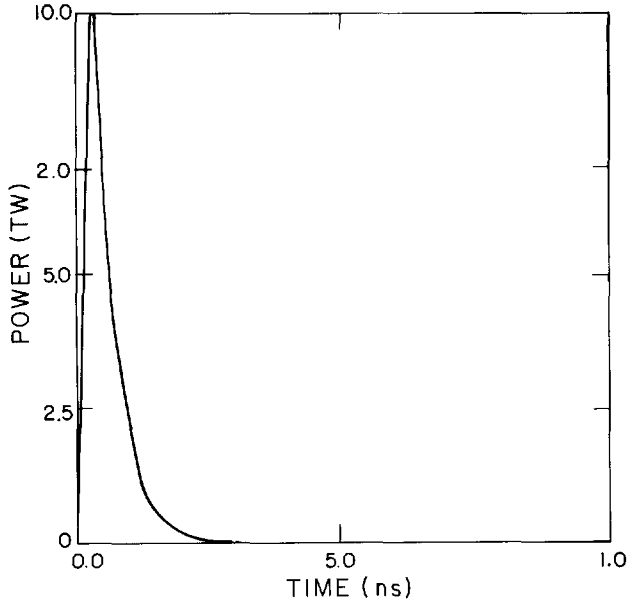

Fig. VI-2. Laser pulse shape.

When we modeled the neutron production, the central fuel region was dudded (not allowed to burn) to avoid overcalculating the effects of spherical convergence. These calculations gave a yield of ~3.4 × 10^9 neutrons, with a peak fuel temperature of ~0.7 keV and a peak fuel ρR of ~0.025 g/cm^2. For comparison, a breakeven yield for the total laser energy into this target would be 2.25 × 10^{15} neutrons, which would be possible if we were able to achieve the thermonuclear ignition conditions of ~3 keV in a fuel mass with a ρR of ~0.3 g/cm^2. Thus we are below breakeven by a factor of 4 in temperature and 12 in ρR. Although the prototype is not completely optimized, we feel that its yield is fairly close to optimum. Furthermore, the design is farily conservative and insensitive to small changes in parameters. Table VI-I shows the change in yield caused by factor-of-2 changes in energy, mass, and density.

As the laser deposits energy on target, the material near the outer boundary of the target is heated and begins to expand at high velocity. (Because the vertical axis is scaled to the initial radius of the target, the outward motion of the outer boundary cannot be seen in Fig. VI-3.) One can see that the shock front reaches the

TABLE VI-I. Yield of Polaris Target at Different Energy, Mass, and Density Yield[a]

Quantity	Quantity Doubled	Quantity Halved
Input energy	2.23	0.0009
Fuel mass	0.42	1.18
Pusher mass	0.13	1.69
Tamper mass	0.62	0.60
Cushion density	0.73	0.91

[a] In units of 3.4 × 10^9 neutrons.

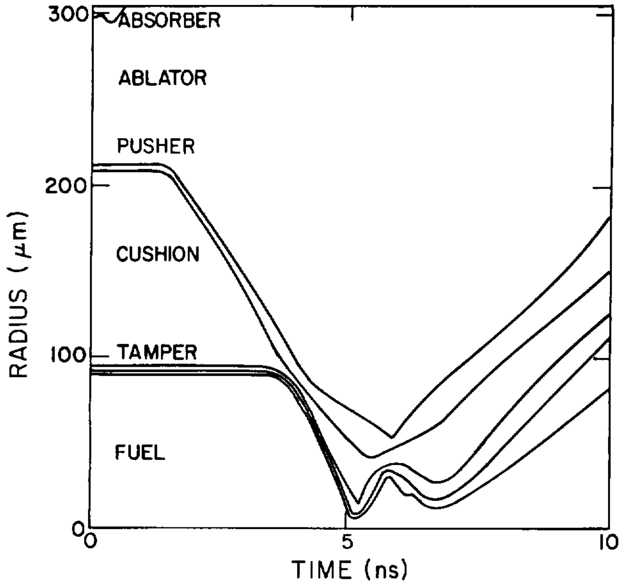

Fig. VI-3. Target interface time histories.

outer boundary of the pusher at $\sim$1.25 ns and reaches the pusher's inner boundary at $\sim$1.5 ns. For the next $\sim$2 ns, the pusher coasts inward with more or less constant velocity, gradually compressing the cushion as it coasts.

Between 3.5 and 4.0 ns, one can see the velocity-multiplying collision between pusher and tamper, which is the whole point of this target. Figure VI-4 presents a closeup of this collision from three different perspectives: spatial development, velocity multiplication, and energy transfer. Because the mass ratio between pusher and tamper is 3.5, an elastic collision would give a velocity-multiplication factor of 1.51 and an energy transfer of 0.65. However, the velocity multiplication, found by dividing the velocity of the tamper at 3.8 ns by the velocity of the tamper at $\sim$3.0 ns, is a ratio of $\sim$1.4, not much under the estimated 1.51. The energy transfer similarly may be estimated at 0.65 in the ideal analogy and at $\sim$0.5 in the calculated target.

Where does the "missing" energy go? Much of it ends up as internal energy in the pusher. For early times [Fig. VI-4 (c)], the kinetic and internal energy lines almost coincide; after the collision, about half the original energy remains as internal energy in the pusher.

As the implosion proceeds past 4.5 ns, the velocities of the gold-glass interface within the tamper and the tamper-fuel interface continue to increase. This is the desired effect of spherical convergence. At 5.0 ns these velocities reach their maximum and begin to decrease rapidly as the tamper delivers energy to the fuel; maximum fuel compression occurs shortly thereafter. Not surprisingly, this time corresponds to the peak in neutron production.

The conditions for ignition are a temperature of $\sim$3 keV in a fuel mass with a ρR of $\sim$0.3. Figure VI-4 shows the conditions achieved in the fuel for this target. Before the implosion, the fuel is at rest in the target at room temperature, at $\sim 10^{-7}$ keV, under a pressure of $\sim$75, or at a density of 0.0167 g/cm^3. As the implosion progresses, the temperature-vs-density curve in Fig. VI-5 shows that the fuel is first shock heated to a temperature of $\sim 10^{-2}$ keV, then compressed more or less adiabatically to a temperature of $\sim$0.7 keV and a density

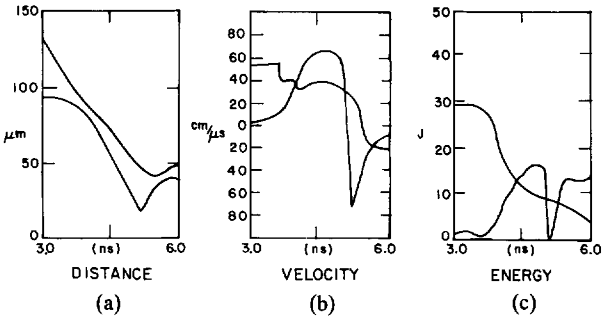

Fig. VI-4. Polaris shell collision from three perspectives.

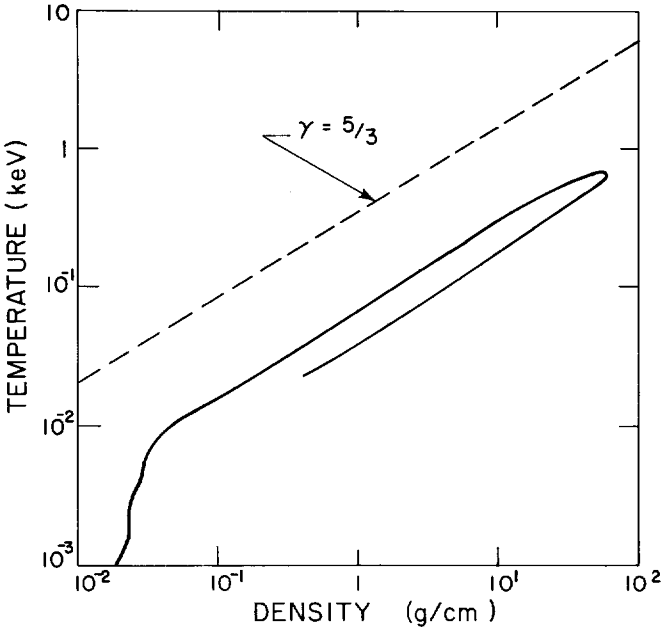

Fig. VI-5. Temperature density history of DT fuel.

of ~60 g/cm^3. As the implosion stagnates, radiation losses become dominant; the fuel expands along a lower adiabat. (A line parallel to the $\gamma = 5/3$ adiabats has been dashed in for comparison.)

For our prototype target, the maximum ρR achieved is only ~0.02, <0.1 the stopping distance of the 4.5-MeV particles produced and not enough for bootstrapping to have a significant effect. We are still in the regime where fuel temperature has the dominant effect on yield.

FUEL TEMPERATURE DETERMINATION FOR ICF MICROSPHERES (D. B. Henderson, D. V. Giovanielli)

A common heuristic formula for the yield of an imploded ICF microsphere is

$$Y = \left(\frac{M}{M_A}\right)^2 \left(\frac{4}{3}\pi R_0^3\right)^{-1} \left(\frac{1}{4}<\sigma v>\right) \tau \quad , \qquad \text{(VI-1)}$$

and

$$\tau \approx \tau_c = f\frac{R_0}{C_s} = f\,R_0\left(\frac{\gamma P_0}{\rho_0}\right)^{-1/2} \quad , \qquad \text{(VI-2)}$$

where Y is the number of reactions (equal to the number of neutrons for DT and twice that number for DD). For DD the term (1/4 $<\sigma v>$) is simply $<\sigma v>$. M is the fuel mass, M_A is the average ion mass, τ_c is the characteristic burn time, and R_0 is the compressed fuel radius. We use the subscript 0 to indicate conditions at maximum compression. Both the reactivity $<\sigma v>$ and sound speed C_s are functions of the peak temperature T_0; P_0 and ρ_0 are the peak pressure and density of the homogeneous fuel; γ is assumed to be 5/3. The factor f is used to account for the dynamics of the implosion; it can be estimated[1] as 0.25, but more usually it is obtained by fits to computer simulations. This formula should be applied only for small fractional yield, $Y \ll (M/M_A)$, which is appropriate for all experiments to date. Although the above formulae are instructive, their deficiencies are soon apparent when inverted to obtain the burn temperature from data (number of neutrons and fuel density) and fixed parameters. Not only is the factor f fixed arbitrarily, but some obviously important parameters are absent. Actual ICF experiments are not conducted with simple spheres of DT but involve layers of other materials.

We consider a model such as the one shown in Fig. VI-6. Here a pusher shell of mass M_s is accelerated by some outer ablator material. This shell then compresses the fuel mass M to a minimum radius $R = R_0$. We assume that the fuel is a homogeneous, perfect gas in which the pressure rises with adiabatic compression to stop the shell and then accelerate it outward. We integrate the yield throughout this process. The principal limiting assumption is our neglect of heat deposition from the burn; for experiments to date this assumption is clearly adequate. Our model does not require any arbitrary parameters such as f.

If the fuel temperature is T, we may simply express the force F accelerating the shell as

$$F = 4\pi R^2 \cdot P \quad ,$$

$$P = \left(\frac{2 \cdot \rho}{M_A}\right) kT \quad ,$$

$$\rho = \frac{M}{4/3\ \pi R^3} \quad ,$$

and

$$T = T_0\left(\frac{\rho}{\rho_0}\right)^{\gamma-1} = T_0\left(\frac{\rho}{\rho_0}\right)^{2/3} \quad ,$$

where the 2 in the expression for pressure P accounts for a fully ionized fuel. Substituting, we obtain

$$F = F_0\left(\frac{R_0}{R}\right)^3 \quad ,$$

and

$$F_0 = 6\left(\frac{M}{M_A}\right)\left(\frac{kT_0}{R_0}\right) \quad .$$

Neglecting any internal dynamics within the pusher shell, we have

$$\frac{d^2}{dt^2}\left(\frac{R}{R_0}\right) = \left(\frac{F_0}{R_0 M_s}\right)\left(\frac{R_0}{R}\right)^3 \quad .$$

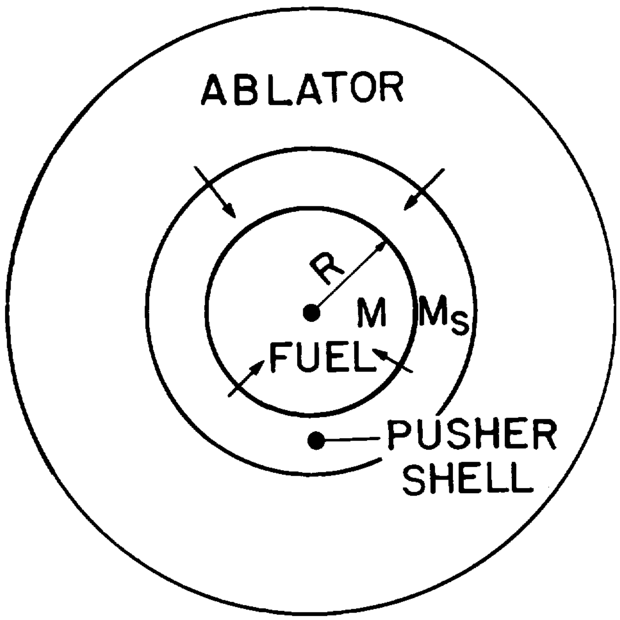

Fig. VI-6. Target model used for fuel temperature. Ablated material is assumed to accelerate the pusher inward causing it to compress the fuel adiabatically. No dynamics internal to the pusher shell are included and the fuel is assumed to be homogeneous.

Defining the origin of time t = 0 at turnaround, dR/dt = 0, and integrating, we obtain

$$R = R_0\left(1 + \frac{F_0 t^2}{R_0 M_s}\right)^{1/2} \quad . \qquad \text{(VI-3)}$$

Integrating the yield rate over the implosion and the explosion (bounce), we have

$$Y = 2\left(\frac{M}{M_A}\right)^2 \int_0^\infty \left(\frac{4}{3}\pi R^3\right)^{-1} \left(\frac{1}{4} <\sigma v>\right) dt \quad .$$

For the reactivity $<\sigma>$, we use a Gamow law fit,[2]

$$<\sigma v> = A_1 T^{-2/3} \exp\left(-A_2 T^{-1/3}\right) \quad , \qquad \text{(VI-4)}$$

where for DT, $A_1 = 3.68 \times 10^{-12}/\text{cm}^3\cdot\text{s}^{-1}(\text{keV})^{2/3}$, $A_2 = 19.94\ (\text{keV})^{1/3}$ and for DD, $A_1 = 9.32 \times 10^{-14}/\text{cm}^3\cdot\text{s}^{-1}(\text{keV})^{2/3}$, $A_2 = 18.76\ (\text{keV})^{1/3}$. For applications of interest between 0.1 and 10 keV, $A_2T^{-1/3}$ is always large, between 8.7 and 41.

Because of the steep dependence of $<\sigma v>$ on temperature, we may substitute a power-law fit within the integration,

$$<\sigma v> = <\sigma v>_0\left(\frac{T}{T_0}\right)^{\ell} \quad ,$$

and

$$<\sigma v> = <\sigma v>_0\left(\frac{R_0}{R}\right)^{2\ell} \quad ,$$

where, from Eq. (VI-4),

$$\ell(T_0) = \frac{1}{3}\left(A_2 T_0^{-1/3} - 2\right) \quad .$$

Integrating, we obtain

$$Y = \frac{3}{8\pi}\left(\frac{M}{M_A}\right)^2 <\sigma v>_0 R_0^{-3} \int_0^\infty (R/R_0)^{-3-2\ell}\, dt$$

$$= \frac{3}{8\pi}\left(\frac{M}{M_A}\right)^2 <\sigma v>_0 R_0^{-3} \int_0^\infty \left[1 + \frac{F_0}{R_0 M_s} t^2\right]^{-3/2-\ell} dt \ .$$

By substituting $X = (F_0/R_0M_s)t^2$, the integral becomes one of the standard definitions of the beta function B. Substituting for F_0 and ℓ, we find

$$Y = \left(\frac{M}{M_A}\right)^{3/2} \frac{M_s^{1/2}}{R_0^2}\, \tilde{Y}(T_0)$$

$$= \left(\frac{4\pi}{3}\right)^{2/3} \frac{M^{5/6} M_s^{1/2} \rho_0^{2/3}}{M_A^{3/2}}\, \tilde{Y}(T_0) \ , \qquad \text{(VI-5)}$$

where $\tilde{Y}(T_0)$ is a function only of the peak temperature T_0;

$$\tilde{Y} = 609. \begin{bmatrix} \text{x1 for DT} \\ \text{x4 for DD} \end{bmatrix} A_1 T_0^{-7/6} \exp\left(-A_2 T_0^{-1/3}\right) B \cdot$$

$$\left[\frac{1}{2}, \frac{1}{3}\left(1 + A_2 T_0^{-1/3}\right)\right] \quad . \qquad \text{(VI-6)}$$

The auxiliary functions $\ell(T_0)$ and $B[1/2,\ 1+\ell(T_0)]$ are plotted for DT in Fig. VI-7. Over our range of interest, we may evaluate B by differentiating and expanding for the large argument. We obtain

$$\frac{d\,\ell n\,B}{d\,\ell n\,T_0} = \frac{1}{6}\left[1 - \frac{1}{4}\,(A_2^{-1}T_0^{1/3}) - \frac{55}{8}\,(A_2^{-1}T_0^{1/3})^2 + \ldots\right]$$

$$= 0.162$$

for $\quad A_2^{-1}T_0^{1/3} = 0.05.$

Thus, a good fit is

$$B = A_3 T_0^{0.162}\ , \tag{VI-7}$$

where A_3 = 0.682 for DT and 0.703 for DD. By substituting into Eq. (VI-6), we obtain

$$\tilde{Y} = \begin{bmatrix} 1.528\times 10^{-9}\ \ T_0{}^{-1.00}\exp(-19.94\,T_0{}^{-1/3})\ \text{for}\ \ \text{DT} \\ 3.99\times 10^{-11}\ \ T_0{}^{-1.00}\exp\ (-18.76\ \ T_0{}^{-1/3})\ \text{for DD} \end{bmatrix} \cdot$$

(VI-8a)

(VI-8b)

Compare Eqs. (VI-1) and (VI-6); by solving for the effective confinement time τ, we obtain

$$\tau = \frac{1}{\sqrt{6}}\sqrt{\frac{M_s}{M}}\,B\,\frac{R_0}{\sqrt{kT_0/M_A}}$$

$$\tau = \sqrt{\frac{5}{9}}\sqrt{\frac{M_s}{M}}\,B\,\frac{\tau_c}{f}\ ,$$

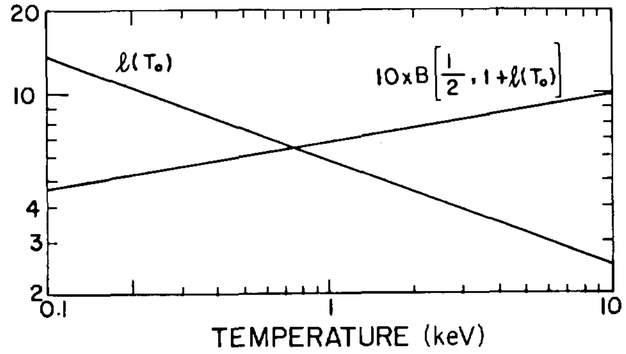

Fig. VI-7. Plot of function ℓ (the exponent in the power-law fit of $<\sigma v>$ to fuel temperature) and β (the beta function) versus fuel temperature.

where τ_c and f are defined in Eq. (VI-2) and B may be evaluated from Eq. (VI-7). Figures VI-8 and VI-9 are plots of $\tilde{Y}$ for DT from Eq. (VI-8a), which cannot be distinguished from Eq. (VI-6). Figure VI-9 is especially useful for the inversion of data. In addition to the function $\tilde{Y}(T_0)$, we have indicated with the dashed line a rather good fit $\tilde{Y}(T_0) = 4.29 \times 10^{-18}T_0^{7.13}$, which has a simple algebraic inversion. For scaling experimental data from the graph, we indicated conveniently chosen typical values of $\tilde{Y}$. Other parameter values may be scaled from these.

The Gamow fit for reactivity $<\sigma v>$ has been supplemented by better fits* for the cross section[3] that are, however, not in as general use. Over the range $0.3 < T_0 < 1$ keV, we have fit Hale's data for DT to Eq. (VI-4), obtaining $A_1' = 3.72 \times 10^{-12}/\text{cm}^3\cdot\text{s}^{-1}(\text{keV})^{2/3}$ and $A_2' = 20.16(\text{keV})^{1/3}$. Using these values, A_3' becomes 0.678 for DT and Eq. (VI-8a) becomes

$$\tilde{Y} = 1.536\times 10^{-9}T_0^{-1.00}\ \exp\ (-20.16\ \ T_0{}^{-1/3})\ \text{for DT}\ . \tag{VI-8a$'$}$$

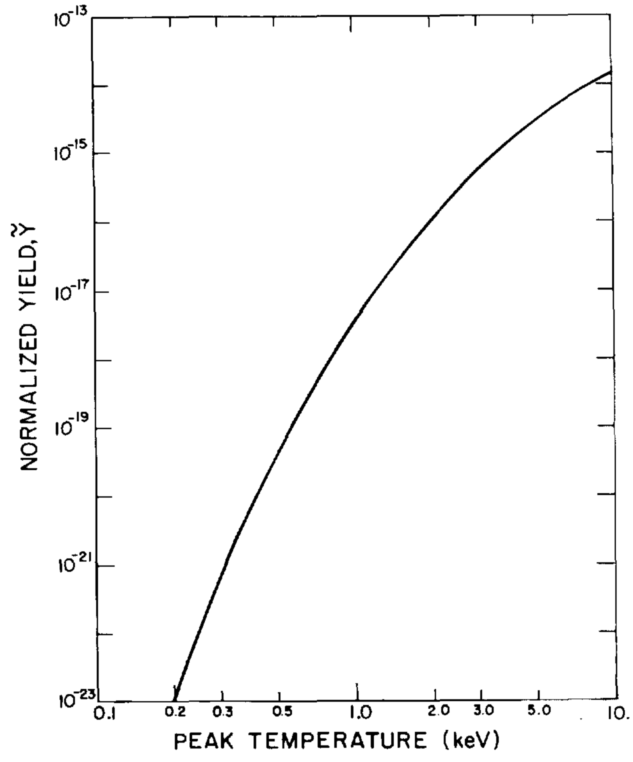

Fig. VI-8. Normalized neutron yield $\tilde{Y}$ versus peak fuel temperature T_0.

---

*From information supplied by G. M. Hale, Los Alamos National Laboratory (1975).

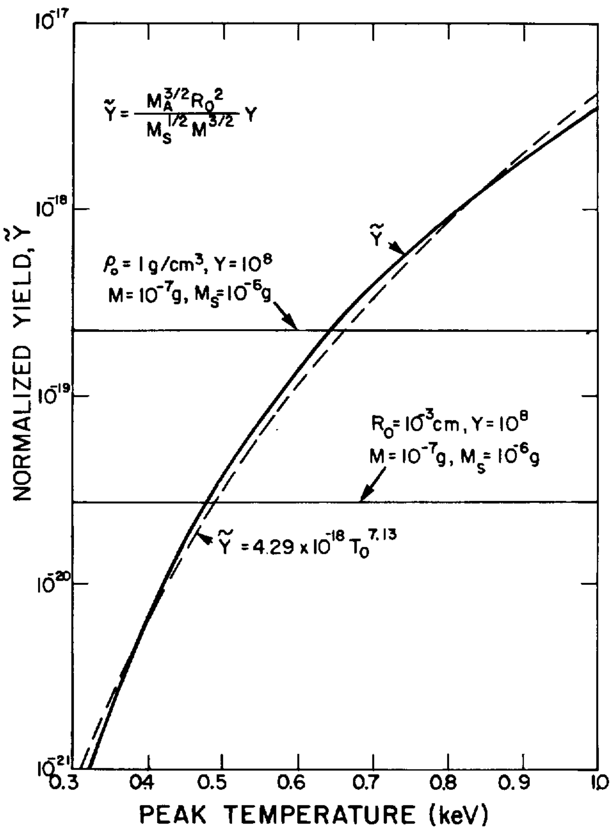

Fig. VI-9. Normalized neutron yield Ỹ versus peak fuel temperature of interest in ICF experiments (solid curve) and an easily inverted power-law fit of Ỹ to T_0 (dashed curve), with the typical values of Ỹ for two arbitrary choices of experimental parameters.

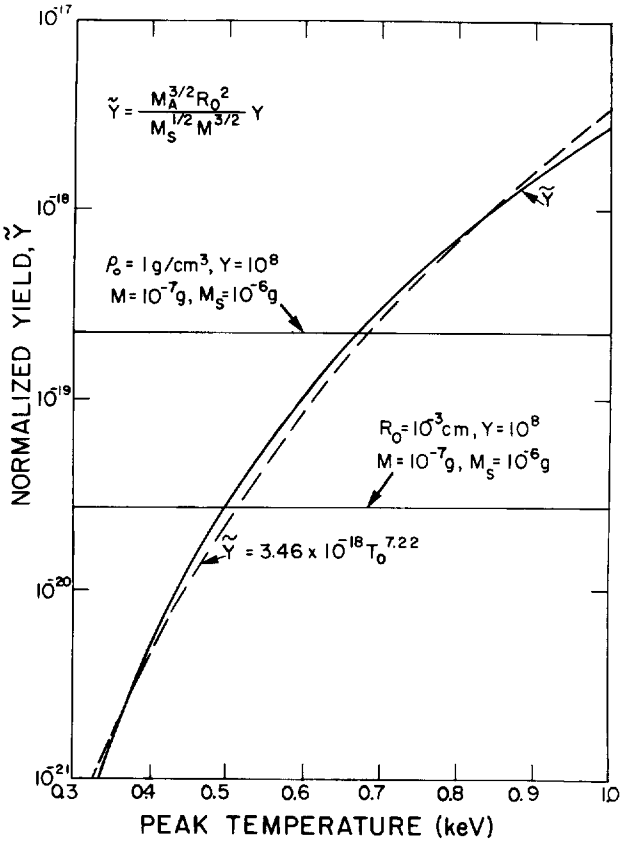

Fig. VI-10. Normalized neutron yield Ỹ versus peak fuel temperature T_0 in ICF experiments, using more current data in the evaluation of the reactivity $<\sigma v>$.

The simple power-law fit becomes $\tilde{Y} = 3.46 \times 10^{-18} T_0^{7.22}$ (Fig. VI-10). Over this range the temperatures implied for given data are higher by 3 to 4%. These values are probably more accurate; however, the differences are masked by typical experimental uncertainties.

SUPPORTING PHYSICS (D. C. Wilson)

Introduction

We continued to concentrate on laser plasma interaction phenomena because in this area the CO_2 laser differs from other prospective ICF drivers. The plasma temperature and density profiles near the critical surface are important in determining the generation of hot electrons by resonant absorption and other plasma processes. Below, we will discuss how the recently observed harmonic emission from CO_2 laser-irradiated plasma in the visible range of the spectrum may be used to diagnose the plasma temperature at the critical surface.

Hot electrons carry the deposited laser energy from the critical-density region into the target. The details of this transport are, therefore, crucial for accurately calculating both the compression and the preheat of a target. In the absence of electric fields, Monte Carlo calculations are adequate to determine the transport of hot electrons. However, at typical laser irradiances, hot electrons are so numerous that self-generated electric fields substantially inhibit their transport. Our LASNEX modeling uses flux-limited diffusion in an electrostatic potential to approximate this inhibition. However, truly self-consistent electric field calculations are needed. A hybrid transport scheme, described below, allows us to calculate self-consistent fields over many plasma periods. This approach is orders of magnitude faster than the traditional PIC calculations and should allow us to calculate electron transport on time scales of hydrodynamic interest.

Visible Harmonic Emission as a Means to Measure Profile Steepening (D. W. Forslund, J. M. Kindel)

Motivated by observations of visible harmonic emission, we have carried out two-dimensional particle simulations where pressure balance produces a highly steepened density profile. Typically, we observe a steepened density profile of 10 to 100 n_c and a lower density shelf of 0.1 n_c, where n_c is the critical density. The simulations are carried out with the electric field polarized in the plane of incidence.

The mode of the incident laser light is converted in the steepened density profile to a surface plasma wave,[4] resulting in a highly nonlinear form of resonant absorption. For this absorption to occur, the incident light wave must either impinge obliquely or be sufficiently focused to produce an electric field component along the density gradient. The plasma wave is highly nonlinear; consequently, it couples to the radiation field, causing the emission at harmonics of the incident light wave. The level of harmonic emission is directly related to both the amplitude of the plasma wave and the absorbed power. However, the plasma wave is primarily dissipated at high intensity because the wave accelerated a small fraction of the electrons in the steepened profile to high energies.[5]

Results from a simulation are shown in Fig. VI-11, in which a linearly polarized, plane light wave is incident from the left at an angle of 23° onto a sharp density profile that is uniform in the direction of periodicity. Pressure balance between the light and the cold, dense plasma produces an upper shelf of density

$$n_u \sim \frac{E_0^2}{8\pi T_c} \simeq 45 n_c \quad ,$$

where E_0 is the incident laser electric field I = 9 × 10^{14} W/cm^2, and T_c is the cold background temperature (T_c = 625 eV). The self-consistent density profile and the corresponding plasma-wave density perturbation are shown in Fig. VI-11. The density plots vs x and y [Fig. VI-11(a) and (b)] vividly display the sharpness of the density profile, with the laser incident from the left. In Fig. VI-11(a), the density changes by 5 to 50 n_c in 0.1 μm. Figure VI-11(b) is a magnified plot at the base of the sharp gradient region that isolates the plasma wave. A large-amplitude, nonsinusoidal surface perturbation travels in the y-direction. The low-density structure extending from the plasma surface is formed by ejected hot electrons from the plasma wave. Steepening of the plasma wave (harmonic generation) is closely associated with the ejection of these hot electrons.

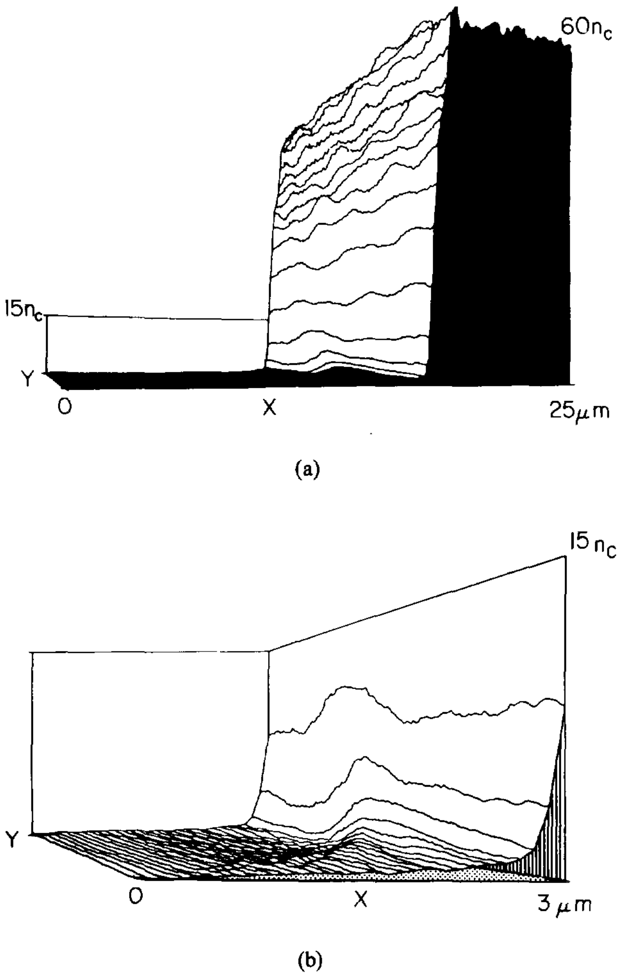

Fig. VI-11. Electron density profile for a wave simulation at $eE_0/m_e\omega_0 = 0.3$, $T_e = 625$ eV, $M_i/m_e = 100$, $T_e/T_i = 10$, and 23° angle of incidence to the density gradient: (a) vs x and y for a self-consistent pressure balance density of 45 n_c, and (b) a blow-up plot of the base of the sharp gradient region that isolates the plasma wave. Contours in (a) and (b) are separated by only 0.1 μm.

In Fig. VI-12 (a), (b), and (c), we plotted the calculated harmonic emission at three different intensities, 10^{14}, 4 × 10^{14}, and 9 × 10^{14} W/cm^2, respectively. At 10^{14} W/cm^2 the steepened profile is 7 n_c, whereas for 4 × 10^{14} W/cm^2 it is 25 n_c. For the low-intensity case, the underdense shelf is at 0.25 n_c, whereas for the intermediate- and high-intensity cases it is 0.1 n_c. The emission at $2\omega_0$ is

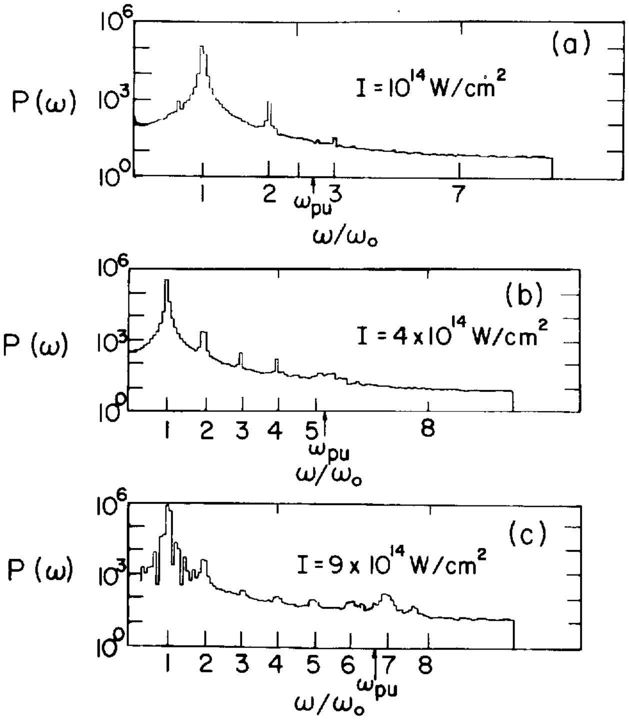

Fig. VI-12. Fourier power spectrum of the light leaving the left boundary of the simulation box for three laser intensities (a) 10^{14} W/cm^2 (that is, $v_0/c = 0.1$), (b) 4×10^{14} W/cm^2, and (c) 9×10^{14} W/cm^2. The emission at harmonics of the laser ω_{pe} corresponds to the plasma frequency at the upper shelf density.

different from the emission at other harmonics and is typically at 1% of ω_0 emission. Emission at the third harmonic is lowered by another order of magnitude. For harmonics above the third, we see an emission of $\sim 10^{-4}$ of the fundamental. As the upper density increases with intensity, we see a flattening of the harmonic number. The cutoff corresponds approximately to the harmonic number at which the upper density shelf becomes underdense. The striking feature is the nearly constant efficiency at which the higher harmonic numbers are generated until cutoff. The effect is clear from the fact that for $\omega < \omega_{pe}$, each harmonic is in resonance in the steep gradient; this should enhance the harmonic content of the plasma wave as well as that of the emitted harmonic light wave. Harmonic emission can develop for $\omega < \omega_{pe}$, but at a substantially lower efficiency. We have verified this scaling of the cutoff harmonic number by choosing a different simulation intensity and plasma temperature, thereby producing the same upper-shelf plasma density. We find that the cutoff harmonic number still lies at the plasma frequency of the upper shelf.

The simulated harmonic emission is in substantial agreement with experimental results, and indicates how these results can be used to infer properties at the critical density. First, the cutoff in the harmonic spectrum immediately yields the density of the upper-density shelf. Gemini data at 8×10^{14} W/cm^2, which show a cutoff at the 20th harmonic, would therefore suggest a steepened profile of 400 times critical density. If we assume pressure balance based on a simple, planar, one-dimensional model, we would infer a temperature for Gemini of <200 eV in the vicinity of the critical density. For Helios, the corresponding profile then must be at least 625 n_c, because a flattened spectrum out to at least the 25th harmonic is observed.

If the harmonic emission is temporally and spatially resolved, we can directly measure the position and velocity of the critical surface front. It is complementary to interferometry and, in particular, provides detailed information around the peak in the laser pulse, where collective processes would be expected to be strongest.

Hot-Electron Transport (R. Mason)

The hybrid transport schemes described in earlier reports[6,7] have employed only approximate schemes for calculating the self-consistent electric fields. A significant advance in computational technique now allows us to perform hybrid or full-particle simulations accurately over time steps Δt large compared to a plasma period $\omega_p\, \Delta t \gg 1$, with the minimum spatial resolution large compared to a Debye length $\Delta x/\lambda_D \gg 1$. The new implicit moment particle simulation technique involves the use of implicitly solved fluid equations to determine electric fields at an advanced time for the stable advancement of Monte Carlo particles. This approach increases the code speed 100- to 1000-fold over traditional PIC methods.

Consider a one-dimensional, collisionless plasma consisting of ions and hot- and cold-electron components represented as particles. These particles are governed by the finite-difference equations

$$u^{(m+1/2)} = u^{(m-1/2)} + \frac{q_\alpha E^{(*)}}{m_\alpha} \Delta t \quad , \qquad \text{(VI-9a)}$$

and

$$x^{(m+1)} = x^{(m)} + u^{(m+1/2)}\, \Delta t \quad , \qquad \text{(VI-9b)}$$

where (m) is the time-step index; (q_α, m_α) are, respectively, (−e, m) for electrons and (Ze, M) for ions, that is, $\alpha \equiv$ h, c, and i (hot electrons, cold electrons, and ions). In the conventional explicit leapfrog scheme, $E^{(*)} = E^{(m)}$, and $E^{(m+1)}$ is computed at the beginning of the *next* cycle from Poisson's equation

$$\frac{\partial E^{(m+1)}}{\partial x} = 4\pi \sum q_\alpha n_\alpha^{(m+1)} \quad , \qquad \text{(VI-10a)}$$

which converts to the following difference equation

$$\frac{E^{(m+1)}(i + 1/2) - E^{(m+1)}(i - 1/2)}{\Delta x}$$

$$= - 4\pi e \left[n_e^{(m+1)} - Z n_i^{(m+1)}\right] \equiv - 4\pi e \Delta n^{(m+1)} \quad , \qquad \text{(VI-10b)}$$

in which i is the cell center index, and $n_e = n_c + n_h$ is the sum of the hot- and cold-electron densities.

Let E(i − 1/2) = 0, then Eq. (VI-10b) rearranges

$$E(i + 1/2) = - (\omega_p \Delta\, t)^2 \frac{\Delta x}{(\Delta t)^2} \frac{m}{e} \; \Delta n/n_e \,\Big|_i \quad , \qquad \text{(VI-11)}$$

with $\omega_p{}^2 \equiv 4\pi e^2 n_e/m$. Suppose we set Δt so that an electron at the mean thermal hot speed $v_h > 0$ crosses a cell in a single time step, that is, $\Delta x = v_h \Delta t$. Then the total energy change for such an electron in Δt is $\Delta\xi = -e\Delta\phi = e\bar{E}\,\Delta x \equiv eE(i + 1/2)\,\Delta x/2$, or

$$\frac{\Delta\xi}{(1/2\ m v_h^2)} = - \frac{(\omega_p \Delta t)^2 \Delta n}{n_e} \quad . \qquad \text{(VI-12)}$$

With $\Delta n/n_e < 0.25$, $\omega_p\, \Delta t \leq 2$ can be tolerated. However, with $\Delta n/n_e = 0(1)$, as at the coronal edge of a laser pellet, the use of large time steps, $\omega_p\, \Delta t \gg 1$, will expose the electrons to fields that are large enough to change the electron mean energy by many multiples in one time step. This, in turn, leads to extreme violation of energy conservation and rapid divergence of the calculations.

One can avoid these difficulties at large Δt by either artificially decreasing the plasma frequency, as in plasma period dilation,[8] or by calculating all, or part, of the $E^{(*)}$ in Eq (VI-9a) implicitly.[9-13] With $E^{(*)} \sim E^{(m+1)}$ the velocities can be controlled to limit the particle excursions and, therefore, the accumulated density deviations $\Delta n^{(m+1)}$. *Thus,* $\Delta\xi$ *remains of order* $m v_h^2 \equiv kT_h$.

The value of an implicit approach has been recognized for some time,[14] but implementation has lagged because of the assumed need for costly iteration of the particle trajectories. In first approximation we skirt this problem by (1) solving the lower fluid moment equations for each cycle in conjunction with Poisson's equation for an implicit $E^{(*)}$, and then (2) advancing the particle equation with this predicted electric field.

Equation (VI-9a) is first replaced, *on the average,* by the particle momentum equation

$$\tilde{j}_\alpha^{(m+1/2)} = j_\alpha^{(m-1/2)} - \frac{1}{m_\alpha} \left[\left(\frac{\partial P_\alpha^{(\dagger)}}{\partial x} - q_\alpha n_\alpha^{(m)} E^{(*)} \right) \right] \Delta t \ . \qquad \text{(VI-13a)}$$

Here, $j_\alpha = n_\alpha U_\alpha$, and $P_\alpha \equiv n_\alpha(kT_\alpha + m_\alpha U_\alpha^2)$ is the second moment sum over the particles, that is, $m \sum u_\alpha^2$. Equation (VI-9b) is replaced by the continuity equation

$$\tilde{n}_\alpha^{(m+1)} = n_\alpha^{(m)} - \frac{\partial}{\partial x} \tilde{j}_\alpha^{(m+1/2)} \Delta t \quad . \qquad \text{(VI-13b)}$$

For one-dimensional problems we can integrate the Poisson equation, Eq. (VI-10), obtaining

$$\tilde{E}^{(m+1)} = 4\pi \int_0^x \sum_\alpha q_\alpha \tilde{n}_\alpha^{(m+1)}\, dx + \tilde{E}^{(m+1)}\ (0) \quad , \qquad \text{(VI-14)}$$

where the integral is arbitrarily started at x = 0. The tildes on $\tilde{n}^{(m+1)}$ and $\tilde{j}^{(m+1/2)}$ in Eqs. (VI-13) and (VI-14) indicate that these quantities are predictions from the moment equations and not necessarily equal to the particle quantities $n^{(m+1)}$, $j^{(m+1/2)}$ that will be established in the next cycle. Thus, $\tilde{E}^{(m+1)}$ is the electric field consistent with these predictions.

The simplest and most stable choice for $E^{(*)}$ is the fully implicit field $E^{(*)} = E_I = \tilde{E}^{(m+1)}$. Alternatively, $E^{(*)} = E_c = 1/4\ [E^{(m+1)} + 2E^{(m)} + E^{(m-1)}]$ is symmetric about (m), offering improved centering, and its levels are weighted to smooth the electron accelerations. Thus, to introduce some flexibility, we have employed

$$E^{(*)} = \theta E_I + (1 - \theta) E_c \quad , \quad 0 \leq \theta \leq 1 \quad . \qquad \text{(VI-15)}$$

Using this expression with Eqs. (VI-13) and (VI-14), we derive the predicted field

$$\tilde{E}^{(m+1)} = \frac{4\pi\left[\int_0^x \sum_\alpha q_\alpha n_\alpha^{(m)}\,dx - \sum_\alpha q_\alpha j_\alpha^{(m-1/2)}\,\Delta t + \sum_\alpha (q_\alpha/m_\alpha)\,(\partial P_\alpha^{(\dagger)}/\partial x)\,(\Delta t)^2\right] + B(x) + C(0)}{(1 + a\omega_p'^2\,\Delta t^2)}$$

$$\equiv \frac{g(x) + C(0)}{f(x)} \qquad \text{(VI-16)}$$

in which $a = 1/4\ (3\theta + 1)$, $\omega_p'^2 \equiv 4\pi e^2(n_e + Z^2\ m/M)/m$, and $B(x) = 1/4\ (1 - \theta)[2E^{(m)} + E^{(m-1)}]$.

In Eq. (VI-16), $C(0) = \tilde{E}^{(m+1)}(0) + 4\pi e \sum_\alpha j_\alpha^{(m+1/2)}(0)\ \Delta t$. At a specular or quiescent left boundary, $j_\alpha(0) = E(0) = 0$, and, therefore, $C(0) = 0$. Alternatively, under periodic boundary conditions, we require that $\phi(0) = \phi(L) = -\int_0^L E\ dx$, and thus, $C(0) = \int_0^L gf^{-1}\ dx/\int_0^L f^{-1}\ dx$. From the particles we accumulate the fluid moments $n^{(m)}$, $j^{(m-1/2)}$, and $P^{(\dagger)}$ at the cell centers, but use the averaged values $j_{i+1/2}^{(m-1/2)} = [j^{(m-1/2)}(i) + j^{(m-1/2)}(i + 1)]/2$ and $n_{i+1/2}^{(m)} = [n^{(m)}(i) + n^{(m)}(i + 1)]/2$ in the calculations at cell boundaries for $\tilde{E}_{i+1/2}^{(m+1)}$. This implicit field is then area weighted to the particle positions and used as $E^{(*)}$ during each cycle in Eq. (VI-9) to advance the particle coordinates.

As a sample application, we have investigated the one-dimensional expansion of collisionless plasma into a vacuum. The input and output have dimensional values, with time in picoseconds and distance in micrometers. We set $Zn_i = n_e = 5 \times 10^{21}\ \text{cm}^{-3}$ initially, and $n_c = 0$ with $T_h = 10$ keV and $T_i = 1$ keV. We used 100 cells at $\Delta x = 0.5\ \mu$m and $\Delta t = 10^{-3}$ ps. Here $v_h = 42.4\ \mu$m/ps, so that the Courant condition for the electrons permits a time step at least five times larger. This method has been subsequently tried and gives nearly identical results.

This calculation ran 3000 cycles with $Z = 10$, $A = M/M_p = 25$, and $M_p/m = 100$, where M_p is the mass of a proton, here reduced to speed up the calculations. We used only 2×10^3 particle electrons and an equal number of ion particles. Before submission as sources into the Eq. (VI-15) field expression, the density, current, and pressure moments were smoothed by passing them through the operator $0(A) \equiv 1/4\ [A(i + 1) + 2A(i) + A(i - 1)]$ four times during each cycle. The results are essentially unaltered (but noisier) when this smoothing is omitted. In the dense, unexpanded plasma $\omega_p = 4 \times 10^3\ \text{ps}^{-1}$, so that $\Delta x/\lambda_D = 47.8$ and $\omega_p\ \Delta t = 4.0$. The ion acoustic speed $v_{i.a.} = (ZT_e/M)^{1/2} = 2.7\ \mu$m/ps. The boundaries are specular.

Figure VI-13 presents the results of the calculation. The vertical fiducial lines mark the distance traveled in 3 ps by a particle moving at the ion-acoustic speed. Each curve, in fact, consists of two overlaid curves: one for n_e and one for Zn_i, but the Eq. (VI-15) field, here in its quasi-neutral limit, locks them into superposition. T_h remains nearly isothermal over the run. For the sequence shown in Fig. VI-14, we have reduced the hot density to 5% of the total, $n_h = 2.5 \times 10^{20}\ \text{cm}^{-3}$. We set the main body of cold electrons and ions at T = 3 keV. We used 10^3 cold-electron particles and 10^3 hot particles, thereby increasing the resolution of the electron distribution tail at least tenfold. Otherwise, the parameters remained unchanged. Upon expansion, the hot electrons rapidly fill the low-density "coronal" region; this is followed by the slower expansion of the main plasma body. Eventually, the fastest ions are reflected by the right computational boundary at x = 50 μm.

For a second test we applied the implicit moment method to the two-beam problem in a warm plasma. The beam drift speeds v_p were ±25 μm/ps, respectively, and

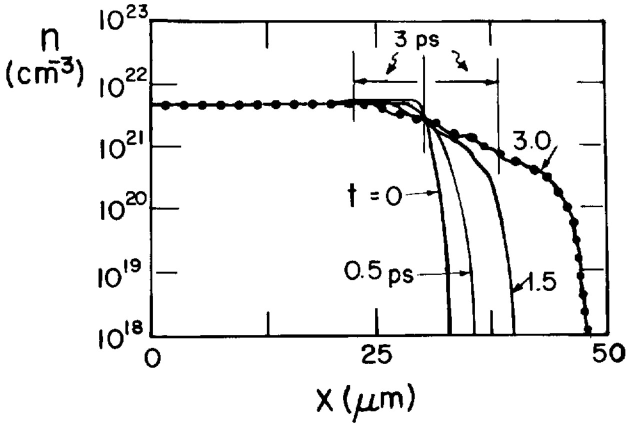

Fig. VI-13. Electron density n_e (dotted line) and ion charge density Zn_i (solid line) curves for the expansion of a $Z = 10$, $A = 25$ plasma with $T_e/T_i = 10$. Evolution to $\omega_p\ \Delta t = 1.2 \times 10^4$ with $\omega_p\ \Delta t = 4$, $\Delta x/\lambda_D = 47.8$.

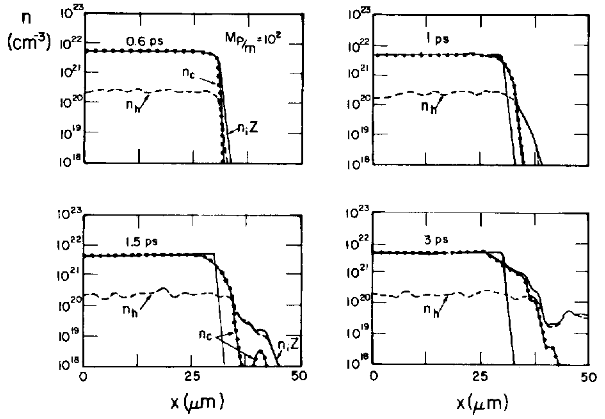

Fig. VI-14. Two-temperature electron-driven plasma expansion: $T_h/T_c = 3.3$ and $T_h/T_l = 10.0$.

the beam temperatures were 0.43 keV, so that their mean themal speeds, $v_h = (T/m)^{1/2}$, were 8.8 μm/ps, and thus, $v_p \equiv \sqrt{2}\, v_h = 12.5$ μm/ps, giving $v_d| = 2v_p$. We used 10^4 simulation particles in each beam, 100 cells, and periodic boundary conditions. The total density from both beams was $n_e = 10^{21}$ cm^{-3}, so that $\omega_p^{-1} = 5.61 \times 10^{-4}$ ps and $\lambda_D = v_h/\omega_p = 4.87 \times 10^{-7}$ cm. The ions were stationary ($M \rightarrow \infty$).

In our first calibrational run, $\Delta t = 2.24 \times 10^{-4}$ ps $= 0.4\omega_p^{-1}$ and $\Delta x = 2.43 \times 10^{-6}$ cm $= 5.0\ \lambda_D$. This setup was, therefore, equivalent to Case V of Ref. 15, except that our time step was 2.5 times longer and our cell size was five times larger. Figure VI-15(a) shows the starting conditions. The particles were loaded at cell centers. Frame (b) shows the development at 40 plasma periods, that is, $\tau = t/T = \omega_p t/2\pi = 40$, $\omega_p t = 251$, after 620 cycles. The coalescing eddies of Ref. 15 are very much in evidence. We see four or five eddies over the 500-λ_D test area, as did Ref. 15 at comparable times. Of course, slightly different initial conditions, and our large Δt and Δx should alter the details. Frame (c) shows the results at $\tau = 190$, cycle 3000. Smearing and coalescence has reduced the number of eddies to one.

Frames (d) and (e) show the results of running the calculation with $\omega_p\, \Delta t = 4.0$, and $\Delta x/\lambda_D = 50.0$. After 62 cycles we obtain frame (d), $\tau = 40$, which shows about three or four eddies in the right 10% of the test area, consistent with frame (b). By $\tau = 400$ (100 cycles), we obtain frame (e), which is comparable to (c). It exhibits about 12 eddies over the full 5000-λ_D test area. As a general rule, we have found that instability sets in later, as we increase $\omega_p\, \Delta t$, but that comparable turbulent states, as limited by the reduced resolution at larger Δx, are obtaining at long times. Frame (f), for example, is the result obtained after 3000 cycles with $\omega_p\, \Delta t = 40$ and $\Delta x/\lambda_D = 500$ at time $\tau = 19\,000$. The left 10% of results of frame (f) corresponds to the results of frame (e) run 100 times longer. This longer interval would, incidentally, correspond to 67 ps and a 243-μm test area, consistent with the corona of a laser pellet.

These two stream results must be viewed with caution. For cold beams the maximum growth should occur near $k = \omega_p/|v_d| = 7.1 \times 10^5$ cm^{-1}, at a rate near $|\gamma| = \omega_p/2$. Assuming that the smallest rate resolved, λ_{min}, is $2\Delta x$, we obtain $k_{max} = 12.9 \times 10^5$, 1.79×10^5, and 0.129×10^5 cm^{-1} for the three time steps considered. Thus, only in the first case is $|\gamma|\Delta t < 1$, and only in this case is the fastest growing mode resolved. In the other two cases the scheme attributes beam coupling to more slowly growing modes. Similarly, nonlinear trapping of the electrons is characterized by a rate $\omega_t = (e\phi/kT)^{1/2} k\ \lambda_D\omega_p$. At $\tau = 40$, with four eddies visible in Fig. VI-15(b), we find that $e\phi = 8$ keV at the eddy peaks, and background has heated to $kT = 2$ keV. The length of the eddies is roughly $L = 8\Delta x = 40\lambda_D(T = 0.43\text{ keV}) = 18.6\ \lambda_D(T = 2\text{keV})$, so that $k = 2\pi/L = 0.34/\lambda_D$. Thus, $\omega_t = (8/2)^{1/2}\ 0.34\ \omega_p = 0.68\ \omega_p$. For our three cases $\omega_p\, \Delta t = 0.4$, 4.0, and 40.0; therefore, we see that $\omega_t\, \Delta t = 0.27$, 2.7, and 27.0, respectively. Only our first case has a reliable $\Delta t < \omega_t^{-1}$, although $\Delta t < T_t = 2\pi\omega_t^{-1}$ may be sufficient because our $\omega_p\, \Delta t = 4.0$ run crudely reproduces the $\omega_p\, \Delta t = 0.4$ structure. The crucial point is that even our calculations for $|\gamma|\Delta t \gg 1$, $k_{max}\, \Delta x \gg 1$, and $\omega_t\, \Delta t \gg 1$ are stable and physically plausible. If greater detail in the evolving structure is desired, smaller time and space steps are required.

CODE DEVELOPMENT

Introduction (E. Linnebur)

The conversion and operation of our main design code, LASNEX, on the CRAY computers under the CTSS was a major accomplishment of 1980. LASNEX has been rewritten and restructured completely to produce a modular and extensively annotated code. By applying structured programming, we made code maintenance easier and facilitated future improvements. On-line graphics have been added to aid the designers. The ICCG algorithm, which is used in thermal electron, ion, and radiation transport calculations, was vectorized to run 15 times faster. As a result of these and other changes, one-dimensional LASNEX calculations are

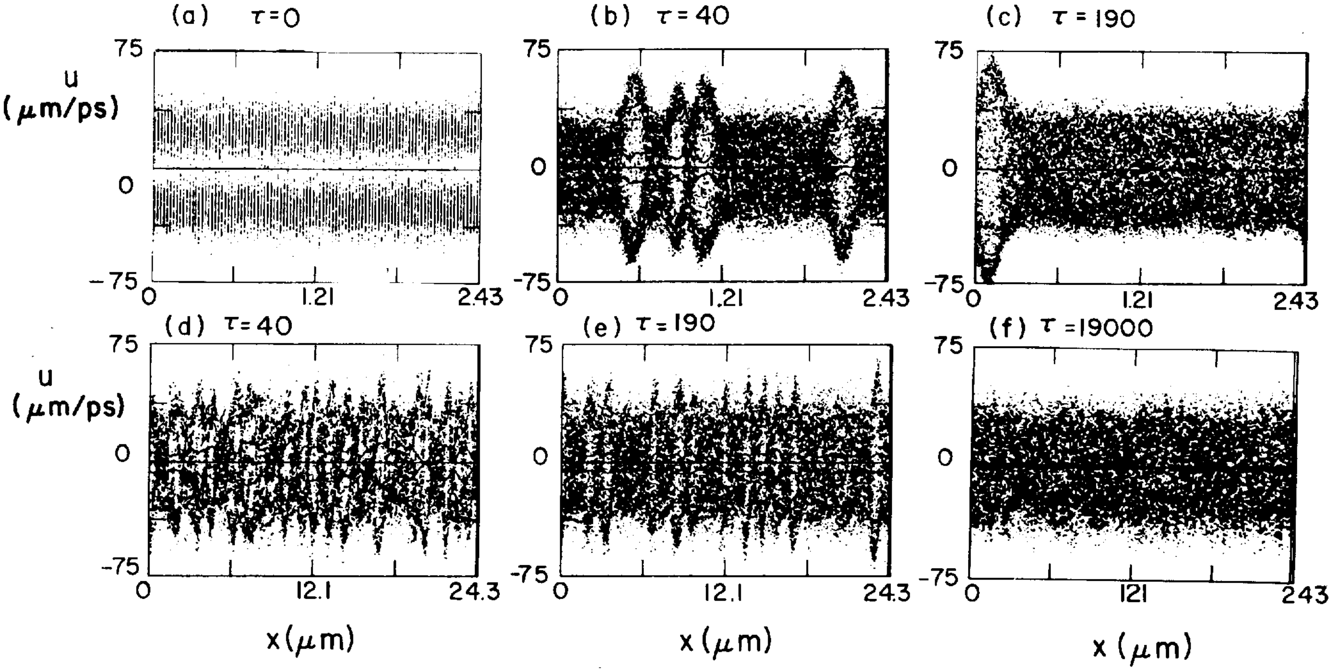

Fig. VI-15. Two-beam instability in a warm plasma calculated with (a)-(c) ωp Δt = 0.4, (d)-(e) ω_p Δt = 4.0, and (f) ω_p Δt = 40.0.

three times faster on the CRAY than on the CDC-7600 computer. Two-dimensional calculations are four times faster.

In the following discussions we describe first the ORBEOS code, which we have used as a testbed for the two-dimensional flux-corrected transport (FCT) algorithm. This discussion is followed by a description of adaptive zoning, a technique that will save user time by reducing the need for manual rezoning of two-dimensional calculations. In addition, this technique will allow us to calculate two-dimensional problems containing large shear stresses and complex deformations.

ORBEOS Code (A. J. Scannapieco)

Studies of fluid instabilities in imploding spherical systems made it obvious that we needed a CDC-7600 computer code that is capable of following the evolution of instabilities into the far nonlinear regime within a reasonable time (that is, in less than 60 min). We wrote ORBEOS specifically to satisfy these requirements.

ORBEOS is a two-dimensional, Eulerian hydrodynamic code that uses tabular equations of state for real substances; it may also operate with an ideal gas equation of state. The geometry used in the code is spherical (that is, r – θ) in which all fluid quantities are independent of the azimuthal angle ϕ. The z-axis is the axis of rotational symmetry. All fluid quantities depend only on r and θ. The physics of the code were originally those of a compressible fluid. This restriction was supposed to isolate the basic aspects of fluid instabilities by excluding the complications introduced by a multitude of physical mechanisms.

The physical equations chosen for study with the code included the equation for mass conservation, the equations of radial and angular momentum density transport, and the energy equation written in terms of the fluid temperature. The equations-of-state relations for pressure, specific energy, and specific heat are obtained from tables compiled for real substances. In ORBEOS we used a generalization to spherical geometry (from a technique described by Zalesak in 1978)[16] to solve the finite-difference equations. By using this technique we avoid introducing explicit artificial viscosity into the code.

The Algorithm. In May 1978, S. T. Zalesak published a paper in which he describes a new alternative form for the flux-limiting phase of the FCT algorithms of Boris, Book, and Hain.[17-19]

He points out several advantages over the flux-limiters previously used; the new flux-limiter

(1) can be generalized to handle multidimensional calculations without resort to Strang-type splitting;[20]

(2) eliminates "clipping" for vanishing velocity and reduces clipping at finite velocities; and

(3) for the first time, makes multidimensional FCT calculations possible for problems not amenable to Strang-type time splitting, such as those involving incompressible or nearly incompressible flow.

This third point is crucial for any algorithm that is used in a hydrodynamic code whose main purpose is to study fluid stability. To understand this assertion, consider the basic equation solved by the FCT algorithm:

$$\frac{\partial w}{\partial t} + \underset{\sim}{\nabla} \cdot \underset{\sim}{f} = 0 \ , \qquad \text{(VI-17)}$$

where w is a generalized density and $\underset{\sim}{f}$ is a generalized flux. Let us consider specifically the situation where $w \equiv \rho$ (that is, a fluid density) and $\underset{\sim}{f} \equiv \rho \underset{\sim}{v}$ (that is, a fluid momentum density), where $\underset{\sim}{v}$ is the local fluid velocity. Equation (VI-17) becomes

$$\frac{\partial \rho}{\partial t} + \underset{\sim}{\nabla} \cdot \rho \underset{\sim}{v} = 0 \quad , \qquad \text{(VI-18)}$$

which is just the equation for conservation of mass. If we further assume that the system is two-dimensional and Cartesian, Eq. (VI-18) written in component form becomes

$$\frac{\partial \rho}{\partial t} + v_x \frac{\partial \rho}{\partial x} + v_y \frac{\partial \rho}{\partial y} + \rho \left(\frac{\partial v_x}{\partial x} + \frac{\partial v_y}{\partial y} \right) = 0 \ . \qquad \text{(VI-19)}$$

Next, assume that $\underset{\sim}{v}$ is a known function of ρ

$$\underset{\sim}{v} = \underset{\sim}{v}(\rho) \ .$$

Equation (VI-19) can be advanced in time in two ways: by Strang-type time-step splitting, or by the use of a fully two-dimensional algorithm. A typical Strang-type time-step splitting scheme is shown below.

$$v_x^0 \equiv v_x(\rho^0) \quad ,$$

$$\rho^{hx} = \rho^0 - \frac{\delta t}{2} \left(v_x^0 \frac{\delta \rho^0}{\delta x} + \rho^0 \frac{\delta v_x^0}{\delta x} \right) \quad ,$$

$$v_x^{hx} = v_x(\rho^{hx}) \quad ,$$

$$\rho^x = \rho^0 - \delta t \left(v_x^{hx} \frac{\delta \rho^0}{\delta x} + \rho^0 \frac{\delta v_x^{hx}}{\delta x} \right) \quad ,$$

$$v_y^x = v_y(\rho^x) \quad ,$$

$$\rho^{hy} = \rho^x - \frac{\delta t}{2} \left(v_y^x \frac{\delta \rho^x}{\delta y} + \rho^x \frac{\delta v_y^x}{\delta y} \right) \quad ,$$

$$v_y^{hy} = v_y(\rho^{hy}) \quad ,$$

and

$$\rho^n = \rho^x - \delta t \left(v_y^{hy} \frac{\delta \rho^x}{\delta y} + \rho^x \frac{\delta v_y^{hy}}{\delta y} \right) \quad ,$$

where δ/δx and δ/δy represent finite-difference approximations to the x and y derivatives, and where the superscript 0 stands for old, hx for half-step x, x for full step x, hy for half-step y, and n stands for new. If we resubstitute into the algorithm and write ρ^n in terms of old quantities, the expression for ρ^n to second order in δt becomes

$$\begin{aligned}
\rho^n = \rho^0 - \delta t \Bigg(& \left(1 - \frac{\delta t}{2} \frac{\partial v_x^0}{\partial \rho^0} \frac{\delta \rho^0}{\delta x} - \delta t \frac{\partial v_y^0}{\partial \rho^0} \frac{\delta \rho^0}{\delta y} \right) \left(v_x^0 \frac{\delta \rho^0}{\delta x} + \rho^0 \frac{\delta v_x^0}{\delta x} \right) \\
& + \left(1 - \frac{\delta t}{2} \frac{\partial v_y^0}{\partial \rho^0} \frac{\delta \rho^0}{\delta y} \right) \left(v_y^0 \frac{\delta \rho^0}{\delta y} + \rho^0 \frac{\delta v_y^0}{\delta y} \right) \\
& - \delta t \left\{ \frac{1}{2} \rho^0 \frac{\delta}{\delta x} \left[\frac{\partial v_x^0}{\partial \rho^0} \left(v_x^0 \frac{\delta \rho^0}{\delta x} + \rho^0 \frac{\delta v_x^0}{\delta x} \right) \right] + v_y^0 \frac{\delta}{\delta y} \left(v_x^0 \frac{\delta \rho^0}{\delta x} + \rho^0 \frac{\delta v_x^0}{\delta x} \right) \right. \\
& \left. + \rho^0 \frac{\delta}{\delta y} \left[\frac{\partial v_y^0}{\partial \rho^0} \left(v_x^0 \frac{\delta \rho^0}{\delta x} + \rho^0 \frac{\delta v_x^0}{\delta x} + \frac{v_y^0}{2} \frac{\delta \rho^0}{\delta y} + \frac{\rho^0}{2} \frac{\delta v_y^0}{\delta y} \right) \right] \right\} + 0(\delta t^2) \Bigg) \ .
\end{aligned}$$

If $\delta v_x^0/\delta x + \delta v_y^0/\delta y \equiv 0$, the above algorithm is true *only* to first order in δt. The condition that the flow be incompressible is not met by this Strang-type time-step splitting algorithm.

Alternatively, a fully two-dimensional algorithm, similar to that described by Zalesak would be:

$$\underset{\sim}{v}^0 = \underset{\sim}{v}(\rho^0) \quad ,$$

$$\rho^h = \rho^0 - \frac{\delta t}{2}\left[v_x^0 \frac{\delta \rho^0}{\delta x} + v_y^0 \frac{\delta \rho^0}{\delta y} + \rho^0 \left(\frac{\delta v_x^0}{\delta x} + \frac{\delta v_y^0}{\delta y} \right) \right] \quad ,$$

$$\underset{\sim}{v}^h = \underset{\sim}{v}(\rho^h) \quad ,$$

and

$$\rho^n = \rho^0 - \delta t \left[v_x^h \frac{\delta \rho^h}{\delta x} + v_y^h \frac{\delta \rho^h}{\delta y} + \rho^h \left(\frac{\delta v_x^h}{\delta x} + \frac{\delta v_y^h}{\delta y} \right) \right] \quad .$$

If $\delta v_x/\delta x + \delta v_y/\delta y \equiv 0$, the above algorithm preserves this condition to all orders of δt. Thus if the flow is incompressible, this algorithm will mirror that fact exactly.

In fluid stability studies this feature of the fully two-dimensional algorithm is important; if $\underset{\sim}{\nabla}\cdot\underset{\sim}{v}$ should be physically zero but is not numerically zero, a virtual source is introduced into the continuity equation that can lead to anomalous peaks and valleys in the solution.

For reasons mentioned above, we used in ORBEOS the fully multidimensional FCT technique described by Zalesak, though generalized to $r - \theta$ geometry.

A natural consequence of using a two-dimensional algorithm is the possibility of treating problems at the origin of coordinates in spherical geometry. This is not possible for a one-dimensional FCT algorithm using Strang-type time-step splitting.

For details of the technique see Ref. 16. The basic philosophy of the FCT technique, simply stated, is that two algorithms are used to carry out the transport of the fluid quantities. An algorithm, low order in space, that is highly diffusive but gives smooth results, is combined through the medium of a flux-limiter, with a high-order algorithm that is very nondiffusive but causes ripples in the solution. The combination produces an algorithm that is accurate to any desired order in space, and to second order in time.

Results. ORBEOS has been used to solve numerous problems; three are discussed below: the imploding spherical shell, the spitting cone, and the imploding spherical shell with perturbations. Artificial viscosity was introduced to handle shocks in none of these cases.

We monitored the code's success in conserving mass and total energy. In each case mass was conserved to an accuracy better than 1% and total energy was conserved to better than 3%.

The three-dimensional display package (DISPLA) used in ORBEOS displays the radius and angle in a rectangular fashion. Three facts must be kept in mind when viewing the figures:

(1) the line at $r = 0$ in the figures is in reality a point and all quantities along that line are equal;

(2) the line at $\theta = 0$ is the axis of rotational symmetry; and

(3) the values along the axis labeled density are, in all cases, on a base 10 logarithmic scale.

Imploding Shell. As the name implies, a shell was imploded symmetrically toward the origin of coordinates. An ideal equation of state was assumed. The maximum angle θ_{max} was 45°, and the maximum radius r_{max} was 50 μm. The computational grid (Fig. VI-16) contained 51 equally spaced points in the radial direction and 5 equally spaced points in the angular direction (that is, $\Delta r = 1$ μm and $\Delta\theta = 11.25°$). The shell was 10 μm thick and centered at the radius $r = 75$ μm. Shell density was 1.0 g/cm^3. The shell contained a gas at density 0.02 g/cm^3, referred to as the fuel, and the outside of the shell was surrounded by a 10-μm layer of a gas at 0.1 g/cm^3. Initially, the pressure of the outside layer of gas was to be 10 times the constant pressure throughout the shell and the fuel. The boundary condition at r_{max} was reflecting.

During the initial phase of the implosion, a shock passes through the shell and compresses the shell to a density of ~4 g/cm^3 (Figs. VI-17 and VI-18). After initial compression, the shell begins to move inward, compressing the low-density fuel. As the shell implodes, several shocks pass into the fuel and reflect at the origin. As the shell approaches the origin, the density of both the shell and the fuel increases (compare Fig. VI-19 with Figs. VI-17 and VI-18) until the shell and fuel configuration reflects at the origin. Immediately after reflection (Fig. VI-20), the density is ~36 g/cm^3.

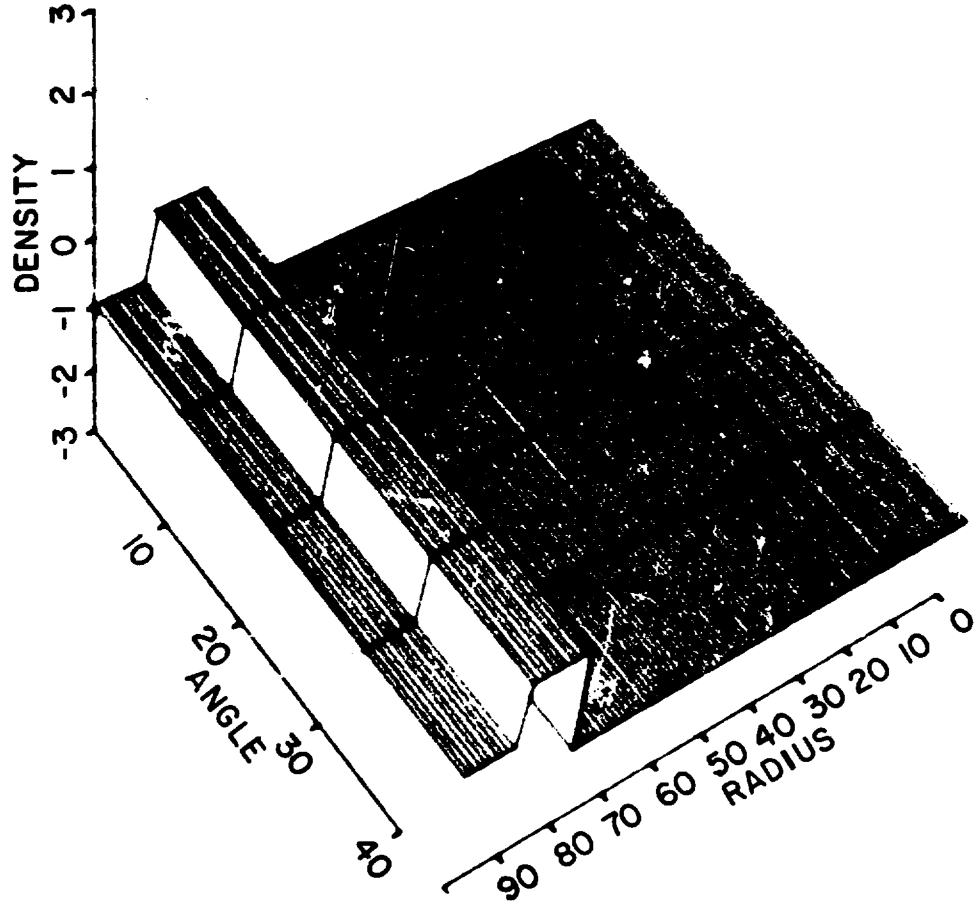

Fig. VI-16. Initial density configuration of imploding spherical shell.

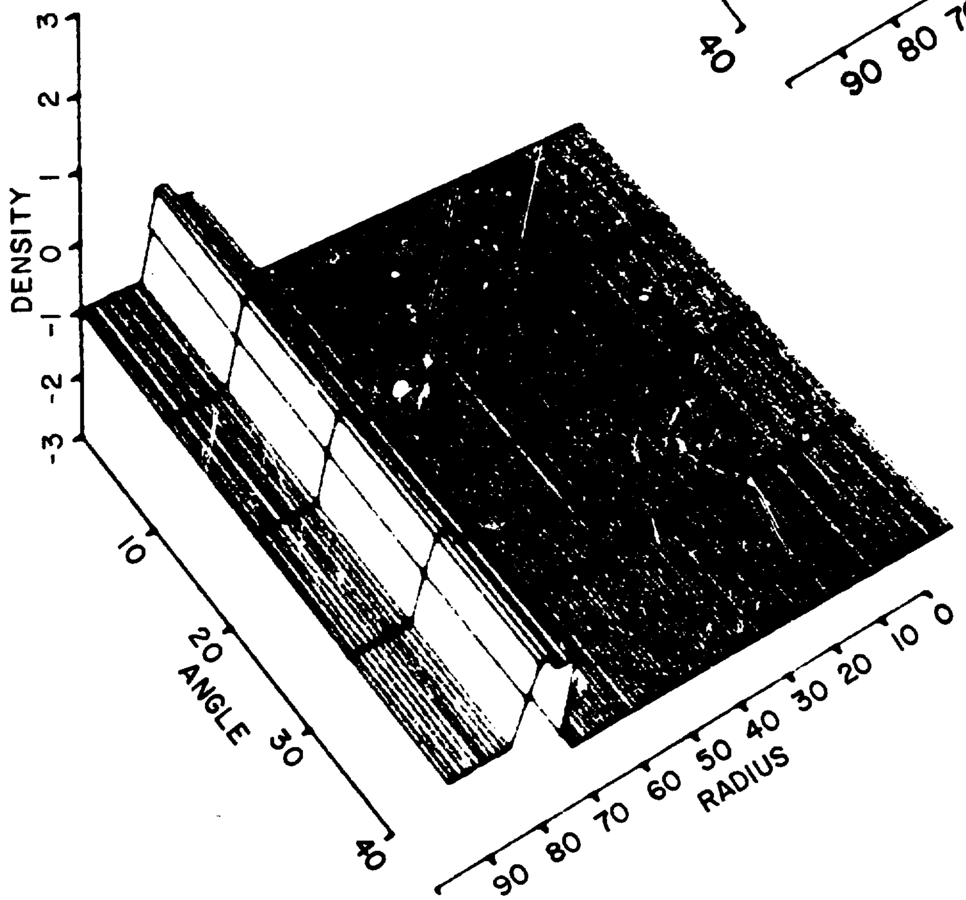

Fig. VI-17. Shock beginning its passage through spherical shell.

Fig. VI-18. Compression of original shell after passage of shock.

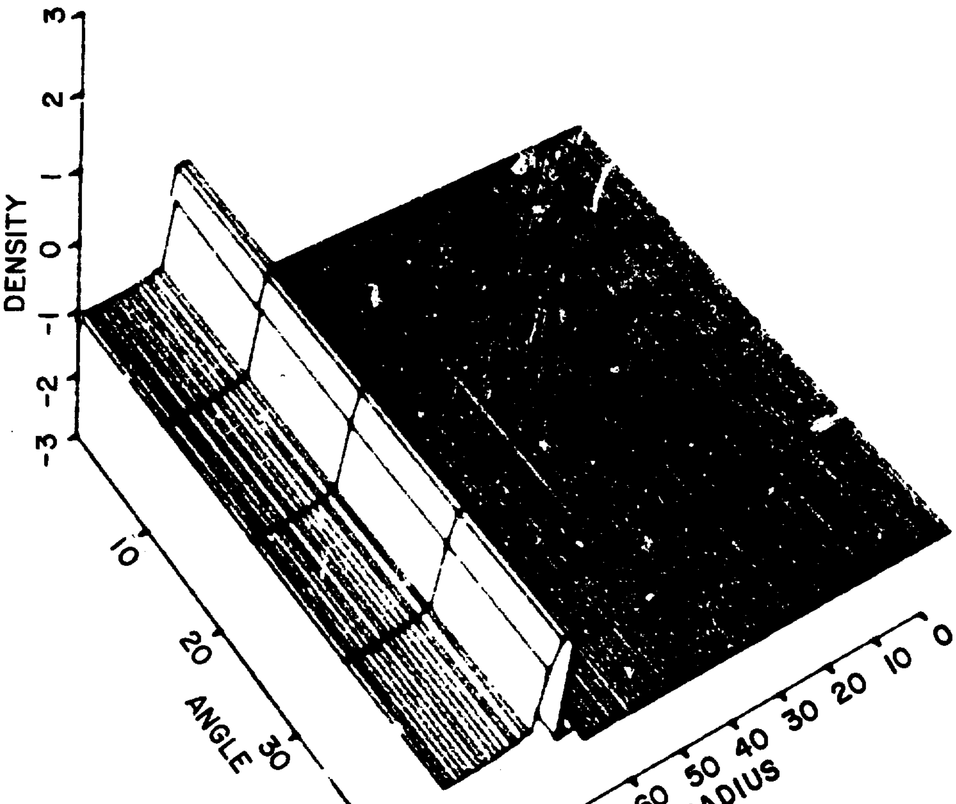

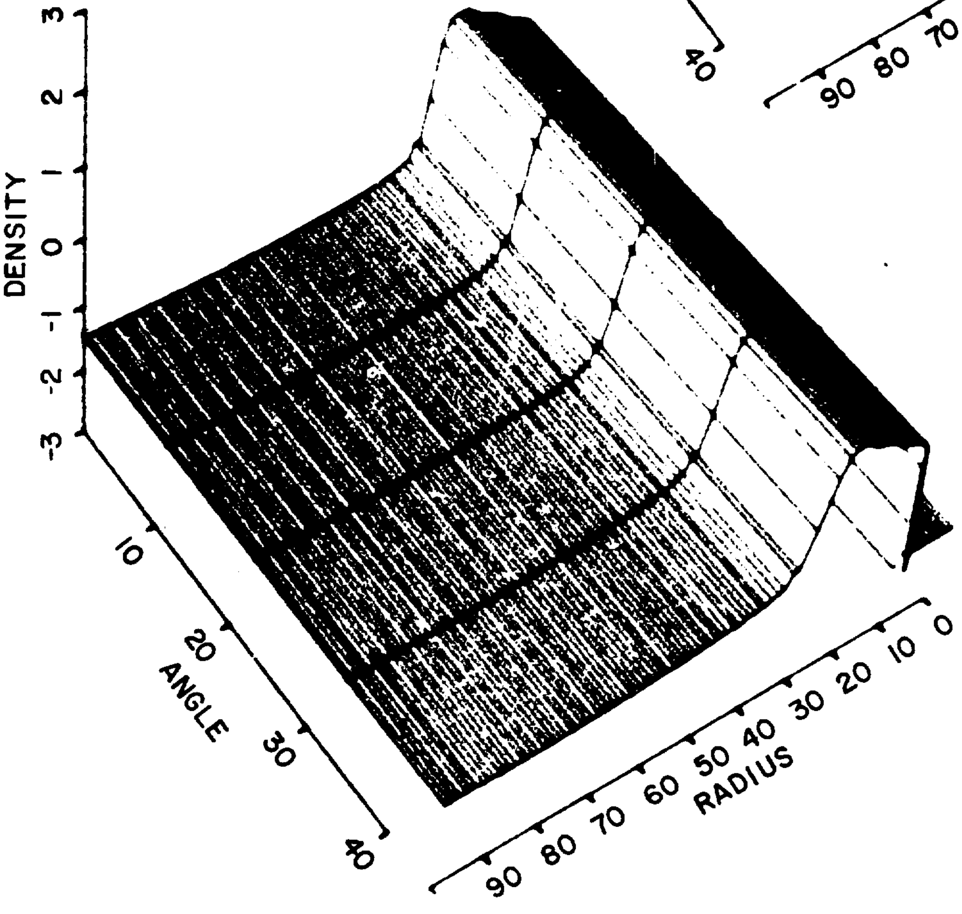

Fig. VI-19. Imploding shell just before hitting the origin of coordinates.

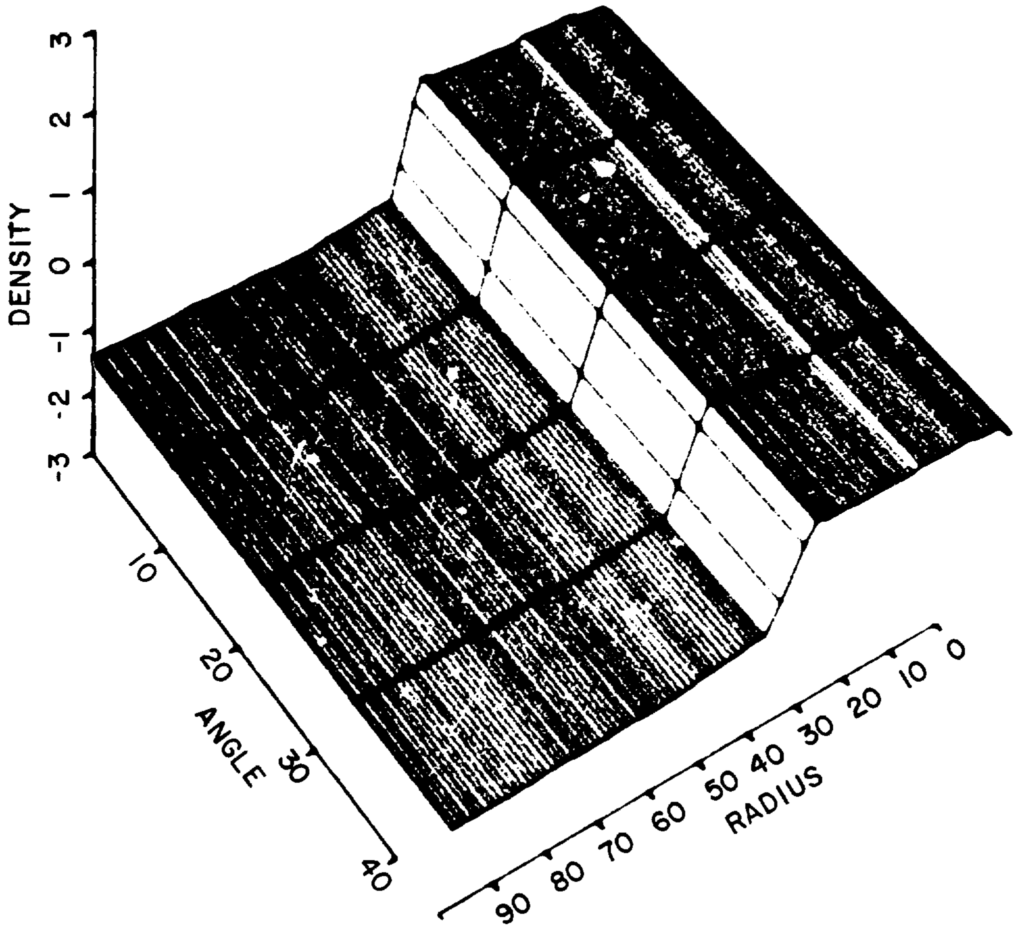

Fig. VI-20. Shell after rebound from the origin.

In this problem we tested the capabilities of ORBEOS in the radial direction without introducing the complications of angular motion. Reflection of the shocks at the origin of coordinates was of particular interest.

Spitting Cone. A cone of 45° half-angle (that is, θ_{max}) was chosen with a constant density of 1.0 g/cm^3 throughout. The temperature in a sheet between $\theta = 25°$ and $\theta = 45°$, running from $r = 0$ to $r = r_{max}$ on the outside of the cone, was chosen to be 25 times higher than the temperature inside this hot sheet. Again, an ideal gas was chosen as the computational medium. This initial configuration leads to an implosion of the gas in the hot sheet towards the axis of rotational symmetry, $\theta = 0°$. The imploding shock reaches the axis of rotational symmetry near the origin first and proceeds outward in r toward r_{max}, hence, the name Spitting Cone. Figures VI-21, VI-22, and VI-23 show the time evolution of this system.

The number of computational points in the radial direction was 26, whereas in the angular direction 25 points were used. The increments in radius and angle were uniform and equal to $\Delta r = 1$ μm and $\Delta\theta = 1.87°$, respectively. In this problem we tested the capabilities of ORBEOS in both the angular and radial direction. We were particularly interested in how the code handled shocks reflected at the axis of rotational symmetry. The boundary condition at r_{max} was reflecting.

Imploding Sphere with Perturbations. A shell was assumed to implode a low-density gas. However, the shell contained a Taylor-unstable sinusoidal perturbation in radius on its outside surface. This problem models the Taylor instability in a converging spherical system. An

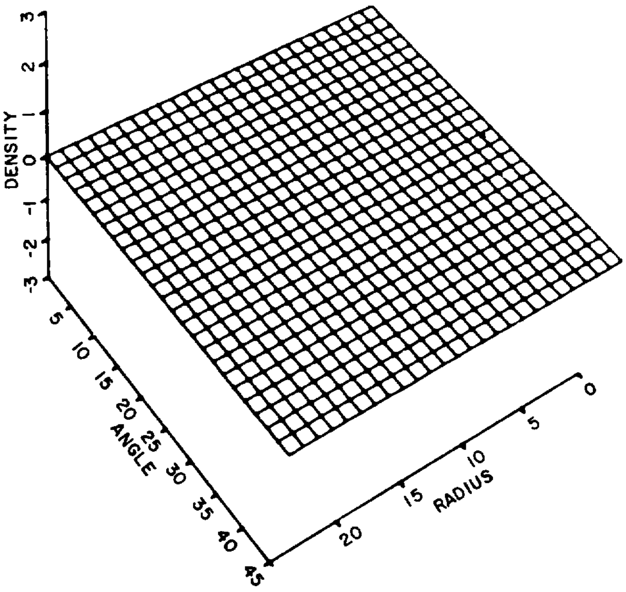

Fig. VI-21. Initial density configuration of the spitting cone problem.

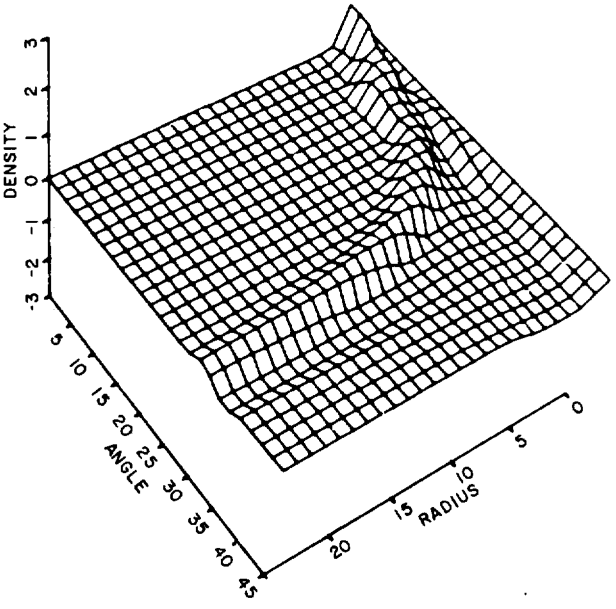

Fig. VI-22. Shock wave just reaching the axis of rotational symmetry near the origin of coordinates; note the structure of the axially directed shock.

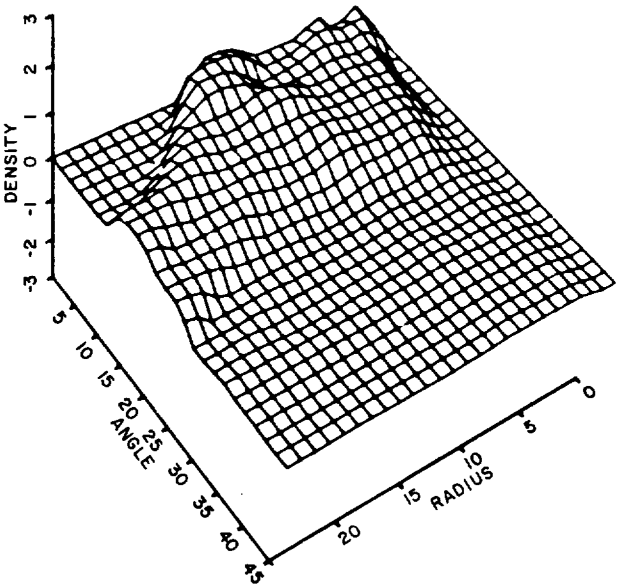

Fig. VI-23. Axial shock propagating along the axis of rotational symmetry.

aluminum equation of state was chosen for the computational medium. The maximum angle θ_{max} was 90° so that the reflecting boundary condition on the surface θ_{max} was physical; this represents a simulation of a full sphere. The maximum radius was 50 μm. The computational grid contained 51 equally spaced points in radius and 36 equally spaced points in angle (that is, $\Delta r = 1$ μm and $\Delta\theta = 2.57°$).

The initial fluid density on the mesh is given algebraically as

$$\rho = \frac{0.02\ \mathrm{g}}{\mathrm{cm}^3}\ , \quad r < 36\ \mu\mathrm{m}$$

$$\rho = \frac{1.0\ \mathrm{g}}{\mathrm{cm}^3}\ , \quad 36 \leq r \leq 39\ \mu\mathrm{m}$$

$$\rho = \frac{(0.1,\ \rho_\theta)\ \mathrm{g}}{\mathrm{cm}^3}\ , \quad 39 < r \leq 50\ \mu\mathrm{m}\ ,$$

where

$$\rho_\theta = \exp\left\{ r \left[1 - 0.022 \cos\left(\frac{6\pi\theta}{\theta_{max}} \right) \right] - \frac{39^2}{D^2} \right\}\ ,$$

and

$$D = \frac{5.0}{\sqrt{-\ell n}}\ (0.1)\ \mu\mathrm{m}\ .$$

The initial pressure was

$$P = 0\frac{\mathrm{Jk}}{\mathrm{cm}^3} \qquad r \leq 39\,\mu\mathrm{m} \ ,$$

$$P = 1.0 \times 10^{-4}\frac{\mathrm{Jk}}{\mathrm{cm}^3} \qquad 39 < r \leq 50\,\mu\mathrm{m} \ ,$$

and the boundary condition at $r_{\max}$ was reflecting.

The wavelength of the initial perturbation was ~21 μm. Figure VI-24 shows the initial density profile. As the system evolved, the perturbations grew in amplitude as seen in Figs. VI-25 through VI-27.

A diagnostic was introduced into the code specifically for this problem:

$$\alpha = \frac{\int \rho U_r^2\, dv}{\int \rho (U_r^2 + U_\theta^2) dV} \ ,$$

which is the ratio of total radial kinetic energy to total kinetic energy. In this problem, even though the fingers appear to have grown to large amplitude, the smallest value of α was ~0.97. This means that only 3% of the total kinetic energy was in the angular direction; therefore, the structures form predominantly because of differences in the radial momentum at different angles.

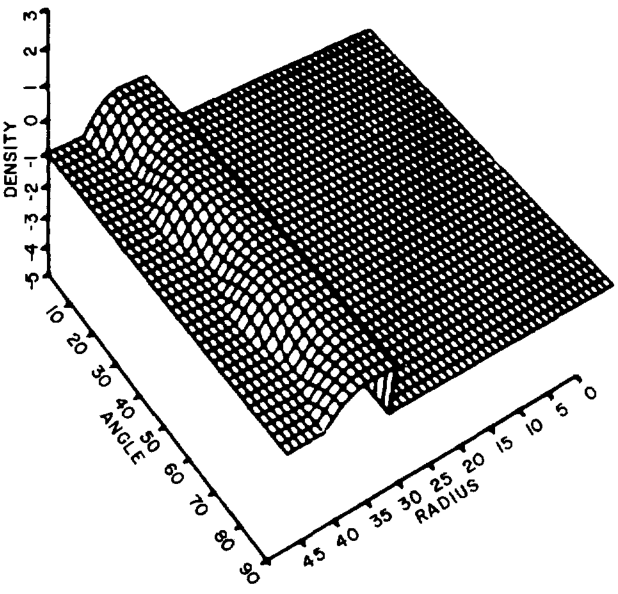

Fig. VI-24. Initial density configuration for imploding spherical shell with perturbations.

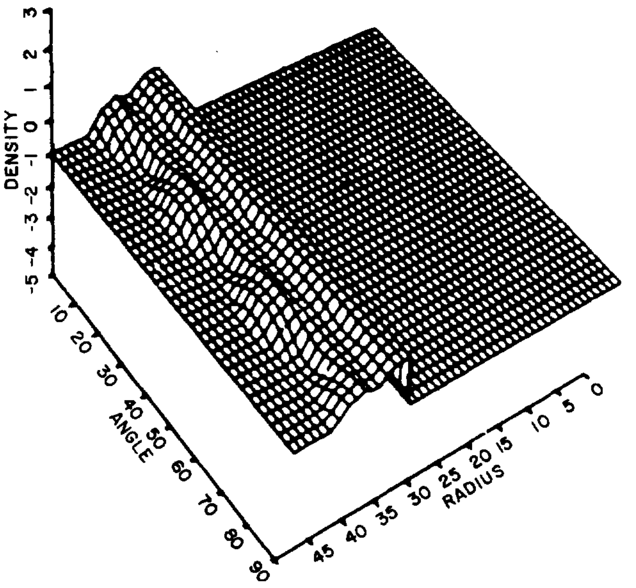

Fig. VI-25. Shell after passage of shock.

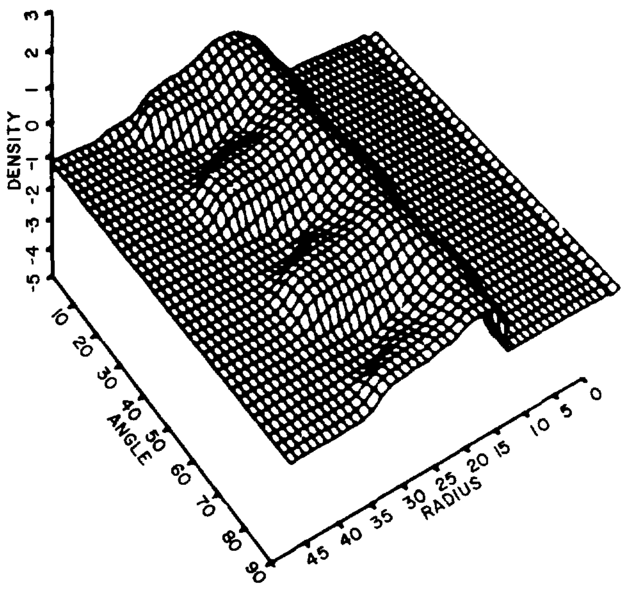

Fig. VI-26. Development of Taylor instability on outside of shell.

Adaptive Zoning for Singular Problems in Two Dimensions (J. U. Brackbill, J. G. Saltzman)

Introduction. Winslow's method[21] for the automatic generation of computation meshes is extended to give discretionary control of the variation of zone sizes and orthogonality of grid lines in the resulting mesh. The additional control is used to adapt the mesh to the problem thereby increasing the accuracy of the result.

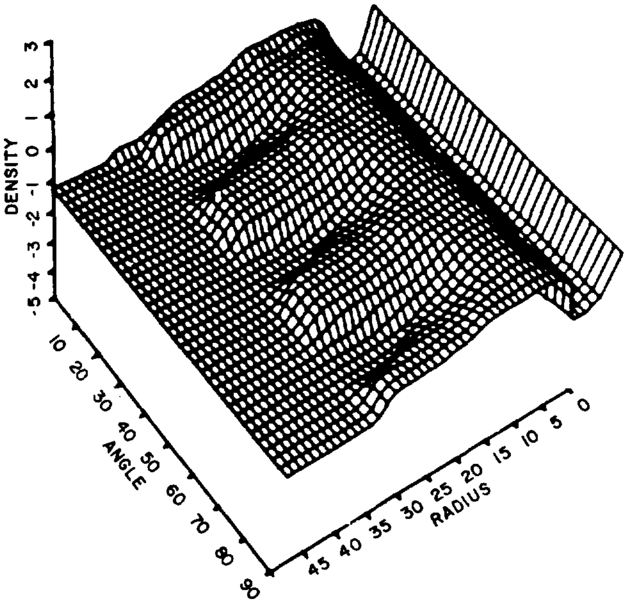

Fig. VI-27. Compare size of Taylor spikes at this later time with those in Fig. VI-26.

Winslow formulates the zoning problem as "a potential problem with the mesh lines playing the role of equipotentials."[21] The formulation requires the solution of a nonlinear, Poisson-like equation to generate a mapping from a regular domain in a parameter space to an irregularly shaped domain in physical space. By connecting points in the physical space that correspond to discrete points in the parameter space, the physical domain can be covered with a computation mesh suitable for solving difference equations.

Winslow's method is widely used, especially for exterior flow problems. His method has received attention from Godunov[22] and from Thompson et al.,[23] among others. Godunov devised an algorithm for generating meshes for initial boundary value problems, in which changes in the boundary data are reflected in changes in the mesh. Thompson developed a method for generating body-fitted coordinates in multiply connected domains. The popularity of these methods arises primarily from their usefulness in giving accurate, numerical representation of the boundary geometry. For example, when calculating flow past an airfoil, the geometry of the boundary is important and its accurate representation is essential to the accuracy of the overall calculation. Thompson's adaptation of Winslow's method makes shaping the boundary convenient.

However, if resolution within the boundary layer in

Fig. VI-24. Initial density configuration for imploding spherical shell with perturbations.

of many flow problems, an embedded region with strong gradients were to develop, then control of the spacing of the mesh far from the boundaries becomes as desirable as accurate representation of the boundary geometry. In reaction diffusion processes, in resistive, magnetohydrodynamic (MHD) flow, and in shocked flows, singular regions may develop far from the boundaries. For these conditions, new methods must be developed that somehow adapt to the data in the interior as well as conform to the shape of the boundaries.

Constructing adaptive mesh generators, those which alter themselves in response to changes in the data, is an area of current interest.[24-30] In many recent studies, adaptability results from source terms added to the potential equations. For example, terms may be added to control the spacing of zones along grid lines to increase resolution in regions of strong gradients.[25] In others, zones are added to regions of the mesh to distribute the error equally.[30]

These studies have shown the value of adaptive zoning, and applications have shown the usefulness of mesh generators of Winslow's type.[31-32] To devise a mesh generator appropriate for arbitrarily shaped domains that both maintain logical connectivity and adapt to the data, the ideas of Winslow[21], Browne,* and Barfield[33] have been combined in a variational formulation similar to the penalty method.[34]

The unifying idea is that a mesh generator can be formulated to optimize several measurable properties of the computation mesh simultaneously. Optimizing smoothness,[21] orthogonality,[33] and the variation in cell volumes give the interior control of the mesh needed for adaptive zoning. The user retains discretion in determining the relative importance given to optimizing each of these properties, or other properties controlled in the same way; this allows the user to fit the adaptive mesh to the problem.

The Mesh Generator. To solve finite-difference equations on a computation mesh, the data are typically stored in ordered arrays of numbers $\phi(i,j)$ in which the indices, $i = 1, \ldots, M$; $j = 1, \ldots, N$, give not only the location of the data in computer memory, but also the physical relationship between the data at one vertex $\underset{\sim}{x}(i,j)$ and another $\underset{\sim}{x}(i',j')$. For example, in a mesh of quadrilateral cells, the neighbors of $\underset{\sim}{x}(i,j)$ are $\underset{\sim}{x}(i+1,j)$, $\underset{\sim}{x}(i,j+1)$, $\underset{\sim}{x}(i-1,j)$, and $\underset{\sim}{x}(i,j-1)$.

---

*From information provided by P. Browne, Los Alamos

additional control is used to adapt the mesh to the problem thereby increasing the accuracy of the result.

In formulating the mesh generator problem mathematically, it is useful to view the mesh, whose vertices are $\underset{\sim}{x}(i,j)$, as the image of a mapping $\underset{\sim}{x}(\xi,n)$ in which only the points corresponding to integer values of the natural coordinates, ξ and η, are realized. (Conversely, the image of a computation mesh of quadrilateral cells is a uniform, rectilinear mesh in ξ,η space with spacing $\Delta\xi = \Delta\eta = 1$.) A mesh generator determines the mapping $\underset{\sim}{x}(\xi,\eta)$.

We have observed that the differential properties of the mapping determine the properties of the computation mesh. For example, $[(\partial x/\partial\xi)^2 + (\partial y/\partial\xi)^2]^{1/2}$ along a level curve of η is related to mesh spacing between vertices with the same index j. Similarly, the volume of computational cells is related to the Jacobean J of the mapping,

$$J = \frac{\partial x}{\partial\xi}\frac{\partial y}{\partial\eta} - \frac{\partial x}{\partial\eta}\frac{\partial y}{\partial\xi} \quad , \tag{VI-20}$$

and the orthogonality of the mesh is related to the scalar, $\nabla\xi\cdot\nabla\eta$, which is zero when conjugate lines of the mesh are orthogonal.

We can write integrals over the computation mesh to measure these properties of the mapping. The global smoothness of the mapping (the variation in mesh spacing along level curves of ξ and η) is measured by the integral,

$$I_s = \int_D [(\nabla\xi)^2 + (\nabla\eta)^2]\, dV \ . \tag{VI-21}$$

The orthogonality of the mapping is measured by

$$I_0 = \int_D (\nabla\xi \cdot \nabla\eta)^2\, dV \ , \tag{VI-22a}$$

or the volume-weighted measure,

$$I_0' = \int_D (\nabla\xi \cdot \nabla\eta)^2 J^3\, dV \ , \tag{VI-22b}$$

and the weighted-volume variation is measured by,

$$I_v = \int_D wJ\, dV \ , \tag{VI-23}$$

where $w = w(x,y)$ is a given function.

Of course, if a property can be measured, it can be controlled. The smoothest mapping can be obtained by minimizing I_s, the most orthogonal mapping by minimizing I_0', and the mapping with specified variation of J by minimizing I_v. However, it is not possible to minimize I_0' or I_v separately, because the solutions to the corresponding minimization problems do not have unique solutions. Thus, to formulate minimization problems with unique solutions, the minimization of I_0' or I_v is combined with I_s (which has a unique solution[23]), as in the penalty method.[35] That is, the integral I is minimized, where

$$I = I_s + \lambda_v I_v + \lambda_0' I_0' \ ,$$

with $\lambda_v > 0$, $\lambda_0' \geq 0$. Numerical solutions that minimize I are obtained for finite values of λ_v and λ_0'.

By interchanging dependent and independent variables, we have derived the Euler equations for the integrals Eqs. (VI-21), (VI-22a), (VI-22b), and (VI-23).

To generate a mapping, finite-difference approximations to the Euler equations are solved by iteration. Because (ξ,η) are continuous variables that take on integer values at the nodes of the computation mesh, they form a uniformly spaced, rectilinear grid in parameter space. The derivatives with respect to the independent variables are easily computed on this grid. Algebraic equations at each node result from substituting the differences for derivatives. The system of equations is solved by a Gauss-Seidel iteration, which continues until the residual errors are everywhere less than the maximum allowed error.

Numerical Examples. The effect of minimizing $I_s + \lambda_v I_v$ rather than I_s alone (Winslow's mesh generator) is illustrated by a simple numerical example. With w given by

$$w = \left[\sin\left(\frac{2\pi x}{X}\right)\sin\left(\frac{2\pi y}{Y}\right) + 1 + \frac{1}{r}\right] \ , \tag{VI-24a}$$

where X and Y are the periodic lengths in x and y, and $2r(\geq 1)$ is the ratio of the maximum to minimum value of the weight function, meshes are generated with periodic boundary conditions for a sequence of λ_v, $0 \leq \lambda_v \leq 16$. With $X = Y = 1$, $M = N = 50$, and $\lambda_v = 0$, Winslow's generator gives the uniform, rectilinear mesh shown in Fig. VI-28. With $r = 100$ and $\lambda_v = 4$, Winslow's generator plus the volume modifier gives the mesh shown in Fig.

VI-29. In the modified mesh, where w is large $[(x,y) = (1/4,1/4)]$, the cells are small; where w is small $[(x,y) = (3/4,3/4)]$, the cells are large.

The results with several values of λ_v, $0 \le \lambda_v \le 16$ are summarized in Fig. VI-30, where I_s, I_v, and the maximum and minimum cell volumes are plotted for a mesh with $r = 100$ and $M = N = 25$. As λ_v increases, I_v, which measures the variance in wJ^2 over the mesh, decreases as the solution $wJ^2 = \text{const}$ is approached. Correspondingly, the maximum cell volume increases and the minimum decreases, although the asymptotic value of the minimum seems to be reached for smaller values of λ_v, and the ratio, V_{max}/V_{min}, approaches the prescribed value, $\sqrt{2r}$, as shown in Table VI-II. However, I_s, which measures the smoothness of the mapping, increases with increasing λ_v. As expected, volume variation is obtained at the expense of smoothness.

Similar control of the volume variation is obtained nearly independently of the direction of variation of w with respect to the principal directions. When w is given by

$$w = \sin\left(\frac{2\pi x}{X}\right) + 1 + \frac{1}{r}\,, \qquad \text{(VI-24b)}$$

with $\lambda_v = 2$ and $r = 100$, the mesh shown in Fig. VI-31(a) results. The cell volumes vary only in the x-direction, with a maximum volume of 2.94 (relative to the unweighted cell volume) and a minimum of 0.59 for a ratio

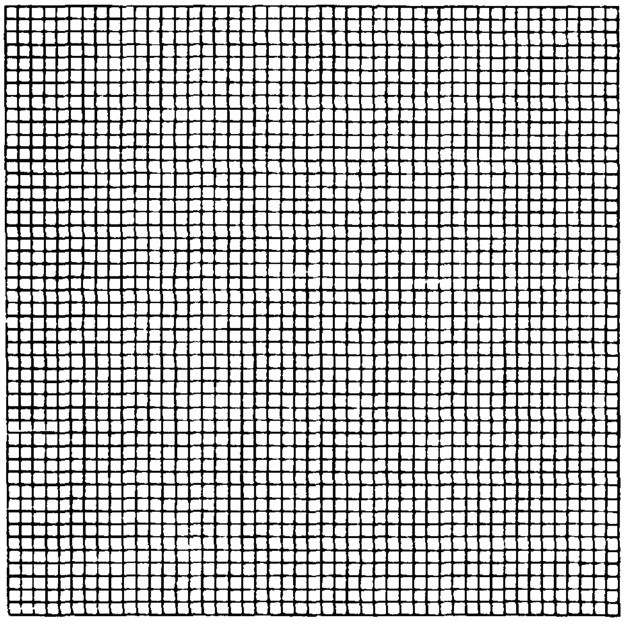

Fig. VI-28. On a square domain with uniformly spaced points on the boundary, minimizing I_s gives a uniform, rectilinear mesh.

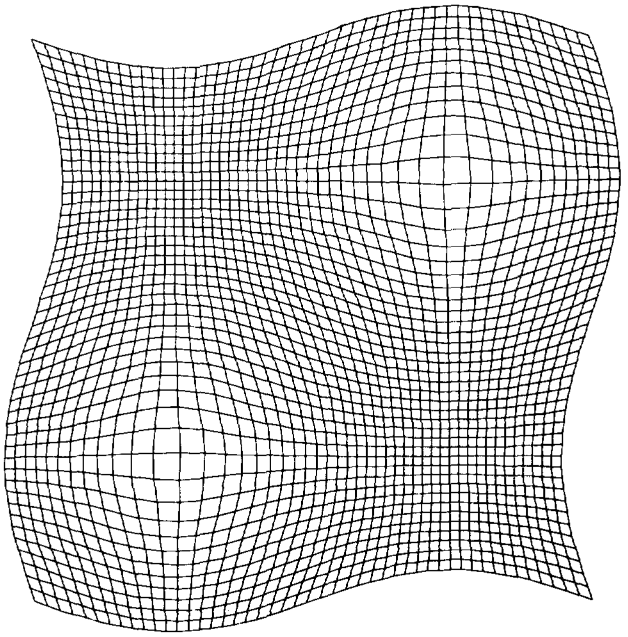

Fig. VI-29. Minimizing $I_s + \lambda I_v$ with $r = 100$, $\lambda_v = 4$, and periodic boundary conditions.

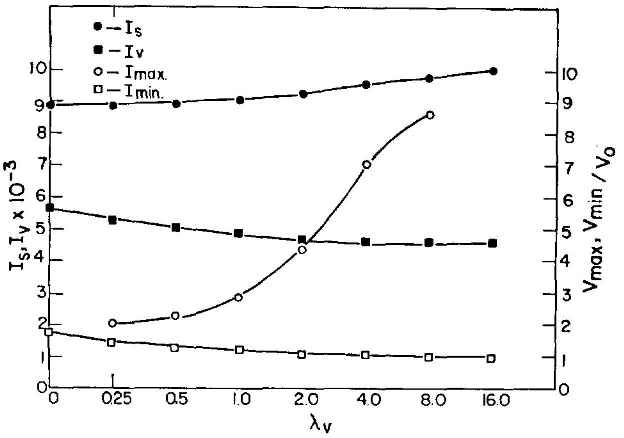

Fig. VI-30. The values of I_s, I_v, and the maximum and minimum cell volumes are plotted for various values of I_v. V_{min} decreases less than V_{max} increases from its value for $\lambda_v = 0$.

TABLE VI-II. Influence of λ_v on Cell Volume[a]

λ_v	V_{max}	V_{min}	V_{max}/V_{min}
0.00	1.74-3	1.74-3	1.00
0.25	2.01-3	1.43-3	1.41
0.5	2.28-3	1.30-3	1.75
1.0	2.89-3	1.17-3	2.47
2.0	4.36-3	1.06-3	4.11
4.0	7.06-3	9.85-4	7.17
8.0	8.60-3	9.40-4	9.15
16.0	---	9.04-4	---

[a] I/J = 25/25, r = 100.

of maximum to minimum equal to 4.98. (This is one-third the prescribed ratio $\sqrt{2r}$ between maximum and minimum value.) When w is given by

$$w = \sin\left[\frac{4\pi(x+y)}{(X+Y)}\right] + 1 + \frac{1}{r} , \qquad \text{(VI-24c)}$$

so that w varies along the diagonal of the mesh, the mesh shown in Fig. VI-31(b) results with $\lambda_v = 2$ and r = 100. The cell volumes vary along the diagonal of the mesh, with a maximum volume of 2.75 and a minimum of 0.62 for a ratio of maximum to minimum equal to 4.43. The 10% difference between this and the ratio above supports the conclusion that the ability to control volume is not strongly dependent on the direction of the gradient in w relative to the principal directions. We also note that by direct measurement, the ratio of the minimum distance between vertices along the gradient of w in Fig. VI-31(a) to the corresponding distance (along the diagonal) in Fig. VI-31(b) is $1/\sqrt{2}$, exactly the ratio one would obtain on a rectilinear mesh between the side and the diagonal.

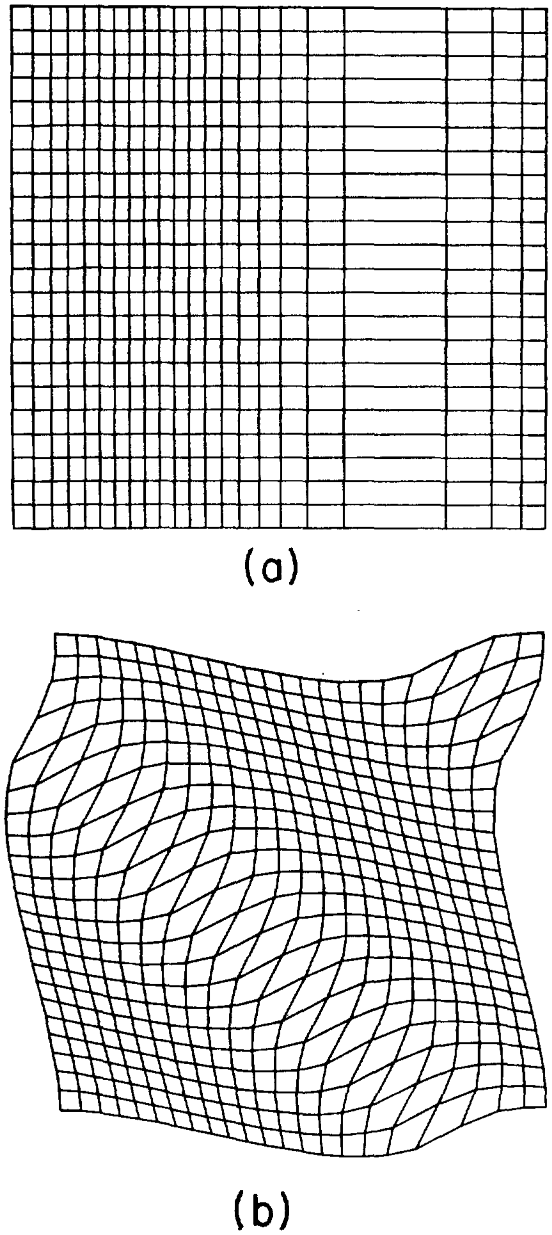

Fig. VI-31. The responsiveness of the volume control is nearly independent of the gradient direction of the weight function relative to the principal directions. The volume variation in (a), with w = f(x), is the same as in (b), with w = f(x + y).

Finally, to determine how closely the computed ratio of cell volumes can be made to approach the prescribed value, λ_v is made as large as possible. The solution to the minimization problem using $\lambda_v \rightarrow \infty$ is not unique. However, only numerical solutions can show how large λ_v can be. With w given by Eq. (VI-24), M = N = 25, λ_v = 16, the mesh shown in Fig. VI-32(a) is obtained. The largest cells in the mesh are distorted, and the iteration does not converge. The maximum volume fluctuates from cycle to cycle even though I_v, I_s, and the minimum volume are nearly constant. However, with I = J = 99 and λ_v = 16, the solution shown in Fig. VI-32(b) is obtained. In this case the iteration converges. The difference between the two cases is the number of zones; therefore, the largest value of λ_v for which solutions can be obtained successfully is influenced by numerical accuracy, but seems to be $\lambda_v \leq O(10)$.

The effect of minimizing $I_s + \lambda_0 I_0$ rather than I_s alone is illustrated by the solutions depicted in Figs. VI-33 and VI-34. A mesh has been generated for $\lambda_0 = 0$, using

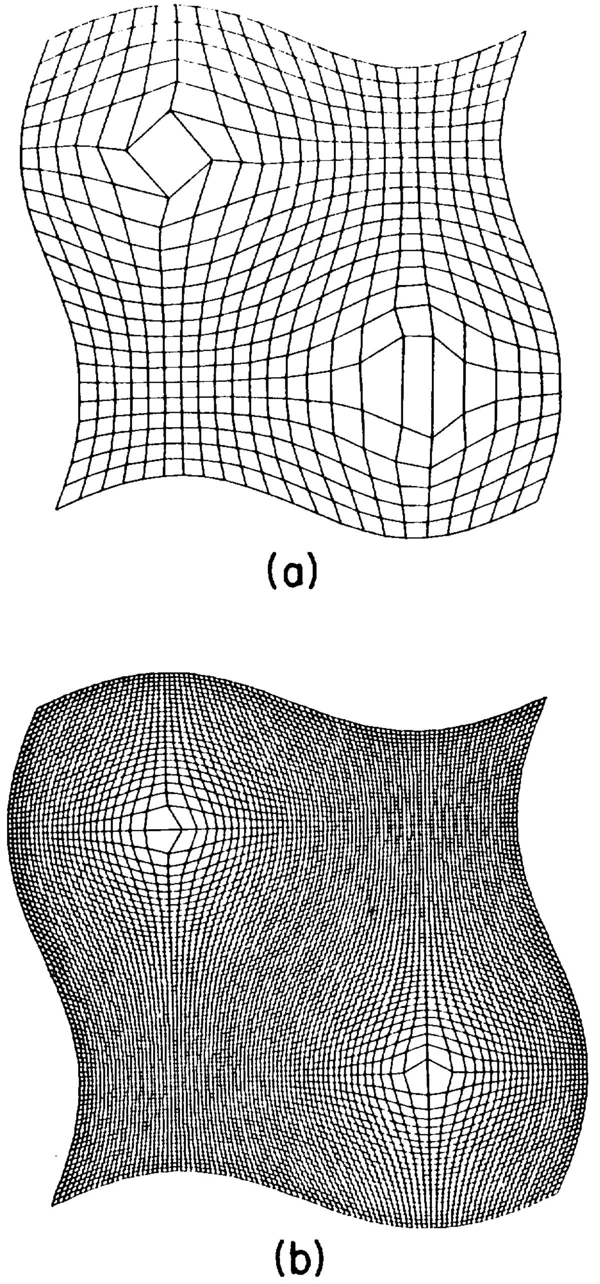

Fig. VI-32. The maximum value of λ_v is influenced by the number of cells in the mesh. When $\lambda_v = 16$, a solution is obtained with the 99 x 99 mesh in (b) but not with the 25 x 25 mesh in (a).

Winslow's generator with Dirichlet boundary conditions and is shown in Fig. VI-33(a). Because the boundaries are skew, the intersections of mesh lines are also skew. Increasing λ_0 to 1000 results in the mesh shown in Fig. VI-33(b), where the intersections of mesh lines appear to be more nearly orthogonal. The mesh is increasingly orthogonal as λ_0 is increased, a fact demonstrated by the

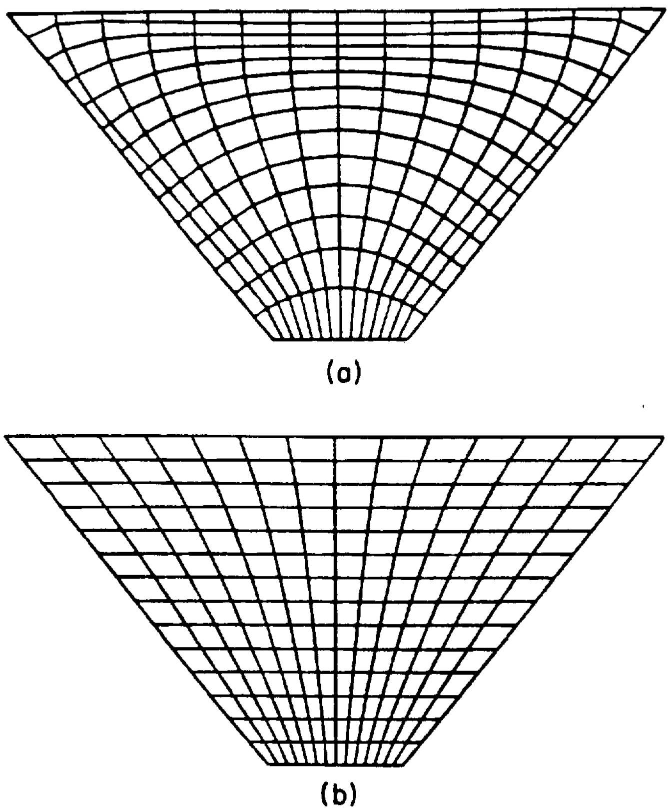

Fig. VI-33. When $I_s + \lambda_0 I_0'$ is minimized, the mesh is made more orthogonal: (a)$\lambda_0 = 0$; (b)$\lambda_0 = 10^3$.

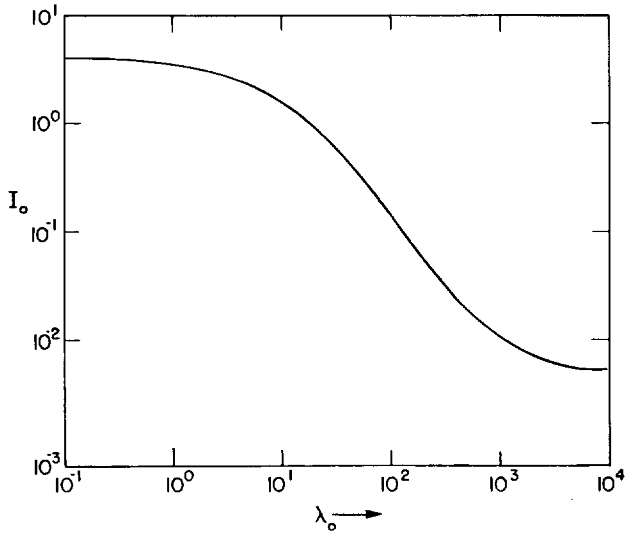

Fig. VI-34. Corresponding to the meshes shown in Fig. VI-33, I_0' decreases as λ_0 increases.

results shown in Fig. VI-34, where the variation of I_0' with λ_0 is plotted. As λ_0 increases from 0 to 10 000, I_0 decreases from 4 to 0.006. Thus, the minimization appears to have the desired effect.

When $I_s + \lambda_v I_v + \lambda_0 I_0'$ is minimized, increasing λ_0 from zero decreases the skewness of the mesh. With w given by Eq. (VI-24), $M = N = 50$, $\lambda_v = 4$, and $\lambda_0 = 0$; the mesh shown in Fig. VI-35(a) is obtained. The largest zones are quite skew. When $\lambda_0 = 1$, the mesh shown in Fig. VI-35(b) results, and the skewness is considerably reduced. However, the maximum zone size is reduced, so that the decrease in skewness is accompanied by a decrease in volume control.

The Adaptive Mesh. The mesh generator described above will now be made part of an algorithm to adapt a computation mesh dynamically to data generated by the solution of finite-difference equations. It will be shown that adapting the mesh reduces numerical error when the resolution of gradients is improved.

To develop the adaptive algorithm, consider Burger's equation in one dimension,

$$\frac{\partial u}{\partial t} + (u + V)\frac{\partial u}{\partial x} - \kappa\frac{\partial^2 u}{\partial x^2} = 0 ,$$

where κ and $V > 0$ are constant. A steady solution to Burger's equation is given by

$$u = \frac{u_0}{2}(g^- - g^+) ,$$

where g^- and g^+ are written

$$g^- = \frac{1}{1 + \exp[-u_0(x - Vt)/\kappa]} ,$$

and

$$g^+ = \frac{1}{1 + \exp[u_0(x - Vt)/\kappa]} .$$

This solution corresponds to a progressing wave propagating in the positive x-direction with speed V_0.

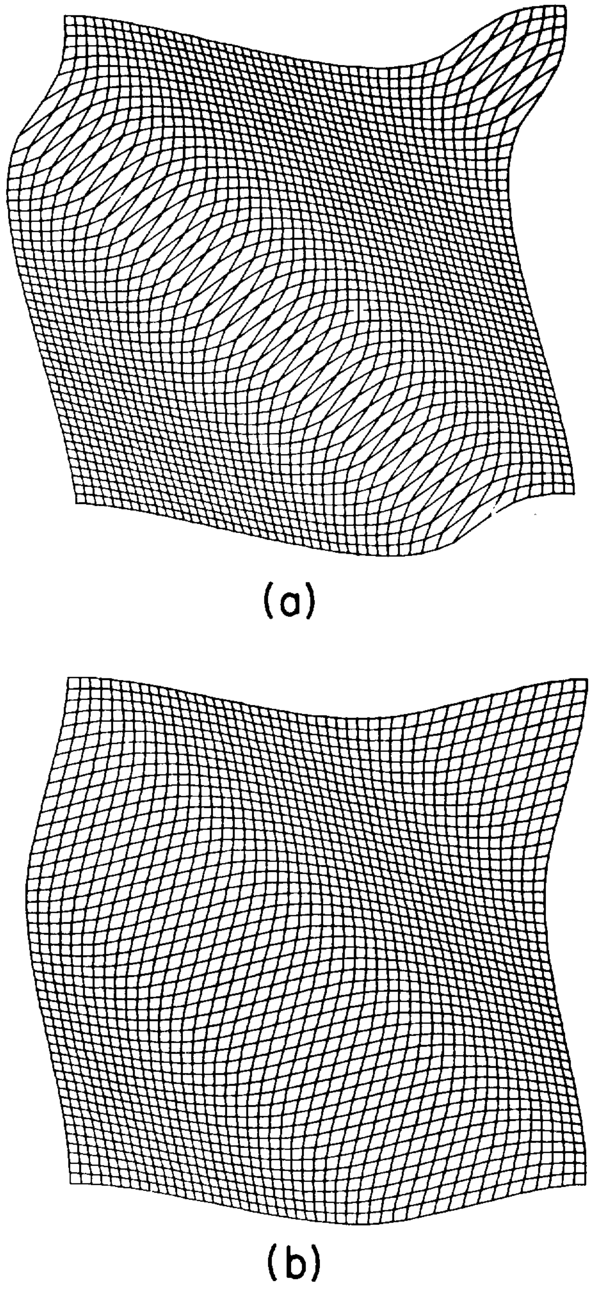

Fig. VI-35. Increasing λ_0 decreases the skewness of the mesh; compare (a) $\lambda_0 = 0$ with (b) $\lambda_0 = 1$.

The solution above is typical for a singular perturbation problem because, as $\kappa \rightarrow 0$, it becomes constant everywhere except at $(Vt - \kappa/u_0) < x < (Vt + \kappa/u_0)$. The derivative of u, written

$$\frac{\partial u}{\partial x} = \frac{u_0^2}{\kappa} g^+ g^- ,$$

becomes large as κ becomes small. In fact, all higher derivatives of u become very large, because

$$\frac{\partial^n u}{\partial x^n} = 0(\kappa^{-n}) \ .$$

There are obvious difficulties in treating problems of this type numerically, because the truncation error becomes very large as $\kappa \longrightarrow 0$. This is clearly seen by considering a typical finite-difference approximation to the derivative,

$$\frac{\partial u}{\partial x} \cong \frac{u_{i+1} - u_{i-1}}{x_{i+1} - x_{i-1}} \ .$$

The truncation error, which is estimated by substituting the correct solution into the difference equation and expanding about $u(x_i)$, can be written

$$\begin{aligned}\epsilon &= \left(\frac{u_{i+1} - u_{i-1}}{x_{i+1} - x_{i-1}} - \frac{\partial u}{\partial x} \right) \\ &= \left\{ \frac{1}{2} \frac{\partial^2 u}{\partial x^2} \frac{(\nabla + \delta)^2 - (\nabla - \delta)^2}{\nabla} \right. \\ &\quad + \frac{1}{6} \frac{\partial^3 u}{\partial x^3} \frac{(\nabla + \delta)^3 + (\nabla - \delta)^3}{\nabla} \\ &\quad \left. + \cdots + \frac{1}{n!} \frac{\partial n^u}{\partial x^n} \frac{(\nabla + \delta)^n - [-(\nabla - \delta)]^n}{\nabla} + \cdots \right\} ,\end{aligned}$$

where

$$\nabla = \frac{1}{2}(x_{i+1} - x_{i-1}) \ ,$$

and

$$\delta = \frac{1}{2}[(x_{i+1} - x_i) - (x_i - x_{i-1})] \ .$$

The derivatives can be evaluated from the recursion relation that satisfies the steady solution to Burger's equation:

$$\frac{\partial^2 u}{\partial x^2} = \frac{u}{\kappa} \frac{\partial u}{\partial x} \ .$$

For a nonadaptive mesh with constant spacing, the mesh interval ∇ can be written in terms of a grid Reynolds number

$$R_e \equiv \frac{u_0 V}{\kappa} \ .$$

At the symmetry point, u = 0, where $\partial u/\partial x$ is largest, the error is given by

$$\epsilon = \left(\frac{\partial u}{\partial x} \right) \left[\frac{\sin h\,(R_e) - R_e}{4R_e} \right] \ . \qquad \text{(VI-25)}$$

As $\kappa \longrightarrow 0$, $\epsilon = \alpha \exp(R_e)$, and if at least one point in the mesh lies in the interval $(Vt - \kappa/u_0) < x < (Vt + \kappa/u_0)$, ϵ becomes very large. This error is caused by the fact that the narrow region at which $\partial u/\partial x$ is large is not resolved when $R_e > 1$.

In contrast, the error on an adaptive mesh generated by minimizing the weighted volume variation with w, given by

$$w = \left[\frac{1}{(u + u_0)} \frac{\partial u}{\partial x} \right] \qquad ,$$

scales differently. In one dimension, the resolution of the singular region is improved because $J = x_\xi$, minimizing the integral I_v, *and thereby minimizes* x_ξ, where $\partial u/\ell x$ is large.

The effect of varying x_ξ on the truncation error is estimated by repeating the analysis above. The mesh spacing is given by

$$\left(\frac{\partial u}{\partial x} \right)^2 x_\xi^2 = c(u + u_0)^2 \ .$$

The constant of integration c is determined by the number N of mesh points in the computational domain, $-X \leq x \leq X$, which is given by

$$\begin{aligned}N &= \int_{-X}^{X} \xi_x' dx' \\ &= \frac{2u_0}{\kappa \sqrt{c}} \int_{-X}^{X} \left[\frac{g^+ g^-}{(g^- - g^+) + 2} \right] dx \ .\end{aligned}$$

The integral is everywhere positive, and for $u_0X \gg \kappa$, is given by

$$N \cong \frac{2}{\sqrt{c}} \ .$$

At the symmetry point where $u = 0$, x_ξ is given by

$$x_\xi = \frac{4\kappa}{u_0N} \ .$$

By differentiation, one finds that

$$\frac{\partial^n x}{\partial \xi^n} = 0(\kappa^n) \quad , \quad n \text{ odd} \ ,$$

and

$$\frac{\partial^n x}{\partial \xi^n} = 0 \quad , \quad n \text{ even} \ .$$

Thus, it will not alter the scaling of the truncation error if the substitution

$$x_\xi^{n-1} = \frac{(\nabla + \delta)^n - [-(\nabla - \delta)^n]}{\nabla}$$

is made. With this approximation, the truncation error is given by

$$\epsilon = \frac{1}{4}\left(\frac{\partial u}{\partial x}\right)\sum_m \frac{1}{(2m+1)!}\left(\frac{1}{N}\right)^{2m} \ .$$

In contrast to the error for the nonadaptive grid, Eq. (VI-25), the error for the adaptive grid does not increase as $\kappa \to 0$.

The conclusion one can draw from this simple example is that, by the proper choice of volume weight function, the effect of the singular nature of the solution on numerical truncation error can be mitigated. This is true in two dimensions as well.[35]

Conclusion. This description of work on adaptive meshes is necessarily incomplete. Among the areas not covered for which results exist, however, are the application of the adaptive mesh to time-dependent problems[35,36] and its extension to three dimensions and to non-Cartesian coordinates.

There are also many unanswered mathematical questions. For example, is the difficulty in obtaining solutions for large λ_0 and λ_v mathematical or numerical in origin? For more complicated systems of equations, how can the choice of weight functions to minimize error be tested a priori?

In spite of all the areas not discussed, a systematic method for measuring desirable mesh properties using several integral measures has been presented. By forming a variational principle using linear combinations of the integral measures, a system of partial differential equations can be derived. These equations were solved numerically by using a relaxation algorithm. The effect of each term in the variational principle on the mesh has been demonstrated. The ability of the mesh technique to resolve singular problems in one dimension was also shown.

REFERENCES

1. G. S. Fraley, E. J. Linnebur, R. J. Mason, and R. L. Morse, "Thermonuclear Burn Characteristics of Compressed Deuterium-Tritium Microspheres," Phys. Fluids **17**, 474 (1974).

2. E. J. Stoval [see S. Glasstone and R. H. Lovberg, *Controlled Thermonuclear Reactions*, (Van Nostrand, Princeton, 1960), p. 20].

3. A. Peres, "Fusion Cross Sections and Thermonuclear Reaction Rates," J. Appl. Phys. **50**, 5569 (1979).

4. J. M. Kindel, K. Lee, and E. L. Lindman, "Surface Wave Absorption," Phys. Rev. Lett. **34**, 134 (1975). The references in this article are also useful. M. M. Mueller, "Enhanced Laser-Light Absorption by Optical Resonance in Inhomogeneous Plasma," Phys. Rev. Lett. **30**, 582 (1973). R. P. Godwin, "Optical Mechanism for Enhanced Absorption of Laser Energy Incident on Solid Targets," Phys. Rev. Lett. **28**, 85 (1972).

5. B. Bezzerides, S. J. Gitomer, and D. W. Forslund, "Randomness, Maxwellian Distribution, and Resonance Distribution," Phys. Rev. Lett. **44**, 651 (1980). K. Estabrook and W. L. Kruer, "Properties of Resonantly Heated Distribution," Phys. Rev. Lett. **40**, 42 (1978). D. W. Forslund, J. M. Kindel,

and K. Lee, "Theory of Hot-Electron Spectra at High Laser Intensity," Phys. Rev. Lett. 39, 284 (1977).

6. "Inertial Fusion Program, January 1—June 30, 1978," Frederick Skoberne, Compiler, Los Alamos Scientific Laboratory report LA-7587-PR (May 1980).

7. Roger B. Perkins and the Laser Fusion Program Staff, "Inertial Fusion Program, July 1—December 31, 1978," Los Alamos Scientific Laboratory report LA-7755-PR (November 1980).

8. R. J. Mason, "Monte Carlo (Hybrid) Suprathermal Electron Transport," Phys. Rev. Lett. **43**, 1795 (1979).

9. R. J. Mason, "Electron Transport in Laser Fusion Targets," in *Laser Interaction with Matter*, Vol. 5, H. Schwartz, H. Hora, M. Lubin, and B. Yaakobi, Eds. (Plenum, New York, 1981).

10. R. J. Mason, "Monte Carlo (Hybrid) Model of Electron Transport in Laser Plasmas," Proc. Informal Conf. on Particle and Hybrid Codes for Fusion, Napa, California, December 10-11, 1979, University of California, Berkeley, Electronics Research Laboratory memorandum UCB/ERL M79/79, paper 23.

11. R. J. Mason, "Monte Carlo Hybrid Modeling of Electron Transport in Laser Produced Plasmas," Phys. Fluids 23, 2204-2215 (1980).

12. R. J. Mason, "Full-Particle PIC-Collisional Calculations of Electron Transport in Laser Produced Plasmas," 1980 IEEE Int. Conf. on Plasma Science, Madison, Wisconsin, May 19-21, 1980, paper IB1.

13. R. J. Mason, "Full-Particle PIC-Collisional Calculations of Electron Transport in Laser Produced Plasmas," Proc. 10th Annual Anomalous Absorption Conf., San Francisco, California, May 28-30, 1980, paper A10.

14. A. B. Langdon, "Analysis of the Time Integration in Plasma Simulation," J. Comput. Phys. 30, 202 (1979).

15. R. L. Morse and C. W. Nielson, "Occurence of High Energy Electrons in the Blowoff of Laser Matter Interactions," Phys. Fluids 12, 2418 (1969).

16. S. T. Zalesak, "Fully Multidimensional Flux-Corrected Transport Algorithms for Fluids," J. Comput. Phys. 31, 335 (1979).

17. J. P. Boris and D. L. Book, "Flux-Corrected Transport I. SHASTA a Fluid Transport Algorithm That Works," J. Comput. Phys. 11, 38 (1973).

18. D. L. Book, J. P. Boris, and K. Hain, "Flux-Corrected Transport II. Generalizations of the Method," J. Comput. Phys. **18**, 248 (1975).

19. J. P. Boris and D. L. Book, "Flux-Corrected Transport III. Minimal Error FCT Algorithms," J. Comput. Phys. 20, 397 (1976).

20. D. Gottlieb, "Strang-type Difference Schemes for Multidimensional Problems," SIAM J. Numer. Anal. 9, 650 (1972).

21. A. M. Winslow, "Numerical Solution of the Quasilinear Poisson Equation in a Nonuniform Triangle Mesh," J. Comput. Phys. 1, 149 (1966).

22. S. K. Godunov and G. P. Prokopov, "The Use of Moving Meshes in Gas-Dynamical Computations," USSR Comp. Math. Phys. 12, 182 (1972).

23. Joe F. Thompson, Frank C. Thames, and C. Wayne Masten, "Automatic Numerical Generation of Body-Fitted Curvilinear Coordinate System for Field Containing Any Number of Arbitrary Two-Dimensional Bodies," J. Comput. Phys. 15, 299 (1974).

24. J. L. Steger and R. L. Sorenson, "Automatic Boundary Clustering in Grid Generation with Elliptic Partial Differential Equations," J. Comput. Phys. (to be published).

25. H. A. Dwyer, R. J. Kee, and B. R. Sanders, "An Adaptive Grid Method for Problems in Fluid Dynamics and Heat Transfer," AIAA J. **18**, 1205 (1980).

26. R. G. Hindman, Paul Kutler, and Dale Anderson, "A Two-Dimensional Unsteady Euler-Equation Solver for Flow Regions with Arbitrary Boundaries," in *Computational Fluid Dynamics Conference in Williamsburg, Virginia, July 23-25, Collection of Technical Papers,* AIAA publication A79-45251 19-34 (AIAA, New York, 1979), pp. 204-217.

27. T. H. Chong, "A Variable Mesh Finite Difference Method for Solving a Class of Parabolic Differential Equations in One Space Variable," SIAM J. Numer. Anal. 15, 4 (1978).

28. William Gropp, "A Test of Moving Mesh Refinement for 2-D Scalar Hyperbolic Problems," SIAM J. Sci. Stat. Comput. 1, 2 (1980).

29. R. J. Gelinas, S. K. Doss, and K. Miller, "Moving Finite Element Method: Applications to General Partial Differential Equations with Multiple Large Gradients," J. Comput. Phys. 40, 202 (1981).

30. I. Babuska and W. Rheinboldt, "Error Estimates for Adaptive Finite Element Computations," SIAM J. Numer. Anal. 15, 736 (1978).

31. D. C. Barnes, J. U. Brackbill, and W. Schneider, "A Numerical Study of High-Beta Stellarator Equilibria," Nucl. Fusion 21, 537 (1981).

32. Jeremiah U. Brackbill, "Numerical Magnetohydrodynamics for High Beta Plasmas," Methods Comput. Phys. 16, 1 (1976).

33. W. D. Barfield, "An Optimal Mesh Generator for Lagrangian Hydrodynamic Calculations in Two Dimensions," J. Comput. Phys. 6, 417 (1970).

34. R. Courant, "On a General Form of Plateau's Problem," Trans. Am. Math. Soc. 50, 40 (1941).

35. J. U. Brackbill and J. S. Saltzman, "Adaptive Zoning For Singular Problems in Two Dimensions," (LA-UR-81-405), submitted to J. Comp. Phys.

36. R. D. Milroy and J. U. Brackbill, "2-D Numerical Studies of a Field Reversed θ-pinch Plasma," Bull. Am. Phys. Soc. 25, 833 (1980).

VII. LASER FUSION TARGET FABRICATION

(R. J. Fries)

Our target fabrication effort, supported by extensive theoretical investigations, supplies pellets containing thermonuclear fuel for laser-driven compression and heating experiments, as well as simpler targets for basic physics experiments. These targets, which range from simple, deuterated, flat plastic films to complex multilayered structures containing cryogenic, solid DT fuel, are optimized for use with high-power CO_2 lasers. After a target design has been created by the theoreticians, we develop the new technologies to produce the materials, shapes, and properties desired and develop methods for measuring and characterizing all these properties. We then select or fabricate the target core, fill it with the desired thermonuclear fuel and diagnostic gases, and assemble the outer layers over it. Finally, we position the target in a target-insertion mechanism so that it will be at the precise laser focus spot in the target chamber.

INTRODUCTION (J. Booth, E. H. Farnum, R. J. Fries)

Our target fabrication effort has two objectives:

- to supply targets for the experimental program as needed, and
- to develop new techniques and materials for the fabrication of future thermonuclear compression targets.

In addition, we provide micromachining, microassembly, and materials-fabrication services to other groups.

Targets of various designs are produced for the first task: thermonuclear compression targets for main-sequence experiments, spatial and modified compression targets for target-essential experiments, and a wide variety of targets for supporting-physics experiments.

Because the design of these targets continually evolves, half of our effort is in the area of new technology: the development of new processes and techniques to produce new targets or improved materials that might be used in future target designs. However, accelerated experimental programs have shifted our emphasis to the fabrication of targets; approximately two-thirds of our personnel are now assigned to this effort. We also develop methods of measuring and characterizing these materials and assembling them into required configurations.

Our initial targets, called Sirius, were GMBs filled with DT gas at pressures up to 30 atm. In Sirius this simple shell acted as an exploding pusher in which the preheated fuel was compressed and further heated. Although these designs did not lead to high gains, they did produce thermonuclear reactions and neutrons. Adiabatic, or ablation-driven, compression was obtained by adding a ~50-μm layer of plastic, which was vaporized by the laser pulse, causing the glass shell to implode hydrodynamically. Such a design, called Sirius-B, attained our 20-times-liquid-density milestone. By coating the GMB with molybdenum or another high-Z metal before plastic deposition, we produce a Rigel target that implodes more efficiently than the Sirius-B.

In Polaris, our most advanced target (Fig. VII-1), a high-Z metal coating will be added as a pusher shell for the fuel. A low-density plastic foam will be added to provide a hydrodynamic cushion, and a second pusher layer will be added outside the foam.

In all our high-performance targets, such as Polaris, the fuel may be frozen as a solid layer of DT ice onto the inside surface of the innermost pusher shell. Calculations show that this cryogenic modification will improve the yield substantially. We are developing techniques to freeze such layers in place within the target chamber.

For these and other targets of recent design, and for diagnostic purposes, we are developing high-Z metal shells with diameter and wall-thickness uniformity deviations of not more than 1% and surface-smoothness variation of 100 Å. We are also developing low-density, small-cell plastic foams, thick layers of plastic chemically loaded with high-Z metals, metal foams, and smooth metal layers of moderate to low Z.

Because any target must be characterized completely to understand its performance, we have devoted much of our effort to measuring and documenting all targets we deliver and to creating new, automated high-resolution methods of characterizing target parts.

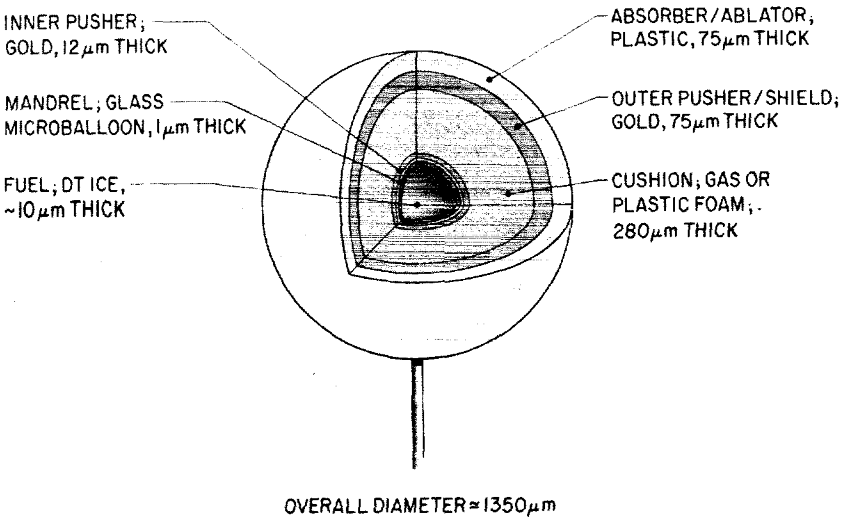

Fig. VII-1. Polaris Prime, a multicoated, multishell laser fusion target designed for Helios and Antares.

TARGET FABRICATION

General

Our primary assignment in target fabrication is the assembly, delivery, and postshot analysis of targets for our operating CO_2 laser systems. We maintain a large and very flexible inventory of materials and techniques so that we can respond rapidly to changes in target design or specifications. As part of target assembly, we also mount and align the targets on the appropriate target-changing mechanism, eliminating the need for any further position adjustment in the target chamber. If desired, we photograph and analyze any remnants to supplement target diagnostics.

Target fabrication typically includes the following steps. A type of GMB is chosen that is most suitable for the desired diameter, wall-thickness, and gas permeation characteristics. Suitable GMBs are optically preselected with an interference microscope. They are filled with DT or DT:Ne gas mixtures by permeation through the wall at elevated temperature and pressure. When nondiffusible diagnostic gases are required in the fuel, GMBs are filled by the drill, fill, and plug (DFP) technique. This technique consists of laser drilling a small hole (1 to 5 μm in diam) in a GMB, covering the hole with a plug of uncured epoxy or low-melting glass, and then filling the GMB by pressurizing it in a small pressure vessel containing the fuel gas. The filled GMB is heated while still in the vessel to flow and cure the epoxy plug or to melt the glass plug thus sealing the hole. The filled GMBs are cleaned and then inspected with an interference microscope in three orthogonal planes. Coatings of metal and/or plastic are then applied to these selected GMBs. These coatings are examined in three views by x-ray microradiography to determine coating smoothness and uniformity, often after each successive layer has been applied. Some targets for laser fusion experiments, such as Polaris, require additional shells of plastic, plastic foam, or various metals. These outer shells have been fabricated in the past by coating suitable spherical mandrels with the desired materials, cutting the coating in half with a laser knife, and then leaching out the mandrel. We now micromachine the outer plastic shells, which are then assembled around the coated GMB to complete the target. Finally, we mount the targets for use in one of our laser systems.

Multishell Target Assembly Development

Polaris Target Assembly Techniques (P. Gobby). Work on assembly techniques for Polaris targets focused on maintaining concentricity of the various spherical shells. A simple Polaris target consists of a GMB centered in an outer spherical shell with a gaseous buffer between the two. To assemble such a target, the GMB must first be centered within an outer hemishell. The second hemishell completes the outer shell with its center coincident with the centers of the GMB and the other hemishell. The joint between the two hemishells thus defines the x-y plane, and the direction perpendicular to this plane is the z-direction.

The centers of spherical surfaces in the x-y plane can be aligned to within 1.0 µm with the apparatus shown in Fig. VII-2. For illustration, a complete sphere is shown at the focal point of the microscope objective. However, any spherical surface whose center is at the focal point of the microscope objective will reflect the laser light back along its incident path. A second lens of longer focal length is used to partially refocus the reflected beam to a screen or quadrant detector. By adjusting the target spherical surface in the x-y plane, we find that alignment in the x-y plane corresponds to a circularly symmetric image at the screen. Measurements show that a 1.0-µm motion in the x-y plane can perceptibly alter this image. If the two hemishells are brought into contact on the flange, their z-alignment will be as good as the hemishells themselves.

Supporting and aligning a GMB inside two hemishells of larger radius also requires new techniques. If we use a gaseous buffer between the GMB and the outer shell, the most appealing technique is to support the GMB between two thin (~500 Å) plastic films that would then be trapped by the hemishells upon assembly. Because the films are transparent, the x-y position of the GMB can be adjusted as described above for the hemishells. The z-alignment of the GMB will depend on how well centered the GMB is in the plastic films. Ideally, the plane of the films will coincide with a diameter of the GMB.

A technique has been developed to determine the centering of the GMB within the plastic films. Figure VII-3 shows a method that has provided 1.0-µm sensitivity in this measurement: a HeNe laser illuminates the GMB mounted between plastic films and produces an interference pattern on a screen. A probe, controlled by micromanipulators, and whose position in the z-direction can be accurately measured, is then advanced to the GMB. As the probe touches the GMB, the interference pattern changes. The probe is then retracted and moved to a new location in the z-direction away from the GMB. Subsequently, the probe is moved toward the film plane until the interference pattern again changes. By measuring the distance the probe moved in the z-direction between interference pattern changes, we can obtain a precise measure of the centering of the GMB within the plastic film when the GMB diameter is known.

Micromachining Laser Fusion Target Parts (J. Feuerherd, E. Farnum). We have designed and assembled a precision air bearing diamond-turning machine. This machine (Fig. VII-4) can produce parts to tolerances of <0.025 µm. It generates very smooth surfaces that are better than required for our present target needs, as shown in a scanning electron micrograph (SEM) of the surface of a spherical copper test piece (Fig. VII-5).

Fabrication of Plastic Hemispheres (W. L. Bongianni, C. Dunning). Hemispherical shells are now

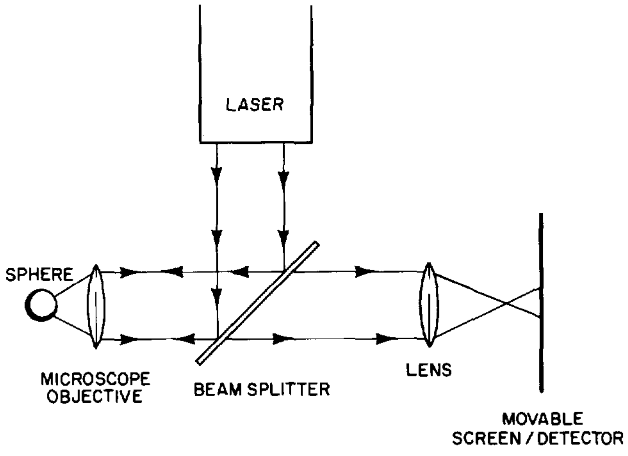

Fig. VII-2. Schematic of confocal alignment.

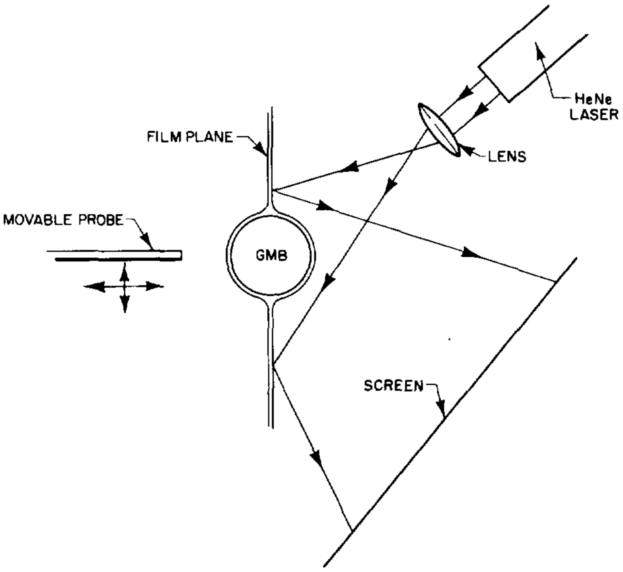

Fig. VII-3. Schematic of GMB centering.

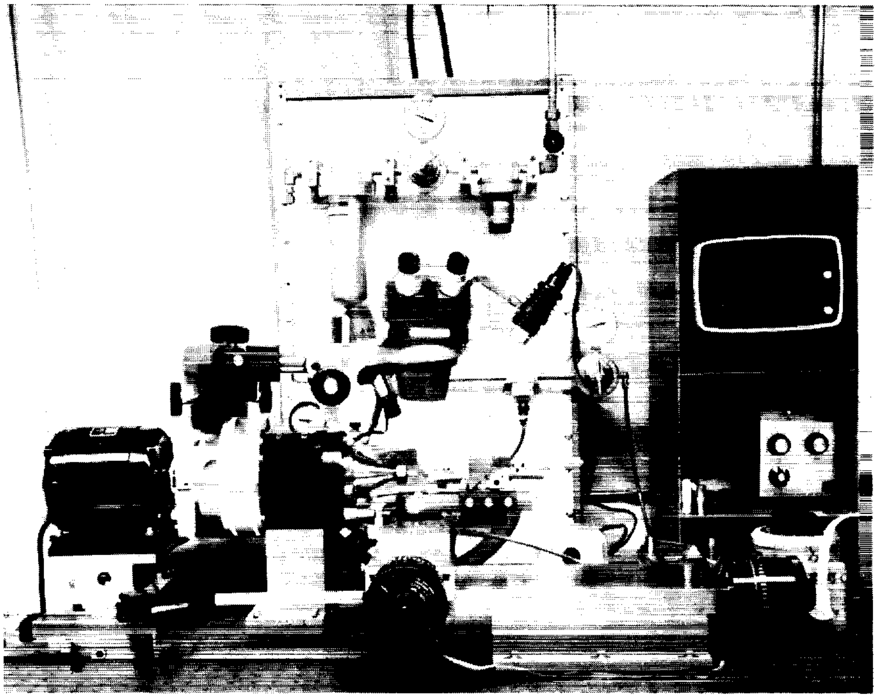

Fig. VII-4. Precision air bearing, diamond-turning machine.

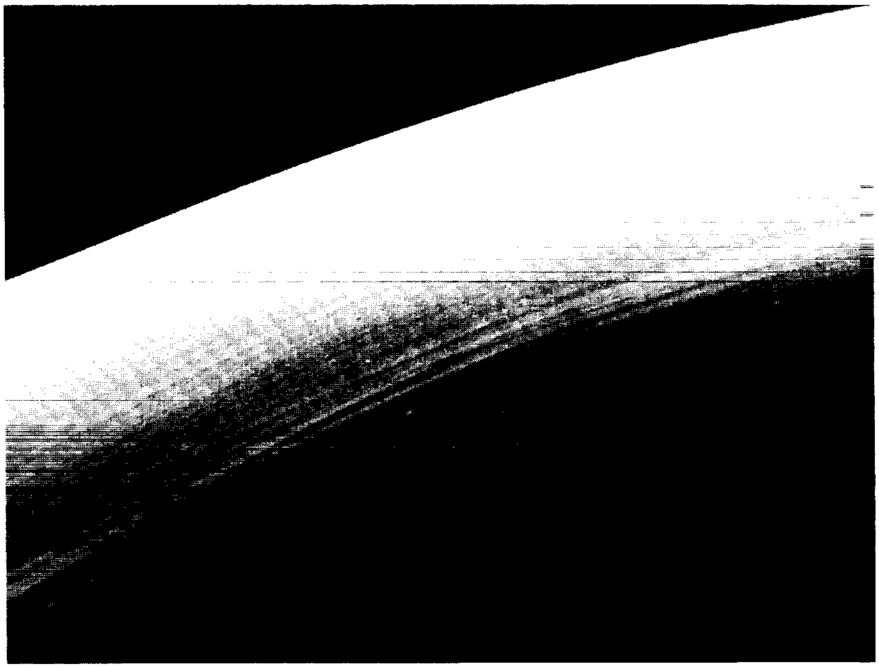

Fig. VII-5. SEM of surface of spherical copper test piece machined in our precision air bearing, SPDT machine.

micromachined individually at considerable expense. We are, therefore, considering a batch process for the production of plastic hemispheres for nested multishell laser fusion targets.

The new approach, the embedded-mandrel technique, consists of precisely embedding solid spherical mandrels in a substrate capable of uniform plastic flow. The key tool for the embedding process is an instrumented micromanipulator that senses pressure and/or resistance on contact and can position a mandrel to an accuracy of ±0.25 μm. In practice, a beryllium-copper spherical mandrel is placed on an anvil held in the micromanipulator. The mandrel is driven toward a mechanically soft surface, such as wax or indium, until contact is recorded. Motion continues, embedding the sphere in the substrate until the desired position is reached. The motion of the anvil is then reversed; when contact with the sphere is broken and its position is recorded, the distance between the two recorded contacts is read as the depth of embedding. Many spheres can be embedded simultaneously in the same substrate by this process.

The substrate and the exposed hemispheres are then coated with parylene by VPP. The SEM in Fig. VII-6 shows an embedded-mandrel mold after it has been coated with 50 μm of parylene. Because proof of the process was the only consideration in this case, no attempt was made at cleanliness, and the coating shown is contaminated with dust. However, the experimental objective, a sharp line of demarcation at the equator, was observed, and the parylene replicates the mandrel surface.

A free-standing hemispherical shell can now be obtained by inverting the mold and ion-milling 50 μm down to the true equator. (The inner part of the hemisphere is still protected by the mandrel.) Alternatively, the inverted coated mandrel could be repotted in a compound harder than parylene, the mandrels removed, and the parylene polished down to the potting compound, leaving the hemisphere.

Development of Polymer Films as Target-Core Supports (B. Cranfill). We have been investigating thin polymer films as support systems for multiple-shell targets. Polystyrene, because of its adhesive properties when heated, is very useful in the assembly of targets. It can be made into 500-Å-thick film, but it begins to tear in about a week if a DT-filled GMB is sandwiched between two such films. However, it can be used as a laminate with another, stronger film. Formvar films are considerably stronger than polystyrene, but they will also tear if radiation damaged. We found that GMBs containing only 10% of DT will cause Formvar films to begin tearing in about 2 months. Other film materials are being investigated.

We have made progress in producing clean, thin plastic films by casting them on glass slides and then floating the coatings off on water. If a slide is too clean, the film will not float off by itself, and therefore a parting agent is required. We have found that residual films from a detergent solution leave an excellent parting agent for these thin plastic films.

Gas Filling Laser Fusion Targets

To understand the performance of GMB laser targets, we must be able to measure the gas fill with a high degree of accuracy. We must also determine the permeation rates of deuterium and tritium through thin layers (shells) of a variety of coating materials at various temperatures. This information enables us to select the conditions under which a given target type should be filled. Permeation data at room temperature and below are also important in selecting the best storage temperature for targets that are filled with the desired quantity of fuel gas or fuel plus diagnostic gas.

Diffusion Filling Metal-Coated GMBs (J. E. Barefield II, B. S. Cranfill). During the last 6 months, we have successfully diffusion filled metal-coated GMBs with DT and D_2. GMBs coated with 10 μm of tungsten were diffusion filled to 70 atm D_2 in 96 h at 923 K, whereas GMBs coated with 2 μm of nickel were filled at 673 K and required 7 days of staging in 210 increments plus an additional day at full pressure.

Diffusion-Filling System (J. E. Barefield II, A. Mondragon). Our DT fill system (Fig. VII-7) is a facility in which targets can be permeation filled with DT fuel. The high-pressure section (Fig. VII-8) of the system was significantly modified and improved. The addition of two independent fill ports now allows us to fill 500 to 600 targets simultaneously at two different gas densities and temperatures. This has significantly shortened the turnaround time between target request and delivery.

Gas removal after a fill was tedious in the past because the efficiency of the cryogenic pump was limited. After a 30-amagat fill, several pumping cycles, lasting hours, were required before the targets could be

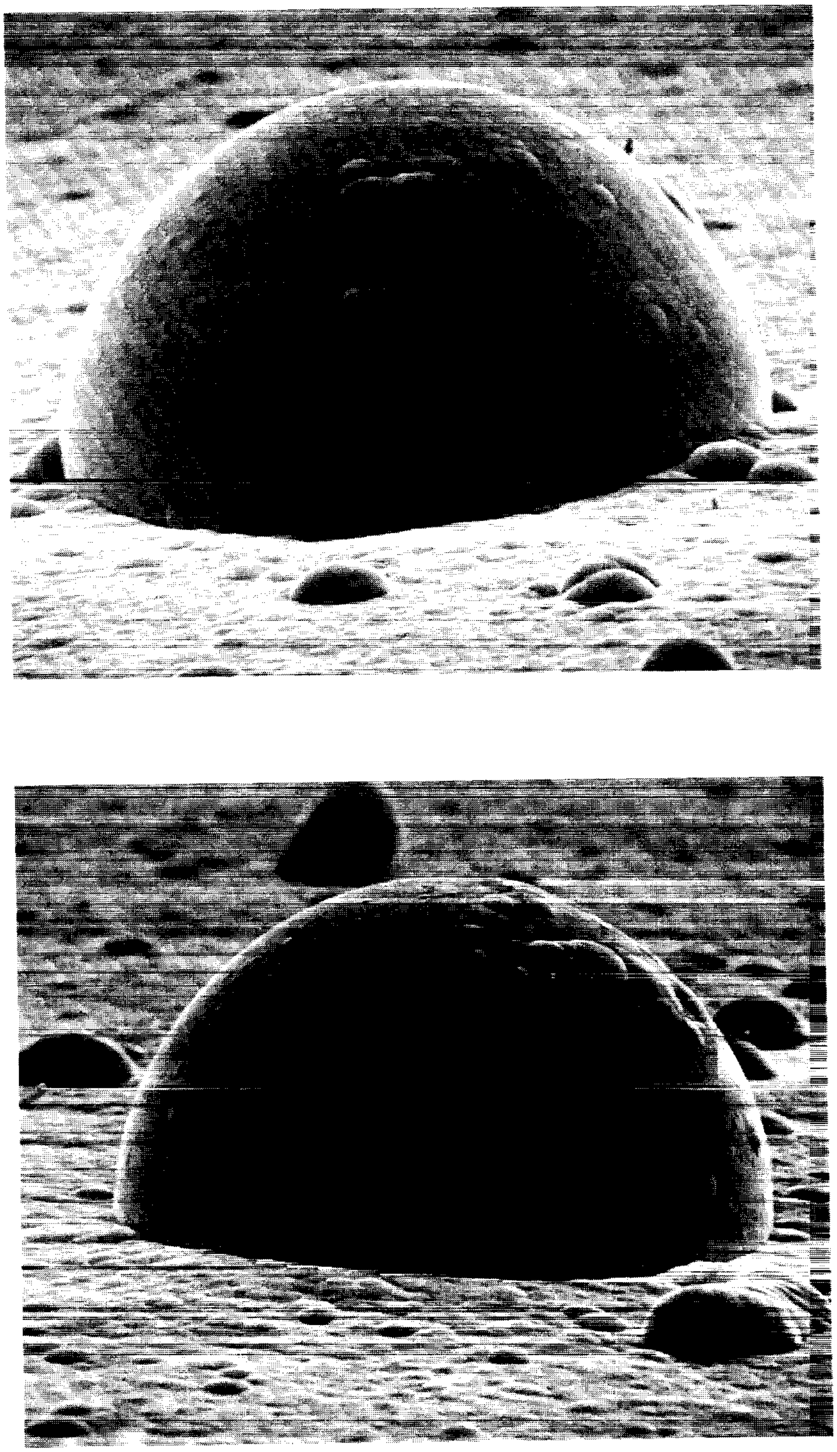

Fig. VII-6. SEM of hemispherical mandrel with 50-μm parylene coating (200 X).

removed. However, the recent addition of a uranium bed with the capacity of absorbing 2 moles of tritium has reduced gas removal time to 2-5 min.

The uranium bed has also greatly reduced the burden on the cleanup system that removes tritium from effluents when the high-pressure fill manifold is evacuated

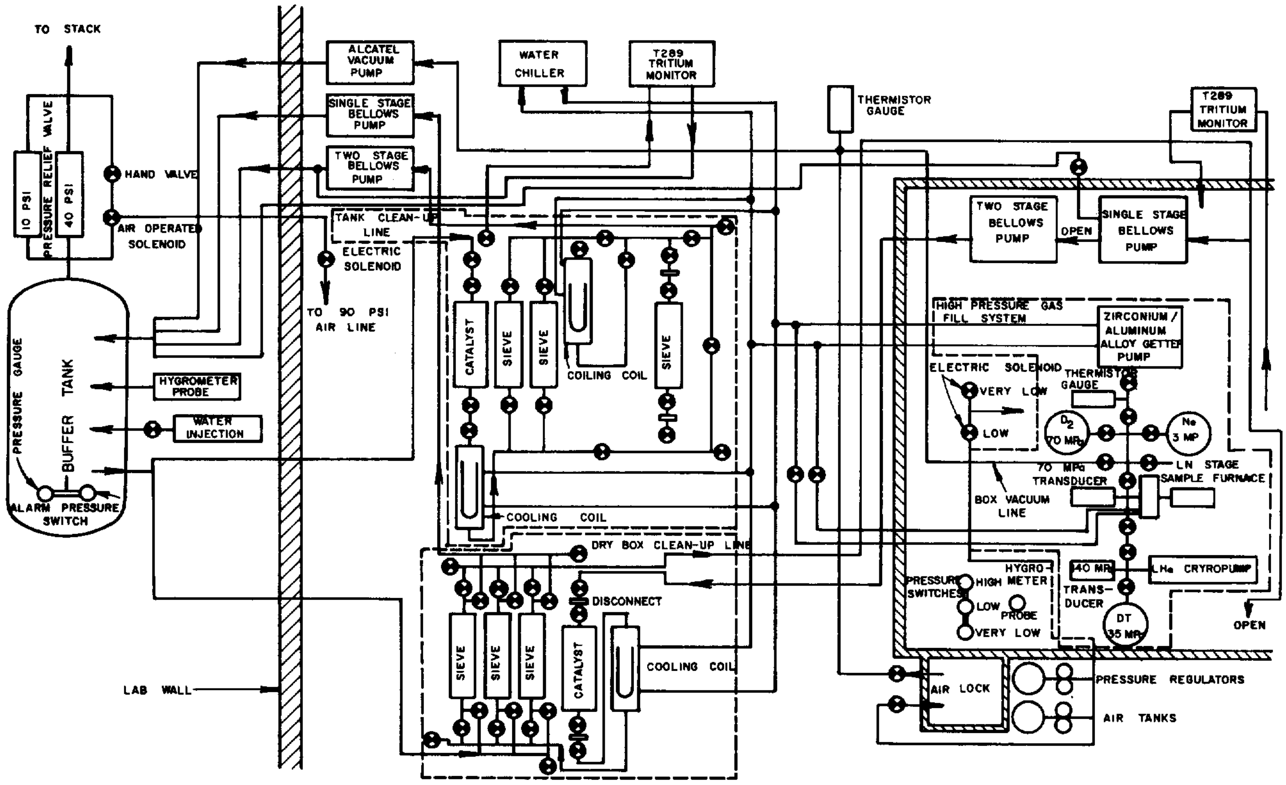

Fig. VII-7. Schematic of DT fill system.

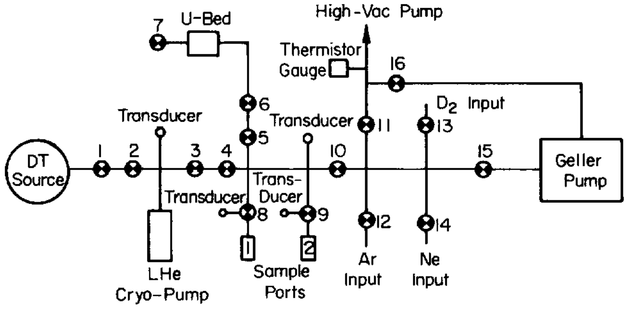

Fig. VII-8. High-pressure gas fill system.

before or after a fill run. After a fill experiment the uranium bed now leaves in the fill ports only extremely small quantities of hydrogen isotopes, which are easily removed by the cleanup system.

TARGET CHARACTERIZATION

Fuel Assay (B. Cranfill)

Determining DT Fill From X-Ray Counts. We have developed an equation for calculating the DT fill pressure of GMBs from the external rate x-ray count. This equation is suitable for use on a programmable hand calculator. Corrections are made for x-ray attenuation in the glass wall and for self-absorption of beta particles at varying gas densities and shell diameters. The equation is empirically derived and has been shown to work very well for GMBs with a 1.5- to 5-µm-thick wall, 150- to 600-µm diam, and for DT fills from 10 to 100 atm. At present, this formula may be used for only one type of glass composition, but a simple recalibration could modify it for other glass types.

To use the equation, the x-ray counter must be calibrated against a reference sample. The fill pressure of a GMB with a different wall thickness, diameter, and fill pressure can then be determined by

$$\text{Fill Pressure} = \frac{Ke^{0.09W}}{e^{0.09W_R}} \times \frac{P^{0.34}}{P_R^{\,0.34}} \times \frac{8.5 \times 10^{-4}\ D + 0.54}{8.5 \times 10^{-4}\ D_R + 0.54}\, e^{0.0039t} C$$

where K is the calibration factor in atm/counts/s/volume;

W is the wall thickness;

P is the estimated fill pressure;

D is the diameter;

C is the number of counts/s/volume;

t is the thickness of the GMB coating; and

W_R, P_R, and D_R refer to the reference sample measurements.

The initial value for P must be estimated because the program is iterative and a closer approximation is used each time. Even with a large error in the estimated P, only a few iterations are needed.

To derive the equation, two of the three parameters considered were held constant and the effect of varying the other was observed. This was repeated for each parameter. Each GMB used was then broken under glycerin to determine the gas fill. When the final equation was derived, the predicted fill pressure was compared to the measured fill pressure; better than 10% agreement was observed. X-ray counter repeatability and tritiated surface particle contaminants appeared to account for anomalous count rates.

The interferometrically measured wall thickness was corrected using the expression $W = nW - 1.02 \times 10^{-4}\ DP$, where W is the measured wall thickness and n is the refraction index of the GMB. This expression was derived experimentally and differs somewhat from the theoretically derived expression that corrects for the refractive index of deuterium and tritium. However, we find the theoretical expression overcorrects for the gas fill and sometimes, at high fill pressures, predicts negative wall thickness.

DT Fill Determination by Breaking Under Glycerin (B. Cranfill). Modified breaking under glycerin is being used to measure the gas fill of GMBs. The GMB is placed in a drop of glycerin and crushed between two microscope slides with a 150-µm-thick cover slip used as a spacer. The bubble formed is nearly cylindrical, and with careful measurements, its volume can be closely approximated. The diameter is measured in at least two orientations, using the average of the inside and outside of the meniscus. Spacing between the slides is also measured with an eyepiece micrometer by placing the slide assembly on its side. Both sides are measured as close to the bubble as possible. Corrections are made for temperature and atmospheric pressure only; DT solubility in the glycerin is negligible. Such measurements of recently filled GMBs agree to better than 10% with the equilibrium fill pressure. This method reduces the errors inherent in trying to measure a moving bubble of DT in glycerin.

Gas Analysis by Quadrupole Mass Spectroscopy (J. E. Barefield II). Our quadrupole mass spectrometer system (Fig. VII-9) was redesigned to improve analysis of the gas content of microballoons. This new design has two microballoon injectors to introduce samples into the system for analysis. For samples with volumes of $\sim 10^{-6}$ cm^3 and pressures to 50 atm, the low-pressure injector is used; the sample is broken directly inside the high-vacuum system. However, for samples containing several hundred atmospheres, we use the high-pressure microballoon injector. In this case, the sample is broken in a calibrated evacuated volume and metered into the high-vacuum mass analysis section through a variable leak valve. The variable leak valve is designed to automatically regulate the gas flow in the range between 1.2×10^{-12} and 500 torr•L/s. The operator can also introduce several gases for calibration by means of gas ports.

This system has been used to obtain calibration curves, which are then used to quantitatively ascertain

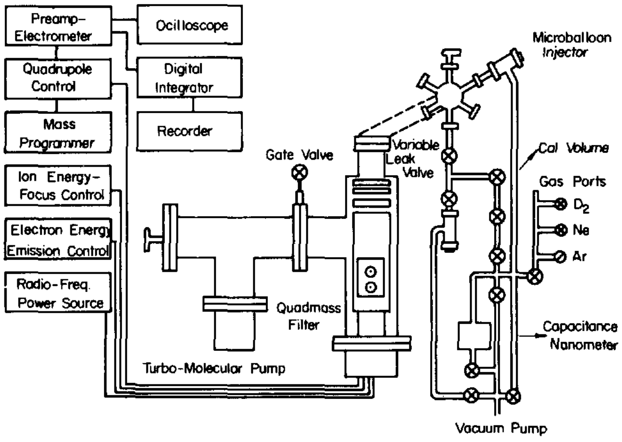

Fig. VII-9. Quadrupole mass spectrometer system.

the gas content in glass and/or metal microballoons. A typical decay curve for a 300-μm-diam GMB that contained 2.0 atm of D_2 gas appears in Fig. VII-10. An example of a calibration curve is shown in Fig. VII-11. The samples used were GMBs filled to 10, 20, 30, and 40 amagats of D_2; 10 samples were analyzed at each gas fill density. The correlation coefficient for the curve shown in Fig. VII-11 is 0.996.

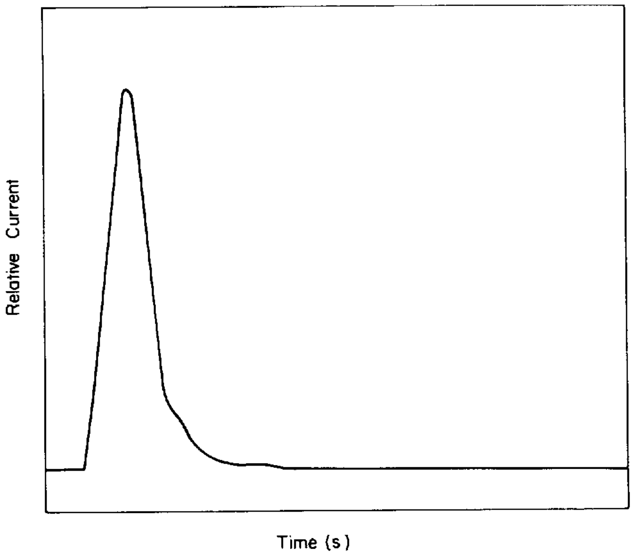

Fig. VII-10. Typical fill-pressure (2.0 atm) decay curve for a D_2-filled GMB.

Samples containing several hundred atmospheres of pressure cannot be broken directly inside the high-vacuum system because the mass filter will saturate. For this type of analysis, the high-pressure microballoon injector is used. The samples are broken in a known calibrated volume, depending upon the desired dilution ratio (that is, pressure/cm^3). The sample is then metered into the high-vacuum system through the variable leak valve. An example of a calibration curve is shown in Fig. VII-12. The calibration volume is 20 cm^3, the range of dilution ratio is 0.1 to 0.4 torr/cm^3, and the correlation coefficient for this curve is 0.99. To analyze an unknown high-pressure sample, the sample is broken in the calibrated volume, metered into the high-vacuum system, and the level of the mass peak is measured. The fitting parameters from the calibration curve are then used to ascertain the pressure/gas density of the unknown sample.

Acoustic Microscope Characterization (W. Bongianni). We have continued our theoretical and developmental work on an electronically scanned acoustic microscope.[1] This type of microscope shows good potential as a characterization tool for applications requiring thickness and diameter tolerances of better than 100 Å over spot dimensions of 20 to 100 μm^2.

A proof-of-principle acoustic microscope has been built and successfully operated. The microscope, which operates at 935 MHz, consists of a single-element

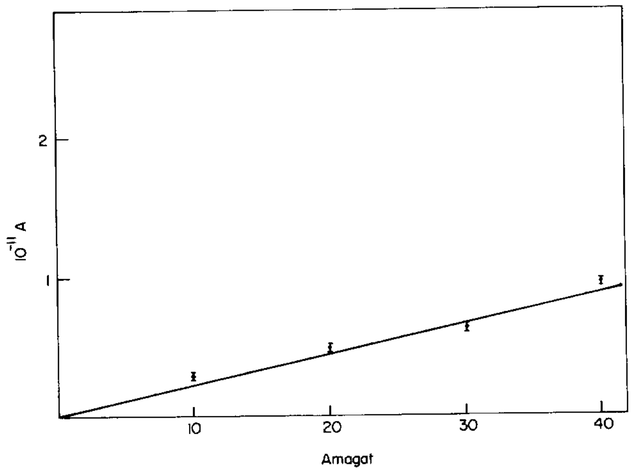

Fig. VII-11. Typical calibration curve for a batch of D_2-filled GMBs.

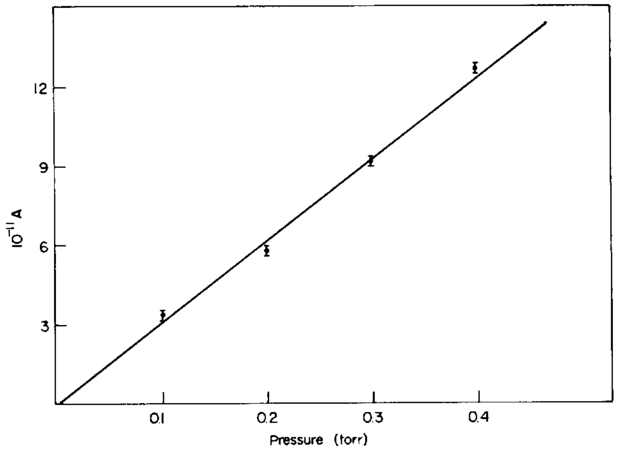

Fig. VII-12. Calibration curve useful for high-pressure microballoon sample analysis.

yttrium-ion-garnet (YIG) lens and has a transverse mechanical object stage. Proof of the principle of operation consisted of measuring the acoustic field of a relatively simple design and comparing the measured value with the results from the magnetoelastic optics code; agreement is not good (Fig. VII-13). Once the code is in agreement with the measured values, we believe that a lens could be designed for any specific target wall characterization.

The microscope consists of a YIG rod oriented along the axis of a dc magnetic field, yielding a maximum field of 1050 G. A solenoid coaxial with magnets provides for field variation and for focuses of the acoustic field at the rod face. The object stage consists of a 125-μm-diam beryllium-brass probe attached to a load cell and capable of translation measured in 0.5-μm steps. Measurements are taken by pressing the probe at discrete positions along the YIG face and measuring the change in amplitude of an acoustic echo; the profile obtained is indirectly related to the acoustic field distribution.

Using a Gaussmeter, we found that the coaxial field deviates from uniformity in the radial direction. Near axis, the distribution increases quadratically with radius; in addition, the field minimum is believed to be displaced slightly from the geometrical axis. The first factor increases the launch surface area (effective aperture), and the second results in a loss of beam symmetry. These deviations have been modeled in the optics code and a fit to the experimental data has been obtained (Fig. VII-14).

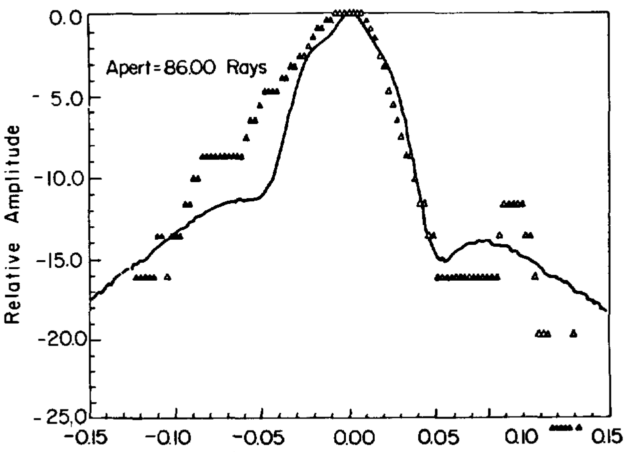

Fig. VII-13. Magnetoelastic beam profile—comparison of theoretical and experimental results.

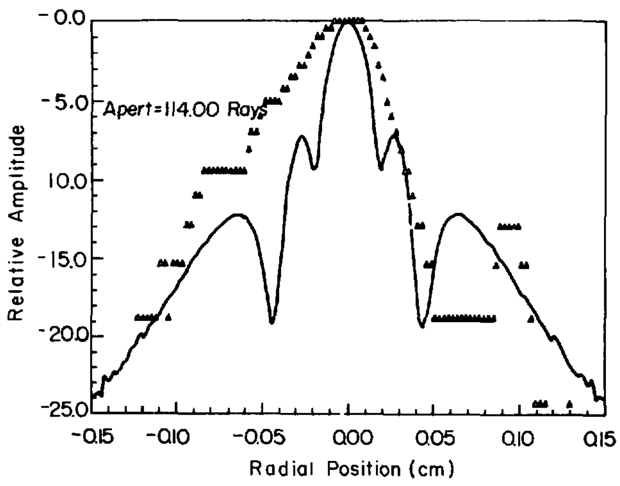

Fig. VII-14. Magnetoelastic beam profile—improved fit of data.

The relative amplitude is measured in dB, and the half-power width at the –3 dB points of the beam is 450 μm, which compares well with a launch surface aperture of 400 μm. Hence the beam is only weakly focused, providing collimation instead of a tightly focused spot at the rod face.

In agreement with this fact, beam width and peak amplitude vary slowly with field. A 3-dB variation in peak amplitude occurs over a range of 100 Oe and a spot size variation of <10 μm.

Although this device has poor transverse resolution, its long depth of field makes it ideal for measuring multilayered targets. For example, nickel thickness resolution in micrometers is directly proportional to pulse width in nanoseconds. The minimum pulse obtained on this device is 25 ns, implying the ability to discriminate between layers 25 μm or farther apart. By tailoring the rf pulse to the naturally occurring dispersion, pulse compression to ~4 ns should be obtained, resulting in the ability to discriminate layers separated by 4 μm or more.

Contact X-Ray Microradiography (D. Stupin). We are developing radiographic and image analysis techniques to detect defects in opaque laser fusion target coatings. To ensure symmetric target implosions, we are required to detect deviations as small as 1% in the concentricity of the inner and outer shells of coatings and 0.1% in coating thickness variations that are caused by warts or dimples. These requirements correspond to a 100-Å and a 10-Å variation, respectively, in a 1-μm-thick coating. Contact radiography is sensitive to

±0.5% variations caused by nonconcentricity and to ±6% variations attributable to warts or dimples that cover a 100-μm^2 area.

Our new technique applies the fact that a change in coating thickness caused by a defect affects the x-ray path length through that part of the microballoon, and consequently, the intensity of an x-ray beam traversing it (Fig. VII-15). We can thus detect defects smaller than 10 µm, which is the resolution limit of optical microscopy. X-ray radiography has another advantage in that it can be used for opaque shells and targets.

During contact microradiography the target is placed directly on a photographic emulsion in the path of a collimated x-ray beam. The resultant image has the same size as the microballoon. The optical density of the emulsion is then digitized, and the digitized image is stored in a minicomputer where an analysis routine finds and quantifies the defects. A microdensitometer digitizes the optical density information on the film.

We search for the three types of defects[2,3] shown in Fig. VII-16. Type I is a coating with spherical inner and outer surfaces where the centers of the two surfaces are not concentric (also called a nonconcentricity or an eccentricity). A Type-II defect is a coating that has either an inner or an outer elliptical surface; a Type-III defect is either a wart or a dimple.

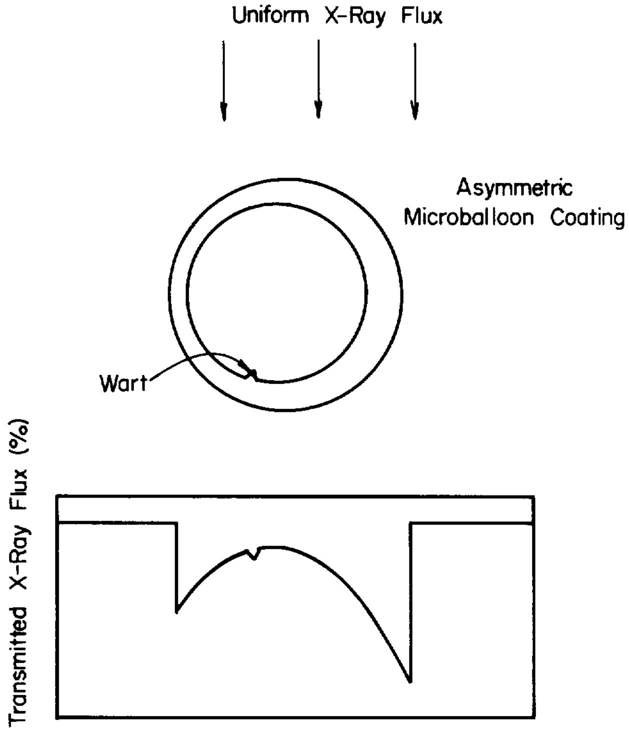

Fig. VII-15. Asymmetric coating thickness and surface irregularities cause variations in the transmitted flux of x rays passing through a microballoon.

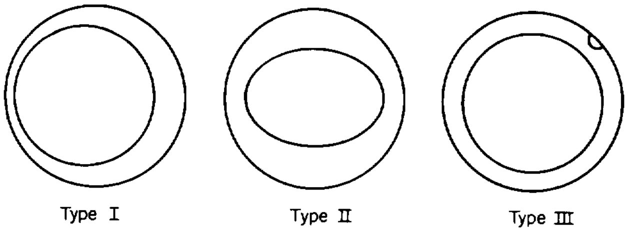

Fig. VII-16. Three types of target defects.

Our computer analysis routine, which uses a FFT, has a ±0.5% sensitivity to Type-I defects and a ±2.5% sensitivity to Type-II defects. In this analysis, the magnitude of the spatial frequencies indicates the percentage of eccentricity for Type-I defects and the percentage of nonsphericity for Type II defects.[4] The phase of the spatial frequency gives the direction of the defects relative to the center of the polar coordinate system.

A statistical test shows a sensitivity limit of ±6% to Type-III defects. To measure Type-III defects, image densities of 90% of a microballoon are analyzed. Image densities that are outside a $\pm 3\sigma$ variation of the average density are classified as Type-III defects. All of the adjacent points that have been classified as Type-III defects are then grouped together into larger defects. Type-III defect sensitivity is a function of the areal extent of the defect; for a 1-μm^2 area, we can detect ±6% variation in coating thickness.

The average coating thickness is measured by comparing the optical density in the center of the microballoon image with the optical densities of a step wedge, or penetrameter, which is made of different, but known thicknesses of the same material as the target coating (Fig. VII-17). Uncertainties in the densities of target coating and penetrameter foils can result in an uncertainty of 10% in the average coating thickness measurement, which is acceptable.

Three orthogonal views of each coated microballoon are required to characterize the entire surface, and each view is computer analyzed. Because contact microradiography scans 90% of the area of the microballoon image, this method is much more sensitive to the detection of defects than methods that use a few diametrical scans through the center of the microballoon.

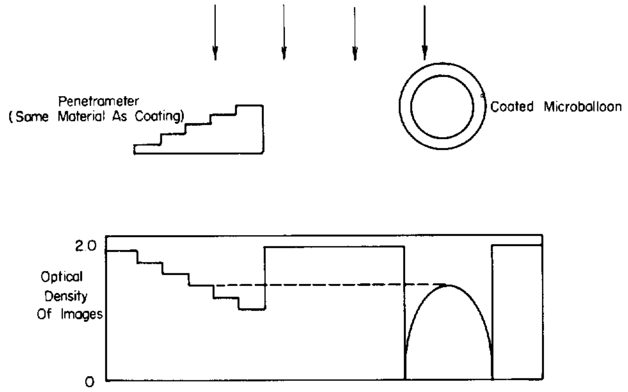

Fig. VII-17. Average coating thickness is measured by comparing the optical density in the center of the microballoon image with the optical density of a penetrameter.

Fig. VII-18. Modified molybdenum target.

Projection X-Ray Characterization of Laser Fusion Targets (R. Whitman). We are continuing to develop a technique of characterizing opaque and/or multishell laser fusion targets by projection radiography. We have concentrated on Type-III defects and made significant progress; in a GMB with a 1-µm-thick wall, we can now detect defects at ±0.1% variation over a defect area of 100 μm^2. This constitutes a considerable improvement over previously reported results of ±3.0 and ±9.0%.

Digital Target Modeling and Analysis (R. Whitman). To broaden our capabilities to model by computer and to digitally analyze contact microradiographs of single-layer targets, we are using a bremsstrahlung x-ray source of 5-50 kV (peak). We are also developing a technique to measure the outer uniformity of a multilayered target and to model such a target.

For modeling single-layer targets, we obtained thickness-to-film density data experimentally by exposing a step wedge of molybdenum or gold. This exposure was obtained by using a bremsstrahlung x-ray source imaged through the step wedge onto either a very high resolution emulsion or a holographic plate emulsion. An example of a modeled molybdenum target using the step-wedge data from a bremsstrahlung source exposure is shown in Fig. VII-18. We had previously digitally analyzed only models of contact microradiographs of 1-µm glass targets based on exposure data from a monochromatic x-ray source. The technique to measure the outer material uniformity of a multilayer target uses a Sobel edge-detector algorithm to define the outer material boundaries. A method of tracking the edges of these boundaries is being implemented. Modeling a multilayer target is a complex process; we are considering a technique in which a step wedge of aluminum is placed perpendicular to a step wedge of copper forming a two-dimensional step wedge that is then exposed to a bremsstrahlung source. This technique provides a density-to-material thickness image formed on holographic plate emulsion. The image is then digitized for use in computer modeling of a two-layered target of copper and aluminum.

Optical Characterization (D. Cooper)

We are also developing high-resolution optical techniques such as transmission and reflection interferometry and light scattering to characterize glass and metal-coated microballoons, diamond-turned metal mandrels, metal-loaded plastic pusher shells, and DT-ice cryogenic fuel layers. Other areas of study include thickness measurements of gold-black films and the use of ellipsometry to measure the thickness of thin polymer films.

Surface-Mapping System. Significant progress has been made on an automated sphere-mapping system based on a LLNL design.* This system will be capable of

---

*This information was provided by B. W. Weinstein, J. R. Monjes, and D. L. Willenberg of Los Alamos National Laboratory.

measuring Type-I, -II, and -III defects in transparent shells, and Type-III defects as well as deviations from sphericity in metal-coated shells. The system will have a defect amplitude sensitivity of 5 nm and a spatial resolution of 1 μm.

Transmission and Reflection Interferometer. To increase interferometer sensitivity to 50 Å, we have developed an ac or phase modulation interferometer. This instrument represents a vast improvement over the Twyman-Green and Michelson interferometers that could only detect path length (phase) changes of 250 to 200 Å. An ac interferometer converts phase information into intensity information by modulating the relative phases of the two arms of the interferometer. Introduction of a phase object, such as a microballoon, in either arm of the interferometer results in an intensity modulation on the output beam. The depth of modulation is simply related to the phase of the sample object and can be easily and sensitively measured by using ac signal-processing techniques. Sensitivities exceeding 5 nm can be achieved.

Figure VII-19 illustrates the current interferometer design. Light from an argon-ion laser (488 nm) plane polarized at +45° is incident on a quartz photoelastic modulator[5] that induces a periodic phase shift between the 0 and 90° components of the linear light. The polarization-modulated beam then encounters a polarizing cube beamsplitter that splits the two components into probe and reference beams. The probe beam is focused twice onto the target sphere by a pair of microscope objectives. The first focus is on a 1-μm spot on the sphere surface and the second focus is (for a metallic sphere) on the center of curvature. The advantage of this scheme is that, as the sphere is rotated by a 4π manipulator, small translations of the sphere along the probe beam axis do not change the total path length of the probe beam. Otherwise, small translations of the sphere would produce the same signal as a surface defect. The probe and reference beams are recombined and then pass through a Soleil-Babinet compensator and Glan-Thompson prism. The compensator introduces a relative phase shift between the probe and reference waves, which is easily adjustable to an accuracy of 5 nm. The Glan-Thompson prism, oriented at +45°, causes interference between the orthogonal probe and reference waves, and the resulting intensity is detected with a photodiode. Introducing a phase shift between the probe and reference beams results in an intensity modulation at the fundamental (50-kHz) oscillation frequency of the photoelastic modulator. This signal is detected by a lock-in amplifier referenced to the modulator.

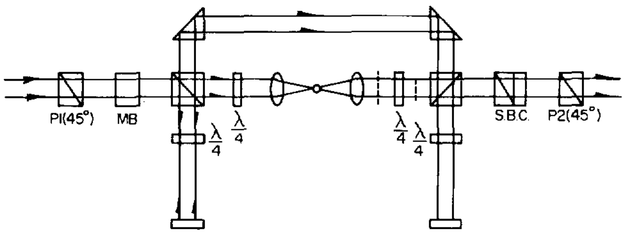

Fig. VII-19. Transmission-reflection interferometer.

For transparent shells we insert a double-sided mirror in the location shown by the dashed line. Both objectives are focused on the front surface of the target and the system is then optically equivalent to a double-pass Twyman-Green interferometer.

In an actual microballoon examination, the target is held in the interferometer by the target rotator tips of a 4π manipulator. The compensator is adjusted to null out any 50-kHz signal. The sphere is then rotated throughout its 4π solid angle by the computer-controlled manipulator, and any path length changes brought about by surface defects or asphericities are detected as a 50-kHz signal by the lock-in. In this way a detailed surface map of the sphere is obtained.

4π Manipulator. The 4π sphere manipulator will be based upon the Topo II design of LLNL.[6] The major difference is that we use a vacuum-opposed, air bearing xy translation stage rather than a conventional ball bearing stage.

The maximum error of straight line motion along each axis of the air bearing stage will be 4 μm, a significant improvement over a conventional stage. The stage will be driven by two dc servo motors, and position indexing will be accomplished with two rotary optical shaft encoders with a resolution of 800 counts/revolution. The stage and the motors will be coupled by precision-lapped 40-pitch lead screws having a guaranteed accuracy of 2.5 × 10^{-16}/in. The rotary shaft encoders will be calibrated by monitoring the actual stage motion with a Hewlett Packard laser interferometer.

A PDP-11 microcomputer will control the stage motion. A Fortran program will issue the command sequence to rotate the sphere under examination while simultaneously monitoring the 50-kHz output of the lock-in amplifier. Examination times should typically be ~5 min for a 500-μm-diam shell.

Ellipsometry. Our capabilities in this area have been upgraded significantly by the acquisition of a versatile Fortran program developed at NBS.[7] From the measurements of various ellipsometric parameters, this program can calculate

- the angle of tilt of the reflecting surface,
- the film thickness,
- the refractive index and film thickness,
- the substrate refractive index,
- the complex refractive index of a film of known thickness,
- the refractive index and thickness of a film with confidence limits, and
- the constants T_c and Δ_c of waveplate.

In addition, the program can be used to generate a table of values of Δ, ψ, and reflection coefficients for a range of film thicknesses and refractive indices.

Analysis of ellipsometry data from a free-standing polymer film has often given incorrect or inconsistent values for film thickness and refractive index. It has been observed that the ellipsometric angles Δ and ψ vary from one region of the film to another, indicating that the films are not homogeneous. Refractive index variations in a polymer film can arise because of density variations, changes in the mole fractions of the constituent polymers, or the presence of small regions of high crystallinity. In our ellipsometer program, we assume that the film is homogeneous over the spatial extent of the analyzing beam (~2 mm). The user inputs an upper and a lower bound for the refractive index of the film of interest, and the program searches for a solution within this range. Inhomogeneous films usually give refractive indices that lie outside the expected range.

Gold Blacks. We have attempted to measure the thickness of gold-black deposits accurately. Gold-blacks absorb strongly throughout the 2- to 15-µm range as well as throughout the visible and near-infrared regions.[8] A 10-to 20-µm-thick gold-black film absorbs essentially all the incident electromagnetic radiation over these regions. This fact precludes the use of reflection or transmission interferometry to measure film thicknesses greater than ~5 µm.

For flat gold-black films, a light-section microscope can be used to reflect a narrow beam of light from the film and the substrate. The film-surface-reflected beam is displaced relative to the substrate-reflected beam and this displacement provides a measure of the film thickness. Films as thick as 300 µm can, in principle, be measured to an accuracy of a few microns. Unfortunately, the very low reflectivity of the gold-black, as well as the diffuse scattering of its rough surface, makes it difficult to obtain accurate measurements. Meaurements can be improved by using a more intense light source with the light-section microscope.

We have also used an alternative technique that depends on the rough gold-black surface. By using dark-field illumination with a Zeiss microscope, we can easily view the surface with a high-numerical-aperture (0.85) microscope objective. This objective has a depth of field of ~0.7 µm. The black surface is brought into optimum focus with the fine-focus adjustment (~2 µm/division), and its position is noted. The substrate surface is then in view and the fine focus is adjusted to bring it into sharp focus. The difference between the two settings on the fine-focus knob then gives the film thickness. Film thicknesses measured by this technique are in reasonable agreement (within a few microns) with measurements made on the light-section microscope but are considerably easier to perform. The main source of error is the roughness of the gold-black surface, which is difficult to define.

Light Scattering. The use of light scattering to measure defects in microballoons may be much faster and considerably easier to implement than interferometry. It has been known for some time that Mie scattering[9,10] from small (70-µm) spherical glass particles is sensitive to small changes in the particle diameter (<0.4%) and refractive index (<0.04%). In conjunction with computer calculations, the scattering pattern can be used to measure particle diameter and refractive index.

We are interested in extending these techniques to the measurement of defects in glass- (Type-I, -II, and -III) and metal-coated (Type-III) microballoons. As a result, a consulting agreement has been initiated with Milton Kerker of Clarkson College; he will modify his existing Mie scattering codes to enable them to calculate the effect of Type-I, -II, and -III defects on the scattered radiation field. These programs should be available to us by late spring of 1981. At that time a comprehensive investigation of the feasibility of light scattering to detect defects in glass and metal shells will be initiated.

LASER FUSION TARGET COATINGS

Inorganic Coating Development

Future targets may require metal shells. So that we will be able to respond to design requirements as they occur, we are developing a variety of methods for applying various metal coatings to several classes of substrates. The substrates of interest are GMBs and Solacels; the coating techniques include electro- and electroless plating, CVD, PVD, and sputter deposition.

Gold-Black (Wallace E. Anderson). Low-density, high-Z, resistive materials have become a possible means of improving laser/target interactions by means of resistive inhibition of electron return currents. We are attempting to form gold-black at a density no greater than 1% that of bulk gold, in thicknesses up to 300 µm.

Target designs have demanded that the material be deposited on planar substrates and as a coating on stalk-mounted microspheres. Experiments with planar targets in the Helios laser facility are complete.

Previous investigators of gold-black appear to have limited their concern to optical properties and areal density, that is, thermal mass. A comparison of deposition parameters reported in the literature with our own experiments suggests that these materials have usually been prepared at about 5% of bulk density and in thicknesses of a few µm or less. An exception, in which volume density was a parameter of primary concern, involved an experiment by Bond et al.[11] This experiment verified an inhibition of return current by gold-blacks 50 µm thick and 1% of bulk density. We find that the volume density of gold-blacks decreases with increasing chamber pressure and increases with increasing evaporation rate. Transport of the black is highly dependent upon convection currents within the process chamber atmosphere. We have exploited the latter by routinely cooling our desired collection area 10°C below chamber wall temperature.

The blacks are formed by melting and wetting gold onto a four-strand, six-turn tungsten filament. The process chamber is filled with argon gas to a pressure of 6 torr, and the gold is evaporated at a rate of 20 mg/min. Source-to-substrate distance is nominally 7 cm. The density of material collected under these conditions is nominally 1.5 ± 0.5% that of bulk gold. We have collected material with a density as low as 0.6% that of bulk gold at a chamber pressure of 10 torr, but with decreased predictability and reproducibility in transport, as evidenced by steep gradients in thickness across the collection fixture.

Electroplating Temperature-Stable Gold Alloys (A. Mayer). Temperature-stable gold or gold alloy electrodeposits are of interest if laser targets must be diffusion filled after deposition of a metallic coating. The Sel-Rex Company suggested an Au-1 wt% Ag alloy, which may tolerate diffusion temperatures without recrystallizing or otherwise degrading. In the first experimental run, spherical samples were track plated in a proprietary gold-silver alloy bath. These samples were prepared for metallographic examination and for mechanical and physical property determinations. The proprietary electrolyte is a cyanide formulation that produces an Au-1 wt% Ag deposit. During the continuous 3-day run, the cathode current density was varied between 17 and 50 A/m^2 in five stages to determine its effect on structure and property of the deposit. Metallography was performed on one of the six spheres. A photomicrograph of an etched cross section is shown in Fig. VII-20. The structure of four of the five layers was fine grained with some evidence of banding. The high-current-density layer was large grained and cracked, probably because of high internal stresses. The hardness of the banded layers was ~130 diamond pyramid hardness (DPH). The as-plated deposit was very brittle and fractured when an attempt was made to cut a ring tensile test specimen from one of the spheres.

In Run 2, additional silver was added to the bath in the form of silver cyanide to determine its effect on composition and properties. After an initial 1.5-h run in the standard bath, the silver content was raised from ~0.2 to 0.8 g/L. Plating was continued for 25 h at 34 A/m^2 without gold or silver additions to the bath. The last 2 h of the run were made with another 0.4 g/L of silver added to the bath. A cross section of the as-plated deposit is shown in Fig. VII-21. The structure was similar to that of the low-silver-alloy deposit of Run 1. After the initial silver addition, the silver content of the deposit rose from ~2 to 15 wt% and then gradually dropped to ~8 wt% over the 25-h electroplating period. Because no metal was added during this time, it appears that the silver was depleted from the bath at a slightly faster rate than gold. It also appears that, with proper control of the bath chemistry, a uniform alloy could be produced from this system. The hardness of the as-plated, very brittle deposit was 160 DPH. Samples were submitted for heat treatment to determine whether they could be made ductile.

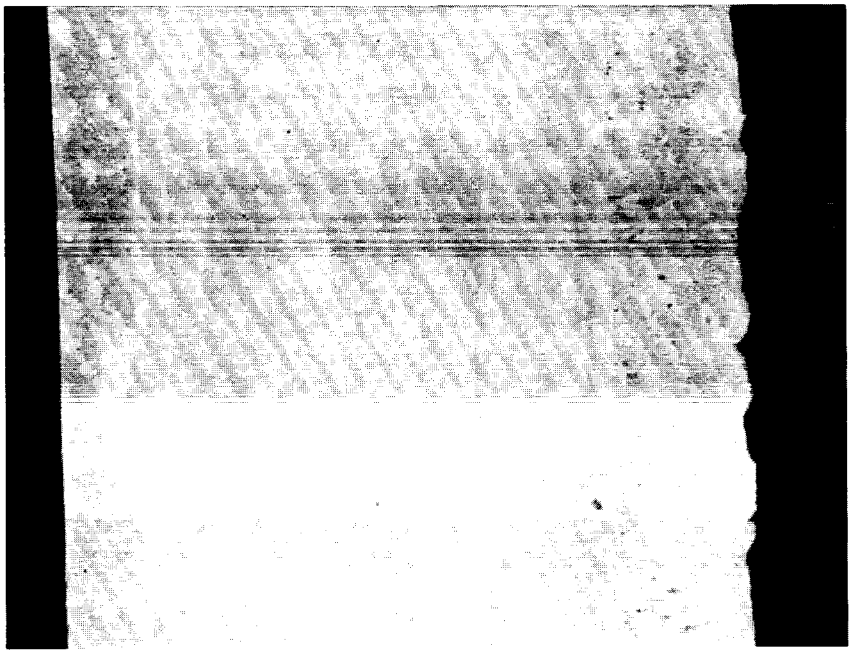

Fig. VII-20. Photomicrograph of a cross section of Au/~1 wt% Ag proprietary electroplate on a Solacel.

Fig. VII-21. Photomicrograph of a cross section of a high-Ag modification to an Au-1 wt% Ag proprietary electroplate on a Solacel.

Electroless Nickel.

Electroless Nickel Plating of GMBs (A. Mayer). Nickel-coated, DT-filled GMBs are required as targets for the ablative implosion experiments planned for Helios. A pie diagram of a typical target is shown in Fig. VII-22.

We have described our work in wet metallization and plating of filled GMBs in an earlier report.[1] No usable targets were obtained by this technique because of the poor coating thickness uniformity and voids in the nickel plate. Several dry metallization processes followed by autocatalytic nickel plating have been evaluated since. GMBs sputtered with ~500 Å of palladium were not usable because of cracks in the highly stressed palladium coating. Inconsistent plating results were obtained when nickel was sputtered directly onto the GMBs; cracked coatings and bare spots were generally observed. The most successful coatings were made with a transitional chromium layer between the glass and the sputtered nickel. When a chromium-flashed nickel sputter target is used, the chromium appears to improve adhesion between glass and metal, reducing the chance of peeled or cracked coatings. Three batches of DT-filled GMBs (15 shells) were chromium-nickel metallized and subsequently nickel plated. Five spheres were usable for targets; the remaining 10 were rejected for various coating defects.

We determined that DT-filling of nickel-plated spheres was feasible, and therefore all subsequent plating experiments were made with unfilled GMBs. Nine batches of preselected GMBs (~20 spheres each) were metallized by sputtering a thin layer with chromium-nickel and then plating with 2 µm of electroless nickel. The yield from these runs was <10%. The two major contributing factors for the low yield are bare spots and poor thickness uniformity in the coating. Photomicrographs of sections through bare spots in these coatings are shown in Fig. VII-23. The spots appear to be caused by incomplete coating during chromium-nickel sputter metallization, possibly because of contamination. The thickness variations, as revealed by micrometallography, were caused by nonuniformities in the sputtered chromium-nickel metal coating. Two distinct layers are shown in Fig. VII-24: the inner chromium-nickel layer on some spheres varied in thickness from nonvisible to as thick as 0.8 µm; the thickness of the outer nickel layer

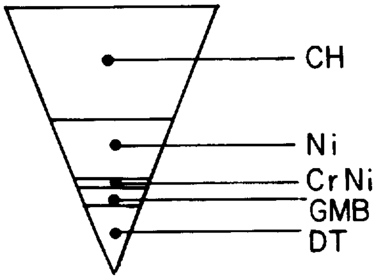

Fig. VII-22. Pie diagram of an ablative implosion target.

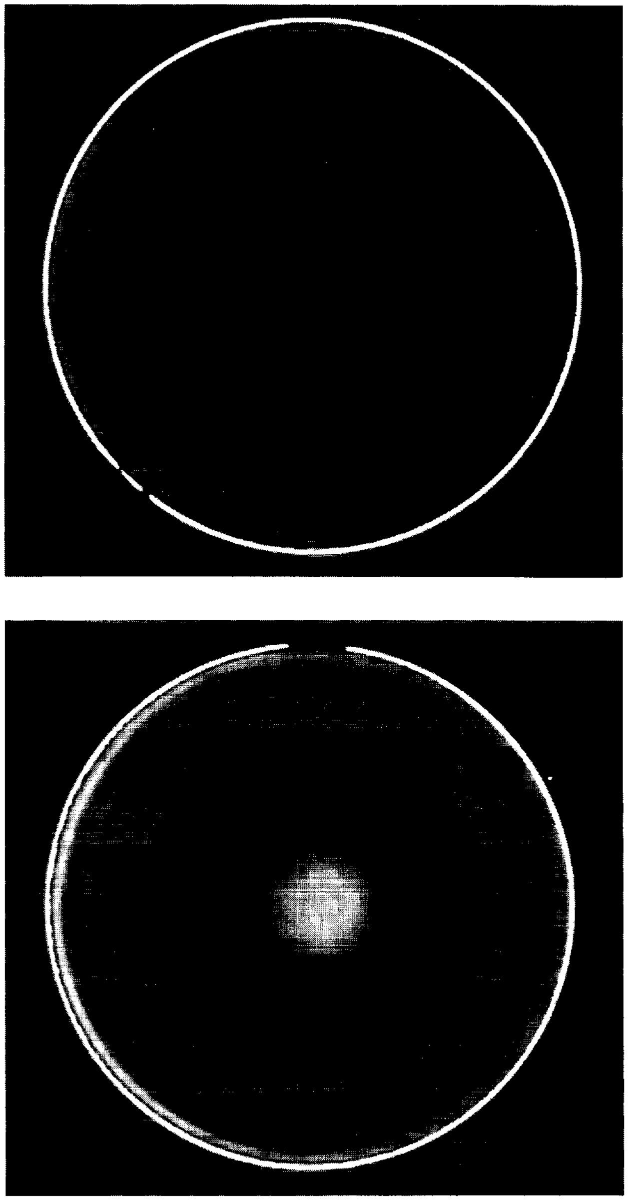

Fig. VII-23. Photomicrographs of sections through bare spots on chromium-nickel flashed 2-µm electroless nickel-plated GMBs. Two distinct layers are evident; the chromium-nickel layer is extremely nonuniform.

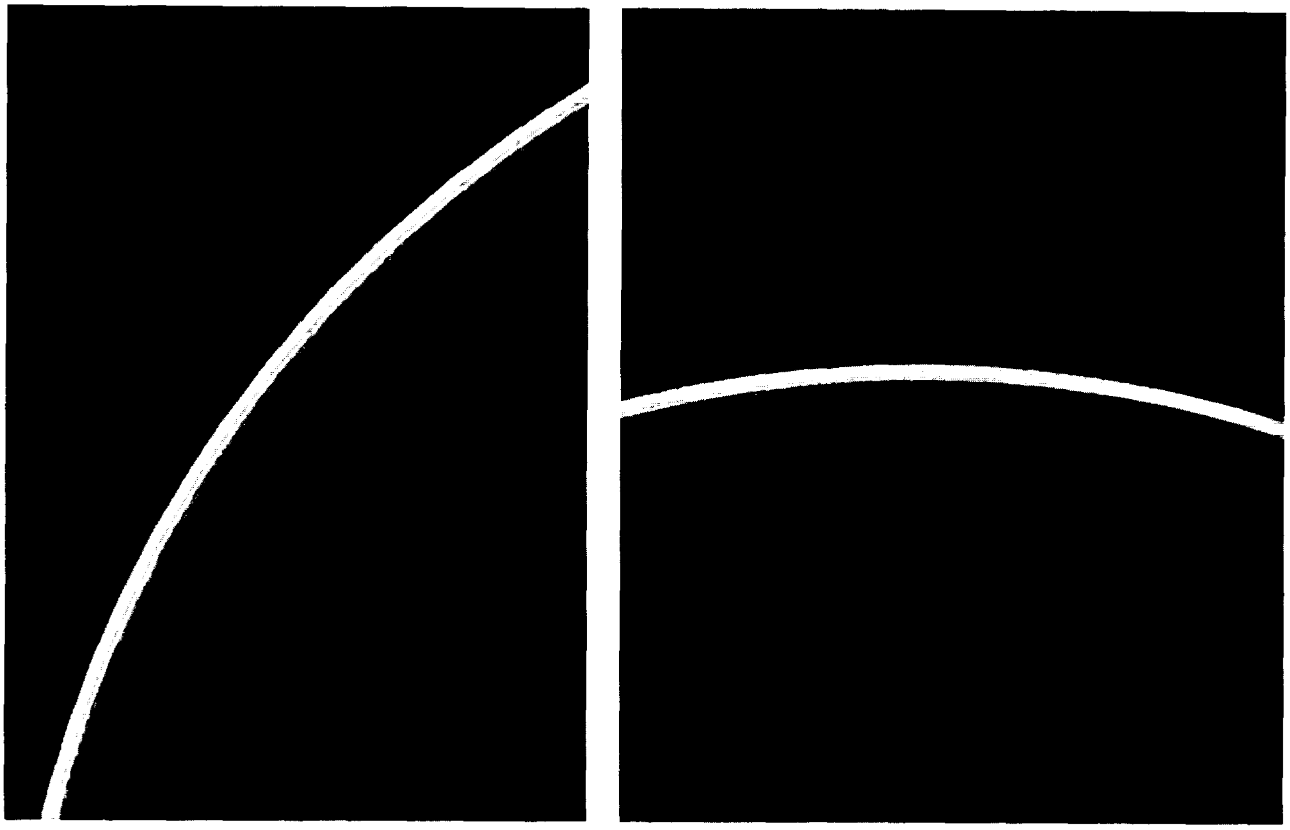

Fig. VII-24. Photomicrograph of chromium-nickel flashed GMB with two distinct layers showing the thickness gradient of the inner chromium-nickel layer.

was fairly uniform. The sputtered chromium-nickel was very nonuniform on some spheres. Further development is required to refine this process.

Another metallization process for depositing a plating base on GMBs consists of applying a thin layer of CVD nickel. A batch of unselected GMBs was coated with a thin layer of CVD nickel; the surface was covered with small nodules that were still observable after 2 μm of nickel plating. CVD-nickel coating of a few preselected GMBs will be pursued as an alternative process for fabricating acceptable nickel-coated spheres.

Targets for Hot-Electron Measurement. A pie diagram of a target for hot-electron measurements is shown in Fig. VII-25. A 3-μm-thick layer of nickel is required between the CH layers. To apply this layer, the surface of the inner plastic shell is sputter metallized first, followed by electroless deposition of nickel to the required thickness. A cross section of this target is shown in Fig. VII-26.

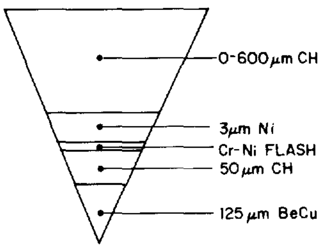

Fig. VII-25. Pie diagram of hot-electron target with a layer of plastic between two metal layers.

Chemical Vapor Deposition (W. McCreary, D. Carroll, J. Vogt).

Metal Coatings Development. We continued to develop CVD metal coatings on GMBs for use as laser fusion targets and to apply metal coatings on selected GMBs.[1] Materials of interest were nickel from $Ni(CO)_4$, Mo_2C from Mo(CO), chromium from Cr(CO), tungsten

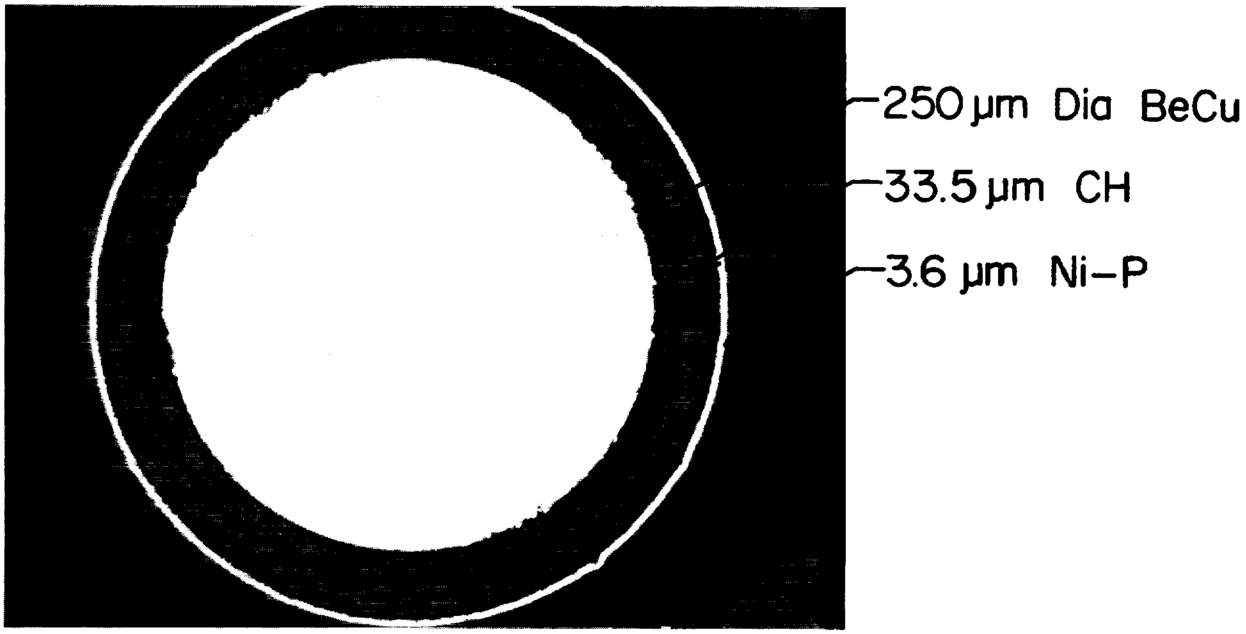

Fig. VII-26. Target for hot-electron measurements.

from WF_6, tungsten from the hexacarbonyl, and cobalt from the 2,4-pentanedionate.

Several DT-filled GMBs were coated with Mo_2C, overcoated with plastic, and coated again with a thin layer of nickel for subsequent electroplating.

Several hundred good quality GMBs were coated with Mo_2C, nickel, and tungsten for diffusion-filling experiments.

We developed a procedure to deposit thick chromium coatings on Solacels in fluid beds with $Cr(CO)_6$ as the reactant gas. These coatings were faceted, resulting in nonspherical Solacels. This program will be continued in an attempt to produce spherical Solacels.

Further work on tungsten coatings from the pyrolysis of $W(CO)_6$ in a hydrogen carrier has been conducted in a limited effort. The major objective for this work is to obtain tungsten coatings 1 to 5 μm thick and 95 at.% purity. Coatings of this thickness can be deposited in 1 to 16 h, the duration depending on the type of substrate. The highest purity obtained to date is only 80 at.% tungsten and further work is needed to improve that percentage.

A quadrupole mass spectrometer has been added to the CVD apparatus for real-time analysis of the exhaust-gas components. Subsequent application of the mass spectrometer to the analysis of the $W(CO)_6$ and H_2 CVD exhaust gas has revealed that the gas composition significantly differs from the calculated equilibrium composition. The major constituents of the exhaust gas are essentially carbon monoxide and hydrogen.

Our experiments with cobalt (II) 2,4-pentanedionate have been carried out in a hydrogen atmosphere at a reaction pressure of 250 torr and temperature of 503 K. The mass transport rate of this cobalt compound has been extremely low (~0.3 mg of coating/min) because the compound has low volatility at 413 K. Consequently, the cobalt coatings have been and will continue to be thin ($\geq$1 μm) at best because of the large surface area in a typical fluidized bed. Also, the surface coatings that have been examined by SEM have been highly granular, demonstrating the need for further work on the interaction of the deposition conditions and surface quality. A single purity determination found the deposited coating to be ~96 at.% cobalt.

CVD Nickel from $Ni(CO)_4$ (W. McCreary, D. Carroll). Prior work resulted in procedures for forming relatively good, thin (<1 μm) nickel deposits on a few (~20) selected GMBs.[1] These GMBs were mixed and coated in a fluidized bed with 1 to 3 cm^3 of microballoons, sized so that the GMBs could be separated by screening after coating.

The major difficulty with CVD nickel in fluidized beds is that the particles stick to other particles and to the coater wall during the process to such an extent that eventually fluid action ceases. Apparently, freely formed CVD nickel readily sticks to itself. Consequently, only short runs can be made and only thin coatings are obtained.

Run times with little or no sticking were increased from ~15 to ~120 min when room air or nitrogen were used as the fluidizing carrier gas, rather than argon or hydrogen. Coatings up to 5 μm thick were obtained, and the smooth, matte nickel surfaces were apparently free of nodules.

$W(CO)_6$: Pyrolysis in H_2 (W. McCreary, D. Carroll). The deposition of tungsten from $W(CO)_6$ is being studied as an alternative process to CVD coating from WF_6 for GMBs. In the earliest stages of WF_6 reduction by H_2, the GMBs are susceptible to HF attack, yielding badly damaged substrate surfaces within the fluidized bed. The alternatives being proposed are (1) coat the GMBs by the $W(CO)_6$ process or (2) flash-coat the glass by the $W(CO)_6$ process for further coating by the WF_6 CVD process.

To date, only extremely thin (<1 μm), but adherent, mirror-like coatings have been deposited. The low coating rate for this CVD process is a direct result of maintaining a high molar feed ratio of hydrogen to $W(CO)_6$ (H/W), as required to minimize oxide, carbide, and free-carbon deposition. The requirement of a high feed ratio, $H/W \simeq 1000$, was determined by thermodynamic calculations for a $W(CO)_6 + H_2$ system.

Chemical analyses of $W(CO)_6$ CVD coatings to determine the relative weight percentages of tungsten, oxygen, and carbon have been performed. The tungsten and oxygen assays have been obtained by neutron activation analysis and the carbon data by using a modified vacuum fusion technique. The available data are summarized in Table VII-I for reaction conditions of 600 ± 10 K mean temperature and 150 ± 10 torr total pressure. The fourth column lists the weight percentages of the total coating for the deposition, as derived by weighing the substrate bed before and after deposition. The final three columns give the results of the various chemical analyses. The data for the two coated Solacel samples indicate that the coatings are ~88 and 86 at.% tungsten. The purity of these coatings falls seriously short of the desired, at least 99 at.% pure tungsten. We believe that the low purity may be improved by increasing both the mean reaction temperature and the pressure, but this supposition has yet to be tested experimentally.

Cobalt CVD: Cobalt (II) 2,4-pentanedionate Pyrolysis (W. McCreary, D. Carroll). The demand for transition-metal coatings on GMBs has generated further interest in a nonhalogen, low-temperature CVD process, particularly for glass substrates. As such, metal 2,4-pentanedionates (or acetylactonates) are promising CVD source materials for pyrolytic decomposition. The crystalline compounds are not poisonous and thus are more easily handled. Also, these metal chelates can be easily evaporated, usually below 473 K, and decomposed at low temperatures (272-773 K). However, because of the metallic-oxygen bond, not all 2,4-pentanedionates will yield metal films. Many chelates yield only oxides, carbides, or mixtures with pure metal.

Our initial investigation has been restricted to cobalt 2,4-pentanedionate because this chelate has been reported to deposit metallic films. For elements in the first transition series and for the platinum metals, 2,4-pentanedionates are commercially available.

Our experiments with cobalt chelate have been carried out in a hydrogen atmosphere of 250 torr with a fluidized bed of either GMBs or Solacels. The deposition experiments were conducted in a simple vertical Pyrex tube that contained a coarse glass frit as the gas distributor and bed support. The cobalt source was located immediately below the frit. The glass reactor was positioned in a two-zone resistance furnace to provide separate zones for chelate evaporation and chelate pyrolysis.

The evaporation temperature in the initial experiments was set at 283 K, yielding deposition rates of ~0.5 mg/min. The initial experiments concentrated on finding the optimum reaction temperature for our experimental apparatus. To date, the most promising metallic coatings have been observed at 600 K within a Solacel fluidized bed. At reaction temperatures near or above 575 K, carbonaceous material was deposited.

CVD Characterization.

CVD Fluidized-Bed Characterization (R. Springer, A. Mayer). We conducted a series of fluidized-bed tests for the evaluation and interpretation of the pressure fluctuation monitor. The response of the monitor was examined over a limited range of particle diameter, particle density, and settled bed height. The tests were conducted in a conical reactor vessel with a 30° included angle and argon as the fluidizing gas.

The dominant frequencies and overall power spectra for the test conditions exhibited a significant shifting to

TABLE VII-I. Chemical Analysis of Coating From $W(CO)_6$ CVD[a,b]

Sample	Feed Ratio (H/W)	Substrate Type	Fraction of Total Coating on Substrate Bed (wt%)	Fraction of Element on Substrate Bed (wt%) W	O	C
Solacel				0.0	1.06 ± 0.03	---[c]
WC06-8	1410	Solacel	18.9	19.3 ± 0.3	0.22 ± 0.04[d]	---[c]
WC06-9	820	Solacel	24.0	24.0	0.34 ± 0.03[d]	---[c]
Aluminum spheroids				<0.001	0.019 ± 0.001	137 ppm
AC06-10	–2000	Aluminum spheroids	6.04	5.62 ± 0.14	0.18 ± 0.002[d]	0.12[d]

[a] Mean reaction temperature, 600 ± 10 K. Total reaction pressure, 150 ± 10 torr.

[b] Estimates of the standard deviation are given.

[c] Data not taken.

[d] Value equals the difference between coated and uncoated substrate.

lower frequencies with increasing particle diameter, particle density, and bed height. In addition, the power spectra for all test beds were dependent on the total flow rate of the fluidizing gas after incipient fluidization, and they became nearly independent of the flow rate at higher velocities.

We believe that a CVD fluidized-bed reactor cannot be maintained at a fixed state of mechanical activity. Because of the inherent time-dependent increase in particle diameter and density, the mechanical activity of a CVD fluidized bed will proceed from a state of higher frequency behavior to that of much lower frequency behavior. With this changing behavior the pressure fluctuation monitor can sensitively assess the relative progress of the reaction as the particle diameter and density increase.

Fluidized-Bed Probes. A development program was initiated late in 1979 to investigate and evaluate the real-time instrumental techniques needed to characterize and distinguish both the type and degree of mechanical behavior in a fluidized-bed CVD reactor. The major effort in 1980 was directed toward assembly, testing, and evaluation of the necessary instrumentation for the proposed probes. The bed sensors will be used to study the effects of significant real-time changes in the dynamic behavior of the fluidized bed during a CVD reaction. The proposed sensors will detect and identify major changes in particle circulation and deposition rate, and should provide sufficient information about a fluidized-bed reactor to ensure reproducible results from batch to batch.

Reaction Efficiency. The exhaust-gas composition will be monitored by a quadrupole mass spectrometer and a photoionization detector. Both units were ordered commercially earlier in 1980, but shipping has been delayed.

The quadrupole mass spectrometer is equipped with a Faraday detector for a 2- to 100-amu range. A high-vacuum sampling system with a rudimentary pressure-reducing scheme has been constructed and tested for leaks; it will be used by the spectrometer in our subatmospheric CVD reactor system.

Resistivity Sensor. The resistivity sensor has only limited application to electrically conductive coatings. Furthermore, the inner electrode penetrates the bed with a conductive tip and will certainly be shorted to the outer surface of the entire penetrating portion during the CVD process. A simple inner electrode without any electrical insulation has been evaluated in limited testing with tungsten-coated spheres in an all-metal coater. Under controlled, non-CVD conditions, the resistivity sensor with a bare inner electrode was difficult to use. Problems with this sensor and a desire to avoid disturbing the bed's fluid activity with an inbed probe will reduce or terminate our use of the resistivity sensor.

Pressure Fluctuation Sensor. Fluctuations in the pressure drop across a fluidized bed can readily be monitored by a sensitive pressure transducer or microphone. Two different types of pressure sensor have been obtained for this purpose: a standard variable-reluctance pressure transducer and a piezoelectric high-sensitivity pressure sensor. Either sensor can be mounted above the bed horizontally through the reactor wall just outside of and above the resistance furnace. Although this location for the sensor is not ideal, several practical constraints, such as temperature, tubing diameter effects, and reactor geometry prohibit the choice of other likely locations.

The electrical output from the fluctuation sensor is processed by a FFT spectrum analyzer for real-time frequency analysis. We have purchased such an analyzer with sufficient analytical capability to derive any required information during deposition. For example, the spectrum analyzer can readily measure dominant frequencies, intensities, bandwidths, and variable-bandwidth power levels.

Experiments were carried out with various fluidized beds to gain experience with the operation of the sensor and with the interpretation of the output signal and its analysis. A typical pressure vs time plot is shown in Fig. VII-27; its power signal appears to be random, yet the occurrence of one or more frequency maxima, such as the two intense peaks at 2.55 and 4.40 Hz in Fig. VII-28, are reproducible features. A time signal and its power spectrum is shown in Fig. VII-29 for the fluidized bed of Fig. VII-27 in an unstable, slugging state. This plot demonstrates the fluctuation sensor's ability to distinguish the major mechanical states of a fluidized bed and to detect the transition between the states. The slugging-bed signal in Fig. VII-29 shows a high periodicity with a dominant frequency at 1.45 Hz and with several higher harmonic frequencies, as indicated in Fig. VII-30.

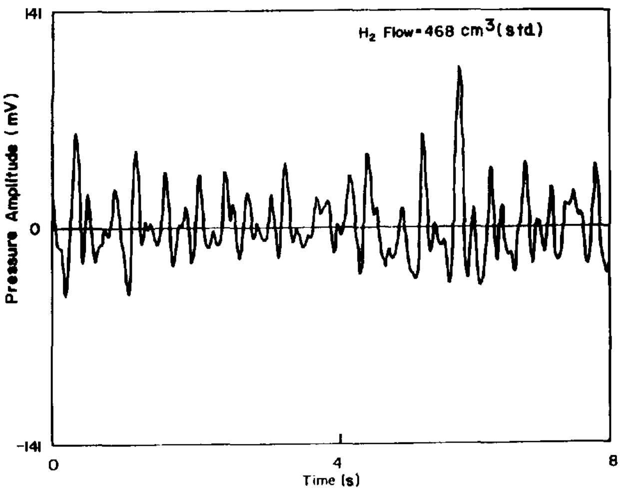

Fig. VII-27. Time signal for a fluidized bed in a bubbling mode.

These observations have been made for fluid beds without the added complication of a CVD reaction. In the case of a $W(CO)_6$ CVD experiment with a low deposition rate, where the total flow rate is held fixed, changes in dominant frequencies, active band, and power levels also appear to be negligible. We plan to use the pressure fluctuation sensor to monitor fluidized beds at faster deposition rates.

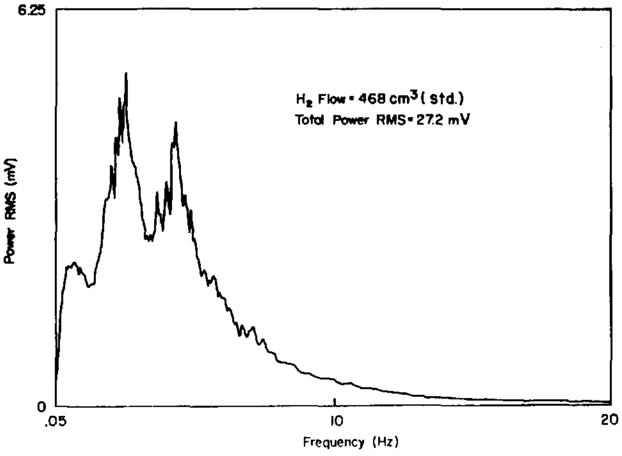

Fig. VII-28. Power spectrum for a fluidized bed in a bubbling mode.

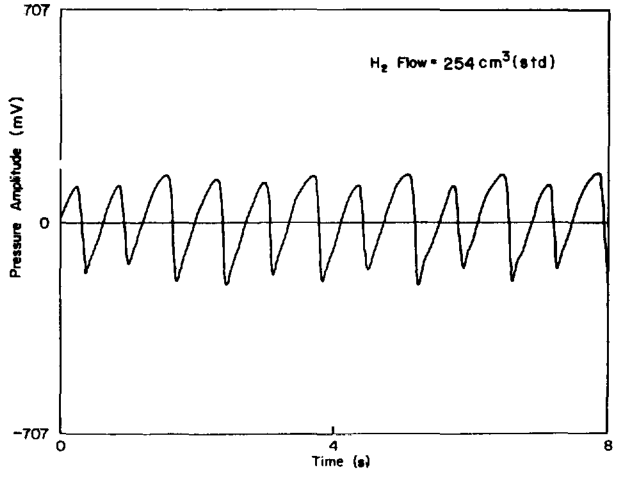

Fig. VII-29. Time signal for a fluidized bed in a slugging mode.

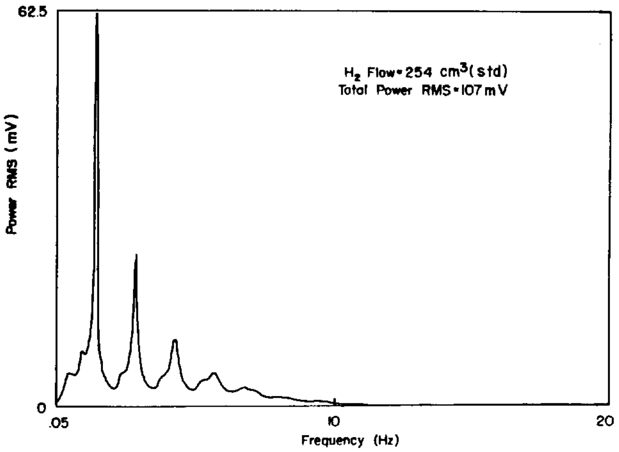

Fig. VII-30. Power spectrum for a fluidized bed in a slugging mode.

Levitation (J. Bunch, D. Brown).

Gas Levitation. We have concentrated on improving the deposition rates of metals on GMBs by using sputter deposition with molecular-beam levitation. Earlier work was performed with an rf magnetron source; maximum power input (hence deposition rate) was limited by an interaction with stray plasma that tended to force the GMB into the levitator. We have discovered that this effect is greatly reduced when the magnetron is operated with a dc, rather than rf, target power supply. We also found that a washer-type levitation structure (Fig. VII-31) provides stable levitation at lower chamber pressures than the dimpled collimated-hole structure used earlier. Increased stability can contribute to higher deposition rates caused by reduced gas scattering of the sputtered metal atoms. We have obtained deposition rates of ~1 µm/h of nickel, and similar rates should be attainable with several other metals. We have attempted to optimize the procedure for sputtering nickel onto levitated GMBs and are striving for the best possible combination of adhesion, surface finish, and thickness uniformity for coating thicknesses up to ~3 µm.

By varying surface pretreatment and deposition rate, which affects grain structure mainly by changing the temperature of the GMB, we have produced highly adherent fine-grained coatings with surfaces smooth within a few hundred Å. However, thickness uniformity is not well controlled. Some targets are uniform within ±10%, whereas others are so highly nonuniform that all the coating is on one side of the GMB. The latter effect may be attributed to torque exerted by electric fields in the sputtering plasma on surface charges residing on bare or otherwise insulating patches on the GMB surface. A possible solution would be to provide a uniformly conducting precoat and reduce the plasma density.

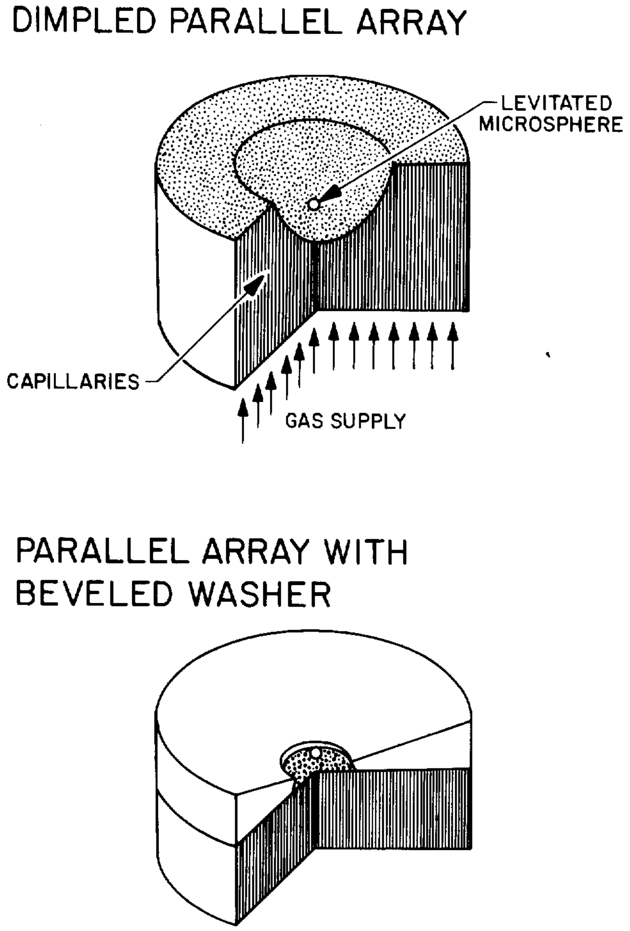

Fig. VII-31. Comparison of dimpled parallel array with washer-type levitation.

We have investigated structures other than a dimpled capillary array for generating the molecular beam used to levitate the GMB. The process described above used a levitator that consisted of a beveled washer resting on a flat glass capillary array with a hole diameter optimized for the desired ranges of GMB diameter and weight. A focusing array did not seem to work as well, but the parameters were not optimized, and variations are still being tried.

To assist in our efforts to optimize coating thickness variation, we have initiated a contract with the Aeronautical Engineering Department at Pennsylvania State University to provide a computer model of the rigid body dynamics of a GMB during coating. This model will take into account the effects of changes in gravitational torque and moments of inertia as the coating thickness increases during deposition.

Bounce Levitation. We have refined the loudspeaker-bounce sputter technique for applying nickel flash coatings on GMBs by driving the apparatus with white noise rather than with a sinusoidal signal. This change prevents the GMBs from collecting at nodes in the vibration pattern.

A chrome-filament evaporation source, with the magnetron sputtering source, now provides a chromium adhesion layer, when necessary, between the GMB and the nickel flash.

Organic Coating Development

General. Plastic coatings are routinely used as absorber/ablator layers on laser fusion targets. The important physical parameters for such coatings are uniformity of wall thickness ($\leq 1\%$ variation) and surface smoothness ($\leq 1\%$ deviations). The thickness of these coatings varies from a few μm to ~600 μm. In addition, some target designs require the inclusion of high-Z elements in the coatings to shield the DT fuel from hot electrons and x rays. The density we are seeking in these high-Z-loaded plastic layers ranges from 1.3 to 2.5 g/cm^3.

LPP Process (R. Liepins, J. Hammond, M. Campbell). One of our main objectives was the deposition of hydrocarbon coatings on metallic (molbydenum, tungsten, and gold) substrates in the fabrication of Polaris Prime targets. Other activities involved the conversion of a monomeric ammonia-borane coating into a polymeric coating and the preparation of perfluorocarbon coatings for S/D studies.

We developed a technique to deposit thick (~26-μm) hydrocarbon coatings on rough molybdenum and tungsten substrates with a multitude of asperities by depositing the coating in several layers and using clean electrodes for each layer deposition. Monomeric ammonia-borane coatings (12-24 μm thick) on GMBs were converted into glassy polymeric coatings by N_2 plasma in our LPP system.

Hydrocarbon Coatings on Metallic Substrates. Of the three metallic substrates (molybdenum, tungsten, and gold), the molybdenum and tungsten substrates were very rough, containing a multitude of asperities that tended to break off during the coating run, generating fine particulate material on the electrode. This in turn caused the generation of very rough hydrocarbon coating surfaces. The problem was minimized by depositing initially only a 3- to 4-μm-thick coating (before much particulate material could accumulate), then exchanging the electrodes for clean electrodes and continuing with the deposition of increasingly thicker coatings after each electrode exchange. The gold substrates were much smoother and without asperities and, as a result, did not require the electrode changes for thick coating depositions.

Ammonia-Borane Coatings (with R. Geanagel). A sublimation technique was developed to deposit uniform, thick (24 μm), ammonia-borane coatings on mounted GMBs. We used high vacuum ($<10^{-6}$ torr), mounted the GMBs next to a liquid N_2 cold-finger, and carefully controlled the monomer sublimation temperature. Equally important, only freshly sublimed monomer was used in this work.

The monomeric coatings were converted into glassy polymeric coatings by an N_2 plasma (300 mtorr) in our LPP system. Preliminary ir spectroscopy indicates that the composition of the polymeric coating is -(BH-NH-)_n with, perhaps, some boron-nitrate included.

Perfluorocarbon Coatings. Perfluorocarbon coatings from perfluoro-2-butyne and perfluoro-2-butene were prepared in the presence of an argon plasma at static and flowing monomer conditions and power densities as low as 0.04 W/cm^2. In general, the above monomers polymerized more easily than many gaseous hydrocarbons at comparable conditions and produced surfaces that were smoother than those of hydrocarbons.

Thick Coatings. In previously reported work, we sought to define the effect of physical and chemical properties of various monomers and background gases on the deposition rates achieved.[12] This effort revealed a strong correlation between the electron-impact ionization potential of the materials and the deposition rates. Coating rates and thickness were inversely proportional to the ionization potentials of the monomer and/or the background gas used. On the basis of these observations, we selected a new monomer, cyclooctatetraene (COT), and achieved 40-μm-thick coatings in our first attempt.

Of the more than 1000 substances surveyed for their ionization potential, a few with some of the lowest values are listed in Table VII-II. We find COT one of the most

TABLE VII-II. Ionization Potentials of Some Hydrocarbons

Substance	Ionization Potential (eV)
P-xylene	8.445
1, 2, 4, - Trimethylbenzene	8.27
Triphenylene	8.02
Cyclooctatetraene	7.99
Anthracene	7.25
Dibenzo(aj)anthracene	6.99
Pentacene	6.73

convenient materials to work with. Similarities in the behavior of a substance in plasma reactions and in mass spectroscopy have been recognized,[12] and we can predict the results of a plasma experiment from the mass spectrum of the starting material. Correlation with activation energies for thermal decomposition appears to follow, in general, the electron impact ionization data, but correlations with electron affinities are less apparent.

We have now deposited 66-μm-thick COT coatings and anticipate no problems in depositing much thicker ones.

When we deposit very thick coatings, the sharp edges of the electrodes are the initial sites at which cracking and peeling of the coating starts. To eliminate these problems, we have designed and tested a series of shaped electrodes. Electrodes with grooved surfaces and large cylindrical edges have been coated to thicknesses exceeding 100 μm without blistering or peeling.

VPP Process (M. DeVolder, R. Liepins). The main objective of the VPP process continues to be deposition of thick coatings in routine target preparations on a short-notice basis. Other activities involved the preparation of thick, transparent coatings, coatings of a very high density, and building of a new automated VPP system.

We prepared transparent coatings as thick as 210 μm. By depositing the poly(p-xylylene) coating at very low temperatures (153 K), we obtained coatings with much higher densities than reported previously. A new semiautomatic VPP system is ~75% complete.

Very Thick Coatings. Currently, the thickest hydrocarbon coating that we have deposited is 600 μm. Because of coating-chamber size limitations, the coating was deposited in layers on the stalk-mounted target and the stalk was machined off after each layer. A microradiograph of the beryllium/copper substrate used for the target and the target itself are shown in Fig. VII-32.

Smooth, Transparent Coatings. Clean substrates, clean atmospheres, and low deposition rates are required to obtain smooth coatings. For optically clear coatings, we positioned a copper screen between the di-radical outlet in the coater and the substrates to be coated. Both characteristics may also be obtained in a coating that has been deposited at a high rate if a comonomer is incorporated in the process. Earlier we had used 10 wt% of 2-chloro-di-p-xylylene as the comonomer[1] and now we find that 2-ethyl-di-p-xylene has the same effect as the chloroderivative. The use of a comonomer that is similar in basic structure but different in detail is sufficient to impede the crystallization of poly (p-xylylene), and thus results in a smooth coating. If the system pressure is constant throughout the coating run, we can deposit very thick (210-μm) transparent coatings.

Coating of Bouncing GMBs. Except for one previous unsuccessful attempt at coating simultaneously more than four free-standing GMBs,[13] no similar work has been reported. We have now coated bouncing GMBs in a chamber cooled to 153 K (−120°C) before admitting the di-radical vapors. We have deposited 5-μm-thick coatings on more than 100 GMBs without agglomeration. One of the key factors in our success is an increased sticking coefficient of the di-radical that is obtained when we lower the temperature of the substrate to be coated.

Automated VPP System. Automation of the VPP system should lead to coatings of improved quality and to a more efficient use of our manpower. We designed an automated coater to allow for fully programmable control of the operation over a period of days. The system is being constructed in two stages, and it will be operational before the programmable portion of it is completed. Thus, in the first stage of the construction, the system will automatically control the vaporizer temperature, pyrolysis furnace temperature, cooling-chamber temperature, and system vacuum pressure. First-stage construction is ~75% complete.

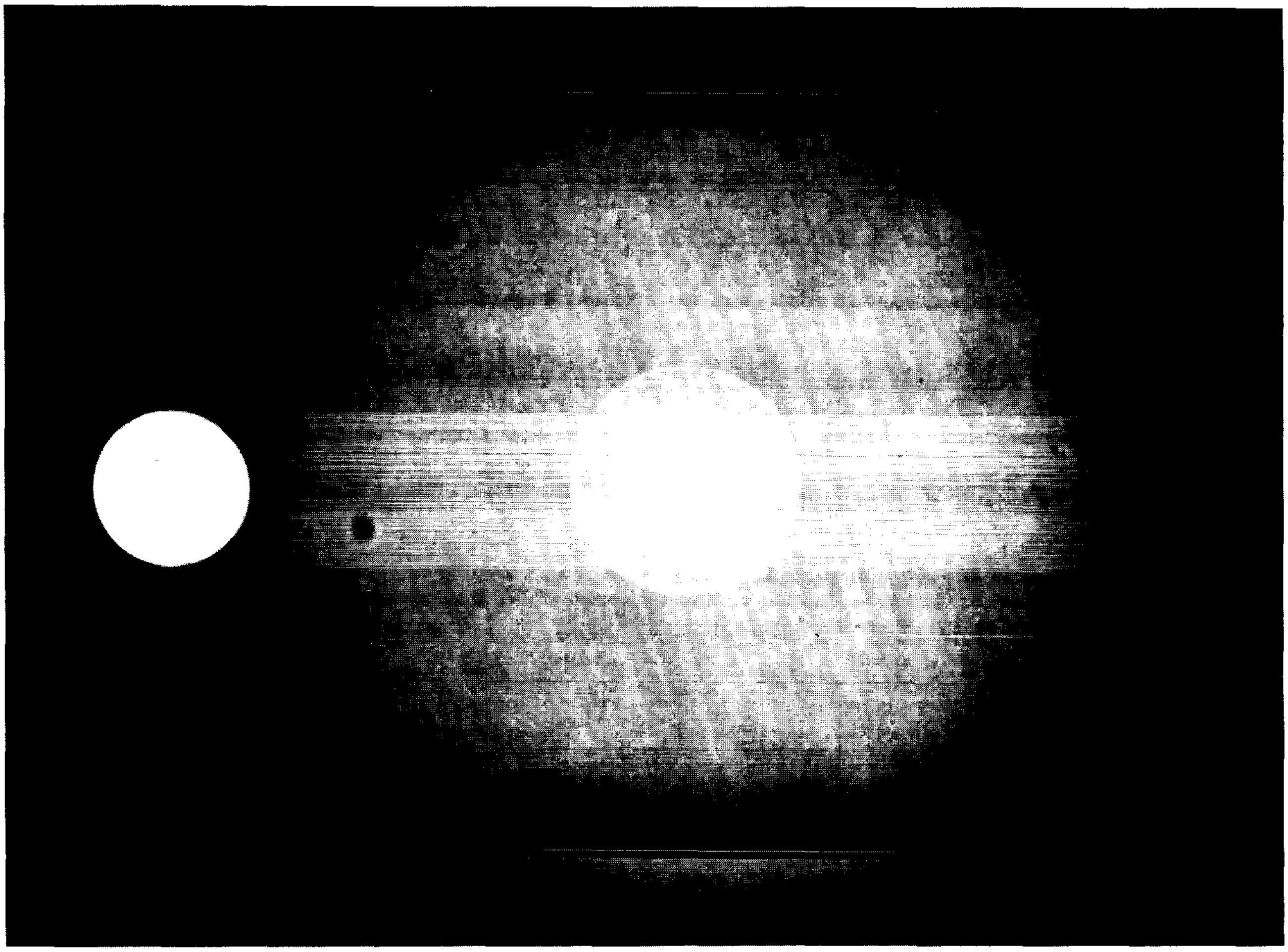

Fig. VII-32. Microradiograph of a thick plastic-coated hot-electron target, 600 µm of parylene on a beryllium/copper substrate.

Organometallic Coating Development (R. Liepins, J. Hammond, J. Clements, M. Campbell)

Deposition of thick hydrocarbon coatings containing various lead concentrations and gradients is the main objective of this effort. Coatings as thick as 28 µm, containing 33.6 wt% (1.41 at.%), have been deposited.

LPP Process Organometallic Coatings, Lead Concentration. In most of our current work we use lead compounds. Tetramethyl lead is obtained as an 80.3% solution in toluene, whereas tetraethyl lead is available as a pure compound. We use both compounds either as received or mixed with COT. Because of the significance of the ionization potential of a substance in LPP processes, simple mixing of two substances with the same boiling point but different ionization potential will not determine the composition of the coating. To obtain a specific metal concentration in a coating, the organometallic and the hydrocarbon components must be metered into the deposition chamber separately at rates to be determined experimentally.

Graded Density. By combining the previously developed techniques for depositing metal-containing coatings[14] and potential monomers with low ionization, it becomes possible to deposit coatings with gradients in density. A microradiograph of a lamellar dual-concentration coating is shown in Fig. VII-33. The coating contains no metal and the outside is a complex layered structure graded in density. The metal is lead, and its

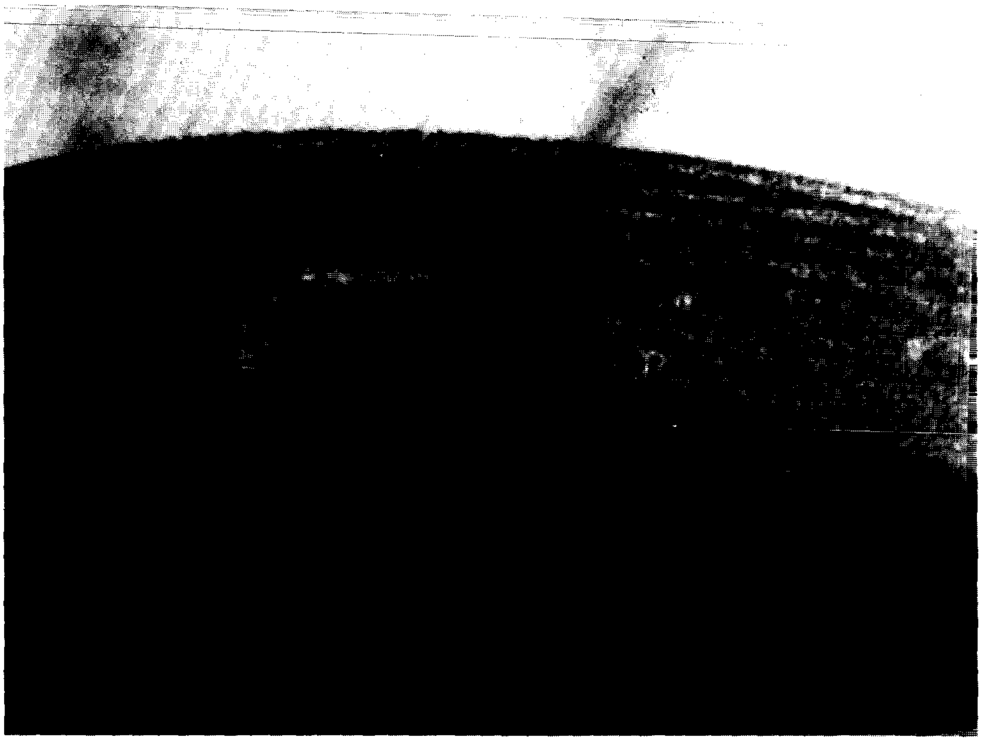

Fig. VII-33. Microradiograph of a graded-density, lead-containing LPP coating on a GMB.

concentration at the outside is ~78%. The hydrocarbon component in these coatings was COT; the concentration gradients were achieved by regulating the organometallic component flow rate and keeping the COT flow rate constant.

Organolead Coating Density. The metal concentration in metal-containing coatings is usually expressed in terms of the density of the coating. Our lead analyses are performed by atomic absorption measurements of films deposited on the electrodes. We cannot yet say how representative such an analysis may be of the lead composition in the coating on GMBs. The lead concentration data of the films on the electrodes and the determined densities on the coatings on the GMBs are summarized in Table VII-III.

Organometallic VPP Process Coatings. The initial work with ferrocene to explore process possibilities has been extended to the incorporation of the metals of

TABLE VII-III. Lead-Containing COT Coating Data

Lead Concentration[a]		Coating Thickness[b] (μm)	Density[b] (g/cm^3)
wt%	at.%		
3.88	0.13	26	1.140
16.77	0.45	33	1.292
80.40	6.67	6	2.626

[a] Films on electrodes.

[b] Coatings on microsphere substrates.

interest (bismuth and thallium) into the coating. To incorporate bismuth we used triphenyl bismuth and a specially constructed vaporizer that was a part of the deposition chamber. We have incorporated 16 wt% of bismuth by using this same vaporizer and thallous formate; we also incorporated 1 wt% of thallium.

S/D Coating Process. A third coating process, S/D, is a conversion process that is still in the early stages of development. It seems to be useful in the generation of plastic and metal-containing plastic coatings, metal-upon-plastic coatings, and coatings graded according to atomic number and density. It does not appear to be limited to any particular elements in the periodic table. This conversion is performed from either the liquid or the gas phase, and microballoons may be coated free-standing or mounted.

The procedure consists of COT-deposition by the LPP process followed by S/D treatment. Plastic-coated microballoons are exposed to a solution containing metals of interest for controlled periods of time, then removed and dried at ambient conditions for ~16 h. The procedure is not limited to COT coatings or to any specific coating thickness. Coatings graded according to Z and density can be prepared by solvent pretreating of the LPP coatings; using solvents with varying solubility parameters; and using solvent mixtures as well as different treatment times, temperatures, and pressures.

In the case of gas-phase treatment, the LPP-coated microballoon is placed in an atmosphere of gaseous metal compounds that are easily vaporized. Because of the high concentration of free radicals, LPP coatings in general are very reactive; the diffusing species will react with these free radicals and become chemically bound to the coating. We have incorporated palladium, mercury, tantalum, tungsten, osmium, gold, platinum, Cl_2, Br_2, boron, and iridium into plastic coatings. Work so far indicates that a large variety of boron-metal-hydrocarbon or boron-metal compositions should be possible. We have also demonstrated the feasibility of depositing gold and platinum metallic coatings onto GMBs without using complicated or advanced techniques.

Metal coatings on plastic coatings are prepared by exposing S/D-treated microballoons to an oxygen plasma in the LPP instrument. The plasma burns away the organic material, leaving behind the diffused metal component as a coating. We have prepared highly adhering gold coatings on plastic, a result that usually is not easily accomplished.

The third, and perhaps most spectacular, result of this process is its surface-smoothing effect. We have submitted coatings with extremely rough surfaces (on the order of many microns) to the S/D treatment and reduced roughnesses to only a few 100 Å (Figs. VII-34 and VII-35). This process has also worked on pure hydrocarbon coatings.

S/D Treatment of Monomeric Coatings. With the development of monomeric ammonia-borane coatings on GMBs, we explored their adaptability to the S/D treatment. This process would then permit the generation of rare and unique boron-metal alloys (compositions), because the conversion of monomeric ammonia-borane coatings into polymer coatings has already been demonstrated. Thus, monomeric ammonia-borane coatings have been S/D-treated with gold, platinum, and palladium metal-containing solutions and, in general, have survived the impregnation process.

Gold and Platinum Coatings on GMBs. There are no simple ways for depositing metallic coatings onto GMBs. About the simplest one is the PVD technique, but it requires specialized equipment. We dip-coat free-standing GMBs in organogold and platinum solutions, dry the coatings at ambient conditions, and then expose them to 823 K (550°C) for 30 min to successfully produce gold and platinum coatings on the GMBs.

LOW-DENSITY ORGANIC FOAM AND FIBROUS MATERIAL DEVELOPMENT

Low-Density Organic-Foam Development (A. T. Young, D. Moreno)

In Polaris multishell targets, a hydrodynamic cushion layer is required between the metal shells to modify the shocks transmitted during implosion. A rigid low-density microcellular foam can be used both as the implosion-shock buffer and as the support structure. A foam layer in laser fusion targets should have a density of <0.1 g/cm^3 (preferably <0.05 g/cm^3), its cell size should be uniform and ~1 μm in diameter, and the cell structure should be open so that voids can be filled with helium gas for cryogenic cooling of the DT fuel. For such targets driven by light-ion beams, the specifications can be relaxed to 0.1 g/cm^3 at uniform cell sizes of 8 to 10 μm.

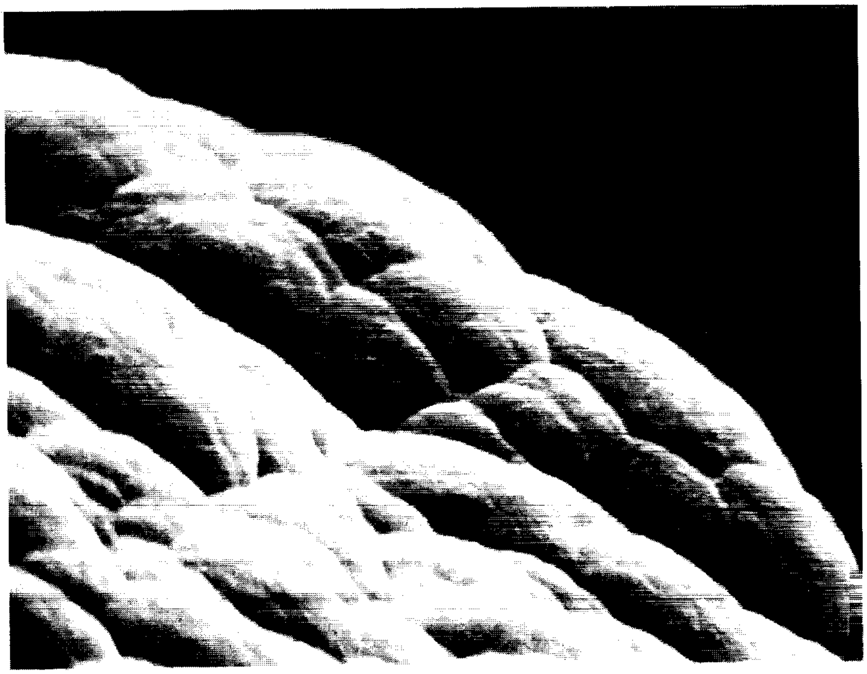

Fig. VII-34. SEM of COT plastic coating on GMB as coated (5000 ×).

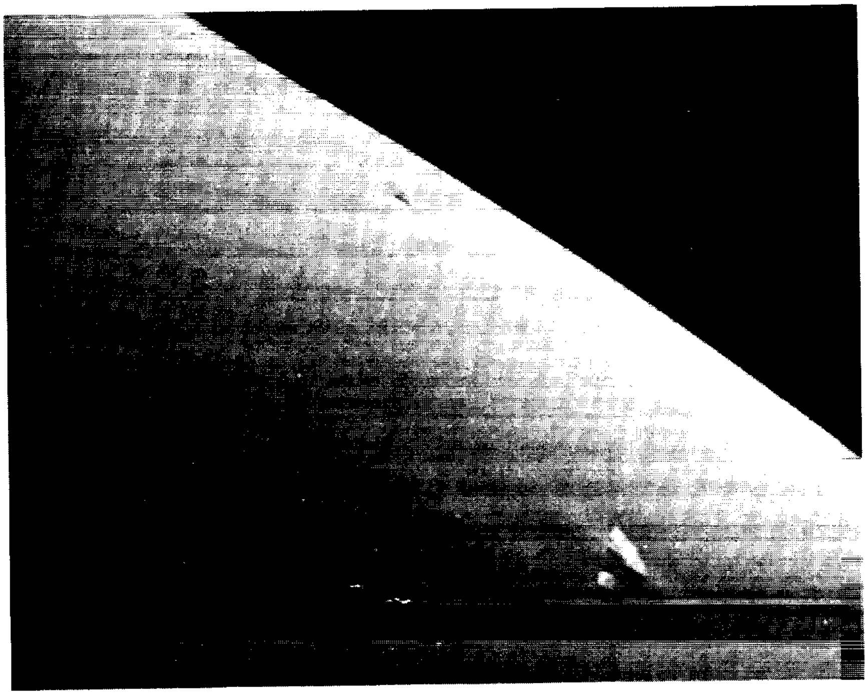

Fig. VII-35. SEM of COT plastic coating on GMB after S/D treatment (5000 ×).

Foam Development and Foam Fabrication. Our studies of low-density, microporous plastic foams have concentrated on Polaris-type multishell laser fusion targets and multishell SNL particle-beam fusion targets.

Target Type	Foam Density (g/cm^3)	AV Foam Cell Size (μm)
Polaris	0.05	2
SNL	0.05	10-20

When we screened a wide variety of foam-forming processes, we found that a thermally induced phase inversion process involving polymer solutions satisfied our requirements. In this process, low-density, microcellular plastic foams could be prepared by dissolving a polymer at high temperature in a material in which the polymer has limited low-temperature solubility and rapidly cooling the resulting solution below the temperature at which the polymer becomes immiscible in the solvent. A polymer matrix is then formed with the solvent filling the voids of the matrix. The structure of this matrix is dependent on the interactive relationships among solvent, polymer, and the system's cooling rate. Foams have been produced successfully from both aqueous and organic solvent systems, the polymer in all cases being substantially insoluble at temperatures used to remove the solvent.

For Polaris multishell ICF targets, aqueous solutions of water-soluble polymers are converted to polymer foams as we force the solvent to separate from the polymer by rapidly freezing the solution in liquid nitrogen. The frozen solvent is then removed by freeze-drying under vacuum.

This process has yielded rigid microcellular foams with measured densities close to theoretical for methyl cellulose, carboxymethyl cellulose, and polyacrylamide. Foams at densities of 0.01 g/cm^3 were almost completely open with the structure consisting only of ribs at the intersections of the faces of a regular dodecahedron, as shown in Fig. VII-36 for methyl cellulose. Foams at densities of 0.05 g/cm^3 (Fig. VII-37) show the more familiar cellular structure with cell sizes for this carboxymethyl cellulose foam in the range of 2 μm. Foams with densities of 0.05 g/cm^3 have been molded into hemispheres with 200-μm radii as potential shells for Polaris-type targets.

A process developed by Armak Co.* exploits a similar preferential phase-separation phenomenon using polyolefins and an organic solvent; this process is better suited for the SNL programs.

The basic process involves a thermally induced phase inversion technique to produce microcellular plastic foams. The polymer that will form the foam structure is dissolved at high temperatures into a material in which the polymer has limited low-temperature solubility. Rapid cooling of this solution results in a separation of the solvent and polymer phases in such a way that a polymer matrix is formed and solvent fills the voids of the matrix. The structure of this matrix also depends on the interactive relationships between the solvent and the polymer and on the cooling rate of the system.

This process has been successful in the preparation of plastic foams containing only carbon and hydrogen; polyolefins such as polyethylene and polypropylene can readily be converted to foams.

We have used this process to study polyolefin foams for the SNL light-ion ICF program, where considerable effort went into the molding of spherical hemishells. Screening a number of different solvent systems for polyolefins such as poly(4-methyl-l-pentene) has identified several solvents that minimize shrinkage of the hemishell in the mold. Poly(4-methyl-l-pentene) foams with densities of 0.03 to 0.11 g/cm^3 and cell sizes in the 10- to 20-μm range have been made in desired configurations. The cellular structure (Fig. VII-38) is rosette and cell sizes are reported as maximum distances between petal surfaces. Mixed solvent systems give very sensitive control over cellular structure and size characteristics of the foam.

Based on the data generated in the SNL study, we developed a low-density, microporous foam (Fig. VII-39). High-molecular-weight poly(4-methyl-l-pentene) was selected as the foam polymer because it is composed only of carbon and hydrogen and has a low bulk density (0.83 g/cm^3). Bibenzyl (1,2-diphenylethane) was chosen as the cell-filling material because it is a good solvent for the poly(4-methyl-l-pentene), shrinks a minimal amount in the final foam (that is, a nonplasticizer for the polymer), and most importantly, is solid at room temperature.

By successfully forming bulk low-density foam, we were able to carry the solution of polymer in bibenzyl through the critical miscibility temperature (the

---

*McCook, Illinois.

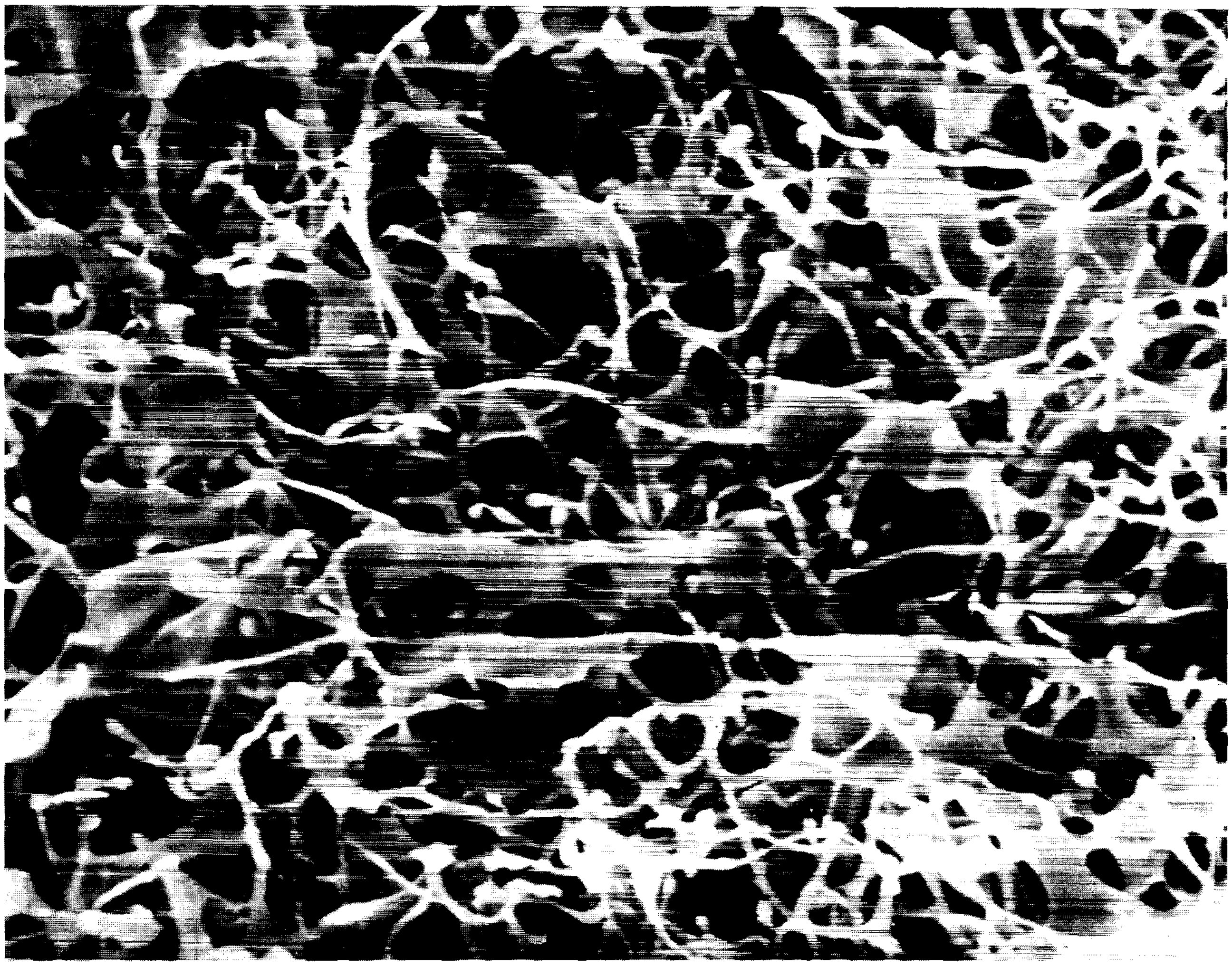

Fig. VII-36. Methyl cellulose foam. Density = 0.01 g/cm^3.

temperature at which the foam matrix is formed). Both the cooling rate through this temperature region and the temperature uniformity throughout the sample had to be controlled tightly to ensure the quality of the final foam.

Once the polymer matrix had been formed, the bulk material could be cooled to a solid state at room temperature. In this state the polymer foam cells are completely filled with the solid bibenzyl, forming a material that feels somewhat waxy to the touch. The bulk material can be machined to very tight tolerances with conventional equipment without adversely affecting the foam structure. This method has distinct advantages over other foam fabrication methods because attempts to fabricate empty-cell, low-density foams into desired configurations usually result in considerable damage to the foam, especially at the surface, with very little control over tolerances. A patent application is being filed covering this unique method of fabricating foam parts of very low density to tolerances never before thought possible.

Microgravity Coating Studies (A. T. Young). Under contract, the Jet Propulsion Laboratory in Pasadena, California, is studying the application of their microgravity techniques to the deposition of uniform coatings on spherical objects, with particular emphasis on ICF target cores. The study will initially center around liquid coatings that could be converted into seamless foam structures. The Armak foam system and the carboxymethyl cellulose foam system may be applicable in this process.

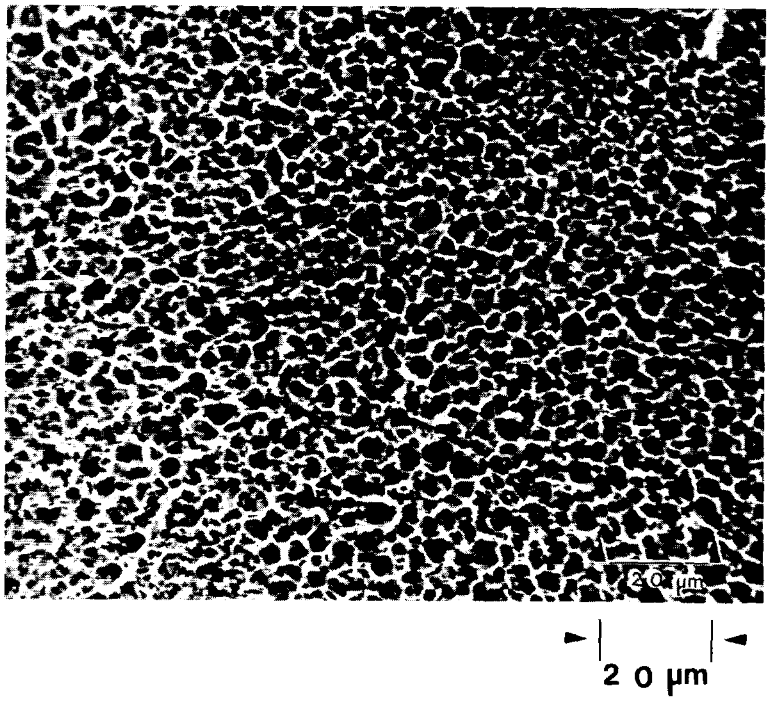

Fig. VII-37. Carboxymethyl cellulose foam. Density = 0.05 g/cm^3.

Low-Density Fibrous Structural Materials
(J. V. Milewski)

Production of low-density structural materials based on fibrous felts has continued. To facilitate initial experiments, we are studying fibrous felts scaled up tenfold in physical dimensions. Good reproducibility in making 4-µm stainless steel fibrous felts and 9-µm polyester fibrous felts has been demonstrated. Sample-to-sample reproducibility of felt density varied by ~5.2% for stainless steel felts and from 3.2 to 7.0% for polyester fibrous felts. Data are presented in Figs. VII-40 and VII-41.

The volume content of solids in the felts can be controlled in two ways. First, the length-to-diameter ratio of the fiber has a significant effect, with longer fibers producing lower-density felts (Fig. VII-42). The solid content almost doubles by changing the fiber length-to-diameter ratio from 50:1 to 250:1.

We can also change the solid content of the felts by coating the felt after its production. The amount of coating on the fibers adds to the solids and bonds the fibers together, substantially increasing the strength of the felt. The compressive strength of the felts has improved significantly by these coating processes (Fig. VII-43).

In laser fusion application, density distribution is as important as the density of the structure itself. Image-analysis techniques are used to study the density distribution of felts, and appropriate computer codes have been developed to support image-analysis procedures. Some preliminary statistical information has been derived; the results are encouraging.

CRYOGENIC TARGET DEVELOPMENT
(J. R. Miller, J. T. Murphy)

Laser fusion targets fueled with cryogenic, liquid or solid, DT offer the advantage of high initial fuel density without the disadvantage of diluent atoms being present as they are in room-temperature solids having a high hydrogen density [for example, lithium in LiDT, carbon in $(COT)_n$, or boron and nitrogen in NH_3BH_3]. In addition, calculations indicate that the yields from targets fueled with liquid or solid DT can be considerably higher than those from targets of the same design, but fueled with high-pressure DT gas. We therefore actively pursued the development of cryogenic targets despite the significant experimental complications encountered in their fabrication and use in laser-target interaction experiments.

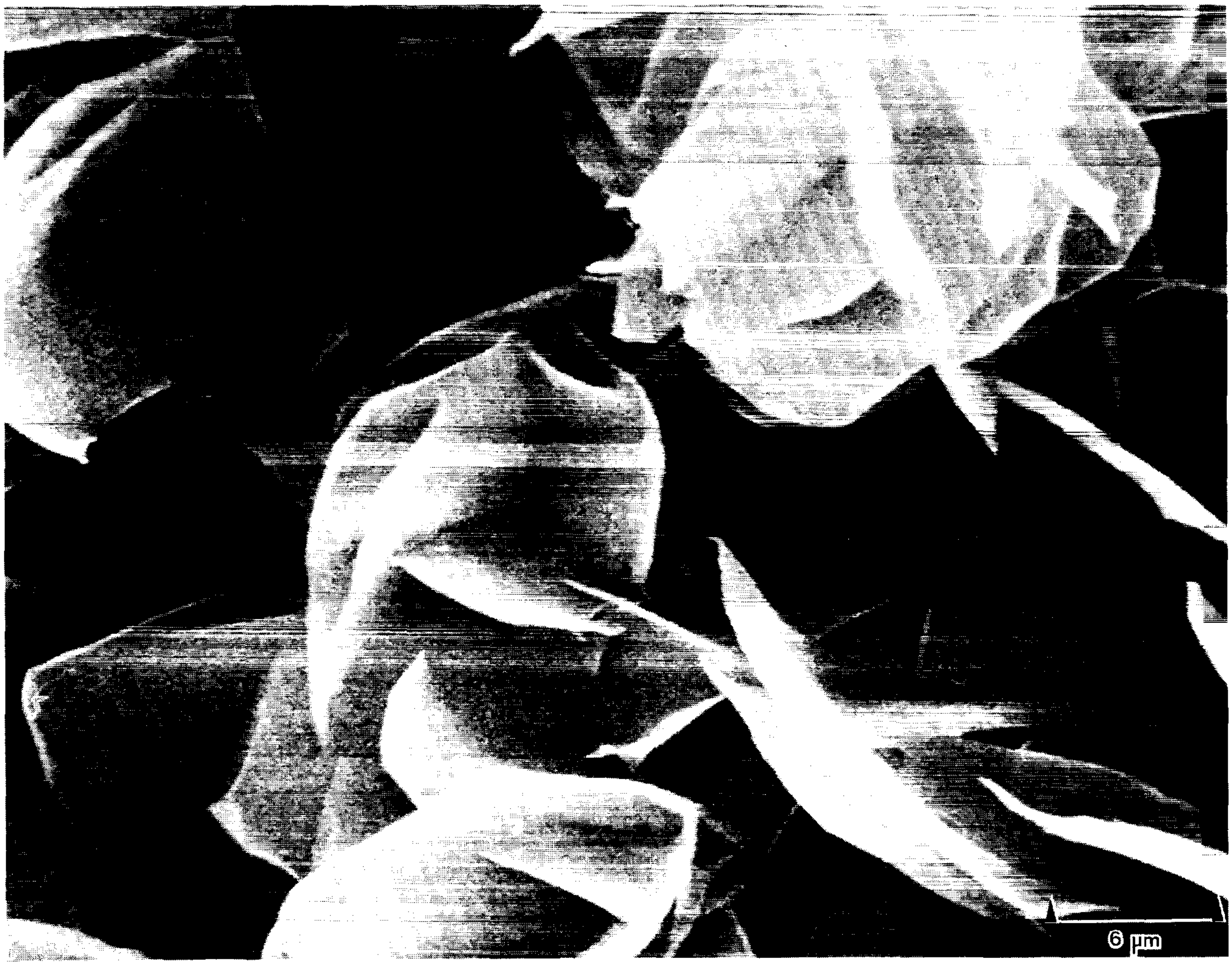

Fig. VII-38. Rosette cell structure of low-density foam.

Fast Isothermal Freezing Method (J. T. Murphy, J. R. Miller)

Targets with uniform layers of solid DT fuel are produced by using the fast isothermal freezing (FIF) technique. This method uses laser light to vaporize previously frozen DT, which then rapidly condenses and freezes as a uniform layer on the GMB wall. Vaporization has been accomplished by focusing a cw laser on the target while it is positioned in a constant temperature, gas-filled cryogenic cell. Shuttering the laser causes rapid, uniform target cooling. A new cryogenic target-production technique is being evaluated that involves replacing the large cw laser and its associated equipment with a single optical fiber and a small laser diode. The target is mounted directly on the optical fiber. We still obtain local target heating, but with significant savings in cost, space, and optical alignment time. Because of the improved cooling efficiency obtained with the new heating laser, the isothermal environment needed for uniform cryogenic layer formation is more easily maintained.

A target mounted on the bare optical fiber is shown in Fig. VII-44. Light-coupling efficiency in the fiber is improved by melting the end of the fiber into a ball, thus forming a collection lens. A chromium coating applied to the fiber minimizes light losses at the right-angle band and at the stalk-fiber glue joint. Evaluation of this local heating source will be tested after the current series of experiments.

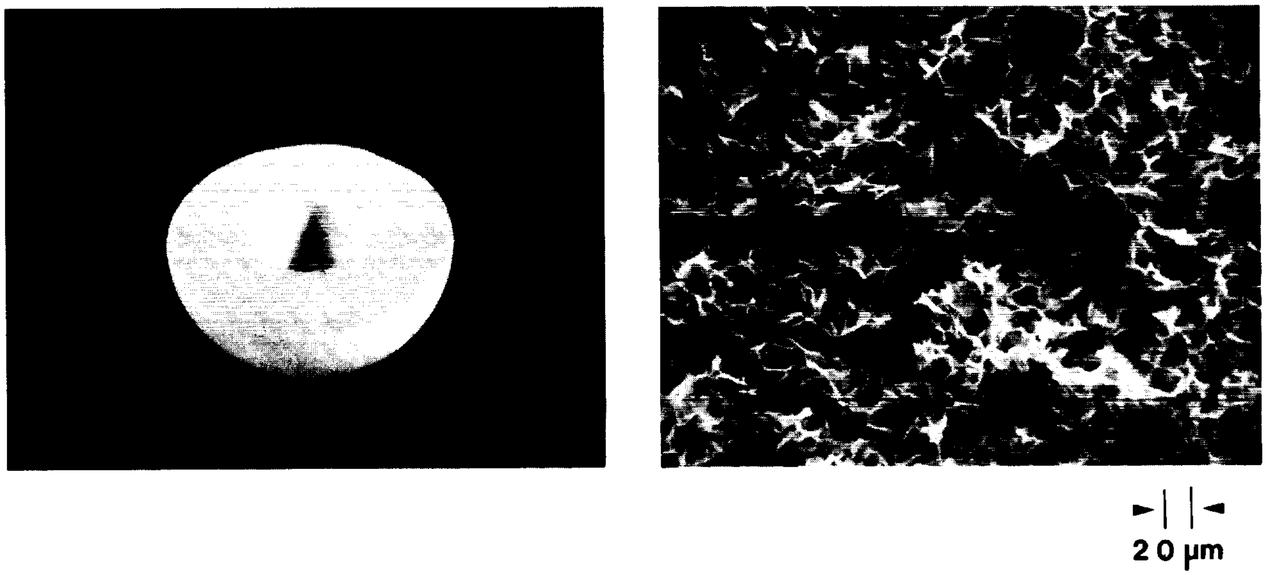

Fig. VII-39. Low-density microporous foam. Density = 0.055 g/cm^3.

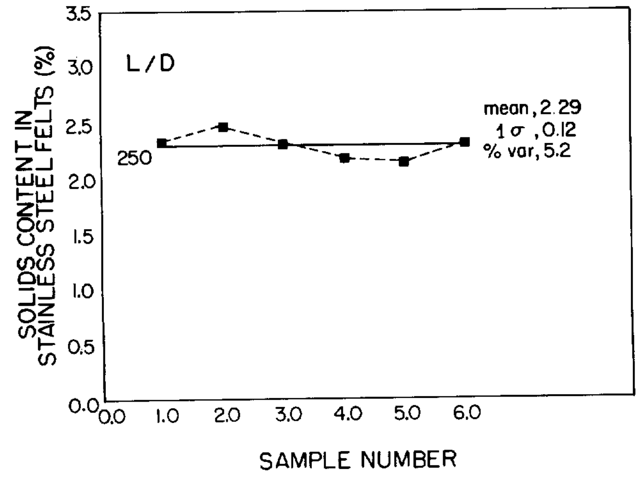

Fig. VII-40. Density variations in felts made from 4-μm-diam stainless steel fibers.

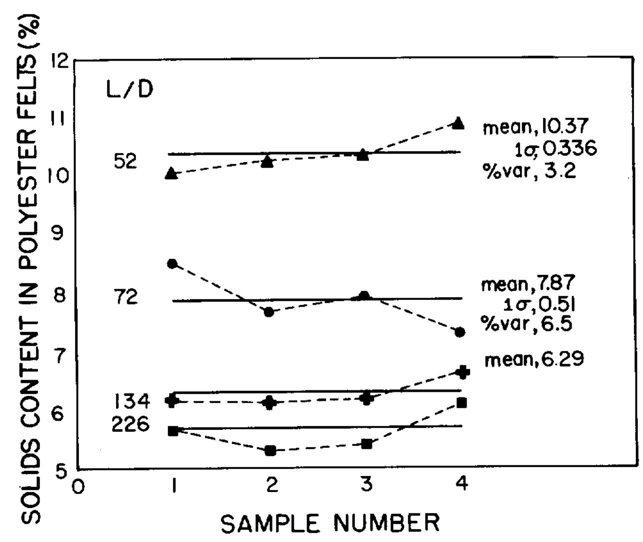

Fig. VII-41. Density variations in felts made from 9-μm-diam polyester fibers.

Status of FIF Calculation (L. Foreman)

There are two routines, F80 and FREEZE, that calculate the liquid cooling time of a layer of DT liquid from the dew point to the freezing point. This time is thought to be the dominating constituent in the total freezing time, which also includes the condensation time and the fusion time. FREEZE is the basis of the work by Miller, Fries, and Press.[15] FREEZE is about half as fast as F80 on standard targets and is also inconvenient to use because it must be changed internally for each target configuration.

F80, developed by W. Press, is designed principally to alleviate the latter objection to FREEZE. It queries the user for target geometry, materials, and initial conditions, and calculates the liquid cooling time on the basis of these inputs. This program is not yet ready for general use for the following reasons.

- Although the result of F80 agrees within ~0.1% with the results of Miller et al.[15] for the simplest target (a 100-µm GMB with a 1-µm DT layer; t_c = 9.2 ms), F80 results do not agree for more complex targets. Recent work indicates that the problem may be caused by changes made in the thermal properties since the generation of results by Miller et al. (Press reports, in support of this possibility, that FREEZE and F80 now agree for a target twice as large as the example above and that both disagree with the results of Miller et al.)
- F80 is not documented.
- F80 does not produce a filmed record of the temperature profile as a function of time. The plotting portions of FREEZE must be rewritten for F80.

The latter two problems are of lesser importance than the numerical discrepancies.

The freezing problem in general deserves some comment. Miller et al. reported an estimate of the time to freeze a layer of liquid DT initially at the freezing temperature based on a model by Cho and Sunderland.[16] These fusion times were insignificant compared to the liquid cooling time ($t_f \simeq 0.3$ ms; $t_c \leq 10$ ms). The freezing time estimate based on the Cho/Sunderland model is certainly too low and perhaps significantly so, because the assumed step-function boundary condition is unrealistic.

We are attempting to check this estimate both experimentally in our laboratory and by means of independent computer models.

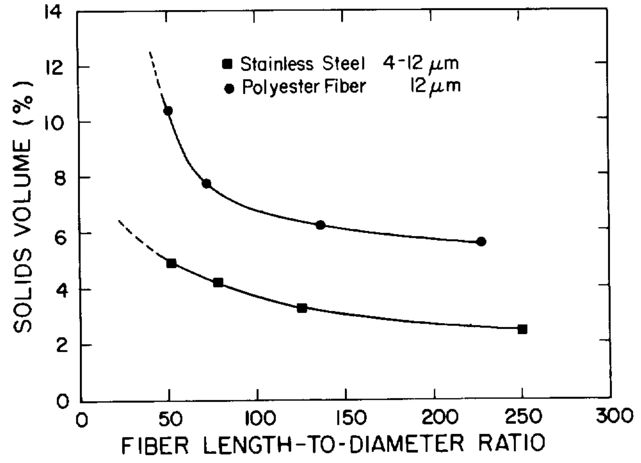

Fig. VII-42. Percentage of solid volume of felts as a function of L/D ratio of the fibers composing them.

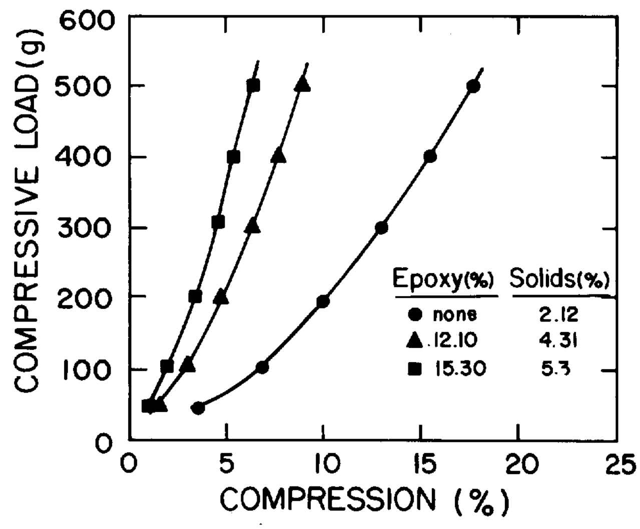

Fig. VII-43. Compressive-stress station curves for stainless steel fiber felts as a function of added epoxy binder.

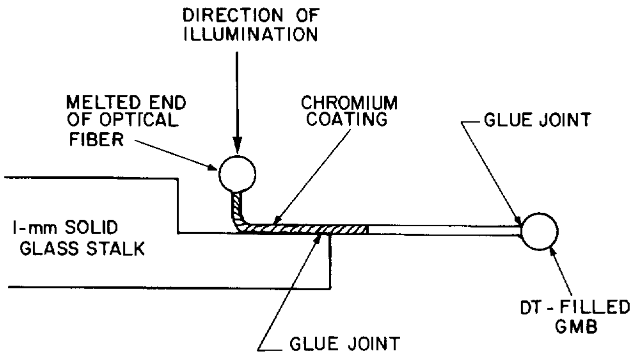

Fig. VII-44. Laser target mounted on a bare optical fiber.

Helios Cryogenic Target Processing Apparatus (J. R. Miller, J. T. Murphy, C. E. Cummings, K. M. Spencer, J. B. VanMarter, T. Farmer)

Targets at room temperature will be loaded into the target chamber, processed with the FIF technique, and then uncovered through rapid retracting of the cryogenic processing shroud just before CO_2 laser irradiation. Final design of the shroud retraction system has been completed and all parts have been fabricated. Assembly and testing of this apparatus is in progress.

An experiment to check the Helios laser for possible parasitic oscillations caused by the cryogenic shroud was completed. Stable laser operation was achieved with a 2.54-cm-diam cylindrical shroud located 3.2 cm from the target, on the target-insertion axis system. Although laser operation was stable, significant shot-induced damage occurred to the copper shroud face. We are evaluating an inertially driven shutter mechanism as a means for preventing this shot-induced damage.

The design of the heat exchanger in the cryogenic processing shroud has been finalized. Refrigerant (liquid helium) is supplied to the high-purity annealed-copper shroud by 0.3-cm-diam tubing and returned through 0.95-cm-diam tubing. To constrain the 0.95-cm tubing during the rapid 12.7-cm retraction cycle, a swing-arm assembly has been developed (Fig. VII-45) that will have the following significant advantages:

- 12.7 cm of travel can be accommodated with a 0.95-cm tubing,
- negligible volume change will result during retraction,
- only axial forces are imposed on shroud support and retractor,
- turbulent flow is minimized by use of short bellows sections, and
- inertial forces (30 g acceleration and 200 g deceleration) act on the swing-arm pivots rather than on the bellows.

The computer-controlled operations program for the cryogenic target-production apparatus has been completed. The required operations have been ordered sequentially, the status checks and check points defined, the jump-out nodes identified, and a system failure analysis completed. The design criterion stipulated that any component or operational malfunction in the cryogenic system would not cause catastrophic failure anywhere in the Helios system. The control electronics have been designed, fabricated, programmed, and bench tested. Mating and final resting of the control system for the cryogenic target apparatus with the retraction and shroud hardware will be completed in a specially fabricated test chamber.

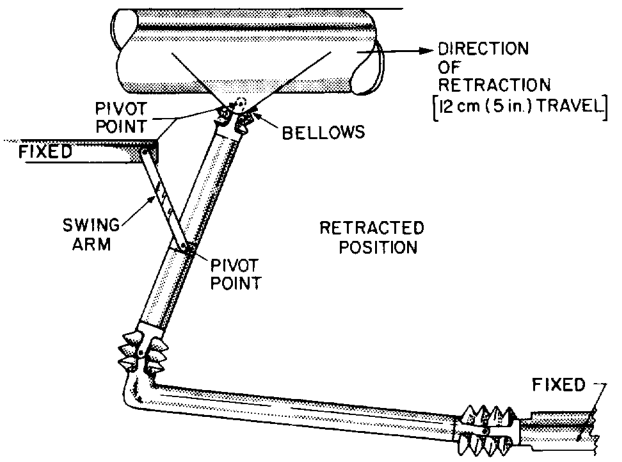

Fig. VII-45. Swing-arm assembly used to retract the cryogenic shroud.

REFERENCES

1. Roger B. Perkins and the Inertial Fusion Program Staff, "Inertial Fusion Program, July 1—December 31, 1979," Los Alamos National Laboratory report LA-8511-PR (October 1981).

2. R. L. Whitman and R. H. Day, "X-Ray Microradiographs of Laser Fusion Targets: Improved Image Analysis Techniques," Appl. Opt. **19**, 1718 (1980).

3. R. L. Whitman, R. H. Day, R. P. Kruger, and D. M. Stupin, "Microradiographs of Laser Fusion Targets: 2-D Modeling and Analysis," Appl. Opt. **18**, 1266 (1979).

4. H. J. Trussell, "Theoretical Explanation of an Image Analysis Technique," Appl. Opt. Lett. **19**, No. 21, 3587-3588 (1980).

5. S. N. Jasperson and S. E. Schnatterly, "An Improved Method for High Reflectivity Ellipsometry Based on a New Polarization Modulating Technique," Rev. Sci. Instrum. **40**, 761 (1967).

6. "Laser Program Annual Report—1978," Brian D. Jarmon, Ed., Lawrence Livermore National Laboratory report UCRL 50021-78 (March 1979), pp. 4-21 to 4-34.

7. Frank L. McCrackin, "A FORTRAN Program for Analysis Ellipsometer Measurement," National Bureau of Standards Technical Note 479 (U.S. Government Printing Office, Washington, April 1968).

8. Louis Harris and John K. Beasley, "The Infrared Properties of Gold Smoke Deposition," J. Opt. Soc. Am. **42**, 134 (1952).

9. Milton Kerker, *The Scattering of Light and Other Electromagnetic Radiation* (Academic Press, New York, 1969).

10. H. H. Blau, D. J. McCleese, and D. Watson, "Scattering by Individual Transparent Spheres," Appl. Opt. 9, 2522 (1970).

11. D. J. Bond, J. D. Hares, and J. D. Kilkenny, "Demonstration of Resistance Inhibition of Fast Electrons from Laser-Produced Plasmas in Low-Density Gold Targets," Phys. Rev. Lett. **45**, 252 (1980).

12. A. Suhr, "Applications of Non-Equilibrium Plasmas to Organic Chemistry," in *Techniques and Applications of Plasma Chemistry* (John Wiley & Sons, New York, 1974), Chap. 2, p. 57.

13. J. W. Haverhill, "1973 Laser Target Activities," Bendix Corp. report BDX-613-1087 (February 1975).

14. Roger B. Perkins and the Laser Fusion Program Staff, "Inertial Fusion Program, July 1—December 31, 1978," Los Alamos Scientific Laboratory report LA-7755-PR (November 1980).

15. J. R. Miller, R. J. Fries, and W. J. Press, "Cryogenic Laser Fusion Target Design Considerations," J. Nucl. Mater. **85-86**, 121-124 (1979).

16. Sung Hwang Cho and J. E. Sunderland, "Phase Change of Spherical Bodies," J. Heat Transfer **13**, 1231 (1970).

VIII. HEAVY-ION DRIVER DEVELOPMENT

(G. A. Sawyer)

Heavy-ion accelerators are being developed as alternative drivers for ICF. Los Alamos has been assigned a leading role for Heavy-Ion Fusion (HIF). Los Alamos efforts in low-velocity accelerator development and ion-beam transport theory are described.

INTRODUCTION

Los Alamos, in carrying out its leading role for HIF, has organized a technical working group with membership from organizations involved in HIF development. The working group meets several times a year to act as a steering committee for the HIF program. Two approaches to heavy-ion acceleration are being pursued: the linear-induction accelerator, being developed mainly at Lawrence Berkeley Laboratory, and the rf linear accelerator, being developed mainly at Argonne National Laboratory.

Los Alamos, in addition to its leading role, is engaged in studying critical issues for HIF. Accelerator development and beam-transport theory are covered, as well as target physics and systems studies as they relate to HIF.

ACCELERATOR DEVELOPMENT (R. H. Stokes)

Development of RFQ Linear Accelerator

Development of the RFQ linear accelerator has continued at a rapid pace for a wide range of applications. Both calculational and experimental studies have confirmed its excellent properties as a low-velocity injector capable of meeting very stringent requirements. We will discuss first the RFQ activities that are of interest to both light- and heavy-ion applications and in the next section will discuss those aspects of the RFQ that are more directly related to its possible use in HIF accelerators.

We continue to develop methods of designing RFQ systems that will have output beams with specified characteristics. Calculational methods to synthesize the beam dynamics of RFQ linacs have been improved and extended. These methods have been used for the first time to design systems with a constant aperture, which require considerably less rf power to excite the RFQ structure. The use of these constant-aperture systems now depends upon our ability to design resonators with the correct longitudinal distribution of vane voltage.

After we synthesize an RFQ design, we analyze its behavior by using multiparticle beam dynamics simulation programs. These programs have been developed further so that there are now two main schemes: one based upon integration over the longitudinal space coordinate, and the other based upon the use of time as the variable of integration. Both include the effects of space charge as well as the effects of electric quadrupole focusing, radio-frequency defocusing, longitudinal bunching, and acceleration. The two methods provide an independent check on our ability to predict the behavior of particle beams under widely variable conditions.

Fundamental studies[1] of emittance growth in rf linacs have been carried out by using the PARMILA beam dynamics simulation program. The Alvarez linac was used as a model, and calculations were made with beam intensities that approach the maximum possible currents. Widely different frequencies, inputs on emittance values, and radial focusing conditions were simulated. Although much more work is needed, these studies have begun to show that certain types of parameter scaling tend to give the same emittance growth behavior.

A highly successful experimental test of an RFQ accelerator in February 1980 constituted a major milestone. The test was designed to accelerate protons from 100 to 640 keV in a length of 1.1 m. The test accelerator operated with a frequency of 425 MHz and was equipped with an array of diagnostic equipment necessary to characterize the output beam. The beam dynamics design of this test and its predicted performance were reported.[2] The test confirmed the general properties of the RFQ linac and gave excellent detailed agreement between the measured characteristics of the output beam and the predicted performance. For example, with a dc input beam of 30 mA, the output beam was 26 mA, and the radial emittance grew by less than a factor of 1.5. The test showed that RFQ operates in a highly stable manner and is insensitive to resonator tuning errors and to errors in the pole tip geometry. It also confirmed the utility of the method for coupling rf power to the RFQ through a coaxial manifold.[3] More detailed descriptions of this experimental test are available in other sources.[4,5]

Heavy-Ion Accelerator Development

One of the problem areas in HIF accelerators has been the low-velocity region. In conventional low-velocity linacs there tend to be severe limits on the beam current that can be accelerated. Also, the largest growth of radial emittance tends to occur in the early linac stages, and this growth is amplified when high-current beams are accelerated. The RFQ linac structure offers a highly attractive solution to these low-velocity problems; its design flexibility allows it to be adapted to a wide range of applications, each of which may require optimization of specific operating characteristics.

One of the important areas of RFQ design is predicting the maximum beam current that a given RFQ accelerator will transmit. This becomes especially important in HIF systems, which place a premium on high currents. An important part of our RFQ design procedure is the development of a calculational method[6] to predict the current capacity of linear accelerators. From these current limit systematics, we have learned that an RFQ can carry higher currents than a conventional linac; this is a result of the initial slow bunching and acceleration cycle that delays the onset of the current limit until the beam has moved downstream to a point where the energy is 10 times higher than at the output.

To demonstrate the heavy-ion capability of an RFQ, we designed a system[7] to accelerate Xe^{+1} from 0.24 to 5.0 MeV. The operating frequency was 12.5 MHz, and the linac was 27 m long. For an input beam of 30 mA, the predicted output beam was 29.1 mA, and the growth in rms radial emittance was a factor of 4.0. In the rf linac approach to HIF, beam currents of 1.0 A are often required; this means that multiple RFQ channels must be used and the beams combined in an arrangement called funneling. In a stepwise manner this scheme[8] combines many initial beams into a single final beam and, in principle, results in no radial emittance growth. We have developed concepts[8] for constructing RFQ linacs in arrays containing four channels per module. These arrays contain parallel beam channels that are closely spaced and offset longitudinally so that funneling can be performed in an efficient, symmetric manner.

The HIF Workshop was held in November 1979 in Berkeley, California. Following the conference, papers[1,7-9] were written and submitted for inclusion in the proceedings. In addition, papers[10] have been submitted to the CLEOS Topical Meeting on Inertial Confinement Fusion held in San Diego in February 1980, and to the International Conference on Low-Energy Ion Beams 2, Bath, England, April 1980.

Critical Review of Heavy-Ion Deposition Models

One of the principal attractions of HIF is the expectation that energy deposition by heavy ions can be characterized in target calculations with little, if any, uncertainty introduced by unknown or little understood effects. However, a critical review of the physics of the interaction is lacking in the open literature. We have undertaken a review to evaluate (1) the sensitivities of target calculations to major features of the interaction and (2) the need, if any, for incorporating into the models of ion deposition reference values from appropriate experimental measurements.

We have begun a detailed study of the model for ion-beam deposition that was developed by T. A. Mehlhorn of SNL.[11] Because this deposition model is employed in the LASNEX code used at Los Alamos for target calculations, parameters in the model are being defined to carry out sensitivity studies in target performance.

Although these extrapolations may appear reasonable, they remain unsupported by experiment. In addition, the energy deposition profiles are expected to be sensitive to the details of the ion interactions in the stopping material, especially in hot, partially ionized material. There are no experimental data of any kind to serve as references in the models that are proposed for the ion stopping mechanisms in such conditions.

In view of the above concerns, we plan to examine the extent to which target calculations depend on variations in the deposition-model input parameters. From this examination, we expect that crucial experimental measurements may be defined and performed, leading to a firmer basis for the credibility of HIF target-performance calculations.

Combination of Ion Beams by Funneling

All proposed schemes for using rf linacs to produce heavy-ion beams for inertial fusion require the beam current to be increased by sequentially combining linac output beams. To accomplish this increase, it has been proposed to funnel together pairs of beams in a manner that increases the beam current with no increase in radial emittance. For this latter step it is possible to use a time-varying electric deflector to interlace the microstructure pulses and make them collinear. This combined beam would be accelerated further in another linac operating at twice the frequency of the first linac stages.

Because the rf deflector is an important element of this system, we studied[12] a wide variety of possible arrangements and found that appropriate deflectors can be designed. However, further overall work is needed to develop a system that provides the necessary radial focusing and bunching during the funneling process.

A High-Current, Four-Beam, Xenon Ion Source for HIF

General. With M. R. Shubaly, we completed at Chalk River Nuclear Laboratories the design and component testing of a four-beam, xenon ion injector for the four-channel RFQ accelerator; this accelerator was proposed at Los Alamos as the initial stage of a heavy-ion, ICF driver.[8] In this scheme, each channel of the RFQ would provide 25 mA of Xe^{+1} for funneling into a system of electrostatically and magnetically focused linear accelerators.

The RFQ has two advantages that greatly ease the injector design. It requires a relatively low injection energy (~250 eV for Xe^{+1}) and has a 97% capture efficiency[7] so that the injector has to provide only 25 mA of Xe^{+1}. The four beams must be in a 10-cm^2 array to match the RFQ channel spacing. A source that provides a high (~90%) fraction of Xe^{+1} would make magnetic separation unnecessary and would permit a close-coupled design that would greatly ease beam transport. High efficiency of the source gas is required to reduce charge-exchange losses and to reduce the gas load. High arc efficiency would ease the requirements for cooling and for power delivery to the high-voltage dome (at 245 kV). A high-current, heavy-ion duopigatron source, developed at the Chalk River Nuclear Laboratories,[13] provides an ideal ion source for this injector. This source has produced xenon beams of up to 100 mA and current densities of over 70 mA/cm^2, with low power and gas consumption.

Injector Description. The proposed injector uses four plasma sources on a 10-cm^2 array because a single source that would provide the desired current density over a large area would require an extremely high arc power. The four sources are mounted on a common extraction and acceleration column that uses an Einzel lens to provide the required focusing. To provide consistent beam characteristics with different pulse lengths and duty cycles, the plasma sources operate continuously, and an extraction electrode is pulsed to give the desired pulse length and duty cycle. The ion sources essentially are duplicates of the Chalk River sources, with minor mechanical modifications to fit them into the available space.

Figure VIII-1 shows one quarter of the extraction and acceleration column and one plasma-source module. The first column electrode holds the molybdenum plasma aperture plate with an 8-mm-diam shaped aperture. For convenience, the potential of this plate is defined as zero. The next electrode is the extraction electrode, which is held at +30 V between pulses to prevent plasma flow into

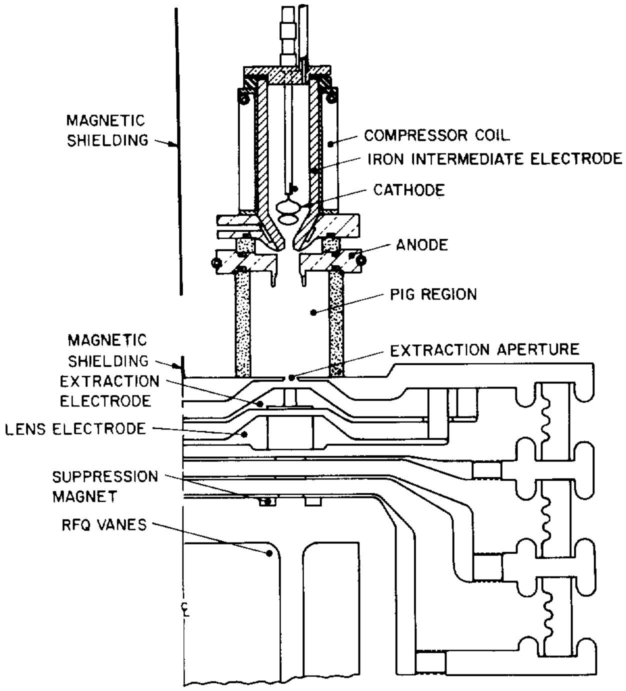

Fig. VIII-1. One quadrant of RFQ accelerator injector.

the column. During a pulse, this electrode is at −45 kV to extract the beam. The next electrode is part of the Einzel lens and is at −10 kV. The following electrodes are at −45, −145, and −245 kV with respect to the plasma aperture plate. The bottom electrode incorporates a magnetic electron-suppression element to prevent damage from backstreaming electrons during the pulse. As is shown, the vanes of the RFQ penetrate into the bottom of the column. The ceramics are convoluted to reduce surface tracking and are well shielded to reduce photoelectron production by bremsstrahlung radiation from backstreaming electrons. The active regions of all electrodes are of molybdenum to reduce beam-induced sparking. The outside of the column is insulated with low-pressure SF_6.

The extraction, focusing, and acceleration optics were designed with the help of BEAM, an ion-beam extraction and acceleration modeling code being developed at Chalk River. Figure VIII-2 shows the configuration of the central region of the electrodes and the calculated ion trajectories for a 29-mA beam. At the entrance to the RFQ, the beam is 1.3 cm in diameter and slightly convergent. The extraction voltage and the voltage on the lens electrode can be varied to change the beam size and divergence, as required by the final RFQ design.

Tests of the system components at Chalk River have verified the feasibility of this injector concept.[14] Results have shown that the shimming to operate these ion sources in an array would be straightforward and that the extrapolated normalized emittance for this configuration would be less than the specified 0.07π mm•mrad.

BEAM TRANSPORT (L. E. Thode, D. S. Lemons)

Ion-beam inertial fusion research has concentrated on the problem of the ballistic propagation and focusing of a high-current ion beam from the accelerator port, across a reactor chamber, to a target pellet. This work has been in support of both proposed heavy- and light-ion fusion schemes. As recommended at a recent HIF workshop,[15] special attention has been paid to propagation in vacuum; the relatively simple problems associated with this propagation mode should be fully understood before considering the more complicated chemistry and plasma physics problems associated with beam, plasma, and neutral gas interactions.

Total ion currents required for inertial fusion applications are high enough that beam defocusing caused by self-space charge fields requires this current to be divided into a number of individually focused beams. Recent heavy-ion target calculations have resulted in higher required ion currents, which in turn have driven the number of individual beams converging on one target pellet to impractically high values (>40).[16] A possible solution to this problem has been previously proposed for light-ion beams:[17] charge- and current-neutralize the ion beam with comoving electrons before it enters the reactor chamber. For this reason, we studied the vacuum propagation and focusing of a neutralized ion beam.

As a neutralized ion beam focuses in configuration space, the electron and ion velocity space must increase so that the particle entropy is conserved or possibly increases; that is, the particles must heat. Electron heating is especially a problem because (1) it is impossible to provide electrons that are initially as cool as the ions, and (2) hot electrons make large excursions from the ion beam, which in turn results in loss of neutralization and ion-beam defocusing. A one-dimensional equation, which describes the evolution of an ion-beam envelope and contains the competing effects of electron heating and pressure, space-charge forces, ion inertia and emittance, and the effect of a background plasma, has been derived to study these processes.[18] The equation assumes two-dimensional adiabatic electron and ion heating; solutions can be displayed in terms of the maximum allowed temperature of the neutralizing electrons for a particular propagation scheme. Such solutions are shown in Fig. VIII-3, in which initial electron temperature is plotted as a function of the number of beams required for several different heavy-ion drivers. If a system of no more than 10 beams is desired,

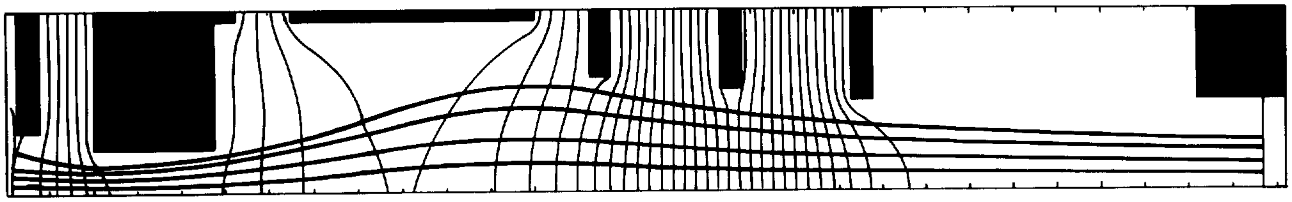

Fig. VIII-2. Computer simulation of ion-beam optics for RFQ accelerator injector.

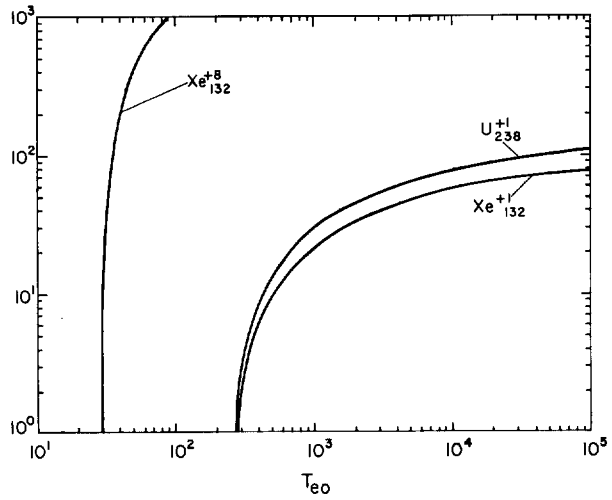

Fig. VIII-3. Number of beams n versus initial electron temperature in eV, T_{e0}, for indicated beam ions and charge state. Other parameters are beam power P_b, ion energy E_b, initial beam radius a_0, focused beam radius a_f, and propagation distance L, where $P_b = 300$ TW, $E_b = 5$ GeV, $a_0 = 10$ cm, $a_f = 0.03$ cm, and L = 10 m.

singly charged heavy ions must be neutralized with temperatures no hotter than ~400 eV, whereas an X^{+8} driver would require electrons no hotter than ~20 eV. We may conclude that the heavy-ion charge could be relaxed somewhat below the singly charged state, even if heavy-ion beams are neutralized.

The basic physics of vacuum propagation and focusing of a neutralized ion beam has also been studied in numerical simulations. Because envelope equation studies[18] indicate that the effect of beam self-magnetic fields is insignificant compared to the effect of the self-electrostatic fields, these simulations were performed by an electrostatic version of the fully electromagnetic two-dimensional PIC code CCUBE. (The former code runs some three times faster than the latter and, therefore, allows us to perform longer simulations. This code only recently became available* and was tested by us.) Simulation results illustrate the processes of ion-beam focusing, electron heating, and consequent ion-beam defocusing caused by self-electrostatic fields. Figure VIII-4 shows ion and electron configuration space plots of a focused beam. The electrons have heated as the beam focused and, as is evident, some of them have made large excursions from the beam. The minimum radius actually reached by the ion beam is, however, about twice as large as the envelope equation predicted from initial conditions. This discrepancy is apparently caused by the unneutralized ion sheath evident at the head of the beam and by the fact that the electrons are heated more than predicted by an adiabatic law. Preliminary indications are that this apparent emittance growth of the neutralizing electrons can have a significant deleterious effect on focusing of neutralized ion beams and should therefore be investigated further.

REFERENCES

1. R. A. Jameson, "Emittance Growth in RF Linacs," Proc. HIF Workshop, Berkeley, California, October 29-November 9, 1979, Lawrence Berkeley Laboratory report LBL-10301 (September 1980), p. 4.

2. K. R. Crandall, R. H. Stokes, and T. P. Wangler, "RF Quadrupole Beam Dynamics Design Studies," Proc. 10th Linear Accelerator Conf., Montauk, New York, September 10-14, 1979, Brookhaven National Laboratory report BNL-51134 (1980), p. 205.

3. J. M. Potter, "An RF Power Manifold for the Radio-Frequency Quadrupole Linear Accelerator," Proc. 10th Linear Accelerator Conf., Montauk, New York, September 10-14, 1979, Brookhaven National Laboratory report BNL-51134 (1980), p. 138.

4. R. W. Hamm, K. R. Crandall, L. D. Hansborough, J. M. Potter, G. W. Rodenz, R. H. Stokes, J. E. Stovall, D. A. Swenson, T. P. Wangler, C. W. Fuller, M. D. Machalek, R. A. Jameson, E. A. Knapp, and S. W. Williams, "The RF Quadrupole Linac: A New Low-Energy Accelerator," in *Low Energy Ion Beams, 1980*, Proc. Int. Conf. Low Energy Ion Beams 2, University of Bath, England, April 14-17, 1980 (Institute of Physics, Bristol, 1981), Conf. Ser. 54, p. 54.

5. R. H. Stokes, K. R. Crandall, R. W. Hamm, F. J. Humphry, R. A. Jameson, E. A. Knapp, J. M. Potter, G. W. Rodenz, J. E. Stovall, D. A. Swenson, and T. P. Wangler, "The Radio-Frequency Quadrupole: General Properties and Specific Applications," Proc. Int. Conf. High Energy Accel., 11th,

---

*The electrostatic version of the particle simulation code CCUBE was developed by Brendan Godfrey of Mission Research Corporation, Albuquerque, New Mexico, under contract to Los Alamos.

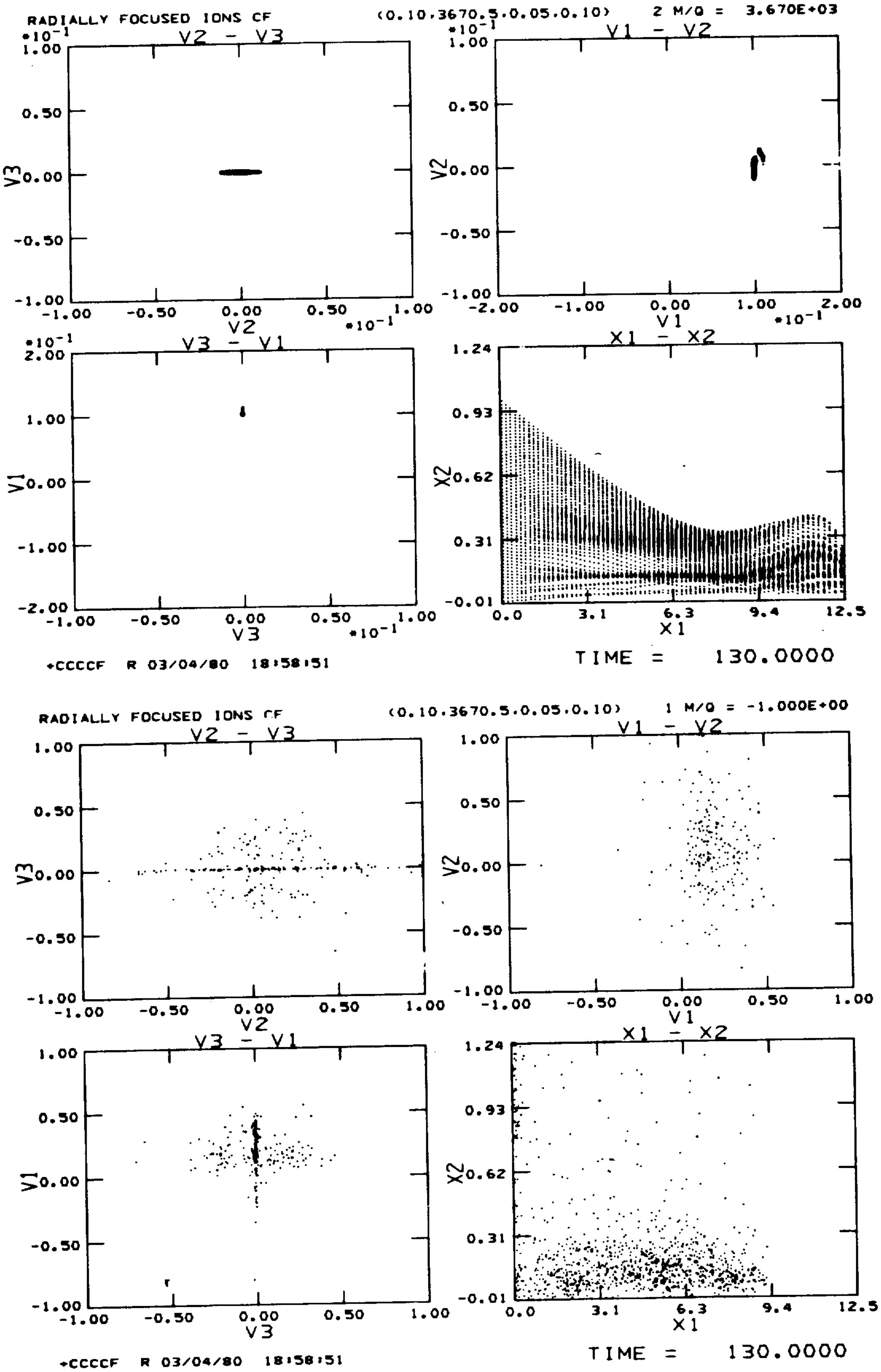

Fig. VIII-4. Configuration space [X1(z) and X2(r)] and velocity space [V1(V_z), V2(V_r), and V3(Vθ)] simulation plots of a focused ion beam neutralized with hot comoving electrons. Normalized beam parameters are velocity v_0/c, focal angle θ, mass ratio m_i/m_e, electron temperature V_{th}/c, $V_0/c = V_0/c = 0.1$, $\tan\theta = 0.1$, $m_i m_e = 3670.5$, $V_{th}/c = 0.05$, $a_0\omega_p/c = 1.0$.

CERN, Geneva, July 7-11, 1980, Experimentia: Supplement 40, 399 (1980).

6. T. P. Wangler, "Space-Charge Limits in Linear Accelerators," Los Alamos Scientific Laboratory report LA-8388 (December 1980).

7. T. P. Wangler and R. H. Stokes, "Application of the RF Quadrupole in Linear Accelerators for Heavy Ion Fusion," Proc. HIF Workshop, Berkeley, California, October 29-November 9, 1979, Lawrence Berkeley Laboratory report LBL-10301 (September 1980), p. 21.

8. D. A. Swenson, "RF Linac Approach to Heavy Ion Fusion," Proc. HIF Workshop, Berkeley, California, October 29-November 9, 1979, Lawrence Berkeley Laboratory report LBL-10301 (September 1980), p. 239.

9. R. A. Jameson, "Summary of Low-Beta Linac Working Group," Proc. HIF Workshop, Berkeley, California, October 29-November 9, 1979, Lawrence Berkeley Laboratory report LBL-10301 (September 1980), p. 6.

10. R. A. Jameson, "Recent Developments in Low-Velocity Linacs for Heavy Ion Fusion," in *Low Energy Ion Beams, 1980,* Proc. Int. Conf. Low Energy Ion Beams 2, University of Bath, England, April 14-17, 1980 (Institute of Physics, Bristol, 1981), Conf. Ser. 54, p. 65.

11. T. A. Mehlhorn, "A Finite Material Temperature Model for Ion Energy Deposition in Ion-Driven ICF Targets," J. Appl. Phys. 52, 6522 (1981).

12. K. Bongardt, "Calculation of the Transfer Matrix T in Six Dimensions for an RF Deflector Element," Los Alamos National Laboratory report LA-8668-MS (January 1981).

13. Murray R. Shubaly, "A High-Current DC Heavy-Ion Source," in *Low Energy Ion Beams, 1980,* Proc. Int. Conf. Low Energy Ion Beams 2, University of Bath, England, April 14-17, 1980 (Institute of Physics, Bristol, 1981), Conf. Ser. 54, p. 333.

14. Murray R. Shubaly and Robert W. Hamm, "A High-Current Four-Beam Xenon Ion Source for Heavy-Ion Fusion," Proc. 6th Conf. Appl. Small Accel. in Research and Industry, Texas State University, Denton, Texas, November 3-5, 1980, IEEE Trans. Nucl. Sci. 28, 1316 (1981).

15. "Report on the Workshop on Atomic and Plasma Physics Requirements for Heavy Ion Fusion," Yong-Ki Kim and Glen Magelssen, Eds., Argonne National Laboratory report ANL-80-17 (1980).

16. C. Olson, "Final Transport in Gas and Plasma," Proc. HIF Workshop, Berkeley, California, October 29-November 9, 1979, Lawrence Berkeley Laboratory report LBL-10301 (September 1980), p. 403.

17. Z. G. T. Guiragossian, "The Light Ion Fusion Experiment (LIFE) Accelerator System for ICF," Proc. HIF Workshop, Berkeley, California, October 29-November 9, 1979, Lawrence Berkeley Laboratory report LBL-10301 (September 1980), p. 426.

18. D. S. Lemons and L. E. Thode, "Electron Temperature Requirements for Ballistically Focused Neutralized Ion Beams," Nucl. Fusion 21, 529-535 (1981).

IX. SYSTEMS AND APPLICATIONS STUDIES OF INERTIAL FUSION

(T. G. Frank, I. O. Bohachevsky)

Systems and applications studies are being performed to analyze the technical and economic feasibility of various commercial and military applications of inertial fusion. Commercial applications include electric power generation, fissile-fuel production from fusion-fission hybrid reactors, and production of synthetic fuels such as hydrogen. Our studies also include assessment of advanced technologies that require development for the ultimate commercialization of inertial fusion. The general objectives of these studies are (1) conceptualization and preliminary engineering of laser fusion reactors and other integrated plant systems for economic and technology tradeoff and comparison studies and (2) the identification of critical technology areas requiring long-term development efforts.

INTRODUCTION

In general, past efforts in systems and applications studies were devoted to investigating the technical and economic feasibility of ICF reactors and total energy conversion systems; therefore, progress has been most significant in this area. Our studies were directed toward developing models and methods for the analysis of technical problems associated with ICF reactor design, arriving at integrated plant layouts, deriving scaling laws (that is, sensitivities to parameter changes), and establishing costing methodology and a corresponding data base.

Integration studies of ICF reactor systems were conducted in two complementary ways: with approximate analytic investigations and with detailed computer modeling. Approximate analytic investigations of ICF reactor systems integration led to simple explicit expressions that relate different reactor parameters and show the dependence of the objective function—unit cost of power—on these parameters. The results indicate directions of parameter changes that lead to system optimization and thus may be used to reduce the time and effort required to arrive at optimum characteristics with detailed computer modeling.

The effort in computer modeling was directed toward revising TROFAN and updating it with subroutines that incorporate the results of recent technical and cost analyses. Revision of the code was motivated by the need to allow complete use of recently accumulated data bases, provide greater flexibility in parametric studies and corresponding outputs, and facilitate future modifications that incorporate new technical results.

In addition to these activities, two subroutines were developed and added to TROFAN. One subroutine optimizes the reactor vessel design by trading off reactor cavity size against the lifetime of its first wall. A summary of the technical analysis supporting development of the subroutine is included in this section.

The second subroutine models the CO_2 laser driver capital cost. This subroutine is based on the results of a design study sponsored by the US Department of Energy and carried out by the AVCO-Everett Research Laboratory. We have generalized these results to increase their usefulness in ICF systems modeling; the generalization is indicated briefly in this section.

ICF SYSTEM INTEGRATION (I. O. Bohachevsky)

Introduction

Successful commercialization of ICF requires integrating a system's subsystems into a functional, reliable, and efficient electric power generating plant. The objective of systems integration is to determine the sizes of reactor subsystems and components in such a way that energy and mass flows are mutually consistent for all flow paths inside the reactor. They must also be compatible with externally imposed requirements such as the desirable or at least economically acceptable size, the relationship between ICF driver-beam pulse energy and fuel pellet yield (that is, the gain curve), and the availability of the necessary technologies.

We use simple analytic considerations to gain insights into ICF reactor systems integration and derive trends. The results may be used as general technical guidelines for parametric system optimizations.

Model, Analysis, and Results

The subsequent analysis is based on the postulate that variations in reactor cost with pellet yield and driver pulse energy are dominated by changes in vessel and driver costs.

We have shown previously[1] that the cost of the reactor vessel is proporational to the 3/2 power of the pellet yield Y. More detailed cost studies* show that the cost-scaling exponent is <3/2 but greater than unity, which is sufficient for the validity of the conclusions derived below.

Costing studies indicate that a proportionality to the α power of the pulse energy E approximates the driver cost with adequate accuracy; the economy-of-scale exponent α is expected to be in the range $0.4 < \alpha < 1.0$.

Combining these cost relations with the net energy production rate, we obtain the following expression for the unit capital cost of power u, which is the objective function in further analysis:

$$u = \frac{nC_V\sqrt{Y} + C_D Y^{\alpha/\beta - 1}}{N[\eta_T(1-q) - (K/\eta_D)Y^{1/\beta - 1}]} , \qquad \text{(IX-1)}$$

where n is the number of reactor vessels, N is the driver repetition frequency, C_V and C_D are cost constants, η_T and η_D are thermal and driver efficiencies, q is the fraction of heat lost through the structure, Y is the fuel pellet yield, and K and β are the parameters that specify the gain curve, that is, for the driver pulse energy E

$$E = KY^{1/\beta} \text{ or } Y = K_1E^{\beta} . \qquad \text{(IX-2)}$$

Optimal Pellet Yield. It is useful to begin the ICF reactor system studies with a derivation of guidelines pertaining to the desirable size of the pellet yield and of the driver to be developed. This is easily accomplished on the basis of Eq. (IX-1). The denominator in Eq. (IX-1) changes slowly with Y because (1) the recirculating fraction (E/η_D) is small and (2) it is weakly dependent on Y because the exponent is small (that is, in general, β is not far from unity). With the approximation that the denominator does not vary significantly, the minimum of the numerator for a constant number of vessels n occurs at

$$Y_0 = \left[2\left(1 - \frac{\alpha}{\beta}\right)\frac{C_D}{nC_V}\right]^{2/[3-(2\alpha/\beta)]} . \qquad \text{(IX-3)}$$

This result shows that the value of the pellet yield, which minimizes the average unit power cost Y_0, depends only on the ratio of the economy of scale-to-gain exponents α/β and on the ratio of the cost constants C_D/nC_V. In general, the values of the ratio α/β are near 1/2 so that the exponent in Eq. (IX-3) is near unity; therefore, Y_0 increases approximately linearly with the ratio of the cost constants.

The variation of optimal pellet yield in the relevant range of parameters is shown graphically in Fig. IX-1. For relatively high driver costs and high values of α/β (that is, either large α, meaning little economy of scale, or small β, meaning shallow gain curve), the values of Y_0 become unmanageably high; however, for values of α/β near 1/2 and lower, the optimal yield is acceptable for any value of the cost ratio.

For representative values of $\alpha = 0.6$, $\beta = 1.2$, $C_D = 350$ M\$, and $nC_V = 2$ M\$, the optimal yield is 175 MJ; this value of Y_0 agrees closely with the results obtained from detailed computer modeling using the TROFAN code[1] for the reactor design employing wetted-wall containment vessels.

Effect of Gain Curve and External Constraints. In studying the effects of the gain curve, it is customary to make comparisons for a constant pulse energy E.[2] In our model this corresponds to determining the variation of the pellet yield Y with β from Eq. (IX-2) for constant K_1 and E. (We assume that variation of the gain curve is modeled by variation in the gain exponent β.)

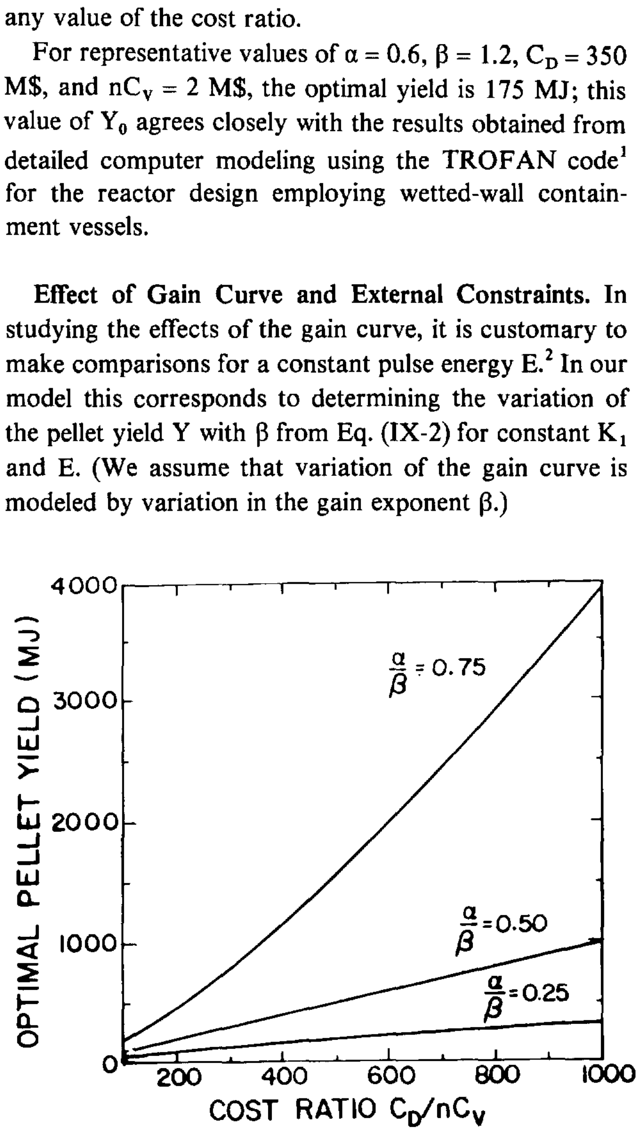

Fig. IX-1. Optimal pellet yield.

---

*Information supplied by Burns and Roe, Inc.

As we indicated previously, the denominator in Eq. (IX-1) changes slowly with Y; therefore, the variation of u with β is given primarily by the variations of the numerator. The calculation of that variation, by using Eq. (IX-1), results in the following expression for the change in unit cost δu corresponding to the change δβ.

$$\delta u = \left\{ \frac{1}{2}\left(nC_V\sqrt{Y}\right) \ln E - \left(C_D Y^{\alpha/\beta-1}\right)\left[\left(1 - \frac{\alpha}{\beta}\right)\ln E + \frac{\alpha}{\beta^2}\ln Y\right]\right\} \delta\beta \ . \tag{IX-4}$$

In general, the driver cost C_D dominates the reactor cost and the ration $\alpha/\beta < 1$; therefore, the above result shows that the unit cost decreases as β increases and that the amount of decrease is proportional to the cost itself. This was to be expected; because of the economy of scale, the driver cost per unit power output decreases as Y increases with β, for constant pulse energy E. However, because of the diseconomy of scale in reactor vessel cost (exponent greater than unity), the unit cost would increase with increasing β (that is, Y) if the vessel cost was dominant; this result is also evident from Eq. (IX-4). Our conclusions are confirmed in calculations performed with TROFAN and illustrated in Fig. IX-2.

To illustrate how essential external constraints are in parameter optimizations, we now recalculate the effect of changing β on unit power cost when the net power is held constant. For a constant driver repetition frequency N, the requirement of constant power implies a functional relationship Y(β) from which we easily derive the expression

$$\left[Y\eta_T(1 - q) - \frac{E}{\beta\eta_D}\right]\frac{dY}{d\beta} = -\frac{K}{\beta^2\eta_D} Y^{1/\beta+1} \ln Y \ . \tag{IX-5}$$

This result indicates that $dY/d\beta$ is always negative. To maintain a constant net power output, the yield Y must be decreased as the steepness of the gain curve increases because of the decrease in recirculating power fraction; this is an intuitively anticipated result.

The effect of a change in β on u can now be inferred from Eq. (IX-1) directly without additional calculations. A decrease in yield Y with an increase in β ($dY/d\beta < 0$) implies an increase in unit cost (because $\alpha/\beta < 1$) when the driver cost dominates (as it usually does) because of the economy of scale in driver cost. (The opposite would be true if the plant reactor cost were dominated by the vessel cost for which there is a diseconomy of scale.) This apparently counterintuitive conclusion may be a consequence of omitting the balance of plant from the analysis. For constant net power output, a decrease in the recirculating power fraction implies a smaller and less expensive turbogenerator; whether the resulting reduction in cost is sufficient to overcome the effect of the increased unit driver cost will depend on the relative magnitudes and scalings of these two costs.

These simple considerations show that the change in unit cost with changing slope of the gain curve β can be either downward or upward, depending whether the driver pulse energy E or the reactor power output is kept constant. This demonstrates the essential dependence of optimization on external constraints.

Reactor Configuration. For a given power plant output, one of the first questions to be answered is whether the reactor should comprise one larger or several small containment vessels. The answer is readily determined from the previously introduced expressions for the cost of the reactor vessel and the driver.

The vessel cost for a one-vessel design is

$$C(1) = C_V Y^{3/2} \ . \tag{IX-6}$$

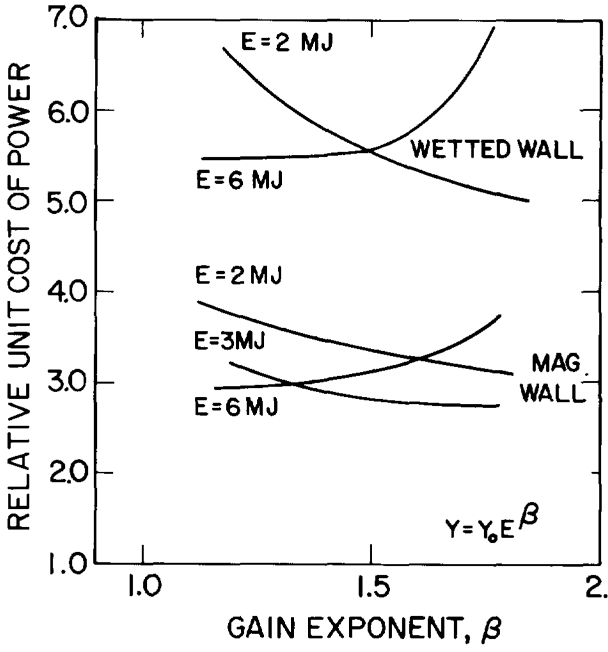

Fig. IX-2. Effect of gain exponent.

Assuming that a technical constraint precluding the possibility to increase the driver repetition frequency to the required level is not encountered, the vessel cost for an n-cavity design is

$$C(n) = nC_V (Y/n)^{3/2} = C(1)/\sqrt{n} \ , \tag{IX-7}$$

because the yield per cavity is Y/n. Therefore, it is advantageous to use several small cavities rather than a single large one if the resulting system complexity (for example, piping and beam switching) does not preclude the above scaling.

The corresponding saving in driver cost is determined analogously. The driver cost for a one-cavity design is

$$D(l) = C_D Y^{\alpha/\beta} \ , \tag{IX-8}$$

and for an n-cavity design it is

$$D(n) = C_D(Y/n)^{\alpha/\beta} = n^{-\alpha/\beta} D(l) \tag{IX-9}$$

(In this case the economy-of-scale argument does not apply because the driver repetition rate does not remain constant.) Because $\alpha/\beta > 0$, the above result indicates that cost will be reduced if the reduction is not canceled by the required increase in frequency capability and system complexity resulting from the addition of beam-switching devices.

In deriving the above simple cost estimates, the net power output remained constant. Consequently, the design policy of using several small containment vessels in place of a single large one will lower the average capital cost of power, which is the usual objective in engineering optimizations.

Containment Vessel Size/Lifetime Tradeoff. The lifetime of an ICF reactor vessel is governed, in general, by either the neutron fluence or by the material loss, both of which are inversely proportional to the first-wall surface area. Therefore, it is natural to look for a tradeoff between the size of the vessel and its lifetime. Let us illustrate the required analysis by deriving the answer to a specific question. If the expenses associated with the need for replacing n containment vessels during the plant lifetime can be eliminated by increasing the size of the vessel, how large can the increase be before it is no longer cost effective?

A plausible estimate of reactor vessel cost with necessary replacements is

$$C(n) = C_V R^2 d(1 + nr)t_0/t_p \ , \tag{IX-10}$$

where C_V is a constant, R is the vessel radius, d is its wall thickness, r is the fractional replacement cost (including installation), and t_p/t_0 is the productive fraction of the reactor lifetime t_0. The cost of a large vessel that would not require replacement is

$$C(0) = C_V R_0^2 d_0 \ ; \tag{IX-11}$$

it will be cost effective if the inequality

$$\frac{R_0^2 d_0}{R^2 d} < \frac{t_0}{t_p}(1 + nr) \tag{IX-12}$$

is satisfied.

This analysis can be refined, for example, by postulating that the number of replacements n is inversely proportional to the surface area $4\pi R^2$ and by deriving a corresponding estimate for the productive fraction t_p/t_0. However, the inequality derived above suffices to indicate the approach.

We illustrate the result with an example. Suppose the containment vessel must be replaced every 3 years during a reactor lifetime of 30 years, that is, $n = 10$; only the first and the inner structural walls need be replaced at 30% of the original reactor vessel cost, that is, $r = 0.30$; and 10% of the lifetime must be devoted to replacement activities, that is, $t_p/t_0 = 0.90$. If, in addition, we postulate that $d_0 = d$, then the inequality reduces to

$$R_0 \leq 2.1\ R \ .$$

The result means that if increasing the radius by any factor <2 will eliminate the need for replacements, then it is cost effective to do so; if, however, the radius must be more than doubled to avoid replacements, then it is not cost effective.

Conclusions. The discussions of trends and tradeoffs presented in this section are not intended to be complete and exhaustive; they illustrate one approach to arrive at a point design and indicate directions of parameter variations that may reduce the value of the objective function. Analyses of this kind, when used judiciously, provide insights into parametric interdependencies and contribute to the solutions of problems encountered in the development of ICF reactors. They may also save significant amounts of time and effort required for detailed studies and/or optimizations with computer modelings.

INERTIAL FUSION COMMERCIAL APPLICATIONS SYSTEMS CODE DEVELOPMENT (J. H. Pendergrass)

Introduction

A project to revise and document the inertial fusion commercial applications systems code TROFAN has been initiated and is well under way. The revision objectives were

- to update and upgrade present physical and capital cost models for all plant components and integrated plant economic performance models to include our most recent information and permit more flexible and accurate modeling;
- to permit more complete use of data bases that have been accumulated;
- to expand TROFAN's capability to conveniently treat commercial applications of inertial fusion other than CO_2 laser-driven electric power generation by using conventional steam cycles;
- to provide documentation of the models in TROFAN and a manual for its use;
- to provide more detailed output when desired and greater flexibility and convenience in data input; and
- to reorganize the code to permit easier modification of TROFAN and incorporate new developments.

The following section describes the revised TROFAN code and lists directives for future work.

Updating and Upgrading Models; More Complete Use of Existing Data Bases

We have accumulated extensive data bases that to date have been used only partially. Much of this information is being incorporated into TROFAN. Many new models and much new information concerning the plant's physical performance, capital cost, and operating and maintenance costs have been developed in recent months. In addition to the CO_2 commercial-applications laser driver capital cost and performance model and reactor cavity-sizing algorithms described elsewhere in this report, we have developed

- new capital operating and maintenance cost and efficiency models for beam-transport systems of CO_2 laser drivers for commercial applications, with emphasis on beam-tube tunnels, last optical surfaces, turning mirrors, and deformable focusing mirrors, using recently acquired data from supporting studies performed by United Technologies Research Center, Rocketdyne (Rockwell International Corporation), and Burns and Roe, Inc.
- new and improved reactor designs and analytical models.
- sizing and costing algorithms for electric power generating station buildings and structures, steam lines, and control cables, based on data supplied by Burns and Roe, Inc.
- new pellet designs and gain curves.

This information and new models have already been or will shortly be incorporated into TROFAN.

Desirable modeling options for plants' economic performance have been identified and the groundwork has been laid for their implementation. These options include

- costs and cash flows expressed in terms of both constant and current dollars;
- the use of simple fixed charge rates and detailed discounted cash-flow methods to obtain levelized cost of production;
- escalation during construction;
- the use of alternative methods for computing interest expense incurred during construction; and
- the consideration of alternative construction schedules.

In addition, we incorporated the usual provisions for variations in economic parameters such as taxes, insurance, interest rates, discount rates, and cash-flow histories.

Expansion of TROFAN Capabilities

The older version of TROFAN provides models and costs for only CO_2-laser-driven Los Alamos wetted-wall and magnetically protected reactor concepts and electric power production by conventional steam cycles. Physical and capital cost models and cost data bases have recently been constructed by Burns and Roe, Inc., for

- lithium boiler, high-temperature blankets coupled with potassium Rankine topping cycles that reject

heat to conventional steam cycles for high plant conversion efficiencies, and
- hybrid fusion/fission power and fissile-fuel production plants.

These models and data will soon be included in TROFAN. We also plan to incorporate heavy-ion accelerator driver and reactor concept models. When economically promising synfuels processes (for example, thermochemical water-splitting cycles or high-temperature electrolysis) reach an appropriate stage of conceptual development, we intend to incorporate models of such processes coupled to inertial fusion into TROFAN. Other large-scale, process heat applications generated by inertial fusion may also be considered.

Code Design Philosophy

TROFAN is already a large, complex code with many subroutines. It will become even larger and more complex through addition of other commercial applications models and data bases. Therefore, logical, retrievable organization, ease of addition for new features, and ease of use are of paramount importance. Efficiency, speed of computation, and minimization of storage requirements are generally not limiting and are therefore secondary goals. Figure IX-3 illustrates the principal organizational features of the new version of TROFAN.

REACTOR STUDIES

Modified Wetted-Wall Reactor Concept (J. H. Pendergrass, I. O. Bohachevsky, T. G. Frank)

A major modification of the wetted-wall reactor concept has been conceived that may eliminate uncertainties in performance and restrictions on operating conditions. We are continuing to investigate the operating characteristics of this reactor.

A layer of liquid lithium protects the interior surface of the cavity wall in the modified wetted-wall reactor from damage from pellet microexplosions. The response of the liquid lithium layer to pulsed neutron and x-ray energy depositions has been investigated analytically and numerically.

We have obtained analytic solutions that are valid when the layer is in a pure liquid state. For the anticipated energy deposition rates, these analyses predict modest wave amplitudes. For example, transverse velocity components generated by pressure perturbations do not exceed a few meters per second. Further development of these analytical solutions will provide insight and direction for interpreting and guiding detailed numerical simulations.

Initial numerical simulations of modified wetted-wall reactor cavity phenomena are performed using the CHART-D hydrodynamics code. The interpulse pressure in the cavity is expected to be reduced to the vapor pressure of the protective lithium layer before each successive pellet microexplosion. Numerical simulations indicate that at this pressure the protective layer will contain a small fraction of the vapor phase. This vapor content is sufficient to lower the sound speed of the protective layer appreciably and to result in the dissipation of pressure pulses generated by x-ray energy deposition before they reach the cavity wall. Only qualitative results have been obtained at this time; however, these results are encouraging and indicate stable performance of the protective lithium layer.

Heavy-Ion-Beam Fusion (W. A. Reupke, J. H. Pendergrass)

Heavy-ion-beam accelerators are a promising alternative to lasers for driving fusion pellet microexplosions. Los Alamos' interest in the heavy-ion-beam option has increased since we were named the lead laboratory for this technology. We have studied several aspects of heavy-ion-beam fusion during this reporting period.

To avoid causing beam instabilities, a very restricted reactor cavity environment is necessary for focused heavy-ion-beam propagation to the fusion pellet. It seems likely that there will be an upper limit on reactor cavity atmosphere density of $\sim 10^{12}$ to 10^{13} atoms/cm^3, corresponding to $\sim 10^{-4}$ to 10^{-3} torr at 1000 K. This particle density is ~ 3 orders of magnitude lower than required for laser beam propagation and has directed attention to new reactor concepts. The reactor cavity designs now being evaluated for possible use with heavy-ion-beam drivers are the modified wetted-wall concept, a dry-wall concept with a carbon protective liner, and a concept with a bare metal wall. We have applied the greatest effort to the modified wetted wall, which is very promising for this application. Our study of the dry- and bare-wall concepts revealed problems concerning the ultimate disposition of the condensable pellet debris.

The interface between reactors and accelerators will require study and innovation. The placement, support,

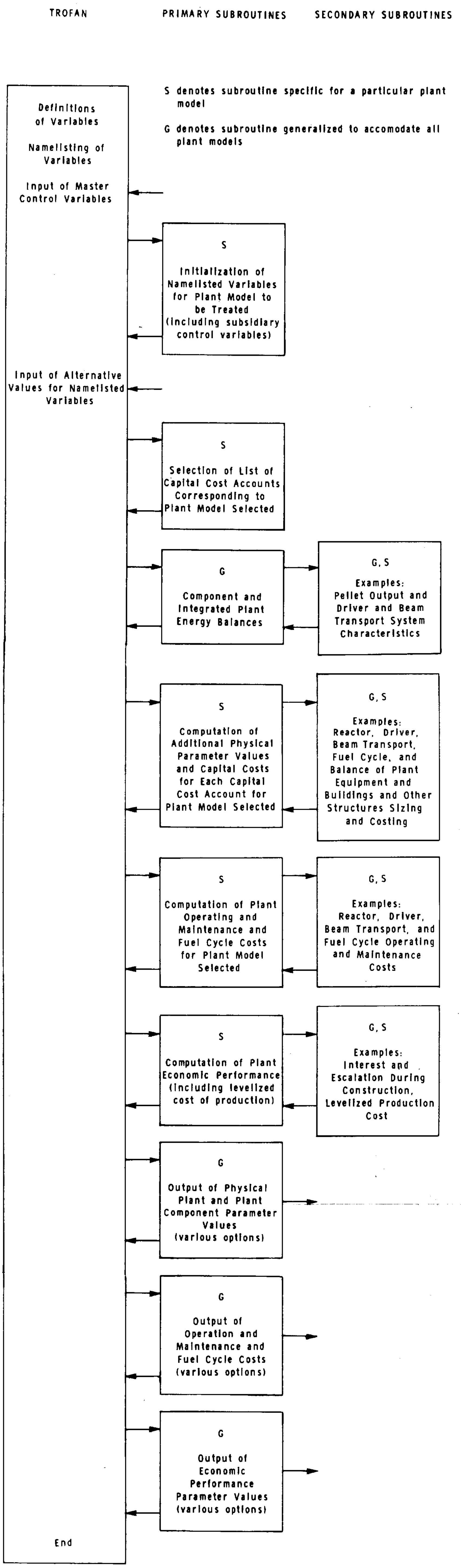

Fig. IX-3. Organization of new TROFAN version, shown as once through for simplicity.

and protection of the required large number of focusing magnets poses significant problems; we are attempting to reduce the size and power requirements of these magnets. For accelerators that use storage rings for current magnification (for example, rf linacs), the permissible gas particle density in the storage rings is ~7 orders of magnitude lower than in the reactor cavities. Because there is direct access between the storage rings and the reactor cavities through the beam-transport system, vigorous differential pumping will be required to maintain this pressure difference. Analysis of this problem has been complicated by the different flow regimes.

The attractiveness of heavy-ion-beam fusion in commercial applications will depend on both its technical feasibility and economic comparisons between it and other energy sources. We conducted a brief preliminary study to compare power production costs between heavy-ion-beam and laser-driven electric generating stations using variable fusion pellet performance (gain) as a parameter. The results of the study indicate that there are no significant differences in power production costs if optimistic pellet performance is assumed; however, heavy-ion-beam driven systems are more economical if pessimistic pellet performance is assumed.

Reactor Cavity Sizing for Optimized Commercial Applications Pellets (J. H. Pendergrass)

Introduction. In inertial fusion electric power generating stations, reactor cavity size directly influences the overall reactor size; reactor and reactor maintenance building, pipeway, and crane gallery sizes; the lengths of primary coolant loop piping, driver beam-transport ducts, tunnels, and control wiring; and the volumes of primary coolants and tritium-breeding materials and the required capacities of processing systems for these materials. All these plant components have high capital costs; significant reductions in their sizes, amounts, and capacities can substantially reduce plant capital cost. On the other hand, reactor maintenance and lost production during downtime will also be costly. Longer service lives between shutdowns mean potentially lower maintenance cost, greater availability, and hence, lower unit production cost. The optimum service-life/cavity-size combination for a first-wall reactor intended for commercial application can only be determined through optimization studies of the entire plant with unit cost of production as a FOM. However, to maximize reactor service life for a specified power level and cavity size by specifying optimum pellet characteristics for each reactor type is an important initial step in plant optimization.

For our TROFAN code we have developed computerized models of several inertial fusion reactor cavity concepts combined with those pellet designs that give minimum cavity size for specified power levels and service lives. These models and the supporting analyses are outlined below.

Wetted-Wall Reactors. In wetted-wall reactor concepts, the first-wall structure is protected from photon and ion damage by interposing thin liquid metal films between the first-wall structure and pellet microexplosions. Their first-wall service life is therefore determined solely by neutron damage under normal operating conditions.

Neutron Damage Considerations. Because life-cycle testing with 14-MeV fusion neutrons is not yet possible, we have no directly applicable experimental data for estimating first-wall structure service lives in wetted-wall reactors. However, fission-spectrum neutron-irradiation tests and ion bombardment simulations of damage processes suggest that to replace a first-wall structure after reaching a thermonuclear neutron fluence of $\sim 5 \times 10^{22}$ n/cm^2 will be conservative for most metallic construction materials that are now being considered. Fortunately, it appears that economically acceptable cavity-size/first-wall service-life combinations will be possible if this conservative value is used. Substantially greater first-wall structure resistance to neutron damage may be possible and would, of course, enhance the prospects for commercial applications of inertial fusion.

The calculation of reactors' minimum cavity size for specified first-wall structure service life and a power level based on fluence limits is straightforward and independent of pellet characteristics as long as neutron energy spectra are not significantly altered by changes in pellet design. The relationship is:

$$R = \sqrt{Y_N Y \nu_R A S_{FWS}/4\pi F_R} \quad , \qquad \text{(IX-13)}$$

where R is the cavity radius (m), A is reactor fractional availability, Y_N is thermonuclear neutron release per unit thermonuclear energy release (3.55×10^{17} n/MJ), Y is pellet energy yield (MJ/microexplosion), ν_R is reactor pulse repetition rate (microexplosions/year), S_{FWS} is desired first-wall structure service life (years), and F_R is neutron fluence (n/m^2) at which the first-wall structure must be replaced. Thus, minimum cavity radius based on neutron fluence limits is directly proportional to the square roots of pellet yield, reactor pulse repetition rate, and desired service life; it is inversely proportional to the square root of the limiting neutron fluence. For example, for the conservative fluence limit of 3×10^{22} n/cm^2, a first-wall structure service life of 2 years, 100% availability, and a pellet yield of 150 MJ, the corresponding minimum wetted-wall reactor cavity radius is 1.03 m.

Hard X-Ray Heating of Inner First-Wall Surfaces. The inner surfaces of cavity structural walls in wetted-wall reactors undergo cyclic heating as a result of energy deposition by hard x rays that penetrate the relatively thin lithium protective layers. The potential for damage caused by this mechanism is greater in wetted-wall reactors than in any other reactor concept because in wetted-wall reactors the protective layers are thinner and cavity radii smaller.

Calculations of x-ray energy deposition in first-wall structures using the x-ray energy deposition code HEX[3] and detailed pellet x-ray spectra indicate that temperature increases can be limited to acceptable values by appropriate choice of pellet design. We considered three prospective wall materials: P22, a low-alloy (2.5 Cr, 1 Mo) steel; 316 stainless steel; and TZM, a molybdenum alloy (0.5 Ti, 0.08 Zr).

For reactor cavities with sufficiently large radii to limit neutron damage rates to acceptable values, temperature increases were <25 K for optimized pellet designs and essentially independent of lithium film thickness in the range 0.1 to 1.0 cm.

Magnetically Protected Reactors.

Introduction. In the Los Alamos concept for first-wall protection by magnetic fields, the pellet debris ions are deflected from reactor cavity walls into specially designed energy sinks, for example, onto sacrificial solids, MHD channels, or liquid metal sprays. Thus, in this concept, reactor cavity first walls are subject only to photon and neutron irradiation, and a graphite sacrificial liner may be used for their protection. The photon damage mechanism that acts on the liner is loss of material by evaporation; this evaporation from the liner's inner surface is a result of pulsed heating to very high temperatures. For reactor concepts involving first-wall surfaces subject to material loss by evaporation and sputtering, we can vary pellet design to modify pellet photon and ion energy yields and spectra, and thereby reduce damage rates. Different pellet designs may be optimum (causing minimum first-wall material loss rate) for different reactor concepts.

Cavity Sizing and Service Life of First-Wall Structure. We examined the potential for reducing graphite material loss rates, and thereby increasing liner service life, by maintaining high-Z gases within magnetically protected reactor cavities. The gas concentrations should be low enough to permit efficient transmission of CO_2 laser beams, which are now estimated at $\sim 10^{15}$/cm^3, but high enough to permit absorption of substantial fractions of pellet photon energy emissions. Much of this energy would be subsequently reradiated to the sacrificial liner; however, it would occur over a sufficiently longer time to allow conduction of thermal energy away from the liner inner surface during energy deposition, significantly reducing evaporation. This time is estimated at up to 1 ms, compared to submicrosecond pellet x-ray emission times. The dependence of liner service life on liner radius and operating temperature (temperature to which the sacrificial-liner surface returns just before the next pellet microexplosion) has also been investigated.

All our calculations for a protective liner of minimum radius R_L (m) as a function of desired liner service life S_L (years) and operating temperature level T (K), cavity protective gas concentrations C_G (molecules/cm^3), and pellet x-ray spectrum S_p begin with calculations of material loss L_1 per pellet microexplosion (cm/microexplosion as a function of photon fluence per pellet microexplosion F (J/cm^2·microexplosion) for specified values of T and C_G for a specified pellet. Thus, we first obtain

$$L_1 = L_1(T, C_G, S_p, F) \ . \qquad \text{(IX-14)}$$

If, in addition, an initial protective liner thickness δ_I (cm), a minimum thickness at replacement δ_F (cm), a pellet yield Y (MJ/microexplosion), a fractional x-ray photon energy yield F_x, a reactor pulse repetition rate ν_R (microexplosion/year), and a fractional availability A are specified, then the liner radius is obtained by solving

$$\frac{S_I - S_F}{A \nu_R S_L} = L_1\left(T, C_G, S_p, \frac{YF_x}{4\pi R_L^2} \right) \ . \qquad \text{(IX-15)}$$

In practice, L_1 (T, C_G, S_p, F) is represented in tabular form for computerized systems studies and in graphical form to hand calculate a particular pellet design. The liner radius of a magnetically protected cavity for constant C_G, T, S_p, F_x, S_L, ν_R, δ_I, and δ_F scales as the square root of the pellet yield. Similarly, liner radius is proportional to the square roots of S_L and ν_R; it is inversely proportional to the square root of $\delta_I - \delta_F$ when all other parameters are held constant. The dependencies of liner radius on liner operating temperature and cavity gas concentration, with all other parameters held constant, are too complex to express in such simple terms. Once the liner radius is determined, the service life of the first-wall structure as set by neutron irradiation can be computed by inverting Eq. (IX-13).

We used the following procedure to obtain the results. A detailed x-ray emission spectrum and history obtained from the pellet burn code of a commercial pellet design is used as input to an x-ray energy deposition code, such as the HEX code developed at Los Alamos. The spatial energy deposition-profile history obtained from the deposition code is used as input to our HOTWALL inertial fusion first-wall heating and evaporation code.

Because x-ray absorption cross-section data were readily available in a form suitable for use with the HEX code for xenon, this inert gas was used as a representative heavy-element cavity gas for first-wall protection. Xenon is a reasonable choice, and results obtained for other heavy elements would be similar. Figure IX-4 summarizes calculated values of liner material loss by evaporation as a function of cavity radius with initial liner surface temperature T and cavity gas density C_G as parameters. The pellet yield for these calculations was 150 MJ, and the optimized pellet design for minimum liner loss by evaporation was used for each range of the parameters. The results presented in Fig. IX-4 suggest that cavity atmospheres can be important in providing additional protection from material loss caused by x-ray heating and consequent evaporation. A number density of 10^{15} xenon atoms/cm^3 (corresponding, for example, to ~0.1 torr at 1000 K) permits reduction in cavity radius from ~6.55 to ~2.25 m for a vacuum, a pellet yield of 150 MJ, a liner operating temperature of 1200 K, and a liner evaporation rate of 10^{-8} cm/microexplosion (~3.2 cm/year in a 10-Hz machine). The strong dependence of liner material loss rate on cavity radius is significant and indicates that liner material loss rates can be reduced to very low values (corresponding to long service life) at very little penalty in increased cavity size compared to the size required for maximum economically acceptable loss rates. As the results presented in Fig. IX-4 illustrate, the effect of variations in operating temperature of the protective liner over the wide range considered has only a modest effect on cavity size for fixed material loss rates.

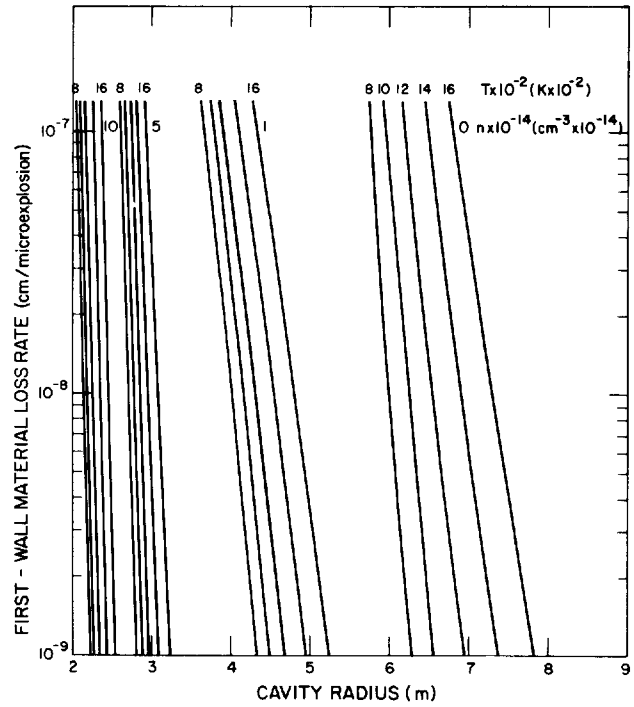

Fig. IX-4. Liner material loss rates caused by surface evaporation in Los Alamos magnetically protected inertial fusion reactions.

One significant aspect of liner ablation that has not yet been addressed is the question of useful redeposition of evaporated liner material. There are indications that net evaporation rates will be at least ~20% lower than those presented in Fig. IX-4. Because the problem of redeposition is complex, geometry-dependent, and has not been adequately investigated, we have been reluctant to include the potential benefits of useful redeposition in our calculations.

On the other hand, the preceding discussion ignores the degradation of protective liners that may result from neutron irradiation and thermal shock.[4] These legitimate questions have not been satisfactorily resolved. Recent estimates of blast-wave overpressures (~3.0 atm) on cavity first walls for 1 torr neon in 10-m-radius cavities for similar pellet x-ray spectra and energy yields indicate that maximum blast-wave overpressures with 0.1 torr xenon will be negligible.[5]

Reactors with Unprotected Sacrificial Liners and with Bare First Structural Wall. We have also evaluated alternatives to protecting the first wall of inertial fusion reactor cavities with liquid metal films and magnetic-field/sacrificial-liner combinations. We have estimated loss rates for sacrificial graphite liners without gas protection (dry-wall concept); we also considered otherwise unprotected cavities in which pellet debris deposited on first-wall inner surfaces provides protection. Minimum cavity diameters for those concepts are determined by liner ablation or pellet debris build-up rates. Service-life limitations of structural components caused by neutron damage are usually secondary considerations; however, structural component replacement schedules must prevent the accumulation of neutron fluences in excess of limiting values.

Dry-Wall Concept. In dry-wall cavities, sacrificial liners lose material through evaporation from their inner surfaces as a consequence of both x-ray and pellet-debris heating and by sputtering from pellet-debris ion bombardment. Estimated material loss rates (per pellet micro-explosion) L_l for a carbon liner and a pellet design considered for commercial applications that cause the lowest loss rates in reactors of this type are presented in Fig. IX-5 for a liner operating temperature of 1200 K and a pellet yield of 150 MJ.

Once again, the effect of variation in liner temperature is relatively minor and affects only that portion of the total material loss-rate curve that is dominated by x-ray heating and by roughly the amounts shown in Fig. IX-4. There are other, more critical conclusions.

- Liner evaporation resulting from heating caused by pellet-debris ion impingement is relatively unimportant.
- Evaporation resulting from x-ray heating sets a practical lower limit on cavity size of ~10 m, even if relatively high loss rates (that is, $\sim 10^{-7}$ cm/microexplosion or ~30 cm/year in a 10-Hz, 150-MJ, 1200 K liner cavity) are considered acceptable.
- Sputtering dominates as a material loss mechanism for large cavity radii. An ~11.0-m radius is required to maintain loss rates of $\sim 10^{-8}$ cm/microexplosion (~3.0 cm/year in a 10-Hz, 150-MJ, 1200-K liner cavity).

Thus, cavities of this type must be large if acceptable service lives are to be achieved. We apply the same type of scaling of reactor size with pellet yield as that discussed for magnetically protected reactor cavities.

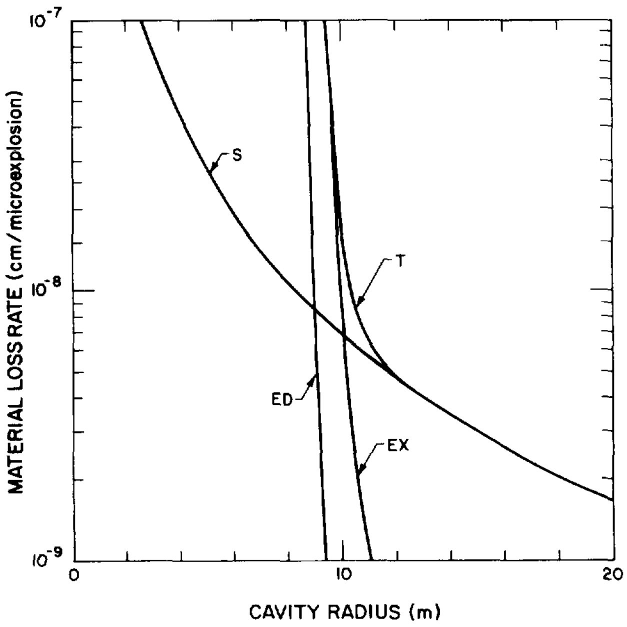

Fig. IX-5. Material loss rates on the inner surface of Los Alamos dry-wall reactor liners caused by evaporation.

Bare-Wall Concept. Because pellet designs for commercial applications involve materials that tend to condense under inertial fusion reactor conditions, we are concerned about the build-up of pellet debris on reactor first walls. Lack of information precludes definitive assessment of this possibility. However, we now include in our studies reactor cavities whose size for a specified service life between maintenance is determined by the rate of build-up of pellet debris on their first walls and by the permissible maximum thickness of pellet-debris build-up.* If M_p is the pellet mass (g); ν_R the reactor pulse repetition rate (microexplosions/year); f_c the fraction of the pellet mass that condenses with acceptable uniformity on cavity first-wall inner surfaces; S_B the desired bare-wall service life between cleanout activities (years); δ_M the maximum thickness of deposited pellet debris that can be tolerated (cm); and ρ_p the density of deposited pellet debris, then the cavity radius

$$R_B = \sqrt{\frac{M_p f_c \nu_R S_B}{4\pi\ \delta_M \rho_p}}$$

for uniform deposition on first walls of spherical reactor cavities. The service life of the first-wall structure, determined by neutron fluence limits, is computed in the usual manner once cavity radius is known.

---

*This protection scheme was proposed by Westinghouse Electric Corporation in a design study sponsored by DOE.

The reactor service life between cleanouts, described above, also assumes that the remainder of the pellet debris is deposited in noncritical locations or is continually removed. This question clearly requires considerable further examination. If deposition is relatively uniform, as might be expected in a spherical reactor cavity, then the strong dependence of ablation (per microexplosion on cavity radius) suggests that a reactor cavity could be sized so that a quasi-equilibrium state is attained in which debris-deposition rates exactly match net ablation rates. However, this ideal situation might be unstable and difficult to ensure.

We calculate the rates of liner material loss by evaporation resulting from x-ray heating in Los Alamos dry-wall reactor cavities by the same sequence of computations and the same tools as we use for magnetically protected reactor cavities. Our first-wall heating and evaporation code HOTWALL and appropriate deposition profiles can be used to calculate evaporation that results from pellet-debris heating; combined x-ray/pellet-debris-induced evaporation can also be treated. Sputtering was calculated with a newly written FORTRAN code called SPUTTER, based on a theoretical treatment of sputtering and detailed pellet-debris ion energy spectra. We must resort to theory to predict sputtering coefficients because no directly applicable experimental data exist for this complex phenomenon.[6]

Summary

In our systems studies, we model four reactor cavity concepts: wetted-wall, magnetically protected, dry-wall, and bare-wall. Our FORTRAN subroutine and our TROFAN commercial applications systems code permit sizing of cavities for these four concepts.

- Radii of spherical wetted-wall reactor cavities (first-wall protection from pellet-debris ions and x-ray photons) are determined as functions of (1) neutron fluence at which the first-wall structure must be replaced because of neutron damage, (2) desired service life of first-wall structure, (3) pellet thermonuclear yield, and (4) reactor pulse repetition rate.
- Liner radii for cylindrical, magnetically protected reactor cavities (first-wall protection by deflection of pellet-debris ions into energy sinks and sacrificial liners for x-ray energy absorption) are determined as functions of (1) cavity atmosphere heavy-element gas concentration, (2) liner operating temperature, (3) initial and minimum acceptable liner thickness, (4) desired liner service life between replacements, (5) fraction of ablated liner material that is usefully redeposited, (6) pellet yield, and (7) reactor pulse repetition rate. First-wall structure service lifetimes are determined as functions of cavity radius, neutron fluence at which first-wall structure replacement is necessary, reactor pulse repetition rate, and pellet thermonuclear yield.
- Liner radii of spherical dry-wall reactor cavities (first-wall protection by sacrificial liners only) are determined as functions of (1) liner operating temperature, (2) initial and minimum acceptable liner thicknesses, (3) liner desired service life between replacements, (4) fraction of ablated liner material that is usefully redeposited, (5) pellet yield, and (6) reactor pulse repetition rate. First-wall structure service lifetimes are determined as functions of cavity radius, neutron fluence at which first-wall structure must be replaced, reactor pulse repetition rate, and pellet thermonuclear yield.
- Radii of spherical bare-wall reactor cavities (first-wall protection by deposition of pellet debris) are determined as functions of (1) maximum (uniform) permissible debris thickness, (2) fraction of pellet debris deposited on first-wall inner surfaces, (3) pellet-debris mass, (4) pellet-debris deposited density, (5) desired cavity service life, and (6) reactor pulse repetition rate. First-wall structure service lives are determined as functions of cavity radius, neutron fluence at which first-wall structure must be replaced, pellet thermonuclear yield, and reactor pulse repetition rate.

Where necessary, we have performed detailed calculations of pellet energy yields and spectra; energy deposition profiles; and first-wall heating, evaporation, and sputtering to provide data bases for cavity sizing and to determine optimum pellet design selections for each reactor type.

HEAT TRANSFER FROM GRAPHITE LINERS TO COOLANTS

Quasi-steady removal of deposited energy to the lithium coolant by conduction through the liner toward the rear liner surface, combined conduction and radiation across the interface between the liner and the first structural wall, and conduction through the first structural wall must occur with a moderate time-averaged temperature drop. Otherwise, the liner operating temperature will be very high, and material will be lost by evaporation so rapidly that the economic viability of the liner concept will be questionable. The following simplified analysis suggests that with typical projected operating conditions, acceptable temperature drops can be achieved through appropriate design.

The plane, one-dimensional geometry of the heat-transfer model that was used to derive the results is illustrated in Fig. IX-6. The model involves the following assumptions and approximations.

- The resistance to heat transfer at the interface of the metallic first structural wall and the lithium coolant can be neglected.
- No credit is taken for heat transfer from the inner surface of the protective liner by thermal radiation or as latent heat from evaporation of ablated material.
- We treat only the worst case of liner heat transfer, that is, immediately following installation of a new liner when it is thickest and hence its resistance to conduction of heat through it is greatest.
- The use of representative, constant thermophysical property values will give results of acceptable accuracy.
- A quasi-steady heat-transfer analysis will give results of acceptable accuracy, assuming that the liner inner surface temperature is that to which the liner inner surface cools just before pulsed energy deposition.

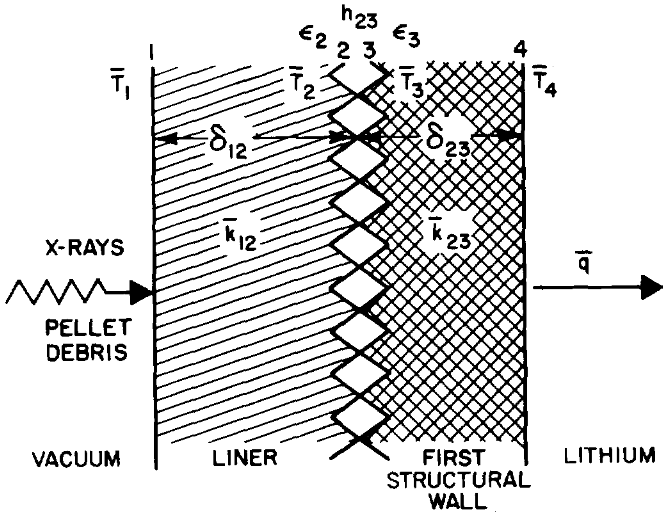

Fig. IX-6. Heat-transfer model for protective liner.

- Gray-body thermal radiation across the interface of the liner and first structural wall is postulated.

Plane, one-dimensional geometry is appropriate because projected liners and first-wall structures are thin relative to reactor cavity radius. A quasi-steady approximation with inner surface liner temperature equal to the premicroexplosion minimum is possible, although the inner surface temperature cycles up and down. This approximation can be used because the region near the inner surface that is exposed to large temperature variations is thin in comparison to total liner thickness, the thermal capacity of the liner is large in comparison to pellet yield, and the largest resistance to heat transfer is expected at the interface of liner and first structural wall. The quasi-steady approximation using the liner inner surface temperature clearly gives conservative results.

The largest resistance to heat transfer is expected at the interface of liner and first structural wall; if the thermal contact is poor, we concentrate our attention on this resistance. The rate of heat transfer through the liner is given by

$$q = \frac{k_{12}}{\delta_{12}} (T_1 - T_2) ,$$

and for the first structural wall by

$$q = \frac{k_{34}}{\delta_{34}} (T_3 - T_4) ,$$

whereas at the plane of contact between the liner and the first structural wall we have

$$q = \frac{\sigma(T_2^4 - T_3^4)}{(1/\epsilon_1) + (1/\epsilon_2) - 1} + h_{23}(T_2 - T_3) .$$

Here q is the quasi-steady heat flux (W/cm^2); k_{12} and k_{34} (W/cm·K) are, respectively, the time- and space-averaged thermal conductivities of the liner and the first-wall structure; and δ_{12} and δ_{34} are their corresponding thicknesses (cm). T_1, T_2, T_3, and T_4 are, respectively, the time-averaged temperatures (K) at the liner inner and outer surfaces and at the first structural wall inner and outer surfaces; h_{23} is the contact transfer coefficient (W/cm^2) of the liner/first structural wall interface; ϵ_1 and ϵ_2 are the gray-body emissivities of the outer liner and inner first structural wall surfaces; and σ is the Stephan-Boltzmann constant (W/cm^2·K^4). The temperature T_1 must be low enough to limit liner evaporative material losses to acceptable values, whereas T_4 must be high enough to permit acceptable power cycle efficiencies.

The critical parameter for heat removal from protective liners appears to be the contact transfer coefficient at the liner/first structural wall interface. The lowest value reported is ~5 × 10^{-3} W/cm^2·K and corresponds to nonflat surfaces and contact pressures of only 2 psi. Our concept for protective liners consists of interlocking blocks of graphite of appropriate shape (spherical or cylindrical shell segments). A typical energy for wall loading that gives acceptable liner evaporative material loss rates is 4.5 J/cm^2 per pellet microexplosion in a 10-Hz cavity, or 45 W/cm^2. The liquid lithium coolant temperature at the first wall is expected to be ~700 K.

Solution for T_2, given T_1, is straightforward and solution for T_3, given T_2, is also straightforward, but the solution for T_3, given T_2, requires an iterative or numerical procedure. Some results of a modest parameter study are presented in Table IX-I; they suggest that contact-transfer coefficients of $\gtrsim 100 \times 10^{-3}$ W/cm^2·K may be required for acceptable performance. Although no directly applicable experimental data appear to exist, data for other systems suggest that very modest contact pressures (only 10 to 100 psi) may suffice to provide contact-transfer coefficients in this range. Thus, there appears to be a broad window in parameter space for which the necessary liner heat transfer rates can be achieved with acceptable temperature drop.

TABLE IX-I. Results of Protective Liner Heat Transfer Parameter Study[a]

k_{23} (W/cm^2·K)	Emissivity		Temperatures[b] (K)			
	ϵ_2	ϵ_3	T_1	T_2	T_3	T_4
0	0.9	0.6	2350	1964	936	823
			2300	----	----	----
5 × 10^{-3}	0.9	0.6	2250	1864	518	405
			2200	----	----	----
20 × 10^{-3}	0.9	0.6	2150	1764	936	813
			2100	1714	780	667
	0.9	0.9	2050	1664	989	873
			2000	1614	828	715
100 × 10^{-3}	0.9	0.9	1650	1264	902	789
			1600	1214	842	729
α[c]	----	----	1200	814	814	701
			100	714	714	601

[a] Fixed Values: q = 45 W/cm^2, k_{12} = 0.4 W/cm·K, k_{34} = 0.35 W/cm·K, δ_{12} = 3 cm, δ_{34} = 1 cm.

[b] $(T_1 - T_2)$ fixed at 386 K, $(T_3 - T_4)$ fixed at 113 K.

[c] Required heat-removal rate cannot be achieved even with T_4 = 0 K.

CO_2 LASER CAPITAL COSTS AND EFFICIENCIES FOR ICF COMMERCIAL APPLICATIONS (J. H. Pendergrass)

Los Alamos' capability for performing accurate parameter and design tradeoff studies for conceptual inertial fusion electric generating stations has been improved substantially by incorporating estimates of overall efficiencies and capital costs for CO_2 lasers. These estimates were derived from a study[7]* funded by the DOE Office of Inertial Fusion, monitored by Los Alamos, and recently completed by AVCO-Everett Research Laboratory. These estimates were generated by exercising a CO_2 laser conceptual design and capital costing code written by AVCO for design parameter values near optimum and then modifying the results to correspond to more economical system geometries developed by Los Alamos. Near-optimum values of principal design parameters are listed in Table IX-II.

AVCO proposed a single ring of multipass laser PAMs closely coupled to power supplies, with axial fans for lasing-medium circulation, heat exchangers to remove pumping energy not extracted as laser light, and suitable expansion and contractions connected to form a circular flow path. Conceptual design details are given in Ref. 7. The laser beams are directed through ducts, called transfer tubes, to a central rotating mirror for redirection to reactors. We have found that for high pulse energies and repetition rates, savings in capital cost can be realized by dividing the large single ring proposed by AVCO into smaller rings, the exact number depending on pulse energy and repetition rates. The savings will be substantial, in spite of the additional costs of appropriate optics and transfer tubes for combination of smaller ring outputs. Reduction in total transfer tube costs constitutes the largest saving.

The differences in capital cost for AVCO single-ring layouts and our multiring geometries are indicated in Fig. IX-7. The dependence of capital cost on pulse repetition rate is illustrated in Fig. IX-8. The curves in these two figures bound the parameter space that was investigated. Table IX-III contains a more complete set of values of capital costs and overall efficiencies for CO_2 lasers with repetition rates of 2 to 40 Hz and output energies of 1 to 10 MJ with salt and aerowindows.

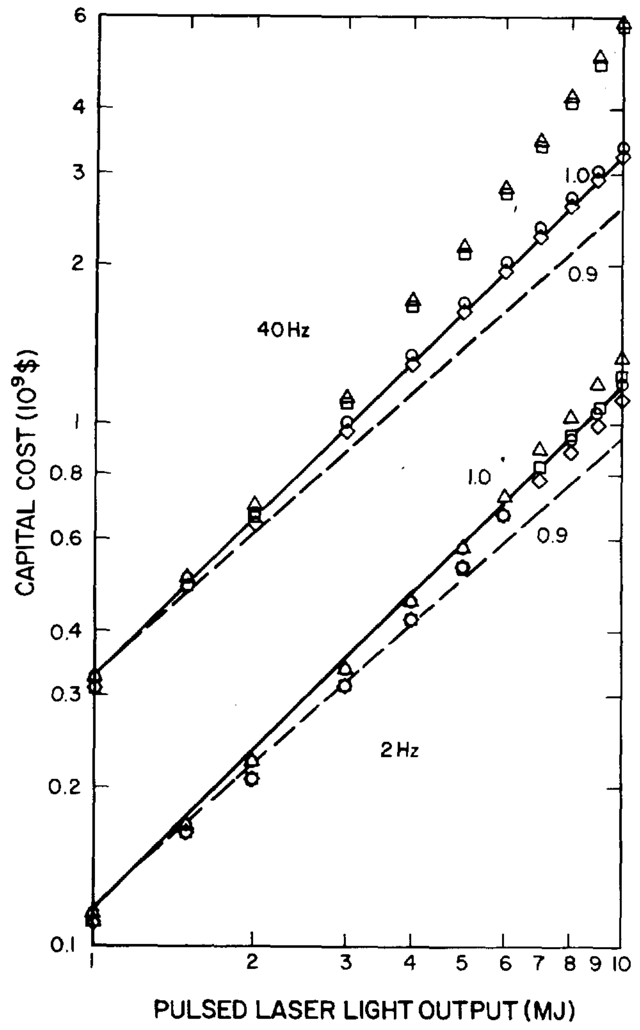

Fig. IX-7. Capital cost as function of driver pulsed-energy output for 2- and 40-Hz CO_2 lasers for inertial fusion commercial applications. Δ, salt window option and AVCO single-ring configuration; □, aerowindow option and AVCO single-ring configuration; ○, salt window option and Los Alamos multiring configuration; ◇ aerowindow option and Los Alamos multiring configuration; and solid line, 1.0 exponent scaling with energy for salt window option that might apply to large construction projects.

TABLE IX-II. Principal Near Optimum Physical Design Parameter Values

Laser energy absorbed per mirror (%)	0.5
Aerowindow aperture flux limit (J/cm^2)	10
Gas loading (J/1 atm)	100
Aerowindows Mach number	0.90
Laser gas mixture (N_2:CO_2)	1:1
Electron density (10/cm^{-3})	2
Number of passes through lasing medium	5
Salt window flux limit (J/cm^2)	2
Laser cavity operating pressure (atm)	1
Laser light pulse width (ns)	5
Small-signal gain	2
Laser gas inlet temperature (K)	300
Electric discharge pulse length (μs)	4

---

*Unpublished report by H. Friedman, C. A. Tavallee, and B. A. Miami, "User Manual for Laser Fusion Driver Economics Model," AVCO-Everett Research Laboratories (November 1979).

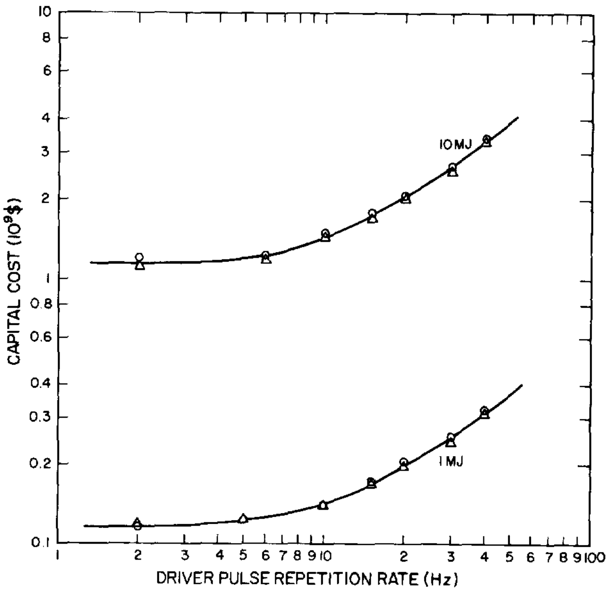

Fig. IX-8. Capital cost as function of driver pulse repetition rate for 1-and 10-MJ CO_2 lasers in Los Alamos multiring configuration for inertial fusion commercial applications (○, salt-window option; Δ, aerowindow option).

The data of Table IX-III reveal that if aerodynamic windows are used, there are sharp increases in driver efficiency, with increases in pulse repetition rate and driver energy for low pulse repetition rate and energy. However, there are only small efficiency variations over the entire parameter space of pulse repetition rate and energy for the salt window option. The difference in efficiency dependencies on pulse energy and repetition rates for the two window options can be explained in terms of the power required for aerowindow operation. The first window provides a pressure interface between the lasing medium and the 0.01-atm environment in the beam-transport tubes. The second window is interposed between the last optical surface and the reactor cavity to provide the pressure interface between the beam-transport system and the reactor cavity and also to protect the last optical surfaces. The aerowindow power requirement data given in Table IX-IV indicate that

- the power requirement of the first aerowindow is independent of pulse energy and
- the power requirement of the first aerowindow decreases substantially with increase in pulse repetition rate, whereas
- the power requirement of the second aerowindow is independent of pulse repetition rate but increases with pulse energy.

The power requirement for the first aerowindow is determined by its aperture, which is proportional to the cross-sectional area of the PAMs. For the data presented in Table IX-III, the height (electric discharge dimension) is constant, but as the pulse repetition rate increases, the flow dimension (width) must decrease to permit laser cavity clearing between pulses. Therefore, the power consumption of the first aerowindow decreases with increase in pulse repetition rate.

The low pulse-energy and low repetition rate cases still involve only a single laser amplifier ring. For the highest pulse energies and repetition rates (10 MJ/pulse, 40 Hz), up to 10 total amplifier rings (no rings smaller than 1 MJ were considered) resulted in lower driver system cost than did any smaller number of rings with higher ring outputs. Laser amplifier-ring radii ranged from 49 m for the 2-Hz, 1-MJ case to 2140 m for the 40-Hz, 10-MJ single-ring (AVCO) configuration and 2140 m for the 40-Hz, 10-MJ, 10-amplifier-ring (Los Alamos) case. Table IX-V is a more detailed list of the optimum values and corresponding radii of laser amplifier rings. The number of laser amplifiers, their size, and intrinsic efficiency are essentially independent of window option for windows that efficiently transmit CO_2 light (both salt and aerodynamic windows). Only single-plane arrangements of laser amplifier rings were considered to keep the analysis within reasonable bounds. Stacking amplifier rings two or three high may result in lower total driver system cost; however, this option has not yet been examined. The multiring layouts considered are illustrated in Fig. IX-9. The distances from the center of multiring configurations to their peripheries (given in Fig. IX-9) are indicative of the minimum lengths for laser duct tunnels that are required to conduct the laser pulses to reactors. The primary tradeoff, of course, is decreased transfer-tube cost versus increased support-structure cost. Preliminary investigations also suggest that somewhat smaller, more efficient, and less costly laser gas flow systems can be devised.

The AVCO driver study was conceptual only, and the two approaches mentioned above to further reduction in capital cost have not been explored adequately. The capital cost and efficiency data presented in Tables IX-III and IX-IV provide useful interim information for CO_2 laser fusion commercial applications. Should further research indicate that the basic physical parameters used in developing this model are not valid, the procedure can be easily repeated to provide an updated model.

TABLE IX-III(A). Capital Cost[a] of CO_2 Laser Drivers for Commercial Applications of Inertial Fusion

Driver Pulse Repetition Rate	Driver Pulsed Energy Outputs (MJ)										
(Hz)	1	1.5	2	3	4	5	6	7	8	9	10
					Salt Window Option						
2	117	174	224	343	464	587	703	828	939	1078	1190
5	126	183	238	362	489	619	756	875	1005	1126	1246
10	143	218	296	435	608	767	908	1060	1220	1357	1538
15	175	259	346	537	718	897	1078	1259	1440	1624	1806
20	208	304	420	628	844	1058	1260	1480	1701	1901	2112
30	260	411	534	801	1071	1342	1614	1878	2152	2428	2705
40	329	510	665	1018	1361	1706	2052	2388	2737	3088	3441
					Aerowindow Option						
2	119	169	213	320	729	541	670	783	895	1009	1122
5	127	178	227	340	455	573	712	831	950	1071	1191
10	142	211	283	411	572	719	880	1031	1179	1326	1471
15	171	248	330	515	686	859	1030	1205	1376	1554	1726
20	201	291	401	602	811	1018	1208	1421	1630	1823	2027
30	250	395	514	771	1031	1292	1554	1808	2072	2338	2605
40	313	491	653	982	1313	1646	1980	2304	2641	2980	3221

[a] Expressed in 10^6 \$.

TABLE IX-III(B). Overall Efficiency[a] of CO_2 Laser Drivers for Commercial Applications of Inertial Fusion

Driver Pulse Repetition Rate (Hz)	Driver Pulsed Energy Ouputs (MJ)										
	1	1.5	2	3	4	5	6	7	8	9	10
						Salt Window Option					
2	9.57	9.88	10.53	10.55	10.82	10.98	10.73	10.86	10.96	10.91	10.99
5	9.60	9.91	10.56	10.57	10.84	11.01	10.75	10.88	10.98	10.93	11.01
10	9.64	9.64	9.64	10.21	10.06	10.33	10.21	10.26	10.29	10.21	10.33
15	9.67	10.04	10.24	10.05	10.24	10.36	10.24	10.33	10.32	10.31	10.36
20	10.13	10.26	10.11	10.26	10.33	10.38	10.33	10.37	10.33	10.36	10.38
30	10.27	10.08	10.27	10.27	10.35	10.40	10.37	10.40	10.39	10.37	10.40
40	10.13	10.28	10.36	10.36	10.36	10.40	10.40	10.42	10.39	10.41	10.43
						Aerowindow Option					
2	4.05	5.10	6.01	7.02	7.81	8.36	8.55	8.89	9.17	9.30	9.50
5	6.20	7.20	8.12	8.80	9.39	9.75	9.78	9.99	10.18	10.23	10.36
10	7.81	8.34	8.63	9.43	9.48	9.84	9.81	9.90	9.98	9.94	10.08
15	8.75	9.36	9.70	9.69	9.97	10.14	10.06	10.17	10.18	10.18	10.25
20	9.15	9.85	9.81	10.05	10.17	10.25	10.23	10.27	10.25	10.29	10.31
30	9.99	9.90	10.13	10.18	10.28	10.34	10.33	10.36	10.35	10.35	10.37
40	9.98	10.17	10.28	10.30	10.32	10.37	10.37	10.40	10.37	10.39	10.41

[a] Expressed as %.

TABLE IX-IV. CO_2 Laser Driver Aerowindow Power Consumption as Functions of Pulse Repetition Rate and Energy

Pulse Repetition Rate (Hz)	Pulse Energy (MJ)	First Aerowindow Power Requirement (MW)	Second Aerowindow Power Requirement[a] (MW)
2	1	28.5	0.62
	4	28.5	2.26
	10	28.5	5.61
15	1	16.2	0.58
	4	16.2	2.26
	10	16.2	5.61
40	1	6.1	0.57
	4	6.1	2.25
	10	6.1	5.60

[a] For a single reactor plant.

TABLE IX-V(A). Number of CO_2 Laser Amplifier Module Rings for Modified Layouts for Both Salt Windows and Aerowindows

Driver Pulse Repetition Rate	Driver Pulsed Energy Ouputs (MJ)										
(Hz)	1	1.5	2	3	4	5	6	7	8	9	10
2	1	1	1	1	1	1	3	3	4	4	4
5	1	1	1	1	1	1	2	3	3	4	4
10	1	1	1	1	1	1	4	5	5	7	7
15	1	1	1	2	2	3	3	4	4	5	5
20	1	1	1	2	3	3	4	5	5	6	7
30	1	1	2	3	4	5	6	7	8	9	10
40	1	1	2	3	4	5	6	7	8	9	10

TABLE IX-V(B). CO_2 Laser Amplifier Module Ring Radii[a,b] for Modified Layouts for Both Salt Windows and Aerowindows

Driver Pulse Repetition Rate	Driver Pulsed Energy Ouputs (MJ)										
(Hz)	1	1.5	2	3	4	5	6	7	8	9	10
2	49	70	87	129	167	205	87	102	87	98	108
5	50	73	91	136	177	218	136	106	115	102	113
10	64	96	128	182	246	299	96	89	102	82	91
15	91	131	171	131	171	145	171	151	171	155	171
20	117	166	225	166	150	186	166	156	177	166	164
30	161	246	161	161	161	161	161	161	161	161	161
40	214	316	214	214	214	214	214	214	214	214	214

[a] Radii measured in meters.
[b] See Fig. IX-9.

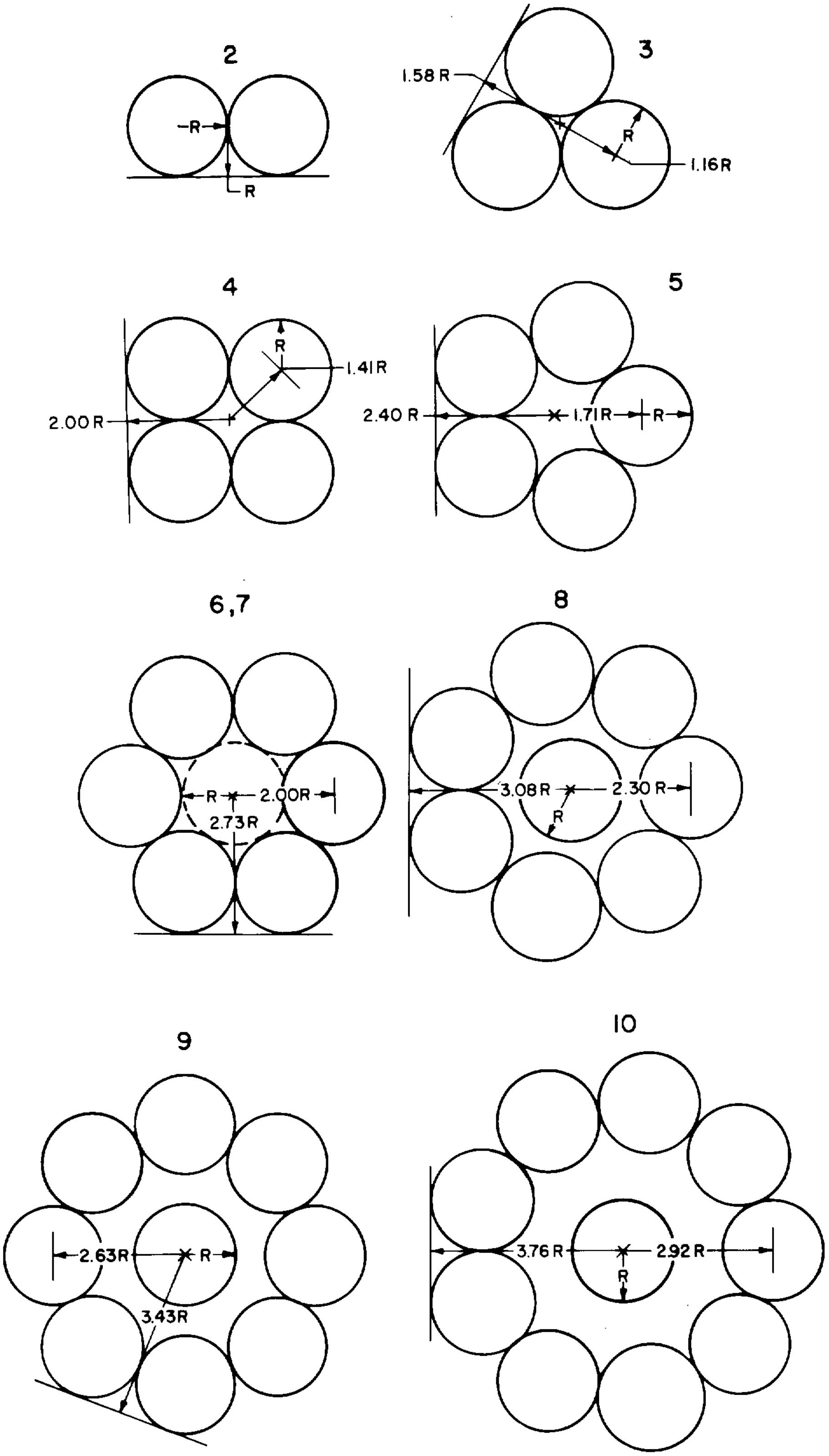

Fig. IX-9. Planar multiring laser amplifier layouts.

REFERENCES

1. I. O. Bohachevsky, L. A. Booth, J. F. Hafer, and J. H. Pendergrass, "Effect of Pellet Yield on Electricity Cost in Laser Fusion Generating Stations," Technology of Controlled Nuclear Fusion, Proc. Am. Nucl. Soc. Top. Meet., 1978, Santa Fe, New Mexico, May 1-11, 1978, Vol. 1, p. 517.

2. L. A. Booth and E. M. Leonard, "A Preliminary Assessment of Heavy-Ion Fusion," 1980 American Nuclear Society Annual Meeting, Las Vegas, Nevada, June 9-12, 1980.

3. S. D. Gardner and W. L. Seitz, "HEX: A One-Dimensional Code for Computing X-Ray Absorption," Los Alamos Scientific Laboratory report LA-5114 (February 1973).

4. K. Miya and J. Silverman, "Thermomechanical Dynamic Behaviour of the Solid Wall of a Pellet Fusion Reactor," Nucl. Technol. 49, 347 (1980).

5. G. A. Moses and R. R. Peterson, "First-Wall Protection in ICF Reactors by Inert Cavity Gases," University of Wisconsin report UWFDM-323 (October 1979).

6. I. O. Bohachevsky and J. F. Hafer, "Sputtering Erosion in Inertial Confinement Fusion Reactors," Nucl. Technol. 41, No. 3, 299-311 (1978).

7. H. W. Friedman, "Fusion Driver Study-Final Technical Report," Department of Energy report DOE/DP/40006-1 (April 1980).

X. RESOURCES, FACILITIES, AND OPERATIONAL SAFETY

Construction of the HEGLF was completed in August 1980. We continued to apply operational safety policies and procedures successfully to minimize the hazards of operating high-power lasers.

MANPOWER DISTRIBUTION

The distribution of employees assigned to the various categories of the Inertial Fusion Program is shown in Table X-I.

FACILITIES

Antares—High Energy Gas Laser Facility (HEGLF)

Construction Packages I and II were completed in August 1980. Los Alamos now occupies all buildings and has assumed responsibility for equipment operation and maintenance.

Target Fabrication Facility

Title-I design for this project is complete; Title-II design (80% complete) is scheduled for completion in February 1981. Construction of the facility is expected to begin in June 1981 and will take 23 months to complete. The design calls for 53 000 ft^2 of laboratory area, including 12 000 ft^2 of clean rooms, 8 000 ft^2 of tritium-handling areas, and 13 000 ft^2 of office space. The facility will consolidate and support target fabrication for the Los Alamos Inertial Fusion Program and the SNL Pulsed Power Program. The total estimated cost for the project is $15.3 million, of which $1.08 million was appropriated in FY 1980 and $7.0 million in FY 1981; the remainder will be appropriated in FY 1982.

OPERATIONAL SAFETY

General

An excellent lost-time injury record was maintained throughout this period with no serious accidents reported.

Laser Safety Publications

"A Practical Approach to Laser Safety" was prepared and will be featured as the cover story in the October 1981 issue of the *National Safety News,* a publication of the National Safety Council.

TABLE X-I. Approximate Staffing Level of Inertial Fusion Program[a]

Tasks	Direct Employees
CO_2 laser development	60
CO_2 laser experiments	133
Target design	40
Target fabrication	47
Diagnostics development	46
Short-wavelength laser development	4
Heavy-ion source development	3
Systems and applications studies	6
Total	339

[a] October 1980 figures.

XI. PATENTS, PUBLICATIONS, AND PRESENTATIONS

PATENTS

Serial numbers, filing dates, patent numbers, and issue dates may not be known for several months after they are assigned. Therefore, for any given period, cases may be missing from these listings if patent activity occurred later in the reporting period.

The following applications were filed in the U.S. Patent Office.

S.N. 143,059—"Broadly Tunable Picosecond ir Source," Anthony J. Campillo, Ronald C. Hyer, and Stanley J. Shapiro.

S.N. 151,870—"Method for Monitoring Irradiated Fuel Using Cerenkov Radiation," Edward J. Dowdy, Nicholas Nicholson, and John T. Caldwell.

S.N. 179,917—"Quasi Random Array Imaging Collimator," Edward E. Fenimore.

S.N. 180,252—"Random Array Grid Collimator," Edward E. Fenimore.

S.N. 191,192—"Coded Aperture Imaging with Self-Supporting Uniformly Redundant Arrays," Edward E. Fenimore.

S.N. 198,028—"Three-Electrode Low Pressure Discharge Apparatus and Method for Uniform Ionization of Gaseous Media," Edward J. McLellan.

S.N. 202,042—"Imaging Alpha Particle Detector," David F. Anderson.

S.N. 204,121—"Device for Detecting Imminent Failure of High-Dielectric Stress Capacitors," George G. McDuff.

The following patents were issued by the U.S. Patent Office.

U.S. Pat. 4,183,671—"Interferometer for the Measurement of Plasma Density," Abram R. Jacobson.

U.S. Pat. 4,189,686—"Combination Free Electron and Gaseous Laser," Charles A. Brau, Stephen D. Rockwood, and William E. Stein.

U.S. Pat. 4,194,813—"Vacuum Aperture Isolator for Retroreflection from Laser-Irradiated Targets," Robert F. Benjamin and Kenneth B. Mitchell.

U.S. Pat. 4,200,846—"Efficient Laser Amplifier Using Sequential Pulses of Different Wavelengths," Eugene E. Stark, Jr., John F. Kephart, Wallace T. Leland, and Walter H. Reichelt.

U.S. Pat. 4,209,780—"Coded Aperture Imaging with Uniformly Redundant Arrays," Edward E. Fenimore and Thomas M. Cannon.

U.S. Pat. 4,211,954—"Alternating Phase Focused Linacs," Donald A. Swenson.

U.S. Pat. 4,228,420—"Mosaic of Coded Aperture Arrays," Edward E. Fenimore and Thomas M. Cannon.

U.S. Pat. 4,236,124—"CO_2 Optically Pumped Distributed Feedback Diode Laser," Stephen D. Rockwood.

PUBLICATIONS

This list of publications is prepared from a stored computer data base.

Target Fabrication

J. E. Barefield, L. H. Jones, and R. Liepins, "Vibration-Rotation Analysis of Deuterium Tritide," J. Mol. Spectrosc. **80**, 233-6 (1980).

R. Liepins and A. T. Lowe, "Coating of Levitated Glass Microballoons," Polym. Plast. Technol. Eng. **15** (1), 51-60 (1980).

R. L. Whitman and R. H. Day, "X-Ray Microradiographs of Laser Fusion Targets: Improved Image Analysis Techniques," Appl. Opt. **19**, 1718 (1980).

Theory

B. Bezzerides and S. J. Gitomer, "Role of Thermalization of Electron Distribution in Resonance Absorption," Phys. Rev. Lett. **46**, 593-6 (1981).

W. P. Gula, "One-Dimensional Computer Simulations of Exploding Pusher Targets for the Los Alamos Helios Laser System," Los Alamos Scientific Laboratory report LA-8458-MS (August 1980).

D. B. Henderson and D. V. Giovanielli, "Fuel Temperature Determination for ICF Microspheres," Los Alamos Scientific Laboratory report LA-8469-MS (August 1980).

D. B. Henderson and D. V. Giovanielli, "Fuel Temperature Determination for ICF Microspheres," Comments on Plasma Physics and Controlled Fusion 6, No. 5, 161 (1981).

R. J. Mason, "On the Monte Carlo Hybrid Modelling of Electron Transport in Laser Produced Plasmas," Phys. Fluids **23**, 2204-2215 (1980).

R. J. Mason, "Implicit Moment Particle Simulation of Plasmas," J. Comput. Phys. **41**, 233-244 (1981).

A. J. Scannapieco, "Atmospheric Type Modes in Laser Fusion Targets," Phys. Fluids **24**, 1699-1705 (1981).

Experiments and Diagnostics

I. Liberman, V. K. Viswanathan, M. Klein, and B. D. Seery, "Automatic Target Alignment of the Helios Laser System," Appl. Opt. **14**, No. 9, 1463-1467 (1980).

I. J. Bigio, S. V. Jackson, A. Laird, and J. Seagrave, "Beam-Diagnostic Techniques for Multiterawatt CO_2 Lasers," Appl. Opt. 19, 914 (1980).

W. Ehler, F. Begay, T. H. Tan, J. Hayden, and J. McLeod, "Effect of Target Purity on Laser-Produced Plasma Expansion," J. Phys. D: Appl. Phys. **13**, L29-32 (1980).

A. W. Ehler, F. Begay, T. H. Tan, and P. H. Castine, "Lateral Transport of Energy from a Laser-Produced Plasma," J. Phys. D: Appl. Phys. **13**, L65 (1980).

F. Begay and J. M. Grilly, "A Novel Photographic Method to Record Images from Cellulose Nitrate Film," Appl. Opt. **19**, 1217 (1980).

J. D. Seagrave, B. L. Berman, and T. W. Phillips, "The Neutron Zero-Energy Total Cross Section and Scattering Lengths for Tritium," Phys. Lett. **91B**, 2, 200-202 (1980).

M. D. Montgomery and J. V. Parker, "The Relativistic Electron Beam Plasma Heating Experiment," Los Alamos Scientific Laboratory report LA-8826-MS (April 1980).

R. U. Datla, L. A. Jones, and D. B. Thomson, "Temperature Diagnostics Using Lithium-Like Satellites," Los Alamos Scientific Laboratory report LA-8324-MS (October 1980).

P. D. Goldstone, R. F. Benjamin, and R. B. Schultz, "Shock Wave Production and Plasma Motion in CO_2-Laser-Irradiated Targets," Appl. Phys. Lett. **38**, 223-5 (1981).

Systems Studies

G. F. Scheele and J. H. Pendergrass, "Rapid Coalescence of Mercury Drops at Planar Mercury-Liquid Interfaces," Chem. Eng. Commun. 5, 7 (1980).

Laser Development

J. F. Figueira and A. V. Nowak, "Carbon Dioxide Laser System with Zero Small Signal Gain," Appl. Opt. 19, 420-421 (1980).

D. E. Watkins, J. F. Figueira, and S. J. Thomas, "Observation of Resonantly Enhanced Degenerate Four-Wave Mixing in Doped Alkali Halides," Opt. Lett. 5, 169-171 (1980).

D. E. Watkins, C. R. Phipps, Jr., and S. J. Thomas, "Determination of the Third-Order Nonlinear Optical Coefficients of Germanium Through Ellipse Rotation," Opt. Lett. 5, 248-249 (1980).

E. T. Salesky and D. Korff, "A New Impact Parameter Theory for Collision-Induced Lineshifts," J. Quant. Spectrosc. Radiat. Transfer 23, 399-402 (1980).

R. K. Ahrenkiel, S. J. Thomas, G. A. Prinz, J. J. Krebs, and W. G. Maisch, "Magneto-Optical Switch for Synchronization of CO_2 and Red Laser Beam," IEEE J. Quantum Electron. QE-16, 253 (1980).

J. B. Marling, I. P. Herman, and S. J. Thomas, "Deuterium Separation at High Pressure by Nanosecond CO_2 Laser Multiple-Photon Dissociation," J. Chem. Phys. 72, 5602-5634 (1980).

J. L. Lyman, R. G. Anderson, R. A. Fisher, and B. J. Feldman, "The Frequency, Fluence and Pressure Dependence of the Absorption of Pulsed CO_2-Laser Radiation by SF_6 at 140 K," Chem. Phys. 45, 325 (1980).

I. J. Bigio, B. J. Feldman, R. A. Fisher, and E. E. Bergman, "High-Efficiency Wavefront Reversal in Germanium and in Inverted CO_2," Sov. J. Quantum Electron. 11, 2318 (1980).

W. W. Rigrod, R. A. Fisher, and B. J. Feldman, "Transient Analysis of Nearly Degenerate Four-Wave Mixing," Opt. Lett. 5, 105 (1980).

R. A. Forber, R. E. McNair, S. F. Fulghum, M. S. Feld, and B. J. Feldman, "Collision-Induced Energy Absorption and Vibrational Excitation by Intense Laser Radiation in CH_3F," J. Chem. Phys. 72, 4693 (1980).

W. H. Reichelt, "Highpower Infrared Optics," Laser Focus 71-75 (June 1980).

R. A. Fisher and B. J. Feldman, "Optical Phase Conjugation," in *McGraw-Hill Yearbook of Science and Technology* (McGraw-Hill, New York, 1980).

R. A. Fisher, B. R. Suydam, and B. J. Feldman, "Transient Analysis of Kerr-Like Phase Conjugators Using Frequency-Domain Techniques," Phys. Rev. A 23, No. 6, 3071-3083 (1981).

Accelerator Development

"Accelerator Technology Program, January—December 1979," Los Alamos Scientific Laboratory report LA-8592-PR (November 1980), p. 138.

"Accelerator Technology Program, January—June 1980," Los Alamos National Laboratory report LA-8736-PR (March 1981), p. 123.

J. E. Stovall, "The PIGMI Program at the Los Alamos Scientific Laboratory," Los Alamos Scientific Laboratory report LA-8525-SR (September 1980).

T. P. Wangler, "Space-Charge Limits in Linear Accelerators," Los Alamos Scientific Labortory report LA-8388 (December 1980).

PRESENTATIONS

Target Fabrication

The following presentations were made at the 27th Annual Symposium of the American Vacuum Society, Detroit, Michigan, October 13-17, 1980.

S. M. Butler and M. H. Thomas, "Glass-Sealed Laser Fusion Targets Containing Gas Not Permeable Through the Wall."

R. Liepins, M. Campbell, J. S. Clements, J. Hammond, and R. Jay Fries, "Plastic Coating of Microsphere Substrates."

W. L. Bongianni, "Acoustic Microscopy for ICF Target Analysis."

J. V. Milewski and R. G. Marsters, "Tensile Testing of Glass Microshells."

J. K. Feuerherd and E. H. Farnum, "Micromachining of Laser Fusion Target Parts."

J. T. Murphy and J. R. Miller, "Improved IF Cryogenic-Target Production Technique."

E. H. Farnum, A. R. Gutacker, and R. Mulford, "A Cleaning Procedure for Inertial Fusion Targets."

The following presentations were made at the OSA/IEEE Conference on Inertial Confinement Fusion, San Diego, California, February 26-28, 1980.

J. E. Barefield II, V. Cottles, and D. P. Campbell, "Nondestructive Analysis of Laser Fusion Targets via Laser Raman Spectroscopy."

W. L. Bongianni, "Glow Discharge of Laser Fusion Targets."

S. Butler and B. Cranfill, "Laser Fusion Targets Containing Gas Not Permeable Through the Wall."

E. H. Farnum and J. K. Feuerherd, "Laser Micromachining for Laser Fusion."

J. V. Milewski, "Elastic Buckling of Glass Microballoons at Elevated Temperatures."

W. E. Anderson, J. M. Bunch, R. Liepins, and A. T. Lowe, "Coating Levitated Glass Microballoons."

J. R. Miller, J. V. Murphy, C. E. Cummings, and J. E. Barefield, "Helios Cryogenic-Target-Producing Apparatus."

D. M. Stupin, M. A. Winkler, R. H. Day, C. K. Crawford, and T. S. Tyrie, "X-Ray Source for Radiographic Inspection of Laser Fusion Targets."

Theory

The following presentations were made at the APS Annual Meeting of the Plasma Physics Divison, San Diego, California, November 10-14, 1980.

C. H. Aldrich, R. D. Jones, and K. Lee, "Comparison Between Theory and Simulation on Density Profile Modification."

B. Bezzerides and S. J. Gitomer, "Role of Thermalization on Electron Distributions Produced by Resonance Absorption."

J. U. Brackbill and D. W. Forslund, "Implicit Field, Particle Methods."

D. W. Forslund and J. M. Kindel, "Harmonic Emission as a Way of Measuring Profile Steepening."

S. J. Gitomer and B. Bezzerides, "Cutoffs of Hot Electron Distribution in Resonance Absorption."

W. P. Gula and G. Magelssen, "Heavy Ion Targets."

R. D. Jones, K. Lee, Y. C. Lee, and T. K. Samec, "Monte Carlo Simulation of the Non-linear Fokker Planck Equation."

J. M. Kindel, D. W. Forslund, and C. H. Aldrich, "Stability and Absorption of Focused Laser Beams at High Laser Intensity."

K. Lee and R. D. Jones, "Transport in the Presence of an Intense Oscillating Electric Field."

K. Lee, "Theory and Simulations on the Modification of Hydrodynamic Flow in Laser-Plasma Interaction."

R. J. Mason, "Full Particle PIC-Collisional Calculations of Electric Transport in Laser Produced Plasmas."

R. J. Mason, "MEFI-Collisional Particles Simulation of Electron Transport in Laser Plasmas."

E. K. Stover and D. B. Henderson, "Computer Simulation of 1.3 Micron Laser Irradiated Thin Plastic Foils."

The following presentations were made at the 10th Annual Anomalous Absorption Conference, San Francisco, California, May 28-30, 1980.

B. Bezzerides and S. J. Gitomer, "Fluid Steepening and Electron Distribution."

R. D. Jones, C. H. Aldrich, and K. Lee, "Laser Induced Density Profiles in an Isothermal Plasma."

J. M. Kindel, C. H. Aldrich, and D. W. Forslund, "Nonlinear Behavior of Stimulated Scattering, Self-Focusing and Bubble Formation."

R. J. Mason, "Full-Particle PIC-Collisional Calculations of Electron Transport in Laser Produced Plasmas."

The following presentations were made at the 1980 IEEE International Conference on Plasma Science," Madison, Wisconsin, May 19-21, 1980.

C. H. Aldrich, R. D. Jones, and K. Lee, "Study of Profile Modifications with Hybrid Simulation Code."

C. H. Aldrich, R. D. Jones, and K. Lee, "Laser Induced Shock Structures."

C. H. Aldrich, R. D. Jones, and K. Lee, "Effect of the Electron Equation of State on the Profile Modification Problem."

S. J. Gitomer and B. Bezzerides, "Prevalence of Cutoff Distribution in Laser Fusion."

W. P. Gula, "Simple Breakeven Targets for Heavy Ion Fusion."

W. P. Gula and G. Magelssen, "Heavy Ion Targets—Spherical Shells."

D. P. Henderson, "Sensitivity of Heavy Ion Fusion Targets."

R. D. Jones, C. H. Aldrich, and K. Lee, "Mechanisms for Compression Shock Formation in Laser Induced Plasma Profiles."

R. D. Jones, C. H. Aldrich, and K. Lee, "Laser Induced Density Profiles in an Isothermal Plasma."

J. M. Kindel, "Recent Theoretical Work on the Nonlinear Behavior of Stimulated Scattering Instabilities in Laser Plasma Interaction."

K. Lee, C. H. Aldrich, and R. D. Jones, "Dependence of Density Profile Modification on Equation of State."

R. J. Mason, "Full-Particle PIC-Collisional Calculations of Electron Transport in Laser Produced Plasmas.

The following presentations were made at the Ninth Conference on the Numerical Simulation of Plasmas, Northwestern University, Evanston, Illinois, June 30-July 2, 1980.

J. W. Painter, "Improvements in the PAL Fluid Algorithm."

A. J. Scannapieco and K. A. Taggart, "Orbeos—A Spherical Fully Dimensional, Flux Corrected Transport Code."

The following presentations were made at the International Quantum Electronics Conference, Boston, Massachusetts, June 23-26, 1980.

J. C. Goldstein, S. J. Czuchlewski, and A. V. Nowak, "Saturation of Hot Carbon Dioxide at 10.6 Micrometers."

J. C. Goldstein, R. F. Haglund, Jr., and J. C. Comly, "Small Signal Gain Spectrum of an 1800 Torr Carbon Dioxide Amplifier."

In addition, the following presentations were made at various institutions.

B. Bezzerides and S. J. Gitomer, "Role of Nonlinear Wave Steepening in Hot Electron Production," Aspen Center for Physics, Aspen, Colorado, June 16-21, 1980.

G. E. Bohannon, "Calculations of Target Behavior with Intense Radially Localized Energy Deposition," High Intensity Target Workshop, Fermilab, Chicago, Illinois, April 28-30, 1980.

D. W. Forslund, "Recent Theoretical Work on the Nonlinear Behavior of Stimulated Scattering Instabilities in Laser Plasma Interaction," University of Alberta, Edmonton, Alberta, Canada, March 24, 1980.

J. C. Goldstein, C. J. Czuchlewski, and A. V. Nowak, "Saturation of Hot Carbon Dioxide at 10.6 Micrometers," International Conference on Lasers and Applications, New Orleans, Louisiana, October 15-19, 1980.

W. P. Gula, "Simple Ion Beam Fusion Target," Workshop on the Penetration of Charged Particles in Matter under Extreme Conditions, New York, New York, January 3-5, 1980.

E. L. Lindman, Jr., "Inertial Fusion Program at LASL," Moorpark College, Moorpark, California, February 21, 1980.

R. J. Mason, "Full-Particle PIC-Collisional Calculations of Electron Transport in Laser Produced Plasmas," University of Osaka, Osaka, Japan, June 26, 1980.

R. J. Mason, "Implicit Moment Particle Simulation of Plasmas," Workshop on Long Time Steps in Particle Simulation, University of California, Berkeley, California, December 8, 1980.

R. J. Mason, "Monte Carlo Hybrid Electron Transport in Laser Produced Plasmas," OSA/IEEE Conference on Inertial Confinement Fusion, San Diego, California, February 26-28, 1980.

Experiments and Diagnostics

The following presentations were made at the APS Annual Meeting of the Plasma Physics Division, San Diego, California, November 10-14, 1980.

P. D. Goldstone and R. F. Benjamin, "Measurements of CO_2 Laser-Driven Shocks Using Streak Shadowgraphy."

R. F. Benjamin and P. D. Goldstone, "Streaked Shadowgraphy Study of CO_2 Laser Irradiated Targets."

R. L. Carman, F. Wittman, and N. Clabo, "Observation of Visible Harmonics in CO_2 Laser Fusion Experiments."

T. H. Tan and G. H. McCall, "The Effects on Hot Electron Temperature of Multi-Laser Beam Illumination."

A. H. Williams and T. H. Tan, "Optical Fibers in Laser-Fusion Diagnostics."

J. F. Kephart, "Measurement of the Angular Distribution of Energetic Ions from Laser-Produced Plasmas."

R. Kristal, "Integrated Absorption Experiments on CO_2 Laser Generated Plasmas."

P. D. Rockett, W. C. Priedhorsky, and D. V. Giovanielli, "Radiation Losses From High Z, 10.6 μm Laser Irradiated Microballoons."

R. F. Benjamin, "Measurements of Electrode Plasmas in a Magnetically Insulated Vacuum Diode."

R. F. Benjamin, "XUV Photography of Imploding Wire Arrays."

R. F. Benjamin, "Time-Resolved Photography of the Axial Assembly of Exploding Wire Arrays."

R. Kristal, "Reflection Probing of Inertial Fusion Targets."

F. Begay, "Scaling of Hot Electron Temperature in the Eight-Beam Helios Laser System."

A. Hauer, "Detailed Radiation Post-Processing Hydrodynamic Simulations."

B. A. Hammel, L. A. Jones, and K. H. Finken, "Observations of the Infrared Emission from a Dense Plasma."

K. B. Riepe, M. D. Montgomery, J. V. Parker, and R. L. Sheffield, "A High-Density Plasma Source Using a Current Driven Ionizing Shock Wave."

R. L. Sheffield, J. V. Parker, M. D. Montgomery, and K. B. Riepe, "Interaction of a Highly Collimated Relativistic Electron Beam with Hydrogen."

The following presentations were made at the OSA/IEEE Conference on Inertial Confinement Fusion, San Diego, California, February 26-28, 1980.

A. Hauer and D. B. van Hulsteyn, "X-Ray Diagnosis of High Density Plasma."

R. F. Benjamin, J. P. Carpenter, and J. J. Hayden, "A New Experimental Diagnostic for Spatial-Filter Design."

P. D. Rockett, "Considerations for X-Ray Interferometry and Thomson Scattering as High-Density Diagnostics."

A. W. Ehler, G. H. McCall, W. S. Varnum, and S. A. Hackenberry, "The Effect of Atomic Mass of a Target on Laser Produced Impulse."

T. H. Tan and G. H. McCall, "High Density Implosion Experiments at Helios."

M. A. Yates, A. H. Williams, and J. T. Ganley, "Radiochemical Diagnostics Development at Helios."

A. H. Williams and V. M. Cottles, "A Precision Calorimeter for Focused CO_2 Laser Light."

The following presentations were made at the 1980 IEEE International Conference on Plasma Science, Madison, Wisconsin, May 19-21, 1980.

S. Singer, J. H. Brownell, K. Finken, L. A. Jones, I. R. Lindemuth, and T. A. Oliphant, "High Temperature, High Density Z-Pinch Devices for Plasma Research."

M. D. Montgomery, J. V. Parker, K. B. Riepe, and R. L. Sheffield, "Generation of Highly Collimated, Intense Relativistic Electron Beams Using a Magnetized, Foilless Diode."

J. V. Parker, R. L. Sheffield, K. B. Riepe, M. D. Montgomery, R. White, J. Harrison, and J. Shannon, "A Relativistic Electron Beam Generator for Plasma Heating Experiments."

L. A. Jones, S. Singer, and K. Finken, "Measurements on a High Density, Laser Initiated Z-Pinch."

D. B. van Hulsteyn, G. H. McCall, S. Whitehill, and J. S. McGurn, "Hot Electron Measurements from CO_2 Laser Irradiated Targets."

The following presentations were made at the 10th Annual Anomalous Absorption Conference, San Francisco, California, May 28-30, 1980.

F. Begay and D. W. Forslund, "Ion Acceleration Processes in CO_2 Laser-Induced Carbon Plasmas."

R. Kristal, "Absorption Experiments on CO_2 Laser Produced Plasmas."

The following presentations were made at the 1980 International Conference on Lasers, Shanghai and Beijing, China, May 5-8 and May 19-22, 1980.

S. Singer, "High Efficiency CO_2 Lasers for Inertial Confinement Fusion."

T. H. Tan, "CO_2 Laser Interaction Experiments."

The following presentations were made at the JOWOG on Irradiation Effects on Materials and Components, Albuquerque, New Mexico, October 6-8, 1980.

P. D. Goldstone and R. F. Benjamin, "Laser Produced Shock Waves in Solids."

L. A. Jones, I. Lindemuth, J. Brownell, K. Finken, A. Dangor, E. Kallne, T. Oliphant, and S. Singer, "The Plasma Produced by a Laser Initiated, Gas Embedded Z-Pinch."

The following presentations were made at the Conference and Workshop on Radiative Properties of Hot Dense Matter, Monterey, California, November 17-20, 1980.

A. Hauer, "Spectroscopic Investigation of Very High Density Laser Compressed Plasma."

A. Hauer, "Line Shift Measurements in High-Density Laser Implosion Experiments."

In addition, the following presentations were made at various institutions.

R. P. Godwin, "Experiments Fundamental to Laser-Irradiated Fusion," XI International Quantum Electronics Conference, Boston, Massachusetts, June 23-26, 1980.

M. A. Yates, "Radiochemical Diagnostic Development at Los Alamos," University of Rochester, Rochester, New York, March 31-April 2, 1980.

F. Begay and D. W. Forslund, "The Effect of Hydrogen in CO_2 Laser-Induced Plasmas," 14th European Conference on Laser Polytechnique, Palaiseau, France, September 15-19, 1980.

M. A. Yates, "Progress in Laser Fusion Experiments at Los Alamos," Network of Women in Science, Albuquerque, New Mexico, May 3, 1980.

R. F. Benjamin and P. Goldstone, "Optical Streak Camera Studies of Transport in CO_2 Laser Produced Plasmas," Annual Meeting of the Optical Society of America, Chicago, Illinois, October 14-17, 1980.

R. L. Carman, "Laser Fusion—Past, Present and Future," University of Chicago, Chicago, Illinois, October 15, 1980.

R. L. Carman, F. Wittman, and N. Clabo, "New Approach to Fusion-Laser Optical Pulse Generation

Has Proven Very Reliable," International Conference on Lasers and Applications, New Orleans, Louisiana, December 14-19, 1980.

D. R. Bach, "Shock Wave Production and Plasma Motion in CO_2 Laser Irradiated Targets," University of Michigan, Ann Arbor, Michigan, November 3, 1980.

A. Hauer, "Diagnosis of High Density Laser Compressed Plasma Using Spectral Line Profiles," 5th International Conference on Spectral Line Shapes, West Berlin, Germany, July 6-12, 1980.

Systems Studies

The following presentations were made at the OSA/IEEE Conference on Inertial Confinement Fusion, San Diego, California, February 26-28, 1980.

I. O. Bohachevsky, D. O. Dickman, and J. C. Goldstein, "Plasma Modeling for the Magnetically Protected Reactor Cavity."

W. A. Reupke, H. S. Cullingford, and T. G. Frank, "Inertial Confinement Fusion Hybrid Reactor Concepts."

E. M. Leonard, L. A. Booth, and J. H. Pendergrass, "Optimization in ICF Systems Engineering."

J. H. Pendergrass and Lawrence A. Booth, "Laser Fusion Driven Synthetic Fuel Production."

E. T. Salesky, H. W. Friedman, and Paul F. Keller, "CO_2 Fusion Driver Study."

The following presentations were made at the 1980 American Nuclear Society Annual Meeting, Las Vegas, Nevada, June 9-12, 1980.

I. O. Bohachevsky and T. G. Frank, "ICF Reactor System Integration."

J. H. Pendergrass, T. G. Frank, I. O. Bohachevsky, and L. A. Booth, "Heavy-Ion-Beam Fusion Reactor Conceptual Design."

The following presentations were made at the Topical Meeting on the Technology of Controlled Nuclear Fusion, 4th, King of Prussia, Pennsylvania, October 14-17, 1980.

W. A. Reupke and H. S. Cullingford, "A Comparison of Wetted Wall and Magnetically Protected Wall ICF Hybrid Concepts."

J. G. Freiwald, J. H. Pendergrass, and T. G. Frank, "Environmental and Safety Envelope Analysis for Inertial Fusion Applications."

J. H. Pendergrass, T. G. Frank, and I. O. Bohachevsky, "A Modified Wetted Wall Inertial Fusion Reactor Concept."

The following presentations were made at the American Nuclear Society Winter Meeting, Washington, D. C., December 17-21, 1980.

J. H. Pendergrass, T. G. Frank, and M. E. Battat, "Neutron Streaming in Laser Fusion Electric Power Generating Stations."

I. O. Bohachevsky, "Pressure Waves in ICF Reactor Blankets."

J. H. Pendergrass, "CO_2 Laser Capital Costs and Efficiencies for ICF Commercial Applications."

In addition, the following presentations were made at various institutions.

W. A. Reupke, "Inertial-Confinement-Fusion Driven Neutron Effects Multiplier," JOWOG-6 Conference, Sandia National Laboratories, Albuquerque, New Mexico, October 7-9, 1980.

Ellen M. Leonard and Thurman G. Frank, "A Potential Inexhaustible Energy Source," AAAS Annual Meeting, San Francisco, California, January 3-8, 1980.

I. O. Bohachevsky, J. C. Goldstein, and D. O. Dickman, "A Plasma Model for ICF Reactor Studies," International Conference on Plasma Physics, Nagoya, Japan, April 7-11, 1980."

I. O. Bohachevsky, "Plasma Modeling for the Study of ICF Reactor Cavity Phenomena," Courant Institute of Mathematical Sciences, New York University, New York, New York, May 22, 1980.

I. O. Bohachevsky, "Plasma Modeling for the Study of ICF Reactor Cavity Phenomena," Department of Applied Physics and Nuclear Engineering, Columbia University, New York, New York, May 16, 1980.

Laser Development

The following presentations were made at the Optical Society of America, 1980 Annual Meeting, Chicago, Illinois, October 13-17, 1980.

J. L. Munroe, "Diffraction-Based Tolerancing for Encircled Energy."

W. H. Reichelt, "Optical Component Engineering in CO_2 Laser Fusion Systems."

K. L. Underwood and G. Woodfin, "Use of the Zernike Polynomials in Evaluating Interferograms."

The following presentations were made at the OSA/IEEE Conference on Inertial Confinement Fusion, San Diego, California, February 26-28, 1980.

C. R. Phipps, Jr., S. J. Thomas, and J. F. Figueira, "Passive Temporal Compression of Laser Pulses in Rigrod-Type Saturable Absorbers."

B. J. Feldman, R. A. Fisher, R. G. Tercovich, N. Barnes, and R. T. Kung, "Evaluation of KrF-pumped Thallium-Doped KCl as a Potential UV Laser Storage Material."

C. R. Phipps, Jr., S. J. Thomas, and D. E. Watkins, "Determination of Nonlinear Susceptibilities in a Gaussian Beam with Intensity-Dependent Brightness Measurements."

C. R. Phipps, J. F. Figueira, D. E. Watkins, and S. J. Thomas, "Survey of Material for Correction of Phase and Pointing Via DFWM in CO_2 ICF Lasers."

S. J. Czuchlewski, C. R. Phipps, Jr., J. F. Figueira, and S. J. Thomas, "Plasma Breakdown Isolators for CO_2 Laser Fusion Systems."

J. F. Figueira, O. H. Nestor, L. H. Greene, and A. J. Sievers, "Solid-State Saturable Absorbers for the IR."

D. E. Casperson, I. J. Bigio, R. F. Haglund, Jr., S. V. Jackson, W. A. Kelly, J. S. Ladish, J. Reay, and G. T. Schappert, "Optical Multiplexing Experiment in the Helios CO_2 Laser Fusion Facility."

J. F. Figueira and A. V. Nowak, "Design and Performance of a Zero-Gain CO_2 Laser System."

W. W. Rigrod, R. A. Fisher, and B. J. Feldman, "Transient Analysis of Phase Conjugators."

C. R. Phipps, Jr., and S. J. Thomas, "Subnanosecond Extinction of CO_2 Laser Signals Through Bulk Photoionization in Germanium."

J. Marling, I. Herman, and S. J. Thomas, "Deuterium Separation by CO_2 Laser Dissociation of Fluoromethanes."

I. Liberman, V. K. Viswanathan, and C. Fenstermacher, "Megajoule CO_2 Laser Fusion Facility."

The following presentations were made at the XI International Quantum Electronics Conference, Boston, Massachusetts, June 23-26, 1980.

D. E. Watkins, S. J. Thomas, and J. F. Figueira, "Phase Conjugation via Resonantly Enhanced Degenerate Four-Wave Mixing in a Doped Alkali Halide."

L. H. Greene, R. T. Warner, W. E. Moerner, A. J. Sievers, and J. F. Figueira, "Passive Modelocking of a TEA CO_2 Laser with Matrix Isolated SF_6."

J. C. Goldstein, S. J. Czuchlewski, and A. V. Nowak, "Separation of Hot CO_2 at 10.6 μm."

B. J. Feldman, R. A. Fisher, Tao-yi Fu, F. A. Hopf, and M. Sargent III, "Transient Phase Conjugation in Resonant Media."

R. A. Fisher, B. R. Suydam, W. W. Rigrod, and B. J. Feldman, "Transient Phase Conjugation in Kerr-like Four-Wave Mixers."

The following presentations were made at the International Conference on Lasers and Applications, New Orleans, Louisiana, December 14-19, 1980.

C. R. Phipps, D. E. Watkins, S. J. Thomas, and J. F. Figueira, "Phase Conjugate Reflectors at 10 μm ICF Laser Components."

P. B. Mumola, J. J. Ewing, W. T. Leland, and C. A. Fenstermacher, "Advanced CO_2 Laser Fusion Driver Concepts."

B. J. Feldman, R. A. Fisher, and S. L. Shapiro, "Practical Implications of Ultraviolet Phase Conjugation."

S. J. Czuchlewski, "Pulse Propagation in CO_2 Laser Gain Media."

D. E. Watkins, C. R. Phipps, Jr., and S. J. Thomas, "Observation of Degenerate Four-Wave Mixing and Amplified Reflection in Germanium."

J. C. Goldstein, S. J. Czuchlewski, and A. V. Nowak, "Saturation of Hot CO_2 at 10.6 μm."

J. E. Sollid, C. W. Bjork, and A. C. Saxman, "Large-Aperture Beam Diagnostics for the Antares I Laser System."

The following papers were presented at the 4th Biennial CUBE Symposium, Lawrence Livermore National Laboratory, Livermore, California, October 22-24, 1980.

M. E. Thuot, "A Hierarchical Control Network for the Antares Laser Fusion Facility."

S. W. White, "TENnet: A Control System Network for UNIX."

The following presentations were made at the 5th International Conference on Spectral Line Shapes, West Berlin, Germany, July 6-12, 1980.

E. T. Salesky, "Calculations of Pressure Broadened Half Widths of HC1 (0-0) Perturbed by Ar."

E. T. Salesky, "Current Status of Line Broadening Theories of Molecular Vibrational-Rotational Lines."

The following presentations were made at the SPIE 24th Annual Technical Symposium, San Diego, California, July 28-August 1, 1980.

Q. Appert, T. Swann, W. C. Sweatt, and A. C. Saxman, "Antares Automatic Beam Alignment System."

W. C. Sweatt, "Alignment and Focusing Device for a Multibeam Laser System."

In addition, the following presentations were made at various institutions.

R. A. Fisher, S. L. Shapiro, and B. J. Feldman, "Ultraviolet Phase Conjugation," Annual Meeting, Optical Society of America, Chicago, Illinois, October 13-17, 1980.

S. J. Czuchlewski, C. R. Phipps, Jr., J. F. Figueira, and S. J. Thomas, "Plasma Breakdown Isolators for CO_2 Laser Fusion Systems," at Fourth Annual DoD Conference on Laser Vulnerability Effects and Hardening, Monterey, California, September 17, 1980.

Q. Appert and T. Swann, "Antares Automatic Alignment," Laser-Optics II, Tutorial Seminar, University of Lowell, Andover, Massachusetts, May 7-8, 1980.

D. Call, "Hierarchical, Distributed Computer Control System for the Antares Laser," International Conference on Plasma Science, Madison, Wisconsin, May 19-21, 1980.

A. C. Saxman, C. Silvernail, W. C. Sweatt, and W. Bauke, "The Antares Opto-Mechanical Interface Solution," Optical Society of America Workshop on Optical Fabrication and Testing, Cape Cod, Massachusetts, September 22-23, 1980.

J. E. Sollid, C. W. Bjork, and A. C. Saxman, "Large-Aperture Beam Diagnostics for the Antares Laser System," AIAA 13th Fluid and Plasma Dynamics Conference, Snowmass, Colorado, July 14-16, 1980.

S. J. Thomas, C. R. Phipps, and R. F. Harrison, "Optical Damage Limitations for Copper Mirrors used in CO_2-ICF Laser System," 12th Boulder Damage Symposium, National Bureau of Standards, Boulder, Colorado, September 30-October 1, 1980.

R. A. Fisher and B. J. Feldman, "Phase Conjugation in the Infrared," Institute of Laser Engineering, University of Osaka, Osaka, Japan, June 15-16, 1980.

V. K. Viswanathan, "Aberration Theories and Their Applications in Optics," University of New Mexico, Albuquerque, New Mexico, May 5, 1980.

V. K. Viswanathan, "Optical Design, Evaluation and Engineering Codes in Use at LASL," OSA Mini-Symposium, Los Alamos, New Mexico, May 12, 1980.

R. A. Fisher and B. J. Feldman, "New Developments in Phase Conjugation," Department of Electrical Engineering, University of California, Berkeley, California, February 25, 1980.

L. H. Greene, A. J. Sievers, J. F. Figueira, and A. V. Nowak, "Nonlinear Properties of Matrix-Isolated SF_6 Gas," American Physical Society Annual Meeting, New York, New York, March 17-19, 1980.

Accelerator Development

The following presentations were made at the International Conference on Low-Energy Ion Beams 2, Bath, United Kingdom, April 14-17, 1980.

R. W. Hamm, K. R. Crandall, L. D. Hansborough, J. M. Potter, G. W. Rodenz, R. H. Stokes, J. E. Stovall, D. A. Swenson, T. P. Wangler, C. W. Fuller, M. D. Machalek, R. A. Jameson, E. A. Knapp, and S. W. Williams, "The rf Quadrupole Linac: A New Low-Energy Accelerator."

R. A. Jameson, "Recent Developments in Low-Velocity Linacs for Heavy Ion Fusion."

In addition, the following presentation was made at another institution.

R. H. Stokes, K. R. Crandall, R. W. Hamm, F. J. Humphry, R. A. Jameson, E. A. Knapp, J. M. Potter, G. W. Rodenz, J. E. Stovall, D. A. Swenson, and T. P. Wangler, "The Radio-Frequency Quadrupole: General Properties and Specific Applications," 11th International Conference on High-Energy Accelerators, CERN, Geneva, July 7-11, 1980.

☆U.S. GOVERNMENT PRINTING OFFICE: 1981—576-088/28

Printed in the United States of America
Available from
National Technical Information Service
US Department of Commerce
5285 Port Royal Road
Springfield, VA 22161

Microfiche (A01)

Page Range	NTIS Price Code	Page Range	NTIS Price Code	Page Range	NTIS Price Code	Page Range	NTIS Price Code
001-025	A02	151-175	A08	301-325	A14	451-475	A20
026-050	A03	176-200	A09	326-350	A15	476-500	A21
051-075	A04	201-225	A10	351-375	A16	501-525	A22
076-100	A05	226-250	A11	376-400	A17	526-550	A23
101-125	A06	251-275	A12	401-425	A18	551-575	A24
126-150	A07	276-300	A13	426-450	A19	576-600	A25
						601-up*	A99

*Contact NTIS for a price quote.

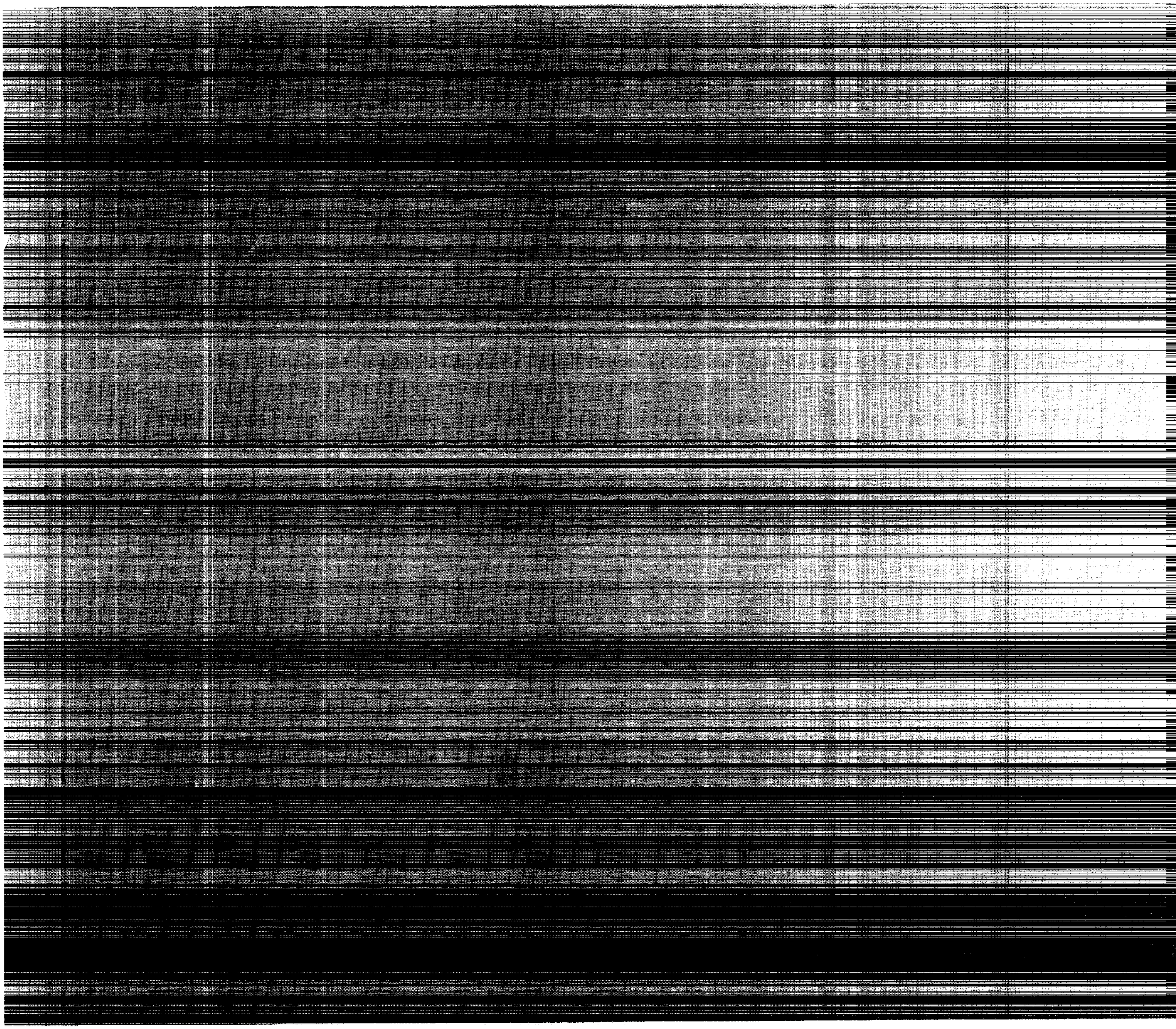

Los Alamos